

2017-2018 Cornell NanoScale Facility Research Accomplishments





250 Duffield Hall • 343 Campus Road • Ithaca NY 14853-2700
Phone: 607.255.2329 • Fax: 607.255.8601 • Email: information@cnf.cornell.edu • Website: www.cnf.cornell.edu

Cornell NanoScale Facility 2017-2018 Research Accomplishments

**CNF Lester B. Knight Director:
Christopher Ober**

**Director of Operations:
Donald Tennant**

Cornell NanoScale Facility (CNF) is a member of the
National Nanotechnology Coordinated Infrastructure
(www.nnci.net)

and is supported by the National Science Foundation under Grant No. NNCI-1542081,
the New York State Office of Science, Technology and Academic Research,
Cornell University, Industry, and our Users.

***The 2017-2018 CNF Research Accomplishments are also available on the web:
http://www.cnf.cornell.edu/cnf_2018cnfra.html***

© 2018



Table of Contents

Technical Reports by Section.ii
Directors' Introductionvi
A Selection of 2017 Patents, Presentations & Publicationsix
Photography Credits... .. .xxvii
Full Color Versions of a few Research Images.. xxviii-xxix
Abbreviations & Their Meanings xxx
Technical Reports 2-233
Indexes.. 234

Biological Applications... .. . 2-63

Topics in Nano-Biophotonics: Fabrication of Plasmonic Metasurfaces that Attract and Spectroscopically Interrogate Cancer Cells 2
 Microfluidic Mixer for Time-Resolved Single-Molecule Fluorescence Experiments using Flip-Chip Bonded SU-8 Structures 4
 Body-on-a-Chip Systems for Drug Development 6
 Micropillar-Based Microfluidic Device for Cell Capture and DNA Analysis 8
 The Number of SNARE Complexes Changing Conformation in Vesicle Fusion Events 10
 Nanoneedles for Intracellular Measurements. 12
 MoS₂ Pixel Sensors for Optical Detection of Redox Molecules. 14
 Silicon Nitride Cantilevers for Muscle Myofibril Force Measurements 16
 DNA Unzipping by Resonator-Based nSWATs.. 18
 Generalized Platform for Antibody Detection Immunosensor 20
 Development of a Salivary Microfluidic Diagnostic Device Using Hot Embossing 22
 Rapid Detection of Antimicrobial Susceptibility at the Point-of-Care 24
 An *in vacuo* Microfluidic Mixer for Biological X-Ray Solution Scattering. 26
 Biomechanics of Bacteria. 28
 Design and Application of Microfluidic Devices to Study Cell Migration in Confined Environments 30





Zero-Mode Waveguides on Thin SiN Membranes for Efficient Single-Molecule Sequencing 32

Microfabricated Devices for Cell Organization. 34

Electrochemical Detection Array Combining Amperometry and Total Internal Reflection Fluorescence 36

Microfluidic Device for Studying HABs. 38

Chip-Based Frequency Combs for High-Resolution OCT 40

Handheld Chem/Biosensor Combining Metasurfaces and Engineered Sensor Proteins to Enhance SPR 42

Scalable Sensor Array Platform for Analysis of Quantal Transmitter Release Events. 44

Droplet-Microfluidic Device for Stem Cell Culture 46

Metasurfaces for Infrared Spectroscopy of Live Cells in a Microfluidic Chamber 48

Listeria Sensor Chip via SPR 50

Gut-on-a-Chip using Microfluidic Devices 52

Retinal Implant Project. 54

Disseminating Glycocalyx Biopolymer-Induced Microvesicle Shedding through Nanoparticle Tracking Analysis and Cryo-Electron Microscopy . . . 56

Investigation of the Mechanical Property of Drosophila Mature Oocytes using Microfluidic Devices 58

Rapid Point of Care Diagnostic for Sepsis Stratification . 60

Patterning of Native Proteins in Supported Lipid Bilayers. 62

Chemistry. 64-79

Fabricating 2D Silica with Atomic Layer Deposition 64

Attonewton Sensitivity Magnet-Tipped Cantilevers and Sample Preparation for Single-Electron Spin Detection. 66

Investigation of Area Selective Atomic Layer Deposition with Microreactor and *in situ* Surface Analysis. 68

Chemical Bonding Across the Periodic Table at High and Ambient Pressures 70

Substrate Preparation for Ultrafast Vibrational Spectroscopy Experiments. 72

A Thin Film Transfer Sample Preparation Technique for Single-Electron Magnetic Resonance Imaging. . . 74

Study on the Electrochemically Stabilizing Effect of the High Dielectric Constant Oxide Artificial Solid Electrolyte Interphase on Electrodes in Aqueous Electrolytes 76

Measuring Refractive Index of Microscopy Slides 78

Electronics 80-95

Vertical Tunneling Field Effect Transistors (Thin-TFETs) Based on BP/SnSe₂ Heterostructure. 80

Self-Assembled Silica Nano-Spheres for Dual Metal Junction-Barrier-Schottky Diodes 82

Room Temperature Microwave Oscillators Enabled by Resonant Tunneling Transport in III-Nitride Heterostructures 84

MBE Grown NPN GaN/InGaN HBTs on Bulk-GaN Substrates. 86

Fabrication of GaN Quantum Well HEMTs. 88

MoS₂/PtSe₂ MOSFETs and CMOS Integration 90

Fabrication of FETs Based on La-BaSnO₃ Perovskite Oxide 92

Micro-Scale Opto-Electrically Transduced Electrodes (MOTES) 94



Materials... ..96-131

New Photopatterning Materials for Advanced Lithography.96

Electrical Characterization of $\text{In}_2\text{Ga}_2\text{ZnO}_7$ Crystallized by Millisecond Heating.98

Fused Silica Substrate and Silicon Absorber Film for use in Laser Spike Annealing (LSA)100

Metal-Organic Complex Photoresists102

Zinc-Based Nanoparticle Photoresist for Extreme Ultraviolet Lithography.104

Critical Size for Bulk-to-Discrete Transition in 2D Layers: Abrupt Size Effect Observed via Calorimetry and Solid-State NMR.106

Manipulating and Controlling Graphene Adhesion.108

Transient Laser Heating Derived Mesoporous Materials Directed by Gyroidal Templates from Block Copolymer Self-Assembly.110

Three-Dimensional Printing of Hierarchical Porous Architectures112

Three-Dimensional Printing of ZnO Macrostructures with Antibacterial Properties and Low Resistivity.114

Novel Platform for Characterization of Nanostructured Polymer Brushes.116

Materials Characterization Work.118

Growth and Characterization of NbN/III-N Heterostructures by Molecular Beam Epitaxy.120

Nanotube Transistor Arrays on a TEM Substrate.122

Stacking of Van der Waals Hetero-Structures124

Characterization of Hexagonal Boron Nitride Thin Films Grown by Molecular Beam Epitaxy126

Utilizing Polymer Nanofibers in Microfluidic Devices for Liquid Separation Applications128

Silica Glass Micropillar Fabrication130

Mechanical Devices..132-147

Thin Films from Atomic Layer Deposition for Membranes, Metamaterials, and Micromachines ..132

Graphene-Based Bimorphs for Micron-Sized Autonomous Machines.134

NEMS Electrostatic Switch for Near Zero Power RF Wakeup136

Origin of Microlayer in Pool Boiling.138

Making a Microfluidic Device to Mimic Flow Through Porous Medium.140

Atomic-Scale Origami for the Fabrication of Micron Sized Machines.142

A MEMS Repulsive Force Accelerometer.144

Microfabrication of Micropillars inside a Microchannel146

Optics & Opto-Electronics148-175

Lithium Niobate Photonic Crystal Nanocavities.148

Lithium Niobate Nanophotonic Waveguides for Tunable Second-Harmonic Generation150

Rabi-Like Oscillations in Photon Pair Correlations152

X-Ray Transmission Optics Development.154

TiO_2 Slot Waveguide for Efficient On-Chip Raman Spectroscopy156

Developing Full Wafer Blazed Grating Fabrication Method Using Stepper158

512-Element Actively Steered Silicon Phased Array for Low-Power LIDAR160

Wide Bandgap Semiconductor Deep UV Devices162

Three-Dimensional Scanner Fabrication164

Development of Single and Double Layer Anti-Reflective Coatings for Astronomical Instruments166

Large Area Electrically Tunable Metalens.168

Multi-Resonant Bianisotropic Metagratings for Ultra-Efficient Diffraction of Mid-Infrared Light.170

Optical Masks for Imaging Exoplanets with Large Ground-Based Telescopes172

Description of the Exploratory Etching and Electrodeposition Project.174



Physics & Nanostructure Physics 176-215

Characterization of Magnetic Thin Films for Actuating Origami Devices176

Development of a MEMS Tool to Study the Physics of Water and Ice.....178

Nanosecond Spin-Orbit Torque Switching of Three Terminal Magnetic Tunnel Junctions with Low Write Error Rate.....180

Reduction of the Spin Hall Angle in Oxygen-Doped Beta Tungsten.182

Study of Spin-Orbit Torques in Transition Metal Dichalcogenide / Ferromagnet Heterostructures184

Spin Hall Effect in CaRuO₃186

Wrapping Microdroplets with Two-Dimensional Materials188

Phase Transition and Equilibrium in Nanoconfinement190

Vortex Dynamics in Nanofabricated Superconducting Devices192

Fabrication of Nanofluidic Cavities for Superfluid ³He Studies194

Fabrication of Nanoscale Josephson Junctions for Quantum Coherent Superconducting Circuits196

Fabrication of Superconducting Devices for Quantum Information Science198

Anomalous Nernst Imaging of Uncompensated Moments in Antiferromagnetic FeRh Thin Films.....200

Manipulating Topological Spin Textures in Spin-Valve Type Nanopillars.....202

Diamond-Based Hybrid Quantum Mechanical Systems204

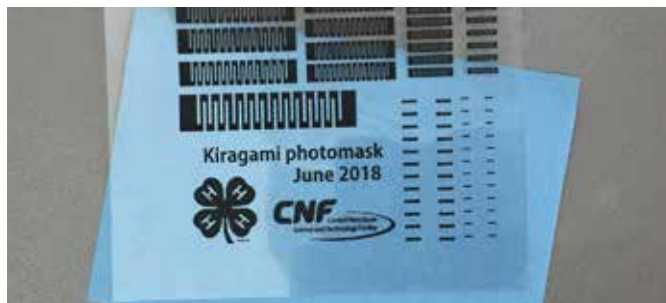
Properties of Isolated Defects in Hexagonal Boron Nitride.206

Extreme Light-Bending and Trapping with a Simple Cubic Optical Photonic Crystal208

Development of Scanning Graphene Hall Probes for Magnetic Microscopy.....210

Gigahertz Surface Acoustic Waves on Periodically Patterned Layered Nanostructures212

Magnetic Imaging of Ionic Liquid Gated Transition Metal Dichalcogenides214



Process & Characterization216-233

Nanoscale Periodic Features with a 5x Autostep i-line Stepper.....216

Development of GaN Vertical Trench-MOSFET with MBE Regrown Channel218

Characterization of (Al_xGa_{1-x})₂O₃ Thin Films Grown on <010> β-Ga₂O₃ by MBE220

Device Processes and Electrical Characteristics of First 1 kV Ga₂O₃ Vertical Power Transistors222

Side-Coupled Microfluidics for Biosensor224

Size Characterization of Plasma Membrane Vesicles, Virus Particles, and Microvesicles226

Hard Mask Fabrication from Block Copolymer Templates and Atomic Layer Deposition228

Photocurable Nanoimprint Lithography (P-NIL): An Enabling Technology for MEMS and Nanophotonics230

PS-PMMA Block Copolymer Lithography for Sub-25 nm Periodic Features232

Indexes.. 234



Directors' Introduction, 2018

It has been many months since we were asked to take on management of most of the capabilities of the Nanobiotechnology Center (NBTC) — I am happy to report that we have now fully integrated these skills to our “2nd floor, outside the cleanroom” laboratory. Along with the new tools, we have added a new training program that does not involve cleanroom access, so bunny suits are not necessary.

Some of you may remember that the NBTC was founded as an NSF-supported science and technology center pioneering the merger of nanoscience and biotechnology. When the center ended, its facility capabilities were mainlined for some time as a separate entity. We were glad that we could help maintain many of these tools and add them to our growing list of biology focused fabrication and characterization skills. We repaired many of the tools, placed them in well-organized labs adding to our existing capabilities and we continue to look for new users. Please check out our website to see what we can do. If you have a group that would like to know more about what we do in this area, please contact us and we can come over and update you.

In addition to nanobiotechnology and the related topic of digital agriculture, CNF has important strengths in areas such as advanced lithography (e-beam and DUV), advanced modeling (Prolith), in-house mask making capabilities and is expanding the number of materials that can be used. CNF has expertise in microfluidics fabrication, processing of Si-nanophotonics, magnetic materials and MEMS. CNF has 2D materials capabilities including a graphene furnace and as you will see below, CNF will be able to make superb AlN films with a new in-house thin film x-ray capability. In partnership with PARADIM, NSF's flagship Materials Innovation Platform that allows users to design and create new interface materials for the next generation of electronic devices, we have first in class capabilities for the design, production, fabrication and testing of 2D materials.

Our users continue to make exciting discoveries using devices made from tools at CNF. To highlight just some of the work being done at CNF, in *Nature Nanotechnology*, Wanunu and his group (Northeastern) and scientists from Pacific BioSciences use the Cornell NanoScale Facility to show that the efficiency of voltage-induced DNA loading into waveguides equipped with nanopores at their floors is five orders of magnitude greater than existing methods. You may recall that that Pacific Biosciences was a CNF startup that is now a \$500,000,000 company. In *Science*, Khodagholy et al. (NYU) and colleagues at Columbia used the Cornell



NanoScale Facility to produce a conducting polymer-based conformable microelectrode array (NeuroGrid) and used it to record local field potentials and neural spiking across the dorsal cortical surface of the rat brain, and combined with silicon probe recordings in the hippocampus, to identify methods of memory consolidation. In *Nanoletters*, McEuen and colleagues at Cornell and Northwestern used the Cornell NanoScale Facility to characterize the delamination of single-layer graphene from monolayers of pyrene tethered to glass in water and maximize the work of separation between these surfaces by varying the density of pyrene groups in the monolayer.

News; New Equipment and Capabilities

The CNF continues to upgrade its capabilities. New processes have been developed by CNF staff over the past year to meet the user demands for new materials or improved process control.



Our staff and CNF fellows have developed new processes for: Photocurable NanoImprint Lithography (P-NIL) using mr-XNIL26 and demonstrated deep silicon etch from imprint patterns; a deep etch of germanium using a modified Bosch etch developed to form Ge x-ray optics; new processes to enhance etching of metals and transition metal dichalcogenides for 2D materials including: MoS₂, SnS₂, WSe₂, NbSe₂, GaSe, InSe, CdSe,

and others. In addition, 2D metal oxides such as WO_3 , V_2O_5 , MnO_2 etches and 2D perovskites such as SrRuO_x and SrLaAlO_x were demonstrated.

We helped design and have now received a new Yield Engineering System (YES) for image reversal in our photolithography area. The new design includes redundant safety features to prevent exposure to ammonia.

The merger with NBTC has built on our expertise in synthesis and ALD coating of nanoparticles by adding two instruments, the Malvern Zetasizer and Nanosight, for nanoparticle characterization to the portfolio as well as bolstering our microfluidic chip facilities.

Our new OEM AlN piezoelectric material deposition system has arrived. Installation is beginning and our group is eager to start characterizing films. To help streamline this we are also acquiring an X-ray Diffraction (XRD) system that will be in the cleanroom. This will allow us to be a leading lab in research related to rf filters and piezo-MEMS.

We are expecting delivery soon of a second AJA Orion 8 sputter deposition system to replace our aging CVC sputter tool. Our first system was so popular, that we just had to clone it to keep all the metal depositions running smoothly.

Last, we are now offering a "Wafer Express" service, whereby researchers from almost anywhere can purchase wafers with high quality silicon dioxide or silicon nitride films grown by our staff. We hope to vastly expand our reach with this simplified access method. Check out our website for details.

Educational Outreach

The CNF participates in numerous educational outreach activities, on campus, off campus, and around the country! For instance, CNF operates both a national and an international version of the NSF Research Experience for Undergraduates (REU) Program. This program takes undergraduate students from across the United States and introduces them to CNF's state of the art facility and our world class staff. In addition to our five REU students, we "adopt" several other interns from programs at Cornell during the 10 week summer REU program, and fund a second group of six students, who spent the summer in Japan (iREU).

We are grateful to the National Science Foundation for its continued funding for our REU activities, and we also seek corporate funds to augment this program. Please

contact Dr. Lynn Rathbun, our REU Programs Manager, to discuss corporate sponsorship (lcr2@cornell.edu).

Every year, CNF hosts many educational tours, workshops, and special events at Cornell. These include our short course, "Technology & Characterization at the Nanoscale" (CNF TCN), open to participants from academia, industry, and government. It includes lectures and demonstrations, and also hands-on lab activities in the cleanroom. The next short course will be offered in January 2019. We welcome inquiries from all researchers about CNF's capabilities and the NNCI network, especially those with no previous experience in nanofabrication, since the outstanding staff members of the CNF are highly skilled at teaching new users.





We have also put out a new edition of *Nanooze*, our educational publication aimed at K-12 students. We send out thousands of copies and we estimate that each year we reach over 10,000 students with the printed version and more through the website version. We are installing a new *Nanooze* display located at Disney's EPCOT center where we expect even more people will see it as they pass by to other Epcot exhibits.

A school teacher tells us

"Years ago, I shared Nanooze with my 5th-graders. As a junior in high school, one of my students came to see me. He said that reading Nanooze was his favorite thing that we had done. He mentioned several articles that we had read. He said that reading Nanooze helped re-awaken his love for school and for science. He hoped that I still use the magazine (which I do) because it was the best part of his entire 5th grade."



If you are interested or know a school that could benefit from this news magazine, email Prof. Carl Batt at cab10@cornell.edu or Dr. Lynn Rathbun at lcr2@cornell.edu.

Over the past year, CNF has hosted visits and tours and staffed events for over 3000 participants; from prospective graduate students and new faculty members, to visiting dignitaries and corporate executives, public events, and visiting groups. These included over 170 distinct visits and events. We again hosted signature outreach events, including the 4H Career Explorations and the Jr FIRST LEGO League. We also enjoy meeting and working with middle and high school students-introducing them to the nano-world we live in. Outreach, that is, sharing our excitement about nanoscience is something we really enjoy doing with the broader community. Contact Melanie-Claire Mallison with your visit request (mallison@cnf.cornell.edu).

Let us close by saying that as always we enjoyed having an excellent group of REU students this last summer. This group of REU students engaged in projects involving use of CNF's advanced tools working on activities that pushed back the frontiers of nanoscience. Their fresh eyes and new perspectives were a boon to our research community. The summer ended with an NNCI network-wide convocation held at the Research Triangle Nanotechnology Network at North Carolina State University.

As always, we welcome your comments about CNF and its operations, as well as suggestions for improvement.



Chris Ober

Lester B. Knight Director, CNF
director@cnf.cornell.edu



Donald Tennant

Director of Operations, CNF
tennant@cnf.cornell.edu

A Selection of 2017 Patents, Presentations & Publications Related to CNF Research

“(How) can selective area atomic layer deposition extend patterning beyond the 7 nm node?”; James R. Engstrom, Keynote address; Advances in Patterning Materials and Processes XXXIV, SPIE Advanced Lithography Conference, San Jose, CA, February 2017. [Cornell University]

“1.1 kV vertical GaN p-n diodes with p-GaN regrown by molecular beam epitaxy”; ZHu, KNomoto, MQi, WLi, MZhu, XGao, DJena and HGXing; IEEE Electron Dev. Lett., 38(8), 1071-1074 (2017). DOI: 10.1109/LED.2017.2720747. [Cornell University]

“2D materials for logic and RF applications”; Xing, HG; The ARL Workshop on 2D materials, College Park, MD, July 2017. [Cornell]

“3-axis MEMS gyroscope calibration stage: Magnetic actuation enabled out-of-plane dither for piezoelectric in-plane calibration”; V. Pinrod, S. Nadig, B. Davaji and A. Lal; Inertial Sensors and Systems (INERTIAL), 2017 IEEE International Symposium on, IEEE, podium. [Cornell University]

“3D Printed Low Density Open Cell Foam”; Christopher Hernandez, Ashley Torres, Pablo Zavattieri; Invention Status Unfiled, Docket No. 8000, Country of Filing: United States, Invention Type: Invention, Disclosure Date 10/5/17. [Cornell]

“5-organ microphysiological system for drug screening”; CT Trinconi, YI Wang, PG Miller, SRB Uliana, ML Shuler; Organ-on-a-Chip World Congress, Boston, MA. July 10-11. [Cornell University]

“50th Anniversary Perspective: Polymer brushes: Novel surfaces for future materials”; Chen, Wei-Liang, Cordero, Roselynn, Tran, Hai, Ober, Christopher K; Macromolecules, 2017, 50 (11), pp 4089-4113. DOI: 10.1021/acs.macromol.7b00450 Publication Date (Web): May 5, 2017, Volume 50, Issue 11, Page(s) 4089-4113. [Cornell]

“600 V GaN vertical V-trench MOSFET with MBE regrown channel”; Li, Wenshen, Nomoto, Kazuki, Lee, Kevin, Islam, S M, Hu, Zongyang, Zhu, Mingda, Gao, Xiang, Pilla, Manyam, Jena, Debdeep, Xing, Huili Grace; Device Research Conference (DRC), 2017 75th Annual, IEEE, Page(s) 43102. [Cornell University]

“64-Pixel Solid State CMOS Compatible Ultrasonic Fingerprint Reader”; J. Kuo, J. Hoopole, M. Abdelmejeed, M. Abdel-moneum, A. Lal; IEEE MEMS 2017. [Cornell University]

“64-Pixel Solid State CMOS Compatible Ultrasonic Fingerprint Reader”; Kuo, JC, Hoopole, JT, Abdelmejeed, M, Abdel-moneum, M, Lal, A; MEMS 2017 IEEE 30th International Conference on, IEEE, Page(s) 43355. [Cornell University]

“A beam path-based method for attenuation correction of confocal micro-X-ray fluorescence imaging data”; Peng Liu, Carol J. Ptacek, David W Blowes, and Y. Zou Finfrock; Journal of Analytical Atomic Spectrometry (2017). doi: 10.1039/C7JA00148G. [Cornell]

“A carbon nanotube reporter maps endolysosomal lipid flux”; Jena, P.V., Roxbury, D., Galassi, T.V., Akkari, L., Horoszkó, C.P., Iaea, D.B., Budhathoki-Uprety, J., Pipalia, N.H., Haka, A.S., Harvey, J.D., Mittal, J., Maxfield, F.R., Joyce, J.A., and Heller, D.A.; ACS Nano, DOI: 10.1021/acsnano.7b04743. PMID: PMC5707631. [Weill Cornell Medical College]

“A CMOS based sensor array platform for analysis of exocytosis events”; M Huang, JCRuelas, SS Rathore, JB Delacruz and M Lindau; 61st Annual Meeting of the Biophysical Society, Biophys. J. 112: 93a. [Cornell University]

“A Highlights from MBoC Selection: Integrin-mediated traction force enhances paxillin molecular associations and adhesion dynamics that increase the invasiveness of tumor cells into a three-dimensional extracellular matrix”; Mekhdjian, AH, et al.; Molecular Biology of the Cell, Volume 28, Issue 11, Page(s) 1467. [Cornell University]

“A Method Utilizing Magnetic Spin Fluctuations to Enhance Spin Currents for Spin-orbit Torque Excitation, Switching and Displacement of Nanoscale Magnetism for Memory, Logic and Electronic Communications Applications”; R Buhrman, Y Ou, D Ralph; Invention Status Filed - by Cornell, Docket No. 7985, Country of Filing: United States, Invention Type: Invention, Disclosure Date 9/28/17. [Cornell University]



- "A microfluidic system for mechanical characterization and stimulus of individual bacteria"; Roberts, M.F., Srivastava, A., Wang, L.M., Hui, C-Y, Genova, L.A., Chen, P., Hernandez, C.J.; European Society of Bioemcahnics, Sevilla, Spain. (2017) Podium. [Cornell]
- "A performance-enhanced planar Schottky diode for Terahertz applications: an electromagnetic modeling approach"; Ghobadi, A, Khan, TM, Celik, OO, Biyikli, N, Okyay, AK, Topalli, K; International J. of Microwave and Wireless Technologies, V9, Issue 10, p 1905-1913. [Bilkent University, Turkey / Utah State Univ]
- "A photon capture approach to Josephson photomultiplier-based qubit measurement"; Alex Opremcak, Ivan Pechenezhskiy, Caleb Howington, Chris Wilen, Matthew Beck, Edward Leonard Jr, Konstantin Nesterov, Maxim Vavilov, Britton Plourde, R McDermott; March Meeting of the American Physical Society Bulletin, 2017, New Orleans, LA. [Syracuse University]
- "A Rapid Diagnostic Testing Platform for Iron and Vitamin A Deficiency"; David Erickson, Saurabh Mehta; Application Status: Filed, Docket No. 7107-01-US, Country of Filing: United States, Application Type: MPR - Manuscript Provisional, Filing Date: 11/13/17, Application Number: 62/585,275. [Cornell University]
- "A Tool to Improve Reproductive Management and Performance of Ruminant Females through Determination of their Reproductive Physiological Status"; David Erickson, Julio Giordano, Magdalena Masello; Invention Status Unfiled, Docket No. 7894, Country of Filing: United States, Invention Type: Invention, Disclosure Date 6/1/17. [Cornell University]
- "Activated skeletal muscle myofibrils have different peak stresses at similar sarcomere lengths when lengthened beyond myofilament overlap"; T Leonard and W Herzog; Biophysical Society Meeting, New Orleans, USA, Feb 11-15, 2017. [University of Calgary]
- "Active microrheology of hydrogels based on oscillations induced by optical radiation pressure"; Leartprapun N., Iyer R.R., and Adie S.G.; OSA Frontiers in Optics, Washington DC, 2017. [Cornell]
- "Adapting Etched Solid Phase Mesh Enhanced Sorption from Headspace (eSPMESH) Coupled to DART-MS for Parallel Extraction and Analysis from Multi-well Plates"; Bee MY, Jastrzembki JA, and Sacks GL; 65th Annual Conference of the American Society of Mass Spectrometry, Indianapolis, IN. June 2017. [Cornell University]
- "Adsorption-controlled growth of La-doped BaSnO₃ by molecular-beam epitaxy"; Paik, Hanjong, Chen, Zhen, Lochocki, Edward, et al; APL MATERIALS Volume: 5 Issue: 11 Article Number: 116107 Published: NOV 2017. [Cornell University]
- "AFM/TIRF force clamp measurements of neurosecretory vesicle tethers reveal characteristic unfolding steps"; MCHarris, DCislo, JSLenz1, CUMBach and MLindau; PLoS ONE 12: e0173993. [Cornell University]
- "AIN GHz Ultrasonic Pulse Diffraction Based Transmit-Receive Oscillator with 1ppm Stability"; M. Abdelmejeed, J. Kuo, A. Lal; TRANSDUCERS 2017 19th International Conference on, IEEE. [Cornell University]
- "An Endoscopic Device for Detection of Cancerous Cells & Tissues Based on Plasmon-tipped Infrared-transparent Fibers"; S Gupta, G Shvets; Invention Status Filed - by Cornell, Docket No. 7743, Country of Filing: USA, Invention Type: Invention, Disclosure Date 3/13/17. [Cornell University]
- "Angle Sensitive Pixel (ASP) - Based Image Processing System, Method, and Applications"; Patrick Gill, Alyosha Molnar, Albert Wang; Application Status: Issued, Docket No. 4893-06-KR, Country of Filing: South Korea, Filing Date: 2/28/13, Application No. 10-2013-7005335, Issue Date: 10/20/17, Patent No. 10-1790601. [Cornell University]
- "Antifouling urinary catheters with shape-memory topographic patterns"; R Dacheng, G Huan; US Patent App. 15/255,241. [Syracuse University]
- "Apparatus and Method for Point-of-Collection Measurement of a Biomolecular Reaction"; D Erickson, S Lee, M Mancuso; Application Status: Issued, Docket No. 6044-03-US, Country of Filing: United States, Filing Date: 3/10/15, Application No. 14/427,049, Issue Date: 6/20/17, Patent No. 9,686,395. [Cornell University]
- "Apparatus for and Method of Terminating a High Frequency Arrhythmic Electric State of a Biological Tissue"; Eberhard Bodenschatz, Flavio Fenton, Robert Gilmour, Valentin Krinski, Stefan Luther; Application Status: Issued, Docket No. 5166-10-CN, Country of Filing: China, Filing Date: 2/9/15, Application No. 2.0151E+11, Issue Date: 4/12/17, Patent No. CN ZL201510065522.4. [Cornell University]
- "Apparatuses with atomically-thin ohmic edge contacts between two-dimensional materials, methods of making same, and devices comprising same"; J. Park, H. Gao, M. H. D. Guimaraes, D. C. Ralph, K. Kang, and S. Xie; Patent Application PCT/US17/37179, filed March 17, 2017. [Cornell University]
- "Atomic and molecular layer processing: Prospects and strategies for selective area atomic layer deposition"; James R. Engstrom, Invited Talk; The 61st International Conference on Electron, Ion, and Photon Beam Technology and Nanofabrication, Orlando FL, June 2017. [Cornell University]
- "Atomic layer MoS₂-graphene van der Waals heterostructure nanomechanical resonators"; Ye, Fan, Lee, Jaesung, Feng, Philip X-L; Nanoscale, Volume 9, Issue 46, Page(s) 18208-18215. [Case Western Reserve University]
- "Automated analysis of evolving interfaces during in situ electron microscopy"; Schneider, NM, Park, JH, Norton, MM, Ross, FM, Bau, HH; Advanced Structural and Chemical Imaging, Volume 2, Issue 1, Page(s) 2. [University of Pennsylvania]
- "Autonomous Gamma, X-Ray, and Particle Detector"; S Czarnecki, A Krol, K Mandal, M Poliks, R Schmidlein, M Thompson, J Turner; Application Status: Issued, Docket No. 6802-02-US, Country of Filing: United States, Filing Date: 3/24/16, Application No. 15/080,073, Issue Date: 3/28/17, Patent No. 9,606,245. [Cornell]



"Autonomous Gamma, X-Ray, and Particle Detector"; Steve Czarniecki, Andrzej Krol, Krishna Mandal, Mark Poliks, Ross Schmidlein, Michael Thompson, James Turner; Application Status: Issued, Docket No. 6802-03-US, Country of Filing: United States, Filing Date: 3/24/17, Application No. 15/468,968, Issue Date: 12/5/17, Patent No. 9,835,737. [Cornell University]

"Bimetallic Effect of Single Nanocatalysts Visualized by Super-Resolution Catalysis Imaging"; Chen, Guanqun, Zou, Ningmu, Chen, Bo, Sambur, Justin B, Choudhary, Eric, Chen, Peng; ACS central science, Volume 3, Issue 11, Page(s) 1189-1197. [Cornell]

"Biocompatible and high stiffness nanophotonic trap array for precise and versatile manipulation"; Ye, Fan, Ryan P. Badman, James T. Inman, Mohammad Soltani, Jessica L. Killian, and Michelle D. Wang; Biophysical Journal 112, 300a (2017). [Cornell University]

"Biomedical Implant for Use in Fluid Shear Stress Environments"; Jonathan Butcher, Chris Frenzl; Application Status: Issued, Docket No. 5624-03-US, Country of Filing: United States, Filing Date: 3/13/14, Application No. 14/344,895, Issue Date: 4/25/17, Patent No. 9,629,713. [Cornell University]

"Bioprocess Engineering: Basic Concepts (3rd Ed)"; ML Shuler, F Kargi, and M DeLisa; Prentice Hall, Englewood Cliffs, NJ. [Cornell]

"Black Phosphorus MOSFETs and CMOS Integration"; K Xiong, L Li, J C M Hwang, A Goritz, M Wietstruck, and M Kaynak; 4th Muju International Winter School Series (MIWS2-2017), Muju, Korea, Feb. 5-9, 2017. [Lehigh University]

"Block Copolymers and Lithographic Patterning Using Same"; T Hayakawa, R Maeda, C Ober, N-h You; Application Status: Issued, Docket No. 5471-04-US, Country of Filing: United States, Filing Date: 9/3/14, Application No. 14/342,657, Issue Date: 1/10/17, Patent No. 9,541,830. [Cornell University]

"Boron-10 nanoparticles filled silicon trenches for thermal neutron detection application"; Wu, Jia-Woei, Weltz, Adam, Koiraal, Machhindra, Lu, James J-Q, Dahal, Rajendra, Danon, Yaron, Bhat, Ishwara B; Applied Physics Letters, Volume 110, Issue 19, Page(s) 192105. [Rensselaer Polytechnic Institute]

"Breast cancer-derived extracellular vesicles stimulate myofibroblast differentiation and pro-angiogenic behavior of adipose stem cells"; Song YH, Warncke C, Choi SJ, Choi S, Chiou AE, Ling L, Liu HY, Daniel S, Antonyak MA, Cerione RA, Fischbach C.; Matrix Biol. 2017 Jul;60-61:190-205. [Cornell University]

"Breather soliton dynamics in microresonators"; Yu, M, Jang, JK, Okawachi, Y, Griffith, AG, Luke, K, Miller, SA, Ji, X, Lipson, M, Gaeta, AL; Nature Communications, Volume 8, Pages 14569. [Columbia University]

"Buhrman group members presented 4 contributed talks"; Buhrman, Robert; 2017 March Meeting of the American Physical Society, March 13-17, 2017, New Orleans, LA. [Cornell University]

"Buhrman group members presented 5 contributed talks"; Buhrman, Robert; 2017 Magnetism and Magnetic Materials Conference in November 6-10 2017, Pittsburgh, PA. [Cornell University]

"Building a "Body-on-a-Chip" to improve drug development"; Shuler, ML; Workshop on Microfluidic Chip and Tissue Engineering. Nanjing, China. June 9-11. [Cornell University]

"Building the (parts for) the nanosubmarine"; Paul McEuen; Fall MRS, Boston, MA; Nov. 27, 2017. [Cornell University]

"Calibration Apparatus, Methods, and Applications"; Amit Lal, Sarvani Piratla; Application Status: Issued, Docket No. 5162-03-US, Country of Filing: United States, Filing Date: 10/17/13, Application No. 14/112,356, Issue Date: 5/9/17, Patent No. 9,645,167. [Cornell University]



"Capacitively Shunted Flux Qubits for Multi-qubit Architectures"; J Ku, M Hutchings, Y Liu, BLT Plourde, J Hertzberg, M Sandberg, M Brink, E Magesan, F olgun, J Chow; March Meeting of the APS Bulletin, 2017, New Orleans, LA. [Syracuse University]

"Cell and nuclear mechanics during migration in 3-D environments"; Lammerding J; Mechanics in Cancer Biology meeting by the French Society of Cancer. Paris, France (Nov. 30, 2017) Invited presentation. [Cornell University]

"Cell Migration in Microfabricated 3D Collagen Microtracks is Mediated Through the Prometastatic Protein Girdin"; Rahman-Zaman, Aniqua, Shan, Shuo, Reinhart-King, Cynthia A; Cellular and Molecular Bioengineering, Page(s) 43110. [Cornell University]

"Characterization of graphene electrodes as piezoresistive SAW transducers"; A. Ruyack, B. Davaji, S. Kulkarni and A. Lal; 2017 IEEE International Ultrasonics Symposium (IUS), Washington, DC, 2017, podium. [Cornell University]

"Characterization of graphene electrodes as piezoresistive SAW transducers"; Ruyack, Alexander, Davaji, Benyamin, Kulkarni, Shrinidhi, Lal, Amit; Ultrasonics Symposium (IUS), 2017 IEEE International, IEEE, Page(s) 43104. [Cornell University]

"Chemical Vapor Deposition Growth of Large Single-Crystal Mono-, Bi-, Tri-Layer Hexagonal Boron Nitride and Their Interlayer Stacking"; Ji, Y, Calderon, B, Han, Y, Cueva, P, Jungwirth, NR, alsalman, ha, Hwang, J, Fuchs, GD, Muller, DA, Spencer, MG; ACS Nano, 2017, 11 (12), pp 12057-12066; DOI: 10.1021/acsnano.7b04841; Publication Date (Web): November 3, 2017. [Cornell University]

"Chiral magnetic excitations in FeGe Films"; Emrah Turgut, Albert Park, Kayla Nguyen, Austin Moehle, David A Muller, Gregory D Fuchs; Phys Rev. B 95, 134416 (2017). [Cornell University]

"Chromosomal instability promotes metastasis through a cytosolic DNA response"; Bakhoum SE, et al.; Nature. 2018. 553(7689): 467-472. [Cornell University]

"Circuits and Devices Based on Spin Hall Effect to Apply a Spin Transfer Torque with a Component Perpendicular to the Plane of Magnetic Layers"; Robert Buhrman, Daniel Ralph; Application Status: Issued, Docket No. 6495-03-US, Country of Filing: United States, Filing Date: 4/18/16, Application No. 15/030,291, Issue Date: 6/27/17, Patent No. 9,691,458. [Cornell University]

“Coherent, directional supercontinuum generation”; Okawachi, Yoshitomo, Yu, Mengjie, Cardenas, Jaime, Ji, Xingchen, Lipson, Michal, Gaeta, Alexander L; Optics letters, Volume 42, Issue 21, Pages 4466-4469. [Columbia University]

“Coherent, directional supercontinuum via cascaded dispersive wave generation”; Okawachi, Yoshitomo, Yu, Mengjie, Cardenas, Jaime, Ji, Xingchen, Lipson, Michal, Gaeta, Alexander L; arXiv preprint arXiv:1708.03717. [Columbia University]

“Collimating Channel Arrays Development at CHESS for High Resolution Confocal X-ray Fluorescence Microscopy”; D.N. Agyeman-Budu, S. Choudhury, I. Coulthard, R. Godon E. Halin, A.R Woll; Gordon Conference for X-Ray Science, 07/30/2017 - 08/04/2017, Stonehill College in Easton MA United States. [Cornell]

“Compact narrow-linewidth integrated laser based on a low-loss silicon nitride ring resonator”; Stern, Brian, Ji, Xingchen, Dutt, Avik, Lipson, Michal; Optics letters, Volume 42, Issue 21, Page(s) 4541-4544. [Columbia]

“Comparison of confined migration and nuclear envelope rupture in a panel of breast cancer cell lines”; McGregor AL, Elacqua JJ, Bell ES, Lammerding J; Physical Science Oncology Network (PS-ON) Annual Meeting. Boston, MA (Oct. 17-18, 2017). AL McGregor was awarded top poster prize in the category “In Vivo & Organoid Models of Growth and Metastasis” Poster presentation selected from submitted abstract. [Cornell]

“Competition between Raman and Kerr effects in microresonator comb generation”; Okawachi, Yoshitomo, Yu, Mengjie, Venkataraman, Vivek, Latawiec, Pawel M, Griffith, Austin G, Lipson, Michal, Loncar, Marko, Gaeta, Alexander L; Optics letters, Volume 42, Issue 14, Page(s) 2786-2789. [Columbia University]

“Conjugation in Escherichia coli biofilms on poly (dimethylsiloxane) surfaces with microtopographic patterns”; Gu, Huan, Kolewe, Kristopher W, Ren, Dacheng; Langmuir, Volume 33, Issue 12, Page(s) 3142-3150. [Syracuse University]

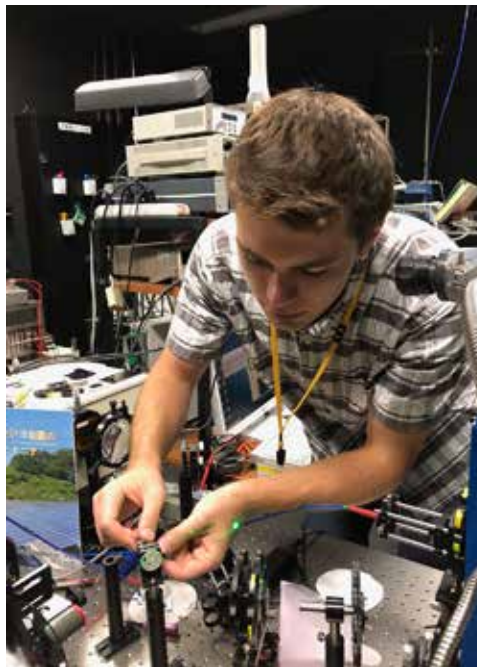
“Control of spin-orbit torques through crystal symmetry in WTe₂/ferromagnet bilayers”; MacNeill, D, Stiehl, G M, Guimaraes, M H D, Buhman, R A, Park, J, Ralph, D C; Nature Physics, Volume 13, Issue 3, Page(s) 300-305 (arXiv:1605.02712). [Cornell University]

“Control of spin-orbit torques through crystal symmetry in WTe₂/ferromagnet bilayers”; Stiehl, GM, MacNeill, D, Guimaraes, MHD, Buhman, RA, Park, J, Ralph, DC; APS March Meeting 2017, abstract id. P47.005. [Cornell University]

“Control of spin-orbit torques through crystal symmetry”; D. C. Ralph; 62nd Annual Conference on Magnetism and Magnetic Materials, Nov. 6-10, 2017, Pittsburgh, PA. [Cornell University]

“Controlling Friction Characteristics of Resilient Members Using Near-Surface Microstructures”; Y Bai, Z He, C-Y Hui, A Jagota, B Levraud; App Status: Filed, Docket No. 7478-02-JP, Country of Filing: Japan, App Type: FOR - Foreign, Filing Date: 8/16/17, App Number: 2017-561613; App Status: Filed, Docket No. 7478-03-US, Country of Filing: United States, App Type: US from PCT, Filing Date: 8/17/17, App Number: 15/551,630; App Status: Filed, Docket No. 7478-04-EP, Country of Filing: Europe, App Type: EPC - European Patent Convention, Filing Date: 8/16/17, App #: 16709857.3. [Cornell University]

“Controlling Nitrogen-Vacancy Center Spins with a Mechanical Resonator”; MacQuarrie, Evan R; Cornell University, Ph.D. Thesis. [Cornell University]



“Convection Enhanced Delivery Apparatus, Method, and Application”; C Foley, RT Matthews, K Neeves, W Olbricht, WM Saltzman, A Sawyer; App Status: Issued, Docket No. 4005-05-US, Country of Filing: United States, Filing Date: 6/25/14, App No. 14/314,119, Issue Date: 12/19/17, Patent No. 9,844,585. [Cornell]

“Cooling a Mechanical Resonator with a Nitrogen-Vacancy Center Ensemble Using a Room Temperature Excited State Spin-Strain Interaction”; Evan MacQuarrie, Matt Otten, Stephen Gray, Gregory D Fuchs; March Meeting of the APS, New Orleans, LA 2017. [Cornell University]

“Cooling a mechanical resonator with nitrogen-vacancy centres using a room temperature excited state spin-strain interaction”; MacQuarrie, E R, Otten, M, Gray, S K, Fuchs, G D; Nature Communications, doi:10.1038/ncomms14358, Volume 8, Page(s) Article number: 14358 (2017). [Cornell University]

“Cooperative communication within and between single nanocatalysts”; N. Zou, X. Zhou, G. Chen, N. M. Andoy, W. Jung, G. Liu, P. Chen; Nature Chem. 2018, doi:10.1038/s41557-018-0022-y. [Cornell University]

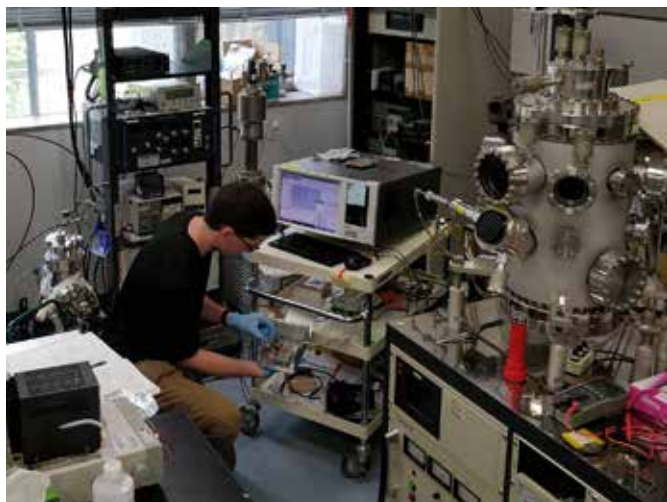
“Creation of Localized Skyrmion Bubbles in Co/Pt Bilayers using a Spin Valve Nanopillar”; Jennifer L Grab, Alison E Rugar, Daniel C Ralph; arXiv:1712.07201 [cond-mat.mes-hall] arXiv preprint arXiv:1712.07201, 2017 - arxiv.org. [Cornell University]

“Critical size for bulk-to-discrete transition and segment-induced size effect melting of 2D aliphatic layers”; Ye, Zichao; UIUC Ph.D. Thesis. [University of Illinois at Urbana-Champaign]

“Cryogenic positioning and alignment with micrometer precision in a magnetic resonance force microscope”; Isaac, Corinne E, Curley, Elizabeth A, Nasr, Pamela T, Nguyen, Hoang L, Marohn, John A; arXiv preprint arXiv:1710.01442 (Review of Scientific Instruments 89, 013707 (2018); https://doi.org/10.1063/1.5008505). [Cornell]

“Decoding reliable oscillations and UV light emission in AlN/GaN resonant tunneling diodes”; Xing, HG; EDISON20, Buffalo, NY, July 2017. [Cornell University]

“Deep reactive ion etched anti-reflection coatings for sub-millimeter silicon optics”; PA Gallardo, BJ Koopman, NF Cothard, SM M Bruno, G Cortes-Medellin, G Marchetti, KH Miller, B Mockler, MD Niemack, G Stacey, and EJ Wollack; Applied Optics Vol. 56, Issue 10, pp. 2796-2803 (2017) https://doi.org/10.1364/AO.56.002796. [Cornell University]



"Deep-UV emission at 219 nm from ultrathin MBE GaN/AlN quantum heterostructures"; Islam, S M, Protasenko, Vladimir, Lee, Kevin, Rouvimov, Sergei, Verma, Jai, Xing, Huili, Jena, Debdeep; Applied Physics Letters / Appl. Phys. Lett. 111, 091104 (2017); <https://doi.org/10.1063/1.5000844>, Volume 111, Issue 9, Page(s) 91104. [Cornell University]

"Delivery Device for a Photocrosslinkable Hydrogel to Repair Intervertebral Disc Herniation"; Lawrence Bonassar, Si Chen, Anny Cunha-Gavidia, Roger Hartl, Monika McCarter, Michael Messina, Gayathri Shibu; Invention Status Filed - by Cornell, Docket No. 7837, Country of Filing: United States, Invention Type: Invention, Disclosure Date 4/28/17. [Cornell University]

"Depth Field Imaging Apparatus, Methods, and Applications"; Suren Jayasuriya, Alyosha Molnar, Sriram Sivaramakrishnan; Application Status: Filed, Docket No. 6955-03-US, Country of Filing: United States, Application Type: US from PCT, Filing Date: 8/30/17, Application Number: 15/554,550; Application Status: Filed, Docket No. 6955-04-EP, Country of Filing: Europe, Application Type: EPC - European Patent Convention, Filing Date: 9/21/17, Application Number: 16713231.5; Application Status: Filed, Docket No. 6955-05-CN, Country of Filing: China, Application Type: FOR - Foreign, Filing Date: 10/25/17, Application Number: 2.0168E+11; Application Status: Filed, Docket No. 6955-06-JP, Country of Filing: Japan, Application Type: FOR - Foreign, Filing Date: 9/15/17, Application Number: 2017-548977; Application Status: Filed, Docket No. 6955-07-KR, Country of Filing: South Korea, Application Type: FOR - Foreign, Filing Date: 10/17/17, Application Number: 10-2017-7029937; Application Status: Filed, Docket No. 6955-08-CA, Country of Filing: Canada, Application Type: FOR - Foreign, Filing Date: 9/14/17, Application Number: 2979836. [Cornell University]

"Design and characterization of a microreactor for spatially confined atomic layer deposition and in situ UHV surface analysis"; Chen, J-R, Zhang, W, Nahm, Rambert K, DiFeo, MA, Engstrom, JR; Journal of Vacuum Science & Technology A: Vacuum, Surfaces, and Films, Volume 35, Issue 6, Page(s) 61604. [Cornell University]

"Design and Modification of Bioreactors Simulating Intestinal Flow"; Acharya, Rohan; Cornell University Ph.D. Thesis. [Cornell]

"Design and Realization of GaN Trench Junction-Barrier-Schottky-Diodes"; Li, Wenshen, Nomoto, Kazuki, Pilla, Manyam, Pan, Ming, Gao, Xiang, Jena, Debdeep, Xing, Huili Grace; IEEE Transactions on Electron Devices, Volume 64, Issue 4, Page(s) 1635-1641. [Cornell University]

"Determination of the porosity in a bifacial fabric using micro-computed tomography and three-dimensional reconstruction"; Zhu, Licheng, Wang, Xungai, Hinestroza, Juan P, Naebe, Maryam; Textile Research Journal, Page(s) 405175000-00000. [Cornell]

"Device and Methods for Molecular Analysis"; B Cipriany, H Craighead, S Levy, P Soloway; App Status: Issued, Docket No. 4837-04-US, Country: USA, Filing Date: 5/14/12, App No. 13/389,259, Issue Date: 3/28/17, Patent No. 9,605,298. [Cornell]

"Devices for Terahertz Signal Generation and Transmitter"; E Afshari, R Han; A Status: Filed, Docket No. 6475-03-US, Country of Filing: United States, App Type: US from PCT, Filing Date: 8/21/17, App Number: 15/552,339. [Cornell University]

"Direct, real-time observation of layer-by-layer growth of a 2D semiconductor using in situ x-ray synchrotron radiation"; Hugh J. Bullen, Rambert K. Nahm, Suresh Vishwanath, Huili Grace Xing and James R. Engstrom; AVS 64th International Symposium, Tampa, FL, October 2017. [Cornell University]

"DNA's Chiral Spine of Hydration"; McDermott, M Luke, Vanselow, Heather, Corcelli, Steven A, Petersen, Poul B; ACS Central Science. [Cornell University]

"Effectively infinite optical path-length created using a simple cubic photonic crystal for extreme light trapping"; Frey, Brian J, Kuang, Ping, Hsieh, Mei-Li, Jiang, Jian-Hua, John, Sajeev, Lin, Shawn-Yu; Scientific Reports, Volume 7, Issue 1, Page(s) 4171. [Rensselaer Polytechnic Institute]

"Effects of asymmetric Schottky contacts on photoresponse in tungsten diselenide (WSe₂) phototransistor"; Islam, Arnob, Feng, Philip X-L; Journal of Applied Physics, Volume 122, Issue 8, Page(s) 85704. [Case Western Reserve University]

"Elastomeric Lightguide Coupling for Continuous Position Localization in 1, 2, and 3D"; Robert Shepherd, Patricia Xu; Invention Status Filed - by Cornell, Docket No. 8051, Country of Filing: United States, Invention Type: Invention, Disclosure Date 11/27/17. [Cornell University]

"Elastomeric Lightguide Coupling for Continuous Position Localization in 1, 2, and 3D"; Robert Shepherd, Patricia Xu; Application Status: Filed, Docket No. 8051-01-US, Country of Filing: United States, Application Type: EPR - Enhanced Provisional, Filing Date: 11/29/17, Application Number: 62/592,073. [Cornell University]

"Electrically Gated Three-Terminal Circuits and Devices Based on Spin Hall Torque Effects in Magnetic Nanostructures"; R Buhrman, L Liu, C-F Pai, D Ralph; Application Status: Issued, Docket No. 6029-05-CN, Country of Filing: China, Filing Date: 4/1/15, Application No. 2.0138E+11, Issue Date: 5/31/17, Patent No. ZL201380051532.1. [Cornell University]

"Electron mobility in polarization-doped Al_{0.2}GaN with a concentration near 10¹⁷ cm⁻³"; MZhu, M Qi, KNomoto, ZHu, BSong, MPan, XGao, DJena and HGXing; Appl. Phys. Lett. 110, 182102 (2017); doi: 10.1063/1.4982920. [Cornell University]

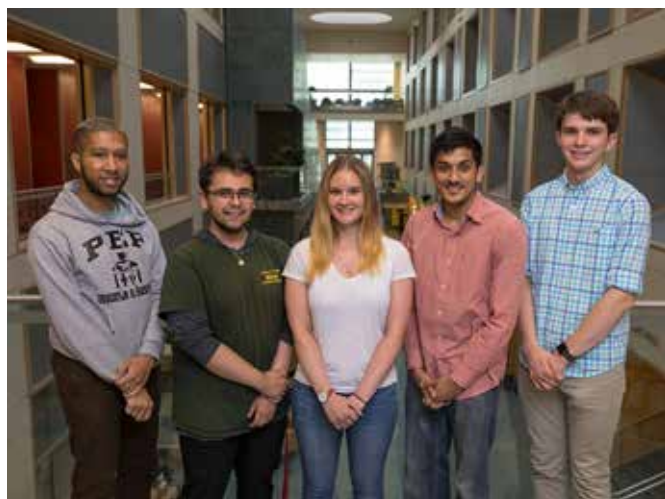
"Electronic structure of the metastable epitaxial rock-salt SnSe 111 topological crystalline insulator"; WJin, SVishwanath, JLiou, LKong, RLou, ZDai, JTSadowski, XLiou, H-HLien, AChaney, YHan, MCAo, JMa, TQian, SWang, MDobrowska, JFurdyna, DAMuller, KPohl, HDing, JIDadap, HGXing, and RMOsgood, Jr; Physics Review X (PRX), 7, 041020 (2017). DOI: 10.1103/PhysRevX.7.041020. [Cornell University]

"Electronics based on GaN and layered materials"; Xing, HG; The KAUST-NSF Research Conference on Interactive Electronics, KAUST, January 2017. [Cornell University]

"Elucidating the patterning mechanism of zirconium-based hybrid photoresists"; Kosma, V, Kasahara, K, Xu, H, Odent, J, Ober, CK, Giannelis, EP; Journal of Micro/Nanolithography, MEMS, and MOEMS, Volume 16, Issue 4, Page(s) 41007. [Cornell University]

"Engineering quantum light on micro/nanophotonic devices"; Q Lin; The 8th International Conference on Metamaterials, Photonic Crystals, and Plasmonics (META), (Invited Talk), Incheon, Seoul, South Korea (2017). [University of Rochester]

- "Engineering quantum light on photonic chips"; Q Lin; SPIE Optics & Photonics, (Invited), San Diego (2017). [University of Rochester]
- "Enhanced subcooled flow boiling heat transfer in microchannel with Piranha pin fin"; Yu X, Woodcock C, Wang Y, Plawsky J, and Peles Y; Journal of Heat Transfer, 139(11), 112402, 2017. [Rensselaer Polytechnic Institute]
- "Enhancement of the spin Hall effect by spin fluctuations near the Curie point"; Robert Buhrman, Daniel Ralph, Yongxi Ou; US Provisional Patent Application No. 62/576,979 filed October 25, 2017. [Cornell University]
- "Enhancement of the Spin Hall Effect by Spin Fluctuations near the Curie Point"; Robert Buhrman, Yongxi Ou, Daniel Ralph; Application Status: Filed, Docket No. 7985-01-US, Country of Filing: United States, Application Type: MPR - Manuscript Provisional, Filing Date: 10/25/17, Application Number: 62/576,979. [Cornell University]
- "Enhancement of the Spin Hall Effect by Spin Fluctuations near the Curie Point"; Robert Buhrman, Yongxi Ou, Daniel Ralph; Application Status: Filed, Docket No. 7985-01-US, Country of Filing: United States, Application Type: MPR - Manuscript Provisional, Filing Date: 10/25/17, Application Number: 62/576,979. [Cornell University]
- "Epigenetic Fingerprinting of DNA using a Solid-State Nanopore"; Alden, J, A Cortese, M Pender, P McEuen; Poster session presented at the NHGRI Advanced Genome Technology Development Mtg, Boston, MA (May 2017). [Esper Biosciences Inc]
- "Estimating the number of SNARE proteins changing conformation in a single fusion event"; Y Zhao, Q Fang and M Lindau; 19th International Symposium on Chromaffin Cell Biology, Sheffield, UK. [Cornell University]
- "Etching of Germanium and Silicon-A Comparison of Mechanisms and Application to X-ray Optics"; V.J. Genova, D.N. Agyeman-Budu and A.R. Woll; Time Multiplexed Deep Reactive Ion, The 61st International Conference on Electron, Ion, and Photon Beam Technology and Nanofabrication, EIPBN 2017, Orlando, FL, USA, May 30 - June 2, 2017. [Cornell University]
- "EUV metal oxide hybrid photoresists: Ultrasmall structures for high-resolution patterning"; Ober, Christopher; 254th ACS National Meeting, Washington, DC, Aug. 20-24, 2017. [Cornell University]
- "Event correlation using data having different time resolutions"; Lindau, Manfred; US9596417B2, US Grant 2017-03-14, US Patent 9,596,417. [Cornell University]
- "Evidence of an application of a variable MEMS capacitive sensor for detecting shunt occlusions"; Apigo, DJ, Bartholomew, PL, Russell, T, Kanwal, A, Farrow, RC, Thomas, GA; Scientific Reports, Vol 7. [New Jersey Institute of Technology]
- "Examination of thin film growth using supersonic molecular beams and in situ real time x-ray synchrotron radiation: from organic small molecule semiconductors to transition metal dichalcogenides"; James R. Engstrom, Invited Talk; 2017 AIChE Annual Meeting, Minneapolis, MN, November 2017. [Cornell]
- "Experimental and Numerical Study on Flow Boiling with an Advanced Structure in Microchannel"; Yu, X; Rensselaer Polytechnic Institute, Ph.D. Thesis. [RPI]
- "Experimental Demonstration of Efficient Spin-Orbit Torque Switching of an MTJ with sub-100 ns Pulses"; Gosavi, T, Manipatruni, S, Aradhya, S, Rowlands, G, Nikonov, D, Young, I, Bhave, SA; IEEE Transactions on Magnetics. [Purdue University]
- "Exploiting kinetics and thermodynamics to grow phasepure complex oxides by molecular-beam epitaxy under continuous codeposition"; Smith, Eva H, Ihlefeld, Jon F, Heikes, Colin A, et al; Physical Review Volume: 1 Issue: 2 Article Number: 023403 Published: JUL 12 2017. [Cornell University]
- "Extended defect propagation in highly tensile strained Ge waveguides"; M Qi, WA O'Brien, CA Stephenson, V Patel, N Cao, BJ Thibeault, M Schowalter, A Rosenauer, V Protasenko, HG Xing and MA Wistey; Crystals, 7, 157 (2017). doi:10.3390/cryst7060157 [Cornell University]
- "Extreme ultraviolet resist materials for sub-7 nm patterning"; Li, L, Liu, X, Pal, S, Wang, S, Ober, CK, Giannelis, EP; Chemical Society Reviews, Vol 46, Issue 16, Page(s) 4855-4866. [Cornell University]
- "Fabrication of 3-Dimensional, Biomimetic GUT on a Chip Composed of Organoids, Microbiota, Cancer Spheroids and Immune Cells"; A Abbaspourrad, M Azizi, S Pajoumshariati; Invention Status Unfiled, Docket No. 7805, Country of Filing: United States, Invention Type: Invention, Disclosure Date 3/30/17. [Cornell]
- "Fabrication of Phosphor-Free III-Nitride Nanowire Light-Emitting Diodes on Metal Substrates for Flexible Photonics"; R Philip, et al.; ACS Omega, Volume 2, Issue 9, Page(s) 5708-5714. [New Jersey Institute of Technology]
- "Fast reliable spin-orbit torque switching of three-terminal magnetic tunnel junctions"; Buhrman, Robert; Governmental Working Group on Magnetic Tunnel Junctions, Nov. 2, 2017, Washington DC; Invited talk presented by R. Buhrman. [Cornell University]
- "Fast response of photorefractive in lithium niobate microresonators"; Jiang, Haowei, Luo, Rui, Liang, Hanxiao, Chen, Xianfeng, Chen, Yuping, Lin, Qiang; Optics letters, Volume 42, Issue 17, Page(s) 3267-3270. [University of Rochester]
- "Fast switching between 2D and direct, 3D XRF imaging using Collimating Channel Arrays and the Maia detector"; Arthur R. Woll and David N. Agyeman-Budu; ICXOM 2017, 25-29 September 2017, Trieste, Italy; Invited. [Cornell University]
- "Fast, low-current spin-orbit switching of magnetic tunnel junctions using Hf interface engineering"; Ou, Yongxi ; 3rd ImPACT International Symposium, Sept. 23-25, 2017, Sendai, Japan; Invited talk presented by Buhrman group member Yongxi Ou. [Cornell]
- "Fast, low-current spin-orbit torque switching of magnetic tunnel junctions through atomic modifications of the free layer interfaces"; Shi, Shengjie, Ou, Yongxi, Aradhya, S V, Ralph, D C, Buhrman, R A; arXiv preprint arXiv:1710.06391. [Cornell]
- "Faster is smoother and so is lower temperature: the curious case of thin film growth of tetracene on SiO₂"; Nahm, R. K., H. J. Bullen, T. Suh and J. R. Engstrom; J. Phys. Chem. C 121, 8464-8472 (2017). [Cornell University]
- "Faster, cheaper, smellier – Accelerating throughput and achieving spatial resolution of plant volatiles with extractive meshes coupled to ambient ionization mass spectrometry"; Jastrzembksi JA, Bee MY, and Sacks GL; Annual National Association of Plant Breeders Meeting, Davis, CA. (Aug 7-10, 2017). [Cornell]



- "Fifty Years of Moore's Law: Towards fabrication at molecular dimensions"; Ober, Christopher; invited talk; Binghamton University, Binghamton, NY, Oct. 18, 2017. [Cornell University]
- "Fifty Years of Moore's Law: Towards fabrication at molecular dimensions"; Ober, Christopher; invited talk; Clarkson University Chemical Engineering Seminar, April 6, 2017. [Cornell University]
- "Flexible Hybrid Electronic Materials: Substrates"; Ober, Christopher; invited talk; S3IP Symposium, Binghamton University, Binghamton, NY, Oct. 25, 2017. [Cornell University]
- "Flexible multi-moduled nanoparticle-structured sensor array on polymer substrate and methods for manufacture"; Zhong, C-J, Luo, J, Wang, L; US20170284953A1 US Application, 2017-10-05. [SUNY College of Environmental Science and Forestry]
- "Flow-Regulated Growth of Titanium Dioxide (TiO₂) Nanotubes in Microfluidics"; Fan, Rong, Chen, Xinye, Wang, Zihao, Custer, David, Wan, Jiandi; Small, 14 June 2017, <https://doi.org/10.1002/smll.201701154>, Volume 13, Issue 30, August 11, 2017, 1701154. [Rochester Institute of Technology]
- "Fluid viscoelasticity promotes collective swimming of sperm"; Tung, Chih-kuan, Lin, Chungwei, Harvey, Benedict, Fiore, Alyssa G, Ardon, Florencia, Wu, Mingming, Suarez, Susan S; Scientific Reports, Volume 7. [Cornell University]
- "Focusing Apparatus for GHz Ultrasonic Waves with Integrated Transistors"; Lal, Amit; Invention Status Unfiled, Docket No. 8007, Country of Filing: United States, Invention Type: Invention, Disclosure Date 10/17/17. [Cornell]
- "Frequency-tunable Quantum Dissipators"; C Wilen, C Wong, N Nehra, I Pechenezhskiy, A Opremcak, JJ Nelson, C Howington, B Plourde, M Vavilov, R McDermott; March Meeting of the APS Bulletin, 2017, New Orleans, LA. [Syracuse University]
- "From Atomic Origami To Cell-Sized Machines, Second International Workshop on Origami Engineering"; Miskin, Marc; Tianjin China, 2017. [Cornell University]
- "GaN power electronics"; Xing, HG; The Government Microcircuit Applications and Critical Technology Conference (GOMAC), Reno, NV, March 2017. [Cornell University]
- "GaN vertical nanowire and fin power MISFETs"; Hu, Zongyang, Li, Wenshen, Nomoto, Kazuki, Zhu, Mingda, Gao, Xiang, Pilla, Manyam, Jena, Debdeep, Xing, Huili Grace; Device Research Conference (DRC), 2017 75th Annual, IEEE, Page(s) 43102. [Cornell University]
- "Generation of High Energy Mid-infrared Laser Pulses"; P Petersen, A Stingel; App Status: Filed, Docket No. 7102-03-US, Country of Filing: United States, Application Type: US from PCT, Filing Date: 12/20/17, Application Number: 15/738,522. [Cornell University]
- "Giant Ferroelectric Polarization in Ultrathin Ferroelectrics via Boundary-Condition Engineering"; Xie, Lin, Li, Linze, Heikes, Colin A, et al; ADVANCED MATERIALS Volume: 29 Issue: 30 Article Number: 1701475 Published: AUG 11 2017. [Cornell]
- "Graphene and Boron Nitride for RF Amplifier Spreaders"; Kennedy, Brian, and Ken Kuang; International Microelectronics Assembly and Packaging Society (iMAPS), Paris, 2017. [Kennedy Labs]
- "Graphene-based bimorphs for the fabrication of micron-sized, autonomous origami machines"; Miskin, Marc; APS March Meeting 2017. [Cornell University]
- "Graphene-based membrane and method of preparation thereof"; Garaj, Slaven, Seunghyun, Hong; US20170144107A1 US Application 2017-05-25. [National University of Singapore]
- "Guiding Pillar Substrate (GPS)-enabled Transferrable Vascular-like Network for Cell Encapsulation Devices"; A Chiu, M Ma, W Song; Invention Status Filed - by Cornell, Docket No. 8042, Country of Filing: USAs, Disclosure Date 11/9/17. [Cornell University]
- "Half-flat vs. atomically flat: Alkyl monolayers on morphologically controlled Si (100) and Si (111) have very similar structure, density, and chemical stability"; DeBenedetti, William JI, Li, Thomas L, Hines, Melissa A; The Journal of Chemical Physics, Volume 146, Issue 5, Page(s) 5-2804. [Cornell University]
- "Handheld highly selective plasmonic chem/biosensor using engineered binding proteins for extreme conformational changes"; Kosciolk, DJ, Sonar, A, Lepak, LA, Schnatz, P, Bendoy, I, Brown, MC, Koder, RL, Crouse, DT; Plasmonics: Design, Materials, Fabrication, Characterization, and Applications XV, International Society for Optics and Photonics, Volume 10346, Page(s) 103462B. [Clarkson University]
- "Harnessing electron spin labels for single-molecule magnetic resonance imaging"; Corinne E Isaac; 254th American Chemical Society National Meeting; Washington, DC; August 20-24. [Cornell University]
- "Hexagonal boron nitride nanomechanical resonators with spatially visualized motion"; Zheng, Xu-Qian, Lee, Jaesung, Feng, Philip X-L; Microsystems & Nanoengineering, Volume 3, Page(s) 17038. [Case Western Reserve University]
- "Hierarchical Fullerene Assembly: Seeded Coprecipitation and Electric Field Directed Assembly"; Stelson, Angela C, Penterman, Sonny J, Watson, Chekesha M Liddell; Small, Volume 13, Issue 17, 1 March 2017, <https://doi.org/10.1002/smll.201603509>. [Cornell]
- "High Performance Wick"; Abraham Stroock, Tobias Wheeler; Application Status: Issued, Docket No. 4197-05-US, Country of Filing: United States, Filing Date: 2/23/11, Application No. 12/990,845, Issue Date: 7/11/17, Patent No. 9,702,636. [Cornell]
- "High quality lithium niobate photonic crystal nanobeams"; H Liang, R Luo, and Q Lin; Proc. Conf. Laser and Electro-Optics/Quantum Electronics and Laser Science (CLEO/QELS), STh4N.2 (2017). [University of Rochester]
- "High Temperature Near-Field NanoThermoMechanical Rectification"; Elzouka, Mahmoud, Ndao, Sidy; Scientific Reports, Volume 7. [University of Nebraska Lincoln]
- "High-performance near-field thermophotovoltaics for waste heat recovery"; B. Zhao, K. Chen, S. Buddhiraju, G. Bhatt, M. Lipson, and S. Fan; Nano Energy, vol. 41, pp. 344-350, 2017. [Columbia]
- "High-quality lithium niobate nanocavities"; H Liang, R Luo, Y He, H Jiang, and Q Lin; Optica 4, 1251 (2017). [University of Rochester]
- "High-quality lithium niobate photonic crystal nanocavities"; Liang, Hanxiao, Luo, Rui, He, Yang, Jiang, Haowei, Lin, Qiang; Optica, Volume 4, Issue 10, Page(s) 1251-1258. [University of Rochester]





“High-resolution facies variability and connections to compositional and mechanical heterogeneity in the union springs formation of central New York”; Mason, John L; Cornell University, Dissertation. [Cornell University]

“Hot Carrier-Based Near-Field Thermophotovoltaic Energy Conversion”; R. St-Gelais, G. R. Bhatt, L. Zhu, S. Fan, and M. Lipson; ACS Nano, vol. 11, no. 3, pp. 3001-3009, 2017. [Columbia]

“Human “Body-on-a-Chip” systems to test drug efficacy and toxicity”; Shuler, ML; Organ-on-a-Chip World Congress, Boston, MA. July 10-11. [Cornell University]

“Human body-on-a-chip systems for drug discovery. (Keynote)”; Shuler, ML; 3D Cell Culture Cambridge Healthtech Inst. Boston, MA. Nov. 6-7. [Cornell University]

“Human in vitro models to improve preclinical testing of drugs”; Shuler, ML; AIChE Ann Mtg. Minneapolis, MN. October 29-Nov. 3. (Invited talk for session in honor of Martin Yarmush). [Cornell]

“Human-based “Body-on-a-Chip” for drug development”; Shuler, ML; Select Bio: Lab on a chip. 2017. Munich Germany. May 10-11. [Cornell University]

“Hybrid reflections from multiple x-ray scattering in epitaxial oxide films”; Smith, Eva H, King, Phil D C, Soukiassian, Arsen, et al; Applied Physics Letters Volume: 111 Issue: 13 Article Number: 131903 Published: SEP 25 2017. [Cornell University]

“ICP-RIE etch of single crystal b-Ga2O3”; LZhang, AVerma, HGXing and DJena; J. J. Appl. Phys. 56, 030304 (2017). <https://doi.org/10.7567/JJAP.56.030304>. [Cornell University]

“Identifying taxane sensitivity in prostate cancer patients”; Giannakakou, Paraskevi, Plymate, Stephen R; US9671405B2 US Grant 2017-06-06. [University of Washington / Cornell University]

“Imaging currents in two-dimensional quantum materials”; K.C. Nowack; APS March Meeting 2017, Volume 62, Number 4, March 13–17, 2017; New Orleans, Louisiana. INVITED TALK. [Cornell]

“Imaging Magnetization Structure and Dynamics in Ultrathin Y3Fe5O12/Pt Bilayers with High Sensitivity Using the Time-Resolved Longitudinal Spin Seebeck Effect”; Bartell, JM, Jermain, CL, Aradhya, SV, Brangham, JT, Yang, F, Ralph, DC, Fuchs, GD; Physical Review Applied, Vol 7, Issue 4, Page(s) 4-4004. [Cornell]

“Imaging Magnetization Structure and Dynamics in Ultrathin YIG/Pt Bilayers with High Sensitivity Using the Time-Resolved Longitudinal Spin Seebeck Effect”; JM Bartell, CL Jermain, SV Aradhya, JT Brangham, F Yang, DC Ralph, and GD Fuchs; Phys. Rev. Appl. 7, 044004/1-8 (2017). (arXiv:1612.07610). [Cornell]

“Imaging Systems and Methods for Particle-Driven, Knowledge-based, and Predictive Cancer Radiogenomics”; Michelle Bradbury, Cameron Brennan, Mithat Gonen, Mohan Pauliah, Ulrich Wiesner; Invention Status Filed - by Joint Owner, Docket No. 7866, Country of Filing: United States, Invention Type: Invention, Disclosure Date 5/16/17. [Cornell University]

“Imbibition triggered by capillary condensation in nanopores”; Vincent, Olivier, Marguet, Bastien, Stroock, Abraham D; Langmuir, Volume 33, Issue 7, Page(s) 1655-1661. [Cornell]

“Immobilized Protein System for Rapid and Enhanced Multiplexed Diagnostics”; Roy Cohen, Alexander Travis; Application Status: Issued, Docket No. 5175-03-US, Country of Filing: United States, Filing Date: 2/7/14, Application No. 14/125,221, Issue Date: 1/17/17, Patent No. 9,547,014. [Cornell University]

“Impact of the synthesis method on the solid-state charge transport of radical polymers”; Zhang, Y, Park, A, Cintora, A, McMillan, SR, Harmon, NJ, Moehle, A, Flatté, ME, Fuchs, GD, Ober, CK; Journal of Materials Chemistry C, Volume 6, Issue 1, Page(s) 111-118. [Cornell University]

“Implantable Therapeutic Delivery System and Methods Thereof”; D An, J Flanders, M Ma; Application Status: Prosecution, Docket No. 6480-04-CN, Country of Filing: China, Application Type: FOR - Foreign, Filing Date: 8/18/17, Application Number: 201580039185.X. [Cornell University]

“In situ Sensing of Water Stress in Plants for High-Throughput Phenotyping”; M Gore, P Jain, D Pauli, A Stroock, O Vincent; Application Status: Filed, Docket No. 7532-01-US, Country of Filing: United States, Application Type: EPR - Enhanced Provisional, Filing Date: 7/28/17, Application Number: 62/538,308. [Cornell University]

“In Vivo Electromagnetic Near-Field Coherent Sensing”; Xiaonan Hui, Edwin Kan; Invention Status Filed - by Cornell, Docket No. 7785, Country of Filing: United States, Invention Type: Invention, Disclosure Date 3/14/17. [Cornell University]

“Increased low-temperature damping in yttrium iron garnet thin films”; C. J. Jermain, S. V. Aradhya, N. D. Reynolds, R. A. Buhman, J. T. Brangham, M. R. Page, P. C. Hammel, F. Y. Yang, D. C. Ralph; Phys Rev B 95, 174411/1-5 (2017), doi:Artn 174411, 10.1103/Physrevb.95.174411 (2017). [Cornell University]

“Indium Gallium Zinc Oxide: Phase Formation and Crystallization Kinetics during Millisecond Laser Spike Annealing”; Lynch, David Michael; Cornell University Ph.D. Thesis. [Cornell]

“Individually Detachable Polymer-Silicon Micro-Parts For Vaporizable Electronics”; V. Gund, A. Ruyack, A. Leonardi, K.B. Vinayakumar, C.K. Ober, A. Lal; IEEE Transducers, 2017. [Cornell]

“Inductively-coupled-plasma reactive ion etching of single-crystal β -Ga2O3”; Zhang, Liheng, Verma, Amit, Xing, Huili Grace, Jena, Debdeep; Japanese Journal of Applied Physics, Volume 56, Issue 3, Page(s) 3-0304. [Cornell University]

“Influence of Surface Adsorption on the Oxygen Evolution Reaction on IrO2(110)”; Kuo, Ding-Yuan, Kawasaki, Jason K, Nelson, Jocienne N, et al; JOURNAL OF THE AMERICAN CHEMICAL SOCIETY Volume: 139 Issue: 9 Pages: 3473-3479 Published: MAR 8 2017. [Cornell University]

“Integrated Circuits Based Biosensors”; Ved Gund, Lal, Amit; Application Status: Issued, Docket No. 6595-03-US, Country of Filing: United States, Filing Date: 7/27/16, Application No. 15/114,814, Issue Date: 6/20/17, Patent No. 9,683,967. [Cornell]

“Integrated Light Management as a Path to Miniaturizing Spectrometers”; N. K. Pervez, T. C. Garza, M. J. Gazes, J. I. Scholtz, M. F. Comerford, and I. Kyymissis; Imaging and Applied Optics 2017 (3D, AIO, COSI, IS, MATH, pcAOP), OSA Technical Digest (online) (Optical Society of America, 2017), paper ATTh2A.3. [Columbia University]

"Integrated Light Management as a Path to Miniaturizing Spectrometers"; Nadia K. Pervez, Tanya C. Garza, Michael J. Gazes, James I. Scholtz, Mark F. Comerford, and Ioannis Kymissis; 2017 OSA Imaging and Applied Optics Congress in San Francisco, 26-29 June 2017. [Columbia University]

"Integrated photon sources for quantum information science applications"; Fanto, M L, Tison, C C, Steidle, J A, Lu, T, Wang, Z, Mogent, N A, Rizzo, A, Thomas, P M, Preble, S F, Alsing, P M; Quantum Information Science and Technology III, International Society for Optics and Photonics, Volume 10442, Page(s) 104420K. [Rochester Institute of Technology]

"Integrin-mediated traction force enhances paxillin molecular associations and adhesion dynamics that increase the invasiveness of tumor cells into a three-dimensional extracellular matrix"; Mekhdjian, Armen H, Kai, FuiBoon, Rubashkin, Matthew G, Prahl, Louis S, Przybyla, Laralynne M, McGregor, Alexandra L, Bell, Emily S, Barnes, J Matthew, DuFort, Christopher C, Ou, Guanqing; Molecular biology of the cell, Volume 28, Issue 11, Pages 1467-1488. [Cornell University]

"Introduction to Spin-Orbit Torques"; D. C. Ralph; Workshop on Multifunctional Interface Materials, Aug 8-9, 2017, Madison, WI. [Cornell University]

"Invited Presentation"; Shalabh Chandra Maroo; 9th US-Japan Joint Seminar on Nanoscale Transport Phenomena, Tokyo, Japan, July 2-5, 2017. [Syracuse University]

"Invited Presentation"; Shalabh Chandra Maroo; Gordon Research Conference - Micro & Nanoscale Phase Change Heat Transfer, Galveston TX, January 8-13, 2017. [Syracuse University]

"Keynote Speaker"; Shalabh Chandra Maroo; ASME 2017 ICNMM, Cambridge MA, August 27-30, 2017. [Syracuse University]

"Kicksat-2 Flight Hardware (Combined with 7830)"; Mason Peck ; Invention Status Will Not File - Tangible Material, Docket No. 7831, Country of Filing: United States, Invention Type: Material, Disclosure Date 4/19/17. [Cornell University]

"Lamin A/C mutant myonuclei experience nuclear envelope rupture and DNA damage that is reduced upon microtubule stabilization"; Kirby T, Earle A, Fedorchak GR, Isermann P, Brightwell C, Fry C, Lammerding J; American Society for Cell Biology (ASCB) Annual Meeting. Philadelphia, PA (Dec. 6, 2017) Platform presentation selected from submitted abstract. [Cornell]

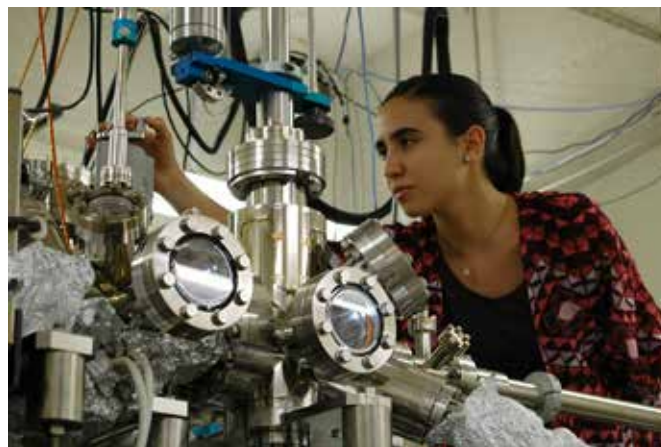
"Lamin mutations cause progressive nuclear envelope rupture in muscle fibers in vitro and in vivo"; Lammerding J; COST School and The Batsheva de Rothschild Seminar: The Nuclear Lamina and Nuclear Organization. Ye'arim, Judean Hills, Israel (June 27, 2017) Invited talk. [Cornell University]

"Lamin mutations linked to muscular disease cause progressive nuclear envelope rupture and DNA damage in muscle fibers"; Earle A, Kirby T, Fedorchak G, Isermann P, Lammerding J; European Intermediate Filament Conference. Saint Malo, France (June 14, 2017) Poster selected from submitted abstract. [Cornell]

"Lamin mutations linked to muscular disease cause progressive nuclear envelope rupture and DNA damage in muscle fibers"; Earle A, Kirby T, Fedorchak G, Isermann P, Lammerding J; European Intermediate Filament Conference. Saint Malo, France (June 14, 2017) Flash talk presentation selected from submitted abstract. [Cornell University]

"Lamin mutations linked to muscular disease result in mechanically-induced, progressive nuclear envelope rupture and DNA damage in muscle fibers"; Earle A, Kirby T, Fedorchak GR, Isermann P, Lammerding J; American Society for Cell Biology (ASCB) Annual Meeting. Philadelphia, PA (Dec. 6, 2017) [Cornell University]

"Lamin mutations responsible for muscular dystrophy cause progressive nuclear damage in muscle fibers"; Lammerding J; Biomedical Engineering Society (BMES) Annual Meeting.



Phoenix, AZ Platform presentation selected from submitted abstract. (October 13, 2017). [Cornell University]

"Large Area Electrically Tunable Lenses Based on Metasurfaces and Dielectric Elastomer Actuators"; She, Alan, Zhang, Shuyan, Shian, Samuel, Clarke, David R, Capasso, Federico; arXiv preprint arXiv:1708.01972. [Harvard University]

"Laser Ablation of the Cell Cortex Reveals a Pressure-Induced Nuclear Transit Mechanism"; Keys J, Isermann P, Lammerding J; Biomedical Engineering Society (BMES) Annual Meeting. Phoenix, AZ (October 12, 2017) Poster presentation selected from submitted abstract. [Cornell University]

"Laser-induced sub-millisecond structural formation kinetics in block copolymers"; Jacobs, Alan G; Cornell University. [Cornell]

"Layer-by-layer assembly of two-dimensional materials into wafer-scale heterostructures"; Kang, Kibum, Lee, Kan-Heng, Han, Yimo, Gao, Hui, Xie, Saien, Muller, David A, Park, Jiwoong; Nature, Volume 550, Issue 7675, Page(s) nature23905. [Cornell University]

"Learning-enhanced coupling between ripple oscillations in association cortices and hippocampus"; Khodagholy, Dion, Gelinis, Jennifer N, Buzsáki, György; Science, Volume 358, Issue 6361, Page(s) 369-372. [Columbia University]

"Length-independent DNA packing into nanopore zero-mode waveguides for low-input DNA sequencing"; Larkin, Joseph, Henley, Robert Y, Jadhav, Vivek, Korlach, Jonas, Wanunu, Meni; Nature nanotechnology, Volume 12, Issue 12, Page(s) 1169. [Northeastern University]

"LETSSGO: Lymphoma-on-Chip Engineered Technology for Single-organoid Sequencing and Genomics"; Ankur Singh, Regan Stephenson; Invention Status Unfiled, Docket No. 7712, Country of Filing: United States, Invention Type: Invention, Disclosure Date 2/15/17. [Cornell University]

"LF-Powered, Piezo-Surface Acoustic Wave Apparatus And Method"; Amit Lal, Steven Tin; Application Status: Issued, Docket No. 4603-06-KR, Country of Filing: South Korea, Filing Date: 7/22/16, Application No. 10-2016-7020153, Issue Date: 4/19/17, Patent No. 10-1729992. [Cornell University]

"Lifshitz transition from valence fluctuations in YbAl₃"; Chatterjee, S, et al; Nature Communications V 8 Article #852 Published: OCT 11 2017. [Cornell University]

"Light Emitting Diodes Using Ultra-thin Quantum Heterostructures"; SM Islam, D Jena, V Protasenko, J Verma, HG Xing; App Status: Filed, Docket No. 7925-01-US, Country of Filing: United States, Application Type: MPP - Manuscript Plus Provisional, Filing Date: 11/15/17, App Number: 62/586,488; Invention Status Filed - by Cornell, Docket No. 7925, Country of Filing: United States, Invention Type: Invention, Disclosure Date 7/3/17. [Cornell]

- "Light Field Image Sensor, Method and Applications"; Patrick Gill, Alyosha Molnar, Albert Wang; Application Status: Issued, Docket No. 4895-07-US, Country of Filing: United States, Filing Date: 8/18/14, Application No. 14/462,039, Issue Date: 5/23/17, Patent No. 9,658,060. [Cornell University]
- "Liquid Free Lithography Utilizing Electrospray of Vaporizable Polymers"; Amit Lal, Christopher Ober; Invention Status Filed - Attorney Instructed to File, Docket No. 7797, Country of Filing: United States, Invention Type: Invention, Disclosure Date 3/28/17. [Cornell University]
- "Liquid/liquid phase separation heat transfer at the microscale"; Xing W, Vutha AK, Yu X, Ullmann A, Brauner N, and Peles Y; International Journal of Heat and Mass Transfer, 107, pp. 53-65, 2017. [Rensselaer Polytechnic Institute]
- "Lithium niobate high quality-factor photonic crystal nanocavity and reversible photorefractive effect"; Liang, Hanxiao, Luo, Rui, He, Yang, Jiang, Haowei, Lin, Qiang; arXiv preprint arXiv:1706.08904. [University of Rochester]
- "Local heat transfer in a microchannel with a pin fin- experimental issues and methods to mitigate"; Wang, Yingying, Nayebzadeh, Arash, Yu, Xiangfei, Shin, Jeong-Heon, Peles, Yoav; International Journal of Heat and Mass Transfer. 106, pp. 1191-1204, 2017. [Rensselaer Polytechnic Institute]
- "Locally deactivated sarcomeres do not over-lengthen in myofibrils"; Tim Leonard, Azim Jinha and Walter Herzog; XXVI Congress of the International Society of Biomechanics, Brisbane, Australia, 23-27 July, 2017. [University of Calgary]
- "Long-Term High-Resolution Imaging of Developing C. elegans Larvae with Microfluidics"; Keil, Wolfgang, Kutscher, Lena Y, Shaham, Shai, Siggia, Eric D; Dev Cell. 2017 Jan 23;40(2):202-214. doi: 10.1016/j.devcel.2016.11.022. Epub 2016 Dec 29. epub date in 2016, physical copy date 2017, Volume 40, Issue 2, Page(s) 202-214. [Cornell University]
- "Low cost, robust, multi-organ microphysiological systems for preclinical development"; Shuler, ML; 6th Workshop on Validation and Qualification of New in vitro Tools and Models for the Pre-Clinical Drug Discovery Process (AIMBE/NIH). Bethesda, MD. May 25-26. [Cornell University]
- "Low-Power Photothermal Self-Oscillation of Bimetallic Nanowires"; R De Alba, TS Abhilash, RH Rand, HG Craighead, and JM Parpia; Nano Letters DOI: 10.1021/acs.nanolett.6b04769 <http://parpia.lassp.cornell.edu/sites/parpia/files/publications/acs.nanolett.6b04769.pdf>. [Cornell University]
- "Magneto-acoustic oscillator"; Gosavi, Tanay A, Bhave, Sunti A; Solid-State Sensors, Actuators and Microsystems (TRANSDUCERS), 2017 19th International Conference on, IEEE, Page(s) 448-451. [Purdue University]
- "Materials challenges in approaching theoretical limit of GaN power devices"; Xing, HG; The MRS Fall Meeting, Boston, MA, November 2017. [Cornell University]
- "MBE growth of 2D materials and heterostructures"; Xing, HG; The MRS Fall Meeting, Boston, MA, November 2017. [Cornell]
- "MBE growth of few-layer 2H-MoTe2 on 3D substrates"; SVishwanath, ASundar, XLIu, AAzcatl, ELochocki, ARWoll, SRouvimov, WSHwang, NLU, XPeng, H-HLien, JWeisenberger, SMcDonnell, MKim, MDobrowolska, JKfurdyna, KShen, RWallace, DJena and HGXing; J. Crystal Growth 482, 61-69 (2017) doi:10.1016/j.jcrysgro.2017.10.024. [Cornell University]
- "MBE-grown 232-270 nm Deep-UV LEDs using monolayer thin binary GaN/AlN quantum-well heterostructures"; SM Islam, KLee, JVerma, VProtasenko, SRouvimov, SBharadwaj, HGXing and DJena; Appl. Phys. Lett. 110, 041108 (2017). DOI: 10.1063/1.4975068. [Cornell University]
- "Measurement of Quantum Interference in a Silicon Ring Resonator Photon Source"; Steidle, Jeffrey A, Fanto, Michael L, Preble, Stefan F, Tison, Christopher C, Howland, Gregory A, Wang, Zihao, Alsing, Paul M; JoVE (Journal of Visualized Experiments), Issue 122, Page(s) e55257-e55257. [Rochester Institute of Technology]
- "Measuring and Manipulating the Adhesion of Graphene"; Miskin, Marc, Sun, Chao, Cohen, Itai, Dichtel, William R, McEuen, Paul; Nano Lett., 2018, 18 (1), pp 449-454. DOI: 10.1021/acs.nanolett.7b04370 Publication Date (Web): December 22, 2017. [Cornell University]
- "Mechanistic Understanding of Early-Evaporation of Microlayer as CHF Enhancement Mechanism"; An Zou, Manish Gupta, Shalabh C. Maroo; ASME 2017 ICNMM, Cambridge MA, August 27-30, 2017. [Syracuse University]
- "MEMS 3-dimensional scanner for handheld confocal microscope"; Liu, Tianbo, Dickensheets, David L; Optical MEMS and Nanophotonics (OMN), 2017 International Conference on, IEEE, Page(s) 4-3102. [Montana State University]
- "MEMS analogous micro-patterning of thermotropic nematic liquid crystalline elastomer films using a fluorinated photoresist and a hard mask process"; Ditter, D, Chen, W-L, Best, A, Zappe, H, Koynov, K, Ober, CK, Zentel, R; Journal of Materials Chemistry C, Volume 5, Issue 47, Page(s) 12635-12644. [Cornell University]
- "MEMS Microtensometer"; Alan Lakso, Vinay Pagay, Michael Santiago, David Sessoms, Abraham Stroock; Application Status: Filed, Docket No. 6335-05-US, Country of Filing: United States, Application Type: CON - Continuation, Filing Date: 8/29/17, Application Number: 15/689,584. [Cornell University]
- "Meshed Photonic Crystals for Manipulating Near-Field Thermal Radiation Across Variable Nano/Micro Gap"; Elzouka, Mahmoud, Ndao, Sidy; ASME 2017 International Technical Conference and Exhibition on Packaging and Integration of Electronic and Photonic Microsystems collocated with the ASME 2017 Conference on ISPS, American Society of Mechanical Engineers, Page V001T04A008. [University of Nebraska Lincoln]
- "Mesoporous titanium and niobium nitrides as conductive and stable electrocatalyst supports in acid environments"; KE Fritz, PA Beaucage, F Matsuoka, U Wiesner and J Suntivich; The Royal Society of Chemistry 2017 DOI: 10.1039/C7CC03232C (Communication) Chem. Commun., 2017, 53, 7250-7253. [Cornell]
- "Mesoscopic quantum effects in a bad metal, hydrogen-doped vanadium dioxide"; Hardy, Will J, Ji, Heng, Paik, Hanjong, et al; Journal of Physics-Condensed Matter Volume: 29 Issue: 18 Article Number: 185601 Published: MAY 10 2017. [Cornell University]
- "Metal oxide cluster compound photoresists for EUV lithography"; Ober, Christopher; invited talk; EIPBN Conference, Orlando, FL, May 30 to June 2, 2017. [Cornell University]



- "Method and Apparatus for Implanting Electrodes in Brain"; DB Shire; Patent Serial # 62/610,635; Filed 12/27/17. [Harvard]
- "Method of Programming the Transformation of 2-D Surfaces into 3-D Shapes"; Itai Cohen, James Pikul, Robert Shepherd; Invention Status Filed - by Cornell, Docket No. 7742, Country of Filing: United States, Invention Type: Invention, Disclosure Date 3/13/17. [Cornell University]
- "Methods of Making Patterned Structures of Fluorine-Containing Polymeric Materials and Fluorine-Containing Polymers"; Hon Hang Fong, Jin-Kyun Lee, George Malliaras, Christopher Ober; Application Status: Issued, Docket No. 4757-05-KR, Country of Filing: South Korea, Filing Date: 5/18/12, Application No. 10-2012-7012907, Issue Date: 8/22/17, Patent No. 10-1771978. [Cornell University]
- "Methods, Systems, and Applications for Solar-Thermal Microfluidic PCR"; David Erickson, Li Jiang, Matthew Mancuso; Application Status: Issued, Docket No. 6032-03-US, Country of Filing: United States, Filing Date: 3/19/15, Application No. 14/429,407, Issue Date: 11/21/17, Patent No. 9,821,314. [Cornell]
- "Microbiome on a Fibrous Membrane: A Microfluidic-based Immobilization Model for Spatially Constrained Bacterial Culture Microbiome"; Alireza Abbaspourrad, Morteza Azizi, Seyedramin Pajoumshariati; Invention Status Unfiled, Docket No. 8022, Country of Filing: United States, Invention Type: Invention, Disclosure Date 10/24/17. [Cornell University]
- "Microcontact-Printed Hydrogel Microwell Arrays for Clonal Muscle Stem Cell Cultures"; Aguilar, Victor M, Cosgrove, Benjamin D; Methods in Molecular Biology: Skeletal Muscle Development, ed: Ryall J. Springer Science + Business Media., Springer, Page(s) 75-92. [Cornell University]
- "Microfluidic blood-brain barrier model provides in vivo-like barrier properties for drug permeability screening"; Wang, Ying I, Abaci, Hasan Erbil, Shuler, Michael L; Biotechnology and bioengineering, Volume 114, Issue 1, Page(s) 184-194. [Cornell]
- "Microlayer Evolution and Contact Line Behavior of a Vapor Bubble on Hydrophobic and Hydrophilic Surfaces"; An Zou, Ashish Chavana, Shalabh C. Maroo; ASME 2017 ICNMM, Cambridge MA, August 27-30, 2017. [Syracuse University]
- "Microphysiological systems: recent development and future prospects. Plenary Talk"; Shuler, ML; Reg Med Forum 2017 - Advanced Disease Models. Berlin, Germany. Dec. 6. [Cornell]
- "Microresonator-based high-resolution gas spectroscopy"; M. Yu, Y. Okawachi, A. G. Griffith, M. Lipson, and A. L. Gaeta; Opt. Lett., vol. 42, no. 21, pp. 4442-4445, 2017. [Columbia University]
- "Microscale Bioreactors for in situ characterization of GI epithelial cell physiology"; Costello, Cait M, Phillipsen, Mikkel B, Hartmanis, Leonard M, Kwasnica, Marek A, Chen, Victor, Hackam, David, Chang, Matthew W, Bentley, William E, March, John C; Scientific reports, Volume 7, Issue 1, Page(s) 1-2515. [Cornell University]
- "Microwave response of vortices in superconducting Nb resonators"; K Dodge, BLT Plourde; March Meeting of the American Physical Society Bulletin, 2017, New Orleans, LA. [Syracuse University]
- "Mobile Device-enabled Detection of Biomarkers in Blood or Urine to Quantify Aflatoxin Exposure"; D Erickson, Z Lu, S Mehta, B Ventkatesh; Invention Status Unfiled, Docket No. 8086, Country of Filing: United States, Disclosure Date 12/20/17. [Cornell]
- "Model-independent quantification of soft tissue viscoelasticity with dynamic optical coherence elastography"; Leartprapun N., Iyer R.R., and Adie S.G.; SPIE, Proc. Vol. 10053, 1005322, 2017. [Cornell]
- "Modeling linear and nonlinear optical wave dynamics in nanophotonic devices"; Q Lin; Advanced Electromagnetics Symposium (AES), (Invited Talk), Incheon, Seoul, South Korea (2017). [University of Rochester]
- "Molecular Photo-Engineering of Super-Resolution Optical Sub-10nm Fluorescent Nanoprobes for Biomedical Applications"; Nikhil Dhawan, Joshua Hinckley, Ferdinand Kohle, Ulrich Wiesner; Invention Status Filed - by Cornell, Docket No. 7815, Country of Filing: United States, Invention Type: Invention, Disclosure Date 4/5/17. [Cornell University]
- "Morphology of Nanostructured Polymer Brushes Dependent on Production and Treatment"; Wei-Liang Chen, Matthias Menzel, Oswald Prucker, Endian Wang, Christopher K. Ober, Jürgen Rühe; Macromolecules, (2017), 50(12), 4715-4724. [Cornell University]
- "Motion Sensor Integrated Nano-Probe N/Mems Apparatus, Method and Applications"; Kwame Amponsah, Lal, Amit; Application Status: Issued, Docket No. 5744-05-CN, Country of Filing: China, Filing Date: 8/4/14, Application No. 201280068948.X, Issue Date: 3/1/17, Patent No. ZL201280068948.X. [Cornell University]
- "Multi-layered Graphene Electrodes, Materials and Precursors Thereof"; Mohammed AlAmer, Yong Joo; Invention Status Filed - by Cornell, Docket No. 7858, Country of Filing: United States, Invention Type: Invention, Disclosure Date 5/15/17. [Cornell]
- "Multi-modal Silicon-graphene Electrodes, Materials, and Precursors Thereof"; Ling Fei, Yong Joo; Application Status: Filed, Docket No. 7966-01-US, Country of Filing: United States, Application Type: PRO - Provisional, Filing Date: 8/14/17, Application Number: 62/545,323. [Cornell University]
- "Multi-modal Silicon-graphene Electrodes, Materials, and Precursors Thereof"; Ling Fei, Yong Joo; Invention Status Filed - by Joint Owner, Docket No. 7966, Country of Filing: United States, Invention Type: Invention, Disclosure Date 8/28/17. [Cornell]
- "Multi-mode Experiments with Superconducting Qubits and Metamaterial Resonators"; Sagar Indrajeet, Matthew Hutchings, Haozhi Wang, Britton Plourde, Bruno Taketani, Frank Wilhelm; March Meeting of the American Physical Society Bulletin, 2017, New Orleans, LA. [Syracuse University]
- "Multi-Organ Microfluidic Platform with Breathable Lung Chamber for Inhalation Drug Screening and Development"; C-YS Chen, E Gao, YI Wang, PG Miller, ML Shuler; Organ-on-a-Chip World Congress, Boston, MA. July 10-11. [Cornell University]
- "Multifocus structured illumination microscopy for fast volumetric super-resolution imaging"; Abrahamsson, S, Blom, H, Agostinho, A, Jans, DC, Jost, A, Müller, M, Nilsson, L, Bernhem, K, Lambert, TJ, Heintzmann, R; Biomedical Optics Express, Volume 8, Issue 9, Page(s) 4135-4140. [Rockefeller University]
- "Multilayer hierarchical control for robotic coax-helicopter based on the H_∞ robustness and mixing control scheme"; Chen, Y, Qin, J, Dong, Z, Liu, S, Zheng, H; Advances in Mechanical Engineering, Volume 9, Issue 10. [Jilin Univ, Changchun, China]





- “Multimodal Sensor, Method of Use and Fabrication”; A Lakso, V Pagay, M Santiago, D Sessoms, A Stroock; Application Status: Issued, Docket No. 6335-03-US, Country of Filing: United States, Filing Date: 12/11/15, Application No. 14/898,003, Issue Date: 9/19/17, Patent No. 9,766,173. [Cornell University]
- “Multiorgan microphysiological systems for drug development: strategies, advances, and challenges”; Wang, YL, C Carmona, JJ Hickman, and ML Shuler; Adv. Healthcare Mater. 2017, 1701000; DOI: 10.1002/adhm.201701000. [Cornell University]
- “Nanoparticle photoresist studies for EUV lithography”; Kazuki Kasahara; Hong Xu ; Vasiliki Kosma; Jeremy Odent; Emmanuel P. Giannelis; Christopher K. Ober; SPIE 10143, Extreme Ultraviolet (EUV) Lithography VIII, Proc. 1014308 (March 24, 2017); doi:10.1117/12.2258187. [Cornell University]
- “Nanoparticle photoresist studies for EUV lithography”; Ober, Christopher; invited talk; SPIE Advanced Lithography, San Jose, CA, Feb. 26-29, 2017. [Cornell University]
- “Nanopore-Containing Substrates with Aligned Nanoscale Electrodes and Methods of Making and Using Same”; J Alden, A Barnard, A Cortese, P McEuen; App Status: Filed, Docket No. 6798-05-CN, Country of Filing: China, App Type: FOR - Foreign, Filing Date: 8/1/17, App Number: 2.0158E+11; App Status: Filed, Docket No. 6798-03-EP, Country of Filing: Europe, App Type: EPC - European Patent Convention, Filing Date: 7/3/17, App Number: 15867804.5. [Cornell University]
- “Nanoscale Imaging of Magnetization Using Time-resolved Plasmonic Heating”; Jason Bartell, Jonathan Karsh, Colin L. Jermain, Jack Brangham, Fengyuan Yang, Daniel C Ralph, Gregory D Fuchs; 62nd Annual Conference on Magnetism and Magnetic Materials, Pittsburg, PA 2017. [Cornell University]
- “Nanoscale magnetic imaging using picosecond thermal gradients”; G D Fuchs; March Meeting of the APS, New Orleans, LA 2017. [Cornell University]
- “Nanoscale Sheets for Rapid Bidirectional and Sequential Folding”; Bircan, Baris; APS March Meeting 2017. [Cornell University]
- “Nanosecond magnetization dynamics during spin Hall switching of in-plane magnetic tunnel junctions”; GE Rowlands, SV Aradhya, S Shi, EH Yandel, J Oh, DC Ralph; Applied Physics Letters 110 (12), 122402. doi: <http://dx.doi.org/10.1063/1.4978661>. [Cornell]
- “Nanosecond-timescale low-error switching of magnetic tunnel junction circuits through dynamic Oersted-field assisted spin-Hall effect”; SV Aradhya, RA Buhrman, DC Ralph, and GE Rowlands; Patent App PCT/US15/462,760, filed March 17, 2017. [Cornell]
- “Near-Field Thermal Radiation for Solar Thermophotovoltaics and High Temperature Thermal Logic and Memory Applications”; Elzouka, Mahmoud; The University of Nebraska-Lincoln, Ph.D. Thesis. [University of Nebraska Lincoln]
- “Negative Tone Nanoparticle Photoresists: New Insight on the Patterning Mechanism”; Ober, Christopher; invited talk; International Conference on Photopolymer Science and Technology, Chiba, Japan, June 27- 29, 2017. [Cornell University]
- “Neural Implants, Packaging for Biocompatible Implants, and Improving Fabricated Capacitors”; Agger, Elizabeth Rose; Cornell University, Ph.D. Thesis. [Cornell University]
- “New tunneling features in polar III-nitride resonant tunneling diodes”; J Encomendero, FA Faria, SM Islam, V Protasenko, S Rouvimov, B Sensale-Rodriguez, P Fay, D Jena and HG Xing; Physics Review X (PRX), 7, 041017 (2017) DOI: 10.1103/PhysRevX.7.041017. [Cornell University]
- “Non-integer harmonics generation by photon acceleration in rapidly evolving nonlinear semiconductor metasurfaces”; Shcherbakov, MR, Werner, K, Fan, Z, Talisa, N, Chowdhury, E, Shvets, G; arXiv preprint arXiv:1710.06966. [Cornell]
- “Non-linear effects for frequency tuning and quadrature compensation of a PZT self-calibration compatible Z-axis gyroscope”; S Nadig, V Pinrod, A Lal; 2017 IEEE 30th International Conference on MEMS, Las Vegas, NV, 2017, pp. 1138-1141. [Cornell University]
- “Nonlinear optical oscillation dynamics in high-Q lithium niobate microresonators”; Sun, Xuan, Liang, Hanxiao, Luo, Rui, Jiang, Wei C, Zhang, Xi-Cheng, Lin, Qiang; Optics express, Volume 25, Issue 12, Page(s) 13504-13516. [University of Rochester]
- “Nuclear Deformability and Expression of Lamin A/C as Predictors of Metastatic Potential in Breast Cancer Cells”; Lammerding J; Biomedical Engineering Society (BMES) Annual Meeting. Phoenix, AZ. Platform presentation selected from submitted abstract. (October 12, 2017). [Cornell University]
- “Nuclear envelope mutations associated with Emery-Dreifuss muscular dystrophy cause softer and more fragile nuclei”; Fedorchak G, Kaminski A, Kirby T, Patel J, Davidson PM, Lammerding J; Muscular Dystrophy Association 2017 Annual Meeting, Arlington, VA (March 22, 2017) Platform presentation and poster selected from submitted abstract. [Cornell]
- “On-Chip Quantum and Nonlinear Optics: From Squeezing to Spectroscopy”; Dutt, Avik; Cornell University, Ph.D. Thesis. [Cornell University]
- “On-chip second-harmonic generation and broadband parametric down-conversion in a lithium niobate microresonator”; Luo, R, Jiang, H, Rogers, S, Liang, H, He, Y, Lin, Q; Optics express, Vol 25, Issue 20, Page(s) 24531-24539. [University of Rochester]
- “On-chip thermo-optic tuning of suspended microresonators”; B. S. Lee, M. Zhang, F. A. Barbosa, S. A. Miller, A. Mohanty, R. St-Gelais, and M. Lipson; Opt. Express, vol. 25, no. 11, pp. 12109-12120, 2017. [Columbia University]
- “Optical Absorption and Emission Mechanisms of Single Defects in Hexagonal Boron Nitride”; Nick Jungwirth and Gregory D Fuchs; Fall Meeting of MRS, Boston, MA 2017; Physical review letters, Volume 119, Issue 5, Pages 57401. [Cornell University]
- “Optimization of SPMESH-DART-MS for quantification of trace-level odorants in real matrices”; Jastrzembki JA, Bee MY, and Sacks GL; 65th Annual Conference of the American Society of Mass Spectrometry, Indianapolis, IN. June 2017. [Cornell University]

- "Organ-body- and disease on-a-chip systems"; Shuler, M; Lab Chip DOI: 10.1039/c7lc90068f. [Cornell University]
- "Origin of spin-orbit torques in thin film heterostructures"; D. C. Ralph; 2017 March Meeting of the American Physical Society, March 13-17, 2017, New Orleans, LA. [Cornell University]
- "Orthogonal Processing of Organic Materials Used In Electronic and Electrical Devices"; M Chatzichristidi, P Dodson, J-K Lee, G Malliaras, C Ober, A Zakhidov; App Status: Issued, Docket No. 4385-04-EP, Country of Filing: Europe, Filing Date: 12/21/10, App No. 9751585.2, Issue Date: 11/29/17, Patent No. 2297613. [Cornell]
- "Orthogonal Processing of Organic Materials Used In Electronic and Electrical Devices"; M Chatzichristidi, P Dodson (f/k/a Taylor), J Lee, G Malliaras, C Ober, A Zakhidov; App Status: Issued, Docket No. 4385-10-FR, Country of Filing: France, Filing Date: 12/21/10, App No. EP09751585.2, Issue Date: 11/29/17, Patent No. 229761; App Status: Issued, Docket No. 4385-11-DE, Country of Filing: Germany, Filing Date: 12/21/10, App No. EP09751585.2, Issue Date: 11/29/17, Patent No. 2297613; App Status: Issued, Docket No. 4385-12-GB, Country of Filing: United Kingdom, Filing Date: 12/21/10, App No. EP09751585.2, Issue Date: 11/29/17, Patent No. 229713; App Status: Issued, Docket No. 4385-13-NL, Country of Filing: Netherlands, Filing Date: 12/21/10, App No. EP09751585.2, Issue Date: 11/29/17, Patent No. 2297613. [Cornell]
- "Parity detection of multiple superconducting qubits"; Caleb Howington, Alex Opremcak, Ivan Pechenezhskiy, Marius Schöndorf, Frank Wilhelm, R McDermott, BLT Plourde; March Meeting of the American Physical Society Bulletin, 2017, New Orleans, LA. [Syracuse University]
- "Passively mode-locked InAs quantum dot lasers on a silicon substrate by Pd-GaAs wafer bonding"; Wang, Zihao, Fanto, Michael L, Steidle, Jeffrey A, Aboketaf, Abdelsalam A, Rummage, Nathan A, Thomas, Paul M, Lee, Chi-Sen, Guo, Wei, Lester, Luke F, Preble, Stefan F; Applied Physics Letters, Volume 110, Issue 14, Page(s) 14-1110. [Rochester Institute of Technology]
- "Path to increasing the coincidence efficiency of integrated resonant photon sources"; Tison, C, Steidle, J, Fanto, M, Wang, Z, Mogent, NA, Rizzo, A, Preble, SF, Alsing, PM; Optics Express, V25, Issue 26, Page(s) 33088-96. [Rochester Institute of Technology]
- "Pathways to Mesoporous Resin/Carbon Thin Films with Alternating Gyroid Morphology"; Zhang, Qi, Matsuoka, Fumiaki, Suh, Hyo Seon, Beaucage, Peter A, Xiong, Shisheng, Smilgies, Detlef-M, Tan, Kwan Wee, Werner, Jörg G, Nealey, Paul F, Wiesner, Ulrich B; ACS nano. [Cornell University]
- "Performance limits for spin torque and spin-orbit torque devices"; Buhrman, Robert; 2017 Lawrence Workshop on Solid-State Technology, Feb. 23-24, 2017, Tempe AZ Invited talk by R. Buhrman. [Cornell University]
- "Phonon-Mediated Quasiparticle Poisoning of Superconducting Microwave Resonators"; U Patel, Ivan V Pechenezhskiy, KR Dodge, BLT Plourde, MG Vavilov, R McDermott; March Meeting of the American Physical Society Bulletin, 2017, New Orleans, LA. [Syracuse University]
- "Phonon-Mediated Quasiparticle Poisoning of Superconducting Microwave Resonators"; U Patel, Ivan V Pechenezhskiy, B L T Plourde, M G Vavilov, R McDermott; Physical Review B 96, 220501(R) (2017). [Syracuse University]
- "Photonic Needles for Light Delivery in Deep Tissue-like Media"; Fain, R, Barbosa, F, Cardenas, J, Lipson, M; Scientific reports, Volume 7, Issue 1, Page(s) 5627. [Columbia University]
- "Physics and polarization characterization of 298 nm AlN-delta-GaN quantum-well ultraviolet light-emitting diodes"; CLiu, YK Ooi, SM Islam, JVerma, HG Xing, DJena and JZhang; Appl. Phys. Lett. 110, 071103 (2017); doi: 10.1063/1.4976203. [Cornell University]
- "Picosecond Ultrasonic Measurements of Surface Acoustic Waves on Patterned Layered Nanostructures"; Gartenstein, SA, MM James, S Mahat, ER Szwed, BC Daly, W Cui, GA Antonelli; American Physical Society March Meeting, New Orleans, LA (March 2017). [Binghamton University]
- "Piezoelectric and Logic Integrated Delay Line Memory"; Justin Kuo, Lal, Amit; Application Status: Abandoned, Docket No. 6542-04-US, Country of Filing: United States, Application Type: CON - Continuation, Filing Date: 9/11/17, Application Number: 15/701,289. [Cornell University]
- "Piezoelectric and Logic Integrated Delay Line Memory"; Justin Kuo, Lal, Amit; Application Status: Issued, Docket No. 6542-03-US, Country of Filing: United States, Filing Date: 8/3/16, Application No. 15/116,441, Issue Date: 9/12/17, Patent No. 9,761,324. [Cornell University]
- "Platforms Enabled by Buried Tunnel Junction for Integrated Photonic and Electronic Systems"; Shyam Bharadwaj, Alexander Chaney, Debdeep Jena, Kazuki Nomoto, Henryk Turski, Huili Grace Xing; Invention Status Filed - by Cornell, Docket No. 8026, Country of Filing: United States, Invention Type: Invention, Disclosure Date 10/26/17. [Cornell University]
- "Polarization Field assisted Heterostructure Design for Efficient Deep Ultra-violet Light Emitting Diodes"; SM Islam, Debdeep Jena, Vladimir Protasenko, Huili Grace Xing; Application Status: Filed, Docket No. 7926-01-US, Country of Filing: United States, Application Type: MPP - Manuscript Plus Provisional, Filing Date: 11/15/17, Application Number: 62/586,466. [Cornell University]
- "Polarization Field assisted Heterostructure Design for Efficient Deep Ultra-violet Light Emitting Diodes"; SM Islam, D Jena, V Protasenko, J Verma, HG Xing; Invention Status Filed - by Cornell, Docket No. 7926, Country of Filing: United States, Invention Type: Invention, Disclosure Date 7/3/17. [Cornell University]
- "Polymeric Physio-Chemical Sensor"; S Bhattacharya, A Huang, R Shepherd, T Wallin; Invention Status Unfiled, Docket No. 8063, Country of Filing: United States, Invention Type: Invention, Disclosure Date 12/1/17. [Cornell University]
- "Potential semiconducting and superconducting metastable Si3C structures under pressure"; Gao, G, Liang, X, Ashcroft, NW, Hoffmann, R; Chemistry of Materials. [Cornell University]
- "Preface: Special Topic on Atomic and Molecular Layer Processing: Deposition, Patterning, and Etching"; Engstrom, James R., and Andrew C. Kummel; Journal of Chemical Physics 2017 Feb 7;146(5):052501. doi: 10.1063/1.4975141. [Cornell University]



"Preparation of Micronutrients Fortified Spirulina Supplemented Rice-Soy Crisps Processed Through Novel Supercritical Fluid Extrusion"; Bashir, S, Sharif, MK, Butt, MS, Rizvi, SSH, Paraman, I, Ejaz, R; Journal of Food Processing and Preservation, Volume 41, Issue 3. [University of Agriculture, Faisalabad, Pakistan]

"Programmable and Reconfigurable Microcolumn Affinity Chromatography Device, System, and Methods of Use Thereof"; H Craighead, J Lis, A Ozer, S Reinholdt, K Szeto; App Status: Issued, Docket No. 6440-02-US, Country of Filing: United States, Filing Date: 10/6/14, App No. 14/507,819, Issue Date: 10/31/17, Patent No. 9/803,192. [Cornell University]

"PZT lateral bimorph based sensor cuboid for near zero power sensor nodes"; V. Pinrod, A. Ruyack, R. Ying, B. Davaji, A. Molnar and A. Lal; 2017 IEEE SENSORS, Glasgow, 2017. [Cornell University]

"PZT lateral bimorph based sensor cuboid for near zero power sensor nodes"; Pinrod, Visarute, Ruyack, Alexander, Ying, Robin, Davaji, Benyamin, Molnar, Alyosha, Lal, Amit; SENSORS, 2017 IEEE, IEEE, Pages 1-3. [Cornell University]



"Quantum control over diamond spins with a mechanical resonator"; G D Fuchs; The Workshop on Innovative Nanoscale Devices and Systems (WINDS), Hapuna Beach, HI 2017. [Cornell University]

"Quantum interference between transverse spatial waveguide modes"; Mohanty, A, Zhang, M, Dutt, A, Ramelow, S, Nussenzveig, P, Lipson, M; Nature Communications, Volume 8, Page(s) 1-4010. [Columbia University]

"Quasi-Linear Spin Torque Nano-Oscillators"; Robert Buhrman, OukJae Lee, Daniel Ralph; Application Status: Issued, Docket No. 6055-03-US, Country of Filing: United States, Filing Date: 7/14/15, Application No. 14/760,999, Issue Date: 2/21/17, Patent No. 9,577,653. [Cornell University]

"Quaternary III-V semiconductor compounds for integrated nonlinear optics"; Shayan Saeidi, Kashif M Awan, Ksenia Dolgaleva; Photonics North (PN), 6-8 June 2017. [University of Rochester]

"Rainer Gross Award Lecture 2016: A Laboratory in Your Pocket: Enabling Precision Nutrition"; Mehta, Saurabh, Colt, Susannah, Lee, Seocho, Erickson, David; Food and nutrition bulletin, Volume 38, Issue 2, Page(s) 140-145. [Cornell University]

"Rapid, sensitive, and spatially resolved measurements of trace volatiles using sorbent meshes and high-resolution ambient ionization mass spectrometry"; Sacks GL, Jastrzembki JA, Bee MY; 254th American Chemical Society Meeting (ACS). Washington, DC. Aug 2017. [Cornell University]

"Rare earth element extraction from pretreated bastnaesite in supercritical carbon dioxide"; Sinclair, L K, Baek, D L, Thompson, J, Tester, J W, Fox, R V; The Journal of Supercritical Fluids, Volume 124, Page(s) 20-29. [Cornell University]

"Recent Progress in EUV Metal Oxide Photoresists"; Kasahara, K, Xu, H, Kosma, V, Odent, J, Giannelis, EP, Ober, CK; Journal of Photopolymer Science and Technology, Volume 30, Issue 1, Page(s) 93-97. [Cornell University]

"Recent progress on THz and energy efficient technologies"; Xing, HG; The NG Next 2nd Semiconductors and Devices Workshop, Redondo Beach, CA, January 2017; The MRS Spring Meeting, Symposium on Terahertz Science and Technologies, Phoenix, AZ, April 2017. [Cornell]

"Recognition-mediated particle detection under microfluidic flow with waveguide-coupled 2D photonic crystals: towards integrated photonic virus detectors"; Baker, JE, Sriram, R, Miller, BL; Lab on a Chip 2017. (Web version: DOI: 10.1039/c7lc00221a) Volume 17, Issue 9, Page(s) 1570-1577. [University of Rochester]

"Reduced confinement and its effect on stability in strong polyelectrolyte brushes"; W-L Chen, M Menzel, T Watanabe, O Prucker, J Rühle, C Ober; Langmuir, (2017), 33(13), 3296-3303. [Cornell University]

"Reduced lateral confinement and its effect on stability in patterned strong polyelectrolyte brushes"; Chen, W-L, Menzel, M, Watanabe, T, Prucker, O, Rühle, J, Ober, CK; Langmuir, Volume 33, Issue 13, Page(s) 3296-3303. [Cornell University]

"Reducing orbital occupancy in VO 2 suppresses Mott physics while Peierls distortions persist"; Quackenbush, NF, Paik, H, Holtz, ME, Wahila, MJ, Moyer, JA, Barthel, S, Wehling, TO, Arena, DA, Woicik, JC, Muller, DA; Physical Review B, Volume 96, Issue 8, Page(s) 8-1103. [Cornell University]

"Reorientable spin direction for spin current produced by the anomalous Hall effect"; Gibbons, Jonathan D, MacNeill, David, Buhman, Robert A, Ralph, Daniel C; arXiv preprint arXiv:1707.08631. [Cornell University]

"Resonance-free light recycling in silicon waveguides"; Y. C. Chang, S. Roberts, B. Stern, M. Lipson; arXiv:1710.02891 [physics.optics]. [Columbia University]

"Resonant tunneling diode: an elusive device in III-nitrides"; Xing, HG; The International Conference on Nitride Semiconductors (ICNS), Strasbourg, France, July 2017. [Cornell University]

"RFID Device, Methods and Applications"; Edwin Kan, Yunfei Ma; Application Status: Issued, Docket No. 5944-03-US, Country of Filing: United States, Filing Date: 1/8/15, Application No. 14/413,523, Issue Date: 5/9/17, Patent No. 9,645,234. [Cornell]

"RFID Device, Methods and Applications"; Edwin Kan, Yunfei Ma; Application Status: Issued, Docket No. 5944-04-CN, Country of Filing: China, Filing Date: 3/2/15, Application No. 2.0138E+11, Issue Date: 8/29/17, Patent No. ZL201380045670.9. [Cornell]

"Rheotaxis-Basis Separation of Motile Sperms Using a Microfluidic Corral System"; Alireza Abbaspourrad, Soon Cheong, Meisam Zaferani; Invention Status Unfiled, Docket No. 8071, Country of Filing: United States, Invention Type: Invention, Disclosure Date 12/13/17. [Cornell University]

"Sample Cell Arrays and Hardware for High-throughput Cryogenic Temperature Small-Angle X-Ray Scattering"; Robert Thorne; Application Status: Filed, Docket No. 7906-01-US, Country of Filing: United States, Application Type: MPR - Manuscript Provisional, Filing Date: 8/4/17, Application Number: 62/541,161. [Cornell University]

"Sample Cell Arrays and Hardware for High-throughput Cryogenic Temperature Small-Angle X-Ray Scattering"; Robert Thorne; Application Status: Filed, Docket No. 7906-02-US, Country of Filing: United States, Application Type: PRO - Provisional, Filing Date: 8/4/17, App Number: 62/541,341; Invention Status Filed - by Cornell, Docket No. 7906, Country of Filing: United States, Invention Type: Invention, Disclosure Date 6/12/17. [Cornell]

"Scanning microwave microscopy of aluminum CMOS interconnect lines buried in oxide and water"; X Jin, K Xiong, R Marstell, N C Strandwitz, J C M Hwang, M Farina, A Goeritz, M Wietstruck, and M Kaynak; European Microwave Conf. (EuMC), Nuremberg, Germany, Oct. 2017. [Lehigh University]

"Scanning microwave microscopy of aluminum CMOS interconnect lines buried in oxide and water"; X Jin, K Xiong, R Marstell, N C Strandwitz, J C M Hwang, M Farina, A Goeritz, M Wietstruck, and M Kaynak; European Microwave Conf. (EuMC), Nuremberg, Germany, Oct. 2017, pp. 975-977. [Lehigh University]

"Scanning SQUID Microscopy of Electronic Transport in Graphene"; Ferguson, G.M., B.T. Schaefer, L. Wang, C. Clement, D.H. Low, L. Ju, P.L. McEuen, J.P. Sethna, K.C. Nowack; APS March Meeting 2017, Volume 62, Number 4, March 13-17, 2017; New Orleans, Louisiana. [Cornell University]

"Selective chemical response of transition metal dichalcogenides and metal dischalcogenides in ambient conditions"; JHPark, SVishwanath, SWolf, KZhang, IKawk, MEdmonds, MBreeden, XLiu, MDobrowska, JKfurdyna, JARobinson, HGXing and ACKummel; ACS Appl. Mater. & Interfaces, (2017) DOI: 10.1021/acsami.7b08244. [Cornell University]

"Self-assembled sub-10 nm structures by millisecond laser assisted annealing of PS-PDMS block copolymers"; Jing Jiang, Brandon Wenning, Clemens Liedel, Alan Jacobs, Michael O. Thompson, Christopher K. Ober; ACS Applied Materials & Interfaces, (2017) 9(37), 31317-31324. [Cornell University]

"Self-contained, low cost Body-on-a-Chip systems for drug development"; Wang, Y, Oleaga, C, Long, C, Esch, M, McAleer, CW, Miller, P, Hickman, J and Shuler, ML; Experimental Biology and Medicine Nov:2 42(17), 1701-1713. DOI: 10.1177/1535370217694101. [Cornell University]

"Self-Powered, Piezo-Surface Acoustic Wave Apparatus and Method"; A Lal, S Tin; App Status: Issued, Docket No. 4603-07-KR, Country of Filing: South Korea, Filing Date: 3/14/17, App No. 10-2017-7007365, Issue Date: 11/29/17, Patent No. 10-1805372. [Cornell]

"Self-referenced temperature sensing with a lithium niobate microdisk resonator"; R Luo, H Jiang, H Liang, and Q Lin; Proc. Conf. Laser and Electro-Optics/Quantum Electronics and Laser Science (CLEO/QELS), SM2N.7 (2017). [University of Rochester]

"Self-referenced temperature sensing with a lithium niobate microdisk resonator"; R Luo, H Jiang, H Liang, Y Chen, and Q Lin; Opt. Lett. 42, 1281 (2017). [University of Rochester]

"Sensitive Imaging of Magnetization Structure and Dynamics using Picosecond Laser Heating"; J Bartell, C Jermain, S Aradhya, J Brangham, F Yang, D Ralph, G D Fuchs; March Meeting of the APS, New Orleans, LA 2017. [Cornell University]

"Separation of 300 and 100 nm Particles in Fabry-Perot Acoustofluidic Resonators"; Sehgal, Prateek, Kirby, Brian J; Analytical Chemistry, Volume 89, Issue 22, Page(s) 12192-12200. [Cornell University]

"Silicon Nanowire Flow Cell Anolyte and Device"; Tobias Hanrath, Benjamin Richards; Invention Status Unfiled, Docket No. 7824, Country of Filing: United States, Invention Type: Invention, Disclosure Date 4/12/17. [Cornell University]

"Single crystal N-polar GaN p-n diodes by plasma-assisted molecular beam epitaxy"; YCho, ZHu, KNomoto, HGXing and DJena; Appl. Phys. Lett., 110, 253506 (2017). doi: 10.1063/1.4989581. [Cornell]

"Single Quantum Defects in h-BN and ZnO"; Nick Jungwirth; March Meeting of the APS (invited), New Orleans, LA 2017. [Cornell]

"Smartphone-Based Apparatus and Method"; D Erickson, S Lee, M Mancuso, S Mehta, D O'Dell, V-V Oncescu; Application Status: Issued, Docket No. 6735-02-US, Country of Filing: United States, Filing Date: 7/21/15, Application No. 14/804,386, Issue Date: 10/10/17, Patent No. 9,787,815. [Cornell University]

"Smartphone-based Platform for Point-of-care Diagnosis of Common Causes of Acute Febrile Illness"; D Erickson, S Lee, S Mehta, D O'Dell; App Status: Filed, Docket No. 6979-01-US, Country of Filing: USA, App Type: MPP - Manuscript Plus Provisional, Filing Date: 8/3/17, App Number: 62/540,887. [Cornell University]

"SNARE Complex Reporter 2: An Improved version of SNAP25 based FRET construct"; Q Fang, Y Zhao, S Sharma and M Lindau (2017); 19th International Symposium on Chromaffin Cell Biology, Sheffield, UK. [Cornell University]

"Sonic Alignment and Tweezer System for Chipllet Placement"; Lal, Amit; Invention Status Filed - Attorney Instructed to File, Docket No. 7684, Country of Filing: United States, Invention Type: Invention, Disclosure Date 1/26/17. [Cornell University]

"Sonic Analog and Logic Test Enabled Designs of Integrated Circuits"; Lal, Amit; Invention Status Filed - by Cornell, Docket No. 7685, Country of Filing: United States, Invention Type: Invention, Disclosure Date 1/26/17. [Cornell University]

"Sonic Testing Method, Apparatus and Applications"; Lal, Amit; Application Status: Filed, Docket No. 7685-01-US, Country of Filing: United States, Application Type: MPP - Manuscript Plus Provisional, Filing Date: 7/17/17, Application Number: 62/533,390. [Cornell University]



"Sonic Touch Sensor"; Lal, Amit; Invention Status Filed - by Cornell, Docket No. 7683, Country of Filing: United States, Invention Type: Invention, Disclosure Date 1/27/17. [Cornell University]

"Spatially-annealed nanoparticle films and methods of making and using same"; Hanrath, Tobias, Treml, Ben E; 2017-02-09 USA 20170040488A1 Patent Application. [Cornell University]

"Spatiotemporally resolved dynamics in B20 chiral FeGe"; Isaiiah Gray, Emrah Turgut, Jason Bartell, Gregory D Fuchs; March Meeting of the APS, New Orleans, LA 2017. [Cornell University]

"Spin and charge excitations in artificial hole- and electron-doped infinite layer cuprate superconductors"; Dellea, G, Minola, M, Galdi, A, et al; PHYSICAL REVIEW B Volume: 96 Issue: 11 Article Number: 115117 Published: SEP 11 2017. [Cornell University]

"Spin currents, interfacial spin transparency and spin orbit torques in Pt alloy-ferromagnet multilayers"; Buhrman, Robert; Workshop on Antiferromagnetic Spintronics, October 25-27, 2017, Grenoble France; Invited talk presented by R. Buhrman. [Cornell]

"Spin Hall Effect Magnetic Apparatus, Method, and Applications"; R Buhrman, L Liu, C-F Pai, D Ralph; Application Status: Issued, Docket No. 5587-09-US, Country of Filing: United States, Filing Date: 8/10/15, Application No. 14/822,807, Issue Date: 2/21/17, Patent No. 9,576,631. [Cornell University]

"Spin-Hall Torques Generated by Rare-Earth Thin Films"; N. Reynolds, P. Jadaun, J. T. Heron, C. L. Jermain, J. Gibbons, R. Collette, R. A. Buhrman, D. G. Schlom, and D. C. Ralph; *Physical Review B*, Volume 95, Issue 6, Page(s) 6-4412. Editors' Selection. (arXiv:1612.01927). [Cornell University]

"Spin-orbit-torque Field Effect Transistor"; A Apsel, C Batten, D Jena, J Martinez, D Ralph, D Schlom, C Studer, HG Xing; Invention Status Unfiled, Docket No. 7875, Country of Filing: United States, Invention Type: Invention, Disclosure Date 5/19/17. [Cornell]

"Squish and squeeze – lamins and nuclear mechanics regulate confined migration of breast cancer cells"; Lammerding J; National Cancer Institute (NCI) Physical Science-Oncology Network (PS-ON) & Cancer Systems Biology Consortium (CSBC) 2017 Junior Investigator Meeting. Bethesda, MD (July 12, 2017) Invited talk. [Cornell University]

"Squish and squeeze – Nuclear mechanics and mechanotransduction in physiology and disease"; Lammerding J; Department of Mechanical Engineering, University of Houston. Houston, TX. Invited seminar for the Distinguished Mechanical Engineering Seminar series. (Nov. 9, 2017). [Cornell University]

"Squish and squeeze – Nuclear mechanics and mechanotransduction in physiology and disease"; Lammerding J; University of Tennessee. Knoxville, TN (September 6, 2017) Invited seminar at the Department of Biochemistry and Cellular and Molecular Biology. [Cornell University]

"Squish and squeeze – Nuclear mechanics and mechanotransduction in physiology and disease"; Lammerding J; Max Planck Institute of Molecular Cell Biology and Genetics. Dresden, Germany (June 8, 2017) Student-invited seminar and tutorial. [Cornell University]

"Squish and Squeeze – Nuclear Mechanics in Physiology and Disease"; Lammerding J; Turku BioNet Seminars, University of Turku, Abo Akademi University. Turku, Finland (June 1, 2017). Invited seminar. [Cornell University]

"Squish and squeeze – the role of the nucleus and lamins in cancer metastasis"; Lammerding J; Physics of Cancer conference. Leipzig, Germany (October 5, 2017) Invited presentation. [Cornell]

"Stabilization of mercury in sediment by using biochars under reducing conditions"; P. Liu, C. J. Ptacek, D. W. Blowes, Y. Z. Finrock, and R. A. Gordon; *J Hazard Mater* 325, 120-128 (2017). doi: 10.1016/j.jhazmat.2016.11.033. [Cornell University]

"Strained GaN quantum-well FETs on single crystal bulk AlN substrates"; MQi, GLi, SGanguly, PZhao, XYan, JVerma, BSong, MZhu, KNomoto, HGXing and DJena; *Appl Phys. Lett.*, 110, 063501 (2017). doi:10.1063/1.4975702. [Cornell University]

"Stress-Based Sensor, Method and Applications"; Leon Bellan, Harold Craighead, Jeevak Parpia, Darren Southworth; Application Status: Issued, Docket No. 5066-03-US, Country of Filing: United States, Filing Date: 1/15/13, Application No. 13/637,861, Issue Date: 2/7/17, Patent No. 9,562,888. [Cornell University]

"Stressed out nuclei – the interplay between the nucleus and cytoskeleton during confined migration and muscle contraction"; Lammerding J; European Cytoskeletal Forum. Helsinki, Finland (June 6, 2017) Invited presentation. [Cornell University]

"Strong Perpendicular Magnetic Anisotropy Energy Density at Fe Alloy /HfO2 Interfaces"; Robert Buhrman, Yongxi Ou, Daniel Ralph; Invention Status Filed - by Cornell, Docket No. 7745, Country of Filing: United States, Invention Type: Invention, Disclosure Date 3/13/17. [Cornell University]

"Strong perpendicular magnetic anisotropy energy density at Fe alloy /HfO2 interfaces"; R Buhrman, D Ralph, Y Ou; US Provisional Patent App No. 62/486,434, filed 4/17/2017. [Cornell]

"Strong perpendicular magnetic anisotropy energy density at Fe alloy /HfO2 interfaces"; Ou, Y, Ralph, DC, Buhrman, RA;



Applied Physics Letters, Volume 110, Issue 19, 192403/1-5 (2017). (arXiv:1701.03933). [Cornell University]

"Structures and Methods for Electronically and Mechanically Linked Monolithically Integrated Transistor and MEMS/NEMS Devices"; Kwame Amponsah, Lal, Amit; Application Status: Issued, Docket No. 5271-04-CN, Country of Filing: China, Filing Date: 7/30/13, Application No. 201180066363.X, Issue Date: 2/15/17, Patent No. ZL201180066363.X. [Cornell University]

"Studying Lipid-Protein Interaction Using Proteinaceous Supported Lipid Bilayers from Cell Membranes"; Hsia, Chih-Yun; Cornell University Dissertation. [Cornell University]

"Sub-100 nm integrated ferroelectric tunnel junction devices using hydrogen silsesquioxane planarization"; Abuwasib, M, Lee, J-W, Lee, H, Eom, C-B, Gruverman, A, Singiseti, U; *Journal of Vacuum Science & Technology B, Nanotechnology and Microelectronics: Materials, Processing, Measurement, and Phenomena*, Volume 35, Issue 2, Page(s) 21803. [University at Buffalo]

"Superconducting metamaterial resonators: analysis of mode structure"; H Wang, MD Hutchings, S Indrajeet, F Rouxinol, M LaHaye, BLT Plourde, B Taketani, FK Wilhelm, A Zhuravel, A Ustinov; March Meeting of the American Physical Society Bulletin, 2017, New Orleans, LA. [Syracuse University]

"Superconducting Qubit with Integrated Single Flux Quantum Controller Part I: Theory and Fabrication"; Matthew Beck, Edward Leonard Jr, Ted Thorbeck, Shaojiang Zhu, Caleb Howington, JJ Nelson, Britton Plourde, Robert McDermott; March Meeting of the American Physical Society Bulletin, 2017, New Orleans, LA. [Syracuse University]

"Superconducting Qubit with Integrated Single Flux Quantum Controller Part II: Experimental Characterization"; Edward Leonard Jr, Matthew Beck, Ted Thorbeck, Shaojiang Zhu, Caleb Howington, JJ Nelson, Britton Plourde, Robert McDermott; March Meeting of the American Physical Society Bulletin, 2017, New Orleans, LA. [Syracuse University]

"Superior spatial resolution in confocal X-ray techniques using collimating channel array optics: elemental mapping and speciation in archaeological human bone"; Choudhury, S, Agyeman-Budu, D N, Woll, A R, Swanston, T, Varney, T L, Cooper, D M L, Hallin, E, George, G N, Pickering, I J, Coulthard, I; *Journal of Analytical Atomic Spectrometry*, Volume 32, Issue 3, Page(s) 527-537. [Cornell University]



Bennett, X Rojas, L Levitin, J Saunders, and JM Parpia; Nature Communications DOI: 10.1038/ncomms15963 [Cornell]

"The Electronic and Vibronic Properties of Single Photon Emitters in Hexagonal Boron Nitride"; G D Fuchs; Fall Meeting of MRS, Boston, MA 2017. [Cornell University]

"The Electronic and Vibronic Properties of Single Photon Emitters in Hexagonal Boron Nitride"; G D Fuchs; FOPS 2017, Stevenson, WA 2017. [Cornell University]

"The exocytotic fusion pore formed by the neuronal SNARE complex"; M Lindau; 19th International Symposium on Chromaffin Cell Biology, Sheffield, UK. INVITED. [Cornell]

"The FcεRI signaling cascade and integrin trafficking converge at patterned ligand surfaces"; Wakefield, Devin L, Holowka, David, Baird, Barbara; Molecular Biology of the Cell, Volume 28, Issue 23, Page(s) 3383-3396. [Cornell University]

"The molecular mechanism of fusion pore formation driven by the SNARE complex"; MLindau; National Institutes of Health, National Institute of Neurological Disorders and Stroke, Bethesda MD, USA. INVITED. [Cornell University]

"The Path to Increasing the Coincidence Efficiency of Integrated Photon Sources"; Tison, C C, Steidle, J A, Fanto, M L, Wang, Z, Mogent, N A, Rizzo, A, Preble, S F, Alsing, P M; arXiv preprint arXiv:1703.08368. [Rochester Institute of Technology]

"The role of nuclear deformation and rupture in breast cancer cell migration"; McGregor AL, Elacqua JJ, Bell ES, Lammerding J; American Association for Cancer Research (AACR) Annual Meeting 2017. Washington, DC (April 4, 2017) Poster presentation selected from submitted abstract. [Cornell University]

"Theory and Practice of Electron Diffraction from Single Atoms and Extended Objects using an Electron Microscope Pixel Array Detector"; MC Cao, Y Han, Z Chen, Y Jiang, KX Nguyen, E Turgut, GD Fuchs, DA Muller; Microscopy DOI:10.1093/jmicro/dfx123 (2017). [Cornell University]

"Thermal Management of Electronics and Power Conversion Devices"; An Zou, Shalabh C. Maroo, Manish Gupta; Patent pending. [Syracuse University]

"Thermal wavefront imaging using GHz ultrasonics"; Abdelmejeed, M, Kuo, JC, Lal, A; Ultrasonics Symposium (IUS), 2017 IEEE International, IEEE, Page(s) 43104; Ultrasonics Symposium (IUS), 2017 IEEE International. [Cornell University]

"Thickness dependence of spin-orbit torques generated by WTe₂"; MacNeill, D, Stiehl, GM, Guimarães, MHD, Reynolds, ND, Buhman, RA, Ralph, DC; Physical Review B, Volume 96, Issue 5, 054450/1-8 (2017). (arXiv:1707.03757). [Cornell University]

"Thin-TFETs for high efficiency logic electronics"; Xing, HG; The Compound Semiconductor Week (CSW), Berlin, Germany, May 2017. [Cornell University]

"Time Resolved BioSAXS at MacCHESS"; Jesse B Hopkins, Richard E Gillilan; CHESS User Meeting, Ithaca NY (June 2017). [Cornell]

"Time-resolved magneto-thermal microscopy: dynamic imaging of magnetic metals and magnetic insulators in devices"; G D Fuchs; Annual Conference on Magnetism and Magnetic Materials, Pittsburg, PA. [Cornell University]

"TINY: the Tiny Isothermal Nucleic acid amplification sYstem"; David Erickson, Ryan Snodgrass; Invention Status Filed - by Cornell, Docket No. 7674, Country of Filing: United States, Invention Type: Invention, Disclosure Date 1/23/17. [Cornell University]

"Top-down and Bottom-up Approaches to Nanoscale Fabrication and Structure Formation"; Ober, Christopher; invited talk; Inha University, Incheon, Korea, Oct. 10, 2017. [Cornell University]

"Superior spatial resolution in confocal X-ray techniques using collimating channel array optics: elemental mapping and speciation in archaeological human bone"; S. Choudhury, D. N. Agyeman-Budu, A. R. Woll, T. Swanston, T. L. Varney, D. M. L. Cooper, E. Hallin, G. N. George, I. J. Pickering, and I. Coulthard; Journal of Analytical Atomic Spectrometry 32 (3), 527-537 (2017). doi: 10.1039/C6JA00297H. (COVER). [Cornell University]

"Surface modified CMOS IC electrochemical sensor array targeting single chromaffin cells for highly parallel amperometry measurements"; MHuang, JBDelacruz, JCRuelas, SSRathore and MLindau; Pflügers Arch. Eur. J. Physiol. 470:113-123. DOI 10.1007/s00424-017-2067-y. Epub 2017 Sep 9. [Cornell University]

"Tech for treatment"; Shuler, ML, JJ Hickman, and C Long; Pan European Networks Health: 12:1. [Cornell University]

"Temperature-dependent far-infrared reflectance of an epitaxial (BaTiO₃)₈/(SrTiO₃)₄ superlattice"; Železna, V, Caha, O, Soukiassian, A, Schlom, D G, Xi, X X; Physical Review B, Volume 95, Issue 21, Page(s) 2-14110. [Cornell University]

"Terahertz spectroscopy of an electron-hole bilayer system in AlN/GaN/AlN quantum wells"; H Condori Quispe, SM Islam, S Bader, A Chanana, K Lee, R Chaudhuri, A Nahata, H G Xing, D Jena and B Sensale-Rodriguez; Appl. Phys. Lett. 111, 073102 (2017), doi: 10.1063/1.4996925. [Cornell University]

"Ternary Gold Hydrides: Designing New, Possibly Superconducting Compounds"; Martin Rahm, Roald Hoffmann, and N W Ashcroft; J. Amer. Chem. Soc., 139, 8740-8751 (2017). [Cornell University]

"Ternary Gold Hydrides: Routes to Stable and Potentially Superconducting Compounds"; Rahm, Martin, Hoffmann, Roald, Ashcroft, N W; Journal of the American Chemical Society, Volume 139, Issue 25, Page(s) 8740-8751. [Cornell University]

"The A-B transition in superfluid helium-3 under confinement in a thin slab geometry"; N Zhelev, TS Abhilash, EN Smith, RG



- "Top-down and Bottom-up Approaches to Nanoscale Fabrication and Structure Formation"; Ober, Christopher; invited talk; Bayreuth Polymer Symposium, Bayreuth, Germany, September 17-19, 2017. [Cornell University]
- "Topological spin dynamics in cubic FeGe near room temperature"; Emrah Turgut, Matthew J Stolt, Song Jin, and Gregory D Fuchs; J. Appl. Phys. 122, 183903 (2017) arXiv preprint arXiv:1705.03397. [Cornell University]
- "Topological spin dynamics in FeGe near room temperature"; Emrah Turgut, Matthew Stolt, Song Jin, and Gregory D Fuchs; 62nd Annual Conference on Magnetism and Magnetic Materials, Pittsburg, PA 2017. [Cornell University]
- "Towards a surface and bulk excited SAW gyroscope"; B. Davaji, V. Pinrod, S. Kulkarni and A. Lal; 2017 IEEE International Ultrasonics Symposium (IUS), Washington, DC, 2017. [Cornell]
- "Towards a surface and bulk excited SAW gyroscope"; Davaji, Benyamin, Pinrod, Visarute, Kulkarni, Shrinidhi, Lal, Amit; Ultrasonics Symposium (IUS), 2017 IEEE International, IEEE, Page(s) 4-3104. [Cornell University]
- "Trace-level volatile quantification by DART-MS following headspace extraction - optimization and validation in grapes"; Jastrzembksi JA, Bee MY, Sacks GL; Journal of Agricultural and Food Chemistry. 2017. 65 (42), 9353-9359 <http://pubs.acs.org/doi/pdf/10.1021/acs.jafc.7b03638>. [Cornell University]
- "Trace-level volatile quantification by DART-MS following headspace extraction - optimization and validation in grapes."; Jastrzembksi JA, Bee MY, Sacks GL; Journal of Agricultural and Food Chemistry. 2017. 65 (42), 9353-9359 <http://pubs.acs.org/doi/pdf/10.1021/acs.jafc.7b03638>. [Cornell University]
- "Tunable excitons in bilayer graphene"; Ju, Long, Wang, Lei, Cao, Ting, Taniguchi, Takashi, Watanabe, Kenji, Louie, Steven G, Rana, Farhan, Park, Jiwoong, Hone, James, Wang, Feng; Science, Volume 358, Issue 6365, Page(s) 907-910. [Cornell University]
- "Tunable nanophotonic array traps with enhanced force and stability"; Fan Y, M Soltani, JT Inman, and MD Wang; Optics Express Vol. 25, Issue 7, pp. 7907-7918 (2017) <https://doi.org/10.1364/OE.25.007907>. [Cornell University]
- "Tunable Optofluidic Apparatus, Method, and Applications"; M Lipson, M Soltani, M Wang; App Status: Issued, Docket No. 5846-04-US, Country of Filing: USA, Filing Date: 9/6/14, App No. 14/383,544, Issue Date: 5/30/17, Patent No. 9,664,500. [Cornell]
- "Tunable superconducting qubits with flux-independent coherence"; Hutchings, MD, Hertzberg, JB, Liu, Y, Bronn, NT, Keefe, GA, Brink, M, Chow, JM, Plourde, BLT; Physical Review Applied, Volume 8, Issue 4, Page(s) 4-4003. [Syracuse University]
- "Tunable Superconducting Qubits with Reduced Sensitivity to 1/f flux noise"; M D Hutchings, JB Hertzberg, Y Liu, JM Chow, BLT Plourde; March Meeting of the American Physical Society Bulletin, 2017, New Orleans, LA. [Syracuse University]
- "Tunnel FET: lateral or vertical?"; Xing, HG; The MRS Spring Meeting, Symposium on Materials for Beyond the Roadmap Devices in Logic, Memory and Power, Phoenix, AZ, April 2017. [Cornell University]
- "Two New Games for Carbon"; Roald Hoffmann; Lecture, Drexel Univ. Nov. 10, 2017. [Cornell University]
- "Two tools for three characterizations of cells: Machine learning for automated cancer cell identification and electrorotation for cancer cell and algae cell electrical property measurement"; Lannin, Timothy Burke; Cornell University, Ph.D. Thesis. [Cornell]
- "Two-Phase Contiguous Supported Lipid Bilayer Model for Membrane Rafts via Polymer Blotting and Stenciling"; Richards, Mark J, Daniel, Susan; Langmuir, Volume 33, Issue 5, Pages 1285-1294. [Cornell University]
- "Ultra-low-loss on-chip resonators with sub-milliwatt parametric oscillation threshold"; X Ji, FAS Barbosa, SP Roberts, A Dutt, J Cardenas, Y Okawachi, A Bryant, AL Gaeta, and M Lipson; Optica Vol. 4, Issue 6, pp. 619-624 (2017) <https://doi.org/10.1364/OPTICA.4.000619>. [Columbia University]
- "Ultra-wide-band slow light in photonic crystal coupled-cavity waveguides"; Lai, Y, Mohamed, MS, Gao, B, Minkov, M, Boyd, RW, Savona, V, Houdre, R, Badolato, A; arXiv preprint arXiv:1706.09625. [University of Rochester]
- "Ultrafast laser annealing processes applied to chemically amplified photoresists and to directed self-assembly"; Ober, Christopher; invited talk; TokyoTech Symposium on Polymer Self-Assembly, TokyoTech, Ookayama, Japan, June 26, 2017. [Cornell University]
- "Ultrafast Self-Assembly of Sub-10 nm Block Copolymer Nanostructures by Solvent-Free High-Temperature Laser Annealing"; Jiang, Jing, Jacobs, Alan G, Wenning, Brandon, Liedel, Clemens, Thompson, Michael O, Ober, Christopher K; ACS Applied Materials & Interfaces. [Cornell University]
- "Ultrasound Transducer Probe and Methods"; Steven Gelber, George Lewis Jr, George Lewis, Sr, William Olbricht; Application Status: Issued, Docket No. 4848-04-CN, Country of Filing: China, Filing Date: 12/11/13, Application No. 2.0128E+11, Issue Date: 2/15/17, Patent No. ZL 201280029034.2. [Cornell University]
- "Ultrawide Band Gap β -Ga₂O₃ Nanomechanical Resonators with Spatially Visualized Multimode Motion"; Zheng, X-Q, Lee, J, Rafique, S, Han, L, Zorman, CA, Zhao, H, Feng, P X-L; ACS applied materials & interfaces, Volume 9, Issue 49, Page(s) 43090-43097. [Case Western Reserve University]
- "Using a "Body-on-a-Chip" including toxicokinetics to predict human response to chemical and drug exposerers"; Shuler, ML; EuroTox, Bratislava, Slovak Republic, Sept. 10-13. [Cornell University]
- "Using a body-on-a-chip including toxicokinetics to predict human response to chemical and drug exposure"; Shuler, ML; Non-animal methods for toxicokinetics: meeting new paradigms in toxicology. Lorentz Workshops, Leiden, Netherlands. October 16-20. Invited talk. [Cornell University]
- "Vanishing polymers: Polymer systems designed to fail"; Ober, Christopher; invited talk; 253rd ACS National Meeting, San Francisco, CA, April 2-6, 2017. [Cornell University]
- "Variability metrics in Josephson Junction fabrication for Quantum Computing circuits"; S Rosenblatt, J Hertzberg, M Brink, J Chow, J Gambetta, Z Leng, A Houck, JJ Nelson, B Plourde, X Wu, R Lake, J Shainline, D Pappas, U Patel, R McDermott; March Meeting of the American Physical Society Bulletin, 2017, New Orleans, LA. [Syracuse University]

Photography Credits

"Vector Electric Field Measurement via Position-modulated Kelvin Probe Force Microscopy"; Dwyer, Ryan P and Smieska, Louisa M and Tirmzi, Ali Moeed and Marohn, John A; Appl. Phys. Lett. 2017 volume 111 number 17 oct2017 pages 173106 doi 10.1063/1.4999172 http://dx.doi.org/10.1063/1.4999172. [Cornell]

"Visualizing weak ferromagnetic domains in multiferroic hexagonal ferrite thin film"; Wang, Wenbo, Mundy, Julia A, Brooks, Charles M, et al; PHYSICAL REVIEW B Volume: 95 Issue: 13 Article Number: 134443 Published: APR 26 2017. [Cornell University]

"Waveguide for Use in Distributive Sensing"; Hedan Bai, Shuo Li, Robert Shepherd, Yaqi Tu; Invention Status Unfiled, Docket No. 8067, Country of Filing: United States, Invention Type: Plant, Disclosure Date 12/8/17. [Cornell University]

"Who's on first? Tracking in real time the growth of multiple crystalline phases of an organic semiconductor: Tetracene on SiO₂"; Nahm, R. K., and J. R. Engstrom; J. Chem. Phys. 146, 052815 (2017). [Cornell University]

"Wideband Material Detection for Spoof Resistance in GHz Ultrasonic Fingerprint Sensing"; J. Kuo and A. Lal; IEEE International Ultrasonics Symposium (IUS) 2017. [Cornell]

"Zero-power sensors with near-zero-power wakeup switches for reliable sensor platforms"; V. Pinrod, L. Pancoast, B. Davaji, S. Lee, R. Ying, A. Molnar, A. Lal; 2017 IEEE 30th International Conference on Micro Electro Mechanical Systems (MEMS), Las Vegas, NV, 2017. [Cornell University]

"Zero-power sensors with near-zero-power wakeup switches for reliable sensor platforms"; Pinrod, V, Pancoast, L, Davaji, B, Lee, S, Ying, R, Molnar, A, Lal, A; MEMS 2017 IEEE 30th International Conference on, IEEE, Page(s) 1236-1239. [Cornell University]

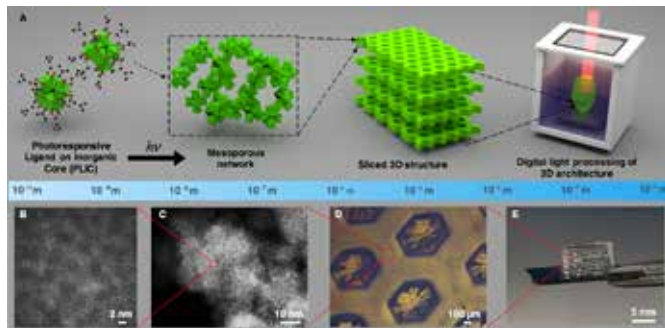
The cover images were used with permission from: 1239-04, Suh, Figure 3, page 68; 1872-10, Rey, Figure 1, page 22; 2065-11, Windsor, Figure 2, page 30; 2214-13, Jadhav, Figure 3, page 32; 2350-15, Shin, Figure 3, page 82; 2406-15, Liu, Figure 1, page 164; 2461-16, De Micheli, Figure 1, page 46; 2471-16, She, Figure 3, page 168; 2499-16, Jovanovic, Figure 2, page 172; 2502-16, Pajoumshariati, Figure 1, page 52; 2574-17, Roberts, Figure 3, page 56; 2641-18, Manzer, Figure 2, page 62.

The photographs on pages i-xxxvi were taken primarily by Don Tennant (youth outreach, CNF REU interns, CNF picnic), but a few were taken by University Photography (Duffield Hall on page i and viii, and the directors photos on page viii), CNF iREU interns in Japan (pages viii, xii, xiii, xvii), and the rest by various CNF Staff and NNCI photographers (like the photo from the 2018 NNCI REU Convocation, featuring Dr. Lawrence Goldberg, NSF, below!).

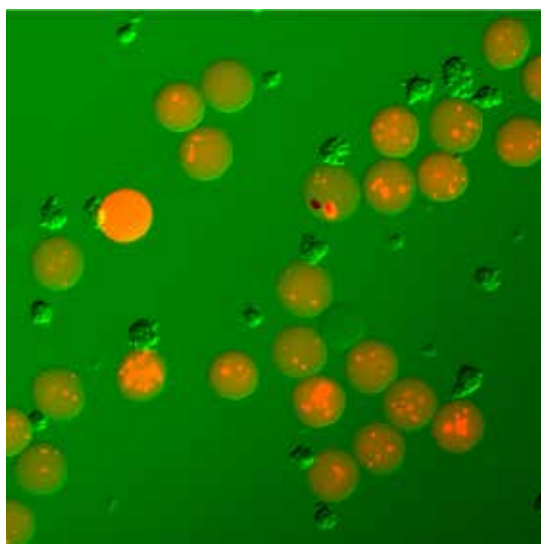
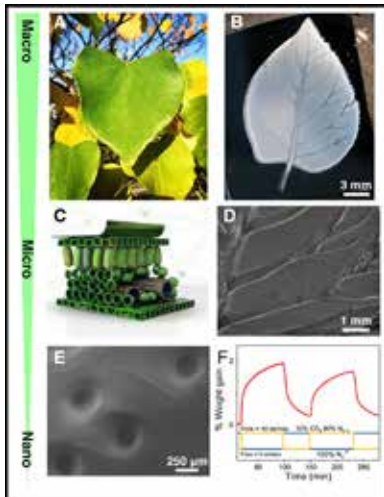
The full color research images on pages xxviii-xxix are each attributed to the appropriate research group and include the page number where you will find their full technical report.



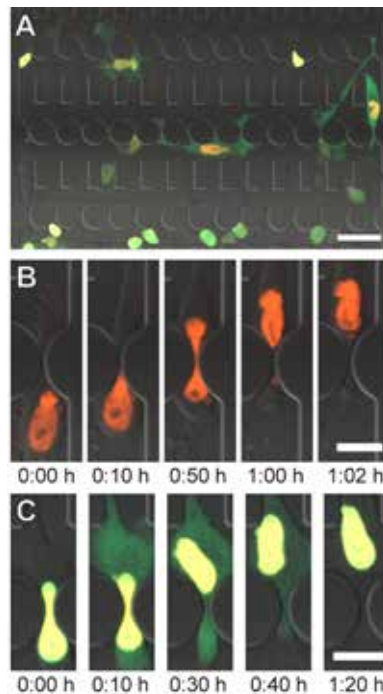
Full Color Versions of a few Research Images



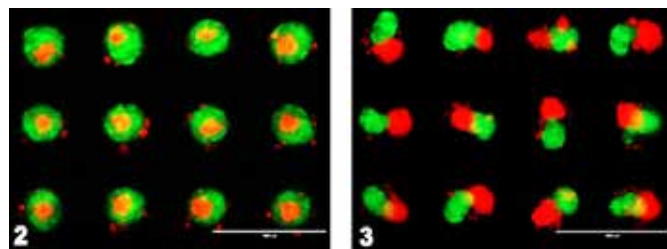
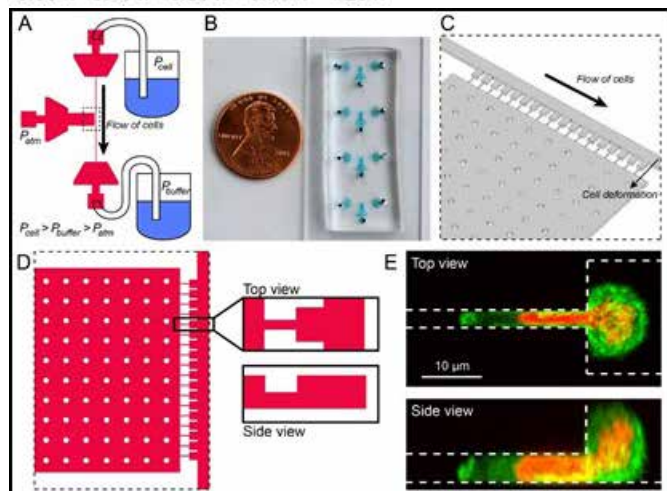
3D Printing of Hierarchical Porous Architectures, CNF Project Number: 1645-08; Figure 1: Three-dimensional printing PLIC assembly. (A) Schematic representation of multi-level control in the printing process. PLIC materials are used as the building units and structured by series of 2D UV images in the 3D printer. (B) The unit cell of zirconia inorganic nanocrystal with methacrylic acid surface ligands. (C) Formation of pores via connecting the building units. (D) An example of printed structure showing shape control for each layer. (E) Centimeter scale resulting parts with layer by layer stacking; Figure 2: Complex devices like artificial leaf can be fabricated with 3D printing PLIC. (A) Photographic image of leaf. (B) Photographic image of artificial leaf. (C) 3D illustration of leaf structure from cross-sectional view. (D) SEM image of channels mimicking veins. (E) SEM of small pores like stomata on the back surface (F) CO₂ capturing capacity of 3D printed artificial leaf; pages 112-113.



Droplet-Microfluidic Device for Stem Cell Culture, CNF Project Number: 2461-16; Figure 1: 100 μm PEG beads coated with the fluorescent (Alexa647) protein laminin (red). Clusters of myoblasts can be seen adhering to the beads; pages 46-47.



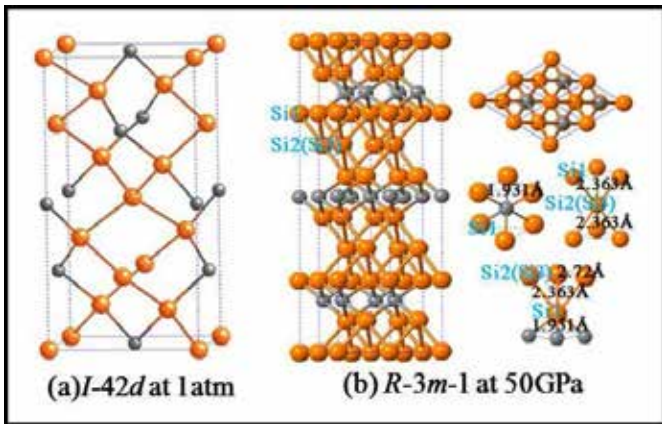
Design and Application of Microfluidic Devices to Study Cell Migration in Confined Environments, CNF Project Numbers: 2065-11, 2642-18; Figure 1, left: Cell migration through microfluidic constrictions. (A) Cells expressing NLS-GFP and H2B-tTomato migrating through a microfluidic device. Scale bar: 50 μm. (B) Time series of a nucleus squeezing through a constriction. Scale: bar 20 μm. (C) Time series of a NE rupture event. NLS-GFP leaks into the cytoplasm upon NE rupture and is reimported into the nucleus as the NE is repaired. Scale bar: 20 μm. Figure reproduced from Elacqua, et al. PLoS one. 2018 [3]; Figure 3, below: Overview of the microfluidic micropipette aspiration device. (A) Design overview, with applied external pressures indicated. (B) Image of four devices integrated onto a single glass slide. (C) Close-up of the design features containing the pockets and micropipette openings. (D) Top and side view of the same feature. (E) Confocal microscope images of a cell inside a pocket, with the nucleus (red) and cytoplasm (green) partially aspirated into the micropipette; pages 30-31.



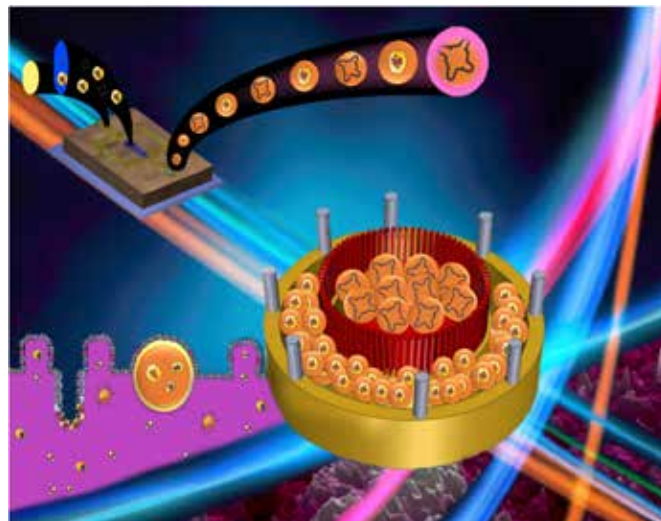
Microfabricated Devices for Cell Organization, CNF Project Number: 2249-13; Figure 2: A fluorescent image of cell segregation of MDA-MB-231 (red colour) and MCF10A (green colour) cells at 1:1 cell seeding ratio over 9 days of culture. Scale bar: 400 μm; Figure 3: A fluorescent image of cell segregation of MDA-MB-231 (red colour) and MCF10A (green colour) cells at 4:1 cell seeding ratio over 9 days of culture. Scale bar: 400 μm; pages 34-35.



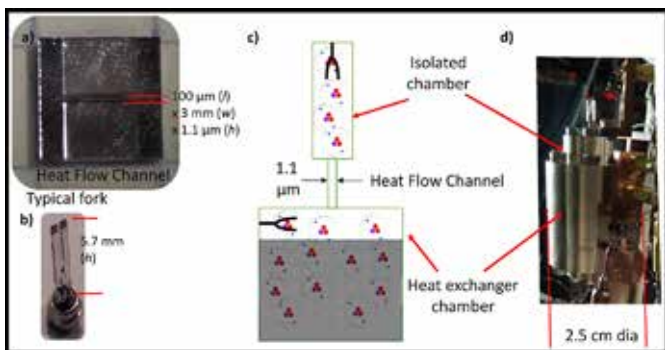
Attoneuton Sensitivity Magnet-Tipped Cantilevers and Sample Preparation for Single-Electron Spin Detection, CNF Project Number: 863-00; Figure 3: Multilayer graphene deposited on top of a coplanar waveguide spin-coated with a 200 nm thick polystyrene film; pages 66-67.



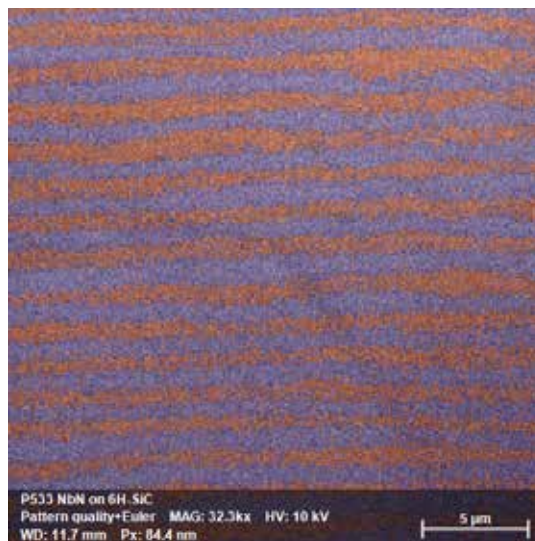
Chemical Bonding Across the Periodic Table at High and Ambient Pressures, CNF Project Number: 1371-05; Figure 1: Predicted I-42d, and R-3m-1 structures for Si₃C at 1 atm, and 50 GPa, respectively. Orange, large balls are Si; grey, small balls carbon. The right panel of (b) presents the top view of the R-3m-1 structure and Si-or C-centered octahedra within the structure; page 70.



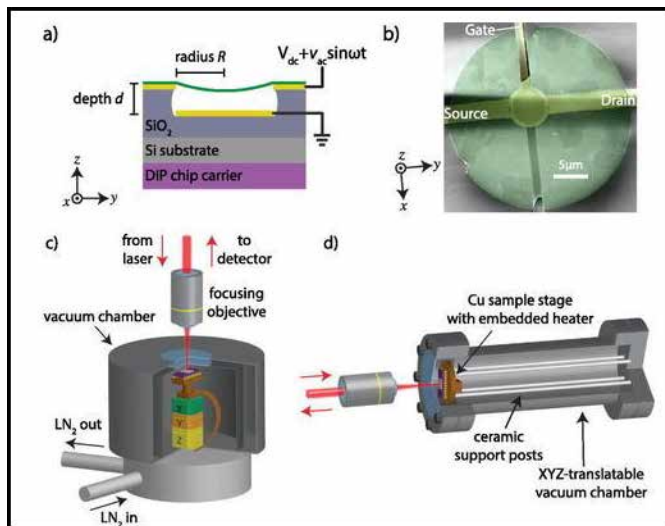
Gut-on-a-Chip using Microfluidic Devices, CNF Project Number: 2502-16; Figure 1: Schematic of the 3D printed insert for co-culture of organoid-embedded microgels along with Peyer's patch embedded microgels; pages 52-53.



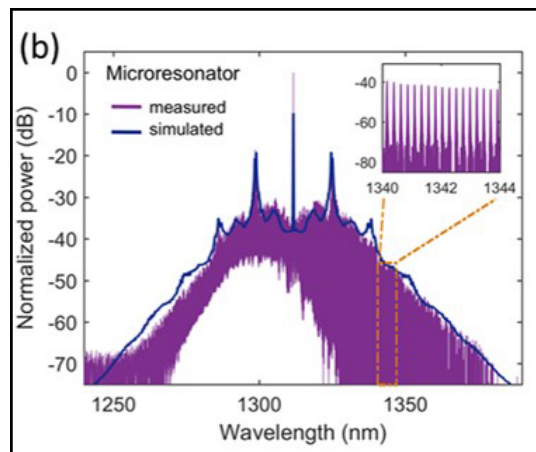
Fabrication of Nanofluidic Cavities for Superfluid 3He Studies, CNF Project Number: 1520-07; Figure 1: A. the bonded heat flow channel (5 mm square) with dimensions alongside. B. typical quartz fork. C. schematic of experiment. D. photograph of experimental chamber [5]; pages 194-195.



Growth and Characterization of NbN/III-N Heterostructures by MBE, CNF Project Number: 2443-16; Figure 2: Crystal orientation map of a 25 μm x 25 μm area of the surface of an 89 nm NbN film on 6H-SiC produced by EBSD using an SEM with an accelerating voltage of 10kV. The color indicates the relative angle of the crystal structure. The parallel array of grains is found to span the entire 1 cm x 1 cm sample. This image shows grains that are approximately 750 nm in width; pages 120-121.



Fabrication of Nanofluidic Cavities for Superfluid 3He Studies, CNF Project Number: 1520-07; Figure 2: A. Cartoon cross-section of a graphene device. Suspended graphene (green) is pulled toward the back-gate via an applied voltage. B. False-color SEM image, showing the suspended graphene (green), metallic Source, Drain, and Gate (yellow), and surrounding SiO₂ substrate (grey). C. Liquid N₂ flow cryostat with optical access. Sample is mounted on a 24-pin Dual In-line Package (purple). D. Heated test chamber with optical window [3].



Chip-Based Frequency Combs for High-Resolution Optical Coherence Tomography, CNF Project Number: 2364-15; Figure 2: Dark grey: Measured frequency comb spectrum generated using the silicon nitride microresonators. Black: Simulated frequency comb; pages 40-41.

Abbreviations & Their Meanings

μl	microliter	BiOCl	bismuth oxychloride
μm	micron, micrometer	BioSAXS	biological small angle x-ray scattering
μN	micro-Newtons	BN	boron nitride
μs	microsecond	BOE	buffered oxide etch
Ω	Ohm	BOX	buried oxide layer
<	is less than	BPB	bisphenol base
>	is greater than	BPF	bisphenol F
~	approximately	Br	bromine
1D	one-dimensional	BRDF	bidirectional reflectance distribution function
2D	two-dimensional	BSA	bovine serum albumin
2DEG	two-dimensional electron gas	BST	barium strontium titanate
3D	three-dimensional	BTO	barium titanate
3DOM carbon	3D ordered macroporous carbon	C	carbon
^3He	helium-3	C	centigrade
^4He	helium-4	C-V	capacitance-voltage
$\alpha\text{-Al}_2\text{O}_3$	sapphire	C_3N_4	carbon nitride
$\alpha\text{-Si}$	amorphous silicon	C_4F_8	octafluorocyclobutane, or perfluorocyclobutane
A&M	Agricultural & Mechanical	CAAC	c-axis-aligned crystalline
AC	alternating current	CaCl_2	calcium chloride
AFM	atomic force microscopy / microscope	CaCO_3	calcium carbonate
AFOSR	Air Force Office of Scientific Research	CAD	computer-aided design
Ag	silver	CaF_2	calcium fluoride
agLDL	aggregated low-density lipoproteins	CCI	Centers for Chemical Innovation
AgNO_3	silver nitrate	CCMR	Cornell Center for Materials Research
AgSR	silver-alkanethiolate	CCS	continuous compositional spreads
AIC	aluminum-induced crystallization	Cd	cadmium
Al	aluminum	CdS	cadmium sulfide
Al_2O_3	aluminum oxide	CdSe	cadmium selenide
ALD	atomic layer deposition	CDW	charge-density-wave
AlGaAs	aluminum gallium arsenide	Ce	cerium
AlGaN	aluminum gallium nitride	CF_4	carbon tetrafluoride or tetrafluoromethane
AM	amplitude modulation	CFD	computational fluid dynamics
APD	avalanche photodiode	CFMA	carbon-fiber microelectrode amperometry
APS	advanced photon source	CH_4	methane
Ar	argon	CHESS	Cornell High Energy Synchrotron Source
ARC	anti-reflective coating	CHF_3	trifluoromethane
ArF	argon fluoride	CIGS	copper indium gallium diselenide
As	arsenic	CION	colloidal iron oxide nanoparticles
AST	aspartate transaminase		
atm.	standard atmosphere (as a unit of pressure)		
ATRP	atom transfer radical polymerization		
Au	gold		
AuNPs	gold nanoparticles		
B	boron		
<i>B. subtilis</i>	<i>Bacillus subtilis</i>		
B_4C	boron carbide		
BAM	bisphenol aminomethyl		
BCL_3	boron trichloride		
BDM	2,3-butanedione monoxime		
BES	bioelectrochemical system		
BHJ	bulk heterojunction		
Bi	bismuth		



Cl. chlorine
 Cl₂. chlorine gas
 Cl₂/SF₆. chlorine sulfur hexafluoride
 cm. centimeter
 CMOS. complementary metal oxide semiconductor
 CMOSFET. complementary metal oxide field effect transistor
 CMP. chemical mechanical polishing
 CNF. Cornell NanoScale Science & Technology Facility
 CNL. charge neutrality level
 CNS. Cornell Center for Nanoscale Systems
 CNTFET. carbon nanotube field-effect transistor
 Co. cobalt
 CO₂. carbon dioxide
 Co₃O₄. cobalt oxide
 COF. covalent organic framework
 CoFeAl. cobalt iron aluminum
 CoFeB. cobalt iron boron
 CoP. cobalt porphyrin
 CPC. colloidal photonic crystal
 CPD. contact potential difference
 CpG. cytosine-phosphate-guanine
 Cr. chromium
 CRDS. cavity ring-down spectrometer
 cryoSAXS. cryogenic small angle x-ray scattering
 CTC. circulating tumor cell
 CTC. composite thermal capacitors
 CTE. coefficients of thermal expansion
 CTL. confinement tuning layer
 Cu. copper
 Cu₂ZnSnS₄. copper zinc tin sulfide
 CuAlO₂. copper aluminum oxide
 CVD. cardiovascular disease
 CVD. chemical vapor deposition
 CW. continuous wave
 CXRF. confocal x-ray fluorescence microscopy
 DARPA. Defense Advanced Research Projects Agency
 DC. direct current
 DCB. double cantilever beam
 DCE. 1,2-dichloroethane
 DCM. dichloromethane
de novo. Latin expression meaning “from the beginning,”
 “afresh,” “anew,” “beginning again.”

DEP. dielectrophoresis
 DFT. density functional theory
 DFT. discrete Fourier transform
 DH-PSF. double helix point-spread function
 DI. de-ionized
 DIC. differential interference contrast
 DMF. dimethyl formamide
 DNA. deoxyribonucleic acid
 DNP. dynamic nuclear polarization
 DODAB. dimethyl dioctadecyl ammonium bromide
 DOE. United States Department of Energy
 DPPC. 1,2-dipalmitoyl-sn-glycero-3-phosphocholine
 DPPG. 1,2-dimyristoyl-sn-glycero-[phospho-rac-(1-glycerol)]
 DRAM. dynamic random access memory
 DRIE. deep reactive ion etch
 DSA. directed self assembly
 dsDNA. double-stranded DNA
 DUV. deep ultraviolet
 e-beam. electron beam lithography
E. coli. *Escherichia coli*
 EB. exchange bias
 EBID. electron beam induced deposition
 EBL. electron beam lithography
 ECD. electrochemical detectors
 ECM. extracellular matrix
 EDS. energy dispersive spectroscopy
 EDTA. ethylenediaminetetraacetic acid
 EELS. electron energy loss spectroscopy
 EG. ethylene glycol
 EIS. electrochemical impedance spectroscopy
 ELISA. enzyme-linked immunosorbent assays
 EMCCD. electron multiplying charge coupled device
 EO. electro-optic
 EOT. equivalent oxide thickness
 EPICs. electronic photonic integrated circuits
 EPR. enhanced permeability and retention
 Er. erbium
 ErAs. erbium arsenide
 ESM. effective screening medium
 EUV. extreme ultraviolet
ex situ. Latin phrase which translated literally as ‘off-site’ -- to
 examine the phenomenon in another setting than
 where it naturally occurs
ex vivo. Latin for “out of the living” -- that which takes place
 outside an organism
 F. fluorine
 FeCOOH. ferrocenecarboxylic acid
 FDA. United States Food & Drug Administration
 FDMA. fluorinated perfluorodecyl methacrylate
 FDMNES. finite-difference method approach to predicting
 spectroscopic transitions
 Fe. iron
 Fe₂O₃. iron oxide
 FeCl₃. iron(III) chloride, aka ferric chloride
 FeDRAM. ferroelectric dynamic random access memory
 FeGe. iron germanium
 FEM. finite element method



FES functional electrical stimulation
FESEM field-emission scanning electron microscopy /
microscope
FET field-effect transistor
FFTs fast Fourier transforms
fg femto gram
FIB focused ion beam
FIR far infrared
fJ femto Joules
FLT field-like torque
FM frequency modulation
FMR ferromagnetic resonance
FOTS fluorosilane, tridecafluoro-
1,1,2,2-tetrahydrooctyltrichlorosilane
FRAP fluorescence recovery after photobleaching
FRET fluorescence resonance energy transfer
FTIR Fourier transform infrared spectroscopy
FWM four-wave mixing
Ga gallium
GaAs gallium arsenide
GaAsN gallium arsenide nitride
GaInNAs gallium indium nitride arsenide
GaN gallium nitride
GaP gallium phosphide
GaSb gallium antimonide
GASP growth advantage in stationary phase
GB glass bead
GBLMA α -gamma butyrolactone methacrylate
GC gas chromatograph
GC-C-IRMS gas chromatography combustion isotope ratio mass
spectrometry
Gd gadolinium
Ge germanium
GEDI μ devices geometrically enhanced differential
immunocapture microdevices
GFET graphene field effect transistor
GHz gigahertz
GI gastrointestinal
GMFI gross mean fluorescence intensity
GMR giant magnetoresistance
GNR gold nanorod
GNR graphene nanoribbons
GPa gigapascal
GPC gel permeation chromatography
GPS global positioning system
GRIN gradient refractive index
GUI graphical user interface
GVD group-velocity dispersion
h hours
H hydrogen
H-NMR hydrogen-1 nuclear magnetic resonance spectroscopy
H₂O₂ hydrogen peroxide
HAMA hydroxyl adamantyl methacrylate
HAuCl₄ chloroauric acid
HBAR high-overtone bulk acoustic resonator
hBN hexagonal boron nitride
HBr hydrogen bromide
hcp hexagonal close packing
HCP1 Heme Carrier Protein 1
He helium
HEMTs high electron mobility transistors
Hf hafnium
HF hydrofluoric acid
HfB₂ hafnium diboride
HFEs hydrofluoroethers
HfO₂ hafnium dioxide
Hg mercury
high- κ high dielectric constant
HMDS hexamethyldisilazane
HMGB high-mobility group box protein
HOMO-LUMO highest occupied molecular orbital
& lowest unoccupied molecular orbital
HOPG highly oriented pyrolytic graphite
HRS high resistance state
HRTEM high-resolution transmission electron microscopy
HS-ssDNA thiol terminated single stranded deoxyribonucleic acid
HSQ hydrogen silsesquioxane
HSQ/FOx negative electron beam resist hydrogen silsesquioxane
Hz Hertz
I-V current-voltage
I/O input/output
IARPA Intelligence Advanced Research Projects Activity
IC integrated circuit
ICP inductively coupled plasma
ICP-MS inductively coupled plasma mass spectroscopy
ICP-RIE inductively coupled plasma reactive ion etcher
IFVD impurity free vacancy diffusion
IGERT Integrative Graduate Education
and Research Traineeship
IGZO indium gallium zinc oxide
IID impurity induced disordering
IIIEI ion implant enhanced interdiffusion
In indium



in situ Latin phrase which translated literally as ‘in position’ — to examine the phenomenon exactly in place where it occurs

in vitro.. . . . Latin for “within glass” — refers to studies in experimental biology that are conducted using components of an organism that have been isolated from their usual biological context in order to permit a more detailed or more convenient analysis than can be done with whole organisms.

in vivo Latin for “within the living” — experimentation using a whole, living organism

InAlN indium aluminum nitride

InAs indium arsenide

InAs NWs indium arsenide nanowires

INDEX Institute for Nanoelectronics Discovery and Exploration

InGaAsN indium gallium arsenide nitride

InGaZnO₄ indium gallium zinc oxide

InP indium phosphide

IPA isopropyl alcohol

IPE Ion & Plasma Equipment, Inc.

IPT in-plane torque

IR infrared

IRMS isotope ratio mass spectrometry

IrO₂ iridium oxide

IrO_x iridium oxide

ISFET ion-sensitive field effect transistor

ITO indium tin oxide

J/m Joules/meter

JP-8 Jet Propellant 8

κ dielectric constant

K Kelvin (a unit of measurement for temperature)

K potassium

kDa kilodaltons

KFM Kelvin force microscopy

kg kilogram

kHz kilohertz

KOH potassium hydroxide

KPFM Kelvin probe force microscopy

L/D length-to-diameter ratio

La lanthanum

LAO lanthanum aluminum oxide

LASSP Laboratory of Atomic & Solid State Physics

LED light-emitting diode

LER line edge roughness

Li lithium

LIDAR light imaging, detection, and ranging

LO local oscillator

low-κ low dielectric constant

LPCVD low pressure chemical vapor deposition

lpm liter per minute

LRS low resistance state

LSPR localized surface plasmon resonance

LTMD layered transition metal dichalcogenide

Lu lutetium

LWGs liquid-core/liquid-cladding waveguides

LWR line width roughness

M-OPTG microring-based optical pulse-train generator

MACE metal-assisted chemical etching

MAMA methyl adamantly methacrylate

MBE molecular beam epitaxy

MCBJ mechanically controllable break junction

MD molecular dynamics

ME magnetoelectric

MEG maleimide-ethylene glycol disulfide

MEMS microelectromechanical systems

MFC microbial fuel

MFMR microfabricated micro-reactors

MgO magnesium oxide

MGs molecular glasses

MHz megahertz

micron micrometer, aka μm

MIFIS+A313 metal-insulator-ferroelectric-insulator-semiconductor

min minutes

ml milliliter

mm millimeter

mM millimolar

MMA-MAA methyl-methacrylate-co-methacrylic acid

mmHg millimeters of mercury; unit of pressure measurement

MnO₂ NPs manganese oxide nanoparticles

Mo molybdenum

MOCVD metal oxide chemical vapor deposition

MONOS metal/oxide/nitride/oxide/semiconductor

MOS metal oxide semiconductor

MoS₂ molybdenum disulfide

MoSe₂ molybdenum diselenide

MOSFET metal oxide semiconductor field effect transistor

MOVPE metal organic vapor phase epitaxy

MPM multiphoton microscopy

MQCA magnetic quantum-dot cellular automata

MQW multiple quantum well

MRA multifunction reconfigurable antenna

MRAM magnetic random access memory

MRFM magnetic resonance force microscopy

MRI magnetic resonance imaging

ms millisecond

MSM metal-semiconductor-metal

MTJ magnetic tunneling junction

mTorr millitorr

mV millivolt

MVD molecular vapor deposition



MWNT multiwalled carbon nanotube
 MΩ megaohms
 N nitrogen
 N₂ nitrous oxide
 nA nanoAmperes
 NaCl sodium chloride
 NASA National Aeronautics & Space Administration
 Nb niobium
 Nb₃Sn triniobium-tin
 NBTC Nanobiotechnology Center, Cornell University
 NCCR National Centers for Research Resources
 NCs nanocrystals
 Nd neodymium
 NEMs nanoelectromechanical systems
 NEXAFS near edge x-ray absorption fine structure
 NH₄F ammonium fluoride
 Ni nickel
 NIDCD National Institute on Deafness
 & Other Communication Disorders
 NIH National Institutes of Health
 NIR near-infrared
 nL nanoliter
 nm nanometer
 NMP n-methyl-2-pyrrolidone
 NMR nuclear magnetic resonance microscopy / spectroscopy
 NNCI National Nanotechnology Coordinated Infrastructure
 NORIS nanometrology optical ruler imaging system
 NPR nonlinear polarization rotation
 NPs nanoparticles
 NPs nanopores
 ns nanosecond
 NSF National Science Foundation
 NSF-SGER .. National Science Foundation Small Grants for
 Exploratory Research
 NSOM near-field scanning optical microscopy
 NSSP nanostructured semipolar
 NV nitrogen-vacancy
 NVM non-volatile memory
 NW FETs ... nanowire field-effect transistors
 NYSTAR ... New York State Office of Science,
 Technology & Academic Research
 O oxygen
 O₃ trioxygen
 OFET organic field effect transistor
 Oh number .. Ohnesorge number
 OLED organic light-emitting diode
 ONO oxide/nitride/oxide
 ONR-MURI Office of Naval Research Multidisciplinary
 University Research Initiative
 OPS optical particle sizer
 OPV organic photovoltaic cells
 OST-MRAM orthogonal spin-transfer magnetic
 random access memory
 OTFT organic thin-film transistor
 P(VDF-TrFE) ... poly[(vinylidene fluoride-co-trifluoroethylene)]
 P/E program/erase
 Pa Pascals
 PAB post-apply bake
 PaC Parylene-C
 PAE power-added efficiency
 PAG photoacid generator
 PAMAM polyamidoamine
 PANOMs ... planarized apertures for near-field optical microscopy
 Pb lead
 PBG photonic bandgap
 PBPK physiologically-based pharmacokinetic
 PbS lead sulfide
 PBS phosphate-buffered saline
 PbSe lead selenide
 PC persistent current
 PC photocurrent
 PCB printed circuit board
 PCBM [6,6]-phenyl-C61-butyric acid methyl ester;
 a fullerene derivative
 PCM phase change material
 PCN photonic crystal nanocavity
 Pd palladium
 PD photodetector
 PDMS polydimethylsiloxane
 PE-GNR polyelectrolyte gold nanorod
 PEB post-exposure bake
 PEC photoelectrochemical
 PECVD plasma enhanced chemical vapor deposition
 PEDOT:PSS.. poly(3,4-ethylenedioxythiophene):
 poly(styrenesulfonate)
 PEG polyethylene glycol
 PEI polyethyleneimine
 pFET p-channel field-effect transistor
 PFM piezo-response force microscopy
 PGMA poly(glycidyl methacrylate)
 pH a measure of the activity of hydrogen ions (H⁺)
 in a solution and, therefore, its acidity
 Ph.D. doctorate of philosophy
 PhC photonic crystal
 PID proportional-integral-derivative
 PL photoluminescence
 pL picoliter
 PLD pulsed laser deposition
 PLGA poly(lactic-co-glycolic) acid
 PMGI poly(methyl glutarimide)



PMMA poly(methyl methacrylate)
PmPV poly(m-phenylenevinylene-co-2,5-dioctoxy-p-phenylenevinylene)
poly-Si polycrystalline silicon
POP polyolefin plastomer
PPM. photolithographic phase masks
PS polystyrene
PS-b-PMMA polystyrene-block-poly(methyl methacrylate)
PSL polysterene latex
PSMO praseodymium strontium manganite
PS μ M phase separation micro-molding
Pt platinum
Pt/Ir platinum/iridium
PtSe₂. platinum diselenide
PTX paclitaxel
PV photovoltaic
PVA poly-vinyl alcohol
PVC polyvinyl chloride
PVD physical vapor deposition
PVDF polyvinylidene fluoride
PVP polyvinylpyrrolidone
Py permalloy, Ni₈₁Fe₁₉
PZT lead zirconate titanate (PbZr_{0.52}Ti_{0.48}O₃)
Q quality factor
QD quantum dots
QW quantum well
QWI. quantum well intermixing
RA. resistance-area
Re number .. Reynolds number
REU Research Experience for Undergraduates Program
RF radio frequency
RF MEMS. radio frequency microelectromechanical systems
RFID radio frequency identification
RIE reactive ion etch
RMS or rms root mean square
RNA. ribonucleic acid
ROS reactive oxygen species
RPEVCD remote plasma-enhanced chemical vapor deposition
RRAM resistive random access memory
RTA rapid thermal anneal
RTD resistance temperature device
RTD resonant tunneling diodes

Ru ruthenium
s seconds
S sulfur
SA-MOVPE selective area metal organic vapor phase epitaxy
SABC surface active block copolymers
SAED selected area electron diffraction
SAMs self-assembled monolayers
SAXS. small angle x-ray scattering
Sb antimony
SBH Schottky barrier height
Sc. scandium
SCAN. single-chromatin analysis at the nanoscale
sccm. standard cubic centimeters per minute
scCO₂ supercritical carbon dioxide
SCOFET single crystal organic field effect transistor
SCORE SNARE Complex Reporter
SDS sodium dodecyl sulfate
Se. selenium
sec. seconds
SECM scanning electrochemical microscopy
SEM scanning electron microscopy / microscope
SERS surface enhanced Raman spectroscopy
SF₆. sulfur hexafluoride
SFLS. supercritical fluid-liquid-solid
SH. second harmonic
Si silicon
Si₃N₄. silicon nitride
SiAlON silicon aluminum oxynitride
SiC silicon carbide
SiH₄ silane
SiN silicon nitride
SiNWs silicon nanowires
SiO₂ silicon dioxide, silica
SIROF. sputtered iridium oxide film
SLBs. supported lipid bilayers
SLG single-layer graphene
SLM. spatial light modulator
SLUG superconducting low-inductance undulatory galvanometer
SML spin memory loss
SMS single molecule spectroscopy
Sn tin
SNARE soluble n-ethylmaleimide-sensitive factor attachment protein receptor complex
SnO₂. tin oxide
SNPs. silver nanoparticles
SNR signal-to-noise ratio
SnSe₂. tin selenide or stannous selenide
SOFC solid oxide fuel cells
SOI silicon-on-insulator
SPCM scanning photocurrent microscopy
SPD switching phase diagram
SPR surface plasmon resonance
SQUID. superconducting quantum interference device
Sr₂RuO₄. strontium ruthenate
SRC Semiconductor Research Corporation



***Cornell NanoScale Science
& Technology Facility***

2017-2018

Research

Accomplishments

Topics in Nano-Biophotonics: Fabrication of Plasmonic Metasurfaces that Attract and Spectroscopically Interrogate Cancer Cells

2018 CNF REU Intern: Vivek Anil

2018 CNF REU Intern Affiliation:

Engineering Science, Physics, The Pennsylvania State University

CNF Project: 2018 Cornell NanoScale Science and Technology Facility Research Experience for Undergraduates Program

CNF REU Principal Investigator: Professor Gennady Shvets, School of Applied and Engineering Physics, Cornell University

CNF REU Mentors: Dr. Steven He Huang, School of Applied and Engineering Physics, Cornell University;

Dr. Maxim Shcherbakov, School of Applied and Engineering Physics, Cornell University

Primary Source of CNF REU Funding: National Science Foundation via the National Nanotechnology

Coordinated Infrastructure (NNCI) Grant No. ECCS-1542081

Contact: vivek3anil@gmail.com, gs656@cornell.edu, hh623@cornell.edu, mrs356@cornell.edu

Website: http://www.cnf.cornell.edu/cnf_2018reu.html

Primary CNF Tools Used: E-beam resist spinners, JEOL 9500, Anatech resist strip, AJA ion mill,

Zeiss Ultra SEM, Zeiss Supra SEM, Even-Hour evaporator, P10 profilometer

Abstract:

Current methods for detecting cancer rely heavily on imaging or tumor markers that are often inaccurate and inefficient. Meanwhile, Fourier transform infrared spectroscopy (FTIR) has been widely studied as a method for label-free biosensing because the characteristic vibrational modes of most biomolecules oscillate at mid-IR frequencies [1]. More recently, plasmonic metasurfaces have drawn interest because they can be engineered to have a resonant electromagnetic response over a broad range of frequencies. Their unique properties enable them to confine light to nanoscale regions (high local field concentration) and have a wavelength-specific response, which is ideal for molecular sensing by spectroscopy [2]. Infrared (IR) plasmonic metamaterials are particularly useful for biosensing: the resonant response of these materials can be tuned to match that of the vibrational modes in biomolecules so that biomolecules can be sensed via surface-enhanced IR spectroscopy. We investigated the use of plasmonic metasurfaces for detection of selected vibrational modes by fabricating gold metasurfaces on an infrared-transparent calcium fluoride (CaF_2) substrate; the metasurfaces were patterned using electron-beam lithography. We successfully fabricated three different types of structures: Fano resonant asymmetric metamaterials (FRAMMs), nanoantennae, and nanoslits, and validated the presence of resonance peaks by performing FTIR on the metasurfaces to obtain reflectance spectra. By adjusting the structures' dimensions, the resonances (quality factor $Q \sim 10$) seen in each structure's reflectance spectra were tuned to match the amide I ($\sim 1650 \text{ cm}^{-1}$) and carbohydrate ($\sim 2900 \text{ cm}^{-1}$) molecular resonances, which are present in cells. Our results demonstrate the potential to develop an improved method of cancer detection via surface-enhanced IR spectroscopy with engineered plasmonic metasurfaces.

Summary of Research:

Introduction. Biomolecular components in cells possess characteristic vibrational modes in the IR, which can be spectroscopically probed to obtain information from cells [1]. The signals from these vibrational modes are often weak, and so we propose using a plasmonic metasurface to enhance these signals. The dimensions and spatial arrangements of the structures were chosen such that the metasurface resonated at frequencies similar to cellular vibrations. Each set of structures with the same dimensions were fabricated together, with consistent spacing between structures, in squares, called pixels. This was done for the sake of testing simplicity: each pixel could be probed as an individual metasurface, and so we could assess how well each set of dimensions enabled us to tune to a particular resonance.

Fabrication. For the FRAMMs and nanoantennae, the fabrication process was as follows: CaF_2 wafers were washed and dried thoroughly, and then $\sim 240 \text{ nm}$ PMMA was spin-coated onto the wafers. The wafer was then baked at 170°C . We patterned the metasurface using the JEOL 9500 electron-beam lithography system. We developed the PMMA from the patterned areas using a methyl isobutyl ketone-isopropanol developer (MIBK:IPA 1:3). We evaporated 10 nm Cr and 70 nm Au onto the substrate at 1 A/s each. Remaining PMMA was lifted-off in an overnight acetone bath. The process for fabricating nanoslits was similar, except that we evaporated Au between cleaning and spin-coating, and added an extra ion mill etching step after development and before lift-off.

FTIR Experiment. The metasurface was integrated into a polydimethylsiloxane microfluidic chamber; a solution — phosphate buffer saline (PBS), ethanol, or DI water — was injected into the chamber, and an IR spectroscopy was done on the metasurface (probing pixel by pixel) in the chamber using a Bruker-Hyperion FTIR-microscope system.

Results and Conclusions:

We were able to successfully tune our FRAMM (pi structure) and nanoantenna resonances to the desired frequencies, as seen in Figure 1 — where the “Pi_5” ($d = 225.1 \text{ nm}$ and $L = 1.727 \mu\text{m}$ as in Figure 2a) and “Nanoantenna_2” ($w = 234.8 \text{ nm}$ and $L = 1.693 \mu\text{m}$ as in Figure 2b) pixels resonate at the amide I frequency ($\sim 1650 \text{ cm}^{-1}$) and the “Pi_3” ($d = 66.19 \text{ nm}$ and $L = 0.9555 \mu\text{m}$ as in Figure 2a) and “Nanoantenna_1” ($w = 238.3 \text{ nm}$ and $L = 0.9624 \mu\text{m}$ as in Figure 2b) pixels resonate at the carbohydrate frequency ($\sim 2900 \text{ cm}^{-1}$). In general, we saw that as we increase the size of FRAMM structures, we decrease the position of the resonant frequency (Figure 3); this relationship proved useful for tuning resonances.

We also successfully fabricated nanoslits and adjusted structure dimensions ($w \sim 50 \text{ nm}$ and $L \sim 700 \text{ nm}$ for “slit_1” and $w \sim 50 \text{ nm}$ and $L \sim 1500 \text{ nm}$ for “slit_2”) such that we observed the interference between the nanoslit peaks and the deionized (DI) water ($\sim 1660 \text{ cm}^{-1}$ and 3400 cm^{-1}) and ethanol ($\sim 3000 \text{ cm}^{-1}$ and 3400 cm^{-1}) resonances (Figure 4). Figure 4 suggests the potential for biosensing by tuning resonances to observe similar interference between biomolecular vibrations in cells and our metasurfaces’ resonances. Furthermore, integrating our metasurface into the microfluidic chamber shows even more promise for developing a device for biosensing by surface-enhanced spectroscopy.

Future Work:

Future work will include refining nanoslit fabrication and resonance tuning, attaching cancer cells to the metasurface and performing FTIR to obtain biomolecular information from cells, comparing nanoantennae and nanoslits to determine which shows greater near field enhancement, and analyzing spectra to understand how we can use them to distinguish between healthy and cancerous cells.

Acknowledgements:

I would like to thank my PI, Prof. Gennady Shvets, my mentors, Dr. Steven Huang and Dr. Maxim Shcherbakov, CNF staff, and the National Science Foundation (NNCI Grant No. ECCS-1542081) for giving me the opportunity to participate in this Research Experience for Undergraduates Program.

References:

- [1] Baker, M. J., et al. (2014). Using Fourier transform IR spectroscopy to analyze biological materials. *Nature Protocols*,9, 1771-1791.
- [2] Wu, C., et al. Fano-resonant asymmetric metamaterials for ultrasensitive spectroscopy and identification of molecular monolayers. *Nature Materials*,11(1), 69-75.

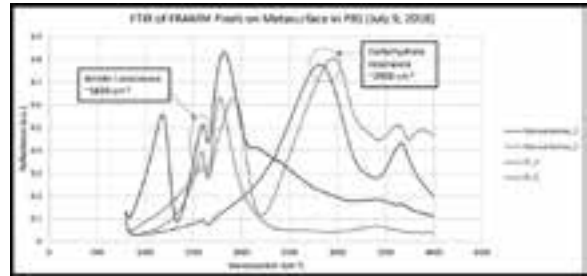


Figure 1: Reflectance spectra of FRAMM and nanoantenna pixels in PBS, tuned to match amide I and carbohydrate resonances.

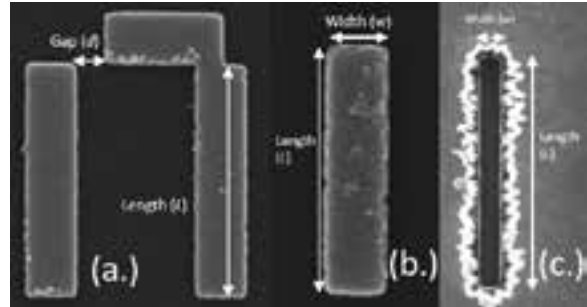


Figure 2: Scanning electron microscopy images (taken at 20.00 kV) of (a) FRAMM (pi), (b) nanoantenna, and (c) nanoslit structures.

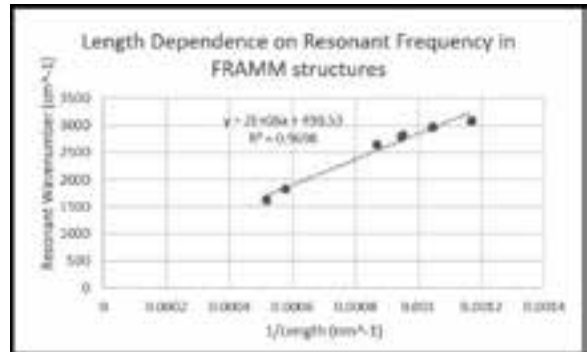


Figure 3: Relationship between length and position of the resonance seen in reflectance spectra for FRAMMs in PBS.

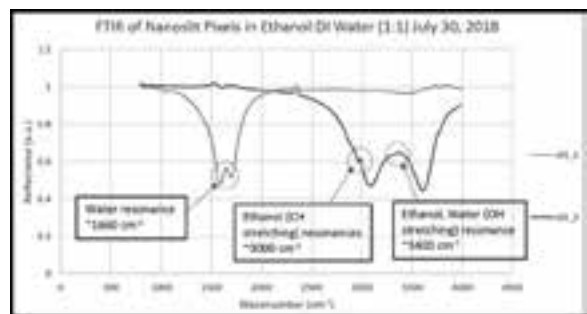


Figure 4: Reflectance spectra for 50 nm wide nanoslits in ethanol-DI water mixture showing water and ethanol resonances.

Microfluidic Mixer for Time-Resolved Single-Molecule Fluorescence Experiments using Flip-Chip Bonded SU-8 Structures

CNF Project Number: 692-98

Principal Investigator: Lois Pollack

User: Alexander Plumridge

Affiliation: Applied and Engineering Physics, Cornell University

Primary Source of Research Funding: National Institute of Health

Contact: LP26@cornell.edu, ap866@cornell.edu

Website: <https://pollack.research.engineering.cornell.edu/>

Primary CNF Tools Used: ABM contact aligner, class 2 resist room, VersaLaser engraver/cutter

Abstract:

We report the fabrication procedure for a microfluidic mixer capable of detecting single, fluorescently labeled biological molecules as they progress through a reaction. Precise flow control and device longevity is achieved using hard materials (SU-8) for fabrication, in place of traditional replica molding.

Summary of Research:

Single-molecule fluorescence experiments are powerful tools for elucidating structural characteristics of biological molecules [1]. Techniques such as fluorescence correlation spectroscopy (FCS) report global molecular size, while Förster resonance energy transfer (FRET) experiments yield distances between labelled residues with Angstrom precision. Critically, these techniques can probe single-molecules, granting detailed information about the underlying population that is smeared out in a bulk measurement. Long measurement times are required to gather statistics from a small ($1 \mu\text{m}^3$) focal volume, often requiring tens of minutes of data acquisition per condition.

While single-molecule experiments are routinely performed at equilibrium, the dynamic nature of biology demands an approach that embraces the time evolution of these systems. A typical strategy to provide time-resolution in fluorescence experiments exploits microfluidic mixing (e.g., ref 2). Molecules are rapidly introduced to initiate a reaction, then spatially separated to provide time-resolution. These technologies are limited to bulk measurements due to the flow speed and exposure times associated with these devices. Furthermore, the length of time required to obtain a single-molecule data set (typically several hours), paired with the pressures required to precisely control the flow ($\sim 1000\text{-}5000 \text{ mbar}$) presents challenges for conventional soft material approaches, though some have been developed and applied [3]. To meet these criteria, we designed and fabricated microfluidic devices from SU-8

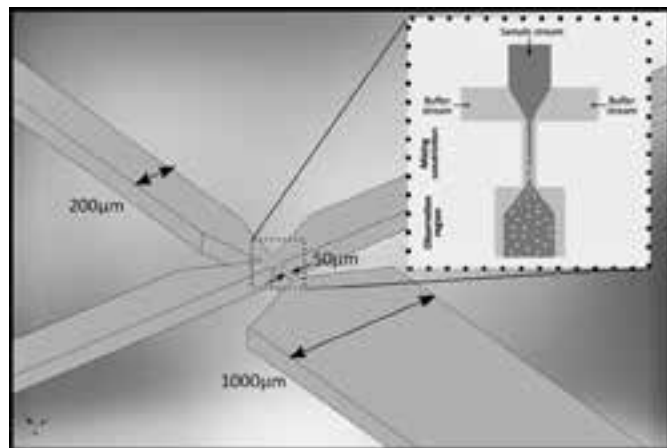


Figure 1: The device design (main panel) is based on the principle of hydrodynamic focusing (inset).

to rapidly mix reagents, then subsequently slow the flow speed to a range compatible with single-molecule detection ($\sim \mu\text{m}/\text{ms}$).

The device design is based on the hydrodynamic focusing principle (Figure 1 inset), where a sample stream is squeezed by flanking buffer streams and forced through a narrow constriction [4]. This yields a micron-sized sample stream in the constriction. Diffusion occurs rapidly across this stream, introducing a reactant from the buffer that initiates a given reaction. This narrow stream is then expanded out into a wide probing channel, which



Figure 2: Stereoscopic image of a completed device.

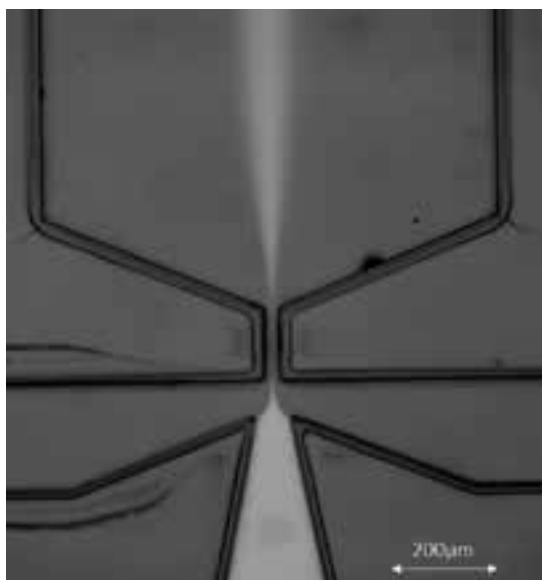


Figure 3: False colored fluorescent image showing a test sample (fluorescent dye Rhodamine 6G, bright) flowing in the device.

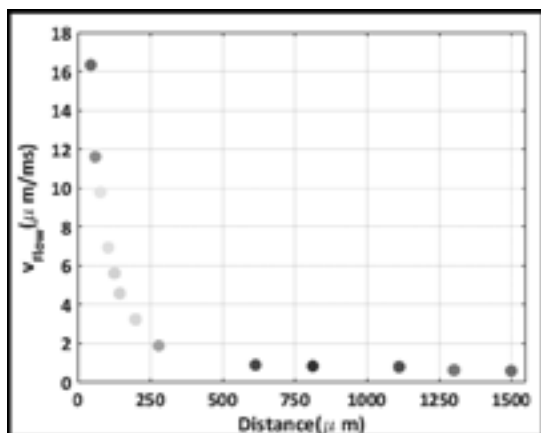


Figure 4: Flow speeds (in microns per millisecond) as a function of distance from the end of the constriction as measured by FCS.

acts to slow the flow speed down to detectable levels. Probing at different spatial locations along the observation channel provides different time delays after the reaction is initiated.

The design in Figure 1 was first replicated in a chrome mask using the Heidelberg 6600 mask writer. The device is then fabricated from four layers: two glass layers that act as windows on the top and bottom, one layer of SU-8 that defines the channel geometry, and one sealing SU-8 layer. In the first process, a 100 μm thick layer of SU-82050 is spun on borofloat, and subsequently exposed, baked and developed to yield the channel geometry. A thin sealing layer of SU-82005 is next deposited over the existing geometry, and a glass cover slide installed on top of this layer. The stack is then baked and exposed through the glass cover slide with the same mask used to pattern the channel geometry. This step acts to polymerize the sealing SU-8 2005 layer in all regions except the underlying channels. Excess SU-8 from the sealing layer that may have entered the channels is then removed by development, yielding fluidic channels which are sealed, clear and flanked solely by glass. A stereoscopic image of a completed device is shown in Figure 2.

To demonstrate the device and flow stream, we used a fluorescent dye (Rhodamine 6G), to act as a control sample, and water on the flanking buffer channels. Figure 3 shows a false colored image of this experiment, where fluorescence intensity is denoted by brightness. The sample stream clearly shrinks in the mixing constriction, before slowing and expanding in the observation region. Measurements of the sample jet widths in the constriction place it between 5-9 μm depending on the flow rates. This results in tunable mixing times between 4-10 ms for added salts and small molecules.

Finally, the flow speed in the observation region can be probed by FCS (Figure 4). For the test system of Rhodamine 6G, the flow can be reduced to less than 1 $\mu\text{m/ms}$, easily compatible with the dwell time required for confocal microscopy. For this system, the flow in the observation region slowed to single-molecule detectable levels at a time point corresponding to 30 ms after mixing is complete. Thus, in this case the device can access time points ranging from 30-3000 ms in the single-molecule regime.

The mixer lends itself well to our future applications in studying the non-equilibrium collapse of regulatory RNA elements. These motifs sense metabolites and ion levels in the cell, and drastically alter their conformation depending on the ligand concentration [5]. Molecular re-arrangements occur on time-scales ranging from 10 ms to many seconds, but detailed characterization of the sub second structural response is lacking due to the absence of appropriate experimental technology.

References:

- [1] Joo, C., et al., *Annu. Rev. Biochem.* 2008, 77 (1), 51-76.
- [2] Park, H. Y.; Qiu, X.; Rhoades, E.; Korlach, J.; Kwok, L. W.; Zipfel, W. R.; Webb, W. W.; Pollack, L. *Anal. Chem.* 2006, 78 (13), 4465-4473.
- [3] Gambin, Y.; Vandellinder, V.; Ferreón, A. C. M.; Lemke, E. A.; Groisman, A.; Deniz, A. A. *Nat. Methods* 2011, 8 (3).
- [4] Knight, J, et al., *Phys. Rev. Lett.* 1998, 80 (17), 3863-3866.
- [5] Montange, R. K.; Batey, R. T. *Annu. Rev. Biophys.* 2008, 37, 117-133.

Body-on-a-Chip Systems for Drug Development

CNF Project Number: 731-98

Principal Investigators: Michael L. Shuler, Harold G. Craighead

Users: Ying Wang, Paula Miller, Danielle LaValley

Affiliations: Nancy E. and Peter C. Meinig School of Biomedical Engineering, Robert Frederick Smith School of Chemical and Biomolecular Engineering; Cornell University

Primary Sources of Research Funding: National Center for Advancing Translational Sciences, National Science Foundation, National Institutes of Health

Contact: MLS50@cornell.edu, hgc1@cornell.edu, ying.wang@cornell.edu, pgm6@cornell.edu, DJL339@cornell.edu

Primary CNF Tools Used: VersaLaser Engraver/Cutter tool, ABM contact aligner, SU-8 hot plates, SUEX/ADEX laminator, PDMS casting station, hot press

Abstract:

Organ-on-a-chips are tissue-engineered microsystems that mimic human organs, modeling both structure and function [1]. Human cell-based multi-organ-on-a-chip systems, or body-on-a-chips (BOC), could be a paradigm-shifting technology for drug development [2]. Such microscale biomimetics of human organs with organ-organ interactions hold the promise to simulate human physiology and disease progression, and thus offer more accurate predictions of human responses to therapeutics and provide mechanistic insights into human diseases, while significantly reduce drug development cost and animal usage. Currently, we are developing several BOC systems, which are fabricated with tools at CNF and will be used to study chemotherapeutic toxicity, model cancer cell metastasis, and simulate immune responses.

Summary of Research:

Tumor-Liver-Bone Marrow Chip. A three-organ microphysiological system has been created to study chemotherapeutic toxicity with relevant drug metabolism and hematological side effects. The device contains three chambers for seeding HCT-116 colon tumor spheroids, HepG₂/C3A hepatocytes, and HL-60 promyeloblasts encapsulated within 3D hydrogels. Microfluidic channels were etched into a layer of poly (methyl methacrylate) (PMMA) and designed to mimic human blood flow rates [3-5]. The silicone cell culture layer and PMMA channel layer were sandwiched between silicone gaskets and outer PMMA housing pieces. All layers were fabricated using the VersaLaser CO₂ laser cutter at CNF. Utilizing gravity-driven flow on a customized programmable rocker, a common medium is recirculated between the two reservoirs.

Colon-Liver Chip. We have developed a colon-liver dual-organ-on-a-chip system to model colorectal cancer (CRC) liver metastasis. The microphysiological system is based on a pumpless platform [6,7]. Two organ chambers representing colon and liver are interconnected and perfused with gravity-driven flow at physiological perfusion rates.

The device is fabricated mainly in PMMA with silicone (gaskets) for sealing. PMMA and silicone sheets are patterned with laser ablation using the VersaLaser CO₂ laser cutter at CNF. The flow dynamics are characterized computationally and experimentally. Flow rates were measured to be within 15% of the designed values. The prototype devices tested with colon and liver cells maintained greater than 85% cell viability.

Using this colon-liver platform, we will incorporate organotypic CRC model and 3D liver constructs and investigate the metabolic stress due to CRC liver metastasis. We will investigate the cellular interaction, differentiation, migration and invasion of primary tumor and metastatic fibroblast tumor microenvironment to evaluate contributing factors in CRC metastasis.

A 5-Compartment Microphysiological System for Drug Screening. We developed a 5-organ BOC system to emulate *in vivo* drug absorption, distribution, metabolism and toxicity, as well as immune responses. The five organ chambers represent bone marrow, inflamed spleen, GI tract, liver and kidney (Figure 1). The 5-Organ Chip consists of five layers: a top cover layer and a bottom

channel layer made of PMMA, a cell chamber layer and a flow dispersion layer made of silicone, and a porous polycarbonate membrane (Figure 1).

The top cover layer and the two silicone layers were patterned using the VersaLaser CO₂ laser cutter at CNF. The bottom PMMA channel layer was fabricated using photolithography and hot embossing. The channel layer pattern was first transferred from a photomask to SUEX epoxy thick dry film using a laminator and standard photolithography technique. A polydimethylsiloxane (PDMS) replica was then created from the SUEX master and was silanized under vacuum overnight. A heat resistant epoxy mold for hot embossing was then created from the silanized PDMS mold using a high-temperature epoxy casting system. The PMMA channel layer was fabricated using a hot press at CNF as shown in Figure 2. The molded PMMA plate was then cut with the VersaLaser to form the channel layer. The assembled device is transparent and allows for real time optical interrogation.

This five-chamber device is being used to study preclinical anti-leishmaniasis drug toxicity and response.

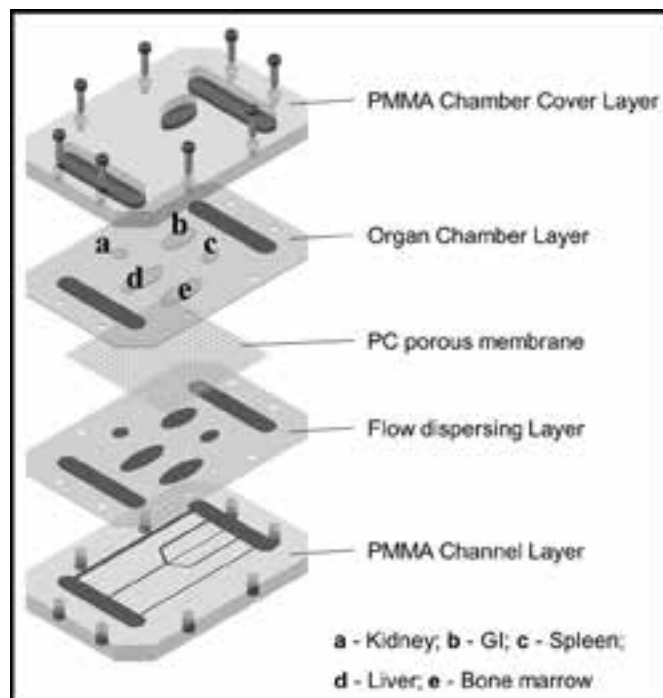


Figure 1: Design of the 5-compartment microphysiological system. Schematic exploded view of the microfluidic platform.

References:

- [1] NIH/NCATS. What are tissue chips, and why are they important? <https://ncats.nih.gov/tissuechip/about/faq#chips>.
- [2] Wang YI, Carmona C, Hickman JJ, Shuler ML. Multiorgan Microphysiological Systems for Drug Development: Strategies, Advances, and Challenges. *Adv Healthc Mater.* 2018;7(2):1701000. doi:10.1002/adhm.201701000.
- [3] Price PS, Conolly RB, Chaisson CF, Gross EA, Young JS, Mathis ET, Tedder DR. Modeling interindividual variation in physiological factors used in PBPK models of humans. *Crit Rev Toxicol.* 2003;33(5):469-503. doi:10.1080/713608360.
- [4] Brown RP, Delp MD, Lindstedt SL, Rhomberg LR, Beliles RP. Physiological Parameter Values for Physiologically Based Pharmacokinetic Models. *Toxicol Ind Health.* 1997;13(4):407-484. doi:10.1177/074823379701300401.
- [5] Forrester DW, Spence VA, Walker WF. The measurement of colonic mucosal submucosal blood flow in man. *J Physiol.* 1980;299(1):1-11. doi:10.1113/jphysiol.1980.sp013106.
- [6] Wang YI, Oleaga C, Long CJ, Esch MB, McAleer CW, Miller PG, Hickman JJ, Shuler ML. Self-contained, low-cost Body-on-a-Chip systems for drug development. *Exp Biol Med.* 2017;(November):153537021769410. doi:10.1177/1535370217694101.
- [7] Sung JH, Kam C, Shuler ML. A microfluidic device for a pharmacokinetic-pharmacodynamic (PK-PD) model on a chip. *Lab Chip.* 2010;10(4):446. doi:10.1039/b917763a.

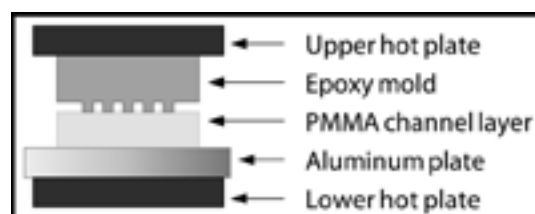


Figure 2: PMMA sheet and epoxy mold assembly for PMMA channel layer fabrication using hot embossing.

Micropillar-Based Microfluidic Device for Cell Capture and DNA Analysis

CNF Project Number: 762-99

Principal Investigator: Harold G. Craighead

User: Harvey C. Tian

Affiliation: Applied and Engineering Physics, Cornell University, Ithaca

Primary Source of Research Funding: Cornell University

Contact: hgc1@cornell.edu, hct33@cornell.edu

Primary CNF Tools Used: Unaxis, ABM contact aligner, photoresist spinning and baking stations

Abstract:

We present a valveless dual-channel microfluidic device for targeted cell capture, imaging, and on-chip DNA analysis. The two channels are positioned with a perpendicular intersection filled by an array of micropillars. These micropillars are functionalized with DNA aptamers, analogous to antibodies, which are used to bind targeted cells such as cancer cells. These bound cells can then be imaged in place or lysed to extract their DNA for further analysis. Our past work has demonstrated high efficiency DNA extraction using micropillar arrays from varying cell counts (hundreds) down to a single cell [1] as well as an improvement to DNA amplification uniformity as compared to conventional methods. Here, we sought to integrate the various capabilities published in our previous work into a single device. We report the device's ability to perform cancer-cell specific capture with the DOV4 aptamer as well target-specific isothermal amplification [2]. Furthermore, we expanded upon our previous year's DNA amplification work to show an improved amplification uniformity in single cell whole genome amplification as measured by exome sequencing. We report a 33.5% improvement in genome mapping and up to 81.08% genome coverage at 10x read depth [3].

Summary of Research:

The dual-channel device shown in Figure 1 is composed of two perpendicularly intersecting microfluidic channels. One channel is designed for cell loading and surface functionalization of micropillars while the other channel is designed for DNA lysis. The intersection of the two channels, shown in Figure 1 (left panel), contain an array of 50 μm diameter pillars rotated 4° to increase cell-pillar collision rates during cell capture. These capture cells are then lysed towards the direction of a second pillar array region consisting of densely spaced 1.5 μm diameter pillars, shown in Figure 1 (right panel).

Through functionalizing the 50 μm diameter pillars with DNA aptamer DOV4 which has been reported as a cancer-cell specific aptamer [4], we were able to capture two cancer cell lines tested, HeLa human cervical cancer cell line and CAOV-3 human ovarian cancer cell line. Our positive controls, performed with human non-cancer ovarian cell lines Ect1/E6E7 and End1/E6E7 did not bind to the DOV4 micropillars indicating successful aptamer driven cell capture. Figure 2 then shows our ability to lyse the captured cells, in this case CAOV-3 cells, and stain and image the DNA in-channel.

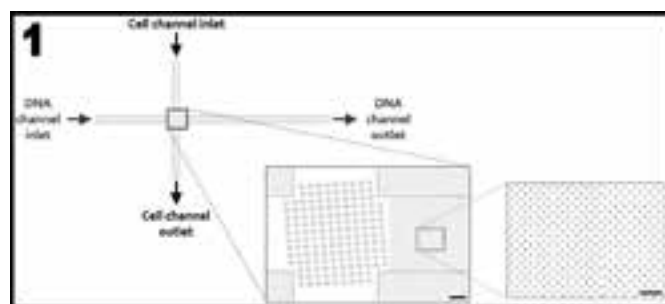


Figure 1: Dual-channel device.



Figure 2: Shows our ability to lyse the captured cells, in this case CAOV-3 cells, and stain and image the DNA in-channel.

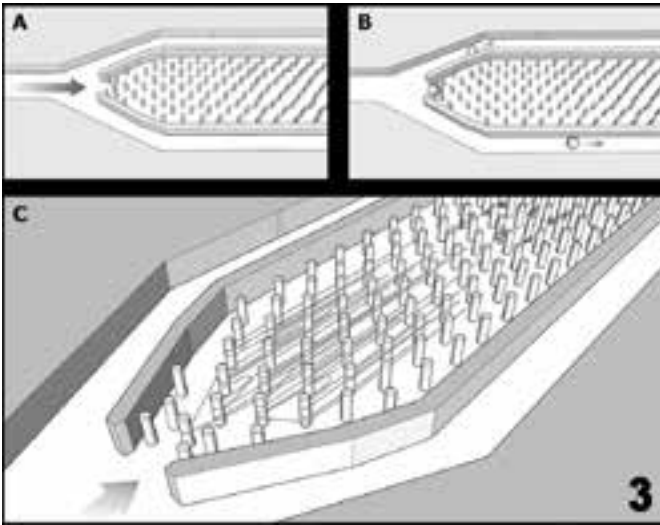


Figure 3: Cartoon of DNA amplification device.

Our DNA amplification device, as depicted by the cartoon representation in Figure 3(A), contains a micropillar array region enclosed by a barrier. At the front of the barrier is an opening wide enough to fit a single cell. In Figure 3(B), a suspension of human cervical cancer cells (HeLa cells) are loaded into the input single cells were captured at the apex of the micropillar array while excess uncaptured cells flow through to the output ports where they were removed. Upon introducing a cell lysis agent into the channel Figure 3(C), the genomic DNA of entrapped cell become physically entangled on the micropillars immediately downstream from the original position of the cell and this gDNA can be used for in-channel chemistries such as DNA amplification or be directly imaged on-chip after fluorescence DNA staining.

The extracted gDNA can then be isothermally whole genome amplified on-chip using commercially available multiple displacement amplification (MDA) reagents. Because the amplified DNA fragments are below the size threshold necessary to become entangled upon the 2 μm diameter micropillars, they flow through the pillars and can be collected at the output port at the end of the amplification.

To assess amplification bias, we compared our amplified DNA pools to DNA amplified within a 96-well plate from single cell isolated through fluorescence activated cell

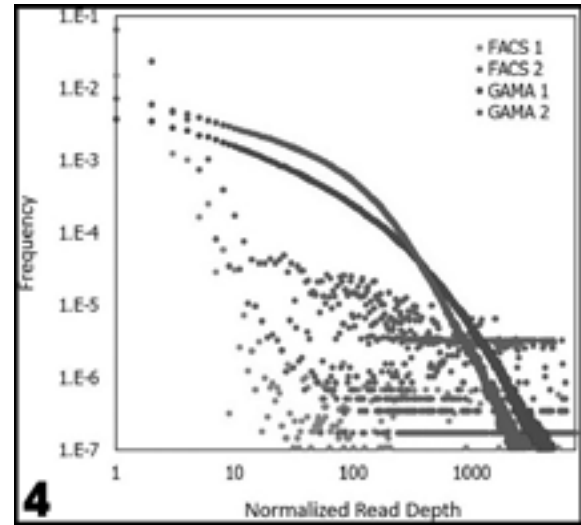


Figure 4: Two on-chip single cell samples.

sorting (FACS). From analyzing the exome sequencing data on more than 20,000 loci across the genome, we determined that we were able to map 98.5% of the reads from our on-chip samples whereas control samples with FACS only reached 65.0% reads mapped.

Shown in Figure 4, the two on-chip single cell samples show a slower decaying distribution of read count as depth increases indicating much more uniform amplification of the genome. Furthermore, we were able to cover 70.35% of the loci with a 1x read depth and 80.8% of the loci with a 1x read depth, comparable to other leading single cell DNA amplification technologies.

References:

- [1] "Microfluidic extraction, stretching and analysis of human chromosomal DNA from single cells", JJ Benitez, J Topolancik, HC Tian, CB Wallin, DR Latulippe, K Szeto, PJ Murphy, BR Cipriany, SL Levy, PD Soloway, HG Craighead, Lab Chip, (2012).
- [2] "Microfluidic Device for Aptamer-Based Cancer Cell Capture and Genetic Mutation Detection", S. J. Reinholt, H. G. Craighead, Analytical Chemistry, (2018).
- [3] "Single cell on-chip whole genome amplification via micropillar arrays for reduced amplification bias", H. C. Tian, J. J. Benitez, H. G. Craighead, PLOS One, (2018).
- [4] "Study of the Molecular Recognition of Aptamers Selected through Ovarian Cancer Cell-SELEX", D. V. Simaey, D. Lopez-Colon, K. Sefah, R. Sutphen, E. Jimenez, W. Tan, PLOS One, (2010).

The Number of SNARE Complexes Changing Conformation in Vesicle Fusion Events

CNF Project Number: 848-00

Principal Investigator: Manfred Lindau

Users: Ying Zhao, Qinghua Fang

Affiliations: 1. Applied and Engineering Physics, Cornell University; 2. Laboratory for Nanoscale Cell Biology, Max Planck Institute for Biophysical Chemistry, D-37077 Göttingen, Germany

Primary Research Funding: NIH Grant GM085808 (to M.L.) and, MH060600 (to W.A.), European Research Council Advanced Grant No. 322699 (to M.L.), NSF Grant ECS-0335765

Contact: ML95@cornell.edu, yz86@cornell.edu, qf24@cornell.edu

Primary CNF Tools Used: Heidelberg Mask Writer DWL2000, ABM Contact Aligner, Oxford 81 Etcher, Oxford PECVD, Dicing Saw - DISCO

Abstract:

The SNARE complex is a core component of the fusion nanomachine, and the zipping of SNARE complexes is thought to provide the force and energy to overcome the energy barrier for membrane fusion. Here, the SNARE Complex REporter2 (SCORE2), a FRET probe of SNAP25, was overexpressed to detect the SNARE complex conformation change during the membrane fusion. Time and location of individual fusion events were detected using microfabricated ElectroChemical Detector (ECD) arrays. Our studies show, under endogenous condition, there are approximately seven (26% of 26.4) endogenous SNAP25 molecules change the conformational during the membrane fusion.

Summary of Research:

In previous studies, we have detected a SNARE conformational change preceding the fusion pore opening [1] in SCORE2 overexpressing SNAP25 KO mouse chromaffin cells. *In vitro* studies [2] have shown that SCORE2 molecules can exhibit the highest FRET efficiency in the presence of excess syntaxin and synaptobrevin 2 by forming the SNARE core complex. In our *in vivo* experiments, the low FRET efficiency of SCORE2 was determined in SCORE2-alone overexpressing. To estimate the *in vivo* high SCORE2 FRET efficiency, SCORE2 were co-expressed with high level of syntaxin by introducing IRES in the transfection construct. By photobleaching the FRET acceptor Venus in both, the low and the high FRET states, the FRET_{high} and FRET_{low} efficiencies were determined as 0.38 (E_{high}) and 0.21 (E_{low}), respectively.

The FRET ratio R can be expressed as a simplified function of FRET efficiency E [2].

$$R = A + B \times \frac{E}{1-E} \quad (1)$$

The measured FRET ratios in the low and high FRET states are R_{low} = 1.01 and R_{high} = 1.85, respectively. Based

on the values of E_{low,high} and R_{low,high}, the coefficients A and B are calculated as 0.37 and 2.42, respectively.

The pre- and post-fusion FRET ratios at the fusion sites R = 1.066 and R = 1.184 [1] correspond to pre- and post-fusion FRET efficiencies of 0.223 and 0.252, respectively, indicating a FRET efficiency increase preceding vesicle fusion within a in a 0.1 μm² area surrounding the fusion site. Assuming that the different apparent FRET efficiencies reflect different fractions of SCORE2 molecules in the two distinct FRET states, the fluorescence intensity ratio becomes

$$R = A + B \times \frac{E_{low} + \alpha \times (E_{high} - E_{low})}{1 - [E_{low} + \alpha \times (E_{high} - E_{low})]} \quad (2)$$

where α is the fraction of molecules in the high FRET state. The fraction α can be calculated from the apparent FRET efficiency

$$E_{app} = E_{low} + \alpha \times (E_{high} - E_{low})$$

$$\alpha = \frac{E_{app} - E_{low}}{E_{high} - E_{low}} \quad (3)$$

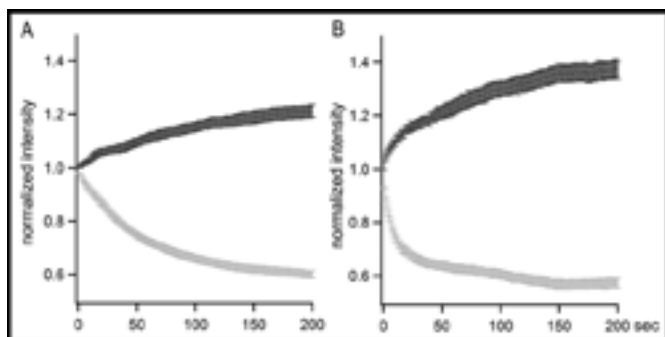


Figure 1: Determination of FRET efficiency by acceptor photobleaching. SCORE2 molecules alone (A) or with 10-fold higher Syntaxin (B) were overexpressed in SNAP25⁺ mouse embryonal chromaffin cells and alternately excited for 100 ms at 442 nm in laser TIRF mode while images were acquired and for 1s with epifluorescence lamp excitation at 510/20 nm to bleach the acceptor. Intensities of Venus and mCerulean3 recorded from individual cells were normalized to the respective values before bleaching and the averaged increase in the mCerulean3 channel indicates an average basal and high FRET efficiency of 21% and 38%, respectively.

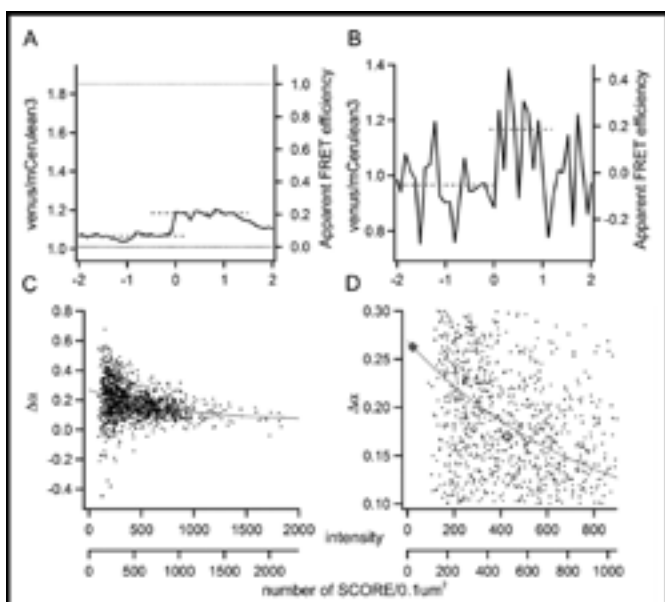


Figure 2: The fraction of SNAP25 molecules undergoing a conformational change as a function of expression level. FRET efficiency changes of all averaged fusion events (A) and of a single event (B), FRET ratio and corresponding apparent FRET efficiency before and after the fusion indicated by red dotted lines. (C-D) plots of $\Delta\alpha$ of individual events versus corresponding mCerulean3 intensities fitted by a single exponential (continuous red line). The open and filled red diamonds indicate the averaged $\Delta\alpha$ at average overexpression level and endogenous SNAP25 level, respectively.

According to equation (3), pre and post-function FRET efficiencies of 0.227 and 0.259 correspond to a value of α 0.076 and 0.247 (Figure 2A), suggesting that $\sim 17\%$ ($\Delta\alpha = E_{\text{app,post}} - E_{\text{app,pre}}$) of the SCORE2 molecules undergo a conformational transition from the low FRET state to the high FRET state just before fusion. With 500 SCORE2 molecules present in the fusion area at typical overexpression levels (data not shown), this corresponds to 85 molecules.

Immunostaining shows, however, that the overexpression level of SCORE2 molecules was ~ 19 fold higher than the amount of wild type SNAP25 molecules in untransfected wt cells, suggesting that only ~ 26 endogenous SNAP25 molecules are present at the vesicle fusion site.

To estimate the number of endogenous SNAP25 molecules undergoing conformational change during fusion, the change of α ($\Delta\alpha$) was calculated for individual events (Figure 2B) and was plotted versus corresponding FRET donor (mCerulean3) intensities at releasing sites, indicating the expression level (Figure 2C).

Due to the low signal-to-noise ratio of individual events the points scatter widely (Figures 2C and 2D), but can be fitted well with a single exponential. In wild type cells we estimate ~ 26 SNAP25 molecules. Extrapolating the fit to this value, the $\Delta\alpha$ value of 0.26 is obtained, suggesting that on average, approximately seven endogenous SNAP25 molecules (26% of 26) undergo a conformational change before a fusion event.

References:

- [1] Zhao Y., et al., SNARE conformational change precedes the fusion pore opening. CNF report 2017.
- [2] An, S. J., and Almers, W. (2004) Tracking SNARE complex formation in live endocrine cells. *Science* 306, 1042-1046.
- [3] Zhao, Y., Fang, Q., Herbst, A. D., Berberian, K. N., Almers, W., and Lindau, M. (2013) Rapid structural change in synaptosomal-associated protein 25 (SNAP25) precedes the fusion of single vesicles with the plasma membrane in live chromaffin cells. *Proceedings of the National Academy of Sciences of the United States of America* 110, 14249-14254.

Nanoneedles for Intracellular Measurements

CNF Project Number: 900-00

Principal Investigator: Paul L. McEuen

Users: Samantha Norris, Yanxin Ji, Alejandro Cortese

Affiliations: Department of Physics, Department of Electrical and Computer Engineering; Cornell University

Primary Source of Research Funding: Multi-University Research Initiative Grant FA2386-13-1-4118

Contact: plm23@cornell.edu, sn588@cornell.edu, yj323@cornell.edu, ajc383@cornell.edu

Website: <http://www.mceuengroup.lassp.cornell.edu/>

Primary CNF Tools used: Odd/even evaporators, Oxford 81 and 100 reaction ion etchers, ABM contact aligner, AJA sputter tool

Abstract:

The ability to measure a cell's membrane potential is crucial to understanding many cellular characteristics such as excitability, intracellular kinetics, and networking behavior. We report on the fabrication of releasable nanoneedle devices for insertion into a cell.

Summary of Research:

Sharp electrode intracellular recording is a standard technique involving piercing the cellular membrane with a micropipette filled with conductive fluid; this micropipette typically has a sub-micron diameter [1].

To more readily investigate the size-scale at which needle insertion can damage or kill cells, we have produced nanoneedle devices that can be released from a substrate, picked up with a micromanipulator, and inserted into cells. Each fabrication layer in the process uses standard photolithographic techniques and all layers are exposed with the ABM contact aligner. The final device before release is depicted in Figure 1.

Devices were fabricated on silicon-on-insulator wafers (SOI) allowing for release of the completed unit after fabrication. The nanoneedles protruding out of the end of the device were made by e-beam evaporation of platinum with a titanium adhesion layer (Ti-Pt) at a 70° angle, to allow for a nanoneedle width smaller than the minimum pattern width achievable with the contact aligner. A scanning electron microscope (SEM) image of a nanoneedle is shown in Figure 2.

After patterning of aluminum release tabs, the Xactix xenon difluoride etcher was then used to etch the silicon handle, resulting in suspended devices. The aluminum was then selectively etched to release the nanoneedle devices into solution. Free-floating devices could then be pipetted up using a standard hand pipette, and dispersed into fluid.

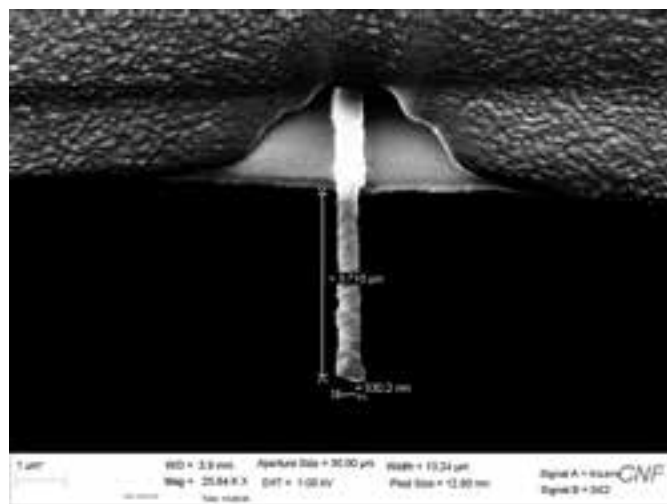
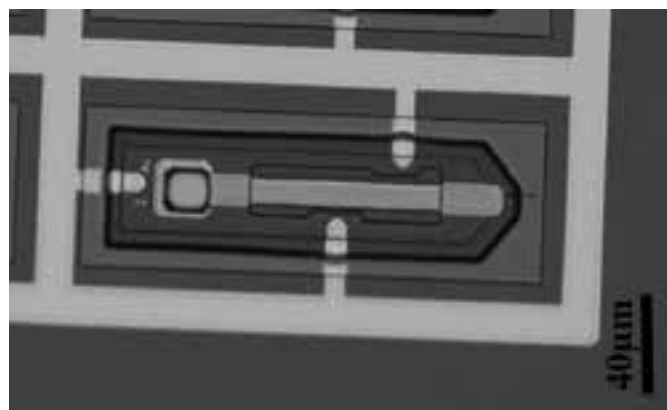


Figure 1, top: An optical microscope image of a completed nanoneedle device. **Figure 2, bottom:** An SEM image of a typical nanoneedle after evaporation.

Although devices survive the full process with remaining nanoneedles, the xenon difluoride etching the oxide under the needles and the pipetting force used cause many needles to break off.

To test the ability of our devices to penetrate the cellular membrane without causing cell death, we cultured HL-1 cardiomyocytes in Petri® dishes. When the cells were approaching confluence, we used a pipette to disperse the nanoneedle devices into the cell media. To monitor cell health while performing experiments, a green fluorescent protein (GFP, Cal-520 AM) was used for concurrent calcium imaging. If the cell membrane is punctured irreparably, the GFP will cause the cell to fluoresce as the calcium present in the surrounding fluid enters the cell.

The nanoneedles devices were then manipulated either by poking into the SU-8 encapsulation layer with a microprobe or using a small micropipette under vacuum to create enough suction to lift the device. Using a micromanipulator, the devices' protruding nanoneedle could then be controllably forced into a cell. In Figure 3, we show a nanoneedle device being manipulated by micropipette suction. The white regions of the cell indicate fluorescence of the GFP. The cell continues to spontaneously blink indicating that the cell has not died; however, the white region near the nanoneedle indicates that membrane penetration may have taken place. The fabrication of an exposed platinum pad at the end of the device opposite the nanoneedle in theory allows for electrical contact to determine whether the nanoneedle is inside, but the large ratio between the surface area of the pad and the surface area of the nanoneedle means that the nanoneedle must have an excellent seal with the membrane to detect the penetration electrically. Further experiments and improvements to the nanoneedle fabrication are being investigated.

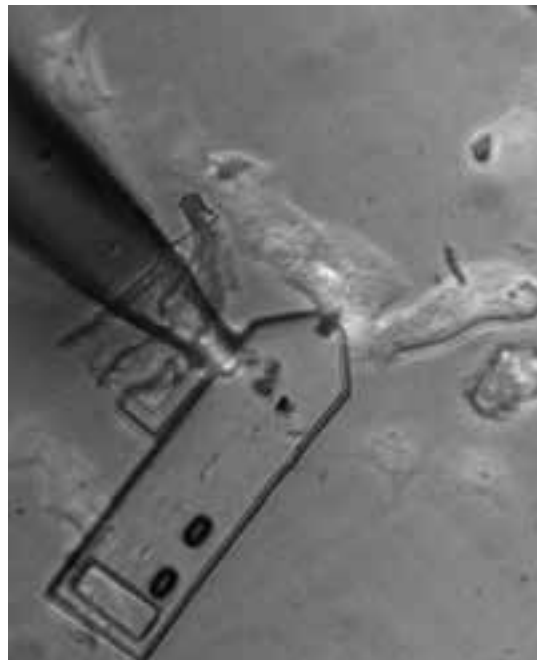


Figure 3: A nanoneedle device being manipulated to puncture a cardiomyocyte.

References:

- [1] Yang, R., et al. Investigation of penetration using atomic force microscope: potential biomarkers of cell membrane. *IET Micro and Nano Letters* 10 (2015).

MoS₂ Pixel Sensors for Optical Detection of Redox Molecules

CNF Project Number: 900-00

Principal Investigators: Paul L. McEuen^{1,2}, Jiwoong Park³, Daniel C. Ralph⁴

Users: Michael F. Reynolds¹, Marcos H.D. Guimarães^{1,2}, Hui Gao^{3,5},

Kibum Kang^{3,5}, Alejandro J. Cortese¹

Affiliations: 1. Laboratory of Atomic and Solid State Physics, 2. Kavli Institute at Cornell for Nanoscale Science, 3. Department of Chemistry and Chemical Biology, 4. Department of Physics; Cornell University, Ithaca NY; 5. Department of Chemistry, Institute for Molecular Engineering, and James Franck Institute, University of Chicago, Chicago IL

Primary Sources of Research Funding: Cornell Center for Materials Research with funding from the NSF MRSEC program (DMR-1719875), Air Force Office of Scientific Research (AFSOR) multidisciplinary research program of the university research initiative Grant FA2386-13-1-4118

Contact: plm23@cornell.edu, mfr74@cornell.edu

Primary CNF Tools Used: Autostep i-line, ABM contact aligner, SC4500 evaporator, Oxford 81 etcher, VersaLine etcher

Abstract:

Spatially-resolved detection of redox molecules in solution is important for understanding chemical and biological systems. Optical detection is advantageously wire-free and easily multiplexed. We demonstrate that monolayer molybdenum disulfide (MoS₂) is a fast, sensitive, optical sensor for redox molecules.

Summary of Research:

Redox molecule detection has applications from detection of neurotransmitters in the brain to trace chemical detection in water samples. Traditional techniques, such as cyclic voltammetry, provide sensitive detection at a single electrode, but do not spatially resolve the variation in redox concentration. More advanced approaches including multiplexed electrode arrays [1,2] and numerous optical detection techniques [3-6] allow researchers to image redox molecules.

We demonstrate a wireless, optical approach for fast, sensitive redox imaging using a flexible, transferrable monolayer of MoS₂. MoS₂ photoluminesces at about 650 nm [7], with an intensity that increases as the concentration of electrons on the MoS₂ decreases, as shown by back-gating [8] and chemical doping [9].

We use the doping dependence of MoS₂ photoluminescence (PL) to detect ferrocene/ferrocenium as a test redox couple. Metal-organic chemical vapor deposition MoS₂ samples [10], grown by Prof. Park's group, are patterned with a two-step fabrication process. First, we pattern contact pads on the MoS₂ with electron-beam evaporation. Second, we etch away the MoS₂ to define our device and pixel geometries, which are shown in Figure 1.

We performed two experiments to demonstrate that our MoS₂ pixel sensors measure the chemical potential of the solution. First, with a fixed total concentration of ferrocene/ferrocenium, we varied the ratio of the

concentration of ferrocenium (Fc⁺) to ferrocene (Fc) in our solution while monitoring the PL of the MoS₂ (Figure 2A). The MoS₂ shows a marked increase in PL as Fc⁺/Fc increases. Second, in a solution without any ferrocene or ferrocenium, we apply a potential to the solution (denoted V_{LG} for liquid gate voltage) while grounding a contacted MoS₂ device. The PL is high at negative values for V_{LG}, but decreases as V_{LG} is swept to positive values (Figure 2B, red curve). We compare the PL *versus* liquid gate voltage to PL *versus* change in chemical potential, where the change in chemical potential of the solution is given by

$$\Delta\mu = \frac{k_B T}{e} \ln \frac{[Fc]}{[Fc^+]},$$

according to the Nernst equation (Figure 2B, blue dots). The good agreement between the two curves indicates that the PL of electrically floating pixels is set by the chemical potential of the solution.

Having characterized the MoS₂ sensors, we measure diffusion to demonstrate their speed and spatial resolution. We apply a voltage pulse to a microelectrode positioned above our MoS₂ pixel array in a solution of 1 mM ferrocene. The pulse oxidizes ferrocene to ferrocenium, which diffuses away from the probe tip, creating a spreading ferrocenium concentration that is imaged by the MoS₂ pixels (Figure 3). From these data, we extract a ferrocenium diffusion constant of about 1.8×10^{-9} m²/s, matching previous measurements [11].

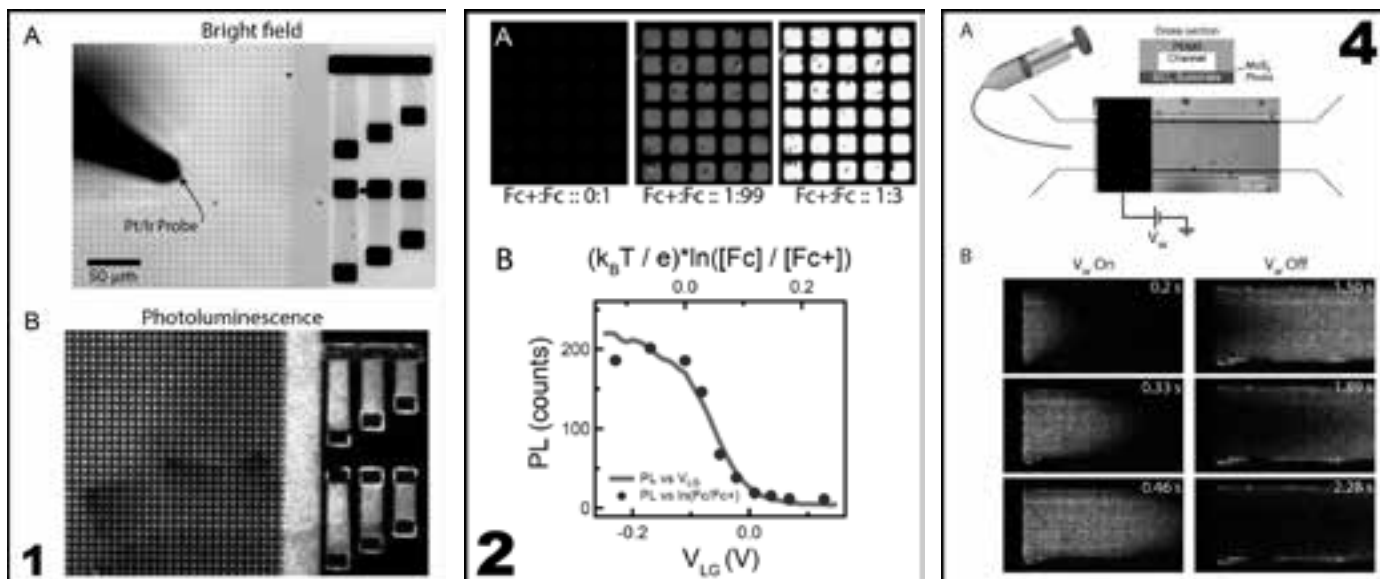


Figure 1, left: A, Bright-field and B, PL (549 nm excitation, 650 emission) images of MoS₂ pixels and devices. **Figure 2, middle:** A, PL images of MoS₂ with varied ferrocenium/ferrocene ratios, showing increased PL with increased ferrocene concentration. B, PL versus liquid gate voltage for grounded device (red line) and versus solution chemical potential (blue dots), showing that MoS₂ sensors are Nernstian. **Figure 4, right:** A, Schematic and bright-field image showing PDMS microfluidic channel placed over MoS₂ pixel array. A pulse on the surface electrode oxidizes ferrocene to ferrocenium while a syringe pump flows the solution through the channel. B, MoS₂ PL imaging flow of ferrocene in the channel.



Figure 3: Frames from PL video imaging diffusion of ferrocenium away from a microelectrode after its potential is pulsed to 0.8 V versus the solution potential.

Finally, we use these sensors to image the flow of redox molecules in microfluidic channels. We mold polydimethylsiloxane (PDMS) microfluidic channels using silicon wafer masters patterned with the Plasma-Therm deep silicon etcher and place them over MoS₂ pixel arrays with platinum surface electrodes (Figure 4A). While flowing a ferrocene solution through the channel, we applied voltage pulses to the surface electrodes to oxidize ferrocene to ferrocenium and image laminar flow of the solution in MoS₂ PL (Figure 4B). These experiments show that MoS₂ can be used for real-time, spatially resolved imaging of redox molecules. The sensor could be improved by increasing the quantum efficiency of the MoS₂ PL in solution. In the future, these sensors could find applications in biological sensing experiments, e.g. spatially resolved detection of dopamine efflux from neurons.

References:

- [1] J. Wang, R. Trouillon, Y. Lin, M. I. Svensson, A. G. Ewing, Individually Addressable Thin-Film Ultramicroelectrode Array for Spatial Measurements of Single Vesicle Release. *Anal. Chem.* 85, 5600–5608 (2013).
- [2] D. L. Bellin, et al., Electrochemical camera chip for simultaneous imaging of multiple metabolites in biofilms. *Nat. Commun.* 7, 10535 (2016).
- [3] X. Shan, U. Patel, S. Wang, R. Iglesias, N. Tao, Imaging local electrochemical current via surface plasmon resonance. *Science.* 327, 1363–6 (2010).
- [4] A. Jane, R. Dronov, A. Hodges, N. H. Voelcker, Porous silicon biosensors on the advance. *Trends Biotechnol.* 27, 230–239 (2009).
- [5] S. Kruss, et al., High-resolution imaging of cellular dopamine efflux using a fluorescent nanosensor array. *Proc. Natl. Acad. Sci. U. S. A.* 114, 1789–1794 (2017).
- [6] D. G. Hafeman, J. W. Parce, H. M. McConnell, Light-Addressable Potentiometric Sensor for Biochemical Systems (available at <http://science.sciencemag.org/content/sci/240/4856/1182.full.pdf>).
- [7] K. F. Mak, C. Lee, J. Hone, J. Shan, T. F. Heinz, Atomically Thin MoS₂: A New Direct-Gap Semiconductor. *Phys. Rev. Lett.* 105, 136805 (2010).
- [8] K. F. Mak, et al., Tightly bound trions in monolayer MoS₂. *Nat. Mater.* 12, 207–211 (2013).
- [9] S. Mouri, Y. Miyauchi, K. Matsuda, Tunable Photoluminescence of Monolayer MoS₂ via Chemical Doping. *Nano Lett.* 13, 5944–5948 (2013).
- [10] K. Kang, et al., High-mobility three-atom-thick semiconducting films with wafer-scale homogeneity. *Nature.* 520, 656–660 (2015).
- [11] Y. Wang, E. I. Rogers, R. G. Compton, The measurement of the diffusion coefficients of ferrocene and ferrocenium and their temperature dependence in acetonitrile using double potential step microdisk electrode chronoamperometry. *J. Electroanal. Chem.* 648, 15–19 (2010).

Silicon Nitride Cantilevers for Muscle Myofibril Force Measurements

CNF Project Number: 1255-04

Principal Investigator: Walter Herzog

Users: Timothy Leonard, Andrew Sawatsky

Affiliation: Faculty of Kinesiology, University of Calgary, Calgary, Canada

Primary Source of Research Funding: Natural Sciences and Engineering Research Council of Canada, Canadian Institutes of Health Research and the Canada Research Chair for Cellular and Molecular Biomechanics

Contact: wherzog@ucalgary.ca, leonard@ucalgary.ca, ajsawats@ucalgary.ca

Website: www.ucalgary.ca/knes

Primary CNF Tools Used: GCA 5X stepper, photolith spinners, Oxford 81 ion etcher

Abstract:

To measure muscle forces in the nano-Newton range, silicon nitride cantilever pairs were manufactured using the GCA 5x-stepper photolithography system and the Oxford 81 ion etching system at the CNF, and then used in our lab in Canada. We investigated titin mechanical properties using a skeletal muscle myofibril model. Our experiments demonstrate sarcomeres in skeletal muscle are not unstable when suddenly made weaker relative to the sarcomeres adjacent to them.

Summary of Research:

Muscle (the smallest functional unit being the sarcomere) generates active force through cyclic interactions between myosin and actin and the amount of active isometric force generated is proportional to the length of the sarcomere [1]. Passive forces in the sarcomere are also length dependent and are supported by the molecular spring-like protein titin [2]. Instability of sarcomeres has been proposed as a mechanism for injury in muscle since sarcomeres arranged in-series must sustain the same force along a myofibril and sarcomeres that are weaker than adjacent ones are expected to over-lengthen since there is a disparity in active force producing potential. This instability results in a sarcomere that is rapidly lengthened (termed “popping”) until only passive structures (titin) sustain the in-series force, with damage occurring to that sarcomere [3]. The purpose of this study was to measure the length of each sarcomere in a single myofibril during activation and then follow these sarcomeres with time as portions of the sample are deactivated to see whether weaker sarcomeres behave as predicted, and do in fact, over-lengthen.

Methods:

Skeletal muscle myofibrils were generated using rabbit psoas muscle as previously described in reference [4] and were placed in an experimental chamber atop an inverted microscope. Single myofibrils (n=6) were attached at one end to a glass needle/motor assembly for specimen

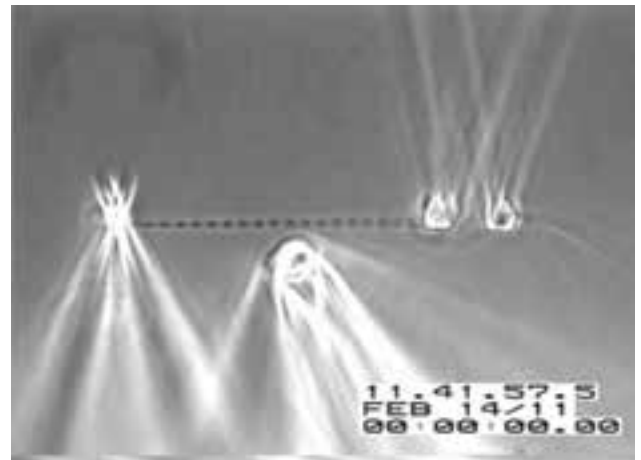


Figure 1: Myofibril attached to a glass needle for stretch-shortening and cantilevers for force measurement. An example of a single myofibril with 19 sarcomeres in-series. The glass tube (center) is used to deliver a focused stream of deactivating solution.

length control and at the other end to a micro-fabricated silicon nitride cantilever pair (68 nN/ μ m stiffness) for measuring force. High-resolution (88 nm per pixel) video data (30 fps) were collected continuously during the experiment and analyzed using custom MATLAB

analysis code. The myofibril was initially in a relaxed state and the myofibril length adjusted to an average sarcomere length (SL) of approximately $2.4 \mu\text{m}$. Then the Ca^{+2} rich activating solution was delivered and once the myofibril was fully activated, a second stream of relaxing solution was targeted to the left side of the myofibril (Figure 1). This resulted in a wave of deactivation that started at the left and propagated rightward until it encompassed the entire myofibril, and the myofibril returned to the relaxed state.

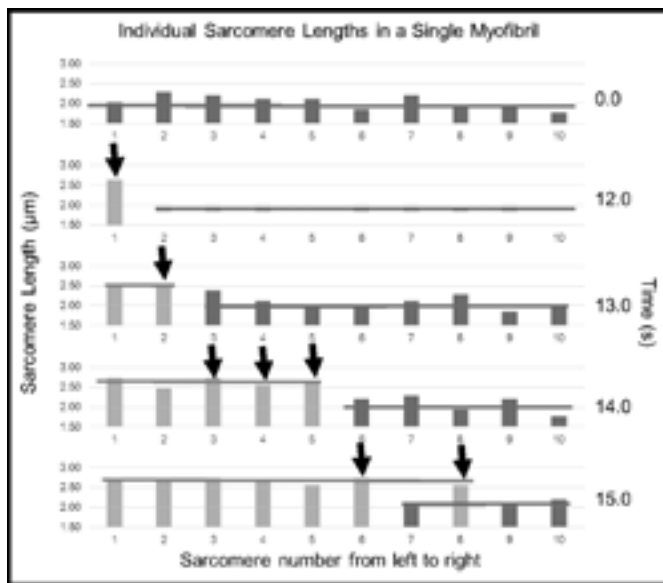


Figure 2: Sarcomere length in an activated myofibril as a wave of deactivation solution moves from left to right. Black arrows highlight activated sarcomeres (dark grey) that transition rapidly to passive (light grey). Dark grey and light grey horizontal bars indicate the mean SL for sarcomeres belonging to groups classified as active or passive.

Results and Discussion:

In Figure 2, for one typical experiment, the mean SL upon activation was $2.1 \mu\text{m}$ and the stress measured (not shown) was $209 \text{ nN}/\mu\text{m}^2$. The infusion of the localized stream of relaxing solution at time-point 12s resulted in the first sarcomere (sarcomere #1) rapidly lengthening from a SL of $2.47 \mu\text{m}$ to $2.65 \mu\text{m}$. At 13s, the next sarcomere

(#2) lengthened from $2.21 \mu\text{m}$ to $2.47 \mu\text{m}$ and at 14s, #3 lengthens from $2.29 \mu\text{m}$ to $2.74 \mu\text{m}$. At time point 15s, more than half of the sarcomeres have relaxed, the total stress is $110 \text{ nN}/\mu\text{m}^2$ and the mean relaxed SL (light grey horizontal line; Figure 1) is $2.65 \mu\text{m}$ and the remaining active sarcomeres have a mean SL of $2.15 \mu\text{m}$ (dark grey horizontal line). At time 15s, seven sarcomeres out of ten have lengthened from their initial active length and are positioned on the descending limb of the force-length relationship. Instability theory would predict these sarcomeres to over-lengthen. In fact, these deactivated sarcomeres would need to lengthen considerably if they were to passively support the $110 \text{ nN}/\mu\text{m}^2$ of stress still detected; A SL of near $4.0 \mu\text{m}$ would be required and passive force does not appear in this preparation until SL of about $2.8 \mu\text{m}$. These passive sarcomeres are presumably sustaining this tension by titin alone, and in this example, with the titin stiffness being modulated so that a relaxed sarcomere at $2.6 \mu\text{m}$ can sustain the load.

Conclusions:

Weak (deactivated) sarcomeres do not “pop”. We speculate that popping is prevented by a “stiffening” of the molecular spring titin. The mechanisms underlying this stiffening of titin need further elucidation.

References:

- [1] Gordon, A.M., Huxley, A.F., Julian, F.J., 1966. The variation in isometric tension with sarcomere length in vertebrate muscle fibres. *J. Physiol.* 184, 170-192.
- [2] Trombitas, K., Greaser, M., Labeit, S., Jin, J.-P., Kellermayer, M.S.Z., Helmes, M., Granzier, H.L.M., 1998. Titin extensibility in situ: entropic elasticity of permanently folded and permanently unfolded molecular segments. *J. Cell Biol.* 140, 853-859.
- [3] Morgan, D.L., 1990. New insights into the behavior of muscle during active lengthening. *Biophys. J.* 57, 209-221.
- [4] Joumaa, V., Rassier, D.E., Leonard, T.R., Herzog, W., 2008. The origin of passive force enhancement in skeletal muscle. *Am. J. Physiol. Cell Physiol.* 294, C74-78. <https://doi.org/10.1152/ajpcell.00218.2007>.

DNA Unzipping by Resonator-Based nSWATs

CNF Project Number: 1738-08

Principal Investigator: Michelle D. Wang

User: Fan Ye

Affiliations: a) Department of Physics, Cornell University; b) Howard Hughes Medical Institute, Chevy Chase, Maryland

Primary Source of Research Funding: Howard Hughes Medical Institute

Contact: mdw17@cornell.edu, fy72@cornell.edu

Website: <http://wanglab.lassp.cornell.edu/>

Primary CNF Tools Used: ASML deep uUV stepper, Oxford 100 plasma etcher, Unaxis 770 deep Si etcher, Heidelberg mask writer DWL2000, SÜSS MA6-BA6 contact aligner, Gamma automatic coat-develop tool, LPCVD nitride - B4 furnace, wet/dry oxide - B2 furnace, AJA sputter deposition, CVC sputter deposition, GSI and Oxford PECVD, SC4500 odd-hour evaporator, Zeiss Supra and Ultra SEM

Abstract:

A nanophotonic trapping platform based on chip-based tunable optical interference allows parallel processing of biomolecules and holds promise to make single molecule manipulations and precision measurements more easily and broadly available. The Wang lab has developed and implemented such an on-chip device based on Si or Si₃N₄ waveguides, coined a nanophotonic standing-wave array trap (nSWAT), that allows for controlled and precise manipulation of trapped nano/micro particle arrays [1-4]. We present here the latest generation of nSWAT devices that contains the following features: (1) local force enhancement are achieved by a resonator-based design; (2) response time of the phase modulation heaters are drastically shortened by a balanced and differential micro heater design; and (3) the thermal drifts of the whole device due to local heating of micro heaters are diminished by a novel sample holder design and cleaver micro heater re-arrangement. With all these crucial improvements, we have for the first time successfully unzipped DNA molecules on an nSWAT device. This is a benchmark achievement, making the nSWAT devices much more relevant in the single molecule field.

Summary of Research:

Optical trapping is a powerful manipulation and measurement technique widely employed in the biological and materials sciences. Miniaturizing bulky and expensive optical trapping instruments onto optofluidic platforms holds promise for high throughput lab-on-chip applications that can be readily integrated with other novel lab-on-chip innovations such as fluorescent detectors or on-chip lasers.

Recently, we have demonstrated a high-throughput, near-field nanophotonic trapping platform that achieved stable trapping with precision controllable repositioning [1-4]. The core concept of the platform is nanophotonic standing-wave interferometry, where laser light travels through a nanophotonic waveguide, is split into two equal intensity laser beams, the two beams are guided by the waveguides and meet each other, which ultimately leads to interference of two counter-propagating laser beams and results in the formation of standing waves. The evanescent field of the antinodes of the standing wave forms an array of stable three-dimensional optical

traps. We call this type of trap a nanophotonic standing-wave array trap (nSWAT). By tuning the phase difference between the two counter-propagating laser beams, the antinode locations can be precisely repositioned, and consequently, the optical trap positions can be precisely manipulated. The nSWAT device holds the capability for high throughput precision measurements on-chip.

In the past year, we have advanced the nSWAT concept in several aspects. (1) We have implemented a resonator-based design for ultimate local intensity enhancement into the nSWAT devices. Among all designs, this resonator design gives the highest force enhancement factor, limited only by the total scattering loss of the trapped beads onto the waveguide. We have measured around three times force enhancement, larger than our previous force-double design [4]. (2) We have implemented a balanced layout and differential operation mode for the micro heaters. This greatly reduced the response time of the micro heaters (from ~30 μ s to ~1 μ s). This is shown to be crucial for maintaining high trapping forces for a

trapped bead under strong biased forces under single molecule manipulations. (3) We have also designed a special sample holder for the nSWAT chip that can greatly reduce (by two orders of magnitude) the thermal drift of the sample caused by the micro heaters. This greatly enhanced the thermal stability of the nSWAT devices.

Thanks to the above described improvements, we have achieved DNA unzipping on the nSWAT devices for the first time. We are currently preparing a manuscript on these latest advancements on the resonator based nSWAT devices.

References:

- [1] M. Soltani, J. Lin, R. A. Forties, J. T. Inman, S. N. Saraf, R. M. Fulbright, M. Lipson, and M. D. Wang, "Nanophotonic trapping for precise manipulation of biomolecular arrays," *Nature Nanotechnology* 9(6), 448-452 (2014).
- [2] F. Ye, R. P. Badman, J. T. Inman, M. Soltani, J. L. Killian, and M. D. Wang, "Biocompatible and high stiffness nanophotonic trap array for precise and versatile manipulation," *Nano Letters* 16(10), 6661-6667 (2016).
- [3] J. E. Baker, R. P. Badman, and M. D. Wang, "Nanophotonic trapping: precise manipulation and measurement of biomolecular arrays," *WIREs Nanomed Nanobiotechnol.* e1477 (2017).
- [4] F. Ye, M. Soltani, J. T. Inman, and M. D. Wang, "Tunable nanophotonic array traps with enhanced force and stability," *Optics Express* 25 (7) 7907-7918 (2017).

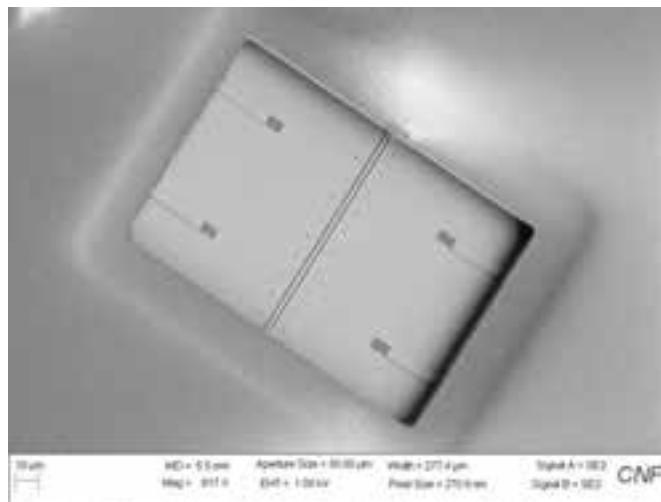


Figure 1: A tilted SEM image of the active trapping waveguides in the fluid pool region (big rectangle) of the latest resonator based nSWAT devices. The two parallel Si_3N_4 waveguides cut through the fluid pool in the middle, with two adjacent arrays of circular dots serving as local fiducial for real time motion tracking for trapped beads. Under operation, two arrays of polystyrene nanospheres (with 380 nm diameter) are trapped onto the two parallel waveguides. DNA molecules attached between two beads on both waveguides can be manipulated and studied by controlling the beads on each waveguide independently. The four wider Si_3N_4 waveguides terminating with free-space coupling gratings are carefully designed local laser intensity indicators for the two trapping waveguides.

Generalized Platform for Antibody Detection Immunosensor

CNF Project Number: 1757-09

Principal Investigator: Christopher K. Ober¹

Users: Roselynn Cordero¹, Wei-Liang Chen²

*Affiliations: 1. Department of Materials Science and Engineering,
2. Department of Chemistry and Chemical Biology; Cornell University*

Primary Source of Research Funding: National Science Foundation

Contact: cko3@cornell.edu, rc634@cornell.edu, wc497@cornell.edu

Primary CNF Tools Used: ABM contact aligner, MVD 100

Abstract:

Immunosensors are diagnostic devices that convert specific antigen-antibody interactions, by means of a transducer, into an electrical signal. Immunosensors are very efficient, simple, affordable, and cost-effective point-of-care systems for medical diagnosis. Our study focuses on the use of polymer chemistry and photolithography to create a unique antibody detection platform. This immunosensor takes advantage of the antibody catalyzed water oxidation pathway (ACWOP) process, in which all antibodies catalyze the production of hydrogen peroxide that can be detected using a colorimetric assay. This report focuses on the fabrication of the platform that make up our immunosensor device.

Summary of Research:

Pandemic infectious diseases have affected many people throughout history, sometimes killing millions of people such as the Plague in 14th century Europe, and the flu. One of the most common methods of detecting such diseases is through antibody detection using a serological assay. In our group, Welch, et al., in 2014 developed an immunobiosensor based on patterned polymer brushes on gold, which demonstrated extremely high sensitivity (2pM) for the specific antibody [1]. This design took advantage of the excellent properties of poly(oligo(ethylene glycol) methacrylate) (POEGMA) polymer brushes by preventing non-specific adsorption and allowing the anchoring of the functional haptens [2].

With that in mind, we would like to improve this sensor by using colorimetric detection as the electrochemical signal in the original design was not as intuitive and required additional parameters complicating our immunosensor. This sensor consists of patterned poly(oligoethylene glycol methacrylate) (POEGMA) polymer brushes on a glass substrate that were polymerized using atom transfer radical polymerization (ATRP), surrounded by a photosensitizer that was functionalized onto the surface of the silica platform.

Photosensitizer is responsible for the production of singlet oxygen reacting with water to produce hydrogen

peroxide. In the past, our group used a ruthenium-based photosensitizer that was electropolymerized on a gold surface. To enable an economic colorimetric design, we selected to utilize Rose Bengal rather than $\text{Ru}(\text{4-vinyl-4'-methyl-2,2'-bipyridine})_3^{+2}$ as photosensitizer due to its high quantum yield (0.75)³, low price and ease of anchoring.

The detection mechanism is based on antibody catalyzed water oxidation pathway (ACWOP)⁴, which is the same as previous work in our group as shown in Figure 1.

The dimension requirement for the sensor is well above the micron level (150 μm line pattern), which could be easily achieved with 365 nm UV photolithography using the ABM contact aligner. The bottom-up patterning process suits this application better for the resulting structural integrity. Since we already know that the monolayer made of silane compounds is unable to completely block all the reactive sites on the silicon substrates, deposition of the second chemical species must be conducted while the photoresist is still present on the surface, otherwise, the mixed chemical species will show up in the pre-defined area.

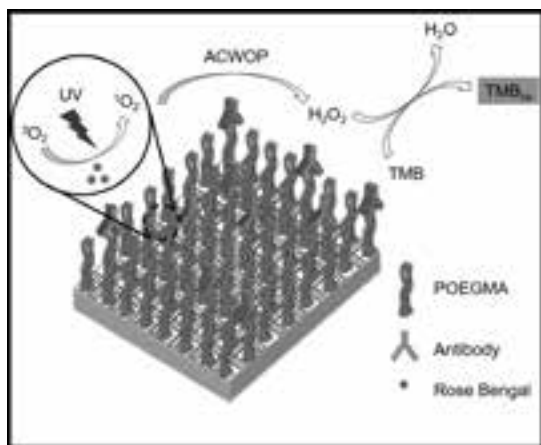


Figure 1: Detection mechanism for the proposed immunosensor. Under UV light exposure, singlet oxygen is formed by exciting Rose Bengal. Hydrogen peroxide is then produced through ACWOP. Hydrogen peroxide subsequently oxidizes TMB resulting in a change from clear to blue color for colorimetric readout. TMB: 3,3',5,5' tetramethylbenzidine.

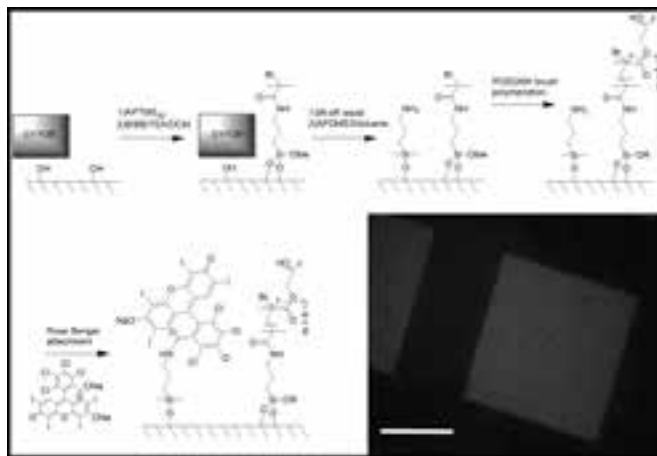


Figure 2: Process flow for the fabrication of the biosensor platform and the picture of the platform taken with a fluorescent microscope.

The CYTOP bottom-up patterning process was then applied to fabricate the functional surface. The fabrication process and results are shown in Figure 2. The 3-aminopropyltrimethoxysilane (APTMS) must be deposited before polymerization since it could also react with the hydroxy group on the POEGMA polymer brushes. This surface functionalization was done using the molecular vapor deposition tool (MVD100). However, it turned out that the Rose Bengal could still adsorb on the surface with POEGMA polymer brushes even though the amount is limited. This happened because an esterification reaction used for anchoring Rose Bengal on an amine could also anchor it on a hydroxy group.

To create more defined patterns, in the future other orthogonal reactions should be selected to anchor the compounds onto the surface. For example, 3-mercaptopropyltrimethoxysilane could be used instead of the APTMS to be the anchoring group, which could be reacted by a thiol-ene click reaction. Another issue that was encountered was that the Rose Bengal monolayer on the surface is not enough to trigger significant signal. Such problems may be further solved by using polymer brushes on the surface to provide more surface area for the anchoring of the Rose Bengal. If the thickness of the polymer brushes is high enough, the amount of the Rose Bengal could be increased to more

than 100 times the amount grafted on the surface and this should be enough to create detectable signal. With the orthogonal anchoring chemistry for the functional groups and polymer brushes for Rose Bengal anchoring, this platform could be more applicable for fabrication and provide easy detection by colorimetric methods.

In conclusion, a CYTOP patterning process could be easily extended to other fields and enable better complex platform fabrication.

References:

- [1] Welch, M. E., et al. Generalized Platform for Antibody Detection using the Antibody Catalyzed Water Oxidation Pathway. *J. Am. Chem. Soc.* 136, 1879-1883 (2014).
- [2] Harder, P., Grunze, M., Dahint, R., Whitesides, G. M. and Laibinis, P. E. Molecular Conformation in Oligo(ethylene glycol)-Terminated Self-Assembled Monolayers on Gold and Silver Surfaces Determines Their Ability To Resist Protein Adsorption. *J. Phys. Chem. B* 102, 426-436 (1998).
- [3] DeRosa, M. Photosensitized singlet oxygen and its applications. *Coord. Chem. Rev.* 233-234, 351-371 (2002).
- [4] Wentworth Jr., P. Antibody Catalysis of the Oxidation of Water. *Science* 293, 1806-1811 (2001).

Development of a Salivary Microfluidic Diagnostic Device Using Hot Embossing

CNF Project Number: 1872-10

Principal Investigator: David Erickson

User: Elizabeth Rey

Affiliation: Sibley School of Mechanical and Aerospace Engineering, Cornell University

Primary Source of Research Funding: National Science Foundation

Contact: de54@cornell.edu, egr42@cornell.edu

Primary CNF Tools Used: Hot press, photolithography room, ABM contact aligner, Unaxis 770 deep Si etcher, Microdrill, Objet30 3D printer

Abstract:

Point of care diagnostic devices allow people to get fast, accurate information about their health and well-being without the need to go to a clinic or hospital. The device that we are designing will determine the concentration of cortisol from a sample of the user's saliva. Cortisol is a steroid hormone associated with stress levels and expressed in human saliva [1,2]. This microfluidic device contains a microbead-based immunoassay, which we are optimizing to determine the cortisol content from a saliva sample. The device is manufactured using a hot embossing process, which uses a silicon master made with traditional lithographic processes. The device is made from a thermoplastic called Zeonor 1020R, which is a transparent, semi-rigid plastic which can be used in large-scale manufacturing processes such as injection molding and hot embossing. Nearly all the fabrication of the device is being done in the Cornell NanoScale Facility.

Summary of Research:

The microfluidic device is made using a hot embossing process, which involves the high-temperature pressing of a mold into a piece of thermoplastic. The mold that we use in our process is made of silicon and is fabricated using photolithographic processes. The design for the mold is made using L-Edit and transferred to a photomask using the Heidelberg mask writer (DWL2000). This mask is then used to transfer a pattern to a photoresist on a silicon wafer. The photoresist (SPR-220-7.0) is spun onto a bare silicon wafer, which has been previously primed in the YES Vapor Prime Oven, to a thickness of approximately 7 μm . After spinning, the photoresist is soft baked on a 115°C hot plate for 2 minutes and 30 seconds. The wafer is allowed to sit for an hour and then exposed using the mask and the ABM contact aligner. The wafer is again allowed to sit for an hour and then is developed using the Hamatech Steag wafer processor. The pattern is now developed and can be used to etch the silicon wafer.

We etched the wafer using the Unaxis 770 deep Si etcher to a depth of 50 μm . We monitored the etch depth and etch rate using the P10 profilometer. Upon reaching the desired depth, we removed the photoresist in the chemical strip bath. We then used the Unaxis 770 again

to deposit a thin layer of fluoropolymer onto the wafer in order to prevent sticking in the hot emboss process. Our masters are then ready to be used in the hot emboss process.

The hot emboss process uses the CRC Prepreg Mini Test Press, which applies heat and even pressure. The silicon master is adhered to a glass backing, for strength, and then the plastic piece is placed on top of the master, with another glass piece on top of that. This whole stack is placed in the hot press once the hot press reaches the desired temperature and pressed for several minutes. The setup is allowed to cool below the glass transition temperature of the plastic and then the pressure is released and the plastic is de-embossed. The pattern is transferred from the master to the plastic. We then drill through-holes in a blank piece of plastic using the custom-made micro drill.

In our own lab, we perform a photografting procedure to increase hydrophilicity of the Zeonor surfaces and improve bonding. This blank piece is then thermally bonded to the patterned piece to create the microfluidic device in the hot press. Our microfluidic device is now



Figure 1: Image of completed microfluidic chip.

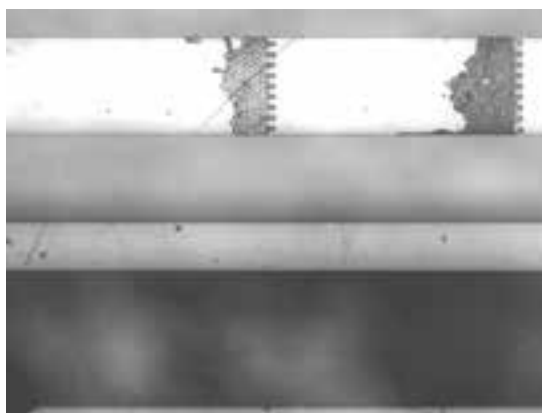


Figure 2: Microscope image of channels, pillars, and different sized bead zones.



Figure 3: Microscope image of fluorescence on beads after flowing of FITC through chip.

complete and ready to be turned into an immunoassay. An example can be seen in Figure 1.

We can now flow differently sized beads into the device to create areas for antibody-antigen-fluorophore interaction. The channels after the beads are successfully added can be seen in Figure 2. The differently-spaced pillars allow two zones with beads with different antibodies to be separated by size. We then flow fluid with cortisol and FITC-labeled antibodies through the device and measure the brightness of the fluorescence at the bead zones with a microscope or with our portable imaging device. A microscope image of the two bead zones with attached fluorophores can be seen in Figure 3.

The portable imaging device is a Raspberry Pi Zero W with a camera attached, fluorescent optics, a lithium-ion battery, LEDs, all assembled in a 3D-printed light-tight case. This case is printed using the Objet30 Pro 3D Printer, and can be seen with all parts assembled in Figure 4.

References:

- [1] Kirschbaum C, Hellhammer DH. Salivary cortisol in psychoneuroendocrine research: recent developments and applications, *Psychoneuroendocrinology*, Volume 19, Issue 4, 1994, Pages 313-333.
- [2] Umeda T, Hiramatsu R, Iwaoka T, et al. (1981). Use of saliva for monitoring unbound free cortisol levels in serum. *Clin Chim Acta* 110:245-253. doi: 10.1016/0009-8981(81)90353-3.



Figure 4: 3D-printed imaging device.

Rapid Detection of Antimicrobial Susceptibility at the Point-of-Care

CNF Project Number: 1872-10

Principal Investigator: David Erickson

User: Sasank Vemulapati

Affiliation: Sibley School of Mechanical and Aerospace Engineering, Cornell University

Primary Source of Research Funding: Atkinson Center Academic Venture Fund

Contact: de54@cornell.edu, sv379@cornell.edu

Primary CNF Tools Used: Objet 3D printer

Abstract:

The rise of antibiotic resistant bacteria poses a serious threat to the United States. In 2014 President Obama issued an Executive Order and the White House published the National Strategy for Combating Antibiotic Resistance [1,2]. This document describes: how as antibiotic resistance continues to increase “we will no longer be able to reliably and rapidly treat bacterial infections”, how “drug choices have become increasingly limited and more expensive and, in some cases, nonexistent”, and imagines a world in which “modern medical advances such as surgery, transplants, and chemotherapy may no longer be viable due to the threat of infection.” Already the Centers for Disease Control and Prevention reports that each year in the US, at least two million people acquire bacterial infections resistant to one or more antibiotics and at least 23,000 people die each year as a result [3]. In this project we are working towards developing a point-of-care diagnostic test that can rapidly provide antibiotic susceptibility information bloodborne organisms causing bacteremia in about four hours following a short blood culture. The integrated sample-to-answer system is based upon two key technologies already demonstrated in our labs: rapid blood sample clean-up using magnetic nano-beads, and a capillary-based system that enhances our ability to monitor bacterial metabolic activity, significantly reduces the time required to determine the efficacy of a given antibiotic dose.

Summary of Research:

In our initial experiments, we have adopted a colorimetric phenotypic testing approach to assess the antibiotic susceptibility of an attenuated *E. coli* K12 strain. The pH indicator phenol red was used to provide a phenotypic indication of bacterial growth.

For our colorimetric phenotypic testing approach, we conducted bacterial growth tests with small sample volumes in a PDMS microchip. The *E. coli* strain with a kanamycin resistance gene as selection marker was first streaked and incubated overnight on LB agar plates containing kanamycin. Single colonies were subsequently picked and propagated in liquid bulk culture. Following overnight bulk culture to stationary phase, small volumes (~1 μ L) of culture were separately incubated on the PDMS chip in wells each containing a 19 μ L mixture of fresh LB media, 0.05% phenol red, and the antibiotics kanamycin (control) and ampicillin (test). The metabolic activity of viable bacteria leads to an accumulation of organic acids in the growth media, which causes the phenol red to change in color from red to yellow, which we expect for the control group as the *E. coli* strain is kanamycin resistant. Images of the chip were taken every hour, and a significant color change was detected after four hours, as seen in Figure 1.

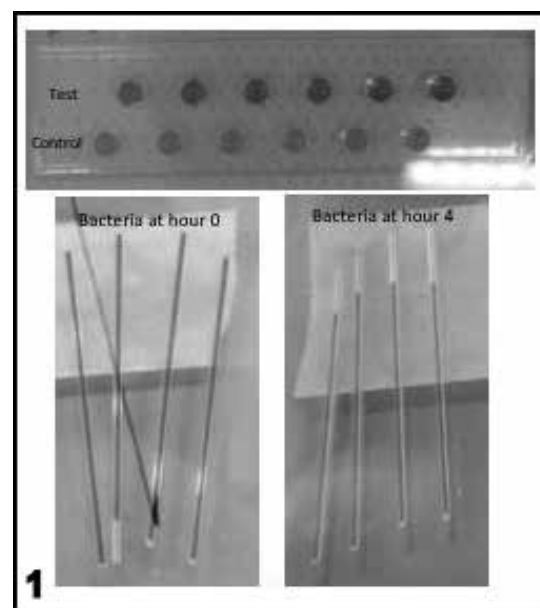


Figure 1: Color change over four hours.

Assessing Bacteria Growth in a Capillary:

A similar experiment was conducted by incubating the bacteria culture in capillary tubes designed to hold microliters of liquid. We hypothesized that the increased surface area to volume ratio of the tubes would induce an accelerated growth rate for the bacteria. First, an overnight experiment was conducted to verify that incubation inside capillary tubes supported bacteria growth. Following this verification experiment, a shorter timescale experiment was conducted with added antibiotics. Similar to the previous experiment, a significant color change was detected in the control group (kanamycin) at the 4-hour mark, as shown in Figure 1. No color change was observed in the ampicillin inhibited group.

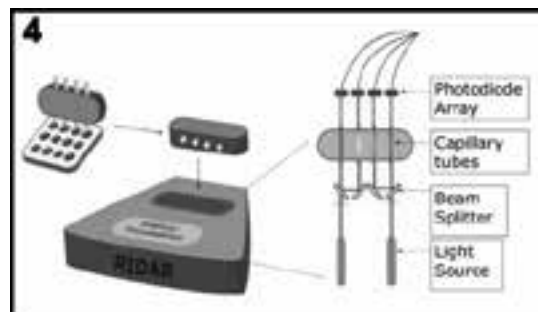
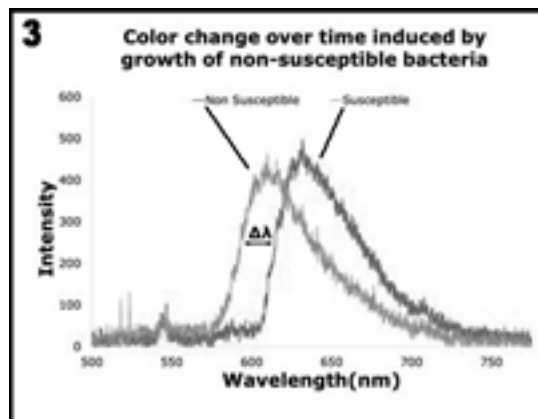
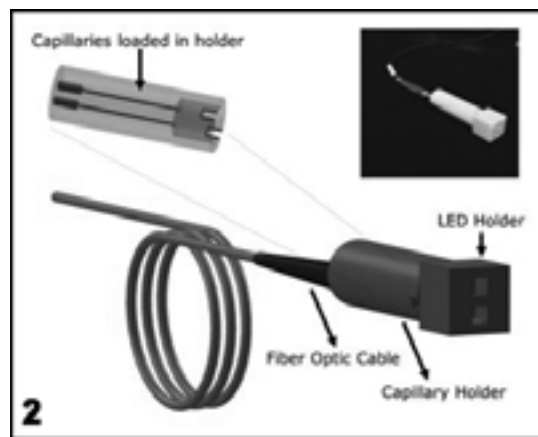
To perform real time detection of bacterial growth, we manufactured a small portable adapter using the Objet 3D printer at Cornell NanoScale Science and Technology Facility (CNF) (Figure 2). White light is incident on one end of the capillary tube and the spectra is measured on the other end using a small portable spectrometer (OceanOptics). A difference in output spectra can give us insight into whether the organism is inhibited by antibiotic presence. As seen in Figure 3, we are able to verify bacterial viability within six hours with an apparent shift in wavelength easily distinguishable by eye.

Future Considerations:

Further testing will include real time tracking of bacteria growth. In particular, we plan on devising a portable imaging system that will allow for real time measurements of the absorbance of phenol red, which we will use as a proxy for tracking bacteria growth. We envision a system as depicted in Figure 4, wherein a simple laser and photodiode system is used to measure absorbance across and along the capillary, thus allowing us to infer the growth of bacteria.

References:

- [1] Report to the President on Combating Antibiotic Resistance - Executive Office of the President and President's Council of Advisors on Science and Technology. 2014; Available from: http://www.whitehouse.gov/sites/default/files/microsites/ostp/PCAST/pcast_carb_report_sept2014.pdf.
- [2] National Strategy for Combatting Antibiotic Resistant Bacteria. 2014; Available from: http://www.whitehouse.gov/sites/default/files/docs/carb_national_strategy.pdf.
- [3] Laxminarayan, R., A. Duse, C. Wattal, A.K.M. Zaidi, H.F.L. Wertheim, N. Sumpradit, E. Vlieghe, G.L. Hara, I.M. Gould, H. Goossens, C. Greko, A.D. So, M. Bigdeli, G. Tomson, W. Woodhouse, E. Ombaka, A.Q. Peralta, F.N. Qamar, F. Mir, S. Kariuki, Z.A. Bhutta, A. Coates, R. Bergstrom, G.D. Wright, E.D. Brown, and O. Cars, Antibiotic resistance—the need for global solutions. *The Lancet Infectious Diseases*. 13(12): p. 1057-1098 (December 2013).



An *in vacuo* Microfluidic Mixer for Biological X-Ray Solution Scattering

CNF Project Number: 1940-10

Principal Investigator: Richard E. Gillilan

User: Jesse Hopkins

Affiliations: Macromolecular Diffraction Facility of the Cornell High Energy Synchrotron Source (MacCHESS),
Cornell High Energy Synchrotron Source (CHESS); Cornell University

Primary Source of Research Funding: National Institutes of Health GM-103485

Contact: reg8@cornell.edu, jbh246@cornell.edu

Website: www.macchess.cornell.edu/MacCHESS/bio_saxs.html

Primary CNF Tools Used: Heidelberg mask writer DWL2000, SUEX laminator, ABM contact aligner

Abstract:

Time-resolved small angle x-ray solution scattering (TR-SAXS) remains a challenging, but increasingly important experiment for structural biologists. Such experiments can tell researchers about multi-step conformational changes biological molecules undergo as part of their function. The continuous-flow mixing that utilizes the chaotic laminar flow regime of fluids provides a means of reaching single millisecond timescales with disposable plastic microchip construction and minimal sample consumption. Photolithographically fabricated mixing chips have been tested *in vacuo* to reduce parasitic x-ray scatter.

Summary of Research:

Small-angle x-ray solution scattering (SAXS) is a widely used technique in structural biology for gaining information about the behavior of molecules in solution. Time-dependent SAXS studies have been conducted for a number of years, with significant advances being made in design, sample consumption, and instrumentation [1]. But adoption of the method by non-specialists has been slow in coming, and the method remains a challenging experiment. To address the need for easier, more practical experiments, we introduced a system based on the principle of chaotic advection [2].

Our previously designed mixing chip, fabricated at CNF, is a composite of SUEX (DJ Microlaminates Sudbury, MA), polymethylmethacrylate (PMMA) and polyimide layers driven by a commercial piezo-controlled pressure system (ELVESYS, Paris, France).

Thin polyimide film (7 μm) serves as low-scatter windows for x-ray transmission. To eliminate x-ray scattering due to air and vacuum windows, we have designed an enclosed sample environment that allows mixing chips to operate in vacuum (Figure 1A). Polyether ether

ketone (PEEK) sample feed tubing enters the vacuum through KF 50 blanks into the cubic sample enclosure (Ideal Vacuum, Albuquerque, NM) and connects to the microfluidic chip via flangeless fittings.

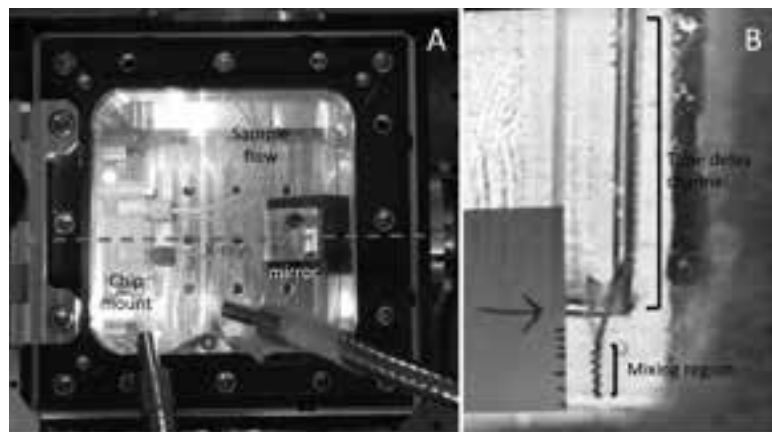


Figure 1: Microfluidic mixing chip for SAXS mounted *in vacuo* at CHESS beamline G1. A: X-rays (red) pass through cubic vacuum enclosure over viewing mirror and through microfluidic cell. B: Mixing region and time-delay channel of chip are visible in camera snapshot.

Positioning of the x-ray beam in the chip channel is accomplished by scanning the cube assembly in the x-ray beam and monitoring transmitted intensity. The chip can be viewed with a remote camera via a diagonal mirror just below the path of the x-ray beam (Figure 1A, right). The mixing and time-delay channels are visible in the camera image (Figure 1B). X-ray tests using a novel compound refractive optic for focusing down to 30 μm showed relatively low parasitic scatter though the time-delay channel.

References:

- [1] Graceffa, R., et al., Sub-millisecond time-resolved SAXS using a continuous-flow mixer and x-ray microbeam. *Journal of Synchrotron Radiation*, 2013, 20: p. 820-825.
- [2] Kane, et al. Microfluidic Mixers for the Investigation of Rapid Protein Folding Kinetics Using Synchrotron Radiation Circular Dichroism Spectroscopy. *Anal. Chem.* 2008, 80, 9534-9541.

Biomechanics of Bacteria

CNF Project Number: 1970-10

Principal Investigator: Christopher J. Hernandez

Users: Melanie F. Roberts, Christine E. Harper, Gabriel Guisado*

Affiliations: Sibley School of Mechanical and Aerospace Engineering, Meinig School of Biomedical Engineering;
Cornell University (* 2017 CNF REU Program Intern)

Primary Source of Research Funding: National Science Foundation 1463084, NSF NNCI Grant No. ECCS-1542081

Contact: cjh275@cornell.edu, mfr75@cornell.edu, ceh272@cornell.edu

Website: hernandezresearch.com

Primary CNF Tools Used: ASML, Oxford 100, AJA sputter deposition, VersaLaser engraver/cutter, MOS clean anneal

Abstract:

The mechanical properties of the bacterial cell envelope influence cell growth, cell division and subcellular localization of membrane proteins. Here we demonstrate the ability to apply mechanical loads to live bacteria, the first step toward determination of mechanical properties of bacterial components *in vivo*. Additionally, we show that devices based on the same concept have the ability to separate bacterial species/strains from one another based on the cell mechanical phenotype.

Summary of Research:

In bacteria, the ability to resist mechanical forces is necessary for survival and growth, allowing cells to withstand osmotic pressures while maintaining cell shape, cell growth and division. Hence, the mechanical properties of bacteria and bacterial structural components influence species competition and resistance to toxins and antibiotics. Our work involves the use of micro/nano fabricated devices as tools for mechanical testing of live bacteria. Within our devices, individual bacteria are flowed into tapered channels travel a distance related to whole cell stiffness: less stiff cells are able to travel further in to the channels (Figure 1).

Key advantages of this microfluidic platform for profiling the biomechanical properties of bacteria include: minimal sample preparation, no chemical immobilization or labeling, and the ability to analyze hundreds of cells at once.

In our first series of experiments we manufactured devices on silica glass wafers using Deep UV photolithography to achieve nano-scale features (250 nm smallest dimension). These glass on glass devices were manufactured using the ASML, Oxford 100, AJA sputter deposition, VersaLaser and MOS clean anneal tools at the Cornell NanoScale Science and Technology Center.

In the first device, design bacteria in liquid culture were submitted to up to 12 different applied pressures to establish the biomechanical profile of two model organisms, *E. coli* and *B. subtilis*.

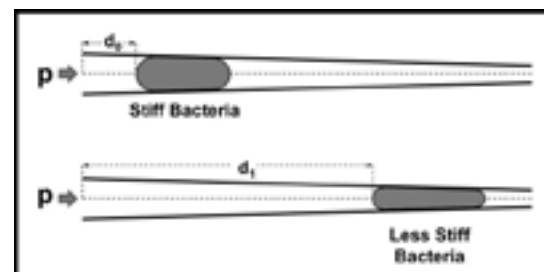


Figure 1: Bacteria under fluid pressure (p) are forced into tapered channels. The distance a cell travels into a tapered channel depends on cell stiffness with more compliant cells traveling further into the channels. The distance traveled by a cell into the tapered channel (d_l) is therefore an indicator of cell stiffness. Viewing the deformation of a cell under two different applied pressures can be used to determine the mechanical properties of the cell envelope.

Our results demonstrated differences in stiffness between *E. coli* and *B. subtilis* (Figure 2) and suggested that a device with a shorter channel length would allow transport of *E. coli*, but not *B. subtilis*, potentially allowing for separation of bacteria based on the biomechanical properties [1]. When combined with theoretical mechanics models it allowed us to determine the stress distribution within individual bacteria and study their response to mechanical stimulation [2].

In our recent work we have explored the effects of mechanical loads on the assembly/disassembly of multicomponent efflux pumps. Multicomponent efflux pumps are three-part channels that cross the inner membrane, periplasm and outer membrane of bacteria and are used to remove toxins (excessive metal ions, antibiotics, etc.). Our data suggests that the assembly and function of multicomponent efflux pumps is sensitive to mechanical stress and strain [4].

References:

- [1] Sun, X., Weinlandt, W.H., Patel, H., Wu, M., Hernandez, C.J. (2014) "A Microfluidic Platform for Profiling Biomechanical Properties of Bacteria." *Lab Chip*. 14 (14), 2491-2498. NIHMS600175.
- [2] M. F. Roberts, A. Srivastava, X. Sun, L. Kreminski, L. Ling, L. Wang, P. Chen, C-Y. Hui, C. J. Hernandez. "A Microfluidic Platform for Generating Non-Uniform Mechanical Stress in Cell Envelopes of Live Bacteria," American Society of Microbiology Annual Meeting. Boston, MA, USA. 2016.
- [3] M.F. Roberts, A. Srivastava, L.M. Wang, C-Y Hui, L.A. Genova, P. Chen, C.J. Hernandez, "A microfluidic system for mechanical characterization and stimulus of individual bacteria," European Society of Biomechanics 2017.
- [4] M.F. Roberts, L.A. Genova, L.M. Wang, P. Chen, C.J. Hernandez, "Non-Uniform Mechanical Stress Promotes Metal Efflux Pump Disassembly," 62nd Annual Meeting, Biophysical Society. San Francisco, CA, USA. 2018.

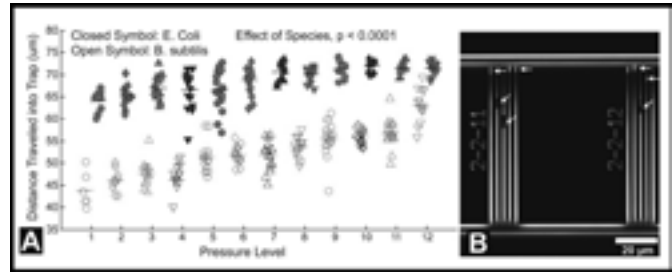


Figure 2: (A) The position of bacteria occupying trap channels at twelve different pressure levels (where level 1 is lowest and level 12 is greatest) in a single experiment are shown. Horizontal lines indicate averages at each pressure level. *E. coli* travel further into the traps than *B. subtilis* overall ($p < 0.0001$, ANCOVA) as well as at each individual pressure level ($p < 0.0001$, *t* tests). (B) Differences in bacteria stiffness between species can be detected in a mixed culture. *E. coli* expressing GFP (green, indicated by the upper horizontal arrows) traveled further into the trap channels than *B. subtilis* (indicated by tilted arrows), demonstrating the possibility of separating bacteria based on mechanical phenotype.

Design and Application of Microfluidic Devices to Study Cell Migration in Confined Environments

CNF Project Numbers: 2065-11, 2642-18

Principal Investigator: Jan Lammerding

Users: Aaron Windsor, Richard Armbruster, Vaishali Balachandran

Affiliations: Biomedical Engineering Department, Weill Institute, Cornell NanoScale Facility; Cornell University

Primary Source of Research Funding: National Institutes of Health award R01 HL082792; National Institutes of Health award 1U54 CA210184; Department of Defense Breast Cancer Research Program Breakthrough Award BC150580; National Science Foundation CAREER award CBET-1254846

Contact: jan.lammerding@cornell.edu, ajw49@cornell.edu, rwa79@cornell.edu, vb324@cornell.edu

Website: <http://lammerding.wicmb.cornell.edu/>

Primary CNF Tools Used: ABM contact aligner, SÜSS MA-6 contact aligner, MVD tool, Unaxis DRIE/RIE etcher, Anatech etcher, CVC sputtering tool, Tencor P-10 profilometer, Oxford 100 etcher, Trion etcher

Abstract:

It is becoming increasingly apparent that the physical properties of cells, including their size and deformability, play an important part in their function. One particular example is cell migration, which is crucial for physiological processes such as development and immune cell function, but also responsible for metastatic spreading in many cancers. To investigate how cells are able to squeeze through interstitial spaces smaller than the cross-section of the cell, we have developed microfluidic migration devices that provided 3D confinement and pore sizes mimicking physiological environments. Using these devices in combination with fluorescence time lapse-imaging, we have been able to confirm the role of nuclear deformability in confined migration, and also shown identified biological consequences of squeezing the nucleus through tight spaces, including transient nuclear envelope ruptures that result in DNA damage.

Summary of Research:

The ability of cells to migrate through tissues and interstitial spaces is an essential factor during development and tissue homeostasis, immune cell mobility, and in various human diseases. However, current methods to study the migration of cells in confining three-dimensional (3D) environments are limited by their imprecise control over the confinement, physiological relevance, and/or compatibility with high resolution imaging techniques.

We designed and built a polydimethylsiloxane (PDMS) microfluidic device composed of channels with precisely-defined constrictions mimicking physiological environments that enable high resolution imaging of live and fixed cells [1]. The device promotes easy cell loading and rapid, yet long-lasting (>24hrs) chemotactic gradient formation without the need for continuous perfusion, and is ideally suited for time-lapse imaging (Figure 1).

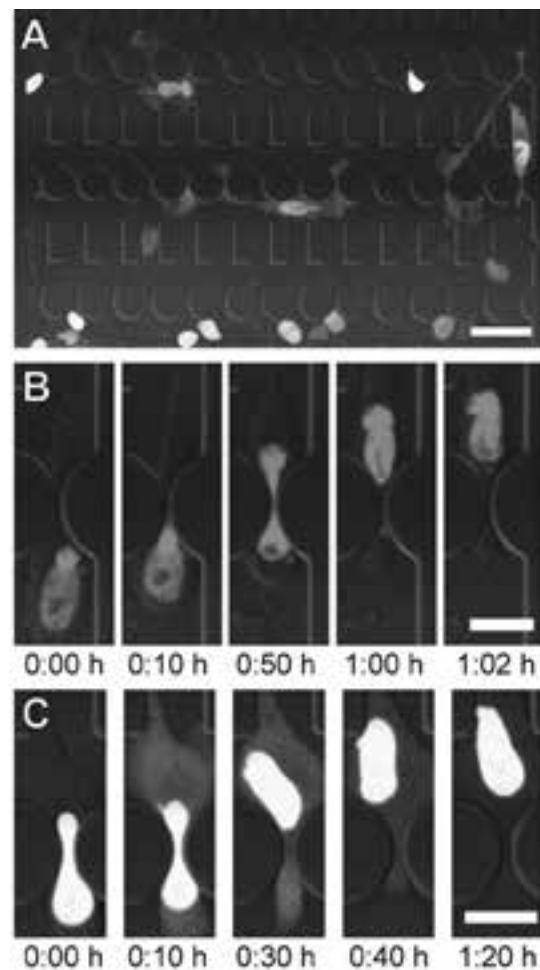


Figure 1: Cell migration through microfluidic constrictions. (A) Cells expressing NLS-GFP and H2B-tdTomato migrating through a microfluidic device. Scale bar: 50 μm . (B) Time series of a nucleus squeezing through a constriction. Scale: bar 20 μm . (C) Time series of a NE rupture event. NLS-GFP leaks into the cytoplasm upon NE rupture and is reimported into the nucleus as the NE is repaired. Scale bar: 20 μm . Figure reproduced from Elacqua, et al. PLoS one. 2018 [3]. See full color version on pages xxviii-xxix.

Using this device, we obtained detailed, quantitative measurements of dynamic nuclear deformation as cells migrate through tight spaces. We found that nuclear deformability, primarily governed by levels of lamin A/C, is a critical factor in determining the ability of cells to move through small constrictions. Furthermore, cells migrating through confined spaces incurred transient nuclear envelope rupture, nuclear fragmentation, and DNA damage, with ESCRT-III proteins playing an important role in restoring nuclear envelope integrity [2,3]. In addition, we showed that the exposure of genomic DNA to the cytoplasm during nuclear envelope rupture leads to activation of the cGAS/STING pathway, which promotes cancer metastasis [4].

The original device design was based on SU-8 soft photolithography [1]. While SU-8 was effective in creating these migration devices, this approach had several fabrication limitations. First, the reproducibility of the smallest SU-8 features ($\sim 1\mu\text{m}$) was difficult to attain, which led to an over use of successful full wafer devices.

The repeated molding and removal of PDMS would overtime weaken the SU-8/silicon substrate bond, eventually resulting in the delaminating of features and device failure. In order to reliably reproduce and preserve our most critical features, we decided forgo SU-8 and instead etch the precise constrictions of our devices directly into the silicon substrate. We accomplished this “bottom-down” approach by using a negative photoresist mask and deep-reactive ion etching (DRIE). This approach enabled us to achieve the critical dimension features with consistent reproducibility (Figure 2), and it also cut the fabrication time in half.

Since our time-lapse studies identified nuclear deformability as a rate-limiting factor in confined migration, we set out to develop a microfluidic device to perform high throughput measurements of nuclear deformability, using the principle of micropipette aspiration.

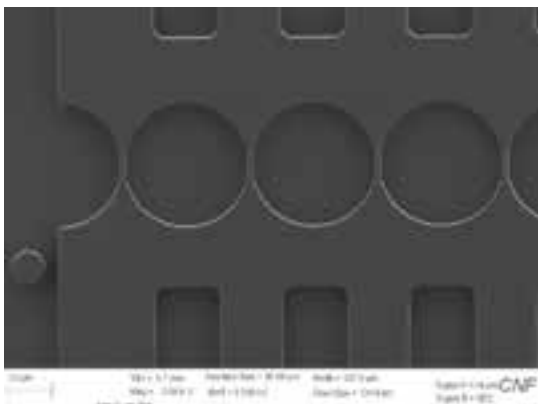


Figure 2: SEM image of a row of $1\mu\text{m}$ constrictions created by etching $5\mu\text{m}$ into silicon by deep-reactive ion etching.

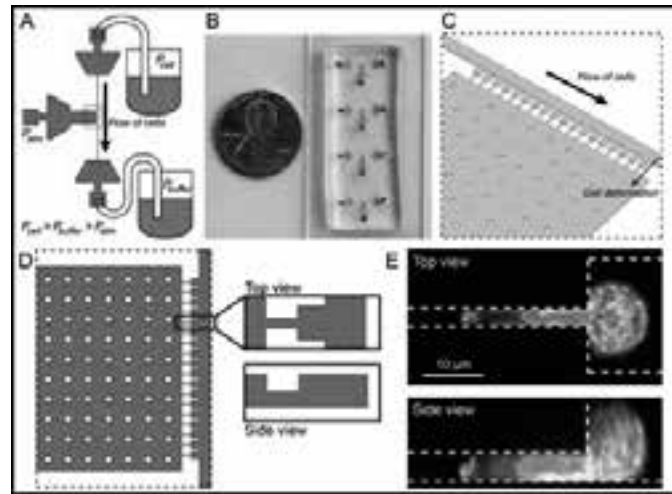


Figure 3: Overview of the microfluidic micropipette aspiration device. (A) Design overview, with applied external pressures indicated. (B) Image of four devices integrated onto a single glass slide. (C) Close-up of the design features containing the pockets and micropipette openings. (D) Top and side view of the same feature. (E) Confocal microscope images of a cell inside a pocket, with the nucleus (red) and cytoplasm (green) partially aspirated into the micropipette. See full color version on pages xxviii-xxix.

Cells in suspension are perfused into the device and segregated into single cells located in individual pockets, each equipped with a small micropipette-like opening (Figure 3). A large pressure gradient across the micropipette results in nuclear deformation (protrusion) into the micropipette, which can be quantified using automated image analysis and used to infer nuclear deformability.

In conclusion, the integration of our migration and micropipette aspiration devices with high resolution time-lapse imaging provides a powerful new approach to study intracellular mechanics and dynamics in a variety of physiologically relevant applications, ranging from cancer cell invasion to immune cell recruitment.

References:

- [1] Davidson PM, Sliz J, Isermann P, Denais C, Lammerding J. Design of a microfluidic device to quantify dynamic intranuclear deformation during cell migration through confining environments. *Integrative Biology*. 7: 1534-1546, <https://www.ncbi.nlm.nih.gov/pubmed/26549481> (2015).
- [2] Denais CM, Gilbert RM, Isermann P, McGregor AL, te Lindert M, Weigelin B, Davidson PM, Friedl P, Wolf K, Lammerding J. Nuclear envelope rupture and repair during cancer cell migration. *Science*. 352(6283): 353-8, <https://www.ncbi.nlm.nih.gov/pubmed/27013428> (2016).
- [3] Elacqua JJ, McGregor AL, Lammerding J. Automated analysis of cell migration and nuclear envelope rupture in confined environments. *PLoS One*. 13(4): e0195664, <https://www.ncbi.nlm.nih.gov/pubmed/29649271> (2018).
- [4] Bakhom S, Ngo B, et al. Chromosomal instability promotes metastasis through a cytosolic DNA response. *Nature*. 553(7689): 467-472, <https://www.ncbi.nlm.nih.gov/pubmed/29342134> (2018).

Zero-Mode Waveguides on Thin Silicon Nitride Membranes for Efficient Single-Molecule Sequencing

CNF Project Number: 2214-13

Principal Investigator: Prof. Meni Wanunu

Users: Dr. Vivek Jadhav, Dr. Mohammad Amin Alibakhshi

Affiliation: School of Physics, Northeastern University

Primary Source of Research Funding: NIH award No. 1R01 HG009186

Contact: wanunu@neu.edu, v.jadhav@neu.edu, m.alibakhshi@northeastern.edu

Website: <http://www.northeastern.edu/wanunu/>

Primary CNF Tools Used: LPCVD CMOS Nitride – E4, JEOL 6300, SC4500 odd-hour evaporator, Zeiss Ultra SEM

Abstract:

Nanopores can generate localized electric fields to focus molecules to 3D positions with high precision. Previously, we have shown that the electrophoretic loading of nanopore zero-mode waveguides (NZMWs) is orders of magnitude more efficient than either diffusion or magnetic bead-based loading techniques. However, serial fabrication of uniform solid-state nanopores arrays is not currently feasible on a large scale. In this work, we demonstrate wafer-scale fabrication of porous membranes containing solid-state nanopore networks for large scale positioning of macromolecules using fabrication techniques derived from molecular layer deposition. These porous membranes will be used to fabricate porous zero-mode wave guides (PZMWs) as large-scale parallel replacements to NZMWs.

Summary of Research:

Zero-mode waveguides (ZMWs) are wavelength-scale apertures in aluminum films, used for single-molecule detection [1]. By immobilizing the DNA-polymerase template at the base of the ZMWs and imaging the incorporation of fluorescently-labeled nucleotide by polymerase a sequence of a single DNAs can be read [2]. Previously, it has been demonstrated that by fabricating ZMWs on 50-nm-thick silicon nitride membranes, and drilling a 3-5 nm pore at the ZMW base, the efficiency of molecular loading is enhanced by orders of magnitude [3]. These ZMW structures were fabricated with e-beam lithography (JEOL 6300) at the CNF.

We continue to fabricate these ZMW devices for our DNA sequencing experiments. Figure 1 shows a darkfield microscope image of a device. The base of the ZMWs is modified by depositing molecule layer deposition to form a porous layer to facilitate more efficient capture of large DNA molecules. The ZMW surface is passivated using by SiO₂ deposited using atomic layer deposition

(ALD) to protect it from electrochemistry with chloride buffer that may occur during voltage bias experiments.

These structures may be used for capturing DNA-polymerase complexes. In Figure 2, we show the SEM image (ZEISS Ultra) of Al pillars before lift-off process. In Figure 3, we show ZMW structure after the lift-off process.

References:

- [1] Larkin, J., et al., Reversible Positioning of Single Molecules inside Zero-Mode Waveguides. *Nano Letters*, 2014. 14(10): p. 6023-6029.
- [2] Eid, J., et al., Real-time DNA sequencing from single polymerase molecules. *Science*, 2009. 323(5910): p. 133-138.
- [3] Larkin, J., Henley, R. Y., Jadhav, V., Korlach, J., and Wanunu, M. Length-independent DNA packing into nanopore zero-mode waveguides for low-input DNA sequencing. *Nature Nanotechnol*, 2017. 12, 1169-1175.



Figure 1: Conventional dark-field microscopy image of ZMWs on a thin SiN membrane after EBL.

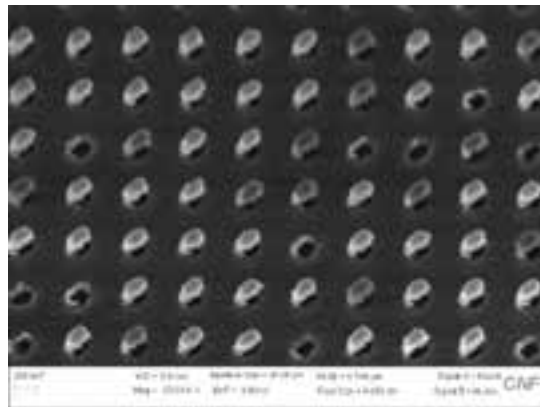


Figure 2: Scanning electron microscope image of Al pillars before lift-off process.

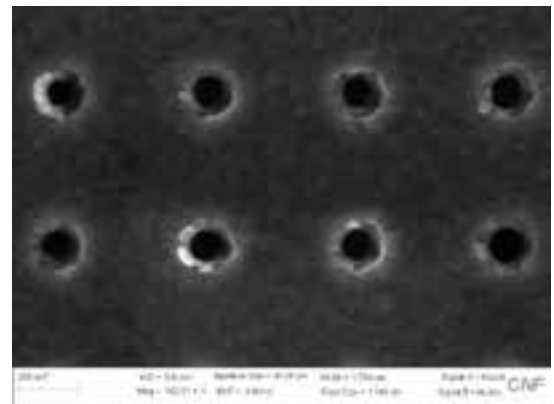


Figure 3: ZMW structure after the lift-off process.

Microfabricated Devices for Cell Organization

CNF Project Number: 2249-13

Principal Investigator: Minglin Ma

User: Wei Song

Affiliation: Department of Biological and Environmental Engineering, Cornell University

Primary Source of Research Funding: American Diabetes Association

Contact: mm826@cornell.edu, ws336@cornell.edu

Website: <http://malab.bee.cornell.edu>

Primary CNF Tools Used: DWL2000 mask writer, ABM contact aligner

Abstract:

Different types of cells dynamically self-assemble and organize themselves in a spatiotemporal and context-dependent manner [1]. In this study, we report the spatiotemporal dynamics of cell organization of a binary cellular mixture (MDA-MB-231 and MCF10A cells) seeded in microfabricated microwells. The initial seeding ratio of binary cells determined the degree of encapsulation of MCF10A cells by MDA-MB-231 cells. When cells were free to grow, the differential proliferation rate of MDA-MB-231 (low growth rate) and MCF10A cells (high growth rate) resulted in a reversed core (MDA-MB-231)-shell (MCF10A) organization at seeding ratio of 1:1 (MDA-MB-231:MCF10A) and a side-by-side aggregate structure at seeding ratio of 4:1 after long-term culture.

Summary of Research:

Fabrication of Polydimethylsiloxane (PDMS) Microwell. The photomask was prepared using DWL2000 mask writer (Heidelberg Instruments). The silicon wafer was spin-coated with SU-8 2150 photoresist (MicroChem) at 500 rpm for 40 sec and then 2500 rpm for 30 sec. The wafer was covered with the photomask and exposed by a UV photolithography machine (ABM contact aligner) for 32 sec. After being developed and post-baked, the SU-8 master wafer was fabricated. The SU-8 master wafer was then used to create PDMS (Sylgard 184, Dow Corning) mold. A mixture (10:1) of Sylgard 184 silicone elastomer components was casted onto the master wafer and cured at 60°C overnight to prepare a PDMS microwell. Figure 1 is a microscopic image of PDMS microwells.

Formation of Cell Aggregates in PDMS Microwells.

PDMS microwells were autoclaved, placed in a 24-well plate, and coated with 1% (w/v) Pluronic® F127 (Sigma) solution before cell seeding to prevent cell attachment on PDMS surface and facilitate formation of cell aggregates. To form cell aggregates, cell suspensions of MDA-MB-231/MCF10A mixture (MDA-MB-231:MCF10A=1:1 and 4:1, total 1.0×10^6 cells) were added to each well of 24-well plate with PDMS microwells inside. After four hours of static culture, the cells that were adhered to

the interspace between microwells were removed by medium change. The cells that fell into the microwells formed cell aggregates after overnight culture. The cell aggregates were cultured in microwells for nine days. The mixed medium (MDA-MB-231 medium:MCF10A medium=1:1 and 4:1) was changed every two days. Figure 2 is a fluorescent image of cell segregation of MDA-MB-231 (red colour) and MCF10A (green colour) cells at 1:1 cell seeding ratio over nine days of culture. Figure 3 is a fluorescent image of cell segregation of MDA-MB-231 (red colour) and MCF10A (green colour) cells at 4:1 cell seeding ratio over nine days of culture.

In summary, the initial seeding ratio and cell proliferation have significant effects on the evolution of cell organization of binary cellular mixture over long-term culture. Depending on the initial seeding ratios, the cell organization is either a core-shell (1:1) or side-by-side (4:1) aggregate by the differential proliferation rates of MDA-MB-231 and MCF10A cells.

References:

- [1] Yoshiki Sasai. Cytosystems dynamics in self-organization of tissue architecture. *Nature* 2013, 493, 318-326.

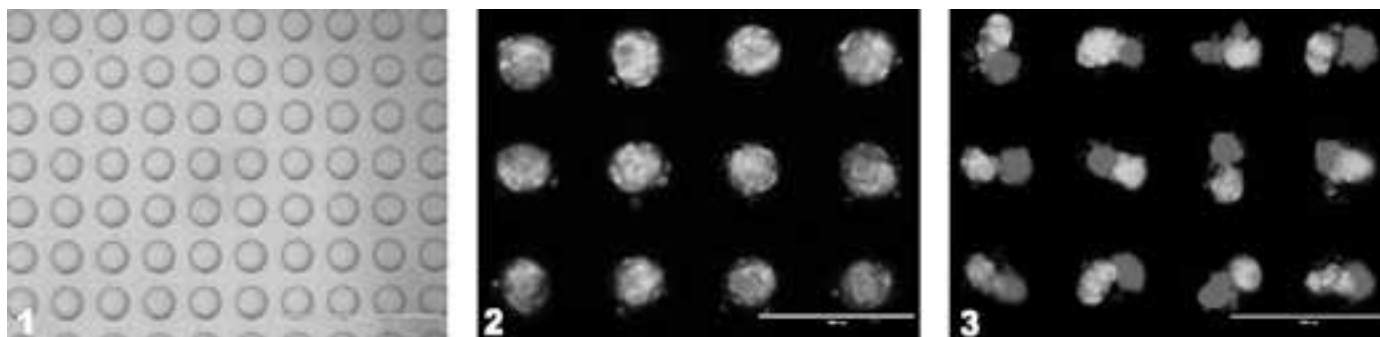


Figure 1, left: A microscopic image of PDMS microwells. Scale bar: 1000 μm . **Figure 2, middle:** A fluorescent image of cell segregation of MDA-MB-231 (red colour) and MCF10A (green colour) cells at 1:1 cell seeding ratio over 9 days of culture. Scale bar: 400 μm . See full color version on pages xxviii-xxix. **Figure 3, right:** A fluorescent image of cell segregation of MDA-MB-231 (red colour) and MCF10A (green colour) cells at 4:1 cell seeding ratio over nine days of culture. Scale bar: 400 μm . See full color version on pages xxviii-xxix.

Electrochemical Detection Array Combining Amperometry and Total Internal Reflection Fluorescence

CNF Project Number: 2260-13

Principal Investigator: Manfred Lindau

User: Meng Huang

Affiliation: School of Applied and Engineering Physics, Cornell University

Primary Source of Research Funding: National Institutes of Health

Contact: ML95@cornell.edu, mh2236@cornell.edu

Primary CNF Tools Used: ABM contact aligner, YES Asher, AJA sputtering system, Aura 1000 resist stripper, Image Reversal Oven, Oxford PECVD, Oxford 81 etcher

Abstract:

Neurotransmitters are released in a quantal event by fusion with membranes. The mechanism of this fusion event remains unknown but is crucial for molecular manipulation and various kinds of disease. We develop and fabricate an electrochemical detection array capable of combining amperometry measurement and total internal reflection fluorescence (TIRF). Amperometry provides the information for the releasing neurotransmitters from vesicles in the cell while TIRF enables direct visualization of vesicles with appropriate fluorescence labels. The combination of the two methods offers a new way for studying the exocytosis process.

Summary of Research:

Exocytosis is the process where neurotransmitters are released into the extracellular space [1]. The amperometry measurement provides precise details about the released transmitters in a single quantal event. While amperometry has the above-mentioned advantages, it measures the releasing contents reaching the electrodes and cannot directly characterize the releasing mechanisms. The total internal reflection fluorescence (TIRF) can detect the fluorescence signals at the substrate surface to visualize the foot print of the cell with its generated evanescence wave. The combination of the two methods offers the availability of monitoring vesicle releasing events and amperometry spikes simultaneously.

To fully utilize the TIRF technology, the specific site of release must be known to locate the fluorescence signal. Therefore, we developed the electrochemical detection (ECD) array with four electrodes between which a cell can be placed, as shown in Figure 1 [1]. Individual fusion events can be detected amperometrically with ~ 200 nm precision, utilizing a map of random walk simulations while the cell surface can be imaged with TIRF microscopy [3].

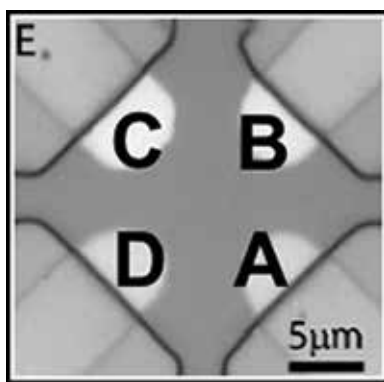


Figure 1: The micrograph showing the geometry of the 4-electrode ECD device.

A 4-inch, 175 μm thick glass wafer was used for the fabrication of the ECDs. Patterns were transferred onto the wafer through general lithography with NFOL 2020 negative photoresist. The photoresist was spin-coated on the wafer with 3000 rpm for 30s, resulting in a thickness of 2 μm . After the soft bake, alignment and exposure was performed with ABM contact aligner for 7s at 12.14 mJ/s. Following the post exposure bake, the photoresist was developed using 726 MIF for 70s. Then 10 nm Ti/150 nm Pt were deposited on the device using the AJA sputtering

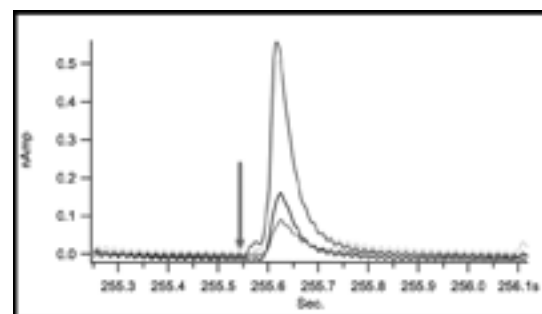


Figure 2: An amperometric spike related to the fluorescent signal in Figure 3. The arrow shows the event start point.

system followed by a lift of process using 1165. A 300 nm thick SiO₂ layer was deposited using Oxford PECVD. By using general lithography and Oxford 81 ether, a window was opened at the tips of the four electrodes to expose them to the environment.

To determine the role of Syntaxin clusters in fusion events in chromaffin cells, fluorescent labelled Syntaxin-CSYS construct was expressed in the cells by overnight infection of semliki forest virus harboring the gene for the expression of Syntaxin-CSYS. Syntaxin-CSYS was cloned into pSFV vector to make virus for the expression in bovine chromaffin cells. A fluorescent image of cell footprint on ECD arrays was collected by the TIRF microscopy. Transmitter release from the single fusion event was detected by the four ECD electrodes as correlated amperometric spikes with different amplitudes, depending on the diffusion distance between the release site and the respective electrode. Fluorescent movie by the TIRF microscopy and release events by the ECD array were recorded simultaneously. A combinatorial fluorescence change with the start of amperometric spike was observed.

A time superresolution analysis of fluorescence loss and amperometric spike start time by ECOM method shows the dispersal of syntaxin clusters coincide with the fusion pore formation.

References:

- [1] Kisler, K., et al., J. Biomater. Nanobiotechnol., 2012. 3(2): p.243-253.
- [2] Liu, X., et al. Analytical Chem., 2011, 83: p. 2445-2451.
- [3] Zhao, Y., et al., PNAS., 2013. 110(35): p.14249-14254.

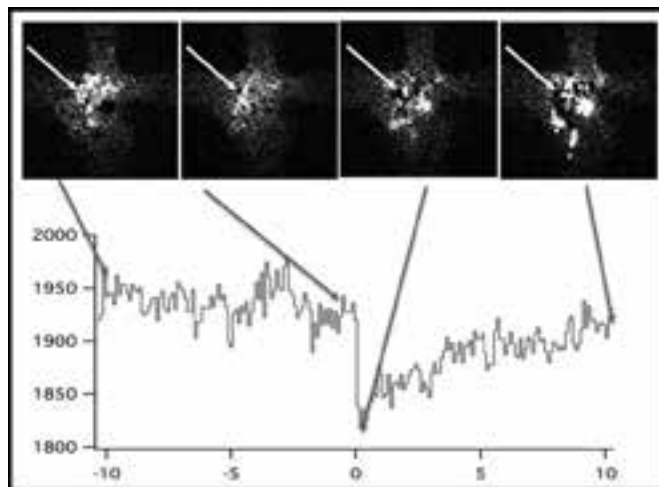


Figure 3: Fluorescent signal correlated with the amperometric spike in Figure 2. The arrows indicate the position of the event and corresponding signal strength.

Microfluidic Device for Studying Harmful Algal Blooms

CNF Project Number: 2262-13

Principal Investigator: Mingming Wu

User: Young Joon Suh

Affiliation: Department of Biological and Environmental Engineering, Cornell University

Primary Source of Research Funding: United States Department of Agriculture

Contact: mw272@cornell.edu, ys668@cornell.edu

Website: <http://biofluidics.bee.cornell.edu/>

Primary CNF Tools Used: ABM contact aligner, YES polyimide bake oven, MVD100

Abstract:

Harmful algal blooms (HABs) are increasing worldwide causing degradation of lake ecosystems, and endangering recreational and drinking water resources. The exact mechanisms that lead to harmful algal blooms remain elusive, but they are often correlated with many chemical and physical environmental cues including nutrients, temperature, and fluid flows. Current assay formats such as in pond and test tubes are not appropriate for probing the role of many environmental factors. Here we developed a microfluidic platform, where cells are cultured in an array of microhabitats with controlled nutrient and chemical gradients. Using this platform, we explored the roles of cell-cell communication signals in the growth, motility and clustering of a common HAB forming cyanobacteria, *Microcystis aeruginosa*. Our ultimate goal is to find a set of environmental conditions under which rapid cyanobacteria growth is triggered and use this knowledge to discover effective control solutions for HABs.

Summary of Research:

Microfabrication of this microfluidic device is challenging since the height of the side channels and the microhabitats are different as shown in Figure 1. The double-layer SU-8 method was chosen to fabricate this device. The wafer was first dehydrated in an oven to remove water vapor. SU-8 2100 was spun on the silicon wafer at 3000 rpm for 30 seconds to form the first 100 μm thick layer. The edge bead was removed using acetone-wetted wipes. Then, a soft bake was performed on the wafer by ramping up the temperature slowly at 2°C/min from room temperature to 65°C in an hour. Then, the temperature was increased to 95°C at 2°C/min and was left on the hot plate overnight. Next day, the wafer was cooled down to room temperature slowly by turning off the hot plate.

The first layer of SU-8 was exposed to the microhabitat pattern using the 365 nm filter at 250 mJ/cm² on a contact aligner (ABM contact aligner, ABM, Inc., Silicon Valley, CA). Then, the second layer of SU-8 was poured and spun at 3000 rpm for 30 seconds. Edge bead removal was performed using the acetone-wetted wipes. Then,

the soft bake was performed. Using 320 mJ/cm² on the same contact aligner using the align marks, both layers of SU-8 were exposed to the pattern of side channels. Then, a post-exposure bake was performed. For post exposure bake, the wafer was heated to 65°C from room temperature at 2°C/minutes and maintained for five minutes. Then, the wafer was ramped up to 95°C at 2°C/min and was maintained for 15 minutes. Then, the wafer was cooled down to room temperature by turning off the hotplate. Then, the wafer was developed using the SU-8 developer. Isopropanol was used to rinse the wafer. Hard bake was performed using the YES polyimide oven. Finally, FOTS treatment was done using the MVD100.

References:

- [1] Beum Jun Kim, Lubna V. Richter, Nicholas Hatter, Chih-Kuan Tung, Beth A. Ahner, and Mingming Wu, An array microhabitat system for high throughput studies of microalgal growth under controlled nutrient gradients, *Lab Chip*, 15: 3687-3694 (2015).

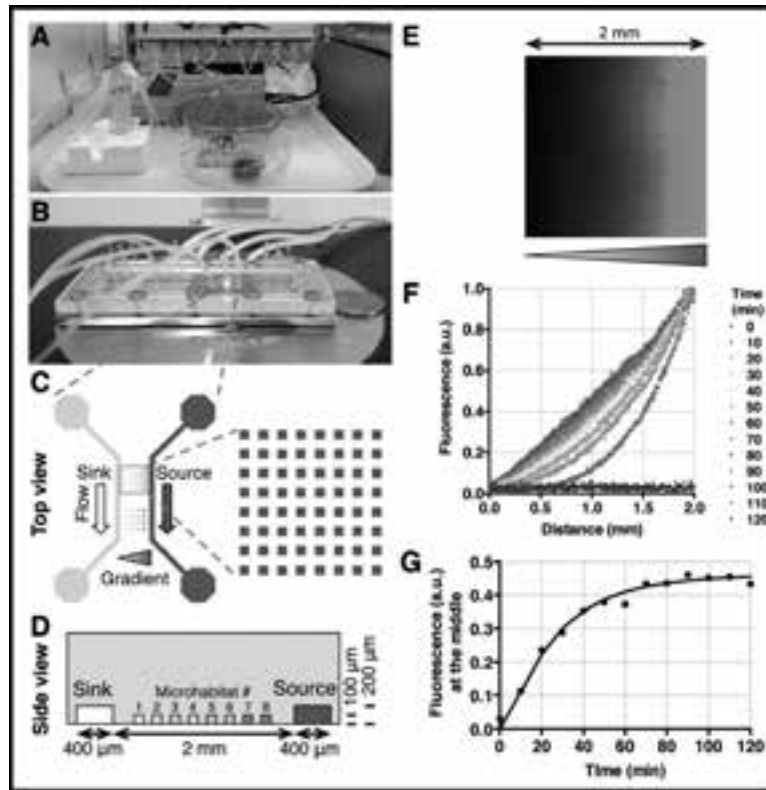


Figure 1: Microfluidic platform design and gradient characterization. A. An image of the microfluidic platform under fluorescent light for the growth of photosynthetic microalgae. The microfluidic platform is enclosed in an upside-down Pyrex® container with water reservoirs for humidity control. A syringe pump is used to perfuse media through the device. B. An image of the microfluidic platform on a microscope stage. Each platform contains four individual devices patterned in an agarose gel membrane. Tubing is used for connecting to the syringe pump for flow control. C. Top view of a device. Nutrients/buffers flow through the two side channels and form a nutrient gradient in the microhabitat array area through molecular diffusion. The top array contains 64 microhabitats, each has a dimension of $100\ \mu\text{m} \times 100\ \mu\text{m} \times 100\ \mu\text{m}$, with a gap of $100\ \mu\text{m}$ between the two adjacent habitats. The bottom array contains 16 microhabitats, each has a dimension of $200\ \mu\text{m} \times 200\ \mu\text{m} \times 100\ \mu\text{m}$, with a gap of $200\ \mu\text{m}$. Cells are pre-seeded before sandwiching the agarose gel membrane between a plastic manifold and a glass slide. D. Side view of a device. The distance between the source and sink channels is $2\ \text{mm}$, and the cross-sectional area of each side channel is $400\ \mu\text{m} \times 200\ \mu\text{m}$. The nutrient concentration is the same for each column of the array, with the column number labeled. E. A fluorescence image of the array microhabitat taken at $t = 1\ \text{h}$, where $t = 0$ is defined to be the time when fluorescein/buffer are introduced into the side channels. F. Time-evolution of fluorescence intensity profile in the array microhabitat area with a $10\ \text{min}$ interval and total time duration of $120\ \text{min}$. Each colored line represents the fluorescence intensity profile at a time point. G. Experimental results (dotted line) are validated against that (solid line) from COMSOL computation. Time evolution of fluorescence intensity in the middle of the array (or $1\ \text{mm}$ away from sink channel) is shown here.

Chip-Based Frequency Combs for High-Resolution OCT

CNF Project Number: 2364-15

Principal Investigator: Michal Lipson¹

User: Xingchen Ji²

Affiliations: 1. Department of Electrical Engineering, Columbia University, New York, NY 10027;

2. School of Electrical and Computer Engineering, Cornell University, Ithaca, NY 14853

Primary Source of Research Funding: Defense Advanced Research Projects Agency

Contact: ML3745@columbia.edu, xj53@cornell.edu

Primary CNF Tools Used: LPCVD, e-beam lithography, Oxford 100 etcher, AJA sputter deposition

Abstract:

We demonstrate chip-based frequency combs as a novel source for optical coherence tomography (OCT). For the first time an OCT image of human tissue is acquired using a silicon nitride microresonator. The potential for ultrahigh-resolution optical coherence tomography (UHR-OCT) is shown.

Summary of Research:

Optical coherence tomography (OCT) is a well-established medical imaging modality that has been used in fields such as ophthalmology, cardiology and dermatology [1-3]. Near infrared light sources with a full width half maximum (FWHM) bandwidth over 150 nm may allow for an axial resolution down to one micrometer in tissue [4]. An OCT broadband light source that can simultaneously achieve both, large bandwidth and deep signal penetration, remains out of reach.

Superluminescent diodes (SLDs), widely used in commercial OCT systems, have typical spectral bandwidths of up to 100 nm. Multiplexing of SLDs represents a viable approach to increase the bandwidth, but the overall achievable bandwidth is still limited by the gain medium. On the other hand, supercontinuum (SC) sources could in principle be used to achieve high resolution OCT. However, SC generation relies on pulsed lasers with kW-range peak power [5] and it suffers from instabilities in the output intensity and irregularities in the spectral shape, as a result of the complex interplay of linear and highly nonlinear effects during its generation [6].

Here we present a novel source for OCT based on chip-scale lithographically-defined microresonators with potential for sub-micrometer axial resolution and deep penetration. When optically pumped with a low-power continuous-wave laser source, they can generate broadband frequency combs. Such frequency combs have been demonstrated in numerous chip-scale platforms in the past decade [7-13]. The parametric gain in these photonic structures enables ultra-broad optical bandwidths which can exceed an octave [11-13] in contrast to traditional gain materials and is not limited by the gain bandwidth tradeoff.

We use an ultra-low loss silicon nitride resonator with a large cavity length of 1.9 mm in order to ensure that the generated frequency

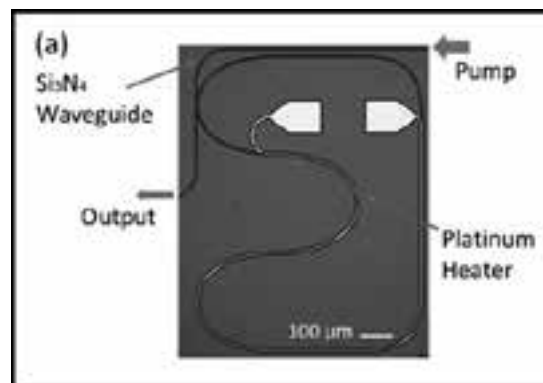


Figure 1: Microscopy image of the silicon nitride on-chip microresonator.

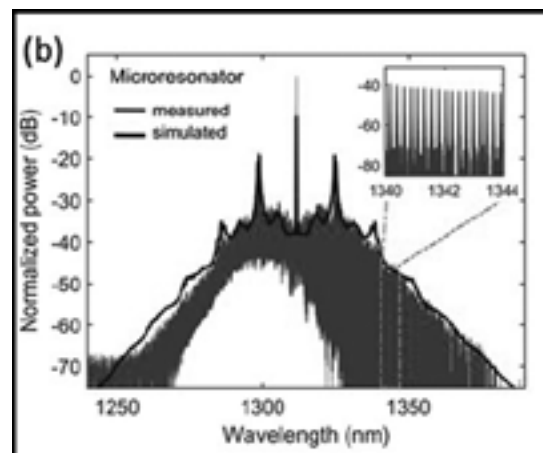


Figure 2: Purple: Measured frequency comb spectrum generated using the silicon nitride microresonators. Black: Simulated frequency comb. See full color version on pages xxviii-xxix

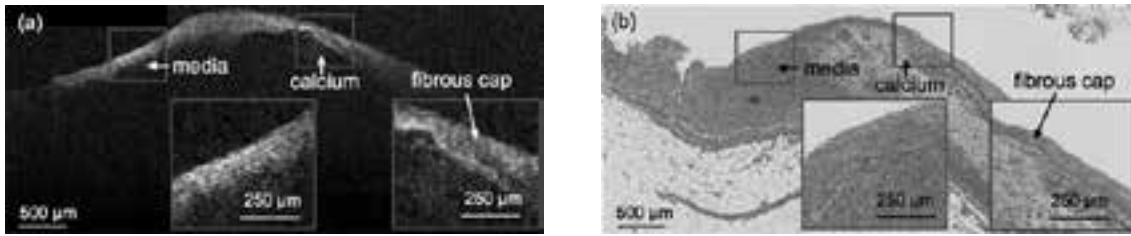


Figure 3, left: A stitched frequency-comb-based OCT B-scan of human coronary artery with a fibrocalcific plaque. Critical features are observed, including fibrous cap thickness, calcium, and media are depicted in OCT images, indicating a great potential for clinic applications. **Figure 4, right:** H&E histology.

comb has small line spacing critical for large imaging range. Our resonator design leads to a line spacing (38 GHz), which makes it compatible with current OCT spectrometers. Figure 1 shows the fabricated resonator. Using optical pump power as low as 117 mW, we generated frequency combs with a 38-GHz frequency spacing (shown in Figure 2).

The generated frequency comb spectrum has a FWHM of 47 nm corresponding to a theoretical axial resolution of 16.3 μm in good agreement with our measured FWHM of the axial point spread function of 18 μm . In order to perform OCT imaging a comb with low temporal coherence is required. We ensure that the comb lines are not locked in phase by tuning of the cavity resonance relative to the pump frequency using a microheater that is integrated on the chip. In order to generate these frequency combs, we use pump source of a low-cost distributed feedback (DFB) laser. The microresonator platform could enable inexpensive sources for OCT since it leverages mass fabrication on wafer-scale and allows miniaturization of OCT systems. Also, this platform has the potential to generate combs an octave span to enable UHR-OCT.

We acquire OCT images of human tissue with a standard commercial spectral domain (SD)-OCT system using the microresonator platform. Figure 3 shows *ex vivo* OCT of human coronary samples imaged with our microresonator frequency comb source using a commercial SD-OCT system. Sections of tissue were stained with hematoxylin and eosin (H&E). A pathologist who specializes in cardiovascular pathology annotated coronary tissue structure in histology image. Figure 3 shows a stitched frequency-comb-based OCT image of a human left anterior descending artery in comparison with the H&E histology in Figure 4. OCT B-scans were stitched using the method previously used in cervical image processing [14]. In the red inset, a gradually decreasing trend of backscattering can be visualized within the transition region from a fibrous

region to the media. The right inset in Figure 3 reveals a typical pattern of a fibrocalcific plaque [15], where a layer of signal-rich fibrous cap is on the top of calcium, a signal-poor region with a sharply delineated border. Importantly, overlying the fibrocalcific plaque region, we observe a thickness change from dense fibrous cap for stable plaque structure to thinner fibrous cap for unstable plaque structure, the latter of which has been found in great frequency in patients with acute coronary syndrome and acute myocardial infarction.

In summary, we have demonstrated the first OCT imaging based on a chip-scale source. We expect that microresonator frequency combs have great potential for UHR-OCT.

References:

- [1] Carrasco-Zevallos OM, et al. *Biomed. Opt. Express* 8(3):1607-1637 (2017).
- [2] Bouma BE, et al. *Biomed. Opt. Express* 8(5):2660-2686 (2017).
- [3] Huang, D., et al. *Sci. N. Y.* NY 254, 1178 (1991).
- [4] Povazay B, et al. *Opt. Lett.* 27(20):1800-1802 (2002).
- [5] Genty, G., Coen, S. and Dudley, J. M. *JOSA B* 24, 1771-1785 (2007).
- [6] Corwin, K. L., et al. *Appl. Phys. B* 77, 269-277 (2003).
- [7] Kippenberg, T. J., Holzwarth, R. and Diddams, S. A. *Science* 332, 555-559 (2011).
- [8] Suh, M.-G., Yang, Q.-F., Yang, K. Y., Yi, X. and Vahala, K. J. *Science* 354, 600-603 (2016).
- [9] Kuyken, B., et al. *Nat. Commun.* 6, 6310 (2015).
- [10] Wang, C. Y., et al. *Nat. Commun.* 4, 1345 (2013).
- [11] Okawachi, Y., et al. *Opt. Lett.* 36, 3398-3400 (2011).
- [12] Pfeiffer, M. H. P., et al. *Optica* 4, 684 (2017).
- [13] Del'Haye, P., et al. *Phys. Rev. Lett.* 107, (2011).
- [14] Gan, Y., et al. *Biomed. Opt. Express* 6, 1090-1108 (2015).
- [15] Tearney, G. J., et al. *J. Am. Coll. Cardiol.* 59, 1058-1072 (2012).

Handheld Chem/Biosensor Combining Metasurfaces and Engineered Sensor Proteins to Enhance Surface Plasmon Resonance (SPR)

CNF Project Number: 2430-16

Principal Investigator and User: Lori Lepak

Affiliation: Phoebus Optoelectronics, LLC

Primary Source of Research Funding: Department of Defense

Contact: llepak@phoebusopto.com

Website: www.phoebusopto.com

Primary CNF Tools Used: DWL2000 photomask writer, JEOL 9500 electron beam lithography, ASML DUV stepper, SC4500 evaporator, Oxford 81 etcher, Zeiss SEM, DISCO dicing saw

Abstract:

Since 2003, Phoebus Optoelectronics has enabled custom R&D solutions in the fields of metamaterials, plasmonics, antennas, and sensors. We work closely with our customers throughout device development, from product realization to small volume manufacturing. Our R&D portfolio spans the spectral ranges of visible light, infrared, terahertz, and microwave radiation, for applications in high resolution infrared imaging systems, wavelength and polarization filtering, tunable optical components, beam forming and steering, solar cells and renewable energy devices, and chemical and biological toxin sensors. Our agile team makes extensive use of the resources at the CNF for our nano/micro fabrication and testing, to provide cost efficiency and rapid turnaround. In the present report, we discuss recent efforts to develop a chem/bio toxin detection system, which provides the state-of-the-art sensitivity of a typical benchtop system with the superior SWaP performance of a handheld system. Our surface plasmon resonance (SPR)-based sensor is expected to be capable of detecting ng/mL concentrations of selected toxins in under five minutes.

Summary of Research:

SPR is a highly sensitive, label-free optical detection technique, whose underlying physics is illustrated in reflection mode in Figure 1. A laser passes through a prism, at an incident angle θ , on a gold film which is in contact with an analyte solution on its opposite side. The illumination produces an evanescent wave (surface plasmon), which significantly reduces the reflectance at a resonant angle. The resonant angle is strongly dependent on the local refractive index, within a few tens of nanometers of the gold surface, and thus is extremely sensitive to enzyme-substrate or antibody-antigen binding events near the surface. The resonance is independent of the geometric configuration of the optical elements (see [8] for mathematical derivation.), such that these results also apply to devices which operate in transmission mode.

As illustrated in Figure 2, Phoebus has combined two recently developed technologies to enable an SPR sensor system, which provides enhanced sensitivity at

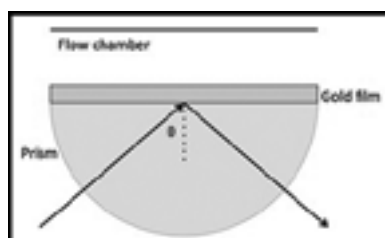


Figure 1: Surface plasmon resonance spectroscopy schematic. Reproduced from reference [8].

lower SWaP, relative to technologies currently on the market. First, Phoebus detects toxins using computationally designed proteins (CDP's), engineered to undergo an exceptionally large conformational change upon binding their specific target. This conformational change increases the density of the protein layer, thereby locally increasing the effective refractive index, which in turn enhances the SPR signal by a factor of 100-1000x competing systems. Second, Phoebus uses the resources of the CNF to fabricate plasmonic chips patterned with a metamaterial surface to enable extraordinary optical transmission (EOT), a phenomenon unique to metastructures in which light is transmitted through apertures much smaller than the incident wavelength, at anomalously large intensities relative to the predictions of conventional aperture theory.

EOT was first observed by T.W. Ebbesen in 1998 [1]. Since its founding in 2003, Phoebus has successfully harnessed EOT by incorporating metasurfaces into devices used

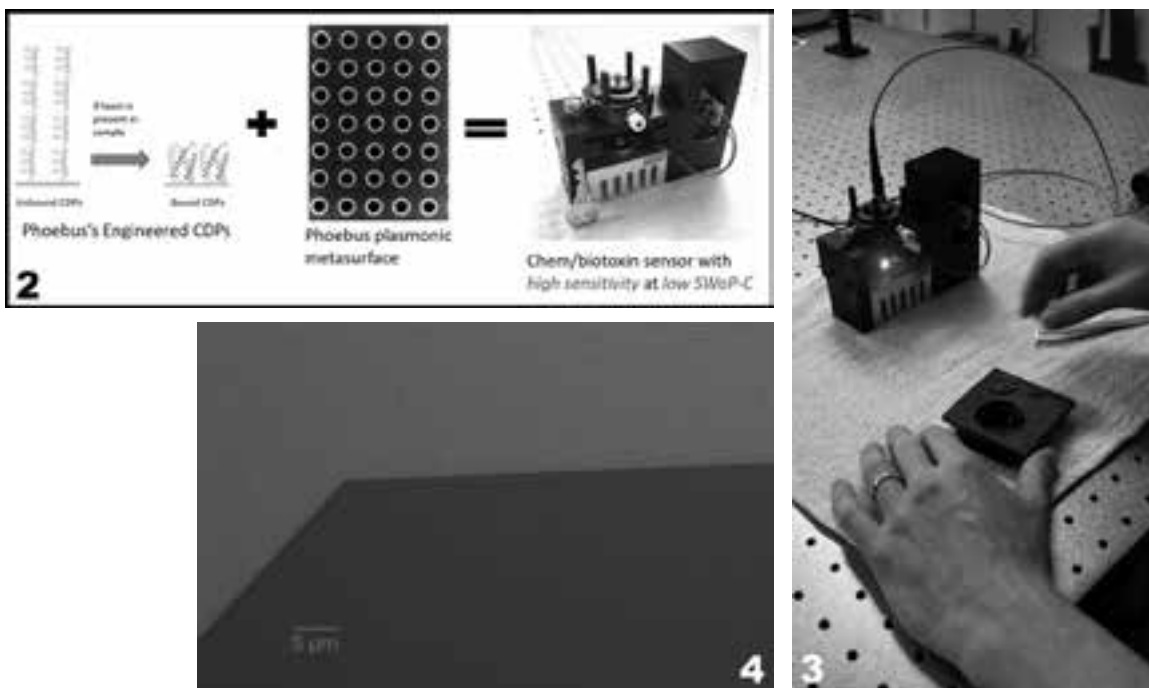


Figure 2, top left: Phoebus-engineered sensor system combines; (a) Designed CDPs which undergo extreme conformational changes upon binding target (b) Gold metasurface, patterned to maximize transmission at SPR resonant wavelength into (c) a high sensitivity, low SWaP-C chem/biotoxin sensor system. **Figure 3, top right:** Complete Phoebus handheld biosensor system. **Figure 4, above:** Optical microscope image of a metasurface used in disposable biosensor chip.

to perform light filtering [2-3], photon sorting [4-5], polarimetric detection [6], high speed optical detection [7], and most recently, in our SPR plasmonic sensor chips [8].

These two innovations are combined by attaching the engineered CDP's to the patterned gold metasurface using standard thiol-based attachment chemistry, to make a disposable sensor chip. As shown in Figure 3, this chip is inserted into the complete 3D printed module. All of the optical elements are already assembled in-line as indicated, for a transmission-based detection system. Except for Phoebus's disposable sensor chip, all of the optical components are inexpensively commercially available, which helps to make our overall system a highly cost-effective toxin sensing solution.

Our second-generation metasurface chips, shown in an optical microscope image in Figure 4, consist of an array of gold pillars, which serve both to bind the designed IDPs and to undergo SPR. To make the chip, we patterned the wires using the JEOL 9500 e-beam lithography system, evaporated Cr/Au, and performed a liftoff. This process is capable of consistently producing lines down to ~200 nm wide, with smooth enough sidewalls for an operable optical device.

References:

- [1] Ebbesen, T.W., et al., "Extraordinary optical transmission through sub-wavelength hole arrays." *Nature*, (1998). 391(6668): p. 667-669.
- [2] Crouse, D. "Numerical modeling and electromagnetic resonant modes in complex grating structures and optoelectronic device applications." *Electron Devices, IEEE Transactions on* 52.11 (2005): 2365-2373.
- [3] Crouse, D., and Keshavareddy, P. "Polarization independent enhanced optical transmission in one-dimensional gratings and device applications." *Optics Express* 15.4 (2007): 1415-1427.
- [4] Lansey, E., Crouse, D., et al. "Light localization, photon sorting, and enhanced absorption in subwavelength cavity arrays." *Optics Express* 20.22 (2012): 24226-24236.
- [5] Jung, Y.U, et al. "Dual-band photon sorting plasmonic MIM metamaterial sensor." *Proc. SPIE 9070, Infrared Technology and Applications XL*, 90702X (June 24, 2014); doi:10.1117/12.2050620.
- [6] Crouse, D., et al. "A method for designing electromagnetic resonance enhanced SOI metal-semiconductor-metal photodetectors." *J. of Optics A: Pure and App Optics* 8.2 (2006): 175.
- [7] Mandel, I, et al. Theory and Design of a Novel Integrated Polarimetric Sensor Utilizing a Light Sorting Metamaterial Grating. *Sensors Journal, IEEE*, (2012): Vol. PP, 99
- [8] Lepak, L., et al. "Handheld chem/biosensor using extreme conformational changes in designed binding proteins to enhance SPR" *Proc. SPIE 9862, Advanced Environmental, Chemical, and Biological Sensing Technologies XIII*, 9862-7 (April 17, 2016); doi:10.1117/12.2222305.

Scalable Sensor Array Platform for Analysis of Quantal Transmitter Release Events

CNF Project Number: 2460-16

Principal Investigators: Xin Liu, Manfred Lindau

User: Meng Huang

Affiliation: School of Applied and Engineering Physics, Cornell University

Primary Source of Research Funding: National Institutes of Health

Contact: ML95@cornell.edu, mh2236@cornell.edu

Primary CNF Tools Used: ABM contact aligner, AJA sputtering system, Unaxis 770 deep silicon etcher, Aura 1000 resist stripper, YES Asher, YES image reversal oven

Abstract:

Neurontransmitters are released in a quantal event by fusion with membranes. We develop and fabricate a CMOS sensor array capable of parallel electrochemical detection of vesicle release events from chromaffin cells. To enable amperometry measurement, polarizable platinum electrodes are deposited on the Al/Cu metal contact on the CMOS chip by sputtering. SU-8 insulation layer is also applied to protect the surface structure of the chip and avoid incomplete coverage of the metal contact by shifting the position of the electrodes as well as form deep wells to trap cells. A silicon wafer with deep etched wells is used as holder for the CMOS chips for better handling and pattern transfer.

Summary of Research:

Neurontransmitters are released into the extracellular space in a process known as exocytosis [1]. The amperometry measurement provides precise details about the released transmitters in a single quantal event. However, amperometric spikes vary from cell to cell even under the same condition [2]. Therefore, a large number of measurements for vesicle release events must be performed to achieve a change in the mean value. Here, we present the CMOS IC sensor array capable of parallel amperometry measurement of vesicle release events and the post-fabrication to enable its functionality.

The CMOS sensor chip is fabricated at MOSIS by On Semiconductor C₅F/N. Polarizable electrode materials such as platinum are not offered in this process. Instead, Al/Cu metal contact are deposited to serve as interconnection of the chip. However, amperometry measurement requires polarizable electrodes for low noise current measurement as the oxidation current is usually on the order of pA. Hence, it is necessary to have a post-fabrication process in the CNF clean room to deposit platinum electrodes directly onto the Al/Cu metal contacts for amperometry measurement. AJA sputtering system is used to deposit Ti(60s)/Pt(500s) bilayer with 400w power on the electrode to have a uniform metal film as well as good side wall coverage.

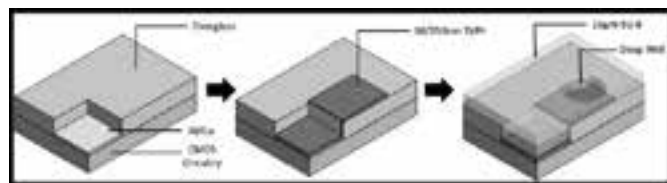


Figure 1: The geometry of shift electrode. The opening of the working area is redefined. In our case, one passivation SU-8 layer is applied with redefined shape (round) of the new opening for better cell trapping.

To avoid possible defect such as incomplete coverage of the Pt electrode, a shift electrode strategy is performed to redefine the position and shape of the working electrodes (Figure 1) [4]. The shifted electrodes also enable cell trapping by SU-8 deep wells. The patterned poly(L-lysine) in register with the electrodes will promote cell adhesion, while poly(ethylene glycol) is applied in between wells will resist cell adhesion [5]. Pt electrodes are deposited over the Al/Cu contact, but instead of just covering the contact window, they are extended to cover some part of the overglass. A 16 μm SU-8 2025 thick layer is fabricated on the surface of the CMOS chip. Deep wells with 20 μm in diameter are opened by general lithography at the redefined electrode position.

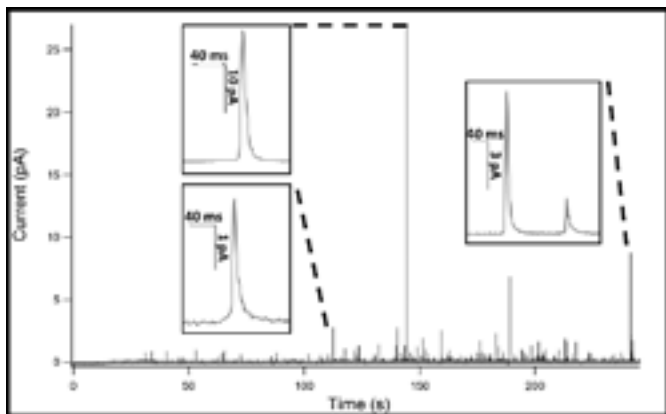


Figure 2: Amperometry recording at one pixel. Many amperometric spikes are observed, validating the function of the device.

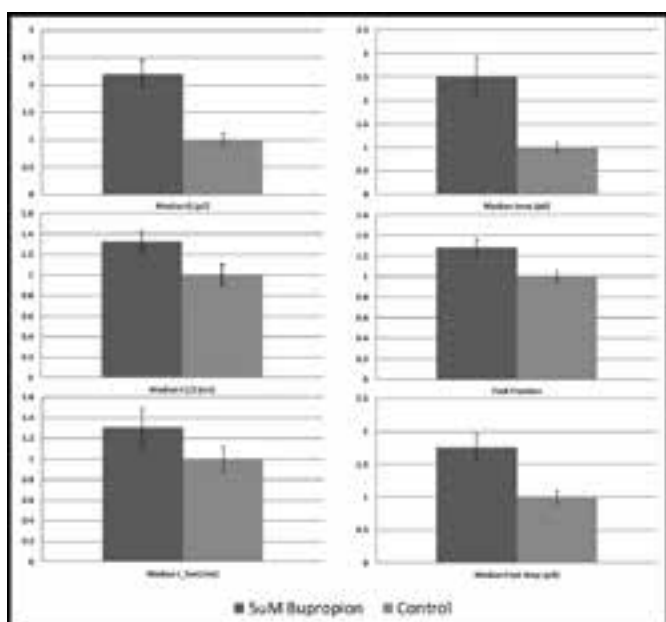


Figure 3: Comparison of various normalized amperometric parameters between the bupropion treated and the control group.

Microcontact printing of poly(L-lysine) and poly(ethylene glycol) will be performed for promotion and resistance of cell adhesion.

Previously we have demonstrated live cell recording on the device. Highly parallel amperometry measurement with low noise is shown in Figure 2 [6]. The device will significantly increase the efficiency of amperometry measurement.

To further utilize the advantages of the CMOS IC with deep wells, effects of several drugs and labels on the quantal release kinetics, such as bupropion, citalopram and FFN511, has been investigated. Figure 3 shows the results for the comparison of various amperometric parameters between the bupropion treated group and the control group. The results were collected from only four experiments from only four separate days, which would normally take weeks or months to get the statistical significance.

References:

- [1] Kisler, K., et al., J. Biomater. Nanobiotechnol., 2012, 3(2): p.243-253.
- [2] Colliver, TL., et al., J. Neurochem., 2000, 74(3): p. 1086-1097.
- [3] Kim, B., et al., Biosens Bioelectron., 2013, 41: p. 736-744.
- [4] Heer, F., et al. Biosens Bioelectron., 2004, 20(2): p. 358-366.
- [5] Liu, X., et al. Analytical Chem., 2011, 83: p. 2445-2451.
- [6] Huang, M., et al. Pflügers Archiv., 2018, 470(1): p. 113-123.

Droplet-Microfluidic Device for Stem Cell Culture

CNF Project Number: 2461-16

Principal Investigator: Benjamin D. Cosgrove

User: Andrea J. De Micheli

Affiliation: Meinig School of Biomedical Engineering, Cornell University

Primary Sources of Research Funding: Cornell Start-Up Funds, NIH Grant # R00AG042491 (Cosgrove)

Contact: bdc68@cornell.edu, ad689@cornell.edu

Website: <http://blogs.cornell.edu/cosgrove/>

Primary CNF Tools Used: Heidelberg DWL66FS/2000, SÜSS MJB4 contact aligner, SU-8 hotplates, SU-2 spinners

Abstract:

We are working on a droplet-microfluidic device to generate microscopic beads of poly(ethylene glycol), a biomaterial we use to study the interaction between muscle stem cells and their environment. The device is made from PDMS cast on a SU-8 patterned wafer generated by standard SU-8 photolithography techniques at Cornell NanoScale Facility.

Summary of Research:

Microfluidics have enabled a more high-throughput and comprehensive examination of biological systems. In particular, the interaction between stem cells and their local environment (the niche) can be studied using biomaterial constructs that attempt to recreate physical and biological aspects of the niche. We used a droplet-microfluidic device (designed and built at CNF) to generate hundreds of thousands of beads of the biomaterial poly(ethylene glycol) (PEG) with various physical and biochemical properties. We will be using these $\sim 100 \mu\text{m}$ PEG beads as artificial microenvironments to screen for muscle stem-cell-niche interactions that are characteristic of muscle physiology.

So far, we have created PEG beads with different levels of incorporated laminin and observed myoblast binding in culture.

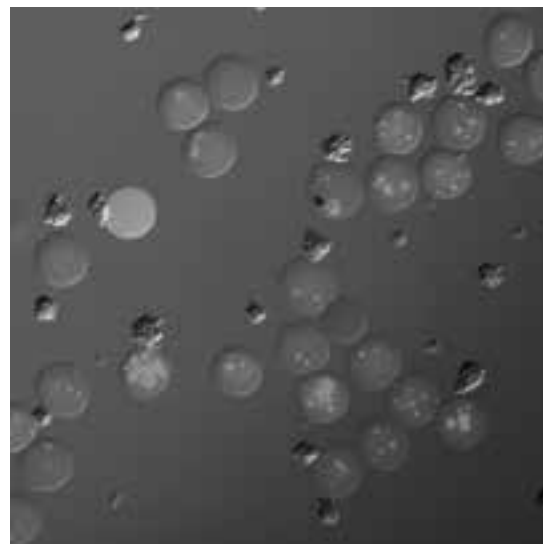


Figure 1: 100 μm PEG beads coated with the fluorescent (Alexa647) protein laminin (red). Clusters of myoblasts can be seen adhering to the beads. See full color version on pages xxviii-xxix



Figure 2: Left: SU-8 wafer with patterned structures. Right: A series of eight PDMS microfluidic devices.

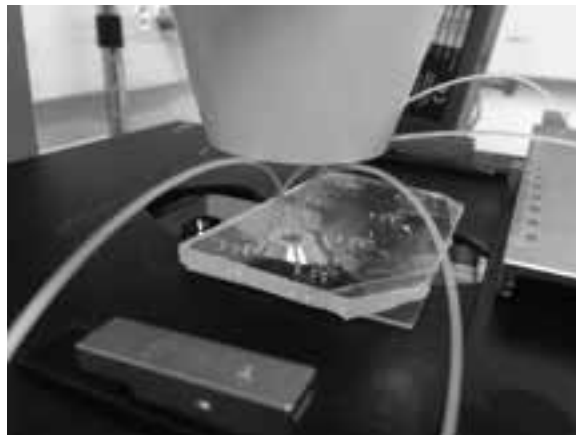


Figure 3: Droplet-microfluidic setup for generating PEG beads. Courtesy De Vlaminck lab.

Metasurfaces for Infrared Spectroscopy of Live Cells in a Microfluidic Chamber

CNF Project Number: 2472-16

Principal Investigator: Gennady Shvets

Users: Glen Kelp, Junlan Lu, Shourya Dutta Gupta

Affiliations: Applied and Engineering Physics, Cornell University; Department of Physics, University of Texas at Austin

Primary Source of Research Funding: Cornell University

Contact: gshvets@cornell.edu, gk389@cornell.edu, JL3286@cornell.edu, sd789@cornell.edu

Website: <http://shvets.aep.cornell.edu>

Primary CNF Tools Used: JEOL 9500, CVC SC4500 evaporator, ZEISS Supra SEM, PDMS casting station

Abstract:

Non-invasive and label-free identification of different cell types allows for early stage diagnosis and leads to more efficacious potential treatment of various human diseases. For example, early stage cancer detection enables many more treatment options and potential cure as compared to detection in the later stage of cancer. In this respect, circulating tumor cells (CTCs) in the blood stream have been shown to be a strong indicator of early stage of various cancers. However, separation, capturing and identification of CTCs still possess significant challenges with regarding to their extremely low concentration as well as the inability of traditional methods to characterize them accurately. Other diagnostic techniques, such all-optical diagnostics of aspiration biopsies, have similar requirements for rapid capture and identification of cancer cells. The following approach is pursued in our lab: simultaneous capture and spectral cytopathology using a combination of dielectrophoresis (DEP) and metasurface-enhanced infrared reflection spectroscopy (MEIRS).

Summary of Research:

Mid-IR spectroscopy is one of the prominent ways of identifying different materials via their fingerprint molecular vibrations. In the past, this has been used for spectroscopically distinguishing cancerous versus non-cancerous tissue. Typically, at least a complete monolayer of cells is required for performing such a characterization. This limitation on the number of cells is a large hindrance for adapting this technique for the detection of CTCs, due to their inherently low concentration in blood. It has been previously shown by our group that mid-IR spectroscopy performed using plasmon resonant metasurfaces (Figure 1) allows one to enhance the sensitivity of this technique significantly and we used this approach to accurately characterize a single protein layer [1]. The increase in sensitivity arises from the highly enhanced optical electric fields created near the structures. Furthermore, the metasurface only probes a small region close to the cell membrane due to the rapid decay of the enhanced fields away from the metasurface.

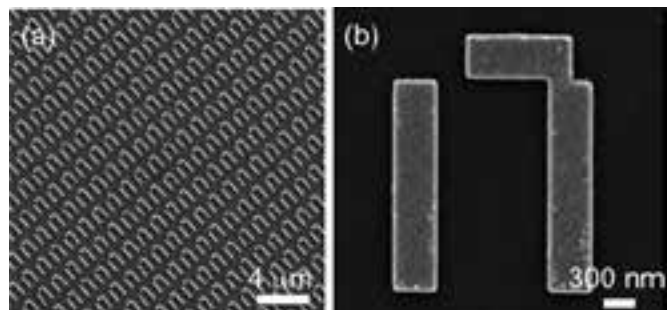


Figure 1: SEM micrographs of the plasmonic metasurface sensor used for MEIRS. (a) Low magnification image showing the periodic plasmonic microstructures. (b) SEM image of a single unit cell of the metasurface. The metasurface is designed to exhibit very high electric fields in the vicinity of the structure. Depicted unit cells are repeated on the substrate plane to form arrays $500 \times 120 (\mu\text{m})^2$ in size. These metasurfaces are made of gold and fabricated on CaF_2 substrates using electron beam lithography.

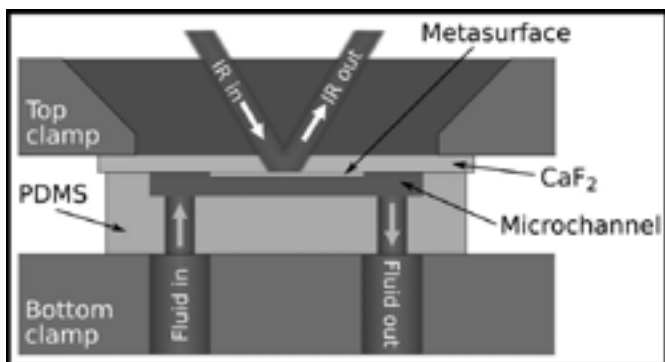


Figure 2: Schematic of a microfluidic device for capturing cells onto the metasurface sensor and measuring their mid-IR spectra. CaF_2 substrate is coupled to a PDMS microchannel allowing cell solution to flow over the sensor surface. PDMS and CaF_2 are fixed together with acrylic clamps compatible with standard microscope slide mounts. Cell solution is pumped through the channel with a syringe pump and voltage is applied on the wire electrodes within the metasurface using a function generator (not shown).

Deposition of cells directly onto the metasurface sensor is achieved with the use of dielectrophoresis. Since cells are essentially dielectric particles, a nonuniform AC electric field can be set up around the metasurface by applying voltage on electrodes embedded in the sensor design, causing cell movement due to DEP force (proportional to electric field gradient). IR spectra of the cells captured and immobilized on the metasurface can then be simultaneously collected under an IR microscope. A schematic of a device constructed to capture cells and collect their mid-IR spectra is shown on Figure 2.

Attachment of cells onto the sensor surface can be further improved by covering the sensor with antibodies. By tuning the frequency of AC signal applied to the electrodes, it is also possible to capture specific cells while repelling other kinds of cells in a multi-species cell solution. Separation of different cell types is especially important while working with blood samples that have very low concentration of CTCs. In the case of CTCs, the separation of tumor and blood cells with DEP is very effective, since those cell types have very different dielectric properties and therefore the frequency of the electric field can be chosen such that CTCs move to the sensor while pushing the blood cells away from it.

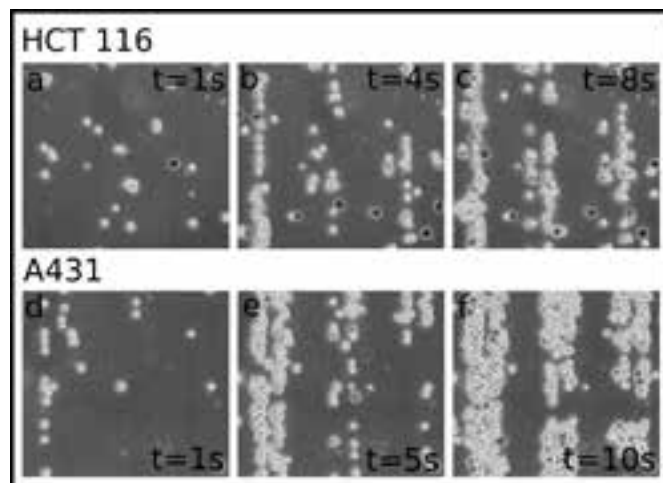


Figure 3: Cells captured on the sensor surface using DEP at different times. (a)-(c) Colon cancer cells (HCT 116). (d)-(f) Skin cancer cells (A431). Three metasurfaces are visible on each image, with two wire electrodes embedded in each metasurface. The DEP force is strongest on the wires, causing cells to form lines on them.

Examples of cells captured onto the wires on the sensor surface are depicted in Figure 3. The device can be mounted on a standard IR microscope, allowing instantaneous collection of cell mid-IR spectra for their identification. We have shown that different cell types (e.g., cancerous and non-cancerous) have different mid-IR fingerprints. The difference in the spectral features between various cell types can thus be used for identifying them. The spectra are acquired in an aqueous environment during flow, which is generally not the case in most of the studies in literature. As the whole experiment is performed within a flow chamber enclosing the metasurface sensor, and over the course of just a few minutes, it paves the way for automated and rapid identification and characterization of cells.

References:

- [1] Fano-resonant asymmetric metamaterials for ultrasensitive spectroscopy and identification of molecular monolayers. Chihhui Wu, Alexander B. Khanikaev, Ronen Adato, Nihal Arju, Ahmet Ali Yanik, Hatice Altug, Gennady Shvets; *Nature Materials* 11, 69-75 (2012).

Listeria Sensor Chip via Surface Plasmon Resonance (SPR)

CNF Project Number: 2498-16

Principal Investigator and User: Lori Lepak

Affiliation: Phoebus Optoelectronics, LLC

Primary Source of Research Funding: National Institutes of Health

Contact: llepak@phoebusopto.com

Website: www.phoebusopto.com

Primary CNF Tools Used: DWL2000 photomask writer, ASML DUV stepper, AJA sputterer, Au electroplating, AJA ion mill, ZEISS SEM, DISCO dicing saw

Abstract:

Since 2003, Phoebus Optoelectronics has enabled custom R&D solutions in the fields of metamaterials, plasmonics, antennas, and sensors. We work closely with our customers throughout device development, from product realization to small volume manufacturing. Our R&D portfolio spans the spectral ranges of visible light, infrared, terahertz, and microwave radiation, for applications in high resolution infrared imaging systems, wavelength and polarization filtering, tunable optical components, beam forming and steering, solar cells and renewable energy devices, and chemical and biological toxin sensors. Our agile team makes extensive use of the resources at the CNF for our nano/micro fabrication and testing, to provide cost efficiency and rapid turnaround. In the present report, we discuss recent efforts to develop a biosensor system, which provides the state-of-the-art sensitivity of a typical benchtop system with the superior SWaP performance of a handheld system. Although our proof-of-concept prototype system is designed to detect *Listeria monocytogenes*, our system may be easily adapted to target any viral or gram-negative bacterial pathogen of interest, simply by designing new detection proteins specific to the new targets. We expect our system to find broad applications in public health and safety, medicine, and agriculture.

Summary of Research:

Metamaterial structures exhibit the unique phenomenon of extraordinary optical transmission (EOT), first observed by T.W. Ebbesen in 1998 [1]. In EOT, light is transmitted through apertures much smaller than the incident wavelength, at anomalously large intensities relative to the predictions of conventional aperture theory. Since its founding in 2003, Phoebus has successfully harnessed EOT by incorporating metasurfaces into devices used to perform light filtering [2-3], photon sorting [4-5], polarimetric detection [6], high speed optical detection [7], and most recently, including the present effort, in our SPR plasmonic sensor chips [8].

SPR is a highly sensitive, label-free optical detection technique, whose underlying physics is illustrated in reflection mode in Figure 1. A laser passes through a prism, at an incident angle θ , on a gold film which is

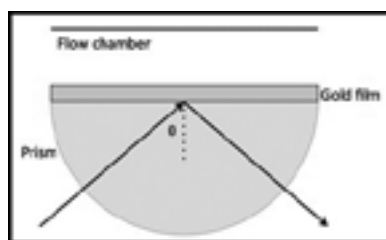


Figure 1: Surface plasmon resonance spectroscopy schematic. Reproduced from reference [8].

in contact with an analyte solution on its opposite side. The illumination produces an evanescent wave (surface plasmon), which significantly reduces the reflectance at a resonant angle. The resonant angle is strongly dependent on the local refractive index, within a few tens of nanometers of the gold surface, and thus is extremely sensitive to enzyme-substrate or antibody-antigen binding events near the surface. The resonance is independent of the geometric configuration of the optical elements (see [8] for mathematical derivation.), such that these results also apply to devices which operate in transmission mode.

Phoebus's technology, for the first time, enables an inexpensive (<\$1,000), hand-held system for the optical detection of *Listeria* via surface plasmon resonance (SPR), with a sensitivity currently only available in

expensive (>\$100,000) benchtop SPR systems. We have achieved this by combining two key innovations: 1) Computationally designed proteins (CDPs), engineered to simultaneously bind their target pathogens with the specificity of wild-type enzymes, while undergoing an exceptionally large conformational change upon binding to maximize the SPR signal, and 2) Disposable plasmonic sensor chips, fabricated using the resources of the CNF, to pattern plasmonic chips with a metamaterial surface to enable as shown in Figure 2.

Our fabricated first-generation metasurface chips, shown in Figure 3, consist of an array of gold wires, which serve both to bind the designed CDPs and to undergo SPR. These two innovations are combined by attaching the engineered IDP's to the patterned gold metasurface using standard thiol-based attachment chemistry, to make a disposable sensor chip. This chip is inserted into a handheld 3D printed module, as shown in Figure 3. All of the optical elements are already assembled in-line as indicated, for a transmission-based detection system. Except for Phoebus's disposable sensor chip, all of the optical components are inexpensively commercially available, which helps to make our overall system a highly cost-effective toxin sensing solution.

References:

- [1] Ebbesen, T.W., et al., "Extraordinary optical transmission through sub-wavelength hole arrays." *Nature*, (1998). 391(6668): p. 667-669.
- [2] Crouse, D. "Numerical modeling and electromagnetic resonant modes in complex grating structures and optoelectronic device applications." *Electron Devices, IEEE Transactions on* 52.11 (2005): 2365-2373.
- [3] Crouse, D., and Keshavareddy, P. "Polarization independent enhanced optical transmission in one-dimensional gratings and device applications." *Optics Express* 15.4 (2007): 1415-1427.
- [4] Lansley, E., Crouse, D., et al. "Light localization, photon sorting, and enhanced absorption in subwavelength cavity arrays." *Optics Express* 20.22 (2012): 24226-24236.
- [5] Jung, Y.U; Bendoyim, I; Golovin, A.B.; and Crouse, D.T. "Dual-band photon sorting plasmonic MIM metamaterial sensor." *Proc. SPIE 9070, Infrared Technology and Applications XL*, 90702X (June 24, 2014); doi:10.1117/12.2050620.
- [6] Crouse, D., and Keshavareddy, P. "A method for designing electromagnetic resonance enhanced silicon-on-insulator metal-semiconductor-metal photodetectors." *Journal of Optics A: Pure and Applied Optics* 8.2 (2006): 175.
- [7] Mandel, I; Gollub, J; Bendoyim, I; Crouse, D. Theory and Design of A Novel Integrated Polarimetric Sensor Utilizing a Light Sorting Metamaterial Grating. *Sensors Journal, IEEE*, (2012): Vol. PP, 99
- [8] Lepak, L., et al. "Handheld chem/biosensor using extreme conformational changes in designed binding proteins to enhance surface plasmon resonance (SPR)" *Proc. SPIE 9862, Advanced Environmental, Chemical, and Biological Sensing Technologies XIII*, 9862-7 (April 17, 2016); doi:10.1117/12.2222305.

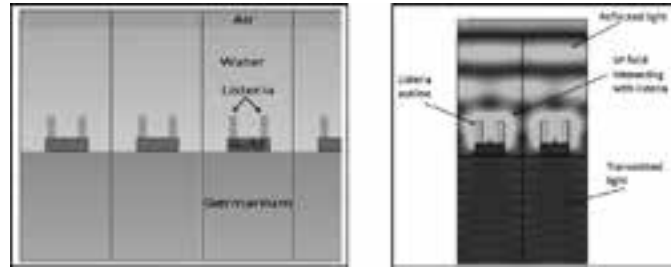


Figure 2: (Left) Unit cell of *Listeria* sensor. The full plasmonic chip consists of an array of these structures. (Right) Electric field profile at SP resonance, when bound to individual *Listeria*.

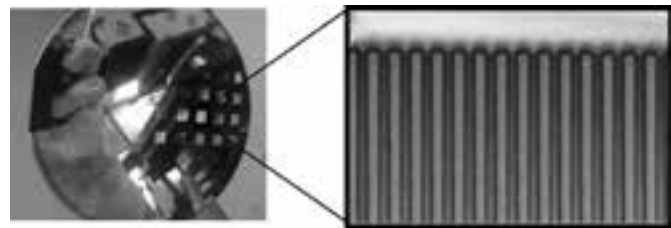


Figure 3: (Left) Wafer of plasmonic chips, fabricated on ASML DUV stepper. (Right) SEM image of a typical metasurface used in sensor chip.

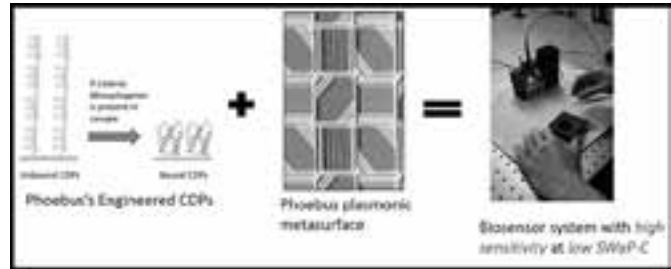


Figure 4: Phoebus-engineered sensor system combines (a) designed CDPs, which undergo extreme conformational changes upon binding target and (b) gold metasurface patterned to maximize transmission at SPR resonant wavelength into (c) a high sensitivity, low SWaP-C chem/biotoxin sensor system.

Gut-on-a-Chip using Microfluidic Devices

CNF Project Number: 2502-16

Principal Investigator: Alireza Abbaspourrad

User: Seyedramin Pajoumshariati

Affiliation: Food Science Department, Cornell University

Primary Source of Research Funding: Principal investigator's start up

Contact: alireza@cornell.edu, sp777@cornell.edu

Website: <https://abbaspourradlab.cornell.edu/>

Primary CNF Tools Used: Object 3D Printer, VersaLaser engraver/cutter, MVD 100, PDMS casting station

Abstract:

Current methods to test genotoxicity and cytotoxicity either use live animals *in vivo*—e.g., a food or drug is administered to a rodent, then monitored for physiological and behavioral changes, histology, and blood results—or we use *in vitro* tests, in which a few bacterial or mammalian cell lines are cultured inside a transwell insert, and then monitored for cell viability. Both have striking limitations. The first one assumes that we can model the pathophysiology of human diseases on animals, an assumption that has led to the costly failure of many clinical drug trials (approximately nine out of ten. It is also unpredictable and fraught with ethical concerns). The second one assumes that a single type of epithelial cancer cell line (i.e., Caco2) inside a transwell insert has the same uptake mechanism and behavior as the diverse microenvironment of the human gastrointestinal tract, which is in fact not composed of only one type of cell but a wide array of crypt stem cells, goblet cells, enterocytes, enteroendocrine cells, tuft cells, Paneth cells, immune cells, and microbiota—all of which influence each other through intricate cross-talking mechanisms such as paracrine and autocrine signaling in order to maintain cell viability.

Summary of Research:

Gut-on-a-Chip. Current *in vitro* models cannot adequately address the complexity of gut environment because of its rapidly changing nature. Herein, we present a “Gut-on-a-Chip” model system to explain intricate crosstalk in the gut microenvironment, using a microfluidic technique to encapsulate the gut constituent cells in the intestinal microenvironment including organoids, immune cells, and microbiome within microgels. Applying this technique, we decouple contact-independent cell-cell interactions from the contact-dependent effects of soluble mediators. This model can be used to evaluate the effect of biopharmaceutical products and food ingredients on the intestinal cells and microbiome and will be served as a unique approach for pathological threat detection in gut environment.

References:

- [1] Pajoumshariati, S. R., M. Azizi, D. Wesner, P. G. Miller, M. L. Shuler, and A. Abbaspourrad. 2018. Microfluidic-Based Cell-Embedded Microgels Using Nonfluorinated Oil as a Model for the Gastrointestinal Niche. *ACS applied materials and interfaces* 10:9235-9246.

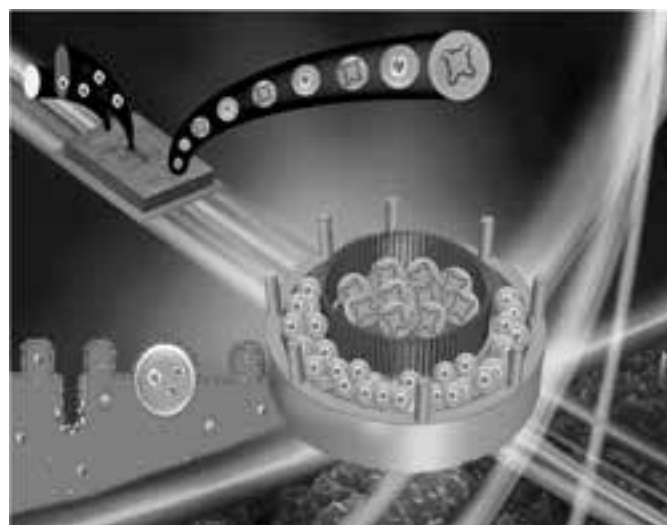


Figure 1: Schematic of the 3D printed insert for co-culture of organoid-embedded microgels along with Peyer's patch embedded microgels. See full color version on pages xxviii-xxix.

Retinal Implant Project

CNF Project Number: 2504-16

Principal Investigator: Douglas Shire, Ph.D.

Users: Marcus Gingerich, Ph.D.^{1,4}, Douglas Shire, Ph.D.^{1,3,4}, Patricia Wong^{2,4}

Affiliations: 1. Department of Electrical Engineering, Cornell University; 2. Department of Neuro-Ophthalmology, Massachusetts Eye and Ear Infirmary; 3. VA Cleveland Healthcare System; 4. Bionic Eye Technologies, Inc.

Primary Sources of Research Funding: Louis Stokes Cleveland VA Medical Center; NIH/NIBIB U01EB018873; NIH/NIBIB R01EB022013, Massachusetts Lions Eye Research Fund

Contact: dbs6@cornell.edu, mdg37@cornell.edu, pwong@bionicvisiontechnologies.com

Website: <http://www.bostonretinalimplant.org>

Primary CNF Tools Used: PT-72, lithography toolset/MA6, DWL2000, evaporators, AJA sputter, Gamma spray coater, SEMs, gold electro-plating, Class 2 lithography toolset, Oxford PECVD, Oxford 100 etcher, Glenn 1000, YES polyimide oven, VersaLaser engraver/cutter

Abstract:

The purpose of the Retinal Implant Project is to restore useful vision to patients who are blind with degenerative retinal diseases. The primary illnesses we hope to treat are retinitis pigmentosa (a primary cause of inherited blindness) and age-related macular degeneration (the leading cause of blindness in the developed world). Both these diseases cause the eventual destruction of the photoreceptor cells — rods and cones — in the retina, leaving intact the ganglion cells which transmit electrical impulses (and hence visual information) to the brain. The ganglion cells may be stimulated, however, with biphasic current pulses from a microfabricated electrode array. Blind surgical volunteers have consistently described visual percepts that resulted from such stimuli, and this has led our team to develop a wireless, implantable retinal prosthesis.

Summary of Research:

The implanted portion of our device consists of power and data secondary receiving coils, and in a sealed titanium (Ti) can a small number of discrete components, and a custom designed application specific integrated circuit (ASIC) which consists of circuitry for clock and data recovery, current drivers for electrodes in a stimulating electrode array, and a programmable function generator capable of stimulating with a wide range of pulse widths and amplitudes. The current outputs drive high-charge capacity sputtered iridium oxide film (SIROF) stimulating electrodes, which in turn give rise to the visual percepts mentioned above.

CNF-fabricated components of this system have included various proof-of-concept test structures and tools used in the research effort and an integrated combination flexible circuit and stimulating electrode array. Si wafers serve as carriers for these freestanding films during processing. The electrode leads are fabricated inside of 'sandwiches' of polyimide and amorphous silicon carbide (SiC), while the SIROF electrodes are reactively sputter-deposited.

Assembly of the intraocular components of the prosthesis is accomplished by flip chip solder ball bonding of the IC and solder attachment of discrete components onto an internal flexible circuit board which is hermetically sealed into an ultraminiature Ti can. The RF coils are soldered and glued to the integrated external flex-array which is in turn thermosonically bonded to the hermetic feedthrough of the Ti can. Finally, the thermosonic bonds are protected and insulated with an over-mold. An external patient interface unit, will consist of a video camera for capturing images, a digital signal processor, and a radio frequency (RF) transmitter and coil to relay power and data to the implanted device.

Scientific challenges still remain in realizing a chronically implantable retinal prosthesis. While our first-generation device was primarily encapsulated in polymers for short term proof-of-concept implant studies, our second-generation system focused on a system which would last many years *in vivo*. Our more recent efforts have focused on developing a device with 256+ stimulation channels

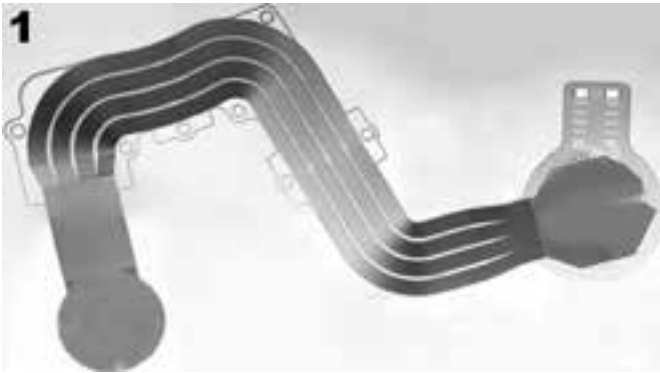


Figure 1, above: A picture of a single complete electrode array.

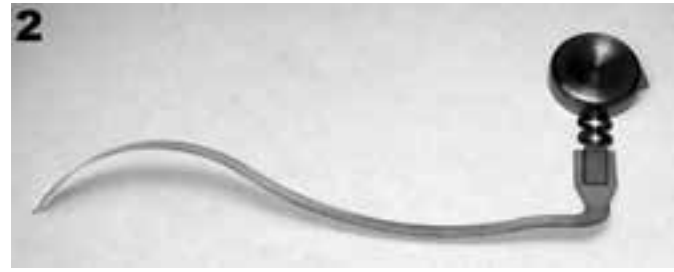


Figure 2, above right: A picture of a VersaLaser-cut mechanical mockup of an indwelling brain electrode system including a titanium hermetic enclosure.



Figure 3, below right: An SEM picture of the partial release of the buried oxide layer of an SOI test sample using the Primaxx vapor HF etch system.

which is still small enough and of a configuration to be easily implanted in the ocular orbit and continue to function for many years *in vivo*. Thus, a major effort has been the development of a technological platform to build a robust, hermetically packaged, high-density subretinal visual prosthesis with a lifetime of > 10 years in biological saline that is scalable to hundreds of I/O channels.

Recent efforts in the CNF have included, among other things, optimizing a reliable microfabrication process for the flexible micro-electrode array (see Figure 1). This included microfabricating a mechanical support for the implantable radio frequency power and communication coil. We have also explored a process of fabricating indwelling electrodes for long-term implantation in brain tissue. A preliminary VersaLaser-cut mockup of such an electrode is shown attached to a titanium hermetic enclosure in Figure 2 in order to evaluate mechanical properties and the overall size and shape. Additionally, we explored a method of fabricating part of that electrode array in Si and releasing it from an SOI substrate using the Primaxx vapor HF etch tool to etch the buried oxide layer (Figure 3).

The project has continued the development and implementation of a microfabrication process to incor-

porate SU-8-based 3D electrodes into a hybrid electrode array to achieve a more optimal interface between the electrode and the target neural cells. Fabrication work at the CNF has included process development required for such high aspect structures including the challenges of lithography with the presence of such extreme topography. Many of these lithography processes have been successfully realized using the Gamma spray coating tool.

The latest microfabrication processes utilize numerous CNF tools including the Heidelberg 2000 mask writer, MA6 aligner, polyimide YES curing oven, PT72 RIE, SC4500 evaporator, Gamma spray coater, Au electroplating station, K and S Au ball bonder, Oxford PECVD, Oxford 100 etch tool, parylene coater, as well as numerous metrology tools.

References:

- [1] J. F. Rizzo, J. Wyatt, J. Loewenstein, S. Kelly, and D. Shire, "Methods and Perceptual Thresholds for Short-Term Electrical Stimulation of Human Retina with Microelectrode Arrays," *Investigative Ophthalmology and Visual Science*, vol. 44, no. 12, Dec. 2003, pp. 5355-5361.

Disseminating Glycocalyx Biopolymer-Induced Microvesicle Shedding through Nanoparticle Tracking Analysis and Cryo-Electron Microscopy

CNF Project Number: 2574-17

Principal Investigator: Matthew Paszek²

Users: LaDeidra Monét Roberts¹, Rose Yin²

Affiliations: 1. Nancy E. and Peter C. Meinig School of Biomedical Engineering, 2. Robert Frederick Smith School of Chemical and Biomolecular Engineering; Cornell University

Primary Source of Research Funding: National Institutes of Health DP2 1DP2GM229133-01

Contact: mjp31@cornell.edu, lmr254@cornell.edu

Website: <https://www.paszeklab.com/>

Primary CNF Tools Used: Malvern NS300 NanoSight

Abstract:

Cancer-derived microvesicles (MVs) have been linked to cancer progression through their ability to propagate an oncogenic phenotype in normal cells. However, the mechanism of their biogenesis is not clearly established. The biogenesis of MVs is inherently a mechanical process where direct vesicle shedding from the plasma membrane requires physical bending. Through scanning electron microscopy, we have found that biopolymers within the sugar-rich coating on the plasma membrane known as the glycocalyx contribute induce membrane bending. Through nanoparticle tracking analysis (NTA), we also have found that molecular crowding within the glycocalyx drives membrane bending for microvesicle biogenesis. Lastly, we show that using nanoparticle tracking analysis in tandem with cryo-transmission electron microscopy (cryo-TEM) allows us to validate and visualize microvesicles and other extracellular vesicle sub-types to better understand mechanisms of biogenesis and shedding.

Summary of Research:

Theory has predicted membrane instabilities and formation of spherical structures in the presence of molecular membrane surface crowding. Remarkably, we have found that increased expression of cancer-associated biopolymers, including mucin-1 (Muc1), induce membrane instabilities as well as drive formation and shedding of spherical microvesicles through conventional scanning electron microscopy (SEM), nanoparticle tracking analysis (NTA) using the Malvern NS300 NanoSight, and cryo-transmission electron microscopy (cryo-TEM). These results suggest that increased glycocalyx biomass might be a general mechanism for MV upregulation. Together, our data suggests that large, cancer associated glycoproteins and glycopolymers, such as Muc1, may perturb cellular communication in cancer through regulation of microvesicle biogenesis. Understanding these physical processes could lead to new therapies that target the mechanical basis of MV biogenesis and cancer.

Together, these experiments and theories describe an entropic mechanism through which the glycocalyx can strongly influence the plasma membrane

shapes. We also find that the plasma membrane in these cells become unstable following inhibition of actin polymerization. These results suggest that the cytoskeleton counterbalances the entropic pressure exerted by cell surface glycopolymers and dynamics play a role in formation and release of microvesicles. Given that glycosylation changes dramatically and in tandem with cell fate transitions, and that the pool of monomers for construction of glycocalyx polymers is tightly coupled to specific metabolic programs, our work raises the intriguing possibility that the glycocalyx may serve as a conduit linking physical morphology to specific physiological and diseased states.

References:

- [1] Antonyak, M.A., PNAS, 2011, 108, 4852-4857.
- [2] Paszek, M.J., Nature, 2014, 511, 319-25.
- [3] Shurer, et al., ACS Biomater. Sci. Eng., 2017, 4, 2, 388-399.
- [4] Shurer, et al., in resubmission, 2018.

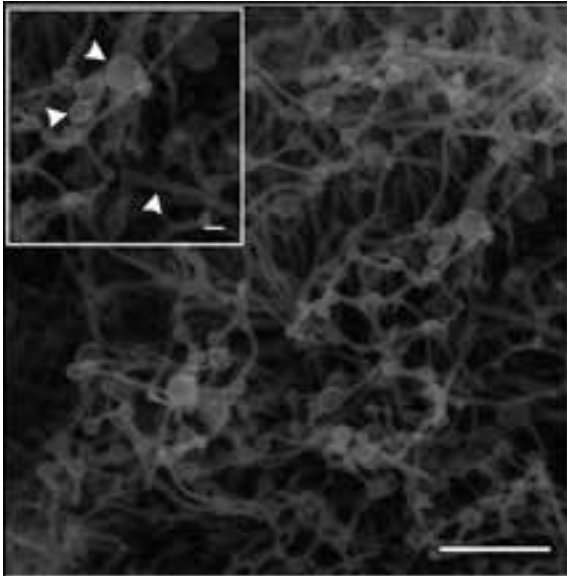


Figure 1: Nanoparticle tracking analysis shows that increased Mucin-1 (Muc1) expression induces membrane tubules and instabilities on the surface of MCF10A cells. (Inset; top left) Microvesicles (indicated by white arrows) present on the membrane tubes (scale bars: 200 nm).

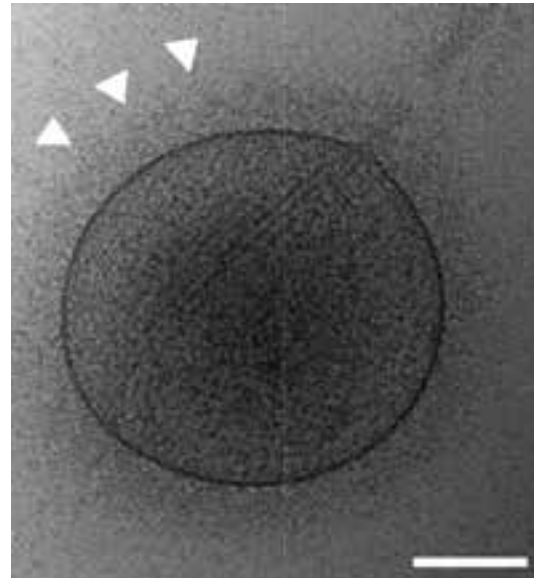


Figure 3: Cryo-TEM of a microvesicle shed from Muc1 MCF10A cells. The ultrastructure of the glycocalyx is indicated by white arrows (Scale bar: 100 nm).

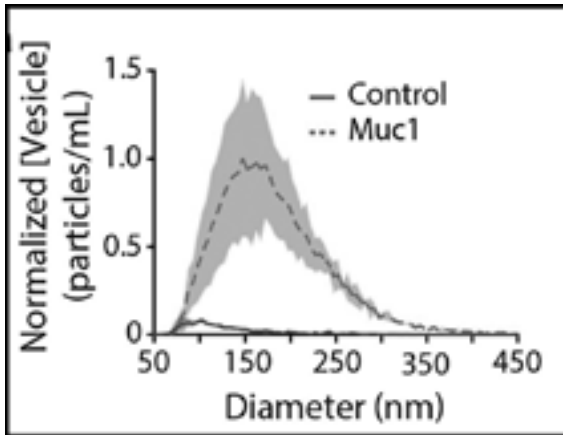


Figure 2: Increased expression of Muc1 induces microvesicle shedding in MCF10A cells compared to control MCF10A cells as shown in nanoparticle tracking analysis (n=3).

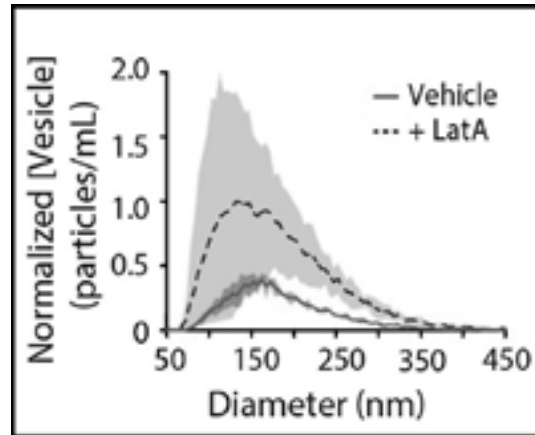


Figure 4: Destabilization of actin through 10 μ M of Latrunculin A treatment in cells with increased Muc1 expression treatment shows enhanced microvesicle shedding compared to control Muc1 cells (n=3).

Investigation of the Mechanical Property of *Drosophila* Mature Oocytes using Microfluidic Devices

CNF Project Number: 2589-17

Principal Investigator: Mariana Wolfner

Users: Qinan Hu, Chih-kuan Tung, Mariana Wolfner

Affiliation: Department of Molecular Biology and Genetics, Cornell University

Primary Source of Research Funding: NIH/NICHD R21-HD088744-02 (Wolfner)

Contact: mfw5@cornell.edu

Primary CNF Tools Used: Lithography toolset, PDMS casting station

Abstract:

This project aims to study the mechanical properties of mature oocytes of the fruit fly *Drosophila melanogaster* using a microfluidic device, to better understand a conserved biological process required for embryonic development, egg activation.

Introduction:

At the end of oogenesis, the mature oocyte is developmentally arrested and needs to be “activated” to transition to embryonic development. Egg activation is conserved across species and is accompanied by a rise of intracellular calcium. In vertebrates, this calcium rise is triggered by fertilization. However, in *Drosophila*, despite conserved downstream events, egg activation is uncoupled from fertilization, and is triggered by mechanical pressure during ovulation. This process can be mimicked *in vitro* by letting the mature oocyte swell in a hypotonic solution containing calcium: the oocyte experiences pressure and takes up calcium-containing fluid from the environment, initiating a calcium rise and activating. The calcium rise initiates at the oocyte poles, and traverses the entire oocyte as a wave (analogous to the calcium waves seen in activating vertebrate and echinoderm oocytes). The *Drosophila* calcium wave can be visualized by our genetically-encoded calcium sensors GCaMP3 and GCaMP6.

Summary of Research:

To better understand the trigger for *Drosophila* egg activation we need to elucidate the mechanical requirement that initiates the calcium wave. Although all-round pressure on the membrane in a French Press can accelerate activation, and all-around pressure on the membrane as the oocyte swells in a hypotonic solution can trigger calcium wave, our preliminary

data have shown that point pressure by a microneedle can only induce a local rise of calcium level that does not propagate like a wave. This suggests to us that a larger regional or circumferential force must be needed to trigger the calcium wave.

To test this, we designed a set of microfluidic chambers with a tunnel-like shape and a narrow constriction in the middle. Mature oocytes can be squeezed through the constriction and we can observe whether a calcium wave starts when the oocyte experiences pressure from the narrow constriction. The wafers used as a mold for the chambers were fabricated at CNF. We then used them to cast our microfluidic devices using PDMS.

GCaMP-containing mature oocytes were loaded into a chamber, pushed through the constriction with syringe-driven fluid flow under a fluorescence microscope to check calcium level changes. To date, we have examined 27 oocytes, but only one of them showed a calcium rise when passing through the constriction in the chamber. Currently we are optimizing the design of the device to increase the chance of inducing a calcium rise and to obtain statistically meaningful results. One way would be to reduce the size of the constriction so that oocytes cannot pass through, allowing us to apply greater pressure using a syringe. The other possibility is to increase the length of constricted part of the tunnel so that oocytes are exposed to pressure for a longer period of time.

Rapid Point of Care Diagnostic for Sepsis Stratification

CNF Project Number: 2636-18

Principal Investigators: David Erickson, Ankur Singh

User: Taylor Oeschger

Affiliations: Biomedical Engineering, Mechanical Engineering; Cornell University

Primary Source of Research Funding: NSF, Atkinson Center Academic Venture Fund

Contact: de54@cornell.edu, as2833@cornell.edu, tmo55@cornell.edu

Primary CNF Tools Used: ABM contact aligner, Class II resist room, Heidelberg 2000 mask writer, profilometer, PDMS casting station, Hamatech wafer developer, UNAXIS 770 deep Si etcher, resist stripper, MVD 100

Abstract:

Sepsis is a rapidly progressing, life threatening immune response triggered by infection that affects many populations worldwide. Therefore, this research aims to create a microfluidic immune cell capture device that is capable of diagnosing sepsis at the point of care. To do this, we created a mold on a silicone wafer using deep silicone etching, which we then cast in polydimethylsiloxane (PDMS) and adhered to a glass slide to create a functional device. A drop of blood is lysed and quenched to remove red blood cells before leukocytes are captured on antibody coated pillars, where they can be quantified and correlated to a sepsis diagnosis. Development of an accurate point of care diagnostic device for sepsis would improve diagnostic speed, reduce hospital costs, and save many lives.

Summary of Research:

Sepsis is a life-threatening condition caused by the body's drastic response to microbial infection, which triggers a cascade of events that can lead to organ failure and death [1]. Neutrophil CD64 expression has been shown to increase under septic conditions making it a potential biomarker for sepsis [2,3]. In response to bacterial infection, neutrophil CD64 has been shown to be upregulated as early as one hour after infection [4]. This project aims to create a microfluidic device that can measure changes in quantities of immune cells and correlate them with a diagnosis of either onset, early stage, or late stage sepsis within hours from a whole blood sample. The long-term goal is to be able to quickly, inexpensively, and reliably determine the on-set and current stage of sepsis at the point of care so that treatment can be properly administered.

The microfluidic device will consist of two main sections: a lysing/quenching region and an antibody chamber for cell capture (Figure 1). Approximately 10 μ L of whole blood will be exposed to lysing buffer followed by quenching buffer over a length of small pipes. This will remove red blood cells in order to obtain pure leukocyte populations. CD4+ T cells, CD4+CD25+ T reg cells, and CD64+ neutrophils will be captured on antibody coated pillars in the antibody capture chamber. These cells will be measured by counters or fluorescence and analyzed by a smart phone.

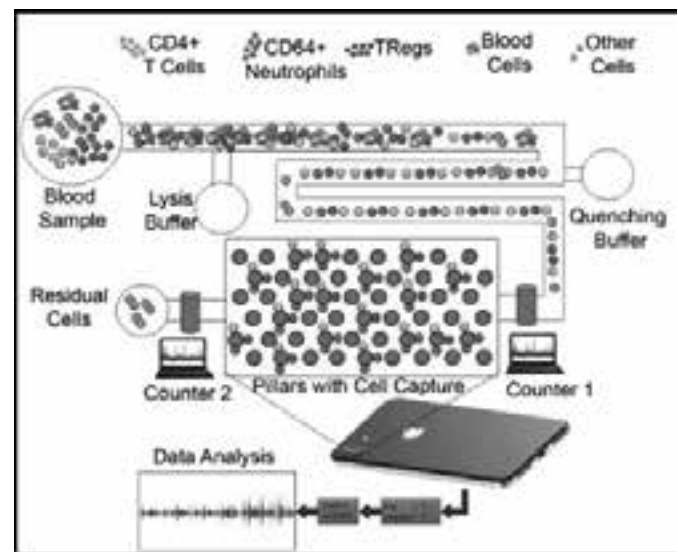


Figure 1: Schematic of microfluidic chip design.

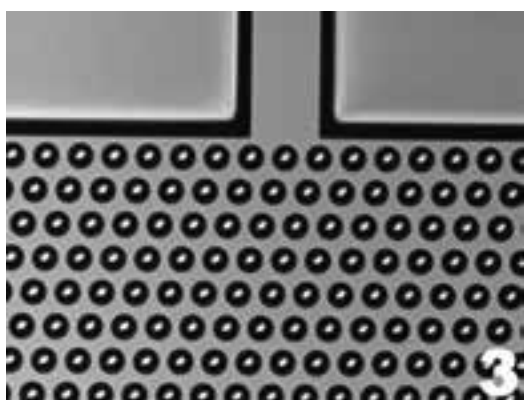
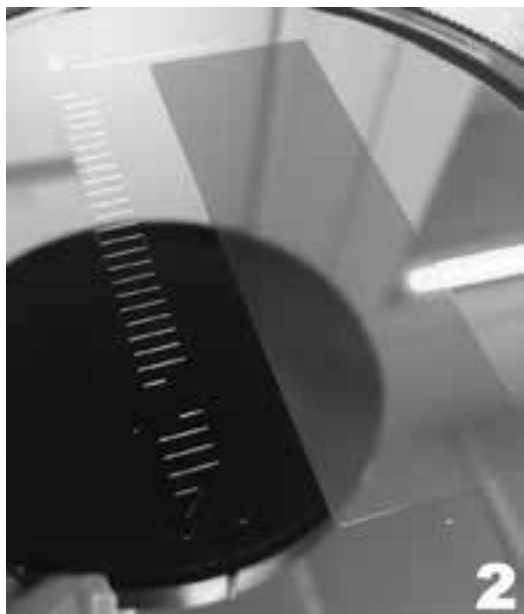


Figure 2, top: Deep etched silicone wafer mold.
 Figure 3, middle: Ten times magnification of silicone mold inlet to antibody capture chamber. Figure 4, bottom: PDMS device cast from the silicon mold.

The Cornell NanoScale Facility was used to create a silicon mold of the antibody chamber and the lysing/quenching region (Figure 2). The antibody capture chamber is approximately 20 mm by 60 mm with ~ 200,000 pillars that are 40 μm in diameter and 60 μm tall (Figure 3).

The mold was first attempted using SU-8 photolithography, but the large area of pillars had trouble staying adhered to the silicon wafer. As an alternative, the UNAXIS 770 deep silicon etcher was used. We were able to achieve uniform pillars much faster and more reliably using this method.

The final device is cast in polydimethylsiloxane (PDMS) and adhered to a glass slide using plasma cleaning (Figure 4). Prior to casting, we coated the silicon wafer mold in (1H,1H,2H,2H-perfluorooctyl)trichlorosilane (FOTS) using the MVD 100 tool to help prevent the PDMS from sticking to the mold.

The next steps are to test the device for functionality and ability to reliably capture and quantify cells.

References:

- [1] Hotchkiss, R. S., and Karl, I. E.; 030109 The Pathophysiology and Treatment of Sepsis. *n engl j med* 3482, (2003).
- [2] Cid, J., Aguinaco, R., Sánchez, R., García-Pardo, G., and Llorente, A. Neutrophil CD64 expression as marker of bacterial infection: A systematic review and meta-analysis. *Journal of Infection* (2010).
- [3] Gros, A., et al. The sensitivity of neutrophil CD64 expression as a biomarker of bacterial infection is low in critically ill patients. *Intensive Care Med.* (2012).
- [4] van der Meer, W., Pickkers Peter, P., Scott, C. S., van der Hoeven, J. G., and Gunnewiek, J. K. Hematological indices, inflammatory markers and neutrophil CD64 expression: Comparative trends during experimental human endotoxemia. *J. Endotoxin Res.* (2007).

Patterning of Native Proteins in Supported Lipid Bilayers

CNF Project Number: 2641-18

Principal Investigator: Susan Daniel

User: Zachary Manzer

Affiliation: Smith School of Chemical and Biomolecular Engineering, Cornell University

Primary Source of Research Funding: National Science Foundation

Contact: sd386@cornell.edu, zam42@cornell.edu

Primary CNF Tools Used: Heidelberg DWL66fs mask writer; ABM contact aligner; Unaxis 770 deep Si etcher; Anatech resist strip, MVD 100, P10 profilometer, FilMetrics F50-EXR

Abstract:

Many *in vitro* experimental studies fail to study membrane proteins in their native cellular environment and instead use solubilized systems in which all cellular components are mixed together and removed from their lipid scaffold. To more directly study these proteins, while still decoupling them from other cellular processes, we aim to create a microfluidic system in which protein embedded cell blebs can be patterned and studied. A supported lipid membrane will keep key membrane bound proteins in their native environment, thus enabling us to study them as if they were still inside the cell. Since the flow characteristics, channel dimensions, and the local environment are readily controlled, this platform gives us a way to easily mimic and manipulate the native cellular environment.

Summary of Research:

The use of a supported lipid scaffold from cellular membrane lipids has been shown by our group and others to preserve protein function in their native environment [1]. Previous work has been done in wells and straight channel devices on the millimeter scale, but the extension of this platform to allow for selective patterning will enable us to more extensively study protein and lipid interactions. These are important in virus binding mechanisms, drug delivery applications, as well as in fundamental studies of membrane dynamics.

A negative mask for a prototype microfluidic design was created using the Heidelberg DWL66fs mask writer and used with the ABM contact aligner to pattern photoresist that was spun onto a silicon wafer. After development, the profile of the patterns was analyzed on the P10 profilometer, a snapshot of which can be seen in Figure 1. Optimization of the process was conducted to produce consistent and even films, as measured by the profilometer and the FilMetrics F50-EXR. Once this was done, the exposed silicon was etched using the Unaxis 770 deep Si etcher, with the final form shown in Figure 2. As can be seen, there is still photoresist on the channels, which was removed by oxygen plasma cleaning in the Anatech resist strip. A final hydrophobic coating (FOTS)

was applied using molecular vapor deposition to allow for PDMS molds to be easily removed once cast. The final wafer can be seen in Figure 3.

Once the mold was fabricated, Sylgard 184 was poured over the mold and cured. This can then be removed and bonded to a glass coverslip by using oxygen plasma cleaning on both surfaces. Synthetic liposomes containing a fluorescent marker was passed into the channels and allowed to incubate, where they will adsorb to the exposed surfaces and form a bilayer structure. Fluidity is confirmed by using a laser to photobleach the dye and then measuring the diffusion rate as the spot recovers. This process can be seen in Figure 4. Future work will involve more complicated device designs as well as leveraging the microfluidic for biotechnology applications, as mentioned.

References:

- [1] Richards, M. J. et al. Membrane Protein Mobility and Orientation Preserved in Supported Bilayers Created Directly from Cell Plasma Membrane Blebs. *Langmuir* 32, 2963-2974 (2016).

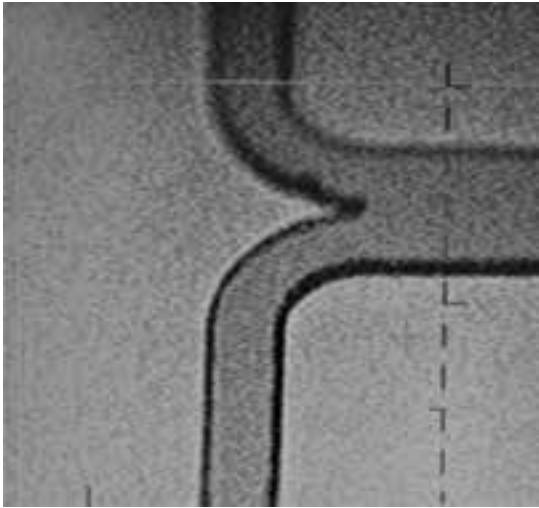


Figure 1: Image taken when measuring profile of exposed features. Depth of film was confirmed using FilMetrics F50-EXR.

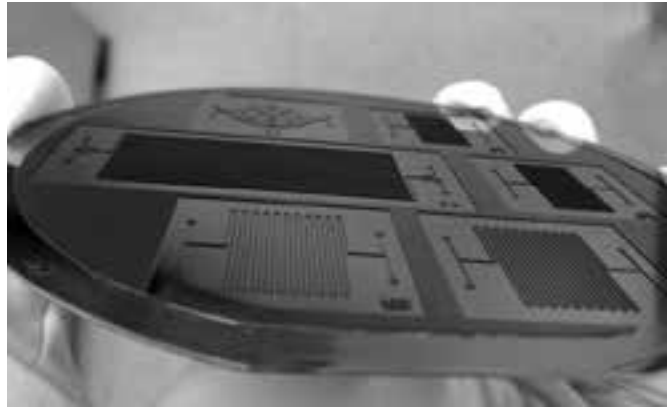


Figure 2: Wafer after being removed from Unaxis 770 deep Si etcher.

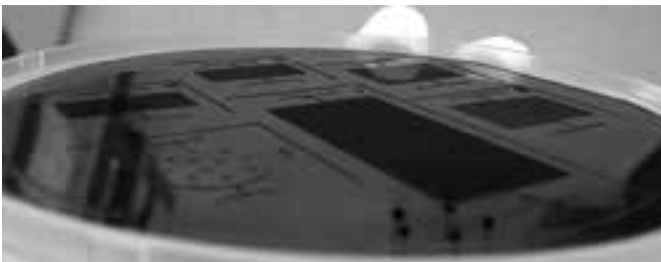


Figure 3: Wafer after being stripped in the Anatech resist strip and coated with FOTS in the MVD 100.



Figure 4: Fluorescence recovery after photobleaching (FRAP) confirms that a supported lipid membrane was formed in the device.

Fabricating 2D Silica with Atomic Layer Deposition

2018 CNF REU Intern: Reed Yalisove

2018 CNF REU Intern Affiliation:

Materials Science and Engineering, University of Michigan

CNF Project: 2018 Cornell NanoScale Science and Technology Facility Research Experience for Undergraduates Program

CNF REU Principal Investigator: Professor James R. Engstrom, Richard F. Smith School of Chemical and Biomolecular Engineering, Cornell University

CNF REU Mentor: Taewon Suh, Richard F. Smith School of Chemical and Biomolecular Engineering, Cornell University

Primary Source of CNF REU Funding: National Science Foundation via the National Nanotechnology Coordinated Infrastructure (NNCI) Grant No. ECCS-1542081

Contact: reedy@umich.edu, jre7@cornell.edu, ts695@cornell.edu

Website: http://www.cnf.cornell.edu/cnf_2018reu.html

Primary CNF Tools Used: Electron-beam evaporator, Oxford FlexAL ALD, general anneal 1 furnace, VCA contact angle, Woollam spectroscopic ellipsometer

Abstract:

Two-dimensional materials exhibit exciting new properties that could have applications for next-generation electronic devices. One such material is two-dimensional silica, called silicatene, which is an SiO_2 bilayer that only binds to a surface via van der Waals forces. Previous research has shown that silicatene can be made via evaporation of silicon and subsequent annealing in oxygen on a few single-crystalline metal surfaces, including Pd, Pt, and Ru. Atomic layer deposition (ALD) is a thin-film deposition technique used in the manufacturing of a variety of devices. This process repeats two self-limiting reaction steps to deposit a thin film, allowing angstrom-scale control of film thickness. The focus of this project was to investigate the use of ALD to deposit silicatene on several metal substrates. The metal substrates were deposited on silicon wafers via electron-beam assisted evaporation, and silica films were deposited with ALD. Post-deposition characterization of deposited film includes ellipsometry, contact angle, and x-ray photoelectron spectroscopy (XPS).

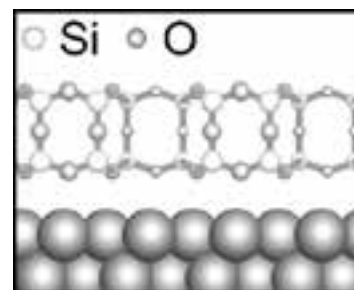


Figure 1: Figure adapted from ref. [1], the structure of silicatene. It consists of a bilayer of SiO_2 molecules attached to a metal substrate via van der Waals forces.

Introduction and Goals:

The thinnest stoichiometric arrangement of silica is a bilayer of silicon dioxide, known as silicatene. This material adheres to its substrate through van der Waals forces (see Figure 1). Silicatene has been fabricated on single crystal palladium (Pd), platinum (Pt), and ruthenium (Ru). Silicon (Si) was evaporated onto the metal substrate with an electron-beam assisted evaporator, then the films are annealed near 800°C and 10^{-6} mbar in an oxygen-rich environment [1]. Atomic layer deposition (ALD) is a thin-film deposition technique in which two self-limiting reactions are repeated, forming a film, atomic layer-by-atomic layer. This method allows low-temperature deposition of highly conformal, uniform films [2]. This research aimed to fabricate silicatene using atomic layer deposition.

Methods:

We chose Pd, Pt, and Ru as metal substrates for SiO_2 ALD. These metals were deposited on *p*-type silicon using an electron beam-assisted evaporator. Each metal film was 150\AA thick, and the Pt film was deposited on a 100\AA thick Ti adhesion layer on Si. Metal substrates [YR1] were characterized with contact angle and ellipsometry. SiO_2 films were deposited with ALD, using tris(dimethylaminosilane) (3DMAS) precursor and O_2 plasma as a co-reactant. Before the precursor was introduced, substrates were reduced in a H_2 plasma. Films were deposited at 200°C , with 5, 10, 20, 50, and 100 cycles of ALD. In addition, a “0 cycle” sample was created, which was not exposed to the Si precursor or the O_2 plasma, and a “20 second-half cycle” sample was created, which was not exposed to the 3DMAS, but did

undergo 20 cycles of the O_2 plasma co-reactant. Samples were annealed in an oxygen environment at 800°C for ten minutes at atmospheric pressure, then were allowed to cool to 300°C . Samples were characterized with contact angle, ellipsometry, x-ray photoelectron spectroscopy (XPS), and angle-resolved XPS (ARXPS) before and after annealing.

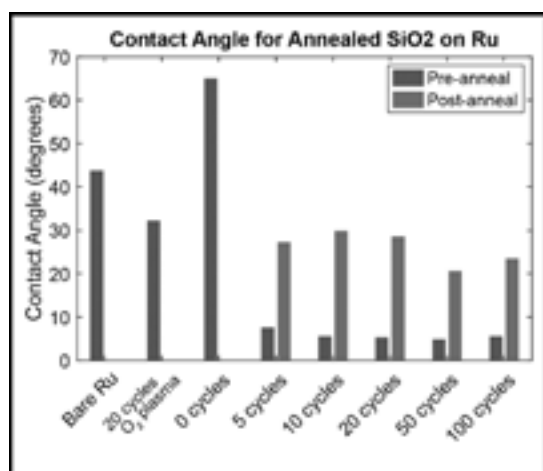


Figure 2: Contact angle data before and after annealing. Before annealing, contact angle is high without the introduction of Si precursor. When the Si precursor is introduced, the contact angle is consistently low. After annealing, the contact angle increases.

Results:

Contact angle showed high angles of water contact for the samples that were not exposed to the Si precursor (bare metal, 0 cycles, and 20 second-half cycles). The contact angles for the pre-annealed samples that were exposed to the Si precursor were uniform and low. This data shows that the exposure to the Si precursor caused a change on the sample surface, suggesting that SiO_2 was deposited. After annealing, contact angles were high, which is inconsistent with the expectation for silicatene. This trend (summarized in Figure 2) was observed for all three. Ellipsometry data shows a linear increase in thickness with the number of ALD cycles for all metal substrates, as seen in Figure 3. This suggests that we

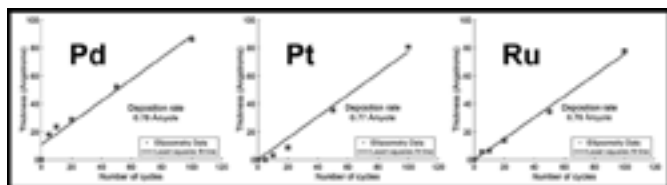


Figure 3: Ellipsometry data before annealing. All metals show a linear increase in thickness with number of ALD cycles.

observed normal ALD behavior, as the formation of silicatene would have led to an asymptote in the film thickness because it is unlikely the complete bilayer would have reacted with additional precursor due to the lack of dangling bonds. Ellipsometry data for the annealed samples was different than that of the pre-annealed samples, and it could not be fit to the expected models. XPS confirmed that the amount and thickness of SiO_2 increased with the number of ALD cycles. ARXPS showed that before annealing, our sample consisted of a thin film of SiO_2 on a buried Ru substrate. After annealing, ARXPS still showed a layer of SiO_2 on top of the sample but the morphology of Ru was inconclusive.

Conclusions:

XPS and ellipsometry suggest that silicatene was not produced. It is likely that during annealing, the SiO_2 combined with the metal to form metal silicides. This is supported by the change in contact angle after annealing and a study showing that Si will diffuse into metals, forming silicides [3]. This would also change the optical constants of the film, which caused the failure of the ellipsometry models.

Future Work:

Successful silicatene fabrication involved single crystal metal substrates [1], whereas our metal films were amorphous due to their evaporation. As a result, we would like to replicate this experiment on single-crystalline metal substrates.

Acknowledgements:

I would like to thank the CNF and its funding via the National Science Foundation NNCI Grant No. ECCS-1542081. Additionally, I would like to thank my PI, James R. Engstrom, and my mentor, Taewon Suh, for their willingness to give me a role in this research. I would like to give special thanks to Aaron Windsor for his patience and help with the evaporator, without which I would not have been able to complete my research.

References:

- [1] Büchner, C., and Heyde, M. (2017). Two-dimensional silica opens new perspectives. *Progress in Surface Science*, 92(4), 341-374.
- [2] George, S. M. (2010). Atomic Layer Deposition: An Overview. *Chemical Reviews*, 110(1), 111-131.
- [3] Petersson, C., Baglin, J., Dempsey, J., D'Heurle, F., and La Placa, S. (1985). Silicides of ruthenium and osmium: Thin film reactions, diffusion, nucleation, and stability. *Vacuum*, 35(6), 237.

Attonewton Sensitivity Magnet-Tipped Cantilevers and Sample Preparation for Single-Electron Spin Detection

CNF Project Number: 863-00

Principal Investigator: John A. Marohn

User: Peter (Hanyu) Sun

Affiliation: Department of Chemistry and Chemical Biology, Cornell University

Primary Source of Research Funding: Army Research Office

Contact: jam99@cornell.edu, hs859@cornell.edu

Website: marohn.chem.cornell.edu

*Primary CNF Tools Used: JEOL JBX-6300FS electron-beam lithography system,
CVC SC4500 e-gun evaporation system, Oxford PlasmaLab 80+*

Abstract:

Magnetic resonance force microscopy (MRFM) is a technique that increases sensitivity and resolution of magnetic resonance imaging beyond that achieved by traditional inductively-detected methods by using a nanomagnet-tipped cantilever as an attonewton-sensitivity force detector. In this report, we detail progress on magnet fabrication and sample preparation at the Cornell NanoScale Science and Technology Facility (CNF) that will enable single electron spin detection via MRFM.

Research Summary:

The Marohn group aims to use MRFM to image three-dimensional structures of biomolecular complexes that are hard to determine using techniques such as x-ray crystallography and cryo-electron microscopy. Achieving the signal-to-noise necessary to detect a single electron requires a nanomagnet with a large field-gradient to maximize the force and force-gradient between sample spins and the cantilever tip. The magnet-tipped cantilever fabrication protocol established by Longenecker separates the cantilever and magnet fabrication processes by depositing magnets first onto patterned chips instead of directly onto the cantilever (magnet-on-chip design) [1]. The fabricated magnet chip is then lifted-off from the wafer and attached to the cantilever with Omniprobe using a dual beam FEI Strata 400 STEM FIB system available at the Cornell Center for Materials Research (CCMR). The batch-serial process prevents the magnet from undergoing extreme conditions during the chemical etching process of the cantilever fabrication, reducing magnet damages. Magnet-tipped cantilevers produced this way have demonstrated record-high field gradients of 5 mT/nm [1], enabling many advances in detection and imaging.

In the past year work done at the CNF focused primarily on reproducing the fabrication protocol for cobalt-tipped cantilevers. The process involves 4-step e-beam lithography patterning on the JEOL JBX-6300FS electron-beam lithography system — alignment marks layout, chip structure, magnetic and under-etch patterning. The alignment and cobalt depositions were achieved with a CVC SC4500 e-gun evaporation system. The chip patterning and under-etch patterning were done in an Oxford PlasmaLab 80+ for silicon etching. The resulting magnet chips are shown in Figures 1 and 2.

The process allows for a 200 to 250 nm magnet overhang at the edge of the cantilever tip. The overhanging magnet design reduces surface noise caused by electrostatic interactions between fluctuating charges in the sample and the relatively large silicon surface of the cantilever tip. Reducing surface noise by increasing this silicon tip-sample separation is crucial to achieving the signal-to-noise necessary for detection and imaging. We are currently in the process of finishing a new batch of magnet-tipped cantilevers at the CCMR by attaching fabricated cobalt magnets onto previously prepared cantilevers.

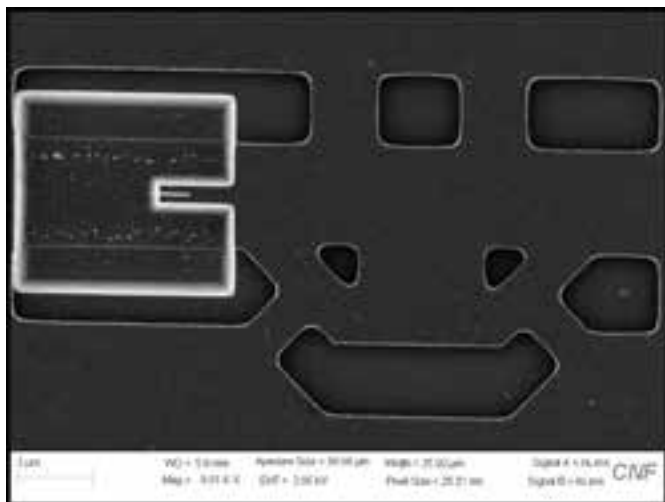


Figure 1: Magnet-on-chip design with an e-beam patterned cobalt. This specific pattern has a magnet of $\sim 1 \mu\text{m}$ in length, 80 nm in width and 200 nm in thickness. The overhang is $\sim 230 \text{ nm}$.

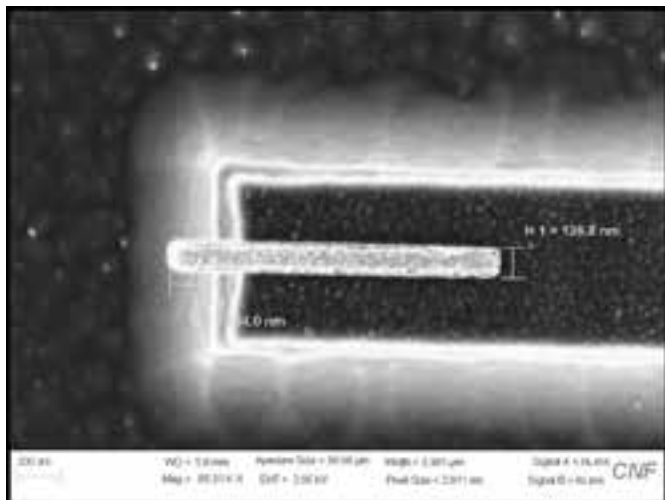


Figure 2: Cobalt magnet overhanging at the edge of the chip design. The magnet patterned is $\sim 1.2 \mu\text{m}$ long, 136 nm wide and 200 nm thick. The overhang is 294 nm.



Figure 3: Multilayer graphene deposited on top of a coplanar waveguide spin-coated with a 200 nm thick polystyrene film. See full color version on pages xxviii-xxix.

To reduce surface noise for MRFM detection, the sample is coated with 12 nm gold film by e-gun deposition and wire-bonded to the ground plane to reduce surface charge accumulation. However, recent experiments suggest the e-gun deposition damages our nitroxide spin probes up to 20 nm in depth. One experimental approach is to use multilayer graphene as a replacement for gold due to its high electrical conductivity and mild conditions for transfer [2].

The substrate for growing multilayer graphene is a silicon wafer (290 nm oxide layer) with a 300 nm nickel film. The nickel film is deposited by the CVC SC4500 e-gun evaporation system at the CNF at a rate of 4 angstrom/s. The graphene is then chemical vapor deposited at 900°C using the furnace from McEuen group (Department of Physics, Cornell University). The multilayer graphene is removed from the substrate and onto the surface of a water bath by a nickel etching process and directly scooped up onto a coplanar waveguide covered in a spin-coated sample. The resulting graphene-coated waveguide is shown in Figure 3. The properties of the graphene are characterized by an Asylum-MFP3D-Bio-AFM-SPM and a Renishaw InVia Confocal Raman microscope at the CCMR and the surface noise is then analyzed in our MRFM microscope.

We have yet to demonstrate surface noise comparable to e-gun deposited gold although more testing is needed. In addition, we are looking forward to further improving our magnet-tipped cantilever fabrication process in terms of increasing yield and reducing magnet damage to increase the sensitivity and resolution of our MRFM microscope.

References:

- [1] Longenecker, et al. ACS Nano 2012, 6 (11), 9637-9645.
- [2] Jo, G., et al. Nanotechnology, 2010, 21, 175201.

Investigation of Area Selective Atomic Layer Deposition with Microreactor and *in situ* Surface Analysis

CNF Project Number: 1239-04

Principal Investigator: James R. Engstrom

User: Taewon Suh

Affiliation: Robert Frederick Smith School of Chemical and Biomolecular Engineering, Cornell University

Primary Source of Research Funding: Semiconductor Research Corporation

Contact: jre7@cornell.edu, ts695@cornell.edu

Website: <http://engstromgroup.cbe.cornell.edu>

Primary CNF Tools Used: ALD, acid hoods

Abstract:

Atomic layer deposition (ALD) is a technique capable of precise control of film thickness and conformal film growth due to self-limiting nature of the precursors. Engstrom research group (ERG) has built a microreactor through which reactants of ALD are delivered and confined in a small region for deposition. This microreactor is coupled to an ultra high vacuum (UHV) chamber for surface characterization such that the deposited film is transferred *in vacuo*, without an air break, to the analysis chamber. In addition to the two reactants used in conventional ALD: ALD precursor and co-reactant, a third species called "co-adsorbate" is introduced for possible area selective deposition to act as a site-blocking layer.

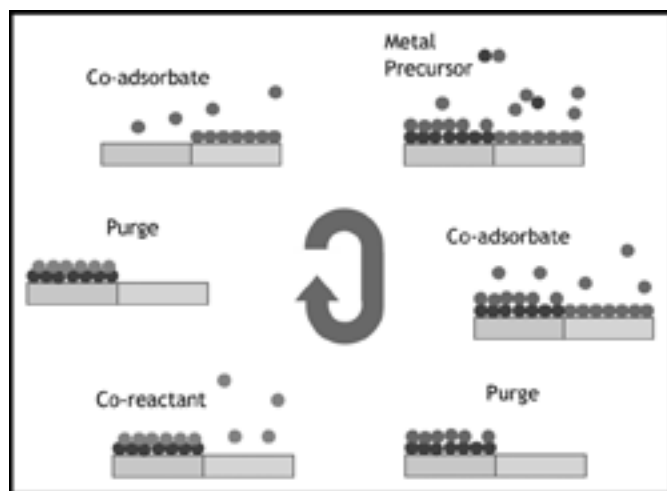


Figure 1: Schematic representation of an ALD cycle with co-adsorbate molecules.

Summary of Research:

In continuous downscaling of semiconductor devices, ALD has emerged as a potential approach capable of meeting required criteria of next generation technologies. The self-limiting nature of ALD precursors brings about two major advantages unique to the technique: precise control of thickness of deposited film and conformal growth [1]. ALD is sequential binary reaction separated by

purge steps to prevent any unwanted parasitic reactions between the precursor and co-reactant in gas phase. ERG takes this deposition technique a step further to study fundamental mechanisms involved in potential area selective ALD. Co-adsorbate molecules are introduced within a conventional cycle of ALD: before, during, and after precursor pulse as in Figure 1, to investigate how this third species potentially allows for area selective deposition. The deposited film is transferred *in vacuo* to and characterized in a UHV chamber coupled with the microreactor using x-ray photoelectron spectroscopy (XPS).

The thickness of deposited film (~ a few nm) is often in the range that is most effectively probed with surface-sensitive characterization techniques that require UHV, $p < 10^{-9}$ Torr. Conventional ALD is typically conducted at low to medium vacuum conditions ($p \sim 10^{-3}$ - 10^{-2} Torr), thus in most cases UHV-based analysis of the deposited thin films occurs in a separate chamber, requiring an air break that may significantly alter the surface composition, oxidation state, structure of the deposited film, and/or underlying substrate. Avoiding this air break is critical for fundamental studies of the growth of ultrathin films, particularly in the early stages. Figure 2 describes how a sample is exposed to precursors at the upper stage and transferred down to the lower stage of the chamber without exposure to air for post-deposition characterization.

In this report, we assess the feasibility of achieving area selective deposition with ALD by employing co-adsorbate molecules. Two substrates of different composition are used as initial surfaces: chemical oxide and metallic copper. Substrate preparation for the dielectric is conducted in the acid hood of CNF at Cornell University. This wet chemical etch includes submerging Si <100> wafer in buffered oxide etch (BOE) (6:1) for two minutes which produces hydrogen-terminated Si, confirmed by hydrophobicity of the surface. The substrate is then immersed in nanostrip for 15 minutes, which generates hydroxyl group termination with known density of $\sim 5 \times 10^{-14}$ OH/cm² [2]. This cycle of removing native oxide and generating chemical oxide is repeated twice. OH-terminated SiO₂ and copper substrates are loaded into the vacuum chamber within a sample holder as shown in Figure 3. This sample holder allows simultaneous exposure of substrates to reactants such that gas-surface reactions will occur under identical experimental conditions.

In area selective ALD experiments, substrates are annealed to substrate temperature of 180°C for an hour prior to exposure. Then co-adsorbate species is introduced to surfaces to form site-blocking layer to prevent incoming ALD precursor from adsorbing on undesired surfaces. The co-adsorbate molecules are present at relatively high ratio compared to ALD precursor during and after the precursor pulse to ensure area selective deposition. After purge of the precursor and co-adsorbate, pulse and purge of co-reactant occurs, just like in conventional ALD cycle. Deposited metal oxide films are characterized with *in situ* XPS using several parameters: photoionization cross section, inelastic mean free path, and kinetic energy, etc. [3]. The absolute atomic density of metal atom is calculated using calibration of semi-infinite Au film and methods described elsewhere [4].

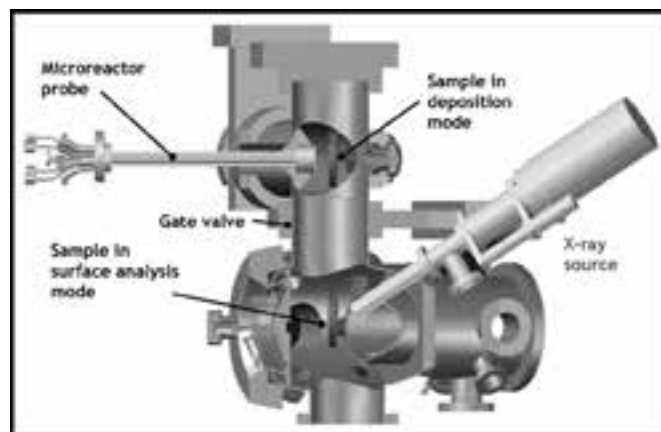


Figure 2: CAD rendering of the microreactor and UHV surface analysis chamber.

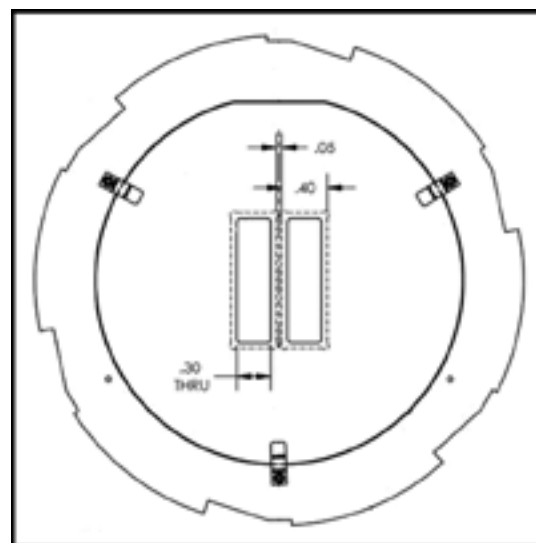


Figure 3: Sample holder capable of holding two copper samples.

References:

- [1] S. M. George, "Atomic layer deposition: An overview," *Chem. Rev.*, vol. 110, pp. 111-131, 2010.
- [2] L. T. Zhuravlev, "Concentration of hydroxyl groups on the surface of amorphous silicas," *Langmuir*, vol. 3, no. 3, pp. 316-318, 1987.
- [3] J. H. Scofield, "Hartree-Slater subshell photoionization cross-sections at 1254 and 1487 eV," *J. Electron Spectros. Relat. Phenomena*, vol. 8, no. 2, pp. 129-137, 1976.
- [4] K. J. Hughes and J. R. Engstrom, "Interfacial organic layers: Tailored surface chemistry for nucleation and growth," *J. Vac. Sci. Technol. A Vacuum, Surfaces, Film.*, vol. 28, no. 5, p. 1033, 2010.

Chemical Bonding Across the Periodic Table at High and Ambient Pressures

CNF Project Number: 1371-05

Principal Investigator: Roald Hoffmann

User: Guoying Gao

Affiliation: Department of Chemistry and Chemical Biology, Cornell University

Primary Source of Research Funding: National Science Foundation, Grant CHE-1305872

Contact: rh34@cornell.edu, gaoguoying@ysu.edu.cn

Website: <http://hoffmann.chem.cornell.edu/roald/>

Primary CNF Tools Used: CNF computer cluster

Abstract:

We address problems of bonding, structure, and emergent properties such as superconductivity in a wide range of materials — from discrete molecules through polymers to extended solids. The behavior of matter under high pressure is of special interest, as it forms a fruitful collaboration with the group of Neil Ashcroft in Physics. The specific project addressed in 2017-18 was the design of a new phase in the Si/C system, stoichiometry Si_3C .

Summary of Research:

As the second most abundant element in the Earth's crust, relatively low cost and an intrinsic semiconductor that can be both *n*- and *p*-doped, silicon has been widely used in the electronic industry. The well-known diamondoid Si(d-Si) structure is a semiconductor with an indirect gap of 1.2 eV and a much larger direct gap of 3.4 eV. As a consequence of the indirect gap nature of d-Si, Si solar cell absorber layers need to be relatively thick to absorb low energy photons. Much theoretical and experimental work has been directed toward the design and synthesis of direct band gap silicon allotropes, at 1 atm and under high pressure, preferably with a band gap value around optimal (~1.4 eV) for effective solar light conversion.

Si_3C is predicted to take on a diamondoid structure (space group: I-42d), at $P = 1$ atm, consistent with the experimental results on a cubic $\text{Si}_{0.75}\text{C}_{0.25}$ alloy. This structure is computed to be a semiconductor with a direct band gap of about 1.3 eV, a desired value. Under pressure, Si_3C may transform to metastable metallic R.3m-2 and R-3m-3 structures at about 25 and 250 GPa, respectively. Both are layered structures with six-coordinate Si and unusual six-coordinate carbon atoms.

The R-3m-1 and R-3m-2 structures (shown in Figure 1, along with the diamondoid structure) are both estimated to be superconductors with T_c of a few Ks. This is the first time that superconductivity in undoped silicon carbides is calculated.

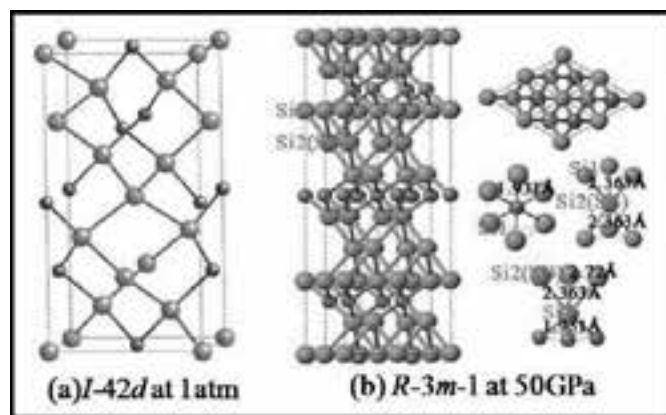


Figure 1: Predicted I-42d, and R-3m-1 structures for Si_3C at 1 atm, and 50 GPa, respectively. Orange, large balls are Si; grey, small balls carbon. The right panel of (b) presents the top view of the R-3m-1 structure and Si-or C-centered octahedra within the structure. See full color version on pages xxviii-xxix.

Substrate Preparation for Ultrafast Vibrational Spectroscopy Experiments

CNF Project Number: 1936-10

Principal Investigator: Poul B. Petersen

User: Stephanie Sanders

Affiliation: Department of Chemistry and Chemical Biology, Cornell University

Primary Source of Research Funding: National Science Foundation

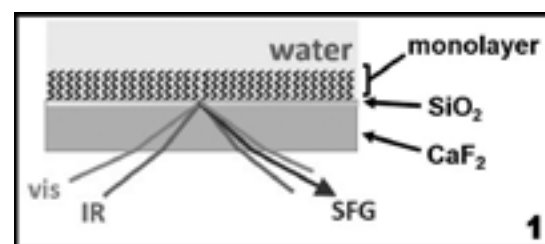
Contact: pbp33@cornell.edu, ses422@cornell.edu

Website: <http://petersen.chem.cornell.edu/>

Primary CNF Tools Used: Oxford ALD FlexAL

Abstract:

Water is ubiquitous and an active component in many natural and technological processes. Vibrational spectroscopy can be used to probe the structure and dynamics of water in a variety of environments. We use sum-frequency generation, a surface specific vibrational spectroscopy, to probe the structure and dynamics of interfacial water at chemically tunable surfaces. Interfaces with tunable surface character are created with self-assembled monolayers. In order to create substrates compatible for both silane self-assembly and sum-frequency generation, infrared and visible transparent CaF_2 windows are coated with SiO_2 . Then after surface functionalization with silane monolayers, the water structure and dynamics at the interfaces can be explored with sum-frequency generation.



Once the SiO_2 is deposited, hydrophobic, hydrophilic, or mixed monolayer are synthesized with self-assembly of silanes on the surface. Figure 1 shows a schematic of the surface in contact with water. Then, the surfaces and water at the surfaces are analyzed with SFG [2-5].

Summary of Research:

Water is an active component in many natural and technological processes [1]. Interfaces terminates the H-bonded network of water. We aim to study the structure and dynamics of water at self-assembled monolayers (SAMs) with varying surface character using sum-frequency generation (SFG) spectroscopy. In SFG, an infrared photon interacts with a dipole transition of the molecule and a visible photon excites the molecule to a virtual electronic state where it can undergo an anti-Stokes Raman transition resulting in a photon at the sum of the two incident frequencies being emitted [2,3]. In order to collect SFG spectra of solid-aqueous interfaces, we must probe through the window so the infrared photons are not absorbed by water. However, silica, a common SAMs substrate, also absorbs in the infrared.

To create an infrared and visible transparent substrate compatible with SAMs syntheses, we start with a CaF_2 window, which is transparent through the visible and infrared. Then approximately 10 nm of SiO_2 is deposited on the CaF_2 window via atomic layer deposition (ALD) with the Oxford ALD FlexAL. The SiO_2 layer is thin enough to not absorb all the IR photons and prevent SFG spectra of the sample from being collected, but thick enough to form a surface compatible with the self-assembly of silanes.

Once the SiO_2 is deposited, hydrophobic, hydrophilic, or mixed monolayer are synthesized with self-assembly of silanes on the surface. Figure 1 shows a schematic of the surface in contact with water. Then, the surfaces and water at the surfaces are analyzed with SFG [2-5].

References:

- [1] Ball, P. *Life's Matrix: A Biography of Water*; University of California Press: Berkeley, 2001.
- [2] Barrett, A. R.; Petersen, P. B. Order of Dry and Wet Mixed-Length Self-Assembled Monolayers. *J. Phys. Chem. C* 2015, 119 (42), 23943-23950.
- [3] Vanselous, H.; Petersen, P. B. Extending the Capabilities of Heterodyne-Detected Sum-Frequency Generation Spectroscopy: Probing Any Interface in Any Polarization Combination. *J. Phys. Chem. C* 2016, 120 (15), 8175-8184.175-8184.
- [4] Sanders, S.E.; Vanselous, H.; Petersen, P. B. Water at Surfaces with Tunable Surface Chemistries. *J. Phys. Condens. Matter* 2018, 30(11), 113001.
- [5] Kocsis, I.; Sorci, M.; Vanselous, H.; Murail, S.; Sanders, S.; Licsandru, E.; Legrand, Y.-M.; van der Lee, A.; Baaden, M.; Petersen, P. B.; Belfort, G.; Barboiu, M. Oriented chiral water wires in artificial transmembrane channels. *Sci. Adv.* 2018 4(3), eaao5603.

A Thin Film Transfer Sample Preparation Technique for Single-Electron Magnetic Resonance Imaging

CNF Project Number: 2125-12

Principal Investigator: John A. Marohn

User: Michael Boucher

Affiliation: Department of Chemistry and Chemical Biology, Cornell University

Primary Source of Research Funding: Army Research Office

Contact: jam99@cornell.edu, mcb344@cornell.edu

Website: marohn.chem.cornell.edu

Primary CNF Tools Used: SC 4500 combination thermal/e-gun evaporation system

Abstract:

Magnetic resonance force microscopy (MRFM) is a type of scanning probe microscopy that uses the excellent force sensitivity of a silicon micro-cantilever in combination with spatially-resolved magnetic resonance made possible by the large local field gradient of the nanomagnet tip to image magnetic spins with theoretical sub-nanometer resolution. The primary goal of this research project is to advance the use of MRFM as a tool for imaging biomolecules and biomolecular complexes such as membrane proteins, whose structure is difficult to obtain by other means. Here we discuss recent developments in measurement sensitivity made possible through cantilever and waveguide fabrication performed at the Cornell NanoScale Science and Technology Facility (CNF) as well as new sample preparation techniques that will enable advances including electron paramagnetic resonance (EPR) detection of individual electron radical spin labels.

Summary of Research:

By employing nanomagnet-tipped attonewton-sensitivity cantilevers developed at the CNF in a magnetic resonance force microscopy (MRFM) measurement, the Marohn group has demonstrated the detection of 500 proton magnetic moments in a 1 mHz bandwidth [1]. In concert with a modified version of the spin modulation protocol first developed by Moore, et al. [2], these cantilevers should have the sensitivity required to image individual nitroxide spin labels on a single biomolecule or biomolecular complex with nanometer resolution.

A major challenge in performing such an experiment is mitigating cantilever frequency noise. One method that has proven effective in reducing this noise is applying a 10-20 nm thick metallic coating to the sample via electron-beam deposition to shield the cantilever from dielectric fluctuations in the sample. Proof-of-concept MRFM-EPR experiments performed on metal coated, tempamine-doped polystyrene samples, have demonstrated noise which is sufficiently low for imaging, however, have demonstrated significantly smaller signal than expected. Numerical simulations suggest the decreased spin signal is due to a 0.20 nm thick "dead layer" at the sample surface in which EPR active radicals are absent (Figure 1). Due to force-sensitivity limitations, this dead layer poses a significant challenge to MRFM detection of single electron spins.

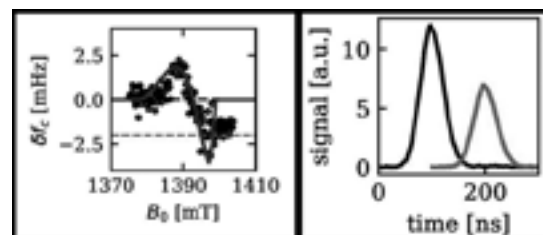


Figure 1, left: Electron spin resonance signal vs. applied magnetic field. The detection protocol developed by Moore, et al. detects the magnetic field gradient produced by sample spins as a modulated shift in the cantilever resonance frequency. Experimental results (black circles) from 30 seconds of signal acquisition, simulated signal of ~50 spins with a 20 nm dead layer (blue line) and expected frequency shift from a single electron near the sample surface (red dashed line).

Figure 2, right: Representative conventional pulsed-EPR measurement demonstrating a reduction in magnetic resonance signal from nitroxide spin probes which had been exposed to gold vapor deposition. Peaks are offset for clarity.

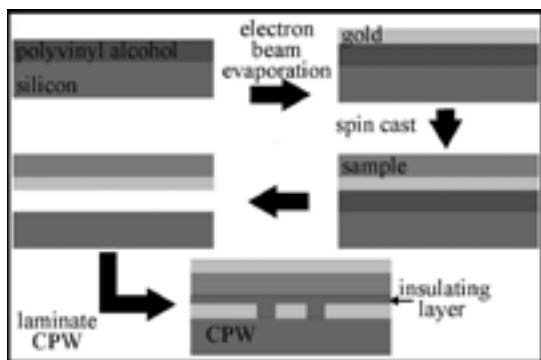


Figure 3: An outline of the sample/top contact transfer process that allows samples to be produced without exposing sensitive nitroxide electron radicals to physical deposition of the gold top contact.

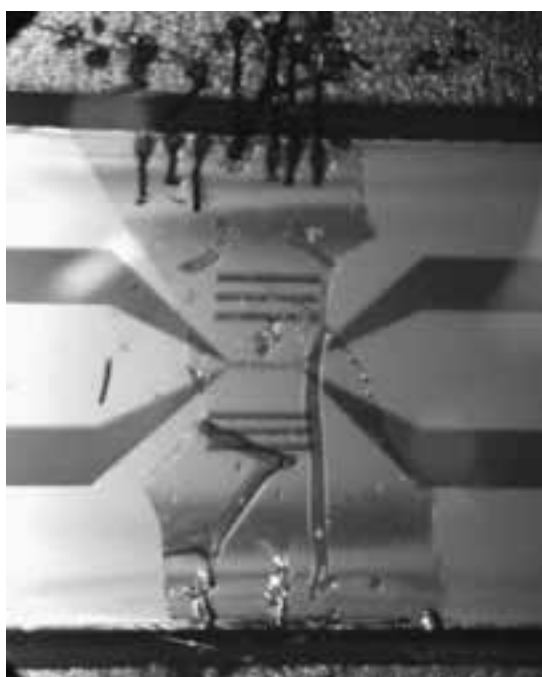


Figure 4: Optical image of a prepared sample/top contact over the tapered microwire region of the waveguide.

Using instrumentation at the National Biomedical Center for Advanced Electron Spin Resonance Technology to perform conventional EPR measurements on prepared 40 nm thick films using identical techniques, we have shown that the total EPR signal is reduced by about 50% after electron-beam vapor deposition of a 10 nm gold top layer — supporting our simulated estimations and suggesting that the process of gold deposition damages the spin probes in the uppermost layers of the sample (Figure 2).

To protect sample spins from direct exposure to the physical vapor deposition of the gold top contact, we developed a new sample preparation protocol. Figure 3 is a schematic of this protocol. A thin layer of polyvinyl alcohol is spin-coated onto a silicon substrate. A 10 nm thick layer of gold is then e-beam deposited on top of the PVA using the SC 4500 combination thermal/e-gun evaporation system at the CNF. The sample in this case, polystyrene doped with 40 mM tempamine, is then spin-coated on top of the gold layer. The Si/Au/polystyrene stack is then placed in a dish containing nanopure water that dissolves the PVA, allowing the Au/polystyrene layers to be transferred directly onto the waveguide to be used to deliver microwaves in the magnetic resonance experiment. Before the transfer, a thin layer of poly(methyl methacrylate) is spin-coated onto the waveguide to prevent shorting through the gold layer. We have found it necessary to transfer only a narrow strip of gold-coated sample because gold contact over the un-tapered region of the waveguide significantly reduces power transmitted through the waveguide. Recent room temperature measurements of the noise over these transferred sample top contacts have demonstrated frequency noise comparable to directly deposited samples.

Application of these newly prepared samples to detection/imaging experiments is currently underway.

References:

- [1] Longenecker, et al. ACS Nano 2012, 6 (11), 9637-9645.
- [2] Moore, et al. PNAS 2009, 106 (52), 22251-22256.

Study on the Electrochemically Stabilizing Effect of the High Dielectric Constant Oxide Artificial Solid Electrolyte Interphase on Electrodes in Aqueous Electrolytes

CNF Project Number: 2447-16

Principal Investigator: Lynden A. Archer

User: Yue Deng

Affiliation: Materials Science and Engineering Department, Cornell University

Primary Source of Research Funding: Private funding from Professor Archer

Contact: laa25@cornell.edu, yd339@cornell.edu

Primary CNF Tools Used: Oxford ALD FlexAL

Abstract:

Aqueous electrolytes, which have huge advantages in fire-hazard safety issues, are now still suffering from their narrow electrochemical stability windows. With the goal to study how ultra-thin oxide coatings can help to extend the stability windows of aqueous electrolytes, and more specifically, how band gap and dielectric constant affect the effectiveness of the oxide coatings, several high dielectric constant (k) metal oxides with different thicknesses were coated onto polished stainless-steel squares. The coated stainless-steel squares were then used to test the stability of aqueous electrolyte in a symmetric cell setup with one molar of lithium sulfate using cyclic voltammetry. The results show that an ultra-thin high k oxide layer helps to increase the stability window of the 1M Li_2SO_4 aqueous electrolyte to about five volts. However, no significant correlation between the width of the stability window and the dielectric constant or band gap of the coating materials was observed.

Summary of Research:

Artificial ultra-thin metal oxide was coated onto 1 cm by 1 cm polished stainless-steel squares (brought from McMaster-Carr Supply Company) by atomic layer deposition (ALD) [1] using the Oxford ALD FlexAL at Cornell NanoScale Science and Technology Facility (CNF). It has been shown in previous research that an ultra-thin (usually around 15 nm) alumina coating

on electrodes can largely increase the electrochemical stability of a rechargeable battery [2]. Therefore, two other high dielectric constant (k) metal oxides, silicon dioxide (SiO_2) and hafnium dioxide (HfO_2) [3], were applied at various thicknesses for studying. For each oxide coating, 1 nm, 5 nm, 10 nm, 15 nm, 20 nm, 25 nm, 30 nm, 35 nm, 45 nm, and 50 nm coatings were investigated. The cyclic

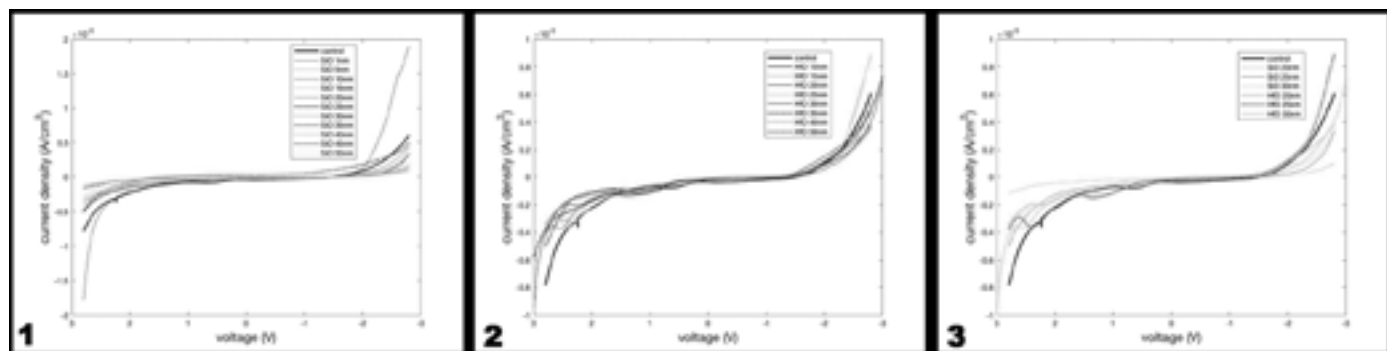


Figure 1, left: The cyclic voltammetry results for a typical symmetric SiO_2 coated stainless steel electrode versus SiO_2 coated stainless steel electrode cell with 1M aqueous lithium sulfate (Li_2SO_4) at various coating thicknesses. **Figure 2, middle:** The cyclic voltammetry results for a typical symmetric HfO_2 coated stainless steel electrode versus HfO_2 coated stainless steel electrode cell with 1M aqueous lithium sulfate (Li_2SO_4) at various coating thicknesses. **Figure 3, right:** A comparison between the cyclic voltammetry results for a symmetric SiO_2 coated half-cell and a symmetric HfO_2 coated half-cell with 1M aqueous lithium sulfate (Li_2SO_4) at various coating thicknesses.

voltammetry results for a typical symmetric SiO_2 coated stainless steel electrode versus SiO_2 coated stainless steel electrode cell with 1M aqueous lithium sulfate (Li_2SO_4) were summarized in Figure 1.

Figure 1 shows that, as the thickness of the SiO_2 layer increases, the stability window of the coin cell is improved. At 20 nm thickness, where the best stability is achieved, the stability window is increased from 3V (baseline generated by the uncoated stainless-steel control cell) to about 5V, which is about 66.7% improvement. For thicknesses beyond 20 nm, no further significant improvement is observed.

Figure 2 contains the cyclic voltammetry for the same coin cell setup with HfO_2 coating instead of SiO_2 . Figure 2 proves that a thin layer of HfO_2 can also improve the stability of such aqueous electrolyte system, especially in the positive potential region. Different from SiO_2 coating, HfO_2 coating gives the best stability window enhancement at thickness around 35 nm. For HfO_2 coating that is thicker than 35 nm, no further significant improvement is observed.

Considering the results from both SiO_2 and HfO_2 coatings, it can be concluded that a semi-conducting or insulating protective layer can expand the stability window for an aqueous battery system. Initially, as the thickness of the coating increases, the stability window also increases. Until a certain thickness (25 nm for SiO_2 and 35 nm HfO_2), the stabilizing effect reaches its maximum and for thickness beyond this value, no further improvement can be achieved.

Figure 3 is a comparison between SiO_2 and HfO_2 coating. It shows that at the same thickness (which is thinner than 35 nm), the SiO_2 coating gives a wider stability window

than the HfO_2 coating does. Additionally, it is observed that there is a reaction peak around 2.2V for HfO_2 coated symmetric half-cell systems, while such a peak cannot be found on the SiO_2 coated symmetric half-cell system. This might indicate that the HfO_2 coating reacts with water or aqueous Li_2SO_4 solution at 2.2V, which suggests that SiO_2 is a more stable coating material to be used in aqueous electrolyte system.

The SEM results of cycled coated electrodes provide evidence. After 11 cyclic sweeps, no HfO_2 could be found at the surface of the electrodes, but SiO_2 was still found evenly covering the entire surface. However, further investigation on the electrolytes after cyclic sweeps is required to make a solid conclusion.

Based on these results, neither band gap nor dielectric constant of the oxide coating has a dominating effect on its ability to stabilize the aqueous system. The chemical reactivity of the coating material against the electrolyte is the crucial factor. Studies of other high κ oxides, such as silicon nitride and hafnium silicate, can help to confirm this hypothesis.

References:

- [1] Jung, Y. S.; Cavanagh, A. S.; Dillon, A. C.; Groner, M. D.; George, S. M.; Lee, S.-H. Enhanced Stability of LiCoO_2 Cathodes in Lithium-Ion Batteries Using Surface Modification by Atomic Layer Deposition. *J. Electrochem. Soc.* 2010, 157 (1), A75.
- [2] He, Y.; Yu, X.; Wang, Y.; Li, H.; Huang, X. Alumina-Coated Patterned Amorphous Silicon as the Anode for a Lithium-Ion Battery with High Coulombic Efficiency. *Adv. Mater.* 2011, 23 (42), 4938-4941.
- [3] Robertson, J. Band Offsets of Wide-Band-Gap Oxides and Implications for Future Electronic Devices. *J. Vac. Sci. Technol. B Microelectron. Nanom. Struct.* 2000, 18 (3), 1785.

Measuring Refractive Index of Microscopy Slides

CNF Project Number: 2673-18

Principal Investigator: Peng Chen

User: Xiangcheng Sun

Affiliation: Department of Chemistry and Chemical Biology, Cornell University

Primary Source of Research Funding: Army Research Office

Contact: pc252@cornell.edu, xs266@cornell.edu

Primary CNF Tools Used: Accurion EP3 imaging ellipsometer, Metricon prism coupler

Abstract:

There are plenty of tools that Cornell NanoScale Facilities (CNF) possesses on materials characterization, which is of vital importance to research. In this project, when we measure the refractive index of the microscopy slides (suspected materials), the CNF refractometer, ellipsometer and Metricon prism coupler were considered to be useful. Finally, Metricon prism coupler was used to measure the refractive index of the material, and the refractive index was obtained under a series of wavelengths. We also used the Cauchy model in that it derived to propose the relation of the refractive index of material with the relation of light wavelengths. Through this study, we verified that the materials measured were the exact ones we would like to study.

Summary of Research:

In this research, materials characterization is of vital importance, and the tool set at Cornell NanoScale Facility (CNF) did just the job that what we needed as there are plenty of tools that help researchers with characterization.

Our project is working on the visualization of single polymer growth using single-molecule fluorescence imaging. Total internal reflection fluorescence microscopy is utilized. We're using sapphire and quartz microscopy slides and prisms, the properties of which are of great importance to our experiments. Especially, the refractive index of materials affects the light path in the materials greatly, which should be known clearly in this research.

Different tools (such as refractometer, ellipsometer and Metricon prism coupler) were considered to measure the refractive index of the slide materials. Firstly, Accurion EP3 imaging ellipsometer was applied to measure the refractive index of bulk materials (microscopy slides). After a series of experiments, it was found that it is challenging to get refractive index of slides through ellipsometry. Generally, ellipsometers are able to measure the thickness or refractive index of a thin layer on the known substrate [1]. This thin layer might include metal

films, oxides, organic coatings or biological molecule layer such as DNA [2]. For our target materials, slides are the bulk materials.

The Metricon model 2010/M prism coupler utilizes advanced optical waveguiding techniques to rapidly and accurately measure both the thickness and the refractive index/birefringence of dielectric and polymer films as well as refractive index of bulk materials. The 2010/M offers unique advantages over conventional refractometers and instruments based on ellipsometry [3,4]. For example, unlike most conventional refractometers, which are single-wavelength (typically 589 nm), the 2010/M can be equipped with as many as five lasers, allowing easy measurement of dispersion across a wide wavelength range.

The Metricon prism coupler was used to measure the refractive index of the material and the refractive index was obtained. We also used Cauchy model in that it derived to propose the relation of the refractive index of material with the relation of light wavelengths. The refractive index values from the Metricon were obtained and shown as follows:

n@446nm: 1.77734

n@637nm: 1.76311

n@824nm: 1.75705

n@1059nm: 1.75287

n@1058nm: 1.74434

With the refractive index at different wavelengths, the Cauchy model was used to fit the data [5], and the equation between refractive index (n) and light wavelength (.) was obtained and shown as follows.

$$n = 1.7412 + 1.2954 \times 10^4 \lambda^{-2} - 1.1617 \times 10^9 \lambda^{-4} \quad (1)$$

Figure 1 shows the measured refractive index under different wavelength and the fitting Cauchy equation. The obtained refractive index of our microscopy slide is consistent with the reported refractive index of sapphire materials.

Through this process, we verified that the materials measured were the exact ones we would like to study.

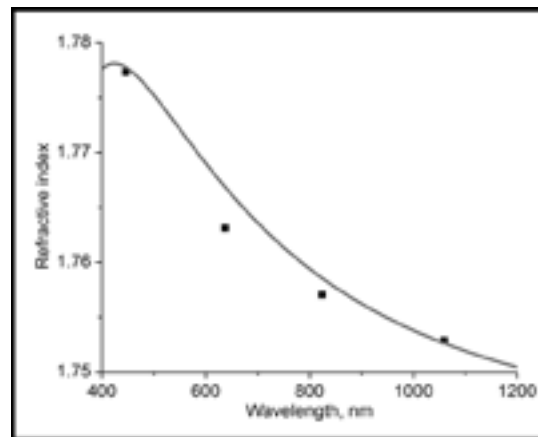


Figure 1: Measured refractive index of the microscopy slide under different wavelength and the corresponding fitting using Cauchy model.

Acknowledgements:

We greatly appreciate the funding from Army Research Office. Xiangcheng Sun thanks the help from CNF staff member, Jeremy Clark.

References:

- [1] Frank L. McCrackin, Elio Passaglia, Robert R. Stromberg, and Harold L. Steinberg, Measurement of the Thickness and Refractive Index of Very Thin Films and the Optical Properties of Surfaces by Ellipsometry, *Journal of Research of the National Bureau of Standards – A. Physics and Chemistry*, 1963, 67A, 363. Janos Vörös, The Density and Refractive Index of Adsorbing Protein Layers, *BioPhysical Journal*, 2004, 87, 553.
- [2] Steven T. Kirsch, Determining the refractive index and thickness of thin films from prism coupler measurements, *Applied Optics*, 1981, 20, 2085.
- [3] J Cardin, D Leduc, Determination of refractive index, thickness, and the optical losses of thin films from prism-film coupling measurements, *Applied optics*, 2008, 47, 894.
- [4] F.A. Jenkins and H.E. White, *Fundamentals of Optics*, 4th ed., McGraw-Hill, Inc. (1981).
- [5] Elena R. Dobrovinskaya, Leonid A. Lytvynov, Valerian Pishchik, *Sapphire Material, Manufacturing, Applications*, Springer (2009).

Vertical Tunneling Field Effect Transistors (Thin-TFETs) Based on BP/SnSe₂ Heterostructure

CNF Project Number: 2324-15

Principal Investigator: Huili Grace Xing

Users: Hyunjea Lee, Xiang Li

Affiliation: School of Electrical and Computer Engineering, Cornell University

Primary Source of Research Funding: LEAST project (Center for Low Energy Systems Technology)

Contact: grace.xing@cornell.edu, HL2255@cornell.edu, XL633@cornell.edu

Primary CNF Tools Used: Autostop i-line stepper, carbon nanotube/graphene furnace, JEOL 6300, AFM – Veeco Icon, AJA sputter deposition, SC4500 odd-hour evaporator, DISCO dicing saw

Abstract:

Two-dimensional materials with clean surface and layered structure have many advantages over three-dimensional counterparts to be used for steep tunneling devices. This work presents two-dimensional heterojunction interlayer tunneling field effect transistors (Thin-TFETs) using black phosphorus (BP)/SnSe₂ heterostructure. Broken gap alignment (type III) between BP and SnSe₂ offers a desirable condition for band to band tunneling, and a solid polymer electrolyte (PEO:CsClO₄) is used to improve subthreshold swing. Graphite electrodes are used to protect air-sensitive BP surface, and most of processing is done in a glove box for the same reason. At room temperature in N₂, the subthreshold swing of the representative device reaches 180 mV/dec for exceeding two decades of drain current, and the I_{on}/I_{off} extends to more than three decades. This work helps the understanding of interband tunneling between layered materials, which forms the basis for low-power tunneling devices.

Summary of Research:

Two-dimensional materials with clean surfaces and layered structures have many advantages over three-dimensional counterparts to be used for steep tunneling devices. This work presents two-dimensional heterojunction interlayer tunneling field effect transistors (Thin-TFETs) using black phosphorus / tin selenide (BP/SnSe₂) heterostructure. Broken gap alignment (type III) between BP and SnSe₂ offers a desirable condition for band to band tunneling, and a solid polymer electrolyte (PEO:CsClO₄) is used to improve subthreshold swing. Graphite electrodes are used to protect air-sensitive BP surface, and most of processing is done in a glove box for the same reason. At room temperature in N₂, the subthreshold swing of the representative device reaches 180 mV/dec for exceeding two decades of drain current, and the I_{on}/I_{off} extends to more than three decades.

Figures 1 and 2 show the optical image of the representative BP/SnSe₂ TFET prior to the application of top-gate dielectric layer and the cross-sectional schematic image of the device. SnSe₂ flake was exfoliated onto a commercially available PDMS film and then transferred to a 285-nm-SiO₂/Si substrate. BP flakes were exfoliated onto another PDMS film and examined under microscope to estimate the layer thickness using optical contrast. The extreme air-sensitivity of BP poses a challenge when it is being exposed to the air during the metal electrode formation process.

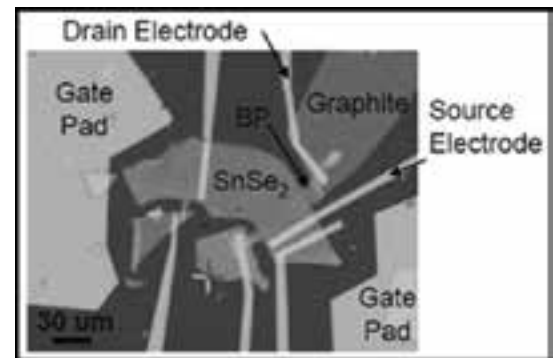


Figure 1: Optical image of the representative BP/SnSe₂ TFET.

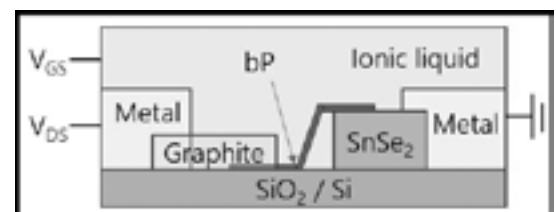


Figure 2: Cross-sectional schematic image of the device.

Semi-metallic graphite flakes were transferred on top of the BP flakes, which is used to make contacts with metal pads acting as a capping layer for BP. To minimize interfacial states resulting from interfacial damage or contamination, all the exfoliation processes were done in a glove box to protect air-sensitive BP and SnSe₂ from being exposed to the air. The substrate was spin-coated with e-beam resist in the glove box and Cr/Au electrodes (5/50 nm) were formed by e-beam lithography followed by lift-off in the glove box. The solid polymer electrolyte, PEO:CsClO₄, was deposited onto the substrate as a gate dielectric that also acts as a capping layer for BP and SnSe₂. When dissolved in PEO, CsClO₄ is ionized into Cs⁺ and ClO₄⁻, forming electric double layers which react to voltage bias.

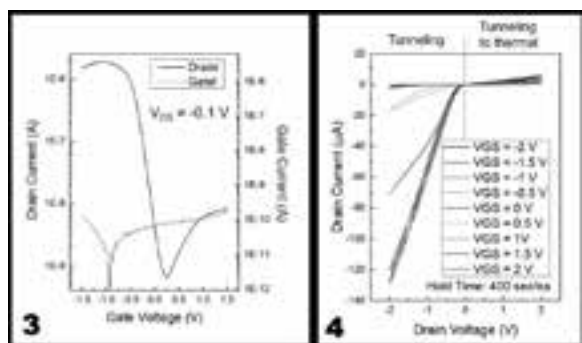


Figure 3, left: Current as a function of gate voltage at V_{DS} = -0.1 V at room temperature in N₂. The black line indicates drain current and the red line indicates gate leakage current. Figure 4, right: Drain current as a function of drain voltage with different gate voltages.

The BP and SnSe₂ form type-III broken band alignment which is favorable to tunneling devices. Since SnSe₂ is degenerately doped, the band of BP can be selectively modulated by gate bias without the change in the band of SnSe₂, which allow to control the band offset between BP and SnSe₂. Figure 3 shows the representative transfer curve of the device when -0.1 V of drain bias is applied. (BP side is drain and SnSe₂ side is source.) This is to open the tunneling window between BP and SnSe₂ so that electrons in the valance band of BP can tunnel into the conduction band of SnSe₂. When the negative gate bias increases, the number of carriers in BP which can move to SnSe₂ side increases, resulting in the increase of drain

current. When the positive gate bias increases, the portion of band to band tunneling decreases as the tunneling window gets smaller. If you keep increasing positive gate bias, the portion of conduction band to conduction band transport increases, and thus the drain current starts increasing. The transfer curve well explains the device characteristics of tunneling field effect transistors. Figure 4 shows the representative output curve of the device. Applying negative drain bias make the tunneling window size larger, increasing the difference between Fermi level of BP and SnSe₂. The drain current increases accordingly as shown in Figure 4. If positive drain bias is applied, the tunneling window decreases and the window get closed at some point. Increasing positive drain bias, however, enhance the thermionic emission of electrons from the conduction band of SnSe₂ to the conduction band of BP as in MOSFETS, leading to the increase of drain current in the opposite direction.

TFETs are said to have subthreshold swing less than 60 mV/dec in ideal case which is lower than so-called Boltzmann limit. In this case, however, the subthreshold swing is 180 mV/dec. The performance of tunneling devices is heavily dependent on interface properties such as interface trap density. If there exist many trap-density of states in the band gap, some portion of applied voltage will be lost to fill up those states. In addition, there is no negative differential resistance (NDR) observed in the output curve, which is one of the characteristic features of TFETs. This can be also attributed to the interfacial states. To see clear NDR behavior, the valley current should be small enough. If there are interfacial states, tunneling can happen even without tunneling window, which means inelastic current will increase the valley current. Electronic grade 2D material film growth as well as process to control interface quality should be developed to achieve high quality TFETs.

References:

- [1] M. Li, D. Esseni, J. J. Nahas, D. Jena, and H. G. Xing, IEEE Elec. Dev. Soc., 3, 200-207 (2015).
- [2] R. Yan, S. Fathipour, Y. Han, B. Song, S. Xiao, M. Li, N. Ma, V. Protasenko, D. A. Muller, D. Jena, and H. G. Xing, Nano Lett., 15, 5791-5798 (2015).
- [3] S. Fathipour, P. Pandey, S. Fullerton, and A. Seabaugh, J. Appl. Phys., 120, 234902 (2016).

Self-Assembled Silica Nano-Spheres for Dual Metal Junction-Barrier-Schottky Diodes

CNF Project Number: 2350-15

Principal Investigators: Prof. Debdeep Jena, Prof. Huili Grace Xing

User: Jae Ho Shin

Affiliation: Department of Materials Science and Engineering, Cornell University

Primary Source of Research Funding: Sixpoints

Contact: djena@cornell.edu, grace.xing@cornell.edu, js3366@cornell.edu

Websites: djena.engineering.cornell.edu, grace.engineering.cornell.edu

Primary CNF Tools Used: ABM contact aligner, wet chemistry bench, Zeiss Supra/Ultra SEM, odd hour e-beam evaporator, AJA sputter, PT-770 ICP RIE, photoresist spinner, hotplate, optical microscope

Abstract:

We report on a time and cost-effective method of selectively depositing thin metal films onto substrates. Silica nanospheres of 50 nm diameter were hexagonally packed using Triton X-100 surfactant on the DI water/air interface, and were transferred onto bulk n type gallium nitride substrates. After inspection using the scanning electron microscope, 20 nm thick metal was deposited on top. After stripping of the silica, a triangular shaped array of metal deposits remained. This technique will enable a quick, simple method of fabricating dual metal junction-barrier-Schottky-diodes, which use the difference in work function of two metals to reduce reverse leakage as in a p - n diode, as well as retain the low turn-on voltage of Schottky barrier diodes.

Summary of Research:

Gallium nitride (GaN), with its superior Baliga's figure of merit, is an excellent candidate for high power, high speed devices. GaN Schottky barrier diodes (SBDs) have shown the highest power efficiency in the < 1 kV breakdown voltage range [1], but show high reverse leakage current compared to those of p - n diodes, which is detrimental to achieving high breakdown voltage. One method of reducing the reverse leakage current is by fabricating a junction-barrier-Schottky-diode. (JBSD) [2]. This structure combines the large breakdown voltage of p - n diodes, and the low turn on voltage of SBDs into one device. Due to the difficulties in ion implantation and regrowth technologies in GaN, designing trench patterns in the p -type GaN and exposing the n -type GaN and making metal contacts on them could circumvent the issue. Results of these trench JBSD devices are further expressed in references. [3] A schematic of the JBSD device is depicted in Figure 1.

The p -type GaN could be viewed as a Schottky metal contact with a work function of ~ 3 eV. Thus, another approach could be taken to replace the p -type GaN with another metal. Due to the difference in work function of the two metals, similar effects as a p -GaN/metal JBSD could be achieved. The goal of this research at CNF was to fabricate a dual metal JBSD. In order to achieve this

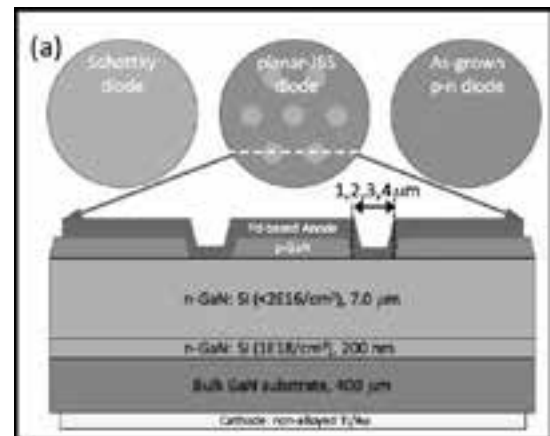


Figure 1: Schematic of trench-JBSD device with p -type GaN and Schottky metal contact on n -GaN [3].

local metal stack structure, a hard mask consisting of self-assembled monolayer of nano-scale silica spheres was used. The densest packing structure of spheres would be hexagonally close packed structures. However, in that packed structure, there would be an interstitial between every three spheres. Our strategy was to use this interstitial to selectively deposit metal.

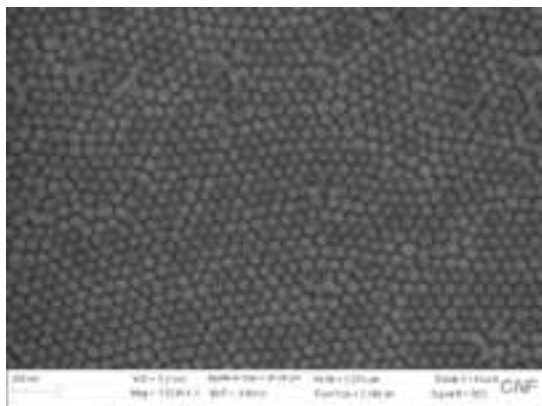


Figure 2: SEM image of HCP monolayer of silica nanospheres with 50 nm diameter.

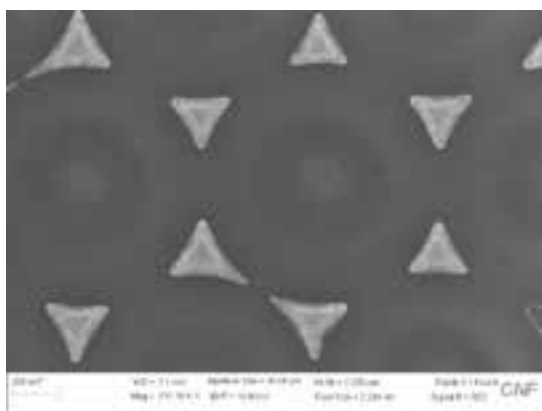


Figure 3: SEM image of 20 nm metal deposition remaining on interstitial area of HCP silica nanosphere monolayer.

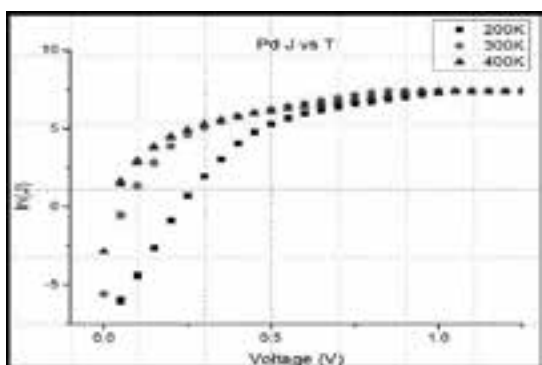


Figure 4: SEM image of 20 nm metal deposition remaining on interstitial area of HCP silica nanosphere monolayer.

Silica nanospheres were self-assembled on the interface between DI water and air using Triton X-100 surfactant, and then was transferred onto an *n*-GaN substrate and dried. After inspection of the layer with SEM, metal was deposited onto the structure. Figure 2 is an SEM image of the monolayer assembled onto a bulk GaN substrate. When the silica was stripped off using hydrofluoric acid, only the metal which was deposited in the interstitial points has remained. Thus, it is able to selectively deposit metal without use of nano-scale patterning such as e-beam lithography. It reduces the process time as well as cost required to pattern nanoscale features. Figure 3 is an SEM image of the resulting metal depositions on a bulk GaN substrate. Here, 20 nm of titanium and 5 nm of palladium was deposited. (Palladium is deposited to protect the highly oxidizing titanium. Since the second layer of metal in future processes would be palladium, the same metal was chosen to be the protective layer.)

After forming local depositions of the first metal, the rest of the process was as if fabricating a normal diode. The diode patterns were formed via photolithography, and 50 nm of palladium was deposited via the odd hour electron beam evaporator. After liftoff of the photoresist, the cathode of the device, consisting of titanium-aluminum-platinum was deposited via the AJA sputter system. The sputter system was used since it had a higher vacuum as well as faster deposition times. S1813 photoresist was deposited on the top surface to protect the devices.

Figure 4 is a temperature dependent J-V curve of the palladium control devices. The goal is to achieve lower turn-on as well as lower leakage than this device in the dual metal JBSD structure.

References:

- [1] S. Chowdhury and T. P. Chow, "Comparative performance assessment of SiC and GaN power rectifier technologies," *Phys. Status-Solidi C*, vol. 13, nos. 5-6, pp. 360-364, 2016.
- [2] B. J. Baliga, "The pinch rectifier: A low-forward-drop high-speed power diode," *IEEE Electron Device Lett.*, vol. 5, no. 6, pp. 194-196, Jun. 1984.
- [3] W. Li, "Design and realization of GaN trench junction-barrier-Schottky-diodes", *IEEE Transactions on Electron Devices*, vol. 64, no.4, pp.1635-1641.

Room Temperature Microwave Oscillators Enabled by Resonant Tunneling Transport in III-Nitride Heterostructures

CNF Project Number: 2443-16

Principal Investigator: Prof. Huili Grace Xing

User: Jimmy Encomendero

Affiliation: Electrical and Computer Engineering, Cornell University

Primary Source of Research Funding: Office of Naval Research under the DATE MURI Program

Contact: grace.xing@cornell.edu, jje64@cornell.edu

Primary CNF Tools Used: Veeco AFM, ABM contact aligner, YES asher, odd-hour evaporator, PT770 etcher, P10 and P7 profilometers, Oxford ALD, Oxford 81 etcher, AJA sputtering deposition

Abstract:

In the present work, we report III-Nitride resonant tunneling diodes (RTDs) operating at room temperature, which exhibit record-high peak current densities up to ~ 220 kA/cm². When the diodes are biased within the negative differential conductance (NDC) region, self-oscillations build up in the biasing circuit. A maximum frequency of oscillation close to 1 GHz is reported. The oscillatory signal and output power are studied in two different RTD designs, showing that their robust negative dynamic conductance can be effectively used as a gain element in high-frequency electronic oscillators.

Summary of Research:

Electronic devices based on III-Nitride semiconductors have emerged as potential solutions to meet the increasing demand for active terahertz (THz) components, due to their high electron velocity, high two-dimensional (2D) electron gas density and high thermal conductivity [1-3]. Toward this end, scaling strategies and parasitic management techniques have been successfully employed to push the cut-off frequencies of III-Nitride high electron mobility transistors (HEMTs) close to the border of the THz band [2,3]. In spite of these advances, amplification at frequencies > 1 THz is yet to be demonstrated. In this context, alternative gain mechanisms such as 2D plasma-waves excited via resonant tunneling injection, have been proposed as a means to engineer THz power amplification [4]. However, resonant tunneling transport across III-Nitride heterostructures has remained an open problem until very recently.

It has been only during the last two years that repeatable resonant tunneling transport was successfully demonstrated in III-Nitride quantum heterostructures [5,6]. Last year, we reported resonant tunneling injection both into the ground state as well as into the first excited state of GaN/AlN resonant tunneling diodes (RTDs) [6]. Furthermore, by precise control over the barrier thickness, peak current densities were enhanced from ~ 6.4 kA/cm² up to ~ 26 kA/cm², raising hopes for the demonstration of high-power RTD oscillators and room temperature THz QCLs.

In the present work, we report III-Nitride RTDs operating at room temperature, which exhibit record-high peak current densities up to ~ 220 kA/cm². When the diodes are biased within the negative differential conductance (NDC) region, self-oscillations build up in the biasing circuit. A maximum frequency of oscillation close to 1 GHz is reported. The oscillatory signal and output power are studied in two different RTD designs, showing that their robust negative dynamic conductance can be effectively used as gain element in high-frequency electronic oscillators.

The device structure of the two different RTD designs are displayed in Figure 1. These heterostructures, grown by molecular beam epitaxy (MBE), were fabricated into diodes using contact lithography, metal evaporation and dry etching processes at the Cornell NanoScale Facility (CNF). The main differences between these diodes are the quantum well width and the extension of the spacer regions next to each of the tunneling barriers (See Figure 1). The incorporation of the desired number of monolayers in the barriers and quantum well was confirmed using high angle annular dark-field (HAADF) scanning transmission electron (STEM) microscopy, as shown in Figure 2.

The typical room temperature current-voltage (*I-V*) characteristics of the devices are displayed in Figure 3. Both RTDs present a characteristic resonant tunneling peak, driving ~ 180 and ~ 6.4 kA/cm², respectively.

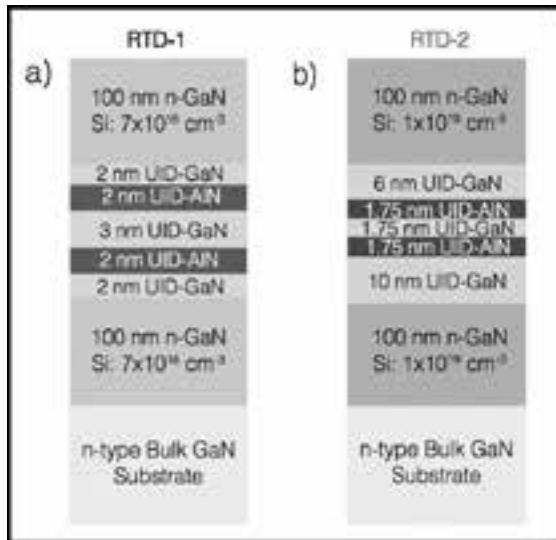


Figure 1: Schematic cross section of the double barrier heterostructures grown by molecular beam epitaxy on single-crystal n-type GaN substrates.

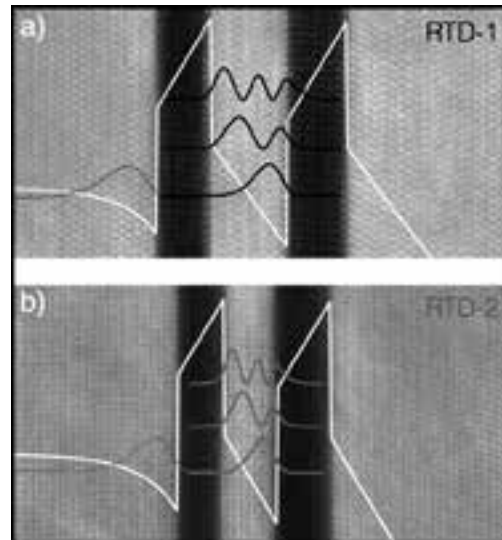


Figure 2: High angle annular dark-field (HAADF) scanning transmission electron microscopy (STEM) images of each of the RTD's active regions. The overlay shows the conduction band profile as well as the confined quantum states.

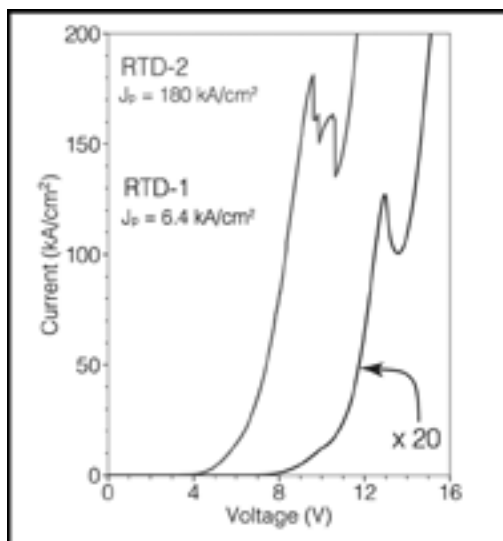


Figure 3: Room temperature current-voltage characteristics of the GaN/AlN RTDs shown in Figure 1. The peak current densities are $\sim 180 \text{ kA/cm}^2$ and $\sim 6.4 \text{ kA/cm}^2$.

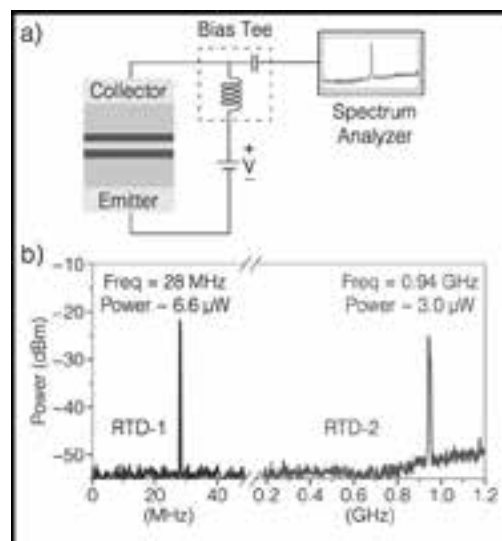


Figure 4: (a) Diagram of the circuit employed to measure the oscillatory signal using a spectrum analyzer. (b) Power spectral density emitted by each of the III-Nitride RTD oscillators.

Microwave oscillators are assembled by connecting the RTDs to a spectrum analyzer using a bias tee and coaxial cables as shown in Figure 4(a). The output power spectrum of each oscillator is displayed in Figure 4(b), showing that a maximum frequency of oscillation of $\sim 0.94 \text{ GHz}$ is produced by the high-current density RTD, generating $\sim 3.0 \mu\text{W}$ of output power. Using an equivalent RTD circuit model, it is shown that the oscillation frequency is limited by the time constant of the external circuit instead of the tunneling time of the RTDs. These results show the great potential of III-Nitride RTDs for the realization of high-frequency electronic oscillators.

References:

- [1] T. Suemitsu, IEECE Electronics Express 12, 20152005 (2015).
- [2] Y. Tang, et al., IEEE Electron Device Letters 36, 549 (2015).
- [3] Y. Yue, et al., Japanese Journal of Applied Physics 52, 08JN14 (2013).
- [4] B. Sensale-Rodriguez, et al., IEEE Transactions on Terahertz Science and Technology 3, 200 (2013).
- [5] T. A. Growden, et al., Applied Physics Letters 109, 083504 (2016).
- [6] J. Encomendero, et al., Phys. Rev. X 7, 041017 (2017).

MBE Grown NPN GaN/InGaN HBTs on Bulk-GaN Substrates

CNF Project Number: 2443-16

Principal Investigators: Huili Grace Xing, Debdeep Jena

User: Kazuki Nomoto

Affiliation: School of Electrical and Computer Engineering, Cornell University

Primary Source of Research Funding: NSF, AFOSR

Contact: grace.xing@cornell.edu, kn383@cornell.edu

Primary CNF Tools Used: Autostep i-line stepper, Heidelberg mask writer DWL2000, P7 profilometer, FilMetrics, AFM Veeco Icon, Zeiss SEM, PT770, Oxford 81, Oxford PECVD, odd-hour evaporator, AJA sputter deposition, RTA AG610

Abstract:

In this work, we demonstrate MBE grown GaN/InGaN/GaN *n-p-n* HBTs on bulk single-crystal GaN substrates with a low leakage current in each *p-n* junction. Good current saturation of the collector current with the collector-emitter voltage was observed. The common-emitter current gain is ~ 1.5 ($V_{CB}=0V$). Visible light emission was observed from the B-C and E-B junctions at forward-bias from 3.5 to 7 V. Two EL peaks at 3.2 eV and 2.9 eV are seen. The origin of this photon peak at 3.2 eV is related with band to band radiative transition in the $In_{-0.04}Ga_{-0.096}N$ base. Though recombination in the base of an HBT hurts its gain and performance, if the recombination is radiative, it also offers potential ways to cool the device, and to communicate with other devices. This first demonstration of an MBE-grown HBT paves the way towards HBT based power electronic devices and circuits in the future.

Summary of Research:

The wide bandgap GaN-based semiconductors are excellent candidates for high-power switching applications. Recently a large number of GaN-based high power switching transistors were reported with high-quality epitaxial growths on bulk-GaN substrates by MOCVD. Buried *p*-type structures are prevalent in GaN vertical power transistors, offering capabilities including reverse blocking, avalanche and reduce surface field. However, it is well-known that *p*-GaN gets passivated by hydrogen in MOCVD grown materials. Furthermore, it is quite difficult to activate the doped-Mg in buried *p*-GaN structures. MBE growth on the other hand enables efficient (Mg) acceptor doping for buried *p*-type layers that do not require activation annealing. In addition to a high degree of control of alloy compositions and heterostructures, the ability to grow buried *p*-layers is a significant advantage of MBE over MOCVD for HBTs, where the *p*-base is critical. And bulk-GaN crystals are necessary to reduce vertical leakage currents.

In this work, we demonstrate MBE grown GaN/InGaN/GaN *n-p-n* HBTs on bulk single-crystal GaN substrates with a low leakage current in each *p-n* junction. High-quality GaN/InGaN epi-layers were successfully grown on a bulk-GaN substrate ($TDD \sim 2 \times 10^7/cm^2$). The In composition in the graded collector-base (C-B) and base-

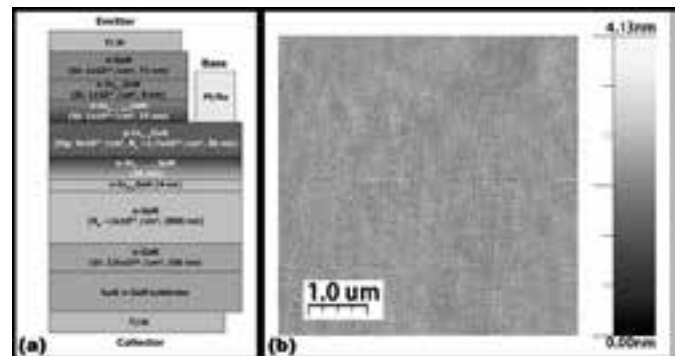


Figure 1: (a) A schematic cross section of MBE grown InGaN/GaN HBTs on bulk-GaN substrates. (b) AFM image of the as-grown InGaN/GaN HBT structure.

emitter (B-E) junctions was graded from 0% to 4% and from 4% to 0% by linearly decreasing and increasing the Ga flux, respectively. A high base hole concentration of $p \sim 1.7 \times 10^{18}/cm^3$ was determined by Hall effect measurement.

Figure 1(a) shows a schematic cross section image of a fabricated GaN/InGaN HBT. A very smooth as-grown epi-surface was confirmed by AFM, as shown in Figure

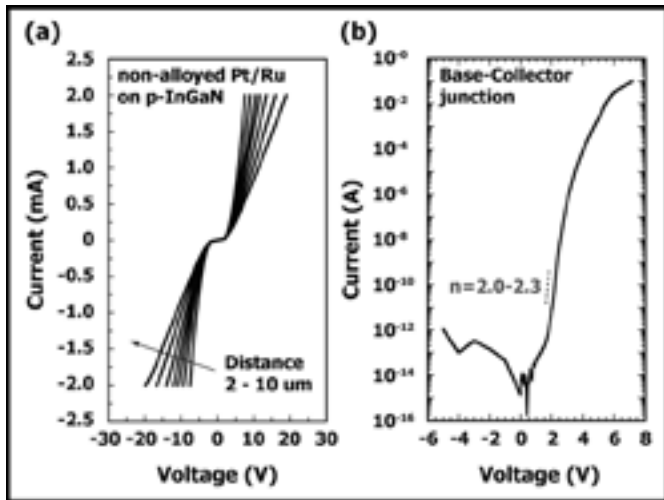


Figure 2: (a) Representative TLM I-V characteristics of Pt-based ohmic contacts on p-InGaN. (b) Forward bias I-V characteristic for a base-collector p-n junction diode.

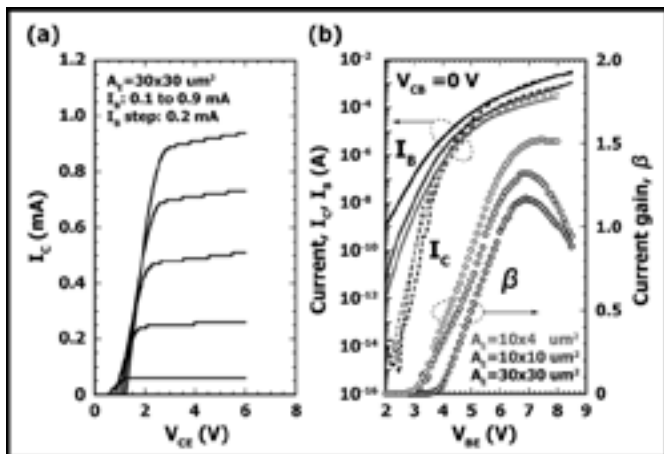


Figure 3: (a) The family curves of a GaN/InGaN n-p-n HBT with $A_E = 30 \times 30 \mu\text{m}^2$ and (b) Gummel plots with various emitter sizes at $V_{CB} = 0\text{V}$.

1(b). Device fabrication started with a two-step mesa etching process for the emitter mesa and device isolation by the Cl-based ICP etching. The base ohmic contacts were formed with Pt/Ru = 20/50 nm by electron beam evaporation. Figure 2(a) shows representative I-V characteristics of ohmic contacts on p-InGaN. For the emitter contacts, Ti/Al metal stacks were deposited and have a contact resistance of $1.7 \times 10^{-4} \Omega\text{-cm}^2$. Finally, Ti/Al stacks were evaporated on the backside of the n-type bulk GaN without patterning as the collector contact.

The representative B-C junction forward/reverse I-V characteristic is shown in Figure 2(b) in log scale. The junction shows rectifying behavior with a low leakage current, 10^{14} on/off ratio and the ideality factor 2, which means that the Shockley-Read-Hall recombination

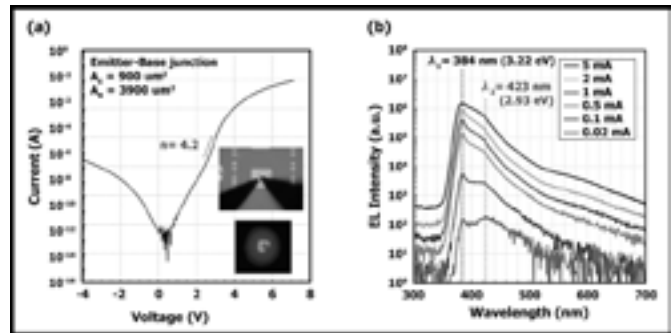


Figure 4: (a) Forward bias I-V characteristic for a base-emitter p-n junction in HBT. Inset figure shows the visible light emission during the measurement. (b) Electroluminescence spectrums of a base-emitter p-n junction in HBT with a forward bias voltage from 3.5 V to 7 V.

current dominates in the junctions [1]. Good current saturation of the collector current with the collector-emitter voltage was observed, as shown in Figure 3(a). Gummel plots for the HBTs with various emitter sizes are shown in Figure 3(b). The common-emitter current gain ($\beta = I_C / I_B$) is ~ 1.5 ($V_{CB} = 0\text{V}$).

In order to improve the current gain, the base resistance needs to be decreased since the measured sheet resistance of the InGaN base layer is $> 100 \text{ k}\Omega/\text{sq}$. Visible light emission was observed from the B-C and E-B junctions at forward-bias from 3.5 to 7 V. The measured electrical forward-bias I-V characteristic and electroluminescence (EL) spectra for the E-B junction are shown in Figures 4 (a,b). Two EL peaks at 3.2 eV and 2.9 eV are seen. The origin of this photon peak at 3.2 eV is related with band to band radiative transition in the $\text{In}_{-0.04}\text{Ga}_{-0.096}\text{N}$ base. The broad EL spectrum after the highest peak comes probably from deep donor-acceptor transition in highly Mg doped layer [2]. The inset in Figure 4(a) shows the visible strong emission even at a low forward voltage of 3.5 V. This result indicates high-quality material and confirms radiative recombination in the p-n junctions. Though recombination in the base of an HBT hurts its gain and performance, if the recombination is radiative, it also offers potential ways to cool the device, and to communicate with other devices. This first demonstration of an MBE-grown HBT paves the way towards HBT based power electronic devices and circuits in the future.

References:

- [1] Z. Hu, K. Nomoto, D. Jena, H. Xing, et al., APL, vol. 107, pp. 243501-1-243501-5, Dec. 2015.
- [2] U. Kaufmann, M. Kunzer, H. Obloh, C. Manz, et al., Physical Review B 59 (1999) 5561-5567.

Fabrication of GaN Quantum Well HEMTs

CNF Project Number: 2470-16

Principal Investigators: Debdeep Jena, Huili Grace Xing

Users: Austin Hickman, Samuel Bader, Reet Chaudhuri

Affiliation: School of Electrical and Computer Engineering, Cornell University

Primary Source of Research Funding: Joint University Microelectronics Program, Semiconductor Research Corporation

Contact: djena@cornell.edu, grace.xing@cornell.edu, alh288@cornell.edu, sjb353@cornell.edu, rtc77@cornell.edu

Primary CNF Tools Used: Autostep i-line stepper, PT770, Oxford 81, e-beam evaporator (odd and even), AFM Veeco Icon, Oxford PECVD, Oxford FlexAL, JEOL 6300, Glen 1000 resist strip, Zeiss Ultra/Supra SEM, profilometers, photolithography spinners/hotplates, solvent and acid hoods

Abstract:

This work focuses on the fabrication and characterization of gallium nitride quantum well HEMTs (QW HEMTs) and GaN pFETs based on the aluminum nitride platform. QW HEMTs provide numerous advantages over the conventional AlGaIn/GaN HEMT, including: improved carrier confinement, higher thermal conductivity, and improved reliability at high voltages. We report high electron mobility transistors (HEMTs) with saturation current densities of 2 A/mm and breakdown fields in excess of 2.7 MV/cm. In addition, we have fabricated an operational *p*-channel field-effect transistor (pFETs) on the same AlN platform with clear gate modulation of drain current. The development of efficient pFETs on AlN could enable complementary logic functionality in nitrides.

Summary of Research:

The QW HEMT offers a wealth of potential for new transport phenomena in III-V nitrides, as well as several improvements to the conventional AlGaIn/GaN HEMT that will allow for improved performance at the limits of high power and high frequency. Our group has previously grown and fabricated QW HEMTs [1-3] with heterostructures currently being grown via MBE at Cornell. The quantum well HEMT structure consists of an AlN buffer (500 nm), GaN channel (30 nm), AlN barrier (5 nm), and a GaN passivation layer (2 nm).

The first component of our fabrication process is MBE-regrown ohmic contacts. To prepare the sample for regrowth, several depositions and etches are performed with CNF equipment. The as-grown sample is cleaned in CNF with acetone, IPA, nanostrip, HF, and HCl. SiO₂ (Oxford PECVD) and chromium (e-beam evaporator) are then deposited on the sample as hard masks. Photolithography (Autostep) is used to pattern the desired regrowth areas. The chromium and SiO₂ are etched (PT770 and Oxford 81). Finally, the sample is etched to expose the 2D electron gas (2DEG) for regrowth of ohmic contacts. By using the tools available in the CNF, we have achieved 2DEG contact resistances as low as 0.25 Ohm mm.

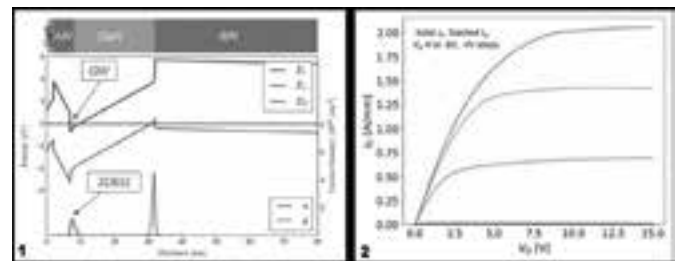


Figure 1, left: The energy band diagram of the GaN quantum well HEMT with electron and hole concentrations. **Figure 2, right:** (a) IDVD for quantum well HEMT. $L_g = 1.5 \mu\text{m}$.

Once the ohmic contact is established via MBE regrown n^{++} GaN, the regrowth is measured via atomic force microscopy (Veeco AFM) to characterize the quality of the GaN. The devices are isolated via i-line lithography and dry etched to ensure proper device dimensions. Ohmic contact metal are defined by i-line lithography, and are deposited via e-beam evaporation. This is followed by gate contacts defined by both i-line lithography and EBL (JEOL 6300), and deposited with e-beam evaporation.

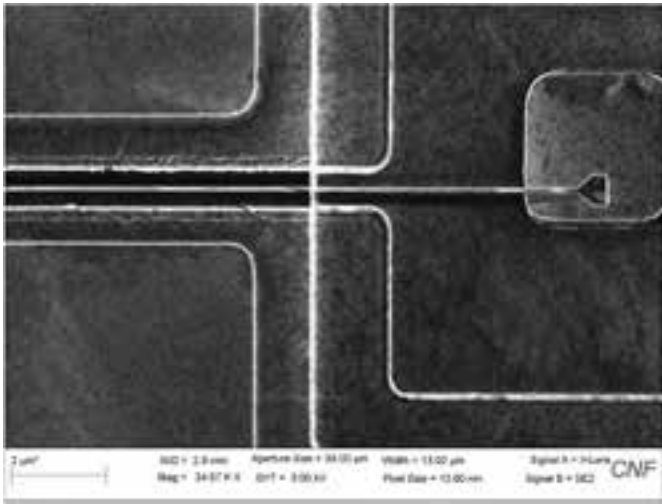


Figure 3: SEM image of a processed RF device. $L_g = 100$ nm.

Finally, the devices are passivated by combinations of SiN, AlN, and Al₂O₃ via ALD (Oxford FlexAL) and PECVD (Oxford PECVD). The final devices are observed via SEM (Figure 3).

In the past year, the first QW HEMT devices were processed and measured at Cornell. After initial optimization of processing, the QW HEMTs have yielded solid DC performance, with saturation currents over 2 A/mm ($L_g = 1.5$ μm) and $g_m = 220$ mS/mm, as well as $E_{\text{breakdown}}$ in excess of 2.7 MV/cm.

In the coming year, the fabrication process will be further optimized for DC and RF performance. With improvements, GaN QW HEMTs can push the limits of high frequency/high power performance of nitride HEMTs, and establish AlN as the optimal platform for the future of nitride electronics.

In addition to high-performance HEMT devices, this platform also provides a natural *p*-channel transistor

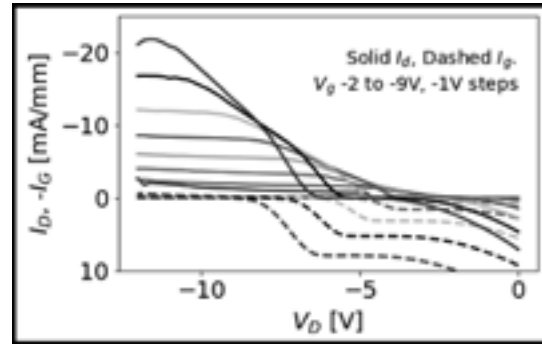


Figure 4: *p*FET IDVD with clear modulation of drain current. Significant gate leakage limits the device.

option based on the hole gas at the GaN-on-AlN interface. Growths focused on optimizing this region have achieved record low 2D hole sheet resistances (below 10 kΩm/sq) for GaN-based devices and, by a similar process to the one described above, have yielded promising preliminary devices. Providing the elusive *p*-channel transistor in a wide-bandgap platform could revolutionize the device of high-power integrated circuits by enabling efficient CMOS-style topologies with compact high-voltage transistors.

References:

- [1] Li, et al., "Ultrathin Body GaN-On-Insulator Quantum Well FETs with Regrown Contacts", IEEE (2012).
- [2] Islam, et al., "First Demonstration of Strained AlN/GaN/AlN Quantum Well FETs on SiC", DRC (2016).
- [3] Qi, et al., "Strained GaN quantum-well FETs on single crystal bulk AlN substrates", APL (2017).

MoS₂/PtSe₂ MOSFETs and CMOS Integration

CNF Project Number: 2509-16

Principal Investigator: James C.M. Hwang

Users: Kuanchen Xiong, Lei Li

Affiliation: Department of Electrical and Computer Engineering, Lehigh University

Primary Sources of Research Funding: This work was supported in part by the U.S. Office of Naval Research under Grant N00014-14-1-0653 and the Air Force Office of Scientific Research and the National Science Foundation EFRI 2-DARE Grant No. 1433459-EFMA

Contact: jh00@lehigh.edu, kux214@lehigh.edu, lel216@lehigh.edu

Primary CNF Tools Used: ABM contact aligner, Autostep i-line stepper, PT720-740 etcher, SC4500 odd-hour evaporator, P10 profilometer

Abstract:

We have used an alternative approach to the current practice of mechanical exfoliation and e-beam lithography in fabricating transitional metal dichalcogenide metal oxide semiconductor field effect transistors (TMD MOSFETs). The alternative uses a CMOS back-end-of-line (BEOL) process and large-scale transfer/dispense or direct thermal conversion. The BEOL process allows buried gates as short as 0.1 μm and high-quality gate insulator to be fabricated before TMD deposition [Figure 1(a)]. Large-scale transfer/dispense or thermal conversion provides large area of TMDs at low temperature tolerable by the BEOL process. After further photolithography, approximately 1,500 RF-probeable MoS₂ or PtSe₂ MOSFETs were fabricated on each chip [Figure 1(c)]. The resulted MOSFETs were then characterized, which showed state-of-art performances with high yields. This work demonstrates that it is practical and promising to integrate TMDs or other 2D devices with CMOS circuits.

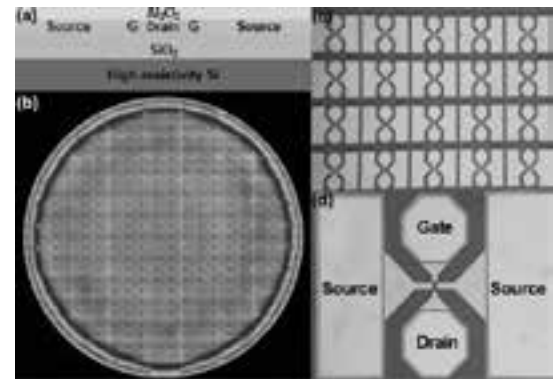


Figure 1: (a) Cross-sectional schematic of buried gates and micrographs of (b) a 200-mm Si wafer with approximately sixty 25 mm \times 15 mm chips, (c) part of a 25 mm \times 15 mm chip with rows and columns of MOSFETs totaling approximately 1,500 on each chip, and (d) details of each RF-probeable MOSFET with gate width of approximately 10 μm and gate length of approximately 0.2, 0.4 or 0.6 μm .

Summary of Research:

For chemical vapor deposited and transferred molybdenum diselenide (MoS₂) films, the fabricated MoS₂ MOSFETs showed yield greater than 50% in terms of effective gate control with less-than-10 V threshold voltage, even for MOSFETs having deep-submicron gate length [1]. The large number of fabricated MOSFETs allowed statistics [Figure 2(c) and (d)] to be gathered and the main yield limiter to be attributed to the weak adhesion between the transferred MoS₂ and the substrate. With cut-off frequencies approaching the gigahertz range [Figure 2(b)], the performances of the MOSFETs were comparable to that of state-of-the-art MoS₂ MOSFETs, whether the MoS₂ was grown by a thin-film process or exfoliated from a bulk crystal.

For solution-processed and dispensed MoS₂ films, nearly 100% yield was achieved and the cut-off frequencies were measured for the first time to be on the order of 100 MHz [2]. Being low temperature, low cost, and large area, solution-processed MoS₂ is attractive for future-generation thin-film and flexible transistors. To obtain the optimum combination of effective gate control and low contact resistance, channel recess was demonstrated for the first time on MoS₂. Specifically, channel recess by CHF₃/O₂ dry etching up to 60s was performed on submicron buried-gate MOSFETs fabricated on 20-nm-thick spin-coated MoS₂. It was found that the channel recess improved the current on/off ratio by three orders of magnitude while maintaining approximately the

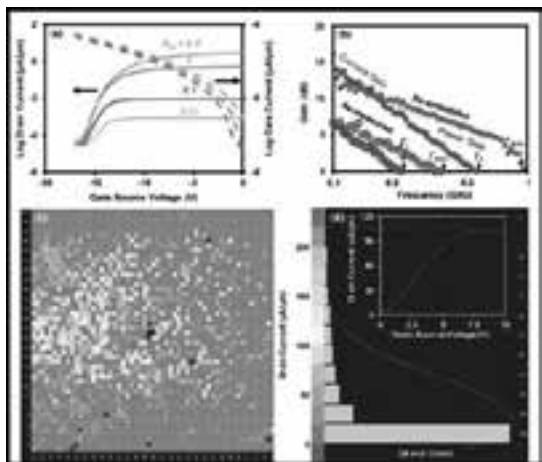


Figure 2: (a) Measured transfer characteristics of a typical MoS₂ MOSFET, (b) forward current-gain cut-off frequency f_T and maximum frequency of oscillation f_{MAX} of a typical MoS₂ MOSFET after annealing at 300°C for 1h in vacuum. $V_{GS} = 0.2$ V; $V_{DS} = 3$ V, (c) wafer map, and (d) histogram of maximum drain-source current measured with gate floating and $V_{DS} = 10$ V across a 15 mm × 15 mm area. The curve in (d) indicates Gaussian fitting with a peak around 30 $\mu\text{A}/\mu\text{m}$. Inset in (d) illustrates drain current saturation behavior.

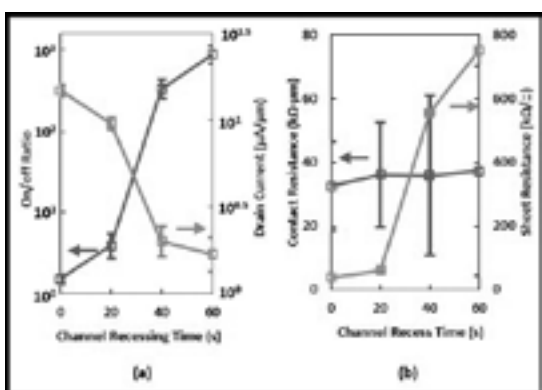


Figure 3: Evolution of (a) on/off ratio ($V_{DS} = 1$ V) and drain current ($V_{DS} = 1$ V, $V_{GS} = 0$), (b) contact and sheet resistances extracted from TLM test structures of 20 nm MoS₂.

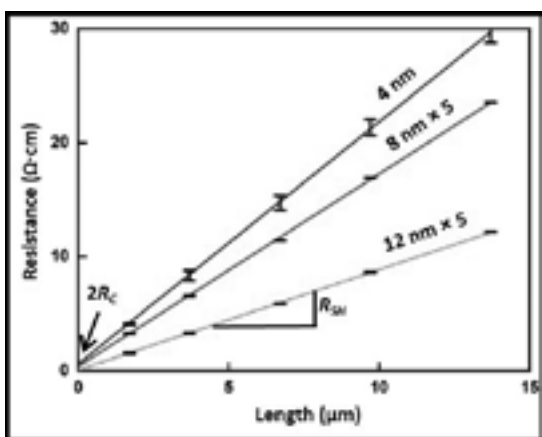


Figure 4: Total resistance R_T measured on TLM structures of different channel lengths and PtSe₂ thicknesses.

same contact resistance and peak transconductance as that of a uniformly 20-nm-thick channel (Figure 3). The resulted performance was among the best of all solution-processed MoS₂ MOSFETs [3]. The same channel recess technique can be used to improve the performance of MOSFETs made of other 2D materials.

Wafer-scale fabrication of platinum diselenide (PtSe₂) MOSFETs was demonstrated for the first time by photolithography on Pt films directly selenized at 400°C. Taking advantage of the unique property of PtSe₂ to transition from semiconductor to semimetal as its thickness increases beyond a few monolayers, channel recess was adapted for improving gate control while keeping the contact resistance as low as 0.008 $\Omega\text{-cm}$ (Figure 4). The wafer-scale fabrication resulted in uniform device characteristics so that average vs. best results were reported, as well as RF vs. DC characteristics.

For example, the drain current at $V_{GS} = -10$, $V_{DS} = -1$ V were 25 ± 5 , 57 ± 8 , and 618 ± 17 $\mu\text{A}/\mu\text{m}$ for 4-, 8-, and 12-nm-thick PtSe₂, respectively [4]. The corresponding peak transconductances were 0.20 ± 0.1 , 0.60 ± 0.05 , and 1.4 ± 0.1 $\mu\text{S}/\mu\text{m}$. The forward-current cut-off frequency of 12-nm-thick PtSe₂ MOSFETs was 42 ± 5 MHz, whereas the corresponding frequency of maximum oscillation was 180 ± 30 MHz. These results confirmed the application potential of PtSe₂ for future generation thin-film transistors.

All MoS₂ and PtSe₂ tested to date show compatibility with complementary metal oxide semiconductor (CMOS) process and state-of-art RF performances. To reduce the contact resistance while maintaining gate control, a channel-recess process was developed which showed promising results. Channel recess will be further optimized in the future.

References:

- [1] K. Xiong, et al., "CMOS-compatible batch processing of monolayer MoS₂ MOSFETs," J. Phys. D: Appl. Phys., vol. 51, no. 15, pp. 15LT02-1-15LT02-6, Mar. 2018.
- [2] K. Xiong, et al., "Large-scale fabrication of RF MOSFETs on liquid-exfoliated MoS₂," in European Microwave Conf. (EuMC), Madrid, Spain, Sep. 2018, pp. 1.4.
- [3] K. Xiong, et al., "Improvement by channel recess of contact resistance and gate control of large-scale spin-coated MoS₂ MOSFETs," IEEE Electron Device Lett., Submitted for publication.
- [4] L. Li, et al., "Wafer-scale fabrication of recessed-channel PtSe₂ MOSFETs with low contact resistance and improve gate control," IEEE Trans. Electron Devices, Submitted for publication.

Fabrication of FETs Based on La-BaSnO₃ Perovskite Oxide

CNF Project Number: 2543-17

Principal Investigator: Darrell Schlom

User: Jisung Park

Affiliation: Department of Material Science and Engineering, Cornell University, Ithaca, NY 14853, USA

Primary Source of Research Funding: Air Force Office of Scientific Research – DOD

Contact: schlom@cornell.edu, gp359@cornell.edu

Primary CNF Tools Used: PVD75 sputter deposition, AJA ion mill, Oxford ALD FlexAL

Abstract:

A field effect transistor based on La-BaSnO₃ (BLSO) has been made. The BLSO is a perovskite oxide material with high mobility and oxygen stability. The BLSO film was grown by molecular beam epitaxy. It has been etched with the AJA ion mill to make a channel layer, and ITO is deposited on the channel layer as the source and drain contact layer by PVD75 sputter deposition. ALD-grown HfO₂ film was deposited on it as a dielectric oxide by Oxford ALD FlexAL. ITO is deposited again by the same tool as a gate electrode. The schematic is shown in Figure 1. The device shows good characteristic curve in terms of I_{ds} - V_{ds} and I_{ds} - V_{gs} . The on-off ratio is over 6×10^6 and mobility is over $20 \text{ cm}^2/\text{V}\cdot\text{s}$. The characteristic curve of the device is shown in Figure 2 and Figure 3.



Figure 1: Schematic of the filed effect transistor based on La-BaSnO₃.

Summary of Research:

Field effect transistor based on La-BaSnO₃ (BLSO) has been fabricated and nice characteristic curves with high on-off ratio over 6×10^6 and mobility over $20 \text{ cm}^2/\text{V}\cdot\text{s}$ has been shown.

References:

- [1] H. J. Kim, U. Kim, H. M. Kim, T. H. Kim, H. S. Mun, B.-G. Jeon, K. T. Hong, W.-J. Lee, C. Ju, K. H. Kim, and K. Char, Appl. Phys. Express 5, 061102 (2012).
- [2] C. Park, U. Kim, C. J. Ju, J. S. Park, Y. M. Kim, and K. Char, Appl. Phys. Lett. 105, 203503 (2014).
- [3] Y. M. Kim, C. Park, U. Kim, C. Ju, and K. Char, Appl. Phys. Express 9, 011201 (2016).
- [4] U. Kim, C. Park, T. Ha, Y. M. Kim, N. Kim, C. Ju, J. Park, J. Yu, J. H. Kim, and K. Char, APL Mater. 3, 036101 (2015).

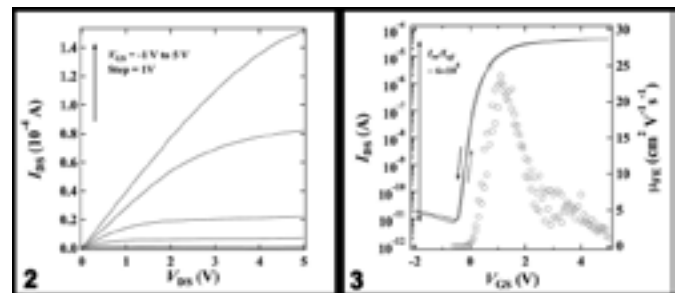


Figure 2, left: Output characteristic curve of the device. Figure 3, right: Transfer characteristic of the device.

Micro-Scale Opto-Electrically Transduced Electrodes (MOTEs)

CNF Project Number: 2578-17

Principal Investigator: Prof. Alyosha C. Molnar

Users: Sunwoo Lee, Alejandro Cortese

Affiliation: Electrical and Computer Engineering, Cornell University

Primary Source of Research Funding: National Institute of Health

Contact: AM699@cornell.edu, SL933@cornell.edu

Website: <https://molnargroup.ece.cornell.edu/>

Primary CNF Tools Used: ABM contact aligner, AJA sputter deposition, Westbond 7400A ultrasonic wire bonder

Abstract:

Recording neural activity in live animals *in vivo* poses several challenges. Electrical techniques often require electrodes to be tethered to the outside world directly via a wire, or indirectly via an RF coil [1], which is much larger than the electrodes themselves. Tethered implants result in residual motion between neurons and electrodes as the brain moves and limits our ability to measure from peripheral nerves in moving animals, especially in smaller organisms such as zebra fish or fruit flies. On the other hand, optical techniques, which are becoming increasingly powerful, are nonetheless often limited to subsets of neurons in any given organism, impeded by scattering of the excitation light and emitted fluorescence, and limited to low temporal resolution [2]. In our work, an untethered electrode unit capable of signal amplification and modulation is powered by, and communicates through a microscale optical interface, combining many benefits of optical techniques with high temporal-resolution recording of electrical signals [3]. To combine conventional complementary metal-oxide semiconductor (CMOS) for electronics and aluminum gallium arsenide (AlGaAs) light emitting diodes (LEDs) for optical functionalities, CNF has provided pivotal supports in fabricating the said hetero-integration.

Summary of Research:

We start our fabrication with a conventional 180 nm process CMOS die, which contains the electronics for signal amplification as well as signal modulation. In order to add an optical link, which powers the electronics by acting as a photo-voltaic (PV) as well as optical transmission by acting as a LED (hence the diode is abbreviated as PVLED), we need to integrate an AlGaAs diode onto the CMOS die. The AlGaAs diodes are first made on a sapphire wafer, then later released from the sapphire substrate with a sacrificial poly(methyl methacrylate) (PMMA) polymer that aids the release and the subsequent transfer processes.

Once the PMMA-coated AlGaAs diodes are transferred onto the CMOS die, the Oxford 81 plasma etcher is used to remove the sacrificial PMMA, leaving only the diode intact with the CMOS die. To establish the electrical contact between the two, and because the CMOS die is often much smaller than conventional wafers (typically in the vicinity of 5 mm × 5 mm), we have used CNF's ABM contact aligner for photolithography with nLoF2020 UV photoresist. To maximize the conformality of the metal coating for contacts, we have employed AJA sputter deposition.

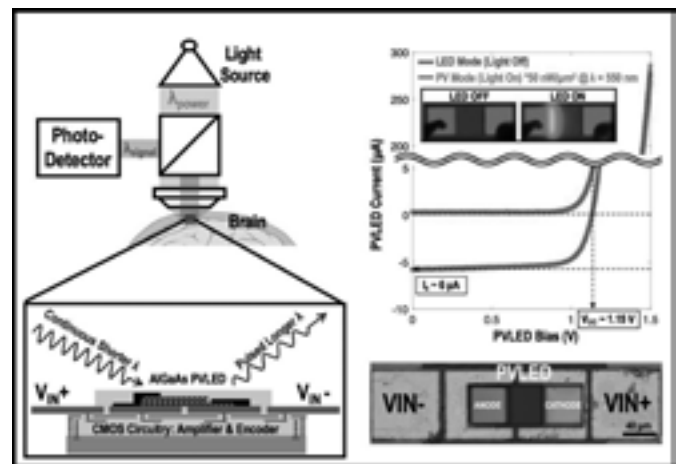


Figure 1: An envisioned implementation of the system. Top-right: characterization of a micro-scale AlGaAs diode device utilized as PV as well as LED. Bottom-right: a micrograph of an assembled system.

In addition, to confirm the functionality of each module (CMOS and the diode), we have relied on Westbond 7400A ultrasonic wire bonder for board-level integration

efforts. We have also employed parylene deposition and the Oxford ALD FlexAL for passivation of the assembled heterostructure. Finally, ZEISS Ultra and Supra scanning electron microscopes (SEMs) are used to inspect the fabricated MOTE that is shown in Figure 1.

The assembled MOTE implements pulse position modulation (PPM) for signal encoding for its high information-per-photon efficiency and the diode, the PVLED delivers sharp (<100ns) current pulses, spacings of which are proportional to the measured electric field of neuronal signals across the measurement electrodes (two outer-most electrodes shown on the bottom right of Figure 1). Furthermore, it should be noted that the PVLEDs with different wavelengths can provide further disambiguation via wavelength multiplexing, providing a path towards many-MOTE probing of neural signals.

To demonstrate the system's capability to encode real neural signals, we have connected the input electrodes to the ventral nerve cord of an earthworm using probes, with a commercial neural amplifier connected in parallel to provide a reference baseline. Figure 2 clearly shows that the composite spikes have been accurately encoded in the output optical pulses, even when communication and power are purely optical.

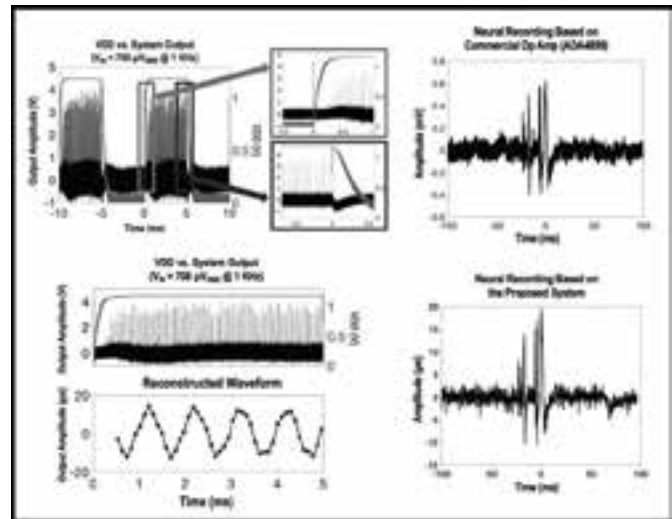


Figure 2: Left: start-up, showing optical pulses (top) and decoded signal (bottom). Right: neural recording on an earthworm ventral nerve using a commercial amplifier (top) and the presented system (bottom).

References:

- [1] R. R. Harrison, et al., "A Low-Power Integrated Circuit for a Wireless 100-Electrode Neural Recording System," in *IEEE J. Solid-State Circuits*, vol. 42, no.1, pp. 123-133, Jan. 2007.
- [2] W. Yang and R. Yuste, "In vivo imaging of neural activity," *Nature Methods*, vol. 14, no. 4, pp. 349-359, April 2017.
- [3] S. Lee, et al., "A 330.m.90.m opto-electronically integrated wireless system-on-chip for recording of neural activities," 2018 IEEE International Solid-State Circuits Conference (ISSCC), San Francisco, CA, 2018, pp. 292-294.

New Photopatterning Materials for Advanced Lithography

2018 CNF REU Intern: Jordan Phillip Howard-Jennings

2018 CNF REU Intern Affiliation: Engineering, Harvey Mudd College

CNF Project: 2018 Cornell NanoScale Science and Technology Facility Research Experience for Undergraduates Program

CNF REU Principal Investigator: Christopher Kemper Ober, Materials Science and Engineering, Cornell University

CNF REU Mentors: Kazunori Sakai, Materials Science and Engineering, Cornell University; Seok-Heon Jung, Materials Science and Engineering, Cornell University; Christopher Alpha, CNF, Cornell University

Primary Source of CNF REU Funding: National Science Foundation via the National Nanotechnology Coordinated Infrastructure (NNCI) Grant No. ECCS-1542081

Contact: jhowardjennings@g.hmc.edu, ks2288@cornell.edu, sj736@cornell.edu, alpha@cnf.cornell.edu

Website: http://www.cnf.cornell.edu/cnf_2018reu.html

Primary CNF Tools Used: ASML DUV stepper, Au/Pt sputter deposition, Hamatech wafer processor, spin coaters

Abstract:

Photolithography, which is a patterning method used to produce micro/nano-scale features, is currently approaching capabilities of producing sub-10 nm features at EUV wavelengths [1]. We present the findings of material development and characterization of model chemically amplified resists (CARs) to study novel photoacid generators (PAGs), as well as of Zn and Zr metal oxide nanoparticle (MO-NP) resists which offer many advantages over CARs.

Background:

For the past decade, the semiconductor industry has been using immersion lithography to make deep-UV lithography critical dimensions smaller [2]. However, and particularly with CARs which utilize PAGs to “amplify” the photo-reaction that occurs upon exposure, two issues arise: defective patterns resulting from the leaching of resist into the immersion fluid [2], and a sensitivity boost at the expense of line-edge roughness (LER) [3,4]. For EUV lithography to become an industry standard, current materials development of EUV resists must address these issues.

MO-NPs have garnered attention for resist development because they offer many potential and realized advantages to current resist technologies: smaller size relative to polymer photoresists [5], and a ligand-exchange photoreactive mechanism that is more controllable than the deprotection reactions that occur with generated photoacids in conventional resists [6], among other benefits. Currently, metal oxide methacrylate resists produced from hafnium and zirconium have been shown to be potential candidates for EUV resists because of their high resolution and sensitivity [6].

Furthermore, the ligand-exchange mechanism occurring between the acid groups on the metal oxides and the generated photoacids that produces a solubility switch in the exposed area is of interest of further investigation. Since there is a direct correlation between scumming (a phenomena associated with high LER) and the

type of PAG used [3], a study of how PAGs alter resist performance is necessary for understanding how newly developed PAGs may provide better compatibility for EUV MO-NP resists.

Materials and Methods; Synthesis

MO-NP Resists. Resist solutions were prepared by combining 91 mg metal oxide, 9.1 mg PAG (N-hydroxynaphthalimide triflate), and 1.9 g PGMEA in a small glass vial. The metal oxide and PAG were dissolved in PGMEA through 12-16 minutes of stirring on a handheld vortex mixer.

Model CARs. Resist solutions were prepared by synthesizing the monomers tert-butyl methacrylate, isobornyl methacrylate, and methacrylic acid with AIBN as an inhibitor. Once this product was formed, it was mixed with a PAG and PGMEA and dissolved by exposure to a heat gun and vigorous hand-mixing for 10-15 minutes.

Materials and Methods; Lithographic Conditions

MO-NP Resists. Resists were spun onto bare silicon wafers at 2000 rpm for 60s and given a 60s soft bake at 40°C (Zr) or 70°C (Zn). The wafers were then exposed using a 248 KrF source ASML DUV stepper at a dose of

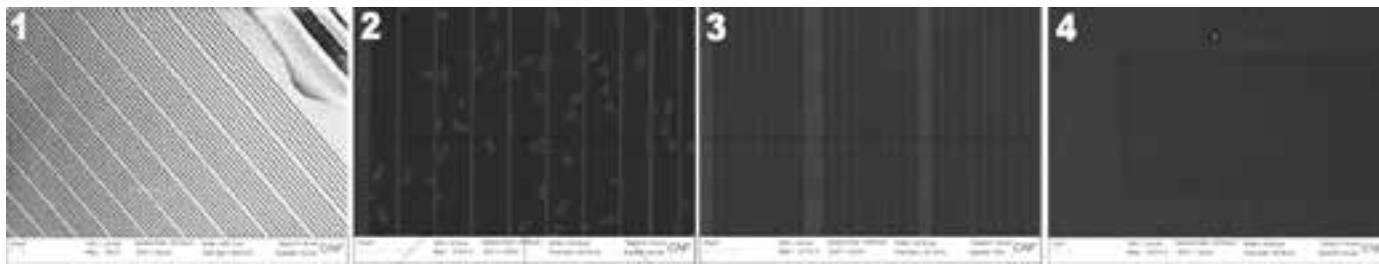


Figure 1: SEM image of various width patterns (largest 1000 nm) of Zn-oxide NP resists. Figure 2: SEM image of a 1000 nm-width pattern from the Zn-oxide NP resist. Figure 3: SEM image of a 500 nm-width pattern (center) from the Zr-oxide NP resist. Figure 4: SEM image of a pattern exposed region from the CARs.

150 mJ/cm², and subsequently developed in a range of solvents including o-xylene and m-xylene (Zr) as well as toluene and decaline (Zn).

Model CARs. DUV-42P bottom anti-reflective coating (BARC) was spun onto bare silicon wafers at 4000 rpm and given a 60s soft bake at 200°C. Resists were spun onto these wafers at 3000 rpm for 60s and given a post-annealing bake (PAB) at 100°C. Exposure took place on the ASML DUV stepper using an exposure dose matrix ranging from 10 to 358 mJ/cm², and subsequently given a 60s post-exposure bake (PEB) at 100°C before development in diluted TMAH for 60s using the Hamatech wafer processor.

Materials and Methods; Characterization

An assortment of optical microscopes capable of imaging nanometer-grade patterns were used to “check” that patterns had registered among the many pre-final lithographic steps. Once developed, scanning electron microscopy was used to qualitatively evaluate resist performance using the Zeiss Supra and Zeiss Ultra models of their SEMs. For the CARs, a pre-SEM step of sputtering a thin Au/Pt layer on the wafer surface was required to reduce SEM overcharging.

Results and Conclusions:

MO-NP Resists. Current resist development demonstrates that while good feature production is possible (Figure 1), randomly dispersed particle defects (Figure 2) and incomplete pattern registering (Figure 3) significantly distort these features. The cause of these defects is not currently understood. For the Zn-oxide resist evaluated, the gradient-matching between the particle defects and the exposed/non-developed regions (lighter area) suggest that there could be issues in material preparation such as mixing of components.

Model CARs. While the appearance of desired patterns offers confirmation that the lithography happened, the model CARs run into two issues: First, randomly

dispersed porous defects dominate both the exposed and non-exposed areas, strongly suggesting that further materials development is needed. Second, the small gradient change between the patterned and non-patterned regions suggests that the height of the patterns is negligible (this observation is confirmed by the optical profilometer), suggesting that lithographic conditions used were not optimal.

Future Work:

Further materials development in conjunction with lithographic parameter optimization is necessary to reduce the preliminary defects observed in both the MO-NP resists and the model CARs. After these defects are eliminated, an expansive design-of-experiments may be implemented to evaluate factor interactions between different material properties (i.e., PAG type/amount, metal oxides, etc.) and lithographic conditions (i.e., spin times, bake times, exposure doses, etc.).

Acknowledgements:

This work was performed in part at the Cornell NanoScale Facility, a member of the National Nanotechnology Coordinated Infrastructure (NNCI), which is supported by the NSF (Grant ECCS-1542081).

References:

- [1] Li, Li, et al. Chemical Society Reviews. doi: 10.1039/C7CS00080D (2017).
- [2] Petrillo, Karen, et al. Advances in Resist Technology and Processing XXII. doi: 10.1117/12.601621(2005).
- [3] Kosma, Vasiliki, et al. “Extreme Ultraviolet (EUV) Lithography IX. doi: 10.1117/12.2297383 (2018).
- [4] Thiyagarajan, Muthiah, Kim Dean, and Kenneth E. Consalves. Journal of Photopolymer Science and Technology. doi: 10.2494/photopolymer.18.737 (2005).
- [5] Krysak, Marie, et al. Advances in Resist Materials and Processing Technology XXVIII. doi: 10.1117/12.879385 (2011).
- [6] Jiang, Jing, et al. Journal of Photopolymer Science and Technology. doi: 10.2494/photopolymer.27.663 (2014).

Electrical Characterization of $\text{In}_2\text{Ga}_2\text{ZnO}_7$ Crystallized by Millisecond Heating

CNF Project Number: 150-82

Principal Investigator: Michael O. Thompson

User: Katherine K. Quinn

Affiliation: Materials Science and Engineering, Cornell University

Primary Source of Research Funding: Air Force Office of Scientific Research (AFOSR)

Contact: mot1@cornell.edu, kkq2@cornell.edu

Website: http://thompson.mse.cornell.edu/

Primary CNF Tools Used: Furnace B2, Oxford 100 PECVD, Plasma-Therm 720, CHA evaporator, SÜSS MicroTech MA6

Abstract:

In this work, we examined the electrical properties of $\text{In}_2\text{Ga}_2\text{ZnO}_7$ films crystallized by laser spike annealing (LSA) for a dwell time of 10 ms. Using the lateral gradient LSA method, samples were annealed and crystallization was visibly observed. Spatially resolved sheet resistance measurements were attempted across the LSA stripe using patterned van der Pauw structures. Films as annealed were insulating with a conductance below 10^{-8} S and exhibited only capacitor-like behavior. Analysis suggests that a thin SiO_2 passivation layer remained on films during processing leading to the observed behavior.

Summary of Research:

Over the past two decades, various amorphous oxide semiconductors have been explored as alternatives to amorphous hydrogenated silicon used in thin film transistors for large area displays. The In_2O_3 - Ga_2O_3 -ZnO (IGZO) material system in particular exhibits promising electrical characteristics including high electron mobility and stable carrier concentration. However, devices fabricated with amorphous IGZO (α -IGZO) are limited by turn-on voltage instabilities. While crystalline forms of IGZO maintain favorable electrical characteristics and do not exhibit device instabilities like α -IGZO, only films formed during heated substrate depositions have been studied. Alternatively, it is possible to crystallize α -IGZO films on short time scales (250 μs to 10 ms) using laser spike annealing techniques, however, very little is known about the electronic properties of metastable crystallized alloys in the IGZO system.

Van der Pauw devices were fabricated on lightly doped p-type Si wafers with ~ 80 nm of thermally grown SiO_2 for the purposes of electrical characterization (Furnace B₂). Amorphous thin film samples of $\text{In}_2\text{Ga}_2\text{ZnO}_7$ were deposited onto rotating substrates using a reactive RF magnetron sputtering system in a 10% O_2 in Ar mix with 120 W power. An ~ 30 nm thick passivating layer of SiO_2 was deposited to protect the IGZO surface (Oxford 100 plasma-enhanced vapor deposition). Samples were photolithographically patterned to form van der Pauw structure arrays, as shown in Figure 1 (SÜSS MicroTech

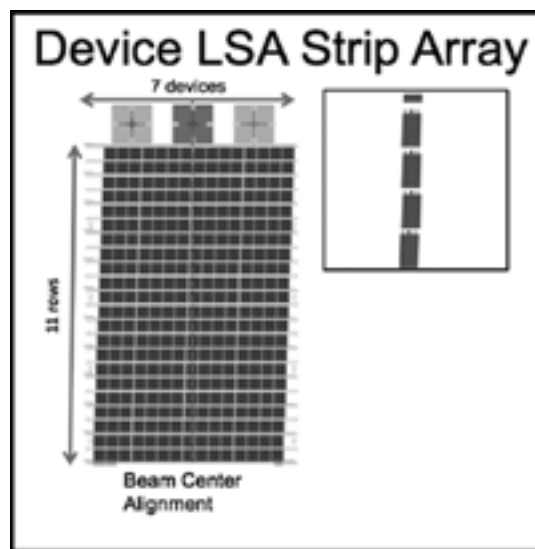


Figure 1: Schematic of van der Pauw device subarray consisting of 11 rows containing seven devices each. Above each subarray are alignment marks used to align the beam center during LSA. Inset is approximate scale of one device stripe on a 2 cm \times 2 cm sample.

MA6). The SiO_2 passivation layer was patterned using fluorine-based dry etching (Plasma-Therm 720) and IGZO was patterned using 2 wt.% HCl wet etching. After patterning, samples were annealed at 350°C with 7 sccm N_2 for 30 min in a quartz tube furnace.

Lateral gradient LSA (lgLSA) was used to crystallize the films. LSA uses a line-focused continuous wave laser beam to scan across a sample for controlled time durations (dwell). In lgLSA, the beam is intentionally non-uniform orthogonal to the scanning direction to produce a lateral temperature profile across the device row, allowing for electrical characterization as a function of peak annealing temperature.

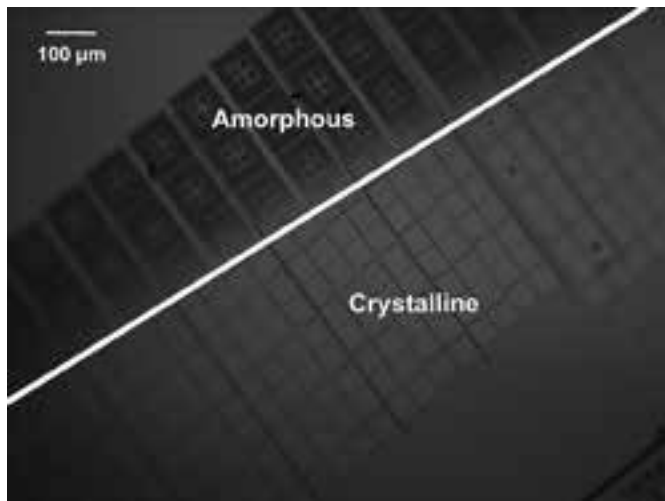


Figure 2: Evident structural transition indicated by color change along row of devices resulting from anneal by diode laser at 70.9 A for 10 ms dwell.

Samples were irradiated with fiber-coupled diode laser (980 nm wavelength, 1.5 mm full width half maximum) for 10 ms dwells, achieving expected anneal peak temperatures above and below a known Si melt temperature of 1414°C. Figure 2 shows a photomicrograph of an anneal stripe that produced a dark to light color gradient across the device rows, confirming a structural transition from an amorphous structure to the crystalline phase within the lateral temperature gradient.

Metal contacts were deposited (CHA Evaporator) and patterned using liftoff. Electrical measurements of devices were conducted using a 4-point manual probe station and a Keithley 2400 Source Measurement Unit (SMU) to supply current and measure voltage. Contact resistance and 4-point van der Pauw resistance measurements were obtained.

Initial resistance measurements ranged in the 60-200 MΩ range, indicating essentially non-conducting films. In contrast to the expected linear behavior of a conductive material, the IV characteristics showed parabolic curvature as seen in the resistance scans in Figure 3. This behavior is consistent with the material acting as a capacitor in that the material charges to a voltage at the application of negative current, then begins discharging symmetrically when the direction of current is reversed. The capacitance of the van der Pauw devices was extracted and found to be 96 pF.

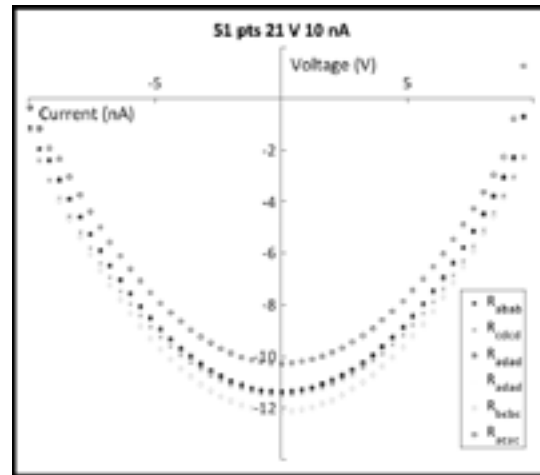


Figure 3: 4-point van der Pauw resistance measurements at 10 nA exhibited a parabolic IV curve, indicating the charging and discharging of current that is characteristic to capacitor behavior.

This implied that a material in the device stack was non-conducting and contributing to the measured device capacitance. The SiO₂ passivation layer, the active IGZO layer, and the thermally-grown SiO₂ layer on the Si substrate were considered as possible sources of the capacitance. After comparing the estimated layer thickness of each material to a calculated thickness required to yield a 96 pF capacitance, it was found that only a thin remainder of the passivation SiO₂ layer could be responsible for the capacitance. The most probable explanation for this observed capacitance is that the SiO₂ passivation layer was not completely etched during processing of the van der Pauw devices, resulting in a dielectric layer between the IGZO and the metal contacts. This motivates future improvements in the etching techniques used in the fabrication of devices.

References:

- [1] Kamiya, Toshio and Hosono, Hideo. (2010). "Material characteristics and applications of transparent amorphous oxide semiconductors." *NPG Asia Materials*. 2, pp. 15-22. DOI: 10.1038/asiamat.2010.5.
- [2] Lynch, David. (2017). "Indium Gallium Zinc Oxide: phase formation and crystallization kinetics during millisecond laser spike annealing." (Doctoral dissertation).
- [3] Yamazaki, Shunpei. (2013). "A possibility of crystalline Indium-Gallium-Zinc-Oxide," *Fifth Asia Symposium on Quality Electronic Design (ASQED 2013)*, pp. 1-5. DOI: 10.1109/ASQED.2013.6643553.
- [4] Chung, Chen-Yang. (2016). "High mobility of sputtered In₂Ga₂ZnO₇ (IGZO) thin film transistors (TFTs)." (Doctoral dissertation).
- [5] Bell, Robert. (2016). "Lateral Temperature-Gradient Method for High-Throughput Characterization of Material Processing by Millisecond Laser Annealing." *ACS Combinatorial Science*. 18, pp. 548.558. DOI: 10.1021/acscmbosci.6b00043.

Fused Silica Substrate and Silicon Absorber Film for use in Laser Spike Annealing (LSA)

CNF Project Number: 150-82

Principal Investigator: Michael O. Thompson

Users: Juliane M. Scholtz, Yi (Johnny) Zhang

Affiliations: Department of Physics, Department of Materials Science and Engineering; Cornell University

Primary Source of Research Funding: Department of Defense through a Multidisciplinary University Research Initiative (MURI)

Contact: mot1@cornell.edu, jms749@cornell.edu, yz2337@cornell.edu

Primary CNF Tools Used: Oxford 100 PECVD, Nikon Eclipse L200N optical microscope, Tencor P10 profilometer

Abstract:

Laser spike annealing (LSA), performed at various dwell times and generating various peak temperatures [1], is used to induce metastable phases in a variety of materials. An alternate LSA setup, which would allow annealing of metals and transparent dielectrics, requires the appropriate choice of a substrate, which is annealed directly, and an absorber film, which conducts heat to the material of interest. We investigate fused silica and silicon as candidates for substrate and absorber film, respectively. An Si thin-film was deposited via plasma enhanced chemical vapor deposition (PECVD) on a fused silica substrate and subjected to LSA with a CO₂ laser (10.6 μm) at various powers. LSA was performed on the glass substrate with a laser diode (980 nm) at various currents and dwell times. Profilometer measurements of the CO₂ anneals suggest Si ablation and potential substrate damage at 20.55W, as well as lesser ablation or an increase in grain size at lower powers. Laser diode annealing of the fused silica substrate caused no damage visible to the eye. Our work contributes to the development of a “universal substrate” for use in the modified laser spike annealing setup.

Summary of Research:

Laser spike annealing (LSA), performed at various dwell times and peak temperatures [1], is used to induce metastable phases in a variety of systems, such as Bi₂O₃ and MnTiO₃ [2]. To allow annealing of additional materials, including transparent dielectrics and metals, an alternate LSA method is in development. Annealing is performed from the substrate side of the sample, allowing an absorber film to conduct the heat to the material under investigation. Appropriate substrate and film choices will therefore withstand anneals that induce a wide range of peak temperatures and occur at different dwell times. Previous research has revealed inadequacies of sapphire substrates for LSA [3]. In this project, silicon (Si) and fused silica were investigated as potential absorber film and substrate, respectively. As peak temperature calibrations for these materials have yet to be performed using our laser setup, we explored the behavior of our substrate and film at varying laser power (or current) and dwell time.

A 100 mm diameter, 500 μm-thick fused silica wafer, polished on both sides, was purchased from the Cornell NanoScale Science and Technology Facility (CNF) and

used as a substrate. Approximately 60 nm of amorphous silicon (α-Si), which crystallized to polycrystalline silicon (poly-Si), were deposited on the substrate via plasma enhanced chemical vapor deposition (PECVD) at 350°C. The deposited film exhibited a transparent, pink-purple color. The absorber film candidate was annealed with a CO₂ laser (10.6 μm) at 1 ms dwell times, at power conditions of 20.55-6.22W. All these powers induced stripes in the thin-film visible to the naked eye (Figure 1).

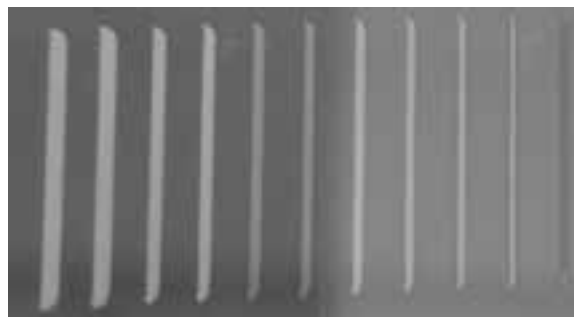


Figure 1: Annealed stripes (20.55W-6.84W, CO₂ laser) on poly-Si surface. Laser power decreases from left to right.

Stripes annealed at powers of 20.55W-10.8W appeared clear, while the film annealed at lower powers displayed a color change to light green.

To understand the physical changes that occurred in the sample during annealing, step heights between the annealed stripe centers and the surrounding thin-film were investigated using a Tencor P10 Profilometer. Stripes annealed at powers of 20.55W and 18.43W, respectively, which appeared clear to the naked eye, evidenced film ablation under profilometer examination. A step height of $1.097\ \mu\text{m}$ (1097 nm) in the former stripe suggests both complete ablation of the 60 nm film and CO₂ laser damage to the glass substrate beneath. This conjecture is supported by an additional set of anneals, in which CO₂ laser annealing at 20.55W directly onto the fused silica produced a damage stripe (Figure 2). The second annealed stripe (18.432W) evidenced $425\ \text{\AA}$ (42.5 nm) between stripe center and unannealed film. This indicates a relatively complete ablation of the thin-film by the CO₂ laser.

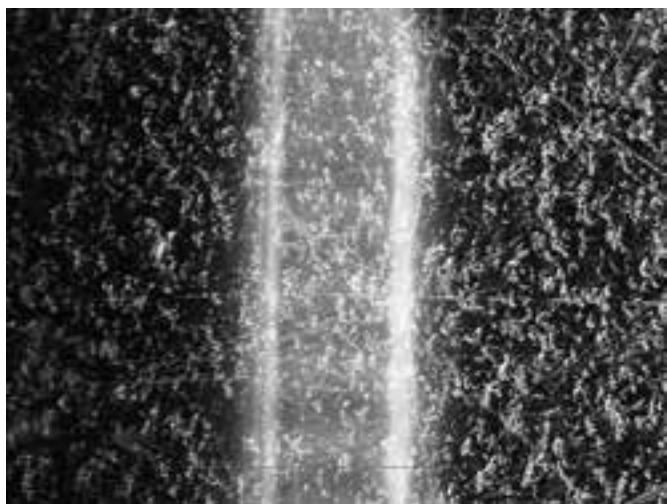


Figure 2: Dark-field view of LSA stripe (20.55W, CO₂ laser) on a fused silica substrate.

Two of the green-colored stripes were also examined with the profilometer. Both the fifth (10.267W) and sixth (9.724W) stripe measurements displayed large amounts of noise in their respective annealed regions. As a result, the Ra (roughness average) was parameter of importance. The fifth stripe had an Ra of $198\ \text{\AA}$, while the sixth evidenced an Ra of $156.4\ \text{\AA}$. Thus, a lower roughness average is observed at lower laser power. Noise observed in the profilometer measurements of the stripes may indicate that the poly-Si has transformed from small-grain to large-grain during the annealing process (Figure 3).

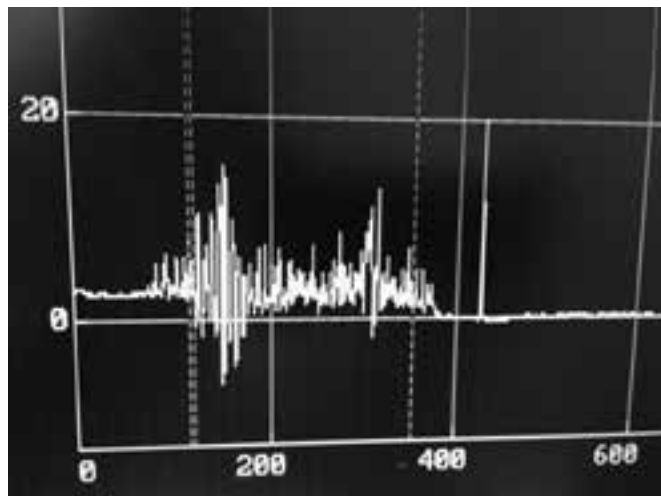


Figure 3: P10 Profilometer measurement of LSA stripe (10.267W, CO₂ laser) on silicon thin-film. Scale: vertical axis: $\times 100\ \text{\AA}$, horizontal axis: μm .

To further examine fused silica's potential as an LSA substrate, the glass was directly subjected to laser spike annealing with a laser diode (wavelength 980 nm). A set of five anneals (5 ms dwell times), with currents increasing from 63.58 Amps to 100.22 Amps, caused no damage to the substrate visible to the naked eye. To perform subsequent anneals at 100 Amps or below, the dwell time was increased. Two anneals, performed at 87.68 Amps and 97.76 Amps, respectively, with dwell time 10 ms, also caused no visible damage to the glass substrate. A further two anneals at 20 ms dwell times and currents of 82.5 Amps and 85.99 Amps, respectively, produced the same result.

We have studied the behavior of fused silica substrates and silicon absorber films under CO₂ and laser diode laser spike annealing. The absence of visible laser-induced damage from the laser diode suggests fused silica is a promising substrate for laser diode LSA. However, this substrate is susceptible to damage from CO₂ lasers, even at relatively low powers. PECVD deposition of α -Si should be performed at the standard 200°C, to prevent premature crystallization and allow for a true study of amorphous silicon as a potential absorber film. Our work contributes to the development of a "universal substrate" for use in the modified laser spike annealing setup.

References:

- [1] R. Bell, et al. ACS Comb. Sci. 18, 548 (2016).
- [2] R. Bell, Ph.D. thesis, Cornell University (2017).
- [3] H.-L. Huang, et al. Cornell NanoScale Science and Technology Facility Report, http://www.cnf.cornell.edu/doc/2017cnfRA/2017cnfRA_222.pdf (2017).

Metal-Organic Complex Photoresists

CNF Project Number: 386-90

Principal Investigator: Christopher Kemper Ober

Users: Kazunori Sakai, Hong Xu, Vasiliki Kosma

Affiliation: Materials Science and Engineering, Cornell University

Primary Source of Research Funding: JSR Corporation

Contact: christoper.ober@cornell.edu, ks2288@cornell.edu, hx49@cornell.edu, vk292@cornell.edu

Primary CNF Tools Used: Zeiss Supra SEM, ASML 300C DUV Stepper, ABM Contact Aligner

Abstract:

The most advanced microelectronics are made by using 193 nm immersion lithography systems, but it is difficult to follow the rapid development of semiconductors due to approaching its physical limits. Extreme ultraviolet (EUV) lithography, which use shorter wavelength (i.e., 13.5 nm), can offer the way to print under 40 nm lines and spaces. EUV lithography requires photoresist to utilize EUV photons because photons generated by EUV exposure are fewer than photons generated by 193 nm light exposure. One of the approaching for utilizing fewer EUV photons is using higher EUV absorption elements such as transition metals. We have continuously developed metal-oxide nanoparticles resists since we reported our first example of hafnium oxide nanoparticle resist [1]. In this report, our recent progress in metal oxide nanoparticle photoresist research will be described.

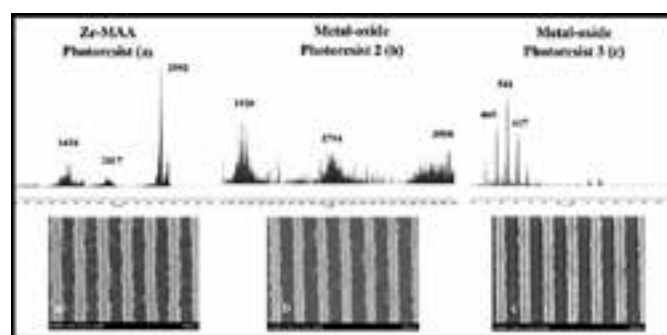


Figure 1: ESI-MS and SEM images after development of different metal oxide photoresists.

Summary of Research:

After we have developed hafnium oxide nanoparticle resist, we have also reported zirconium oxide nanoparticle resist. The features of these materials are very fast sensitivity with severe bridging and scumming. In order to elucidate what induced severe bridging and scumming, analysis with electron spray ionization mass spectrometry (ESI-MS) was investigated [2]. ESI-MS spectra and scanning electron microscope (SEM) images of three different resists are summarized in Figure 1. There is a connection between molecular weight and bridging and scumming. This result indicates that metal oxide resist should be smaller molecular weight and narrower size dispersion to print patterns without bridging and scumming. With this hypothesis, we have developed two

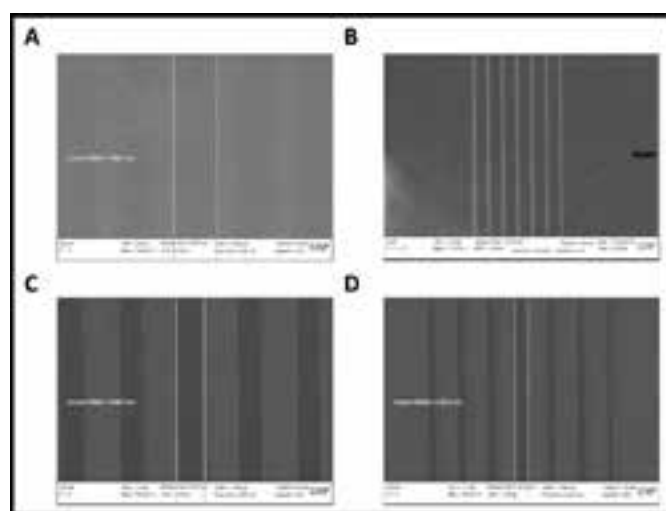


Figure 2: SEM images of DUV exposure results. (A) Zirconium nanoparticle (Zr-NP) 500 nm line-and-space (LS). (B) Zr-NP 250 nm LS. (C) Mono-crystal zirconium (MC-Zr) 500 nm LS. (D) MC-Zr 250 nm.

new materials; one is mono-crystal zirconium resist and the other are metal oxide nanoclusters with a controlled size distribution. The mono-crystal zirconium resist results are summarized in Figure 2. While large amounts of residues can be easily found at unexposed areas in the case of zirconium nanoparticle, mono-crystal zirconium resist demonstrate good 1:1 line-and-space patterns with a feature size from 500 nm to 250 nm.

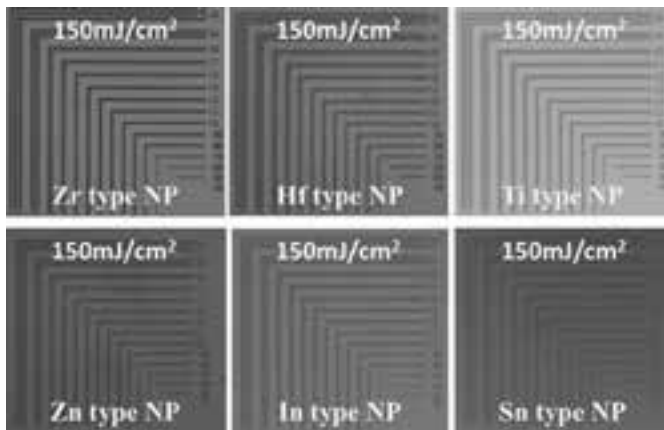


Figure 3: Optical microscope images of micro-scale patterning using the ABM contact aligner.

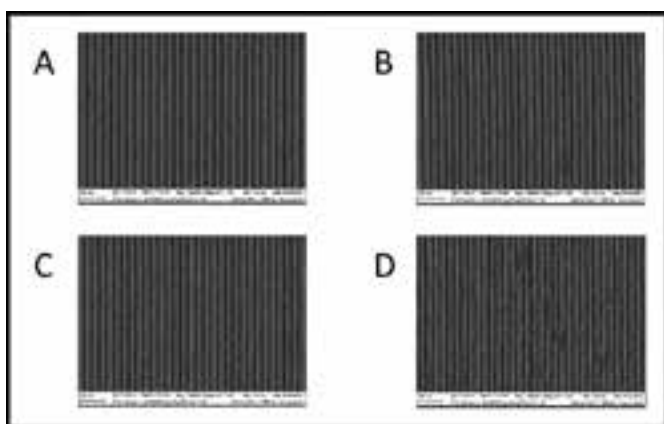


Figure 4: SEM of EUV exposure results with zinc nano-cluster resist. (A) 16 nmLS with 45 mJ/cm². (B) 15 nmLS with 47 mJ/cm². (C) 14 nmLS with 36 mJ/cm². (D) 13 nmLS with 35 mJ/cm².

We have synthesized zirconium, hafnium, titanium, zinc, indium and tin nanocluster and obtained microscale patterning result with 150 mJ/cm² exposure dose, a typical value at 248 nm exposure are summarized in Figure 3.

The zinc nanocluster is expected to absorb more EUV light than the zirconium nanocluster and we have evaluated zinc nanocluster with EUV light. SEM images are summarized in Figure 4 and demonstrates good 1:1 line-and-space patterns with the feature size of 16 nm, 15 nm, 14 nm and 13 nm, with a dose of 45, 47, 36 and 35 mJ/cm², respectively [3].

In this report, we described our recent progress in metal oxide nanoparticle photoresist. Currently we are performing further investigations to improve our material's lithography performance.

References:

- [1] Ober, C. K., Xu, H., Kosma, V., Sakai, K., Giannelis, E. P., EUV Photolithography: Resist Progress and Challenges. Proc. SPIE 2018, 10583, 1058306.
- [2] Kosma, V., Kasahara, K., Xu, H., Odent, J., Ober, C. K., Giannelis, E. P. Elucidating the patterning mechanism of zirconium-based hybrid photoresists. J. Micro/Nanolithography, MEMS, and MOEMS 2017, 16, (4), 041007.
- [3] Xu, H., Sakai, K., Kasahara, K., Yang, K., Herbol, H. C., Odent, J., Clancy, P., Giannelis, E. P., Ober, C. K., MOF-inspired metal-containing building units for high resolution patterning, Chem. Mater. accepted.

Zinc-Based Nanoparticle Photoresist for Extreme Ultraviolet Lithography

CNF Project Number: 386-90

Principal Investigator: Christopher Kemper Ober

User: Kou Yang

Affiliation: Departments of Materials Science and Engineering, Cornell University

Primary Source of Research Funding: JSR Corporation

Contact: cko@cornell.edu, ky373@cornell.edu

Primary CNF Tools Used: ABM contact aligner, ASML 300C DUV stepper, Zeiss Ultra SEM

Abstract:

Extreme ultraviolet (EUV) lithography, using 13.5 nm radiation, is considered one of the most prominent candidates for next generation lithography. The main challenge for EUV resists is to simultaneously satisfy resolution, line-width roughness (LWR) and sensitivity requirements. Over the past few years, our main effort has been to focus on ZrO_2 and HfO_2 nanoparticle-based photoresists. However, both Zr and Hf are relatively low EUV absorbing metals [1], and integration of high EUV absorption elements is a more promising route to further improve lithographic performance under EUV radiation. Zinc is a promising metal for higher EUV absorption. In this work, we synthesized a set of zinc-based nanoparticle photoresists with different kinds of toluic acid ligands. These nanoparticles possess small particle size, good solubility in spin-coating solvents, good film-forming abilities and patterning by incorporating a photo-acid generator.

Summary of Research:

HfO_2 - and ZrO_2 - nanoparticle based photoresists are well-known in the novel inorganic-organic hybrid nanoparticle system [2-6] developed by researchers at Cornell. With significantly higher etch resistance and smaller particle size, these nanoparticle photoresists show promising lithographic performance using DUV, e-beam and EUV exposure. Meanwhile, their superior etch resistance and extremely small constituent size, are clear advantages for ultimate resolution patterning.

However, the Zr and Hf are relatively low EUV absorbing metals [1], and integration of high EUV absorption elements was considered to be one promising route to further improve lithographic performance under EUV radiation. Under this notion, we then developed a series nanoparticle using high EUV absorption element Zn as the metal core. Zinc has shown higher EUV photo-absorption compared to both zirconium and hafnium, thus has a higher potential to achieve the high-sensitivity desired for EUV lithography.

In this work, we synthesized and tested new nanoparticles based on zinc oxide (ZnO). Zinc is a higher EUV absorption metal compared to Zr and Hf. With a similar approach we used for zinc *m*-toluic acid (ZnO-*m*TA), zinc *p*-toluic acid (ZnO-*p*TA) and zinc *o*-toluic acid (ZnO-*o*TA) were synthesized to improve patterning ability of zinc-based nanoparticles. The result shows that

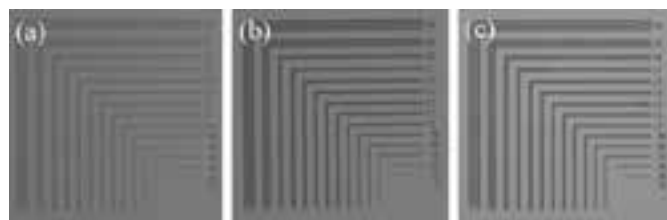


Figure 1: Optical microscopic images of zinc-based nanoparticles: (a) ZnO-*o*TA; (b) ZnO-*m*TA; (c) ZnO-*p*TA.

both ZnO-*p*TA and ZnO-*o*TA give good quality patterns after mid-UV exposure and DUV exposure, which indicates these nanoparticles are good candidates for EUV lithography.

Middle-Ultraviolet (mid-UV) Lithography:

Preliminary lithographic evaluations were carried out using the CNF ABM contact aligner (254 nm UV). The resist test formulation contains 5 wt% nanoparticles and PGMEA as solvent. The resist was spin-coated onto a silicon wafer at 2000 rpm for 1 min, then exposed under 254 nm at 150 mJ. Development was conducted immediately after exposure.

As shown in Figure 1, clear patterns can be obtained after mid-UV exposure. Pictures were taken by Nikon Microscope Cameras in CNF.

Deep Ultraviolet (DUV) Lithography:

With similar lithographic conditions in mid-UV exposure, the zinc-based nanoparticles are further exposed upon 248 deep-UV radiation using ASML 300C DUV Stepper in CNF. The film is exposed at 150 mJ/cm² as normal condition and developed in acetone. Developing time varies by different nanoparticles. Well-defined 1:1 line-and-space patterns negative tone patterns with feature size from 1000 nm to 250 nm were obtained, as indicated by scanning electron microscope (SEM) images (Figure 2 to Figure 4), taken by CNF Zeiss Ultra SEM.

In summary, we developed new ligands for zinc-based nanoparticles used in extreme ultraviolet lithography. These zinc-oxide based nanoparticles possess good solubility in spin-coating solvents, good film-forming ability and moderate patterning performance under mid-UV and deep-UV radiations. Considering the high EUV photo-absorption of zinc metal, this preliminary

work indicates such zinc-based nanoparticles would be promising candidates for EUV lithography. Further structure analysis, patterning mechanism study and lithography tests including EUV lithography patterning tests are ongoing using these zinc-based nanoparticles.

References:

- [1] B. L. Henke et al., X-Ray Interactions: photoabsorption, scattering, transmission, and reflection at E = 50~30,000 eV, Z = 1-92. At. Data Nucl. Data Tables, 54, 181-342 (1993).
- [2] M. Trikeriotis, et al., Development of an inorganic photoresist for DUV, EUV, and electron beam imaging. Proc. SPIE 7639, 76390E (2010).
- [3] W. J. Bae, et al., High refractive index and high transparency HfO₂ nanocomposites for next generation lithography. J. Mater. Chem. 20, 5186-5189 (2010).
- [4] M. Kryszak, et al., Development of an inorganic nanoparticle photoresist for EUV, E-beam, and 193nm lithography. Proc. SPIE 7972, 79721C (2011).
- [5] M. Trikeriotis, et al., A new inorganic EUV resist with high-etch resistance. Proc. SPIE 8322, 83220U (2012).
- [6] S. Chakrabarty, et al., Increasing sensitivity of oxide nanoparticle photoresists. Proc. SPIE 9048, 90481C (2014).

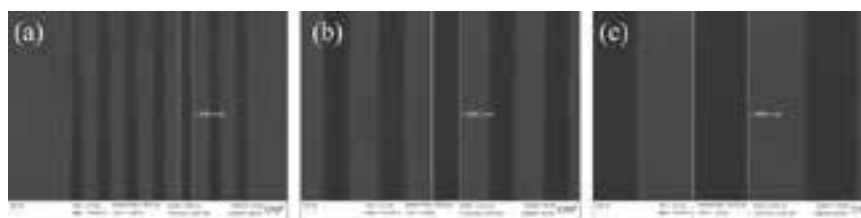


Figure 2: SEM images of ZnO-oTA nanoparticles: (a) 250 nm; (b) 500 nm; (c) 1000 nm.

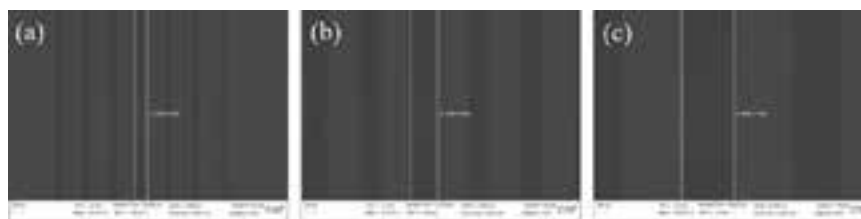


Figure 3: SEM images of ZnO-mTA nanoparticles: (a) 250 nm; (b) 500 nm; (c) 1000 nm.

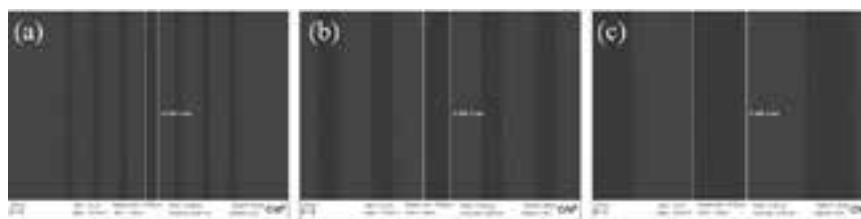


Figure 4: SEM images of ZnO-pTA nanoparticles: (a) 250 nm; (b) 500 nm; (c) 1000 nm.

Critical Size for Bulk-to-Discrete Transition in 2D Layers: Abrupt Size Effect Observed via Calorimetry and Solid-State NMR

CNF Project Number: 522-94

Principal Investigator: Leslie H. Allen

User: Zichao Ye

Affiliation: Materials Science and Engineering, University of Illinois at Urbana-Champaign

Primary Sources of Research Funding: National Science Foundation Division of Materials Research (#1409953, #1006385 and #0735286); University of Illinois Research Board (#13187)

Contact: allen9@illinois.edu, zye3@illinois.edu

Website: <http://allen.matse.illinois.edu>

Primary CNF Tools Used: Photolithography (aligner, developer, spinner, baking), e-beam evaporator, Oxford reactive ion etching tool, base wet etching hood, NH₃ image reversal chamber

Abstract:

Anomalous changes of physical properties are observed in an abrupt bulk-to-discrete transition in layered silver alkanethiolate (AgSC_n, $n = 1-16$). A critical chain length of $n_{cr} = 7$ marks the sharp boundary between the bulk (uniform, $n \geq 7$) and discrete (individualistic, $n \leq 6$) forms of AgSC_n. Solid-state ¹³C NMR analysis reveals that none of the carbons share identical chemical environment in the discrete range, making each AgSC_n with $n = 2-6$ uniquely different material, even though the crystal structure is preserved throughout. Extraordinary changes of thermodynamic properties appearing at this bulk-to-discrete transition include ~500% increases of melting enthalpy (ΔH_m), ~50°C increases of melting point (T_m), and an atypical transition between size-dependent T_m depression and T_m enhancement.

We develop a new comprehensive Gibbs-Thomson model with piecewise excess free energy (ΔG_{excess}) to predict the nature of the abrupt size effect melting. A new 3D spatial model is constructed to divide the aliphatic chains of AgSC_n into three bulk or discrete segments: (a) tail segment containing three carbons, (b) head segment containing two carbons, and (c) bulk mid-chain segment containing ($n - 5$) carbons. Odd/even effect of T_m and ΔH_m is described by a constant ΔG_{excess} over the entire chain length range of AgSC_n and is exclusively attributed to the localized tail segment. Bulk-to-discrete transition occurs when material properties are dominated by the discrete head and tail segments at $n < n_{cr}$. Values of n_{cr} are independently measured by both calorimetry and ¹³C NMR. This analysis is generalized to other aliphatic layers including *n*-alkanes with $n_{cr} \approx 11$.

This work is seminal to the design of novel aliphatic layers with tailorable properties (e.g., T_m) and has applications in molecular electronics and biophysics.

Summary of Research:

We observed an abrupt bulk-to-discrete transition occurring at a critical chain length of $n_{cr} = 7$ in AgSC_n ($n = 1-16$) layers, with extraordinary changes of chain melting properties, chemical environment, and relaxation time. Calorimetry and solid-state ¹³C NMR are coupled to probe the global and local characteristics of atoms within the discrete regions of aliphatic lamellae. Bulk (long chain) AgSC_n ($n \geq 7$) exhibits fixed NMR chemical shift and T_1 values, and size-dependent melting predictable by the classical GT model. In contrast, discrete (short

chain) AgSC_n ($n = 2-6$) presents a short-chain effect, with completely different values of these parameters for every single change of chain length. None of the carbons share an identical chemical environment. The anomalous melting is well predicted by a new comprehensive GT model with variable ΔG_{excess} . AgSC₁ is an outlier with a different crystal structure. A new 3D spatial model is constructed to divide the alkyl chains of AgSC_n into two discrete (head, tail) and one bulk (midchain) segments. The discrete segments dominate the material at $n < n_{cr}$.

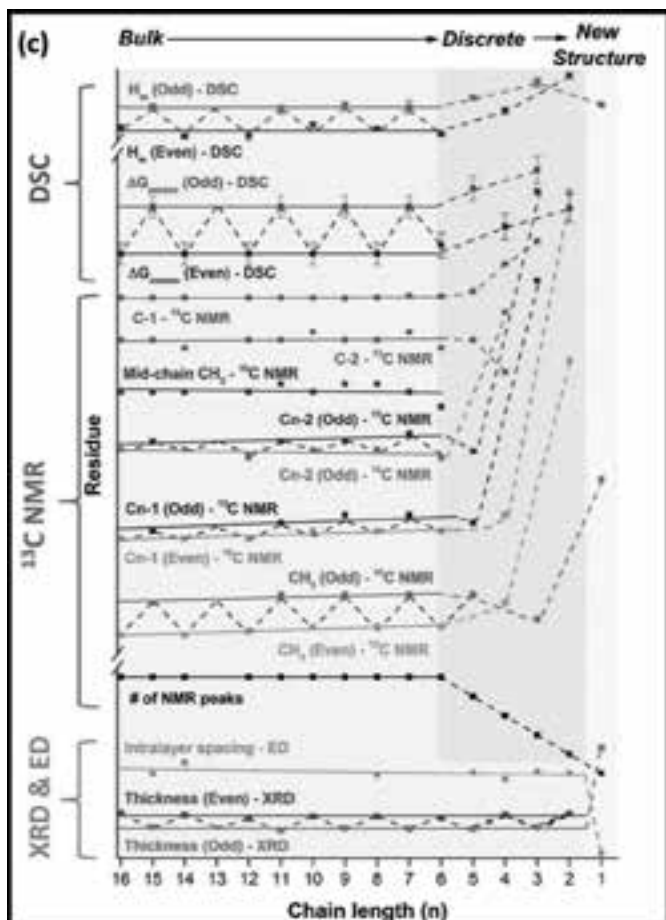


Figure 1: Plot summarizes the structural and property parameters (by DSC, ^{13}C NMR, XRD, and electron diffraction) of AgSCn ($n = 1-16$) as the change of chain length. Each parameter is plotted as residue with regard to its linear fitting of certain bulk AgSCn . The thickness and intralayer spacing data are replotted from our prior paper and are preserved all through $n = 2-16$.

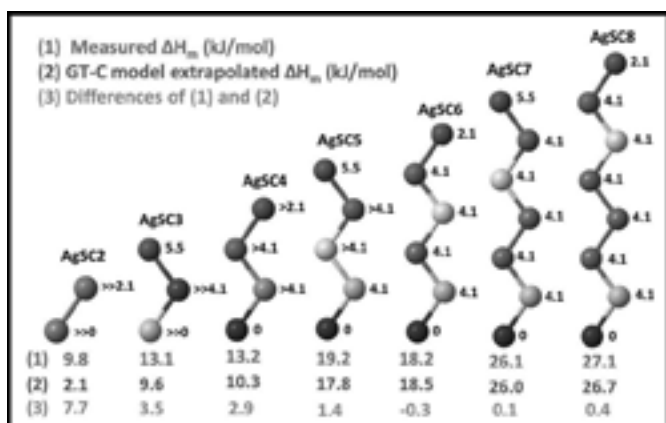


Figure 2: Cartoon shows the deconvolution of ΔH_m of AgSCn ($n = 2-8$) into contributions from each carbon (values beside carbons). The three rows of values represent (1) measured ΔH_m , (2) ΔH_m extrapolated from GT-C linear fitting, and (3) differences of (1) and (2).

An odd/even effect is detected in both the melting and NMR chemical shift of AgSCn and is exclusively attributed to the nature of the tail segment. This analysis is generalized to other extremely small aliphatic layers with discrete regions, including n -alkanes with $n \approx 11$. This finding is instructive to the design of novel alkyl-based layers with controllable properties (e.g., T_m), through the manipulation of molecular segments (e.g., interfacial groups). Potential applications include the optimization of molecular electronics and the study of biological membranes.

References:

- [1] Z. Ye, L. de la Rama, M. Y. Efremov, J.-M. Zuo, L. H. Allen, "Approaching size limit of organometallic layers: synthesis/characterization of ultra-short chain lengths AgSCn ", *Dalton Trans.* 2016, 45, 18954-18966.
- [2] Z. Ye, L. de la Rama, M. Y. Efremov, J.-M. Zuo, A. Sutrisno and L. H. Allen, "Critical Size for Bulk-to-Discrete Transition Aliphatic Layers: Calorimetry Solid-state ^{13}C NMR" *J. Phys. Chem.-C*, 121, 13916 (2017).
- [3] M.Y. Efremov, E. A. Olson, M. Zhang, F. Schiettekatte, Z. Zhang, and L. H. Allen, "Ultrasensitive, fast, thin-film differential scanning calorimeter"; *Review of Scientific Instruments*, 2004. 75(1): p. 179.
- [4] L. Hu, L. de la Rama, M. Y. Efremov, Y. Anahory, F. Schiettekatte, L. H. Allen, "Synthesis and Characterization of Single-Layer AgSCn Lamellar Crystals"; *J. Am. Chem. Soc.*, 133 4367 (2011) <http://pubs.acs.org/doi/abs/10.1021/ja107817x>
- [5] S. L. Lai, J. Y. Guo, V. Petrova, G. Ramanath and L.H. Allen, "Size-dependent melting properties of small Tin particles: Nanocalorimetric measurements"; *Phys. Rev. Lett.* 77, 99 (1996). http://prl.aps.org/abstract/PRL/v77/i1/p99_1.
- [6] de la Rama, L.P., et al., "Size Effect and Odd-Even Alternation in the Melting of Single and Stacked AgSCn Layers: Synthesis and Nanocalorimetry Measurements"; *J. Am. Chem. Soc.*, 135, 14286 (2013). <http://pubs.acs.org/doi/abs/10.1021/ja4059958>.
- [7] Z. Ye, Z. Ma and L. H. Allen, "Chapter 20. Application of *in situ* resistance and Nanocalorimetry measurements for Nanoelectronic thin-film materials, Metrology Diagnostic Techniques Nanoelectronics", ISBN 978-981-4745-08-6, 1013 (2016).

Manipulating and Controlling Graphene Adhesion

CNF Project Number: 900-00

Principal Investigators: William R. Dichtel¹, Paul L. McEuen²

User: Chao Sun¹

Affiliation(s): 1. Department of Chemistry and Chemical Biology, 2. Department of Physics; Cornell University

Primary Source of Research Funding: National Science Foundation grant DMR-1120296

Contact: wdichtel@northwestern.edu, plm23@cornell.edu, cs925@cornell.edu

Primary CNF Tools Used: E-beam evaporator, Oxford atomic layer deposition

Abstract:

We present a technique for patterning, measuring, and tuning surface energies between atomic layered materials and substrates under water. It is simple to implement, provides versatile, high precision measurements, and enables the development and engineering of adhesives at the nano scale. We use this technique to characterize the use of molecular pyrenes bound on glass, and optimize the pyrene density for maximum adhesion. Surface energy control immediately enables a graphene-transfer protocol that is resilient to adhesion failure under sonication. We further study the reproducibility and the hysteresis of adhesion and find a dramatic difference between peeling and re-adhesion that are insensitive to their timescales. More generally, our technique opens the door to a more complete and systematic approach to engineering stimuli-responsive adhesives and mechanical technologies at the nanoscale.

Summary of Research:

Figure 1A illustrates the fabrication sequence that results in lithographically defined patterns of distinct surface energies. Chemical modification using succinimidyl ester-terminated molecules yields release-layer-covered glass coverslips patterned with exposed glass surfaces functionalized by molecular glues (Figure 1B). Figure 1C shows an optical micrograph of five graphene/SU-8 cantilevers of varying widths, imaged in aqueous conditions in reflection mode. The force of adhesion can be directly measured by peeling the cantilever off the surface using a micromanipulator, as illustrated schematically in Figure 2A. We use interferometry to precisely determine the torque applied by the cantilever and the position of the interface between the bound and free regions of graphene.

Using energy conservation, the effective surface energy γ required for peeling can be calculated from the curvature κ in steady state and the Young's modulus E and thickness t of the SU-8 cantilever. For the data in Figure 2, this yields $\gamma_{\text{peel}} = 0.1 \text{ N/m}$. Figure 3 shows measurements of γ_{peel} for a variety of surfaces illustrated schematically in

Figure 3A, ranging from bare glass (very low adhesion) to a mix of pyrene and a diluent (maximal adhesion).

Finally, we explore the reproducibility and hysteresis of the peeling process (Figure 4).

Our technique led to the discovery of a dramatic difference of surface energy between peeling and re-adhesion. We further envision opportunities for switching adhesion properties by engineering adhesive molecules that change in response to optical, chemical, or thermal signals. In each of these cases, our experimental protocol can be readily adopted to provide the necessary information to tune, tailor, and design interfacial adhesives for atomically thin materials.

References:

- [1] Miskin, M. Z.; Sun, C. (co-first authors); Cohen, I.; Dichtel, W. R.; McEuen, P. L. Measuring and Manipulating the Adhesion of Graphene. *Nano Lett.* 2018, 18, 449-454.

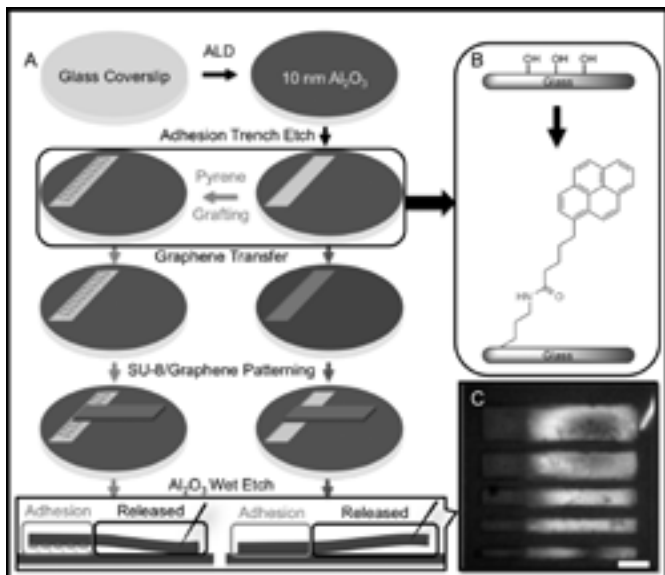


Figure 1: Controlled adhesion using pyrenes. A. Defining distinct patterns of surface energies between graphene and glass using lithography. B. Chemical functionalization on surface with bound, monolayer pyrenes. C. An optical micrograph of five graphene/SU-8 cantilevers bound by the patterned pyrene monolayer (left ends) after the Al_2O_3 release layer was removed.

Scale bar: 50 μm .

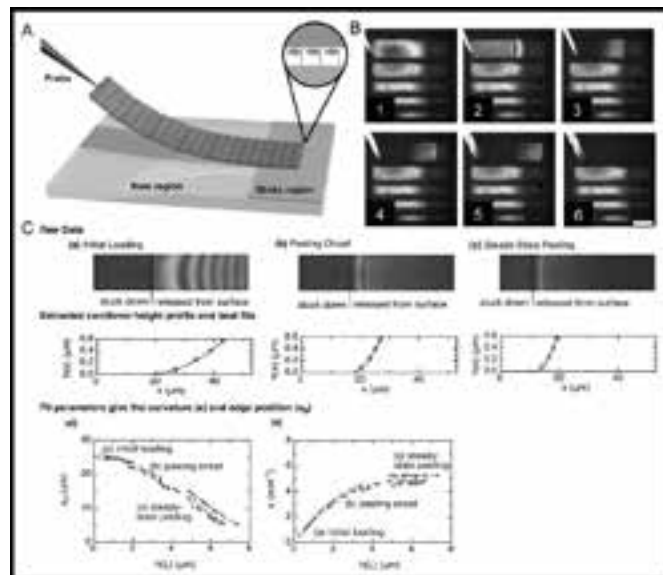


Figure 2: Peeling graphene. A. Loading a cantilever of monolayer graphene stiffened by SU-8 on top with a micromanipulator. The end of the cantilever is anchored on glass made sticky by surface-bound organic monolayers. The rest of the cantilever is released from the unfunctionalized glass surface. B. Reflection white-light micrograph series capturing the delamination of an anchored graphene cantilever. (Scale bar: 50 μm). All images have undergone linear contrast adjustment. C. Data analyses of peeling experiments: (a-c). Reflection white-light micrographs of a graphene/SU-8 cantilever at three stages of peeling: initial loading (a), peeling onset (b), and static-state peeling (c). Below each micrograph is their corresponding extracted cantilever height profiles and best fits. (d). A plot describing the change of lengths of a cantilever's bound portion as peeling progresses. The edge position x_0 is defined as the interface between the bound and the free portions of graphene, with respect to the left end of the cantilever. $h(L)$ describes the elevated height of the manipulator. (e). A plot describing the changes of the cantilever's radius of curvature as peeling progresses.

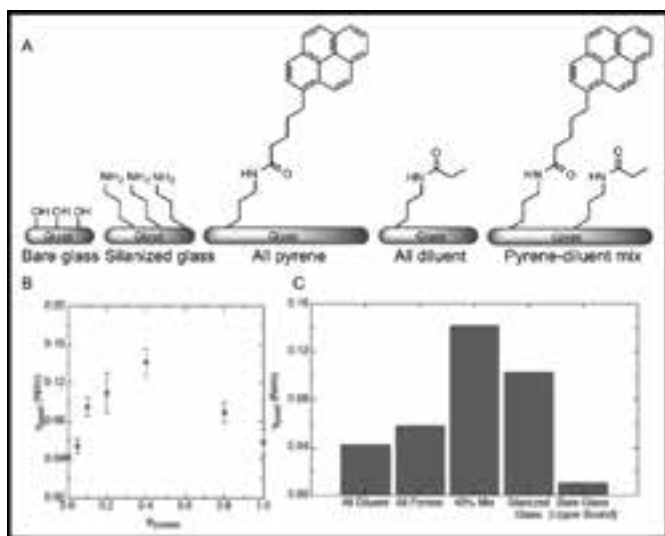


Figure 3: Optimizing adhesion using molecular adhesives. (A) Controlling surface energies using different surface organic monolayers. Surface-bound pyrene moieties serve as a molecular glue to enhance graphene adhesion. An acetyl-terminated moiety is used as a surface diluent to modulate the pyrene density. Amine-terminated moieties from direct glass silanization explore the adhesion enhancement via cation- π interactions. Bare glass is used as control. (B) Plot of graphene peeling measurements on surfaces treated with different pyrene loading% during surface adaptation. (C) Histogram of peeling surface energies on surfaces treated with all diluent loading, all pyrene loading, 40% pyrene loading, amine-terminated silanes, and bare glass.

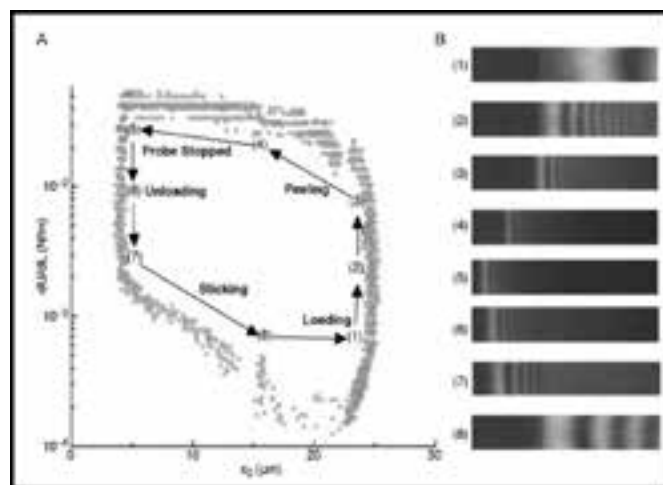


Figure 4: Reversibility and hysteresis of adhesion. A. A peeling-sticking cycle plotted by elastic energy changes per unit area (dU/dL) vs. the position of the peeling front with respect to the bound ends of the cantilever (x_0). B. Reflection white-light micrographs corresponding to different stages of the cycle.

Transient Laser Heating Derived Mesoporous Materials Directed by Gyroidal Templates from Block Copolymer Self-Assembly

CNF Project Number: 1356-05

Principal Investigator: Ulrich Wiesner

Users: Qi Zhang, Fei Yu

Affiliation: Department of Materials Science and Engineering, Cornell University

Primary Source of Research Funding: National Science Foundation (DMR-1719875)

Contact: ubw1@cornell.edu, qz224@cornell.edu, fy84@cornell.edu

Website: <http://wiesner.mse.cornell.edu/>

Primary CNF Tools Used: TFT N+/P+ polysilicon furnace – A4, Oxford 81 etcher

Abstract:

Gyroidal thin films were fabricated from co-assembly of poly(isoprene)-*block*-poly(styrene)-*block*-poly(ethylene oxide) (ISO) and resorcinol formaldehyde resols through solvent vapor annealing. Upon crosslinking the resols and carbonizing the thin films, mesoporous carbon templates were obtained. Low-pressure chemical vapor deposition (LPCVD) was utilized to deposit amorphous silicon into the templates, which melted and crystallized during pulsed excimer laser irradiation to achieve conformal backfilling of the templates. Finally, by removing the carbon template, we successfully prepared 3D continuous crystalline silicon with the inverse gyroidal nanostructure.

Summary of Research:

Templates enable the manufacturing of materials with intricate and complicated structures. Templates at the nanoscale allow for bottom-up fabrication of nanomaterials, which could find applications in catalysis or electronics. Block copolymer self-assembly offers pathways to complex nanostructured templates, which can be combined with laser annealing for pattern transfer to produce porous ordered nanomaterials after template removal.

We first prepared such nanoscale organic templates derived from block copolymer self-assembly. To this end, poly(isoprene)-*block*-poly(styrene)-*block*-poly(ethylene oxide) (PI-*b*-PS-*b*-PEO, or ISO) was synthesized via sequential anionic polymerization as described elsewhere [1]. The resorcinol formaldehyde resols are hydrogen bonded to the PEO block of the amphiphilic ISO terpolymer, which underwent ISO-directed co-assembly in solvent vapor annealing and formed what is known as cubic co-continuous gyroidal structures in the appropriate swelling ratio window [2]. After the resols were crosslinked and carbonized at high temperatures, mesoporous carbon thin-film templates with gyroidal nanostructures were prepared (Figure 1).

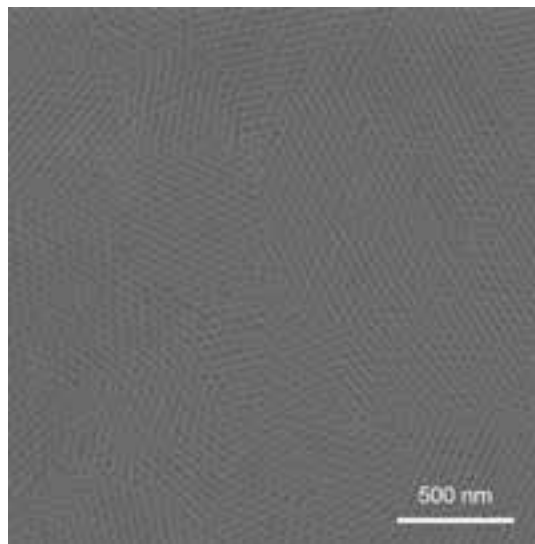


Figure 1: Scanning electron microscopy (SEM) plan view of the mesoporous gyroidal carbon template, derived from ISO-resols hybrid carbonized at 450°C.

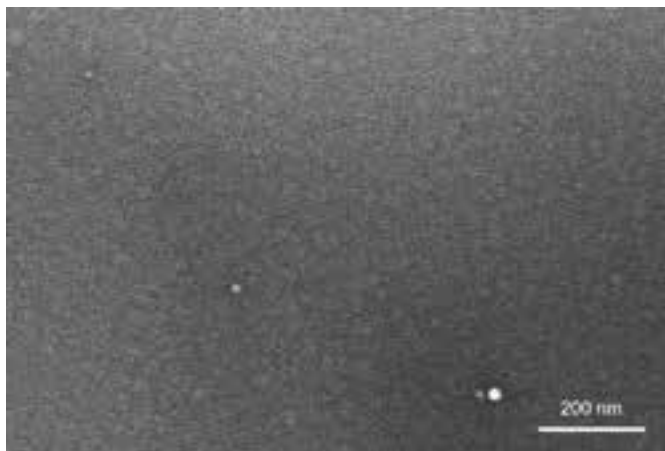


Figure 2: SEM plan view of the carbon template with silicon deposited through LPCVD. There is a silicon overlayer on top of the template, showing grains of silicon.

These thin films derived from organic precursors are stable and amenable to nanomaterials fabrication and processing techniques, a prerequisite for any structure-directing template. We used LPCVD in A4 polysilicon furnace at CNF to backfill the mesopores with undoped silicon (Figure 2). Following TFT MOS cleaning procedures, the native oxide layer between the carbon templates and silicon wafers was removed by dipping them in diluted 20:1 hydrofluoric acid (HF) without compromising the ordered mesostructure of the organic templates. The resulting thin films have small grains of silicon filling the pores with a silicon overlayer on top.

In order to achieve conformal backfilling with crystalline materials, carbon templates with amorphous silicon deposited were subject to pulsed laser annealing at ambient atmosphere. Previous research [3] has demonstrated that shorter heating times promote the thermal stability of organic materials. Transient excimer laser irradiation at nanosecond time scales delivered sufficient energy to melt the silicon (melting temperature around 1250°C). The resulting crystallized silicon displayed polycrystallinity, with the carbon template remaining intact after the heating process.

A combination of dry and wet etching was utilized to remove the carbon template from the carbon/silicon hybrid. Using the Oxford 81 etcher at CNF, reactive ion etching was carried out with CF_4 and oxygen and brief dipping in HF exposed the carbon template to the outside. We subsequently immersed the samples in piranha solution at elevated temperatures to decompose the carbon template. The 3D continuity of gyroids ensures complete removal of the template. Periodically ordered crystalline silicon with the inverse nanostructure of the carbon template was finally obtained via brief dipping in HF to remove silicon oxide (Figure 3).

References:

- [1] Bailey, T. S., et al. A Noncubic Triply Periodic Network Morphology in Poly (Isoprene-*b*-Styrene-*b*-Ethylene Oxide) Triblock Copolymers. *Macromolecules* 35, 7007-7017 (2002).
- [2] Zhang, Q., et al. Pathways to Mesoporous Resin/Carbon Thin Films with Alternating Gyroid Morphology. *ACS Nano* 12, 347-358 (2018).
- [3] Jung, B., et al. Kinetic Rates of Thermal Transformations and Diffusion in Polymer Systems Measured during Sub-millisecond Laser-Induced Heating. *ACS Nano* 6, 5830-5836 (2012).

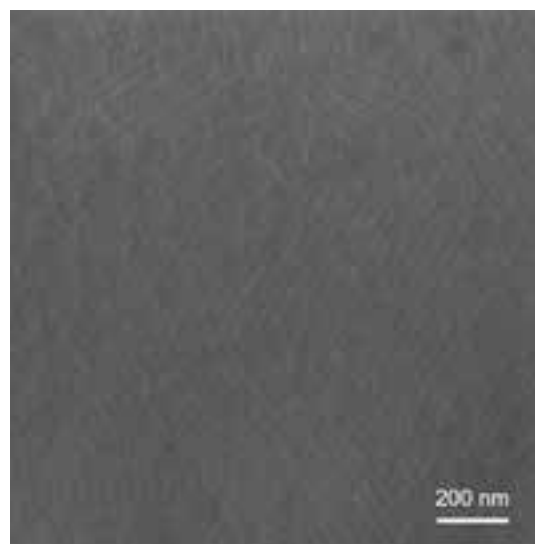


Figure 3: SEM plan view of crystalline silicon gyroid nanostructures after template removal, leaving behind interconnected trenches.

Three-Dimensional Printing of Hierarchical Porous Architectures

CNF Project Number: 1645-08

Principal Investigator: Tobias Hanrath

User: Jen-Yu Huang

Affiliation: Robert F. Smith School of Chemical and Biomolecular Engineering, Cornell University

Primary Source of Research Funding: National Science Foundation

Contact: th358@cornell.edu, jh2486@cornell.edu

Primary CNF Tools Used: Leica supercritical dryer; SEMs, microscopes, ABM aligner, lithography room

Abstract:

Concurrent advances in nanomaterial synthesis and additive 3D manufacturing have created a rich and exciting opportunity space fabricate novel materials and devices. Particularly, integrating high surface area porous materials into structured devices for energy storage, separation system, catalysis and sensing presents interesting scientifically interesting and technologically relevant challenges. Here, we introduce three-dimensional printing of superstructures with multi-level porous networks starting from simple light-controllable building blocks, zirconia core with 12 methacrylic acid ligands. We introduce a new photoresin based on photoresponsive ligand on inorganic core to enable a bottom-up route to program structure, composition and function across seven orders of magnitude in length scale! As a proof of concept, we demonstrate a 3D printed biomimetic artificial leaf with nature-comparable framework and functions such as carbon dioxide capture. This work demarks a significant step forward in creating programmable hierarchical mesoporous structures that approach the complexity common in natural systems.

Summary of Research:

Porous materials are notoriously difficult to process, so synthetic materials are mostly in the form of powder but lacking the mesoscale structure found in natural systems. We introduce photoresponsive ligand on inorganic core (PLIC) design to overcome outstanding challenges related to the processing of porous materials in programmable hierarchical structures. We demonstrate a novel method for generating hierarchical 3D superstructures with nano- to macroscopic controls by three-dimensional (3D) printing of ~ 2 nm metal-containing building units into centimeter-level predesigned complex monoliths.

Figure 1 schematically illustrates how the hierarchical fabrication approach provides a bottom-up route connecting seven orders of magnitude in length scale. Analogous to metal-organic-frameworks (MOFs), the intra-particle and inter-particle pores will form when the PLIC nano-units are connected together. Unlike solvothermal reactions traditionally on MOFs, our fabrication scheme uses light to spatially program where the porous materials are formed. With PLIC as 3D printing inks, we can manipulate predesigned structures in different length scale on a single printing

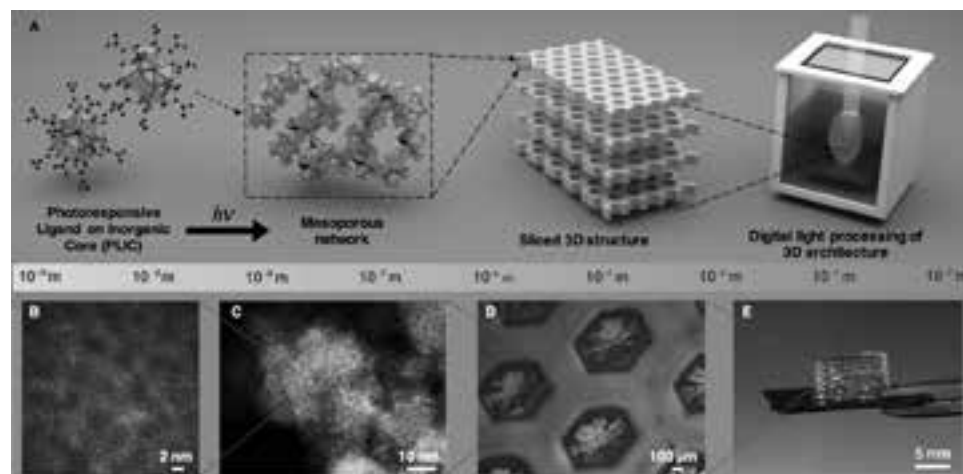


Figure 1: Three-dimensional printing PLIC assembly. (A) Schematic representation of multi-level control in the printing process. PLIC materials are used as the building units and structured by series of 2D UV images in the 3D printer. (B) The unit cell of zirconia inorganic nanocrystal with methacrylic acid surface ligands. (C) Formation of pores via connecting the building units. (D) An example of printed structure showing shape control for each layer. (E) Centimeter scale resulting parts with layer by layer stacking. See full color version on pages xxviii-xxix.

procedure. This process combines the inherent porosity of connecting PLIC units at the nanoscale and the advantage of additive manufacturing at macroscopic scale that enables conventional powder-like porous materials be constructed to intricate designed architectures unattainable with conventional fabrication schemes.

The fundamental building block of the PLIC 3D printing resin is based on $Zr_6O_4(OH)_4$ with 12 methacrylic acid (MAA) ligands (Figure 1A). The structure extends from prominent zirconium-based MOF (UiO-66), possessing attractive thermal and chemical stability with ultrahigh surface area. The methacrylic acid ligands serve two functions: first to provide colloidal stability and second as a molecular connector by photopolymerizing the carbon double bond.

As demonstrated below, we note that additional functionalities can be obtained by exchanging the surface-bound ligands after processing. The inherent compatibility with a broad spectrum of ligand chemistries makes this approach interesting for applications separation applications that rely on programmable interactions between the fluid and the functionalized surface of the particle.

To underscore the practical utility of the mesoporous structures that can be fabricated using the method, we demonstrate the proof-of-concept 3D printing of a highly porous artificial leaf. In nature, the structure of plant leaves has been refined through billion years of evolution to endow all levels of hierarchy from macropores for fluid and nutrient transportation, micropores for gas diffusion and nanopores for gas adsorption to perform complicated and optimal functionalities.

In light of the inherent multi-functionality enabled by the hierarchical porous superstructure of natural leaves, we 3D printed an artificial leaf as shown in Figure 2. We 3D printed the designed leaf with macroscale veins like channels in the middle layer, microscale stomata like pores only on the back surface and nanoscale spongy mesophyll cells like voids. Figure 2 indicates the printed features of both structure and functions in multilevel scale. The channels provide the similar function for mass transportation and the stomata is for gas diffusion. Furthermore, we employed the thio-ene chemistry to post synthesize the residual carbon double bond with

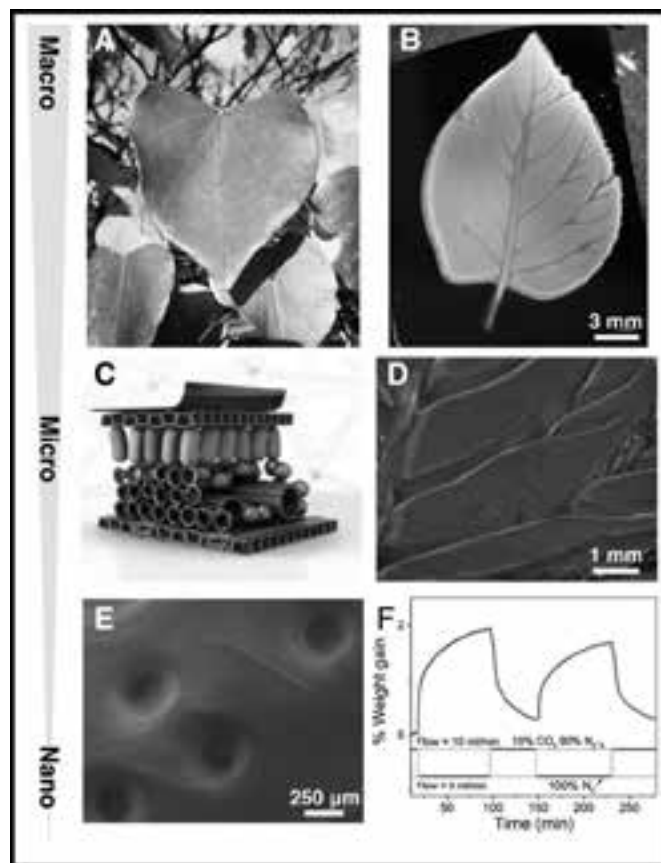


Figure 2: Complex devices like artificial leaf can be fabricated with 3D printing PLIC. (A) Photographic image of leaf. (B) Photographic image of artificial leaf. (C) 3D illustration of leaf structure from cross-sectional view. (D) SEM image of channels mimicking veins. (E) SEM image of small pores like stomata on the back surface (F) CO_2 capturing capacity of 3D printed artificial leaf. See full color version on pages xxviii-xxix.

cysteine ($C_3H_7NO_2S$), anchoring the amine group into the nanoscale pores. To underscore ability of the artificial leaf to capture CO_2 , we exposed the leaf to 10% carbon dioxide 90% nitrogen under 30°C and 1 atmosphere. The nanoscale pores in artificial leaf show the ability to adsorb up to 1.92 weight% carbon dioxide per gram of the leaf.

The artificial leaf not only identifies the benchmark to build complex porous material-based devices but also opens pathways to research the benefits of biomimetic structures.

Three-Dimensional Printing of ZnO Macrostructures with Antibacterial Properties and Low Resistivity

CNF Project Number: 1645-08

Principal Investigators: Christopher Kemper Ober¹, Tobias Hanrath²

User: Dung-Yi Wu¹

Affiliations: 1. Materials Science and Engineering, 2. School of Chemical and Biomolecular Engineering; Cornell University

Primary Source of Research Funding: National Science Foundation

Contact: christopher.ober@cornell.edu, dw567@cornell.edu

Website: <http://cober.mse.cornell.edu/index.html>

Primary CNF Tools Used: Scanning electron microscope (SEM)

Abstract:

We report the first 3D-printable ZnO nanoparticles (NPs) for digital light processing that enable the fabrication of arbitrary and complex 3D metal oxide patterns at room temperature. By modifying photosensitive methacrylic acid on ZnO NPs (ZnO-MAA NPs), we demonstrate the continuous production of programmed 3D structures purely from the nanoscale building blocks. The printed image had good resolution and a height variation of only several nanometers. Printed ZnO-MAA NPs possessed better antibacterial properties than commercial PMMA. Also, calcined ZnO structures demonstrate lower resistivity and rectifying behavior.

Summary of Research:

Additive manufacturing, also known as three-dimensional (3D) fabrication, is a rapidly advancing technique that uses layer-by-layer deposition of materials to construct 3D objects [1]. Compared with traditional manufacturing techniques, 3D printing has significant advantages such as the availability of a wide selection of printing materials, the absence of a need for molds and the ability to create highly complex products [2].

In recent years, digital light processing (DLP) has proven to be one of the most promising 3D printing techniques due to its high resolution, faster printing speed and lower manufacturing cost [3]. DLP is analogous to photolithography as they both create structures using a photosensitive material to crosslink the matrix when exposed to ultraviolet (UV) light [4]. Extensive research has focused on printing polymer-based materials for applications such as micro-fluidic devices, biochips and scaffolds [5]. However, printing materials other than organic polymers, such as metal oxides, is still a challenge for the DLP method. Although some research has been devoted to overcoming this material limitations, the main ingredient in this process remains an organic polymer. Therefore, it is essential to develop a way to process inorganic ingredients to broaden the material choice for 3D printing.

Metal oxides possess many impressive properties, such as optical and environmental resistance. ZnO is one of the most commonly studied metal oxide. It is well-known for its wide and direct band gap, transparency, nontoxicity, good stability, antibacterial properties and biocompatibility [6], which enable applications in semiconducting devices, environmental remediation and as antimicrobial agents. Herein, we propose 3D-printable ZnO building blocks having photoresponsive ligands, specifically methacrylic acid (MAA), on the surface of NPs.

Figure 1 demonstrates a schematic diagram on how 3D structures were precisely constructed from the nano-to macro-scale based on the crosslinking of the building units. MAA ligands play a critical role in increasing colloidal stability, and act as a molecular connector that

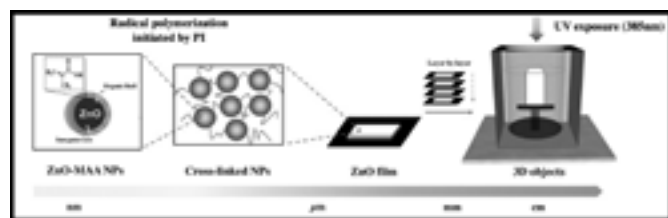


Figure 1: A schematic diagram illustrating the reactions of precursor ZnO-MAA NPs that crosslinked to form a ZnO film. The film was built up layer-by-layer to form three-dimensional (3D) objects.

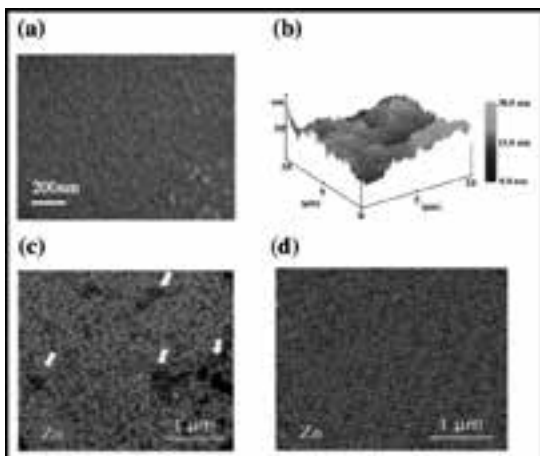


Figure 2: (a) Scanning electron microscopy (SEM) image of a layer of ZnO film. (b) AFM images of ZnO films showing 3D topographies (scale bar: $10 \mu\text{m} \times 10 \mu\text{m} \times 30 \text{nm}$). (c) SEM-EDX spectroscopy analysis of a ZnO-MAA NPs film formed by photopolymerization.

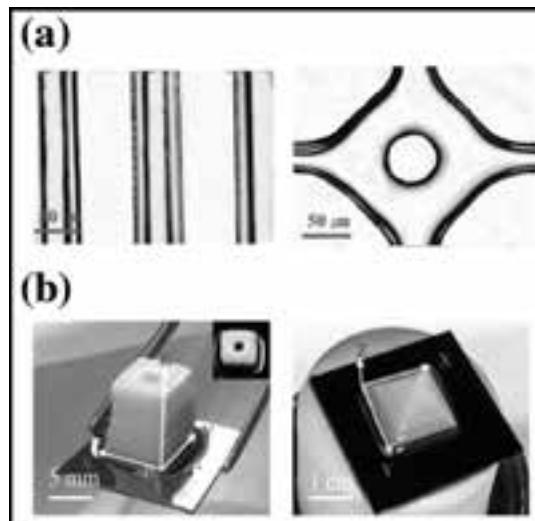


Figure 3: (a) Parallel lines, bent corners and a square array with voids. (b) Honeycomb, butterfly and Cornell logo microstructures printed by the digital light processing technique. (c) Hollow cuboid, pyramidal and townhouse 3D structures manufactured by this technique.

offers interconnection strength for building up the 3D structures. In Figure 2 (a), it is shown that the surface of the film made by ZnO NPs is smooth and uniform. Figure 2(b) shows 3D topographies of an amorphous ZnO film imaged in the tapping mode. The height variation was less than several nanometers. Compared to physical blending, SEM-EDS spectroscopy analysis of ZnO film building from ZnO NPs indicates ZnO particles are distributed more homogeneously in Figure 2(c). The height variation was less than several nanometers.

We used optical microscopy and SEM images to judge the resolution limitation in Figure 3(a). They revealed that the printed sample had good resolution reaching $50 \mu\text{m}$ and Figure 3(b) shows printed ZnO 3D structures. Furthermore, the antibacterial activity was assessed using *E. coli* and *S. aureus* bacteria; a strong inhibition effect was observed with the 3D-printed ZnO sample in Figure 4 (a). After calcination, the resistivity of 3D-printed ZnO dropped to $62 \Omega\cdot\text{m}$ and showed rectifying behavior in Figure 4(b). This study suggests the possibility, but not limited to, of using metal-oxide customized 3D printed structures to make antimicrobial products and semiconducting devices.

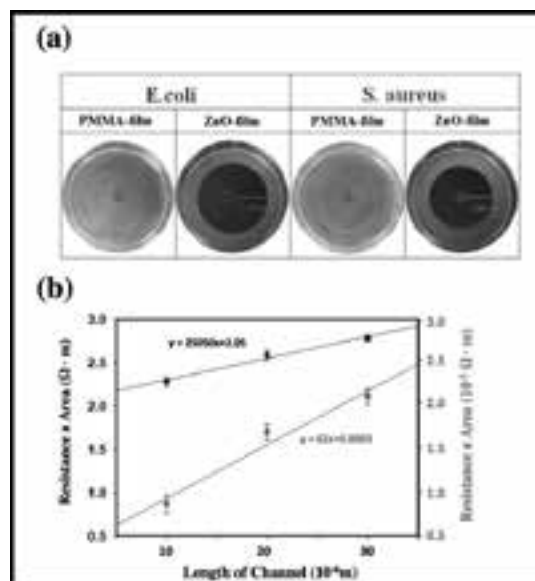


Figure 4: (a) Exposure course of the inhibition zones and (b) Cell counts for the growth of *E. coli* and *S. aureus* cells on PMMA and ZnO films. Resistivity of ZnO film (c) before (black dots) and after calcination (red dots) at 700°C .

References:

- [1] Ligon, S. C., Liska, R., Stampfl, J., Gurr, M., and Mulhaupt, R. Chem. Rev. 117, 10212-10290 (2017).
- [2] Manzano, J. S., Weinstein, Z. B., and Sadow, A. D. ACS Catal. 7, 7567-7577 (2017).
- [3] Tumbleston, J. R., et al. Science, 347, 1349-1352 (2015).
- [4] Kasahara, K., Xu, H., Kosma, V., Odent, J., Giannelis, E. P., and Ober, C. K. J. Photopolym. Sci. Technol. 30, 93-97 (2017).
- [5] Zanchetta, E., et al. Adv. Mater. 28, 370-376 (2016).
- [6] Qi, K., Cheng, B., Yu, J., and Ho, W. J. Alloys Compd. 727, 792-820 (2017).

Novel Platform for Characterization of Nanostructured Polymer Brushes

CNF Project Number: 1757-09

Principal Investigator: Christopher Kemper Ober²

User: Wei-Liang Chen^{1,2}

Affiliations: 1. School of Chemical and Biomolecular Engineering,
2. Department of Materials Science and Engineering; Cornell University

Primary Source of Research Funding: National Science Foundation

Contact: cko3@cornell.edu, slps9061008@gmail.com

Website: <http://cober.mse.cornell.edu/index.html>

Primary CNF Tools Used: ASML 300C DUV stepper, SC4500 evaporator, Oxford PlasmaLab 80+ etch system, ZEISS SEM, Oxford ALD FlexAL, Unaxis 770 deep silicon etcher, Veeco Icon AFM

Abstract:

For further characterization of polymer brushes by neutron and laser scattering, a specific platform was fabricated. The platform allows the anchoring of the polymer brushes on the sidewall of the trenches only, which makes the scattering signals responsive to the change of the polymer brush morphologies. Such methods could increase the sensitivity of the characterization and make probing of more complicated structures possible. Poly(2-(dimethylamino)ethyl methacrylate) brushes were synthesized by atom transfer radical polymerization on the grating. The polymer brushes grown on the sidewall have gradient profiles with a maximum thickness at the bottom of the grating, which is due to the lack of confinement on the top. Such a platform lays down the foundation for the future characterization.

Summary of Research:

Polymer brushes have already demonstrated their application in many fields and their structures have been studied widely in different conditions as described [1]. However, studies focusing on the more complicated structures of polymer brushes, such as molecular brushes, are still in need. It is critical to characterize the polymer brushes in wet state since the tension applied on them is amplified and thus forms more ordered structures. This requirement inspires us to develop a platform, which has polymer brushes anchored on the sidewall of the grating only. When having such platforms in the wet medium, the morphological change of the polymer brushes then controls the opening of the grating which could subsequently be captured by laser and neutron scattering [2]. By using the grating, the response of the polymer brushes would be amplified and allow us to reveal more details in polymer brush structures.

To have a single crystalline silicon (Si)-based grating, a top-down process had to be developed to fabricate the platform. On the other hand, since there is no method to perfectly deposit thin films on top and bottom of the trenches, a sacrificial layer based on silicon dioxide (SiO₂) is needed on the sidewall of the trenches to make sure the sidewalls are free of any residual chromium. The developed process is shown in Figure 1.

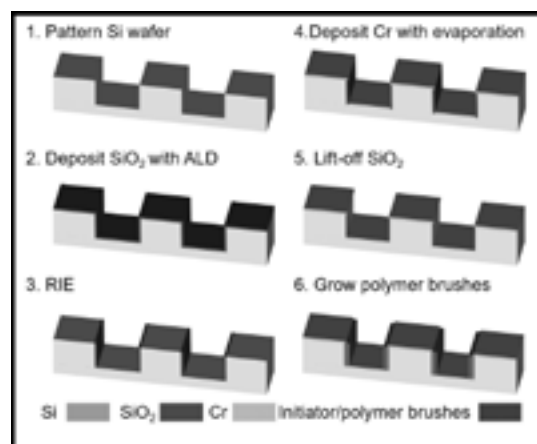


Figure 1: Fabrication process of grafting platform.

Atomic layer deposition (ALD) technique is selected for its layer-by-layer depositing mechanism allowing it to create precise, conformal layer on the grating. After deposition of thin silicon dioxide on the grating, the reactive ion etching process (RIE) is selected to remove only the top and bottom materials to achieve selectivity between sidewall and flat surface on the grating. After depositing thin chromium layers, the lift-off process with

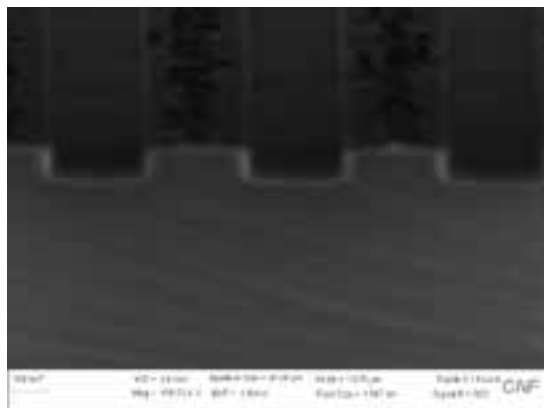


Figure 2: SEM cross-sectional image of grating after ALD SiO₂ deposition.

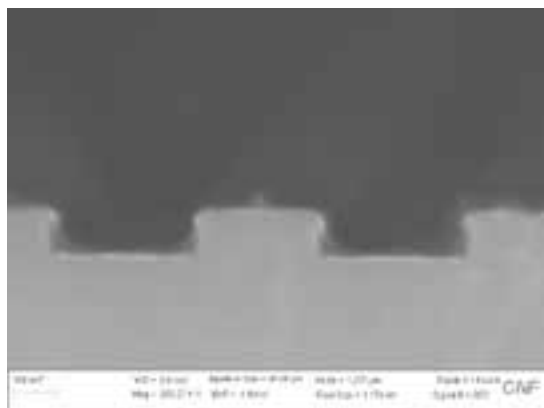


Figure 3: SEM cross-sectional image of grating with PDMAEMA brushes anchoring on sidewall.

hydrofluoric acid could remove undesired chromium on the sidewall and the required grating is obtained for the growth of sidewall-only polymer brushes.

The ALD formed SiO₂ is tuned to have a low density that facilitates the lift-off. The target chromium film thickness is still 5 nm for preservation of the grating original dimension.

Poly(dimethyl aminoethylmethacrylate) (PDMAEMA) brushes were then synthesized on the grating after lift-off BOE immersion. The cross-sectional scanning electron microscope (SEM) images are shown in Figure 2. It is

shown that ALD successfully deposited SiO₂ conformally on the grating and subsequently both the top and bottom SiO₂ layers were removed by anisotropic RIE treatment. It was found out that the few dirt-like materials aggregated to the top of the grating are residues of the lithographic materials. Those residues could be removed with longer RIE treatment. The grating was then used to synthesize PDMAEMA brushes and the result is shown in Figure 3.

It could be observed that the PDMAEMA only anchored on the sidewall of the grating and have the maximum thickness at the bottom of the grating. This is reasonable for the fact that the confinement is no longer existing on the top of the polymer brushes, which makes them like the patterned polymer brushes as studied in the literature [4]. Without the lateral confinement (on the top of the grating in this case) the polymer chains feel no steric repulsion and therefore the stretching level of the polymer chains decreases from the bottom to top of the grating so as the thickness of the polymer brushes.

In conclusion, here we demonstrated the successful fabrication of reflective grating with polymer brushes anchored on the sidewall only. These gratings would make it possible for the neutron/laser scattering characterization responding to the change of the brush in a liquid environment and reveal further details in the structure/dynamic of polymer brushes. It is then expected that not only cationic, but also anionic/zwitterionic polymer brush characterization will soon become available after the preliminary characterization, which is still required to finalize the setup of the experiment instruments.

The synthesis of the polymer brushes with ATRP and characterization of the grafting density has been also explored and this will help fabrication of the well characterized samples. In the future, this will be used to reveal the structure of grafted molecular brushes that have more delicate 3D structures.

References:

- [1] *Macromolecules* 2017, 50 (11), 4089-4113.
- [2] *ACS Appl. Mater. Interfaces* 2015, 7 (22), 11857-11862.
- [3] *IEEE Sens. J.* 2012, 12 (7), 2374-2379.
- [4] *Macromolecules* 2017, 50 (12), 4715-4724.

Materials Characterization Work

CNF Project Number: 2407-15

Principal Investigator: Jefferson W. Tester

Users: Ivan Beentjes, Jay Bender

Affiliation: Chemical Engineering, Cornell University

Primary Source of Research Funding: Departmental

Contact: jwt54@cornell.edu

Primary CNF Tools Used: Scanning electron microscope, laser-scanning confocal microscope

Abstract:

Spallation induced by rapid hydrothermal heating was investigated as a possible method of drilling rock.

Summary of Research:

In this study, an electrically-heated hydrothermal jet was impinged on the surface of cylindrical Barre Granite samples (basement rock) contained in an autoclave reactor to induce localized thermal stress. Comminution of the rock surfaces was achieved at supercritical water conditions, temperatures from 535-580°C and pressures of 22.5-27 MPa. These conditions simulate those encountered in drilling deep, water-filled wells at depths greater than about 2300m. Preferential removal of quartz grains from the rock matrix was observed.

The experimental results of the comminution tests were quantified by examining the sample's top surface prior to the spallation experiments with the scanning electron microscope (SEM), determining the crystal/mineral composition to a resolution of $\sim 10 \mu\text{m}$. After spallation they were examined with a laser-scanning confocal microscope (LSCM), which acted as a profilometer measuring the amount of mineral removed (see Fig. 1).

The comminution tests consistently resulted in heterogeneous removal of surface material. Comparing the diminished areas to the SEM mineral map it was determined that exposing Barre Granite to a supercritical water jet preferentially removes quartz crystals, see Figure 1. Additionally, the boundaries of the subducted quartz grains are very distinct which further strengthens an argument for preferential removal of silica; however, no rock spalls were recovered from these experiments.

These experimental results were published at the 43rd Stanford Geothermal Conference.

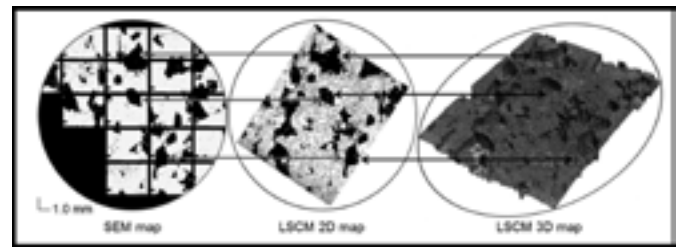


Figure 1: Left to right, the SEM scan of the silicon element (Si) on the unspalled rock sample's top surface identifying the silica rich quartz zones to a resolution of $\sim 10 \mu\text{m}$, compared against the LSCM 2D scan of the same sample's post-comminution test surface. The color-corrected 'black' quartz crystals in the SEM image and the 'black' subducted areas in the 2D LSCM comminuted image correspond to each other and the 3D colored LSCM map. Observation indicates that quartz crystals are preferentially removed.

Growth and Characterization of NbN/III-N Heterostructures by Molecular Beam Epitaxy

CNF Project Number: 2443-16

Principal Investigators: Debdeep Jena, Huili Grace Xing

User: John Wright

Affiliation(s): Materials Science and Engineering, Electrical and Computer Engineering; Cornell University

Primary Sources of Research Funding: ONR grant #N00014-17-1-2414 monitored by Dr. Paul Maki is gratefully acknowledged; CCMR Seed DMR-1120296

Contact: djena@cornell.edu, grace.xing@cornell.edu, jgw92@cornell.edu

Primary CNF Tools Used: Veeco Icon AFM, Zeiss SEM, e-beam evaporators, AJA sputter deposition, Oxford 81 etcher, PT770 etcher, JEOL 9500, ABM contact aligner, Autostep i-line stepper

Abstract:

Films of the metallic superconductor niobium nitride (NbN) have been grown on 6H-SiC substrate and GaN substrate. The surface morphology, grain structure, and electronic transport properties of the films are characterized and used to optimize the growth conditions with the goal of fabricating epitaxial heterostructures incorporating NbN and the III-N family of semiconductors.

Summary of Research:

NbN is a metallic type-II superconductor that can crystallize in both cubic and hexagonal crystal structures [1]. It has been demonstrated [2] that NbN can be grown epitaxially on silicon carbide (SiC) and gallium nitride (GaN) substrates by molecular beam epitaxy (MBE). Multilayer structures incorporating NbN, GaN, and AlN have also been produced and used to demonstrate the possibility of semiconductor devices integrating epitaxial superconducting thin films [3].

In this work we have characterized NbN thin films and NbN/GaN heterostructures grown by MBE using atomic force microscopy (AFM), x-ray diffraction (XRD), electronic transport measurements, and electron backscatter diffraction (EBSD) techniques. We demonstrate that by altering growth conditions such as Nb/N ratio, growth rate, and substrate temperature, the surface morphology, lattice parameters, stoichiometry, and superconducting properties of NbN thin films can be controlled. The goal of this project is to enable the controlled growth of NbN/III-N heterostructures. To enable the growth of III-N semiconductor films with sufficiently low defect density that electronic properties are not significantly degraded the growth of NbN films must be optimized to achieve smooth, continuous, and highly crystalline and epitaxial films.

Our MBE system utilizes an electron beam evaporator to provide Nb flux, while standard effusion cells can be used to provide Ga, Al, In, and various dopant materials. The nitrogen is provided by an RF plasma source.

The CNF Veeco Icon AFM has been used to study the surface morphology. With the goal of producing epitaxial heterojunctions with atomically sharp interfaces the surface morphology of the NbN thin films as measured by AFM is considered an important material parameter to optimize. By controlling deposition temperature, growth rate, and Nb/N ratio we have produced NbN films on 6H-SiC and measured RMS roughness below 0.5 nm by AFM over a scan area of $10\ \mu\text{m} \times 10\ \mu\text{m}$, as shown in Figure 1.

NbN crystallizes in many polymorphs. Asymmetric XRD diffraction analysis indicates that the NbN films primarily possess cubic crystal symmetry oriented with the $\langle 111 \rangle$ crystallographic axis aligned to the growth axis. GaN possesses the wurtzite hexagonal structure, and 6H-SiC possesses a similar hexagonal structure, with the $\langle 0001 \rangle$ crystallographic axis aligned to the growth direction in both cases. This means that for both growth on GaN and 6H-SiC, the NbN films have lower order symmetry about the growth axis than does the substrate. Therefore, two orientations of the NbN crystal differing



Figure 1: $10\ \mu\text{m} \times 10\ \mu\text{m}$ AFM height scan of a 55 nm thick NbN film grown on 6H-SiC. RMS roughness is measured to be 0.32 nm. Barely visible are parallel stripes that are explained by depressions in the films at the site of boundaries between NbN grains whose crystal orientation differ by a 60° rotation about growth axis.

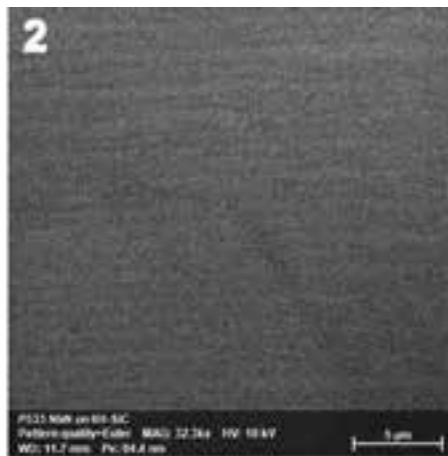


Figure 2: Crystal orientation map of a $25\ \mu\text{m} \times 25\ \mu\text{m}$ area of the surface of an 89 nm NbN film on 6H-SiC produced by EBSD using an SEM with an accelerating voltage of 10kV. The color indicates the relative angle of the crystal structure. The parallel array of grains is found to span the entire $1\ \text{cm} \times 1\ \text{cm}$ sample. This image shows grains that are approximately 750 nm in width. See full color version on pages xxviii-xxix

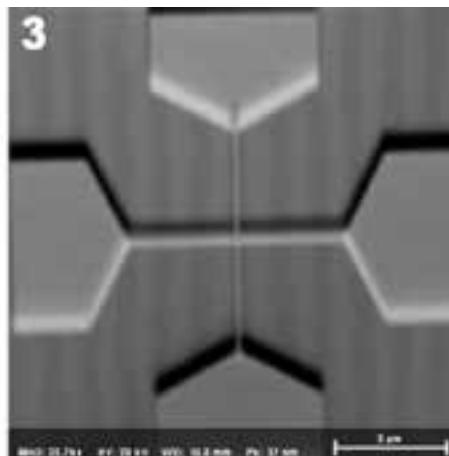


Figure 3: SEM image of a developed resist mask that is used as an etch mask to create structures to test the effect of grain boundaries on the electronic transport properties. The mask, created through EBL, is aligned to the grain structure of the sample. One arm of the cross is parallel to the grains and crosses no grain boundaries; the other arm is perpendicular and crosses several grain boundaries.

by a 60° rotation about the growth axis are equivalent with respect to the substrate crystal structure.

We have found using EBSD techniques to determine the orientation of the NbN crystal about the out of plane direction that the NbN crystallizes with two orientations corresponding to 60° rotation about the out of plane axis. For NbN films on 6H-SiC, we have found that the boundaries between grains of different crystal orientation are parallel and span at least hundreds of microns across the surface of the film, as shown in Figure 2. The width between boundaries has been found to vary, with the largest grains found to be approximately $1\ \mu\text{m}$ wide. No such parallel grain orientations have been observed for NbN films grown on GaN.

In an effort to determine the effect these grain boundaries have on both superconducting and metallic electron transport, a combination of e-beam lithography,

photolithography, and plasma etching were used to etch the NbN film, leaving small crosses of NbN oriented with respect to the grain boundaries, as seen in Figure 3. One arm of the cross lies within a single grain, and the perpendicular arm crosses many grains. Processing and characterization of these structures is ongoing.

References:

- [1] Oya, G., et al., "Transition temperatures and crystal structures of single crystal and polycrystalline NbN films", *Journal of Applied Physics*, 1974 vol: 45 (3) pp: 1389-1397.
- [2] Katzer, D., et al. "Epitaxial metallic β -Nb₃N films grown by MBE on hexagonal SiC substrates", *Applied Physics Express* 8 (2015), no. 8, 085501.
- [3] Yan, R., et al., "GaN/NbN epitaxial semiconductor / superconductor heterostructures", *Nature* 2018 vol: 555 (7695) pp: 183-189.

Nanotube Transistor Arrays on a TEM Substrate

CNF Project Numbers: 2486-16, 900-00

Principal Investigators: Jonathan Alden, Paul L. McEuen

Users: Jonathan S. Alden, Joshua S. Alden, Alejandro J. Cortese

Affiliations: Esper Biosciences, Inc; Department of Physics, Cornell University

Primary Source of Research Funding: National Institutes of Health, National Science Foundation

Contact: jonathan.alden@gmail.com, plm23@cornell.edu, ja698@cornell.edu, ajc383@cornell.edu

Primary CNF Tools Used: Low pressure chemical vapor deposition (LPCVD) furnaces (oxide, nitride), Autostep i-line stepper, ABM contact aligner, SC4500 evaporators, Oxford 80 RIE

Abstract:

We use photolithography to fabricate nanotube transistor devices on substrates with thin nitride windows, which can be imaged using transmission electron microscopy (TEM). Our device architecture permits us to characterize a given nanotube both electrically, and by high-resolution TEM. In low-dimensional systems, such as nanotubes, where nanoscale surface and defect structure can have profound influences on the electrical properties, we expect this combined nanoscale imaging and electrical characterization to yield insights that will inform the design of nanoscale sensors.

Summary of Research:

The study of low-dimensional materials, such as carbon nanotubes, graphene, and molybdenum disulfide, has been an area of growing interest over the past decades, in part due to their promise as molecular sensors. Due to their one-to-few-atom thickness, the properties of such materials often depend sensitively on surface adsorbates, substrate-surface interaction and defect structure. Improving sample cleanliness, for example, enabled the first observations of spin-orbit coupling in carbon nanotubes [1] and, more recently, the fractal quantum Hall effect, known as Hofstadter's butterfly, in graphene [2]. In order to understand these nanoscale structures and subsequently design improved sensors, a device architecture is needed that combines the atomic-level characterization afforded by TEM with the electronics characterization ability enabled by a gated, transistor-like geometry.

We demonstrate that we can produce arrays of gated nanotube sensors devices, with reasonably high yield that can be characterized afterwards by TEM. Our design also keeps parasitic capacitance from our electrodes to the highly resistive silicon substrate low enough to enable electronic measurements of our transistors at MHz bandwidth.

We fabricate nanotube devices on TEM grids using a combination of photolithography and standard nanotube growth and transfer techniques [3]. Figure 1 shows one of such devices, having 26 source-drain electrode pairs and two top gates. Between a few of

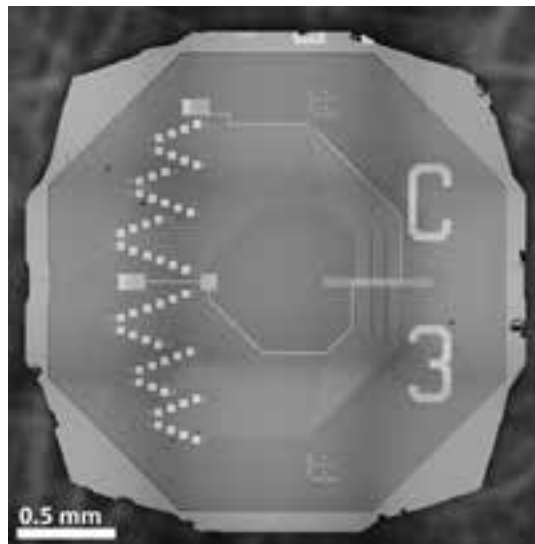


Figure 1: Optical image of microfabricated TEM grid with 26 pairs of source-drain electrodes, a top gate, and a thin nitride window for TEM imaging after top-gate is removed via chemical etching.

the electrode pairs are individual nanotubes, which have been transferred prior to the deposition of a gate dielectric, and top-gate. The device fabrication involves using nine masks to define the various structures, which have been designed to yield nanotube devices with good gating characteristics, as well as low capacitive coupling between nearby electrodes.

The outline of the fabrication procedure is as follows. We begin by using low pressure chemical vapor deposition (LP CVD) to deposit the low-stress nitride on a 300 μm -thick silicon substrate, which will ultimately become our TEM window. We later deposit electrodes, and use backside alignment followed by reactive ion etching (RIE) to expose rectangles on the back of the wafer that will later be used for a potassium hydroxide (KOH) through-etch. Arrays of parallel nanotubes are grown by CVD on a separate quartz substrate, coated with poly(methyl methacrylate) (PMMA), lifted off with KOH, and transferred onto the device substrate [3], where unwanted areas are patterned and etched using RIE. We use atomic layer deposition (ALD) to deposit a gate dielectric, after which we pattern and evaporate a gold top-gate. The surface is then coated with a KOH protection layer, and the devices are placed in hot KOH, which etches the silicon exposed on the back, to both release individual grids and to etch the silicon away from behind the nitride window. Later, the nanotube devices will be imaged through this window using TEM. The protection layer is then removed, and the grids are cleaned with oxygen plasma. Our fabrication process typically yields at least one electrically-connected, gated nanotube on 75% of the TEM grids.

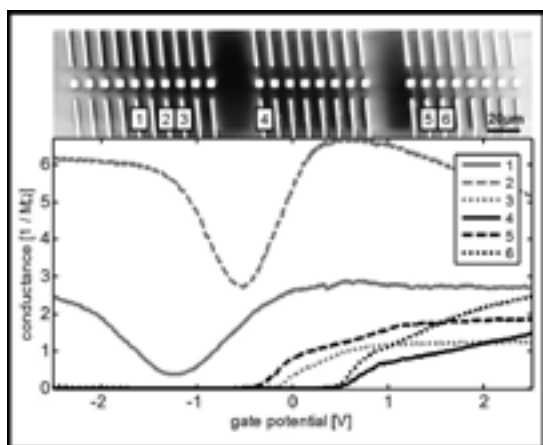


Figure 2: Upper: SEM image of nanotubes between source-drain electrodes, passing over thin nitride windows. Lower: Corresponding conductance measurements as a function of top gate voltage showing six conducting nanotubes with varying characteristics.

Figure 2 shows an SEM image of nanotubes patterned between the source-drain electrode pairs, imaged prior to top-gate deposition. The squares in the center are thin nitride windows for low-background TEM imaging. After completion of the device fabrication, these nanotubes are characterized electrically, shown in the lower portion of Figure 2. All of these nanotubes can be gated to have resistance lower than 1 $\text{M}\Omega$ ($50\text{k}\Omega/\mu\text{m}$) showing that they have a low defect density, and good coupling to the top gate. Nanotubes 1 and 2 can be seen to be metallic, while nanotubes 3-6 are semiconducting.

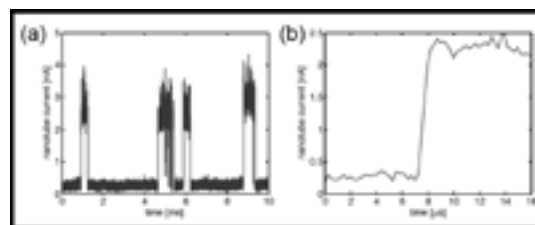


Figure 3: High-speed measurement of nanotube random telegraph signal showing (a) fluctuations in nanotube current and (b) measured rise time of less than 1 μs .

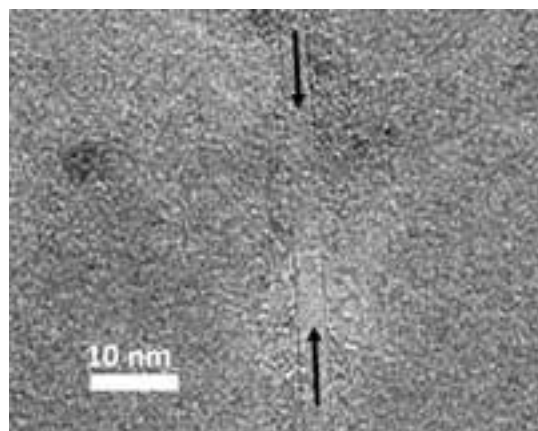


Figure 4: TEM image of a nanotube imaged through a thin nitride window, after top-gate removal.

Furthermore, we can probe the electrical characteristics at high speeds in the MHz range. Previous research has shown that single charge fluctuations in a dielectric can be detected by semiconducting carbon nanotubes as random telegraph signals [4]. As shown in Figure 3, our devices are also capable of measuring such signals, but at higher speeds with rise times less than 1 μs .

After characterizing the nanotubes electronically, we can etch away the gold top-gate, and image them by TEM to determine, for example, the nanotube diameter. Figure 4 shows one such nanotube, which can be seen to be single-walled (single dark lines running parallel to the arrows), and 4 nm in diameter (the width between those lines).

In principle, our fabrication procedure can be applied to many different CVD-grown low-dimensional materials with only minor modifications, and may lead to the development of improved nanoscale sensors capable of high-speed molecular sensing.

References:

- [1] F. Kuemmeth, et al., Nature 452 448-452 (2008).
- [2] C. R. Dean, et al., Nature 497, 598-602 (2013).
- [3] L. Jiao, et al., J. Am. Chem. Soc. 130, 12612-12613 (2008).
- [4] T. Sharf, et al., Nano Lett. 14 (9) 4925-4930 (2014).

Stacking of Van der Waals Hetero-Structures

CNF Project Number: 2528-17

Principal Investigator: Brian Kennedy

Users: Brian Calderon, Brian Kennedy

Affiliation(s): Kennedy Labs, Ontario, Canada

Primary Source of Research Funding: Self-funded

Contact: brian.kennedy@kennedylabs.tech, brc65@cornell.edu

Primary CNF Tools Used: SC4500 even hour evaporator, wire bonder, Oxford 81 etcher

Abstract:

We demonstrate the transfer of Van der Waals (vdW) hetero-structure stacks composed of hexagonal boron nitride (hBN) and graphene (Gr). The stacks were fabricated to study their optical absorption.

Summary of Research:

The ability to layer two dimensional vdW solids has proven to have wide reaching applications due to the ability to tune material properties by intercalating different layers [1]. Recent theoretical results have demonstrated that encapsulating Gr layers in hBN would lead to out of plane interactions that may change the bandgap of Gr [2], lead to ballistic electron transport [3] and have interesting optical properties [4]. For this study we are interested in the optical absorption characteristics of monolayer and bilayer Gr encapsulated between hBN.

The monolayers of Gr and hBN used in this study were CVD grown on Cu foils.

A wet transfer scheme, as shown in Figure 1, was used to transfer the monolayers from the Cu foil onto the target substrate, which in this case was hBN/Cu. The same transfer process was used for both hBN and Gr transfer. A prototypical stack consisted of four hBN layer followed by one or two Gr layers followed by four hBN layers. A gold pad was then evaporated onto the final stack (9-10 layers) using a CVC SC4500 evaporator, this pad was used as a top contact and the bottom contact was the original Cu substrate.

Figure 2a shows a depiction of the final stack.

The constructed vdW stacks are currently under testing in order to determine their optical absorption properties and understand the influence of the layering order on the response.

References:

- [1] W. Aggoune, C. Cocchi, D. Nabok, K. Rezouali, M. A. Belkhir and C. Draxl, "Enhanced light matter interaction in Graphene-hBN van der Waals heterostructures," *The Journal of Physical Chemistry*, vol. 8, pp. 1464-1471, 2017.
- [2] A. K. Geim and I. V. Grigorieva, "Van der Waals heterostructures," *Nature*, vol. 499, pp. 419-425, 2013.
- [3] G. Giovannetti, et al. "Substrate-induced band gap in graphene on hexagonal boron nitride: Ab initio density functional calculations," *Physical Review B*, vol. 76, p. 073103, 2007.
- [4] A. S. Mayorov, R. V. Gorbachev, et al. "Micrometer-scale ballistic transport in encapsulated graphene at room temperature," *Nanoletters*, vol. 11, pp. 2396-2399, 2011.

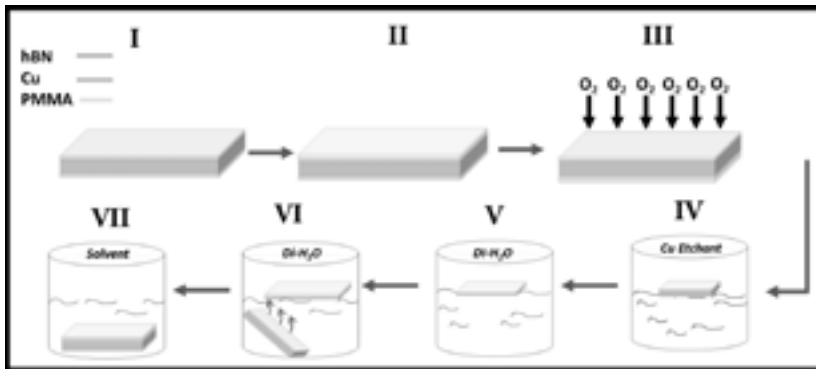


Figure 2: A depiction of the final fabricated vdW stack with a top Au contact and bottom Cu contact.

Figure 1: Depiction of wet transfer process used to fabricate the vdW stacks. (I) Original CVD grown hBN on Cu (II) 5.5% PMMA in anisole was spun onto one side of the monolayer in (I). (III) The back side of the hBN/Cu was etched under an O_2 plasma using the Oxford 81 plasma etcher to remove the hBN on this side. (IV) The PMMA/hBN/Cu stack was floated in Cu etchant CE-100 from Transene Inc. (V) Once the Cu was visibly removed in the prior step the remaining PMMA/hBN stack was then transferred to a DI-water container to remove particulates left over from the Cu etching step. (VI) the floating PMMA/hBN stack was scooped-up onto the target substrate and left to dry. (VII) The scooped-up substrate from step (VI) was left in solvent (1165) over night to remove the remaining PMMA layer.

Characterization of Hexagonal Boron Nitride Thin Films Grown by Molecular Beam Epitaxy

CNF Project Number: 2562-17

Principal Investigator: Dr. Debdeep Jena

User: Ryan Page

*Affiliation(s): Department of Materials Science and Engineering,
School of Electrical and Computer Engineering; Cornell University*

Primary Source of Research Funding: Air Force Office of Scientific Research

Contact: djena@cornell.edu, rlp238@cornell.edu

Primary CNF Tools Used: Veeco Icon AFM, SC4500 odd-hour evaporator

Abstract:

Hexagonal boron nitride (hBN) is a layered material with a wide variety of promising applications, from being used as a substrate and dielectric in Van der Waals heterostructures, to hosting bright, room temperature single photon emitters. Here we report molecular beam epitaxy (MBE) growth and characterization of hBN thin films on sapphire substrates. Films up to 20 nm thick were grown at substrate temperatures up to 1750°C to study the interplay between substrate temperature and source material flux on the morphology and crystallinity of the films. It was observed that films grown at high temperatures (greater than 1650°C) and low boron fluxes (3E-9 torr beam equivalent pressure) resulted in the smoothest and highest quality films. Films were characterized extensively in the Cornell NanoScale Science and Technology Facility using the Veeco Icon atomic force microscope.

Summary of Research:

Hexagonal boron nitride (hBN) is an atomically thin crystalline material, isostructural to graphene, consisting of sheets of boron and nitrogen atoms arranged into a two-dimensional hexagonal net. While the in-plane bonds between each boron and nitrogen atoms in each sheet are very strong, the sheets themselves are bound to one another only by weak Van der Waals forces. Hexagonal boron nitride, along with other so-called two-dimensional materials such as graphene and the family of transition metal dichalcogenides (TMDs) have been the subject of intense research interest in recent years due to the prospect of devices and heterostructures based on stacked monolayers of different 2D materials [1]. The realization of such devices and applications will depend critically on hBN for use as a substrate and dielectric layer. Additionally, hBN has applications in deep ultraviolet photonics and lighting, exhibiting strong emission in the UV-C spectrum [2]. Finally, point defects in hBN layers have recently been discovered as bright, room temperature single photon emitters, opening up this material to applications in quantum cryptography and precision sensing [3].

Despite all of these applications, the synthesis of hBN, particularly epitaxial layers, has proven to be a challenge. In this work, we focus on the growth and characterization of hBN thin films grown by molecular beam epitaxy (MBE) on sapphire substrates. The films are grown at ultra-high substrate temperatures (1600 to 1800°C) in order to overcome kinetic barriers of the crystal growth. The quality and morphology of the films were studied extensively with the Veeco Icon

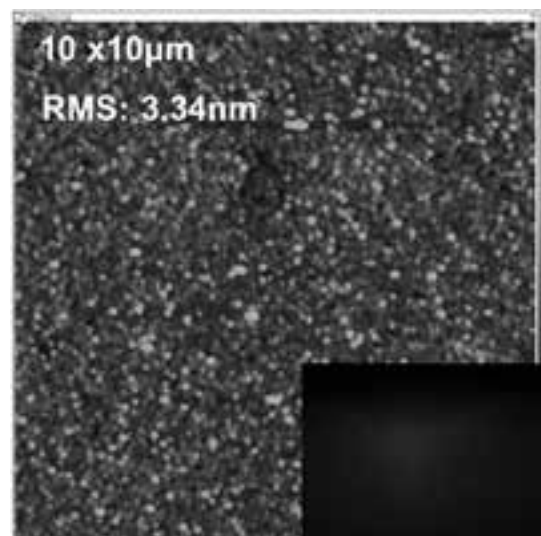


Figure 1: Atomic force microscope image of lower substrate temperature (1600°C) hBN film shows rough, polycrystalline morphology. Inset: diffuse, ringed RHEED pattern.

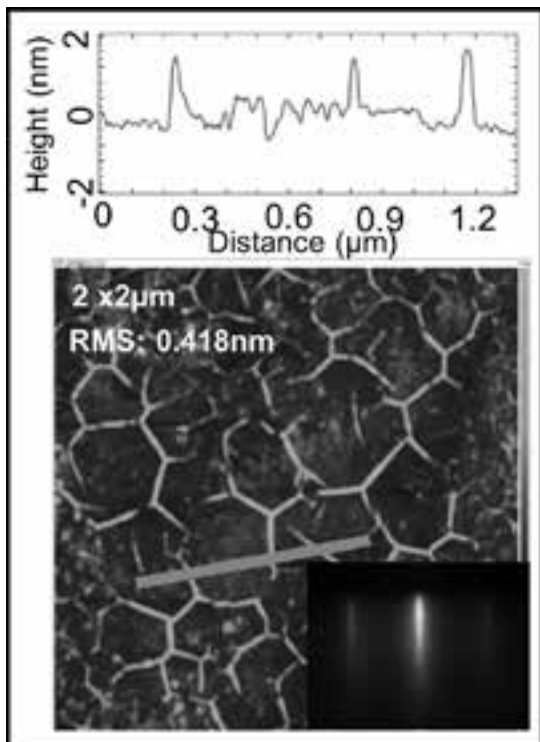


Figure 2: Atomic force microscope image of higher substrate temperature (1650°C) hBN shows smooth surface with network of ripple-like folds, line height profile of inset line shown above. Inset: bright, streaked RHEED pattern.

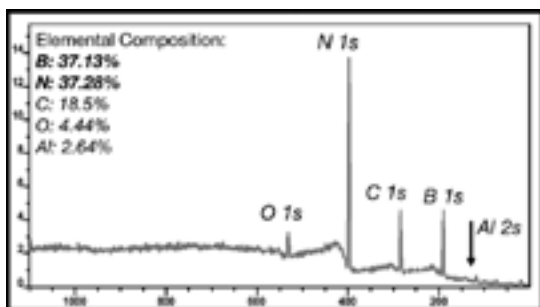


Figure 3: X-ray photoelectron spectroscopy of hexagonal boron nitride grown on sapphire confirms the chemical composition of the film is 1:1 boron to nitrogen.

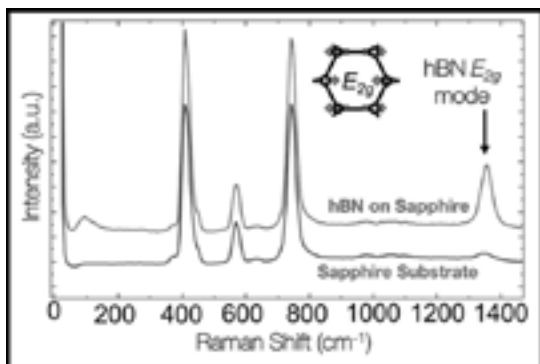


Figure 4: Raman spectrum of hBN film grown on sapphire exhibits clear hBN E_{2g} peak near 1365 $1/cm$. Spectrum of sapphire substrate shown for comparison.

atomic force microscope (AFM). The films were also characterized by Raman spectroscopy, ultraviolet absorption spectroscopy, spectroscopic ellipsometry, and x-ray photoelectron spectroscopy to elucidate their structural, optical, and chemical properties. To study the effect of MBE growth conditions (e.g. boron and nitrogen fluxes and substrate temperature) on the morphology and quality of the films, films throughout the growth parameter space were grown. We observed a variety of different surface morphologies, wherein several trends are noted: at lower temperatures (less than 1600°C) the hBN films consistently exhibited visible rings in the *in situ* reflection high energy electron diffraction (RHEED) patterns, indicating a polycrystalline growth mode. Subsequently, these films had very rough surface morphologies as seen in the AFM. At higher temperatures (1600 to 1750°C), clear streaks were seen in the RHEED pattern, suggesting a higher quality film growth, while we observed in the AFM images smooth films with a dense network of ripple-like features. These ripples have been reported in hBN flakes grown by chemical vapor deposition, where they are attributed to the thermal expansion mismatch between the hBN and the substrate causing the hBN to wrinkle and fold up on itself [4]. At each temperature range, there was an incident boron flux, provided by a high temperature boron effusion cell, past which the films would also become rough and polycrystalline. At all temperatures, this threshold flux was very low (approx. $3E^{-9}$ torr beam equivalent pressure), but it increased with temperature. All growths are done in excess nitrogen conditions using a radio frequency plasma nitrogen source.

X-ray photoelectron spectroscopy of these films confirmed a 1:1 boron to nitrogen ratio with no evidence of carbon contamination. The films also exhibit a sharp absorption peak centered near 6 eV, the band gap of hBN. In the Raman spectra, the hBN E_{2g} peak is observed near 1365 $1/cm$, confirming the phase of the grown films. Notably, hBN was also grown with isotopically purified nitrogen-15; the E_{2g} peak exhibited an approximately 15 $1/cm$ redshift corresponding to the heavier atoms. The demonstrated isotopic control in the films allows for future studies into the electron-phonon interactions of hBN.

In conclusion, hexagonal boron nitride thin films were grown by molecular beam epitaxy and characterized by a variety of techniques to probe the structural, chemical, and optical properties of the layers. It was found that ultra-high growth temperatures and low boron fluxes produce the highest quality films. This work represents a step toward the integration of high quality hBN into a wide range of devices and applications.

References:

- [1] Geim, A., and Grigorieva, I. Nature 499, 419-425 (2013).
- [2] Watanabe, K., Taniguchi, T., and Kanda, H. Nature Materials 3, 404-409 (2004).
- [3] Jungwirth, N., Calderon, B., Ji, Y., et al. Nano Lett. 16, 6052-6057 (2016).
- [4] Kim, K., Hsu, A. Jia, X., et al. Nano Lett. 12, 161.166 (2012).

Utilizing Polymer Nanofibers in Microfluidic Devices for Liquid Separation Applications

CNF Project Number: 2603-17

Principal Investigator: Professor Margaret Frey

User: Mesbah Najafi

Affiliation: Department of Fiber Science and Apparel Design, Cornell University

Primary Source of Research Funding: USDA National Institute of Food and Agriculture

Contact: mfw24@cornell.edu, mn574@cornell.edu

Primary CNF Tools Used: Hot press, UV-Ozone, Microdrill

Abstract:

The purpose of this project is to examine the efficacy of polymer nanofibers inside microfluidic analytical devices for liquid purification applications. To achieve that, the microfluidics device was made from poly(methyl methacrylate) (PMMA) plates and nanofiber fabrics using hot press and UV-Ozone equipment. Methylene blue dye solution was used for the adsorption experiment. The results showed that the nanofibers inside the device channels can effectively capture the dye from the solution.

Summary of Research:

In this study, composite electrospun nanofibers were first developed for dye adsorption application. This was achieved by adding a percentage of poly methyl vinyl ether-alt-maleic anhydride (PMA) to polyvinyl alcohol (PVA), which resulted in composite nanofibers with combined properties of appropriate adsorbent properties (from PMA) and high mechanical properties (from PVA) [1,3]. The obtained nanofibers were then used in a microfluidic analytical device. To achieve that, the nanofibers fabric was collected for 15 min by electrospinning method. The brass template with raised channels (30 mm × 1 mm × 50 μm) was used for embossing the PMMA sheets.

The hot press was heated up to 110°C. A 5 cm × 5 cm PMMA square was placed between the channel template and a blank piece of metal. Then, the upper hot plate was moved to touch the sandwiched PMMA for about 5 mins. Next a pressure of about 1000 lbs was applied for 5 min. Inlet and outlets holes were drilled into the PMMA using a 1.2 mm drill bit. PMMA sheets were activated in an ozone generator (oxygen flow rate 0.5 L/min) and with UV-light for 10 min. Then, the nanofiber fabric was placed between the PMMA pieces and the assembly was placed inside the hot press with the temperature

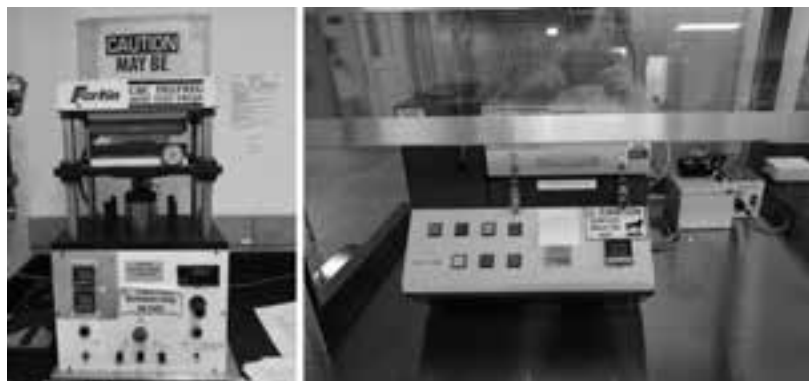


Figure 1: Hot press and UV-Ozone equipment used for making microfluidic device.

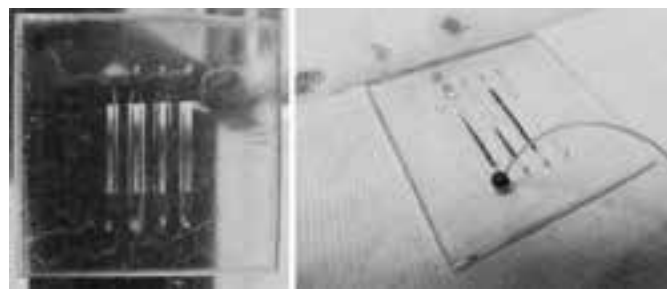


Figure 2: Nanofibers fabrics inside microfluidic channels before (left) and after (right) methylene blue adsorption.

of 80°C. A cover plate was added and both plates were thermostatically controlled for 5 min.

A pressure of 1100 lbs was used for 5 min and then the plates were allowed to cool to room temperature [3,4].

Figure 2 shows the nanofiber fabric inside the microfluidic device before and after dye adsorption experiment. The capture of the dye by the nanofibers can be clearly seen. The adsorption mechanism is based on the electrostatic attraction between the negatively charged nanofibers and the positively charged dyes. PMA has functional groups maleic anhydride, which is hydrolyzed/ionized into carboxyl groups. Once in contact with water, these carboxyl groups ionized into COO⁻ — which results in negative surface charges on the nanofibers [5].

Future step would be utilizing these nanofibers for separation of proteins from a mixture.

References:

- [1] D. Cho, S. Lee, and M. W. Frey, "Characterizing zeta potential of functional nanofibers in a microfluidic device," *J. Colloid Interface Sci.*, vol. 372, no. 1, pp. 252-260, 2012.
- [2] L. Matlock-Colangelo, B. Coon, C. L. Pitner, M. W. Frey, and A. J. Baeumner, "Functionalized electrospun poly(vinyl alcohol) nanofibers for on-chip concentration of *E. coli* cells," *Anal. Bioanal. Chem.*, vol. 408, no. 5, pp. 1327-1334, 2016.
- [3] L. Matlock-Colangelo, D. Cho, C. L. Pitner, M. W. Frey, and A. J. Baeumner, "Functionalized electrospun nanofibers as bioseparators in microfluidic systems," *Lab Chip*, vol. 12, no. 9, p. 1696, 2012.
- [4] D. Cho, L. Matlock-Colangelo, C. Xiang, P. J. Asciello, A. J. Baeumner, and M. W. Frey, "Electrospun nanofibers for microfluidic analytical systems," *Polymer (Guildf.)*, vol. 52, no. 15, pp. 3413-3421, 2011.
- [5] M. Xiao, J. Chery, and M. W. Frey, "Functionalization of Electrospun Poly(vinyl alcohol) (PVA) Nanofiber Membranes for Selective Chemical Capture," *ACS Appl. Nano Mater.*, p. acsanm.7b00180, 2018.

Silica Glass Micropillar Fabrication

CNF Project Number: 2632-18

Principal Investigator: Dr. Shefford Baker

User: Zachary Rouse

Affiliation: Materials Science and Engineering Department, Cornell University

Primary Source of Research Funding: Corning Inc.

Contact: spb14@cornell.edu, zwr6@cornell.edu

Primary CNF Tools Used: AJA sputter deposition, Autostep i-line stepper, PT770 etcher, Oxford 100 etcher, Oxford 81 etcher

Abstract:

A method for the fabrication of a large number of silica glass micropillars has been developed. This method writes a pattern onto photoresist, which is used as a mask to etch a sputtered chromium film. The residual chromium is then used as a mask for a deep silica glass etch, resulting in the formation of pillars of various heights (5 to 12 μm). An initial proof-of-concept fabrication led to pillars that had unsatisfactory surface roughness, but nonetheless led to very interesting compression results viewed with *in situ* SEM. Improvements to the fabrication method are underway and will lead to smoother sidewalls and taller pillars.

Summary of Research:

Although silicate glasses are brittle materials, in small volumes they can undergo extensive plastic deformation. The character of this deformation controls the induced stress and strain state of the contact, and ultimately dictates the fracture initiation and propagation of the bulk material. By far the most common experimental technique for the study of plasticity in ceramics is indentation, however interpretation of plasticity from indentation tests is obscured by the complex, mechanism dependent stress and strain state underneath the indentation. Micropillar compression tests are much less commonplace, but have the tremendous advantage of a well-defined stress and strain state [1], as well as the ability to observe and quantify the plastic deformation *in situ* through SEM.

The most common technique for micropillar fabrication is annular milling using a focused ion beam. While this technique is wide spread, it is extremely low-throughput, is technically challenging in electrically insulating materials, and has been shown to induce structural damage in the pillars, potentially skewing any obtained mechanical data. In this project, a methodology for the simultaneous etching-based fabrication of a large number of silica glass micropillars (> 1 million) for compression testing is developed.

This method starts by using the AJA sputter deposition tool to apply a thick chromium film onto a standard 100 mm silica glass wafer. This process required significant optimization as significant stresses can develop within chromium depending on sputtering conditions and care has to be taken to avoid delamination of the film.

Once the chromium has been sputtered, anti-reflective coating and thick ($\sim 3 \mu\text{m}$) i-line photoresist is spun on top of the chromium. The photoresist is then exposed on the AS200 stepper tool in order to pattern arrays of circles of unexposed photoresist with various diameter. The exposed photoresist is then developed, leaving unexposed cylinders of photoresist behind on the chromium film.

After etching away the anti-reflective coating of the Oxford 81 etcher, the photoresist pattern is used as a mask for a chromium etch on the PT770 etcher. The damaged photoresist is stripped in the Oxford 81 etcher, leaving patterned cylinders of chromium on the silica glass wafer. The wafer is then loaded into the Oxford 100 etcher where it undergoes a long fluorine based etch using the remaining chromium as a mask. After the etch is sufficiently deep, the remaining chromium is etched away in the PT770, leaving arrays of silica glass micropillars.

An initial fabrication yielded pillars of satisfactory height, but lacked smooth sidewalls which makes the determination of the stress state during compression more difficult. As shown in Figure 1, significant plastic deformation can be achieved in these *in situ* SEM micropillar compressions. Optimization of the process hopes to address the smoothness of the pillar sidewalls by ensuring more vertical sidewalls of the chromium mask.

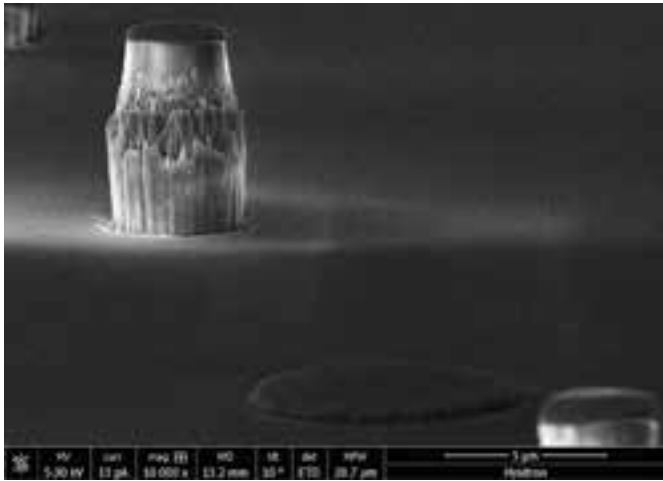


Figure 1: (Background) An uncompressed silica glass micropillar from initial fabrication showing high sidewall roughness. (Foreground) A highly compressed silica glass micropillar with little to no fracture present. This level of ductility can be achieved by exposing the pillars to high electron beam fluxes during compression.

References:

- [1] Fei, H., et al. (2012). "Evaluation of Micro-Pillar Compression Tests for Accurate Determination of Elastic-Plastic Constitutive Relations." *Journal of Applied Mechanics* 79(6): 061011-061011.

Thin Films from Atomic Layer Deposition for Membranes, Metamaterials, and Micromachines

CNF Project Number: 900-00

Principal Investigators: Paul McEuen¹, Itai Cohen¹

Users: Kyle Dorsey², Tanner Pearson², Edward Esposito¹, Baris Bircan², Helen Xu³

Affiliations: 1. Laboratory of Atomic and Solid State Physics, 2. School of Applied and Engineering Physics, 3. Sibley School of Mechanical and Aerospace Engineering; Cornell University, Ithaca, NY

Primary Source of Research Funding: AFOSR MURI Grant FA2386-13-1-4118, NSF Grant DMR-1435829, (NSF) Major Research Instrumentation Award DMR-1429155 Kavli Institute at Cornell for Nanoscale Science CCMR Shared Facilities through the NSF MRSEC program (DMR-1719875)

Contact: plm23@cornell.edu, itai.cohen@cornell.edu, kjd96@cornell.edu, tgp34@cornell.edu, epe3@cornell.edu, bb625@cornell.edu, yx85@cornell.edu

Primary CNF Tools Used: Oxford FlexAL ALD, Arradance ALD, Autostep AS200 i-line stepper, CVC e-beam evaporators, Oxford 81/82 etchers, PT770 and PT740 etchers, Anatech Asher, Zeiss SEMs, Veeco atomic force microscope, Tencor P7 profilometer, Filmetrics UV, Woollam ellipsometer, DISCO dicing saw, Heidelberg DWL2000

Abstract:

Ultra-thin films of inorganic materials are well-suited for fabrication of micron-scale actuators because they can sustain small radii of curvature, have large force outputs, are compatible with semiconductor processing, and are chemically robust. We leverage atomic layer deposition (ALD) on sacrificial substrates to produce micron-scale free-standing mechanical devices with sub-5 nm film thicknesses. We fabricate cantilever springs from ALD films and characterize the material's bending stiffness and elastic properties. We find values for the bending stiffness that are consistent with expectations from elasticity theory. The mechanical properties of ALD are further modified by lithographic patterning of the ALD. Lattices imposed into the film decrease its effective Young's modulus. We integrate these results and device concepts to produce magnetically actuated three-dimensional devices with applications in micromachinery. Our results establish thin ALD films as a scalable basis for micron-scale actuators and robotics.

Summary of Research:

Self-folding is a strategy for producing both static and dynamic three-dimensional devices from two-dimensional sheets at all size scales [1,2]. This conceptual framework is particularly well suited to the fabrication of micron-scale machinery because the dominant mode of manufacturing microscopic features is two-dimensional lithography. Folding therefore enables production of three dimensional parts by lithography. Furthermore, process integration with electronics fabrication is retained in this approach.

The relevant energy scale for design of micro-actuators is the actuator's bending stiffness. Micro-actuators that produce large deflections for small energy inputs must be made out of a material with low bending stiffness. Our approach is to scale hard materials to atomic-scale thicknesses [3-5]. In this work, we demonstrate that sub-10 nm thin films produced by atomic layer deposition (ALD) can serve as the backbone of small machinery.

We fabricate mechanical devices using ALD on films of aluminum, as is described in Figure 1. The aluminum

serves as a sacrificial layer that can be undercut during wet-etching in dilute developer solution to release completed devices from the fabrication substrate. We manipulate devices in aqueous environments with surfactants to avoid stiction between the films and the substrate.

We use optical forces supplied by an infrared laser to actuate cantilever beams fabricated from 5 nm thick films of SiO₂ (Figure 2a). Although these forces are very weak, they can produce large deflections in the beam because of the low spring constants achievable. A force-distance curve from a representative device (Figure 2b) shows reversible elastic behavior with a spring constant on the order of 10⁻⁸ N/m, over nine orders of magnitude lower than typical AFM cantilevers.

The tailorable elastic response of springs fabricated from thin ALD films inspires design of stretchable metamaterials composed of panels and hinges. Figure 3a shows a sheet with a triangular lattice patterned with metallic panels. The cut pattern is shown in the inset.

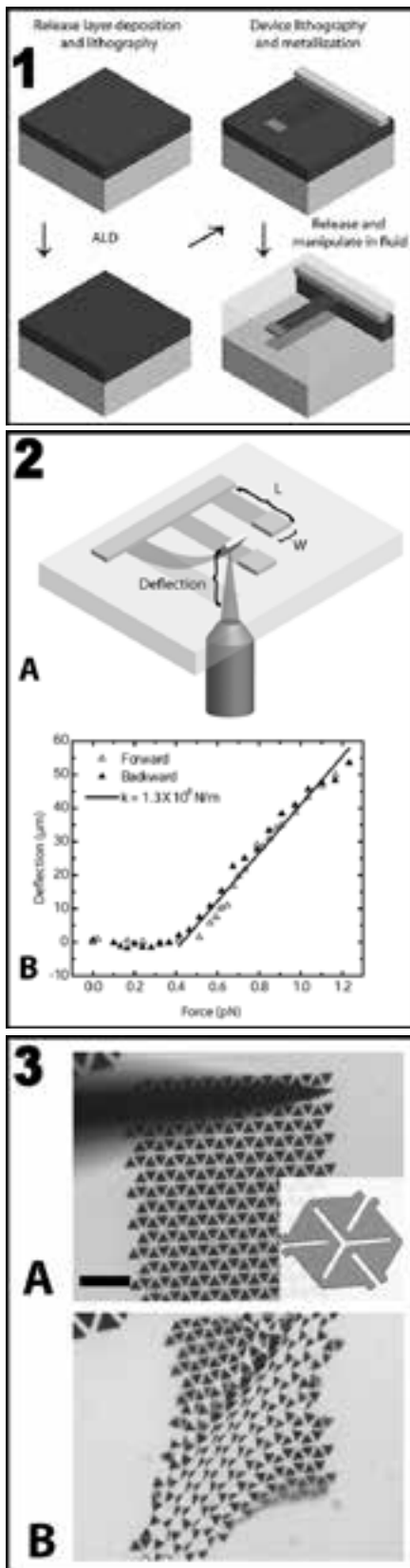


Figure 1, top: Fabrication of free-standing films from atomic layer deposition. **Figure 2, middle:** Mechanical characterization of 5 nm thick films of SiO₂. **Figure 3, bottom:** Stretchable meta-materials fabricated from SiO₂ hinges (scale bar 30 µm).

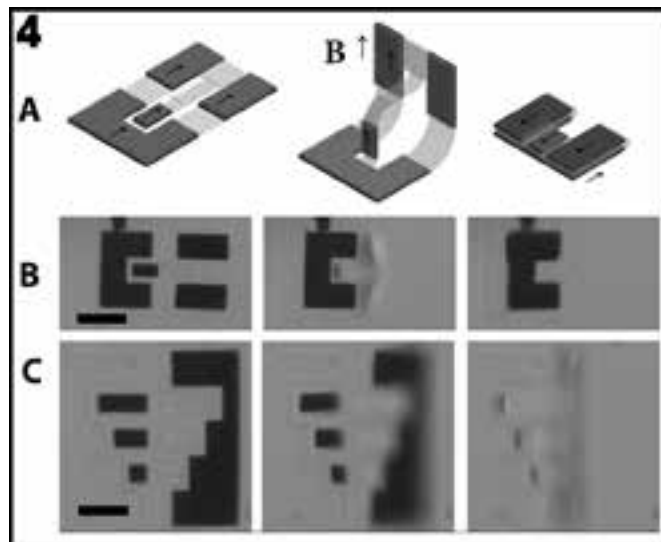


Figure 4: 3D magnetically actuated pop-up structures (scale 10µm).

Upon application of strain with a micromanipulator, the sheet can be stretched in both directions to ~ 100% beyond its original length without failure (Figure 3b).

We further manipulate these devices by patterning thin cobalt films to act as magnetic handles. A device concept is illustrated in Figure 4a. Application of external fields allow rotation of free hinges as shown in Figure 4a. Further rotation of the external field can close a latch structure formed with a second magnet. This concept is realized in Figure 4b, which shows a three-dimensional “pop-up” structure being rotated from the fabrication substrate into its 3D target geometry. It is then closed and remains shut. This simple design paradigm can be extended to more complicated 3D structures such as the micron-scale staircase shown in Figure 4c. We envision the materials and design concepts described herein to be used as the building blocks of more sophisticated 3D machinery at the micron scale.

References:

- [1] Leong, Timothy G., Aasiyeh M. Zarafshar, and David H. Gracias. “Three-Dimensional Fabrication at Small Size Scales.” *Small* 6, no. 7 (April 9, 2010): 792-806.
- [2] Miskin, Marc Z., Kyle J. Dorsey, Baris Bircan, Yimo Han, David A. Muller, Paul L. McEuen, and Itai Cohen. “Graphene-Based Bimorphs for Micron-Sized, Autonomous Origami Machines.” *Proceedings of the National Academy of Sciences*, January 1, 2018, 201712889.
- [3] Davami, Keivan, Lin Zhao, Eric Lu, John Cortes, Chen Lin, Drew E. Lilley, Prashant K. Purohit, and Igor Bargatin. “Ultralight Shape-Recovering Plate Mechanical Metamaterials.” *Nature Communications* 6 (December 3, 2015): 10019.
- [4] Eigenfeld, Nathan T., Jason M. Gray, Joseph J. Brown, George D. Skidmore, Steven M. George, and Victor M. Bright. “Ultra-Thin 3D Nano-Devices from Atomic Layer Deposition on Polyimide.” *Advanced Materials* 26, no. 23 (June 1, 2014): 3962-67.
- [5] Wang, Luda, Jonathan J. Travis, Andrew S. Cavanagh, Xinghui Liu, Steven P. Koenig, Pinshane Y. Huang, Steven M. George, and J. Scott Bunch. “Ultrathin Oxide Films by Atomic Layer Deposition on Graphene.” *Nano Letters* 12, no. 7 (July 11, 2012): 3706-10.

Graphene-Based Bimorphs for Micron-Sized Autonomous Machines

CNF Project Number: 900-00

Principal Investigators: Paul McEuen^(a,b), Itai Cohen^(a,b)

**Users: Marc Miskin^(a,b), Baris Bircan^(c), Kyle Dorsey^(c),
Edward Esposito^(a), Alejandro Cortese^(c), Michael Reynolds^(c)**

*Affiliations: a) Laboratory of Atomic and Solid State Physics, Cornell University, b) Kavli Institute at Cornell,
c) Department of Applied and Engineering Physics, Department of Physics, Cornell University*

Primary Sources of Research Funding: This work was supported by Cornell Center for Materials Research Grant DMR-1719875, National Science Foundation (NSF) Major Research Instrumentation Award DMR-1429155, NSF Grant DMR.1435829, Air Force Office of Scientific Research (AFSOR) multidisciplinary research program of the university research initiative Grant FA2386-13-1-4118, and the Kavli Institute at Cornell for Nanoscale Science

Contact: plm23@cornell.edu, ic64@cornell.edu, mm2325@cornell.edu

Primary CNF Tools Used: Oxford Flex ALD, Arradance ALD, Oxford Cobra ICP etcher

Abstract:

We are developing origami into a tool for fabricating autonomous, cell-sized machines. In our approach, devices can interact with their environment, be manufactured en masse, and carry the full power of modern information technology. Our approach starts with origami in the extreme limit of folding 2D atomic membranes. We make actuators that bend to micron radii of curvature out of atomically thin materials, like graphene. By patterning rigid panels on top of these actuators, we can localize bending to produce folds, and scale down existing origami patterns to produce a wide range of machines. These machines change shape in fractions of a second in response to environmental changes, and perform useful functions on time and length scales comparable to microscale biological organisms. Beyond simple stimuli, we are currently developing voltage responsive actuators that can be powered by on-board photovoltaics. These new electronic actuation technologies are currently being combined with silicon-based electronics to create a powerful platform for robotics at the cellular scale.

Summary of Research:

Our group is shrinking down origami-robotics to become the fundamental platform for nanorobotics by folding atom's thick paper. In origami robotics, actuators, patterned on a sheet, are used to fold complex, reconfigurable 3D structures. This platform is prime for miniaturization because fabrication can be done in plane with tools like photolithography, designs are scale invariant, and flat panels linked by the folds provide a natural place to integrate electronics.

The most basic challenge to miniaturizing origami robots is in actuator design. A single actuator must be capable of bending to micron radii of curvature, produce force outputs large enough to lift embedded electronics, and maintain electrical conductivity across folds while bending. Through research conducted at the CNF, we have shown how actuation technologies based on atomic membranes, like graphene, can achieve these key functional requirements.

First, atomic origami devices can bend to micron radii of curvature using strains that are 100x smaller than the fracture strain for inorganic hard materials, thus maintaining electrical functionality across the actuator. Second, the devices are extremely stiff, capable of lifting the weight equivalent of a 500 nm thick silicon chip, enabling embedded electronics. Third, they can be fabricated and deployed en masse: 10 million devices fit on a 4-inch silicon wafer. Finally, devices can change shape from flat to folded in fractions of a second. Overall, the size, speed, stiffness and strength of these new actuators offer a new perspective on what is possible with nanoscale mechanical technology.

As our first prototypes, we designed and built actuators out of graphene and nanometer thick layers of glass.

These glass layers were deposited at CNF using the Oxford Flex atomic layer deposition tool. By patterning

2- μm -thick rigid panels on top of bimorphs, we were able to localize bending to the unpatterned regions to produce folds. Although only nanometers thick, the graphene glass bimorphs were able to lift these panels, the weight equivalent of a 500-nm-thick silicon chip. Using panels and bimorphs, we showed how to scale down existing origami patterns to produce a wide range of machines. We demonstrated that these machines were capable of changing shape in fractions of a second when crossing a tunable pH threshold.

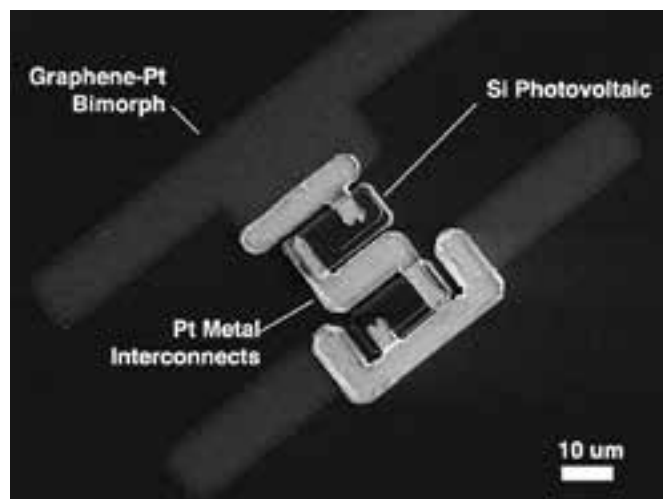
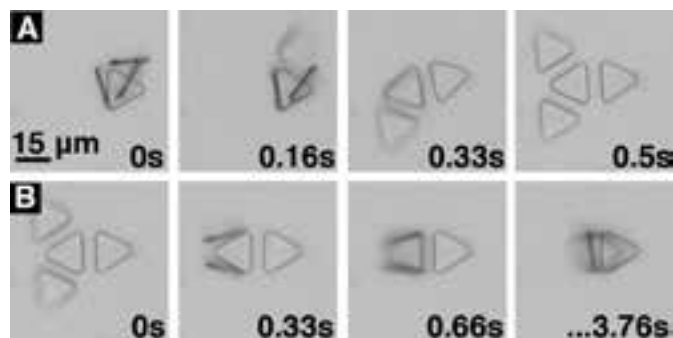
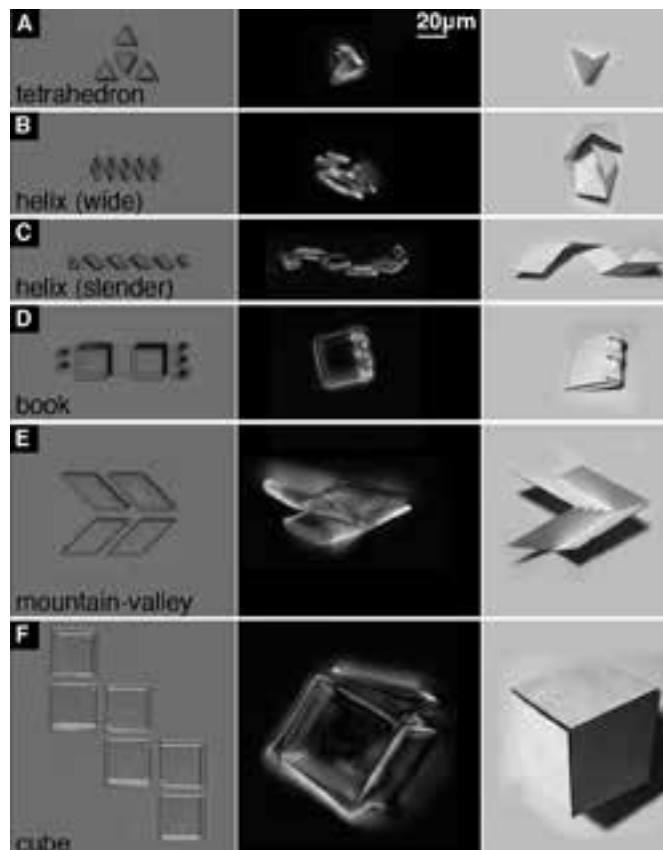
Combined, the work developed a platform for building machines that sense their environments, respond, and perform useful functions on time and length scales comparable with microscale biological organisms.

Currently we are taking key steps in moving towards true robotic systems at the cellular scale by integrating nanoscale origami actuators with electronics. We are now capable of designing and building high efficiency actuators for self-folding machines that are powered by voltage. This advance relies on new metal atomic layer deposition capabilities through the CNF's Arradiance atomic layer deposition tool. These devices can be powered and controlled using standard CMOS electronic components like photovoltaics and transistors. As a first step, we are building basic prototypes that use on-board photovoltaics to power origami actuators. The resulting device can then change shape from flat to folded when external power is supplied through light fields. By combining this actuation technology with origami motifs, we are working to create a walking, autonomous robot no bigger than a few red blood cells in size.

References:

- [1] Miskin, et al., Graphene-based bimorphs for micron-sized, autonomous origami machines, PNAS, 2018.

Figure 1, top right: Graphene origami can be used to fabricate numerous 3D structures at the micrometer scale. Shown here are tetrahedron (A), helices of controllable pitch (B and C), high-angle folds and clasps (D), basic origami motifs with bidirectional folding (E), and boxes (F). In Left, we show the device flattened and still attached to the release layer during fabrication. After the release layer is etched, the bimorphs self-assemble to their targeted 3D geometries (Center). **Figure 2, middle right:** Graphene origami devices are capable of rapid actuation due to the extreme slenderness of the working materials. Here a graphene origami tetrahedron changes shape from flat to folded and back in response to variations in local electrolyte content. The folding processes is fast, taking place in less than second. **Figure 3, bottom right:** A first prototype integrating a silicon based photovoltaic with atomic origami actuators. These origami actuators are capable of transforming from flat to folded by applying a voltage of only a few hundred millivolts and nanowatts of power. The photovoltaics supply rough 3x more voltage than is needed and roughly three orders of magnitude more power. The resulting machine will be capable of walking to explore its environment, fully untethered, using the actuators for locomotion and the photovoltaics for power.



NEMS Electrostatic Switch for Near Zero Power RF Wakeup

CNF Project Number: 1262-04

Principal Investigator: Amit Lal

User: Alexander Ruyack

Affiliation: Electrical and Computer Engineering, Cornell University

Primary Sources of Research Funding: Defense Advanced Research Projects Agency (DARPA) project; Near Zero Power RF and Sensor Operations (N-ZERO)

Contact: amit.lal@cornell.edu, arr68@cornell.edu

Primary CNF Tools Used: ASML 300C DUV stepper, Heidelberg DWL2000, Gamma automatic coat-develop tool, Zeiss Ultra SEM, Zeiss Supra SEM, Oxford 81, 82, and 100 etchers, AJA ion mill, Hamatech hot piranha, Primaxx vapor HF etcher, Plasma-Therm deep Si etcher, Uniaxis 770 deep Si etcher, DISCO dicing saw, wire bonder, Aura 100, Zygo

Abstract:

A near zero-power laterally actuated nanoelectromechanical systems (NEMS) electrostatic radio frequency (RF) switch with multi-gate DC tunable threshold is presented as a portion of an overall wireless sensor node with less than 10 nW power consumption. Previously these switches were demonstrated as means of signal detection from a suite of zero power sensors. Various design updates and fabrication improvements have since been implemented to reach the desired -100 dBm RF sensitivity. The addition of folded trusses, compliant contacts and selections in contact material allow the device to be operated at resonance and reduce bending and variation, improving performance and reducing failure rate. Furthermore, processing with the Plasma-Therm Versaline deep reactive ion etch (DRIE) tool has resulted in 300 nm features within 5% of the drawn dimensions in CAD.

Introduction:

Sensor node reliability is limited by the longevity of the energy sources used to power them [1]. In order to maximize the sensor node operation time, power consumption by all components must be minimized. The power consumed by the sensors of the sensor node is especially critical because the sensors must operate all the time to generate a wakeup trigger for the digital and communication components. Previously, we demonstrated MEMS inertial, magnetic and acoustic sensors made of piezoelectric materials, which promise sensing without any power consumption [2]. These sensors, in conjunction with NEMS switches [3] showed successful classification of a portable electrical generator in different operation modes (on, off, eco) [4]. However, since these sensor nodes are wireless, detection of an RF wake-up signal is equally important and there must be an asleep-yet-aware detection method for RF signals. For this, we used the NEMS switch again with a reworked design and fabrication process in order to achieve the desired -100 dBm sensitivity.

Summary of Research:

A single photomask process is used to fabricate the NEMS switches on a silicon-on-insulator (SOI) substrate.

Previously, alumina was used as a hard mask for a reactive ion etch (RIE) with subsequent alumina etch, metal deposition for conductivity, and release with wet hydrofluoric acid (HF) via critical point drying or vapor HF. This process resulted in over etched features, significant scalloping and large out of plane bending of released devices. By moving to a photoresist (PR)-only process with the Plasma-Therm VersaLine DRIE tool, the over-etching was minimized, scalloping reduced to < 20 nm, and out of plane bending minimized. Furthermore, additional design modifications were made to help push the sensitivity of the switch to -100 dBm. Folded springs and trusses help reduce bending and a compliant contact helps reduce contact lifetime and resistance. Additionally, smaller gaps were achievable with the new process, increasing the electrostatic force and helping sensitivity. Figure 1 shows a top down micrograph of a finished, unreleased device.

Figure 2 is a micrograph showing a 350 nm contact gap measurement. DRIE scallops can be seen on the left side of the image within the two release holes. The Figure 2 inset shows a Zygo white light interferometry image showing the out of plane bending of a released device. At the contact, there is a 30 nm out of plane displacement,

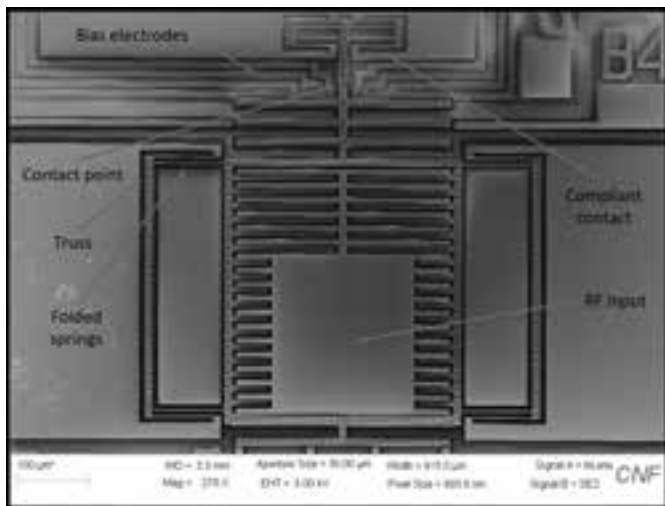


Figure 1: SEM micrograph of NEMS switch from above showing important electrical contacts and features.

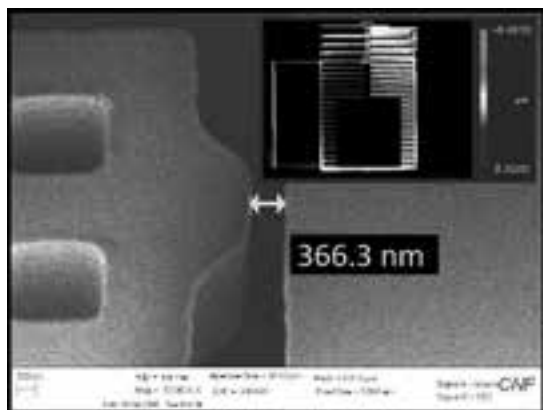


Figure 2: SEM micrograph with contact gap measurement. (Inset) Zygo optical profilometry measurement of out-of-plane bending of released device.

which is small compared to the $2\ \mu\text{m}$ device layer and $1\ \mu\text{m}$ oxide layer.

Testing was done in a custom-built vacuum probe station (Figure 3a). An example image of a device under test can be seen in Figure 3b. Testing is currently underway for probability of detection (POF) and false alarm rate (FAR) using a high gain low noise Stanford Research Systems 570 TIA for detection, Keithley 2400s for biasing and a Rhode and Schwarz SMC100A RF signal generator.

Additional work still needs to be done to ensure reliable and repeatable contacting of the device. Efforts are underway to coat the contact interfaces with platinum (Pt) using a focused ion beam (FIB). Figure 4 shows an example device contact area (with three contact points) that has been completely covered with Pt and then re-cut with the ion beam to form approximately $100\ \text{nm}$ contact gaps. There is also additional work being done to translate these devices to an out-of-plane design

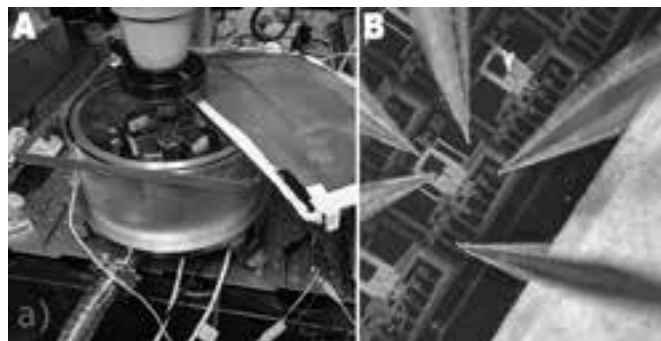


Figure 3: (a) Custom vacuum probe station. (b) Example image of device under test in probe station.

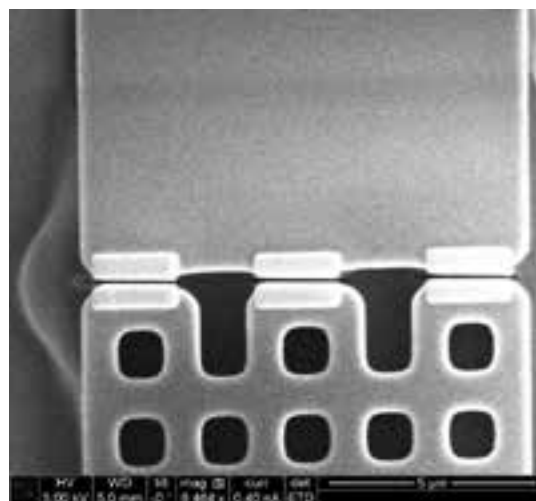


Figure 4: SEM micrograph after FIB Pt deposition and subsequent cutting with ion beam, resulting in near $100\ \text{nm}$ gap.

instead of in-plane. These devices are made via a flip-chip bonding process between a similar SOI chip and patterned lithium niobate (LiNbO_3 or LN) chip with graphene. These devices have the advantage of much larger electrostatic area (for better sensitivity) and RF filtering capabilities on the LN.

References:

- [1] J. Yick, B. Mukherjee, and D. Ghosal. "Wireless sensor network survey," Computer networks 52, no. 12 (2008): pp 2292-2330.
- [2] S. K. Gupta, V. Pinrod, S. Nadig, B. Davaji and A. Lal. "Vibration Powered RF-Transponder for Sensing Low Frequency Motion Events," PowerMEMS 2016.
- [3] K. Amponsah, N. Yoshimizu, S. Ardanuc, and A. Lal, "Near-kT switching-energy lateral NEMS switch," IEEE NEMS 2010, pp. 985-988.
- [4] V. Pinrod, A. Ruyack, R. Ying, B. Davaji, A. Molnar, A. Lal, "PZT Lateral Bimorph Based Sensor Cuboid for Near Zero Power Sensor Nodes," IEEE Sensors 2017.

Origin of Microlayer in Pool Boiling

CNF Project Number: 2123-12

Principal Investigator: Shalabh C. Maroo

Users: An Zou, Manish Gupta

Affiliation: Department of Mechanical and Aerospace Engineering, Syracuse University, Syracuse, NY 13244

Primary Sources of Research Funding: Startup funds from Department of Mechanical and Aerospace Engineering at Syracuse University; National Science Foundation Career Award NO. 1454450

Contact: scmaroo@syr.edu, azou@syr.edu and magupta@syr.edu

Website: <http://maroo.syr.edu>

Primary CNF Tools Used: CHA thermal evaporator, E-beam evaporator, CVC sputter, Oxford PECVD, GSI PECVD, Glen 1000 Plasma, Oxford 81/82 etcher

Abstract:

Microlayer evaporation is one of the major heat transfer mechanisms of boiling. In our work, the microlayer thin film is visualized *in situ* in a vapor bubble during pool boiling. Contrary to current understanding, bubbles originate on hydrophilic and silane-coated hydrophobic surfaces without a three-phase contact line, i.e. the microlayer completely covers the bubble base. The occurrence of such a wetted bubble base is found to be dependent on the liquid-solid interaction, which is validated by molecular dynamics simulations of nucleation of liquid argon on hydrophilic and/or single-layer hydrophobic atoms on hydrophilic surfaces. The work reported here is part of a journal article which is currently under review.

Summary of Research:

Microlayer is a thin liquid film trapped underneath a vapor bubble next to three-phase contact line. The base of the bubble can be divided into three regions: nanoscale non-evaporating film region, microscale evaporating film region, and millimeter scale bulk meniscus (Figure 1). Extremely high heat flux occurs in the microlayer region due to its low thermal resistance, which is proportional to liquid layer thickness. Microlayer evaporation serves as one of the major heat transfer mechanism. Better understanding of the microlayer has led to novel approaches for boiling heat transfer enhancement: microstructures fabricated on pool boiling surface causes early evaporation of microlayer, resulting in ~120% enhancement in the critical heat flux [1]. In our work, we studied origin of microlayer by *in situ* visualizing the microlayer in a vapor bubble in pool boiling, and performing molecular dynamics simulations of bubble nucleation.

We used laser heating to create a vapor bubble on a surface submerged in a pool of deionized (DI) water at room temperature. The surface consists of several metal layers for laser heating technology (Figure 2): a 40 nm thick tungsten was deposited on a glass substrate to absorb the laser and heat the surface; a 1 μm thick PECVD SiO_2 was deposited to serve as hydrophilic surface (contact angle: $33.4 \pm 2.7^\circ$); two 10 nm thick Ti layers were deposited acting as adhesion layer. To form the vapor bubble, a blue CW laser beam (wavelength of $447 \pm 5 \text{ nm}$) was introduced into an inverted microscope, passed through a $50\times$ objective, and focused on the sample to generate a highly localized heating area corresponding to an equivalent beam diameter of $\sim 15 \mu\text{m}$. The same objective was used to image the bubble which was illuminated from above with a 632 nm HeNe laser. This configuration creates a bubble image with a dark annulus ring as light has to refract across multiple interfaces in that region. A high-speed camera was used to record the bubble formation process.

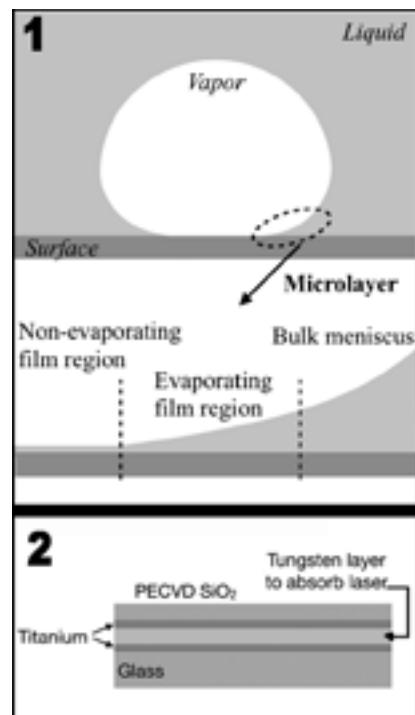


Figure 1, top: Microlayer underneath a vapor bubble in pool boiling. Figure 2, bottom: Sample surface with metal layers to absorb laser.

The microlayer is *in situ* visualized using this setup because fringes would be observed in microlayer region. These fringes were observed due to thin film interference of monochromatic incident light with partially reflected light within the thin liquid microlayer. As the generated dark and bright fringes correspond to constructive and destructive interference respectively, these fringes are separated by an optical path difference which is half wavelength, and the position of the fringes can be used to build microlayer profile.

In our experiments, the fringes are surprisingly seen throughout the bubble base on the surface, indicating that the microlayer liquid film covers entire bubble base and no three-phase contact line forms (Figure 3). In order to understand the physics behind the completely wetted bubble base, molecular dynamics simulations were performed in LAMMPS [2] software with liquid argon present between two walls. The upper wall was moved outward at a certain speed to decrease the pressure in the liquid and initiate nucleation. The lower wall was modeled as the hydrophilic surface by using a 12-2 Lennard Jones potential between the wall and argon atoms. Similar to the experiments, a liquid film is present between the bubble and the surface (Figure 4). Statistical analysis from molecular dynamics simulation shows that due to the strong interaction between the hydrophilic wall and argon atoms, high density liquid layers form near the wall, leading to significantly high pressure in that region. Thus, a bubble forms above these liquid layers as it is thermodynamically favorable to achieve lower pressures required for nucleation, resulting in a liquid film being present underneath the bubble. This mechanism can be amplified/weakened with different wall-liquid combinations, for e.g., interaction between SiO_2 and water were much stronger as polar atoms are involved, leading to thicker high-density liquid water film that is measurable in experiments. However, the completely wetted bubble base will not likely be observed on weak interacted wall-liquid combinations (if either is non-polar).

In summary, we observed that the bubble, at its early growth stage, had a bubble base that is completely covered by the microlayer; similar observation was found in molecular dynamics simulations. This entirely wetted bubble base is due to the strong wall-liquid interactions, the thickness of microlayer is determined by the wall-liquid interactions.

References:

- [1] A. Zou, D. P. Singh, and S. C. Maroo, *Langmuir* 32, 10808-10814 (2016).
- [2] S. Plimpton, *J. Comput. Phys.* 117, 1-19 (1995).

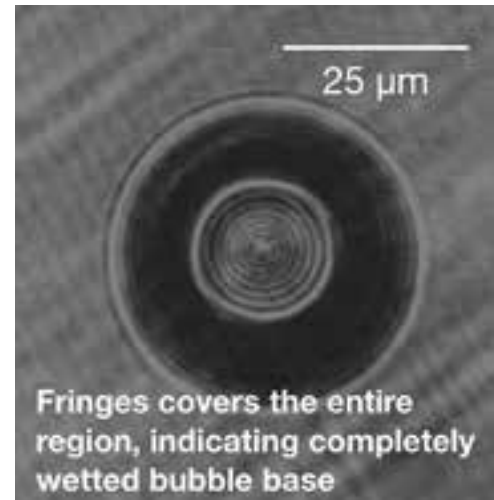


Figure 3: Image of a vapor bubble with completely wetted bubble base.

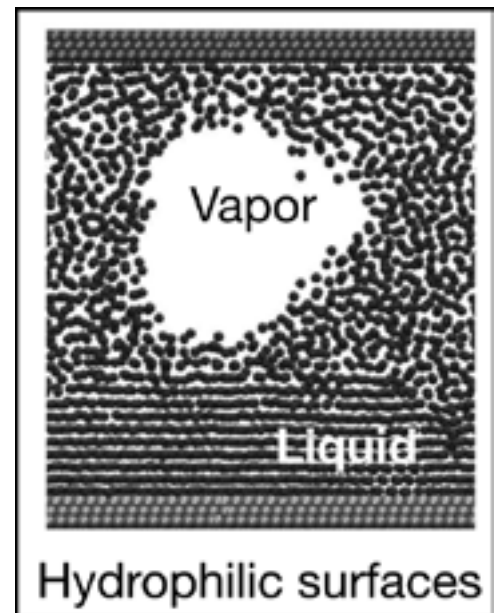


Figure 4: Bubble with completely wetted base in molecular dynamics simulation.

Making a Microfluidic Device to Mimic Flow Through Porous Medium

CNF Project Number: 2385-15

Principal Investigator: Brian Kirby

User: Katherine Polhemus

Affiliation: Sibley School of Mechanical and Aerospace Engineering, Cornell University

Primary Source of Research Funding: IGERT Program for Earth Energy

Contact: kirby@cornell.edu, kcp44@cornell.edu

Primary CNF Tools Used: CAD software L-Edit, photolithography tool set, ABM contact aligner, hot press, CorSolutions microfluidic probe station

Abstract:

With the rapid depletion of known oil reserves, detecting properties of the oil reservoirs and optimizing oil extraction is critical. By measuring the aqueous properties of the reservoirs, decisions can be made on which reservoirs to drill and the available quantity of oil to extract, with minimal environmental impact. Utilizing hairy nanoparticles in testing can provide a variety of information about the reservoir. The objective of the proposed work is to characterize the behavior of hairy nanoparticles at the oil-water interface in order to optimize their use as subsurface sensors. In order to complete the optimization, a microfluidic model for the environment needs to be developed. This past year's work involves making microfluidic devices to mimic water flowing through the subsurface and oil trapped in pores. The design and mold to make the mold was developed in the CNF first using photolithography to create a mold with negative photoresist that was used to make microfluidic channels out of polydimethylsiloxane and later using positive photoresist and etching to create a mold to make microfluidic channels out of polypropylene.

Summary of Research:

This research at the CNF has consisted of using microfabrication techniques to make a microfluidic device. Using the CAD software L-Edit, we make patterns to transfer to a mask using the Heidelberg mask writer. In the past year, we have made two types of masks: one for positive photoresist and the other for negative photoresist. The first set of microfluidic devices we made used the negative photoresist (SU-8) to make a mold.

The process of making a mold with photoresist (photolithography) consist of the steps; 1) Pour and spin photoresist onto a wafer (using CNF spinner), 2) Bake photoresist (using CNF hot plates), 3) Wait time, 4) Expose photoresist (using ABM contact aligner), 5) Second wait time, 6) Development photoresist. At the end of the process, we have a mold out of SU-8 on top of a wafer.

In the Kirby research group's lab, we made microfluidic devices by pouring PDMS on top of the mold, and then baking and attaching the molded PDMS to a glass slide through plasma cleaning. Unfortunately, for our application, we need the PDMS to be very hydrophobic

and PDMS was not hydrophobic enough for these experiments. Therefore, we switched to making devices out of a polypropylene — a much more hydrophobic material.

To make the molded polypropylene pieces, we use hot embossing, which is done on the CNF hot press. Because of the large pressure applied during embossing, we needed a stronger mold than SU-8, so we switched to making molds out of silicon.

To make a mold out of silicon, a positive photoresist is spun instead of negative and after the photolithography process, the wafer is etched on the deep reactive ion etcher in the CNF. The mold is used in the CNF hot press to hot emboss the pattern onto polypropylene, which is then bonded using the hot press. We also used the CorSolutions microfluidic probe station for a time as a connection method for the tubes to the device. However, we determined that epoxy was a better method for the connecting tubes to the microfluidic device due to the pressure exerted by the CorSolution arm causing particles to clog.

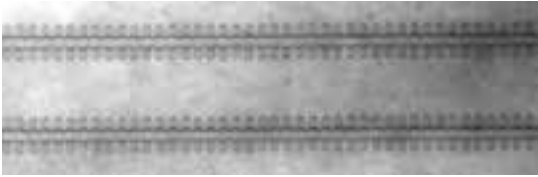


Figure 1: Developed positive resist pattern on wafer.



Figure 2: Embossed channels in polypropylene.

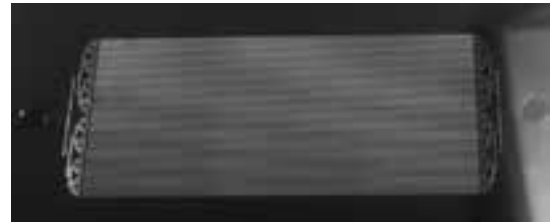


Figure 3: Device on CorSolutions microfluidic probe station.

Atomic-Scale Origami for the Fabrication of Micron Sized Machines

CNF Project Number: 2416-16

Principal Investigators: Itai Cohen, Paul L. McEuen

Users: Marc Z. Miskin, Baris Bircan, Edward P. Esposito, Tianyu Ma

Affiliations: Kavli Institute at Cornell for Nanoscale Science, School of Applied and Engineering Physics, Laboratory of Atomic and Solid-State Physics, Department of Physics; Cornell University

Primary Sources of Research Funding: National Science Foundation, Contract: DMR-1719875; Army Research Office, Contract: W911NF-18-1-0032

Contact: itai.cohen@cornell.edu, plm23@cornell.edu, mm2325@cornell.edu, bb625@cornell.edu, epe3@cornell.edu, tm478@cornell.edu

Primary CNF Tools Used: Oxford ALD FlexAL, Arradiance ALD Gemstar-6, Oxford 81 etcher, ABM contact aligner, SC 4500 odd-hour, Glen 1000 resist strip, Heidelberg DWL2000

Abstract:

Origami allows the creation of complicated three-dimensional structures from simple two-dimensional patterns. We are inspired to use origami for the fabrication of three-dimensional microscopic machines. The first step in such technology is the ability to fold thin sheets on-demand. Our work has demonstrated multiple mechanisms to actuate the folds in microscopic origami patterns, using standard processing techniques of the semiconductor industry.

Summary of Research:

Origami has emerged recently as a promising design strategy for creating arbitrarily complex three-dimensional structures from two-dimensionally patterned thin sheets [1,2]. As long as the two-dimensional pattern contains the proper array of mountain and valley folds, with a suitable actuation mechanism, we can create complicated three-dimensional origami structures that assemble themselves. Our work has demonstrated actuation mechanisms that works for nanometer-thin sheets, patterned using standard semiconductor processing technologies. This promises the smallest possible scale of origami devices.

Our devices rely on the bi-morph principle for actuation. One device, made from a stack with different materials in each of two layers, can be made to bend if the two layers strain by different amounts in response to an external stimulus, such as changing the temperature, or as in our previous work, the pH. Introducing a strain mismatch between the layers causes one layer to be in tension and the other to be in compression. By placing the bimorph stacks only in pre-specified regions, we can use the appropriate external stimulus to cause a thin sheet with an origami pattern to fold all at once.

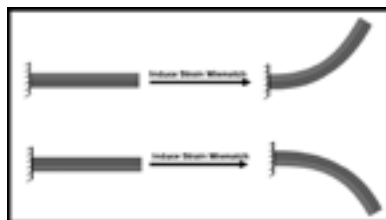


Figure 1: By introducing a strain mismatch between the bi-morph layers, we can cause a cantilever beam to bend.

Our prior work focused on bimorphs of silica (SiO_2) and graphene [3]. We first evaporate a sacrificial aluminum release layer onto a boro-silicate glass substrate, and then deposit a 2 nm layer of SiO_2 using the Oxford ALD FlexAL atomic layer deposition (ALD) tool. We then transfer graphene onto the SiO_2 layer, photolithographically pattern hinges and beams in any regions we would like to introduce a fold, and deposit pads of rigid SU-8

polymer over any regions we would like to remain flat. Finally, we remove the sacrificial aluminum layer with a wet etch to release our devices from the substrate into solution. Ion exchange causes the SiO_2 layer to swell.

Transferring graphene to the substrate is difficult and time-consuming as compared with deposition of an SiO_2 layer using the ALD tool, so it is beneficial to deposit both bimorph layers using ALD. We explored some of the materials available, and have settled on bimorph stacks of SiO_2 and silicon nitride (Si_3N_4), where each layer is 2 nm thick. The ion exchange mechanism is slightly different for the two layers, so lowering the pH still introduces a strain mismatch, causing cantilever beams to bend to roughly 10 μm radii of curvature, as in Figure

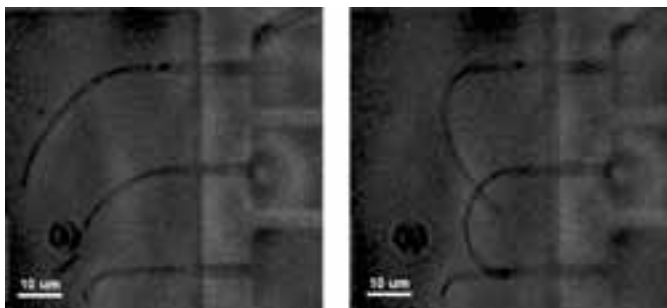


Figure 2: Bending of $\text{SiO}_2 / \text{Si}_3\text{N}_4$ bimorph cantilever beams by means of pH-induced ion exchange. Simply changing the solution from basic to acidic causes the beams to bend.

2. Bimorphs with Si_3N_4 avoid some of the pre-stressing that occurs when using other materials.

Some work this year has focused on process development to allow us to use more sophisticated folding patterns. Devices fabricated with a single kind of bimorph stack are constrained to have all mountain or all valley folds, whereas most origami patterns require a single sheet to have both mountain and valley folds in different locations. We need devices capable of bi-directional folding. We have developed and refined a process that allows the fabrication of one bimorph stack together with the inverted bimorph stack as part of a single device, allowing beams with the two bi-morph stacks to fold into an S-shape, as in Figure 3. This has unlocked a whole realm of complex origami patterns. Professional origami artists have developed software that automatically generates design files we can include in mask designs.

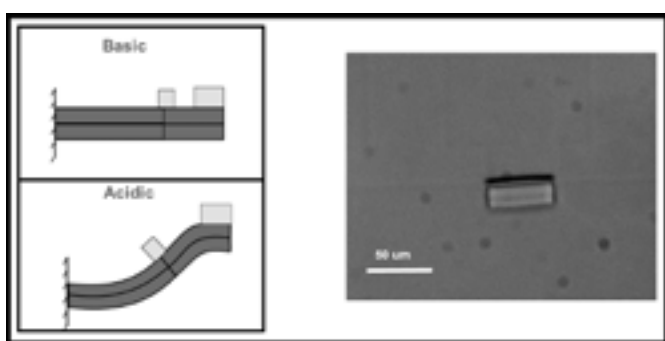


Figure 3: Schematic and experimental demonstration of bi-directional folding in $\text{SiO}_2 / \text{Si}_3\text{N}_4$ bimorph cantilever beams. The flat rectangle is a rigid SU-8 pad, parallel to the substrate, while the dark line above it is an SU-8 pad of the same size perpendicular to the substrate.

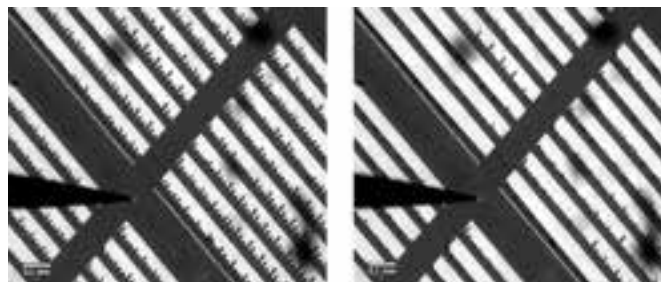


Figure 4: Applying a potential difference across an array of graphene / platinum bimorphs causes the entire array to fold at once.

Our pH-based ion exchange mechanism allows us to change devices from the flat to the folded state at will, but it does not allow precise control over the radius of curvature in our devices when bent. As a promising new direction, part of our team has developed devices offering such precise control. Here, we use graphene with a 5 nm layer of platinum as our bimorphs. To actuate folds, we apply a voltage across our devices, and this potential difference allows ions from the solution to be absorbed into the platinum, swelling that layer as compared with the graphene, bending the device as before. By varying the applied potential difference, we can control the amount of bending, as shown in Figure 4. This technique allows an unprecedented control over the final three-dimensional configuration of our bending-actuated devices.

Our actuation mechanisms are well-suited for origami patterns in which all folds may be actuated at once. However, this is only a subset of all origami patterns. More complicated patterns require folds to be actuated in a specified sequence. Therefore, a major future direction of our work is to uncover techniques for actuating various folds sequentially.

References:

- [1] Benbernou, N., Demaine, E. D., Demaine, M. L. and Ovadya, A. A universal crease pattern for folding orthogonal shapes. arXiv preprint arXiv:0909.5388 (2009).
- [2] Felton, S., Tolley, M., Demaine, E., Rus, D. and Wood, R. A method for building self-folding machines. *Science* 345, 644-646 (2014).
- [3] Miskin, M., Dorsey, K., Bircan, B., Han, Y., Muller, D., McEuen, P., and Cohen, I. Graphene-based bimorphs for micron-sized autonomous origami machines. *Proceedings of the National Academy of Sciences*, 115: 466-470 (2018).

A MEMS Repulsive Force Accelerometer

CNF Project Number: 2446-16

Principal Investigators: Shahrzad Towfighian, Ronald N. Miles

User: Mehmet Ozdogan

Affiliation: Mechanical Engineering Department, State University of New York at Binghamton

Primary Source of Research Funding: National Science Foundation Project ECCS grant # 1608692 titled "A New Approach to Capacitive Sensing: Repulsive Sensors"

Contact: stowfigh@binghamton.edu, rmiles@binghamton.edu, mozdoga1@binghamton.edu

Website: <https://www.binghamton.edu/labs/mems/>

Primary CNF Tools Used: Heidelberg mask writer - DWL2000, LPCVD N+/P+ polysilicon -wet oxide-CMOS nitride, MOS clean anneal, AS200 i-line stepper, Unaxis 770 deep Si etcher, Oxford 81-100 etchers, Logitech Orbis CMP, Zeiss Ultra SEM, SC4500 evaporator, RTA - AG610, DISCO dicing saw, Leica critical point dryer

Abstract:

This study reports fabrication and experimental characterization of a microelectromechanical systems (MEMS) capacitive accelerometer that utilizes repulsive force electrode configuration consisting of three fixed and one moving electrode. This configuration generates a net upward force on the moving electrode that is attached to a movable proof mass. The net force pushes the moving structure away from the substrate and produces an out-of-plane motion. Having this design comes with various benefits such as elimination of pull-in instability that severely limits functioning of electrostatic devices and causes permanent structural damages. This repulsive configuration concept has been investigated for actuator applications; however, it has not been employed for sensing purposes in the literature. Our goal is to create an accelerometer that works based on the repulsive sensing concept. The accelerometer is designed and fabricated with four-mask process. Following the fabrication, it is fixed on a shaker and tested under various DC bias and excitation levels to characterize its dynamic behavior. Laser Doppler Vibrometer (LDV) is used to measure its dynamic response under base excitation provided by the shaker. At 2.5 kHz excitation frequency, we measured the mechanical sensitivity of the sensor as 0.17, 0.13, and 0.09 $\mu\text{m/g}$ at 40-50-60 V bias, respectively. Experimental results indicate that sensitivity of the accelerometer is the function of operating DC bias, excitation level and the excitation frequency. One can tune the sensitivity of the device by playing with these variables without experiencing pull-in instability, which is a great contribution.

Summary of Research:

The repulsive electrode configuration has been shown to be pull-in safe [1], which enables MEMS devices to have large travel ranges and proper functioning at high DC loads [2]. This method utilizes fringe electrostatic field to generate a net force that pushes away the proof mass from the substrate which eliminates the pull-in possibility. Main goal of this project is to exploit the benefits of utilizing repulsive electrode design in a capacitive sensor. The sensor design consists of fixed and moving electrodes which are attached to a rotating proof mass, see Figure 1. The design includes three sets of electrodes: grounded moving fingers, grounded aligned fixed fingers and voltage loaded unaligned fixed fingers. The moving and aligned fixed fingers are vertically separated with 2 μm initial gap.

The fabrication process flow of the accelerometer is shown in Figure 2. The process starts with a 100 mm silicon wafer. First, LPCVD silicon dioxide is grown as an insulation layer. Following this step,

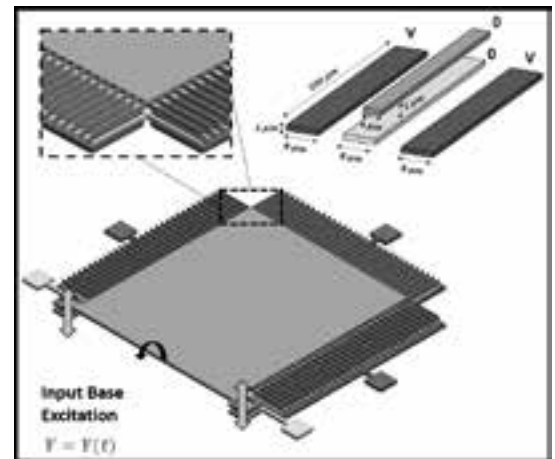


Figure 1: 3D model of the designed sensor showing the details of the proof mass and the electrodes.

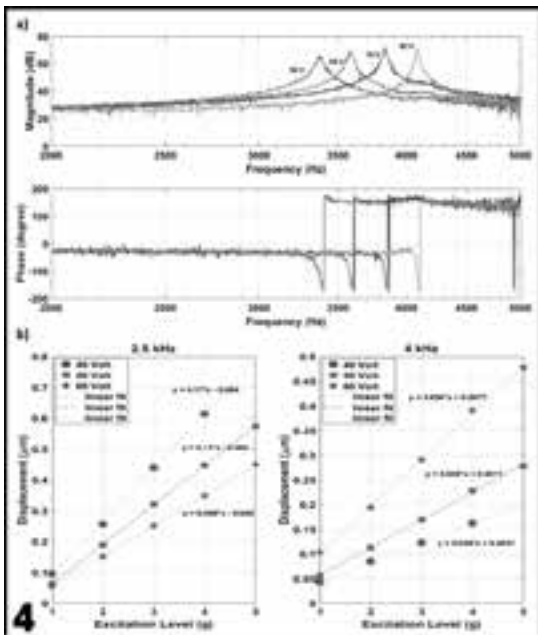
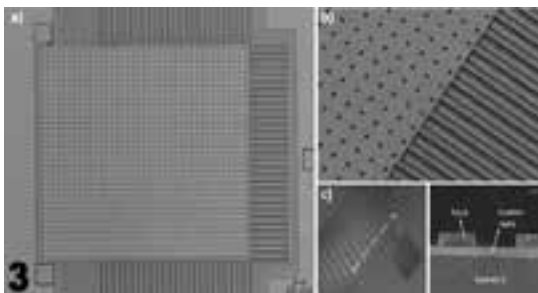
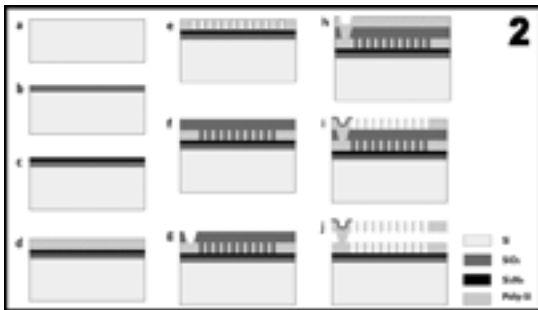


Figure 2, top: Fabrication process flow of the sensor. (a) 4-inch, 525 μm thick silicon wafer. (b-c) Insulation layers growth and deposition, respectively. (d) First layer of 2 μm thick phosphorus doped polysilicon deposition. (e) RIE etch of polysilicon. (f) Sacrificial layer deposition and CMP processes. (g) Anchor etch on sacrificial layer. (h) Second 2 μm thick polysilicon deposition. (i) Polysilicon etch and gold deposition on the pads. (j) Proof mass release in HF:HCl mixture. **Figure 3, middle:** Images of the fabricated device. (a) Top view of the proof mass. (b) Moving and fixed fingers for the released device. (c) Fixed fingers and the cross-sectional view. **Figure 4, bottom:** Experimental results. (a) Shows the transfer function of the device which is performed to measure the resonance frequency of the sensor under various DC bias. (b) Shows the mechanical sensitivity (slope) of the sensor.

LPCVD low stress silicon nitride is deposited on top of the oxide layer. After deposition of insulation layers first structural polysilicon layer is deposited using LPCVD furnace. Unaxis 770 plasma etcher is used to form fixed fingers out of this layer. On top of these fixed fingers, a sacrificial layer of LPCVD high-temperature-oxide (HTO) is deposited. Then, Logitech Orbis chemical mechanical polisher (CMP) is used to remove the step difference between fixed fingers and the proof mass. After the CMP process, vias are formed by etching the oxide layer using Oxford PlasmaLab 100 etcher. Later, second polysilicon layer is deposited and followed by annealing to reduce the residual film stresses. This layer is etched to form the proof mass attached with fingers and suspending torsional springs. Next, we deposit Cr and Au on the pads using evaporation tool SC4500 evaporator. After the evaporation process the wafers are diced and released in HF:HCl mixture. The fabricated device is presented in Figure 3.

The device is attached and wired to a PCB that is mounted on the head of a shaker. The device is excited in a vacuum environment. The side fingers are applied a DC bias while the shaker is vibrating with an AC harmonic signal which is the source of the base excitation. Laser Doppler vibrometer interfaced with data acquisition box is used to monitor the time-response of the device. The results are presented in Figure 4. Figure 4a shows the change of the resonance frequency of the device as the DC bias changes. Due to the fringe electrostatic forcing, as the DC load increases effective stiffness of the structure increases which results in shift of the resonance frequency. Figure 4b shows the relative motion of the proof mass when it is subjected to different excitation levels varying from 1g to 5g. Experimental results show that mechanical sensitivity (Figure 4b) of the device is the function of the applied DC bias and the frequency of the excitation. We are currently performing experiments to measure the response of the device to various shock impulses such as half-sine.

References:

- [1] S. He and R. B. Mrad, "Design, Modeling, and Demonstration of a MEMS Repulsive-Force Out-of-Plane Electrostatic Micro Actuator", *Journal of Microelectromechanical Systems*, Vol. 17, no. 3, pp. 532-547, June 2008. doi: 10.1109/JMEMS.2008.921710.
- [2] Towfighian S, He S, Ben Mrad R. "A Low Voltage Electrostatic Micro Actuator for Large Out-of-Plane Displacement.", *ASME. IDETC/CIE*, Vol. 4: doi:10.1115/DETC2014-34283.

Microfabrication of Micropillars inside a Microchannel

CNF Project Number: 2474-16

Principal Investigator: Dr. Yoav Peles

User: Faraz Khalil Arya

Affiliation: Mechanical and Aerospace Engineering, University of Central Florida

Primary Source of Research Funding: University of Central Florida Research Foundation Inc

Contact: yoav.peles@ucf.edu, arya@knights.ucf.edu

Primary CNF Tools Used: AutoCAD, AJA sputter deposition, photolithography processes, AJA ion mill

Abstract:

Boiling generates bubbles and predicting the movement of these bubble can be challenging. In this research, we fabricated micropillars and heaters in specific locations inside a microchannel and operate the heaters in calculated sequences. We moved the bubbles in the direction that we planned, and these movements pushed the liquid inside the channel toward the outlet.

Summary of Research:

The microfabrication process was conducted at the Cornell NanoScale Science and Technology Facility (CNF). Photolithography masks were designed and drew with AutoCAD and fabricated before they were taken to the CNF to be used during the fabrication process.

The fabrication was started on a Borofloat® wafer with the thickness of 500 μm and the diameter of 100 mm. Borofloat wafer was chosen because of the low heat conductivity ($1.2 \text{ W}/(\text{m}\cdot\text{K})^{-1}$), outstanding thermal resistance, very good temperature stability, excellent resistance to thermal shock, and a low coefficient of linear thermal expansion of around $3.25 \times 10^{-6} \text{ K}^{-1}$.

The Borofloat wafer was first cleaned with hot Piranha. After this step, the cleaned wafer was taken to the deposition tool so that 0.5 μm of Si_3N_4 was deposited on the substrate. This layer provides insulation between layers and acts as a mechanical isolation/buffer membrane. Depositing the vias and heaters was the next step.

The wafer was placed in the sputter deposition tool so that a 7 nm layer of titanium (Ti) could be deposited on it to enhance the deposition of a 30 nm layer of platinum (Pt). This layer of Pt is going to form the heaters of the device. Finally, a 1 μm layer of aluminum (Al) was deposited to provide the electrical connections. The first photolithography process was performed next and the excessive Al was removed by wet etching. After another photolithography process, the ion mill was used to etch the excess Pt and Ti. To insulate the heaters and vias layers from the flow inside the channel, a 1 μm layer of SiO_2 was deposited on the substrate. Contact pads should be the only parts of the wafer without the insulating layer of SiO_2 , therefore, another process of photolithography was performed and the surplus SiO_2 layer was removed by dry etch.

To start the fabrication of the channel and the micropillars from SU-8, the wafer was first dehydrated in the oven. SU-8-100 was chosen as the appropriate SU-8 type and spun on the wafer in the spinning room. To conduct the soft bake step, the wafers were gradually heated up and kept at the temperature of 65°C for two hours and then baked at 95°C for a few more hours. The contact aligner was the selected tool to expose the SU-8 to the microchannel and micropillar designs that

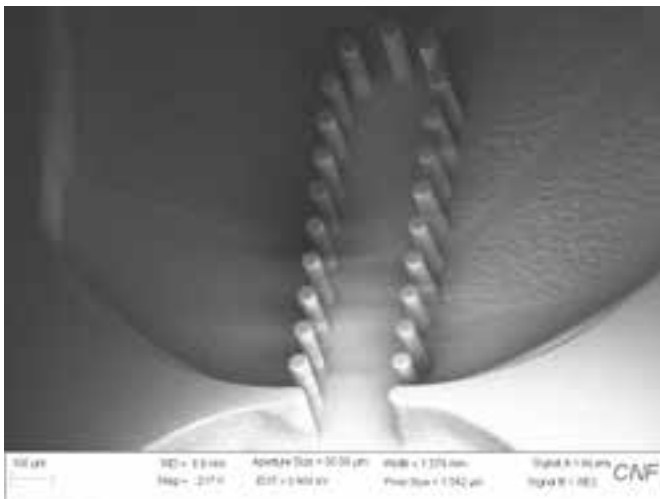


Figure 1: An image of the micropillar section of the microchannel that has been captured with a scanning electron microscope (SEM).

were fabricated on the photolithography mask then a post exposure bake was carried out to prepare the SU-8 for development. The development phase included submerging the wafer upside down in SU-8 developer to remove the SU-8 from the unexposed part of the SU-8 layer. At the end of the SU-8 development process, the wafer was rinsed with isopropanol and SU-8 developer, and then blow dried with nitrogen.

To fabricate the top part of the device, double-coated film bonding tape was attached to a cleaned bare Borofloat wafer. A CO₂ laser machine drilled the holes into the top wafer by vaporizing the substrate. These holes were arranged in a way that after attaching to the bottom wafer, the contact pads would be accessible to operate the heaters. Next, the flow inlet and outlet on the bottom wafer were drilled. Top and bottom wafer was taken to the contact aligner once again to be attached to each other precisely. The final step in the fabrication process was cutting the wafer. A dicing saw was employed to cut the marked lines on the wafer to separate it into individual devices.

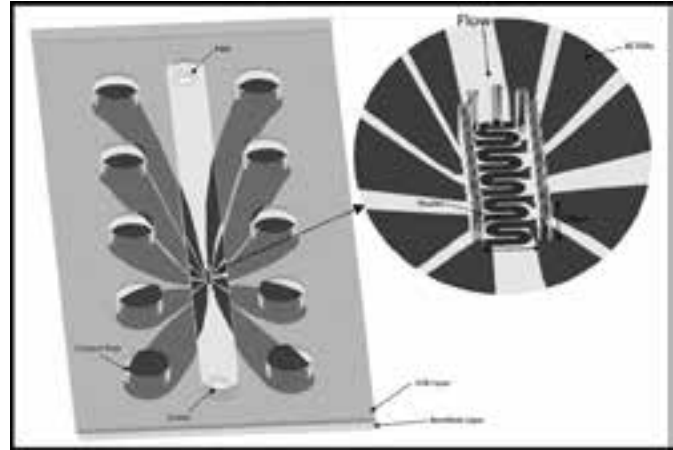


Figure 2: Schematic illustration of microchannel, which consists of arrays of micropillars within.

Lithium Niobate Photonic Crystal Nanocavities

CNF Project Number: 1997-11

Principal Investigator: Qiang Lin

Users: Hanxiao Liang, Mingxiao Li

Affiliation: Department of Electrical and Computer Engineering, University of Rochester

Primary Source of Research Funding: National Science Foundation (ECCS-1509749, ECCS-1610674)

Contact: qiang.lin@rochester.edu, hanxiao.liang@rochester.edu, mli53@ur.rochester.edu

Website: <http://photonlab.hajim.rochester.edu/>

Primary CNF Tools Used: JEOL 9500 electron-beam lithography, AJA ion mill

Abstract:

Lithium niobate, with its wide applications in optics and mechanics, is a chemically inert material, and fabrication techniques for microscale and nanoscale structures of lithium niobate are to be developed. In this report, we demonstrate fabricating high-quality lithium niobate 1D and 2D photonic crystal cavities, using electron beam lithography and ion milling. Our devices exhibit high optical Q factors, paving the way for cavity nonlinear optics and cavity opto-mechanics of lithium niobate.

Summary of Research:

Lithium niobate (LN) exhibits outstanding electro-optic, nonlinear optical, acousto-optic, piezoelectric, photorefractive, pyroelectric, and photoconductive properties, that have found very broad applications in telecommunication, nonlinear/quantum photonics, microelectromechanics, information storage and sensing, among many others. Recently, significant interest has been attracted to develop LN photonic devices on chip-scale platforms, which have shown significant advantage in device engineering compared with conventional approaches [1-4]. Miniaturization of device dimensions dramatically enhances optical field in the devices which enables a variety of nonlinear optical, quantum optical, and optomechanical functionalities. In our work, we demonstrate LN 1D and 2D photonic crystal with more than optical Q around 10^5 , more than two orders of magnitude higher than other LN nanocavities reported to date. In our 1D LN photonic crystal, the high optical quality together with tight mode confinement leads to extremely strong nonlinear photorefractive effect, with a resonance tuning rate of ~ 0.64 GHz/aJ, or equivalently ~ 84 MHz/photon, three orders of magnitude greater than other LN resonators. In particular, we observed intriguing quenching of photorefractive effect that has never been reported before. The devices also exhibit strong optomechanical coupling with gigahertz nanomechanical mode with a significant $f \cdot Q$ product of 1.47×10^{12} Hz.

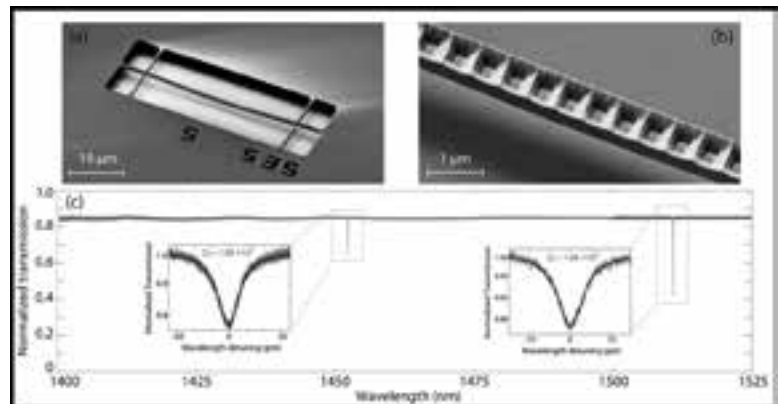


Figure 1: (a) (b) SEM images of a LiNbO_3 photonic crystal nanobeam. (c) Normalized transmission spectrum of the photonic crystal cavity, measured by two tunable lasers operating at different wavelength ranges (indicated as black and grey curves). Insets show detailed transmission spectra of the fundamental TE (TE_0) mode and second-order TE (TE_1) mode, respectively.

The fabrication process of our devices is pretty standard. First, we start with an X-cut lithium niobate-on-insulator wafer, which has a device layer of 300 nm sitting on a buried silicon oxide layer of $2 \mu\text{m}$; then we spin ZEP-520A on the top of the wafer, and do patterning with JEOL 9500 electron beam lithography. Second, lithium niobate is etched with AJA ion milling, with ZEP-520A as the mask. Next, the remaining resist is removed by YES Asher oxygen plasma etcher. Finally, diluted hydrofluoric acid is utilized to remove buried silicon oxide and release our suspended structures.

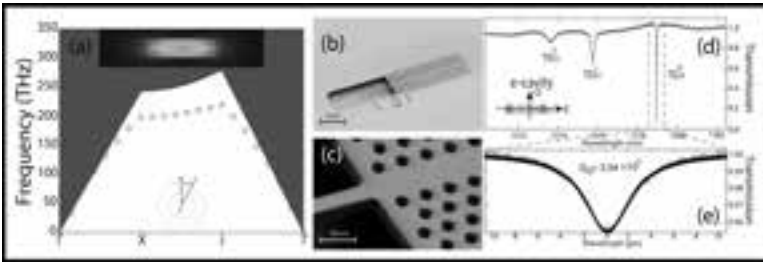


Figure 2: (a) Dispersion property of the fundamental transverse-electric-like (TE-like) guided mode inside the designed 2D photonic crystal slab. Optical mode field profiles of the fundamental mode are shown on the top. (b) Scanning electron microscopic image of a fabricated 2D LN PhC slab. (c) Zoom-in image of a section of the photonic crystal slab. (d) Laser-scanned transmission spectrum of an e-cavity. (e) Detailed transmission spectra of the fundamental cavity modes, with the experimental data shown in grey and the theoretical fitting shown in black.

Figure 1 (a)(b) shows the SEM images of a LiNbO_3 photonic crystal nanobeam, which show clearly the quality of device etching and dimension control. By launching a continuous-wave tunable laser into the cavity with a tapered optical fiber and monitoring the cavity transmission, we obtained the cavity transmission spectrum shown in Figure 1(c) for the transverse electric (TE) optical field with polarization lying in the device plane. Figure 1(c) shows two distinct cavity modes located at 1452 and 1511 nm, which correspond to the fundamental (TE₀) and second-order (TE₁) TE modes of the device, respectively. In particular, the two cavity modes exhibit optical Q as high as 1.09×10^5 and 1.08×10^5 , respectively, which are more than two orders of magnitude higher than current state-of-the-art LN photonic crystal devices.

Figure 2 shows our design and fabrication result for our 2D LN photonic crystal. The dispersion property

of the fundamental transverse-electric-like (TE-like) guided mode inside the designed 2D photonic crystal slab is shown in Figure 2 (a). Optical mode field profiles of the fundamental mode are shown on the top. The scanning electron microscopic image of a fabricated 2D LN PhC slab, shown in Figure 2 (b) and Figure 2 (c), indicates our high etching quality. For convenience, we denote the one perpendicular to the optical axis as an e-cavity since the dominant electric field polarizes along the optical axis, corresponding to the extraordinary polarization (Figure 2 (d)). Accordingly, we denote the one in parallel with the optical axis as an o-cavity as the dominant cavity field polarizes along the ordinary polarization. The highest Q we achieved in our O-cavity is 3.34×10^5 . In particular, the peculiar anisotropy of photorefraction quenching and unique anisotropic thermo-optic nonlinear response have never been reported before.

In conclusion, we have developed the fabrication of high quality photonic crystal on lithium niobate-on-insulator platform using electron beam lithography and ion milling. High-quality etching of lithium niobate is verified by 1D photonic crystal nanocavities with Q of 10^5 and 2D photonic crystal nanocavities with Q of 3.34×10^5 . Our work is of great potential for nonlinear optics, quantum photonics of lithium niobate on chip.

References:

- [1] M. Roussey, et al., Appl. Phys. Lett. 89, 241110 (2006).
- [2] G. Zhou and M. Gu, Opt. Lett. 31, 2783 (2006).
- [3] N. Courjal, et al., Appl. Phys. Lett. 96, 131103 (2010).
- [4] R. Geiss, et al., Appl. Phys. Lett. 97, 131109 (2010).

Lithium Niobate Nanophotonic Waveguides for Tunable Second-Harmonic Generation

CNF Project Number: 1997-11

Principal Investigator: Qiang Lin

Users: Rui Luo, Yang He

Affiliation: Department of Electrical and Computer Engineering, University of Rochester

Primary Sources of Research Funding: National Science Foundation (ECCS-1641099, ECCS-1509749), DARPA (W31P4Q-15-1-0007)

Contact: qiang.lin@rochester.edu, ruiluo@rochester.edu, yhe26@ur.rochester.edu

Website: <http://photonlab.hajim.rochester.edu/>

Primary CNF Tools Used: JEOL 9500 electron beam lithography, AJA ion mill

Abstract:

We report on-chip second-harmonic generation (SHG) that simultaneously achieves a large tunability and a high conversion efficiency inside a single device. We utilize the unique strong thermo-optic birefringence of LN to achieve flexible temperature tuning of type-I inter-modal phase matching. We experimentally demonstrate spectral tuning with a tuning slope of 0.84 nm/K for a telecom-band pump, and a nonlinear conversion efficiency of 4.7% W⁻¹, in a LN nanophotonic waveguide only 8 mm long.

Summary of Research:

Lithium niobate (LN) has attracted considerable attention in nonlinear optics for decades, due to its wide bandgap and large $\chi^{(2)}$ nonlinearity that support efficient second-harmonic generation (SHG), sum-/difference-frequency generation, and parametric down-conversion, which are conventionally enabled by quasi-phase matching in periodically-poled LN waveguides made from reverse proton exchange [1-3]. Recent advance in LN nonlinear photonics has shown the great advantages of the LN-on-insulator platform, which exhibits not only sub-micron mode confinement that enhances nonlinear conversion efficiencies, but also more degrees of freedom in waveguide geometry for dispersion engineering [4-8], which offer potentials for novel functionalities. Here, we demonstrate highly-efficient thermal control of phase-matched wavelengths for SHG in a LN nanophotonic waveguide, with a measured tuning slope of 0.84 nm/K for a telecom pump [9]. Our device is of great potential for on-chip wavelength conversion that produces highly-tunable coherent visible light, essential for various integrated photonic applications such as particle and chemical sensing in aqueous environments, while taking advantage of the mature telecom laser technology.

In order to effectively tune the phase-matching window of SHG, we need a controlling mechanism that is able to induce a significant relative change in effective indices at the two involved wavelengths. We take advantage of the large thermo-optic birefringence of LN, i.e.

$$\left| \frac{dn_e}{dT} \right| \gg \left| \frac{dn_o}{dT} \right|,$$

which allows us to introduce disparate index changes between two interband modes with orthogonal polarizations, by simply varying the temperature [10,11]. This effect is maximized on a Z-cut wafer, which supports high-purity polarization modes. Thus, in a Z-cut LN waveguide [see Figure 1(a)], we designed the geometry for phase matching between $TE_{0,tele}$ in the telecom and $TM_{2,vis}$ in the visible [see Figure 1(b)(c)]. As presented in Figure 1(d)(e), by simulation with the finite-element method (FEM) that takes temperature- and wavelength-dependent thermo-optic effects into account [10], we get a phase-matched pump wavelength λ_{PM} of around 1540 nm at $T = 20^\circ\text{C}$, and it is shifted to 1574 nm at $T = 70^\circ\text{C}$, with a fitted tuning slope of 0.69 nm/K [see Figure 1(f)].

To confirm our simulation results, we fabricated waveguides on a Z-cut LN-on-insulator wafer with electron-beam lithography and ion milling [6,9,11]. Scanning electron microscope (SEM) pictures [see Figure 2(a), insets] show very smooth sidewalls, indicating a low propagation loss. Then we conducted experiments for SHG, with the setup shown in Figure 2(a), where pump light from a continuous-wave tunable telecom laser is coupled into a LN waveguide via a lensed fiber, and collected together with the frequency-doubled

light by a second lensed fiber; after being separated from its second-harmonic by a 780/1550 WDM, the telecom pump light is directed to an InGaAs detector for monitoring, while the generated visible light is sent to a spectrometer for detection. We employed a waveguide with a length of about 8 mm. The fiber-to-chip coupling loss is about 5 dB/facet, and the waveguide propagation loss is estimated to be 0.54 dB/cm. By scanning the laser wavelength, we could find pump wavelengths that generate second-harmonic light.

As shown in Figure 2(b), at $T = 18.7^\circ\text{C}$, significant SHG is achieved by pump light around 1559 nm, with a sinc²-like spectrum, from which we extract a peak conversion efficiency of $4.7\% \text{W}^{-1}$. As we increase the device temperature, λ_{PM} , the phase-matched pump wavelength that exhibits the peak conversion efficiency, is gradually shifted to longer wavelengths.

As shown in Figure 2(c), the experimentally measured $d\lambda_{\text{PM}}/dT$ is 0.84 nm/K , which agrees very well with our

simulation [see Figure 1(f)]. The larger experimental value potentially results from a positive contribution by pyroelectric and thermo-expansion effects that were not considered in the simulation.

References:

- [1] M. M. Fejer, et al., IEEE J. Quantum Electron. 28, 2631 (1992).
- [2] N. I. Yu, et al., Opt. Lett. 27, 1046 (2002).
- [3] H. Jin, et al., Phys. Rev. Lett. 113, 103601 (2014).
- [4] L. Chang, et al., Optica 3, 531 (2016).
- [5] J. Lin, et al., Phys. Rev. Appl. 6, 014002 (2016).
- [6] C. Wang, et al., Opt. Express 25, 6963 (2017).
- [7] A. Rao, et al., Appl. Phys. Lett. 110, 111109 (2017).
- [8] R. Luo, et al., Opt. Express 25, 24531 (2017).
- [9] R. Luo, et al., arXiv:1804.03621 (2018).
- [10] L. Morettia, et al., J. Appl. Phys. 98, 036101 (2005).
- [11] R. Luo, et al., Opt. Lett. 42, 1281 (2017).

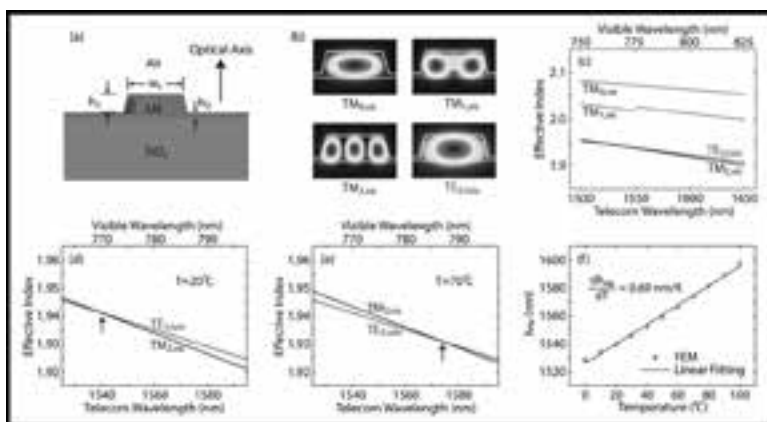


Figure 1: (a) Schematic of our Z-cut LN waveguide. FEM simulation of (b) mode profiles, and (c) effective indices as functions of wavelength, of $\text{TE}_{0,\text{tele}}$ in the telecom band and $\text{TM}_{j,\text{vis}}$ ($j = 0, 1, 2$) in the visible, where $w_t = 1200 \text{ nm}$, $h_1 = 460 \text{ nm}$, $h_2 = 100 \text{ nm}$, and $\theta = 75^\circ$, at 20°C . The discontinuity in the effective index of $\text{TM}_{1,\text{vis}}$ is due to its coupling with $\text{TE}_{2,\text{tele}}$ (not shown). Zoom-in of the wavelength-dependent effective indices of $\text{TE}_{0,\text{tele}}$ and $\text{TM}_{2,\text{vis}}$ at (d) 20°C , and (d) 70°C , with black arrows indicating phase matching. (f) Simulated λ_{PM} as a function of temperature.

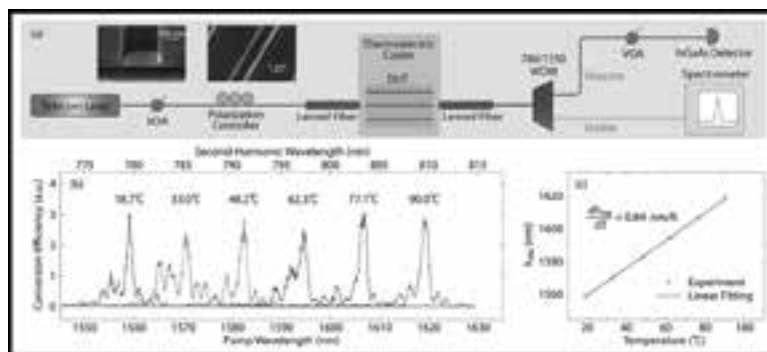


Figure 2: (a) Experimental setup. Insets are SEM pictures showing the waveguide facet and sidewall. (b) SHG spectrum at different temperature. (c) Measured λ_{PM} as a function of temperature.

Rabi-Like Oscillations in Photon Pair Correlations

CNF Project Number: 1997-11

Principal Investigator: Qiang Lin

User: Steven Rogers

Affiliation: Department of Physics and Astronomy, University of Rochester

Primary Source of Research Funding: National Science Foundation (Grant Number: ECCS-1351697)

Contact: qiang.lin@rochester.edu, steven.rogers@rochester.edu

Primary CNF Tools Used: JEOL 9500, UNAXIS 770, YES Asher

Abstract:

We have produced a new quantum coherence phenomenon via photon generation within ultra-high- Q silicon microdisks. The Rayleigh-scattering-induced strong coupling of counterpropagating modes opens up discrete energy pathways for pair creation, leading to Rabi-like oscillations in the biphoton second-order coherence. Additionally, the pump resonance splitting may be used to coherently control the internal structure of the oscillations by enabling the quantum interference between multiple creation pathways.

Summary of Research:

Optical microresonators have proven to be excellent chip-scale sources of heralded single photons and entangled photon pairs [1-3]. In this report, we will show that they possess a new and fascinating functionality not seen in any other system to date. We propose and demonstrate that the Rayleigh-scattering-induced strong coupling between counterpropagating cavity modes within microresonators can be used to achieve Rabi-like oscillations in the biphoton second-order coherence.

Figure 1 illustrates the system and the intracavity processes that lead to this phenomenon. A scanning electron microscope image of the actual silicon microdisk is shown in the inset, with a radius of $4.5 \mu\text{m}$, thickness of 260 nm and average intrinsic optical Q s above one million. The device pattern was defined using the JEOL 9500 electron beam lithography system and transferred to the silicon layer using the UNAXIS 770 etcher. A pump laser is evanescently coupled into the microdisk, wherein cavity-enhanced spontaneous four-wave mixing (SFWM) occurs between the pump (p), signal (s) and idler (i) modes. In the absence of a coupling mechanism, each cavity mode admits two degenerate eigenmodes, forward and backward traveling. However, the extreme enhancement of the light-matter interaction strength in our system enables the small Rayleigh scattering at the boundary of the cavity to induce a strong coupling between the forward and backward modes, which manifests as the well-known resonance splitting [4]. Thus, the single photons may coherently cycle between forward and backward modes, as depicted by the use of bidirectional arrows in Figure 1. The photons are coupled out of the cavity and detected by superconducting nanowire single-photon detectors. A coincidence counter histograms the detection of photon pairs as a function of their arrival time differences, which yields the biphoton coherence waveforms, $g^{(2)}(\tau)$, seen in Figures 2-4.

In analogy to the formation of dressed states in an atom-cavity system [5], the strong coupling between counterpropagating modes implies that it is no longer possible to describe forward or backward independently. And given that the biphoton coherence properties are

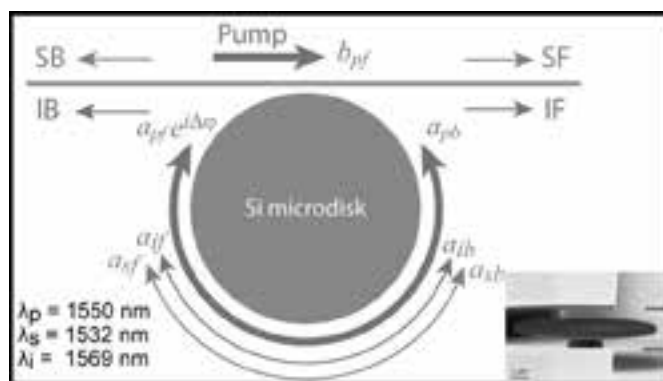


Figure 1: Illustration of the intracavity physics leading to oscillations in the biphoton correlations. The input pump field is evanescently coupled into intracavity pump mode, leading to spontaneous four-wave mixing. The intracavity fields are labeled a_j , where $j = p, s, i$ for pump, signal and idler, respectively, and $k = f, b$ denotes forward and backward. Signal (S) and idler (I) photons are coupled from the optical cavity into the waveguide in the forward (F) and backward (B) directions, resulting in four path configurations for cross-correlations. The inset depicts a scanning electron microscope image of the suspended silicon microdisk.

established by the cavity [6], we expect that the strong coupling must be imprinted on the biphoton correlations. This is precisely what we observe in Figures 2-4.

The measured biphoton correlations display a stunning difference compared with other chip-scale sources, which exhibit monotonically decaying profiles. In Figure 2, we see that at certain delay times the photon pairs in the signal forward-idler forward (SF-IF) channels are highly correlated, then diminish to nearly zero, before being revived in an oscillatory manner.

Figure 3 depicts the biphoton correlations between the signal forward-idler backward (SF-IB) channels. Here, we clearly see a complementary effect compared to Figure 2. Taken together, we understand that as the correlations are diminishing in the copropagating configuration they are intensifying in the counterpropagating configuration, and vice versa. Thus biphoton correlations oscillate between configurations, and an estimate of the modulation period infers that the process originates from a resonance splitting of approximately 1 GHz, which is in good agreement with the measured splitting of the signal and idler resonances.

In Figure 4, we measure the biphoton correlations for the SF-IB configuration using two different values of pump-cavity frequency detuning. Although we are measuring the same channel configuration, we are able to achieve oscillatory features that are completely out of phase with each other. Varying the detuning causes the counterpropagating intracavity pump fields to develop different relative phases (see Figure 1), which may be used to conveniently control the oscillations.

We have shown for the first time that optical microresonators can be used to achieve Rabi-like oscillations in photon pair correlations. We have also demonstrated that the oscillations may be controlled by varying the relative phase of the counterpropagating intracavity pump fields. Given the vital role that second-order coherence assumes in many quantum photonic systems [7], we expect that this new phenomenon will have a broad impact. Photon pairs produced by SFWM are intrinsically time-energy entangled, and we have demonstrated that their correlation properties may be highly coupled to the path configuration of our system. Consequently, we envision that our device may be used to explore quantum state generation and new entanglement properties, as well as the potential for quantum logic operations.

References:

- [1] D. V. Strekalov, et al. *J. Opt.* 18, 123002 (2016).
- [2] X. Lu, et al. *Optica* 3, 1331-1338 (2016).
- [3] S. Rogers, et al. *ACS Photonics* 3, 1754-1761 (2016).
- [4] D. S. Weiss, et al. *Opt. Lett.* 20, 1835-1837 (1995).
- [5] R. J. Thompson, et al. *Phys. Rev. Lett.* 68, 1132-1135 (1992).
- [6] X. Lu, et al. *ACS Photonics* 3, 1626-1636 (2016).
- [7] J. O'Brien, et al. *Nat. Photonics* 3, 687-695 (2009).

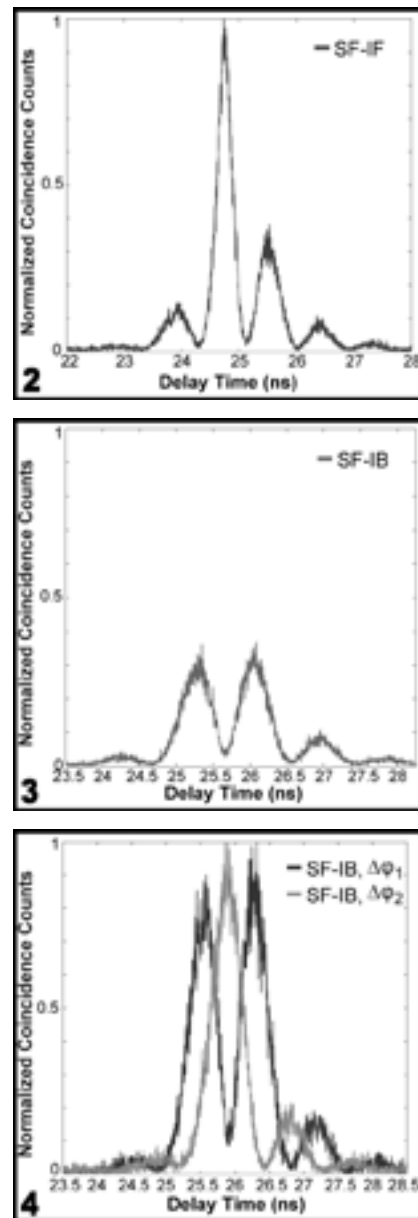


Figure 2, top: Cross-correlation between signal forward (SF) and idler forward (IF). Figure 3, middle: Cross-correlation between signal forward (SF) and idler backward (IB). Figure 4, bottom: Cross-correlation between signal forward (SF) and idler backward (IB), with the black data taken with the counterpropagating intracavity pump modes in phase and the light gray data taken with a relative phase shift of nearly 180 degrees.

X-Ray Transmission Optics Development

CNF Project Number: 2172-12

Principal Investigators: Arthur Woll², Joel Brock^{2,3}, Ernie Fontes²

User: David Agyeman-Budu¹

Affiliations: 1. Materials Science and Engineering, 2. Cornell High Energy Synchrotron Source (CHESS), 3. Applied and Engineering Physics; Cornell University

Primary Sources of Research Funding: CHESS is supported by the NSF and NIH/NIGMS via NSF award DMR-1332208

Contact: aw30@cornell.edu, jdb20@cornell.edu, ef11@cornell.edu, da76@cornell.edu

Website: <http://www.chess.cornell.edu/>

Primary CNF Tools Used: Plasma-Therm deep Si etcher, Xactix XeF₂ etcher

Abstract:

We report the development and performance tests of x-ray transmission mirrors (XTM) fabricated using a new process that is both simpler and has higher yield than prior techniques. The new approach requires only two etch steps, and yet yields more structurally stable devices and accommodates greater versatility for tailoring devices to specific applications. The performance of these devices, namely their transmission and reflection characteristics in the x-ray regime, were tested at the G2 station at the Cornell High Energy Synchrotron Source and agree with theoretical models.

Summary of Research:

X-ray transmission mirrors (XTMs) are a novel class of x-ray optics. As with traditional x-ray mirrors, they operate on the principle of total external reflection (TER): for a given incidence angle, only x-ray energies below a certain critical angle are reflected, so that the mirror acts as a low-pass filter for x-rays. However, unlike a regular x-ray mirror, XTMs transmit the incident x-ray beam rather than absorbing it and can thus act as an efficient high-pass filter. This operating mechanism is illustrated in Figure 1. Because XTMs operate at glancing incident angles, transmitting the incident beam with minimal absorption losses requires XTMs to be designed as thin as possible.

Despite being introduced over 30 years ago [1], XTMs have not been adopted widely in the synchrotron community owing, primarily, to practical challenges of fabricating such optics to be structurally stable. There are many potential applications of XTMs. First, they function as a high-pass x-ray energy filter with sharper energy cut-off and rejection than absorption filters [1,2]. Secondly, together with a total reflection mirror, transmission mirrors can be used as a high flux, tunable x-ray bandwidth optic for applications such as Laue diffraction [3]. They also show promise as a front-end x-ray optic to alleviate the high heat load of a white x-ray beam by reflecting the lower energy components of the spectrum. In this report, we present a new nanofabricated approach developed to fabricate XTMs in a silicon wafer substrate that has resulted in a higher yield of XTIM optics fabricated.

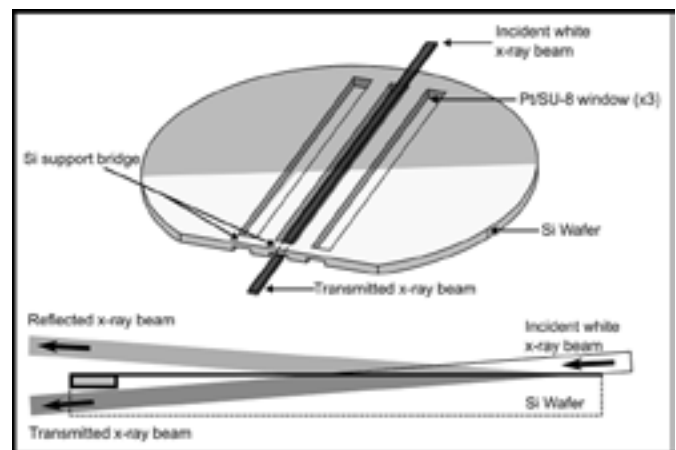


Figure 1: The drawing of a transmission mirror optic showing a 3D representation (top) and a 2D cross-sectional view (bottom) illustrating the mode of operation. By taking advantage of aspect ratio dependent etching (ARDE), a bridge as indicated is created at the downstream of the optic, which functions as the supporting structure for holding up the thin XTM.

Figure 1 shows the principle of operation of an XTM operating at glancing angles. Ideally, the exit path of both the reflected and transmitted beam after interacting with the mirror must be clear. This requirement indicates there should not be any structures at the downstream of wafer in the path where the beam exits the mirror. To avoid blocking the reflected beam, our XTM design was made to support the membrane from the bottom. This support structure was accomplished with a custom

designed etch mask designed to induce a spatial etch rate variation on same wafer using a single deep reactive etch (DRIE) run. In this case, we get to choose which areas of the final optic etches faster and which areas are etched slower.

Starting with a double-side polished silicon wafer, a silicon dioxide etch mask is patterned on the backside to define the eventual support frame of the XTM when the wafer is etched deep. A special, thin formulation of SU-8 (SU-8 TF 6000, ~ 300 nm thick) is spun-on the front side of the wafer. Because the SU-8 film functions as the template membrane for the XTM mirror, care is taken to ramp up the spin speed of the wafer chuck to minimize the overall wafer thickness variation of the SU-8 film. To crosslink the SU-8, a flood exposure on the SÜSS MicroTec MA6 for 4s at a power of 12 mW/cm² is enough, which is followed by a 300°C 3hr anneal to relieve any inherent stresses built-up in the SU-8. A 10-nm thick platinum film is sputtered over the SU-8 on the topside of the wafer. The rest of the processing is a deep reactive ion etch (DRIE) on the backside to create the XTM windows after which an isotropic XeF₂ etch finishes off the support bridge structures of the XTM and clears any residual silicon to fully expose the XTM window membranes.

The mirrors were tested at the G2 station at the Cornell High Energy Synchrotron Source (CHESS). The incident beam used was a 0.1 mm tall by 0.5 mm wide x-ray beam. The mirror was then rocked in the beam while the reflection and transmission response was recorded by the MYTHEN single-photon-counting silicon microstrip detector located further downstream of the mirror.

Figure 2 shows the 2D plot of the captured reflection and transmission response for each rotation angle. Integrating the reflected and transmitted beam intensities shows the complementary response function of the mirror which agrees to the predicted behavior as seen in Figure 3.

References:

- [1] Lairson, B. M., and D. H. Bilderback. "Transmission x-ray mirror -A new optical element." Nuclear Instruments and Methods in Physics Research 195, no. 1-2 (1982): 79-83.
- [2] Cornaby, Sterling, and Donald H. Bilderback. "Silicon nitride transmission X-ray mirrors." Journal of synchrotron radiation 15, no. 4 (2008): 371-373.
- [3] S. Cornaby, D. M. E. Szebenyi, D.-M. Smilgies, D. J. Schuller, R. Gillilan, Q. Hao and D. H. Bilderback. "Feasibility of one-shot-per-crystal structure determination using Laue diffraction." Acta Crystallographica Section D: Biological Crystallography 66, no. 1(2010): 2-11.

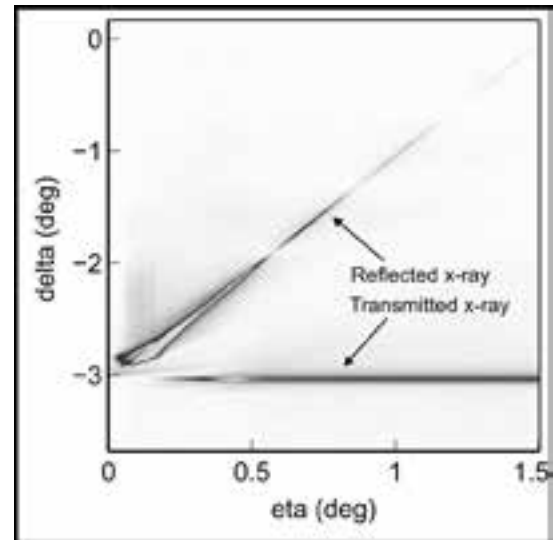


Figure 2: A 2D representation of the reflected and transmitted beam exiting an XTM optic at different incident grazing angles.

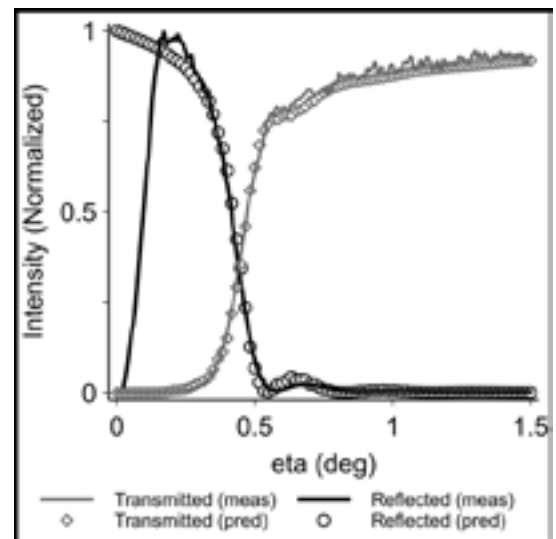


Figure 3: Measured (scaled) and calculated integrated intensities of the reflected and transmitted x-ray beams.

TiO₂ Slot Waveguide for Efficient On-Chip Raman Spectroscopy

CNF Project Number: 2255-13

Principal Investigator: Jin Suntivich^{1,2}

User: Chengyu Liu³

Affiliations: 1. Materials Science and Engineering Department, 2. Kavli Institute at Cornell for Nanoscale Science, 3. School of Applied and Engineering Physics; Cornell University

Primary Source of Research Funding: Samsung Advanced Institute of Technology (SAIT)

Contact: js2765@cornell.edu, CL986@cornell.edu

Primary CNF Tools Used: PVD75 sputter deposition, AJA sputter deposition, JEOL 9500, PT770 etcher, Oxford 100 etcher

Abstract:

On-chip integrated Raman spectroscopy offers an attractive route to on-chip sensing, owing to its portability and signal enhancement in comparison to conventional Raman spectroscopy [1-3]. In order to further improve the Raman conversion efficiency over the previous work, we design a titanium dioxide (TiO₂) slot waveguide, which has a stronger overlap with the surrounding molecule and a reduced mode volume, which when combined with the high refractive index of TiO₂, allows the theoretical conversion efficiency to be five times higher than strip waveguides. We fabricate the proposed TiO₂ slot waveguides using a combination of e-beam lithography and chromium (Cr) hard mask. The propagation loss is about 15 dB/cm at 780 nm wavelength, which makes this platform promising for the next-generation integrated on-chip Raman sensors.

Summary of Research:

Fully-integrated on-chip Raman sensors are a critically needed technology for medical diagnostics, threat detection, and environmental-quality monitoring. By utilizing a waveguide design using the evanescent field outside of a dielectric to pump and collect Raman scattering, we have demonstrated an integrated-evanescent Raman sensor on TiO₂ [2]. In order to further improve this on-chip Raman sensing platform, we propose a slot waveguide structure that has an air gap between two parallel bus waveguides to improve the Raman efficiency. In this slot waveguide structure, the electric field discontinuity at the TiO₂/air interface leads to a high confinement of the optical field in the slot region, which makes this structure appealing for sensing applications.

We fabricate the proposed TiO₂ slot waveguides using a combination of e-beam lithography and Cr hard mask. The fabrication flow is shown in Figure 1. Since the design slot width is around 100 nm, which is beyond the resolution of conventional photolithography, we switch to e-beam lithography from our previous work [2].

We start with a silicon substrate with thermal oxide on top and sputter TiO₂ thin film using PVD75 deposition tool. Above TiO₂ thin film, we first sputter a thin layer of Cr as a hard mask and then the e-beam resist for e-beam lithography (Figure 1a). After e-beam exposure and development (Figure 1b), we transfer the slot pattern to Cr layer by dry etching in PT770 ICP (Figure 1c). Then we remove the residual e-beam resist by oxygen plasma (Figure 1d) and transfer the slot pattern to TiO₂ layer by dry

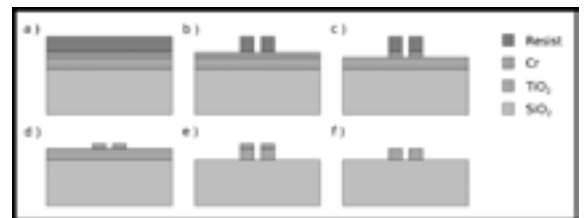


Figure 1: The fabrication process of TiO₂ slot waveguides.

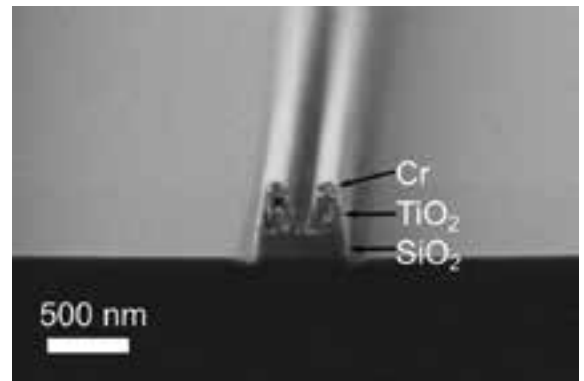


Figure 2: A SEM image of the TiO₂ slot structure after TiO₂ dry etching.

etching in Oxford 100 ICP (Figure 1e). Finally, we remove the Cr hard mask by wet etch (Figure 1f) to form TiO₂ slot waveguides. Figure 2 is a representative scanning electron micrograph (SEM) of the cross section of a fabricated TiO₂ slot waveguide after TiO₂ dry etching step. By utilizing a thin layer of Cr as the hard mask for TiO₂ etch, we are able to define an air gap between two parallel bus waveguides for Raman sensing purpose.

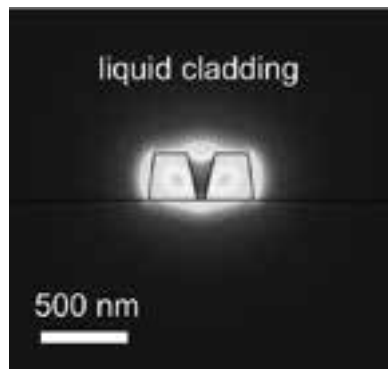


Figure 3: Calculated guiding mode profile of the slot waveguide structure at 780 nm.

In order to characterize this device's performance, we measure the propagation loss using the top-view camera method around 780 nm wavelength in air. We couple a 780 nm laser light into the slot waveguide by an objective lens and capture the waveguide scattering by a camera mounted on the top. We measure the scattering as a function of waveguide length, subtracting the average baseline signal (non-zero dark regions away from the waveguide), and plot the scattering intensity as a function of distance. Then we fit this data to a linear regression model and extract a loss value of about 15 dB/cm. Compared with the previous result by a conformal atomic layer deposition re-coating method to create TiO₂ slot waveguides (767 dB/cm at 664 nm wavelength) [4], our fabrication method has dramatically decreased the device propagation loss, which makes this platform more practical for on-chip Raman sensing application.

We notice that TiO₂ slot etching generates non-vertical sidewalls, so we include those dimension changes and simulate the mode profile in our TiO₂ slot waveguide structure. Figure 3 shows that our fabricated slot structure can support a quasi-TE guiding mode, which is highly confined in the gap region. Based on our previous model of waveguide-based spontaneous Raman scattering conversion efficiency η_0 [2], η_0 is related to the overlap

between guiding light and sensing chemistry. This quasi-TE mode in the slot structure has a stronger overlap with the surrounding molecule than that in strip waveguides, which makes the slot waveguide structure more in favor of Raman sensing than a strip waveguide structure. Our calculation reveals that our TiO₂ slot waveguide design has a five-fold η_0 than optimized strip waveguides that were made of TiO₂ as well.

In conclusion, we propose a slot structure on TiO₂ integrated optics platform for efficient on-chip Raman sensing. We fabricate TiO₂ slot waveguides and the low loss (15 dB/cm) of our TiO₂ waveguide puts it as one of the best performing slot waveguide. Future work will focus on the control of the fabrication variation and repeatability and the demonstration of high-performance sensing.

References:

- [1] Dhakal, A., Subramanian, A. Z., Wuytens, P., Peyskens, F., Le Thomas, N., and Baets, R. (2014). Evanescent excitation and collection of spontaneous Raman spectra using silicon nitride nanophotonic waveguides. *Optics letters*, 39(13), 4025-4028.
- [2] Evans, C. C., Liu, C., and Suntivich, J. (2016). TiO₂ Nanophotonic sensors for efficient integrated evanescent Raman spectroscopy. *ACS Photonics*, 3(9), 1662-1669.
- [3] Dhakal, A., Wuytens, P., Peyskens, F., Subramanian, A., Skirtach, A., Le Thomas, N., and Baets, R. (2015, May). Nanophotonic lab-on-a-chip Raman sensors: A sensitivity comparison with confocal Raman microscope. In *BioPhotonics (BioPhotonics)*, 2015 International Conference on (pp. 1-4). IEEE.
- [4] Häyriinen, M., Roussey, M., Säynätjoki, A., Kuittinen, M., and Honkanen, S. (2015, February). Slot waveguide ring resonators for visible wavelengths in ALD titanium dioxide. In *Integrated Optics: Devices, Materials, and Technologies XIX* (Vol. 9365, p. 936513). International Society for Optics and Photonics.

Developing Full Wafer Blazed Grating Fabrication Method Using Stepper

CNF Project Number: 2292-14

Principal Investigator: Cori Bargmann

Users: Sara Abrahamsson, Philip Kidd

Affiliation: Lulu and Anthony Wang Laboratory for Neural Circuits and Behavior, Rockefeller University, NYC NY

Primary Source of Research Funding: Lab funds

Contact: cori.bargmann@rockefeller.edu, sara.abrahamsson@gmail.com

*Primary CNF Tools Used: ASML stepper, Heidelberg DWL2000 Laserwriter,
Oxford 80 etcher, AFM, Hamatech wafer processing tools*

Summary of Research:

With the help of John Treichler and Garry Bordonaro we were able to devise a method to print a blazed grating on an entire 100 mm fused silica ("glass") wafer, and to cut out four standard 29 mm circular filter size pieces from each wafer. These diffractive optical components will be used as a chromatic correction element in a multi-camera microscopy system for 3D imaging of neural circuits.

512-Element Actively Steered Silicon Phased Array for Low-Power LIDAR

CNF Project Number: 2364-15

Principal Investigator: Michal Lipson

Users: Steven A. Miller, Christopher T. Phare, You-Chia Chang, Xingchen Ji, Oscar A. Jimenez Gordillo, Aseema Mohanty, Samantha P. Roberts, Min Chul Shin, Brian Stern, Moshe Zadka

Affiliation: Department of Electrical Engineering, Columbia University, New York, NY 10027

Primary Source of Research Funding: DARPA

Contact: ML3745@columbia.edu, spr2127@columbia.edu

Website: lipson.ee.columbia.edu

Primary CNF Tools Used: BOSCH etcher, AJA sputter deposition, CVC sputter deposition, Cu electroplating tanks, Oxford 100 ICP RIE

Abstract:

Solid-state beam steering using large-scale optical phased arrays is of great interest for LIDAR and free-space communication systems, enabling wide-angle, long distance ranging or transmission of data in a robust platform. Ideally, a widely steerable narrow output beam that can reach to long distances requires a large aperture containing a large number of independently phase-controlled elements while remaining at a reasonable total power consumption. Applications at distances of tens to hundreds of meters require element-counts of several thousands, such that independent phase control overwhelmingly dominates power consumption and has prohibited larger element-count demonstrations thus far. We demonstrate the highest yet-reported element count actively-steered optical phased array with record low array power consumption of < 1.8 W. We show 2D steering over a $70 \times 14^\circ$ field of view while pumped by an integrated InP/silicon laser.

Summary of Research:

Here, we demonstrate low-power 2D beam steering with a 512-element active silicon optical phased array—to our knowledge the largest independently controllable phased array to date. We achieve low power operation by using a resonance-free light recycling device to recirculate light multiple times through a single thermo-optic phase shifter, thus multiplying its efficiency by approximately the number of circulations [1]. We place a 5-pass light recycling structure on every element (Figure 1b). Phase shifter power and voltage is sufficiently low to be directly driven by off-the-shelf digital to analog converter integrated circuits. The input laser light is split in a binary splitter tree into 512 channels, each of which then have a high-efficiency thermo-optic phase-shifter. The phase-shifters are separated by $20 \mu\text{m}$ to minimize thermal crosstalk, and are then fanned-in to a $1.3 \mu\text{m}$ emitter spacing.

Finally, a 1D array of 1-mm-long sidewall gratings [shown in Figure 1(c)] direct the beam upwards out of the chip and allow for 2D beam steering via wavelength

tuning of our integrated laser in the vertical direction due to the $0.3^\circ/\text{nm}$ wavelength sensitivity of the grating emission. Two layers of aluminum metal on the photonic chip route signals and a common ground to peripheral bond pads, where they are attached to a single layer of aluminum on a silicon interposer. The interposer is then mounted and wire bonded to a standard printed circuit board and its wires routed to control circuitry. The packaged chip is shown in Figure 1(a).

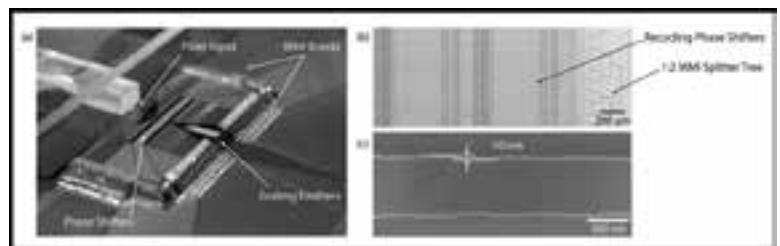


Figure 1: (a) 512-element silicon photonic array chip wire-bonded to interposer. (b) Microscope image of a section of the array of recycling phase shifters and tree of 1:2 MMI splitters (light flows right to left). (c) Scanning electron micrograph of sidewall grating on 450 nm wide emitter waveguide.

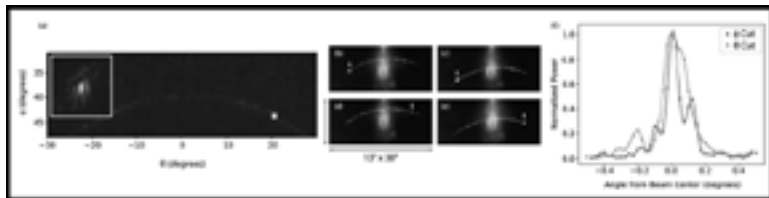


Figure 2: Measured far-field optical power for a beam steered 20° off-axis in the phase-tuned direction. (a) Widefield scan showing beam at 20° off axis. Faint arc is residual power confined by the grating, but not completely confined by the phased array. Inset is a detail $2^\circ \times 2^\circ$ view of the beam. (b-e) Fourier-plane camera images of beams pointed to θ , ϕ of (b) -20° , 42° , (c) -20° , 48° , (d) $+20^\circ$, 42° , (e) $+20^\circ$, 48° . Sidelobe power is exaggerated due to limited camera dynamic range. (f) Cuts in ϕ and θ axes through the center of the beam in (a).

For our laser source, we fabricate an external laser cavity in silicon using vernier ring filters and couple it to an off-the-shelf facet-emitting reflective semiconductor optical amplifier (RSOA). This compact integrated laser source is both broadly tunable over tens of nanometers, while exhibiting sub-MHz narrow linewidth. For this demonstration light is coupled between separate laser and phased array chips with a single mode optical fiber.

We show a 2D-steerable phased array with a beam width of $\sim 0.15^\circ$ in both axes. To converge a single beam for each angle in the 2D phi-theta space and to compensate for as-fabricated phase mismatch between channels, we use a single-element photodiode placed physically in the far-field and a global optimization algorithm [3]. A far-field scan of the beam is shown Figure 2(a) as well as a fine scan in Figures 2(b) and 2(c), showing a peak-to-sidelobe ratio of 8.0 dB. Beam divergence and peak-to-sidelobe in the phase-controlled axis are slightly diminished from the theoretical values of 0.13° and 13 dB due to low phase shifter yield (63%) from a metal-

layer fabrication error. The beam width of 0.15° in the grating axis confirms an effective grating length of approximately 1 mm. We demonstrate 2D beam steering of $\pm 35^\circ$ in the phase-tuned axis (ϕ in Figure 2) and a $\pm 7^\circ$ in the wavelength tuned axis (θ in Figure 2) grating axis by tuning the laser bandwidth over a 45 nm (controlled by microheaters on the vernier ring filters). For accessing any steering point, the phased array consumes 1.5-1.8 W.

This large size array is already adequate for application around 10m operation for ranging or communication applications. Further optimization of our beam-forming algorithm coupled with improved phase-shifter efficiency and additional phase re-circulation can yield several factors improvement to scale up toward hundreds of meters. Considering that the laser efficiency is on the order of 4% [2], for input laser light of 50 mW (corresponding to the maximum output power of typical RSOAs), we estimate total power consumption less than 3W, enabling the array to be operated by a compact battery pack.

References:

- [1] You-Chia Chang, Samantha P. Roberts, Brian Stern, and Michal Lipson, "Resonance-Free Light Recycling." arXiv:1710.02891 (2017).
- [2] Brian Stern, Xingchen Ji, Avik Dutt, and Michal Lipson, "Compact narrow-linewidth integrated laser based on a low-loss silicon nitride ring resonator." Opt. Letters 42, 4541-4544 (2017).
- [3] Christopher T. Phare, Min Chul Shin, Steven A. Miller, Brian Stern, and Michal Lipson, "Silicon Optical Phased Array with High-Efficiency Beam Formation over 180 Degree Field of View." arXiv:1802.04624 (2018).

Wide Bandgap Semiconductor Deep UV Devices

CNF Project Number: 2387-15

Principal Investigator: Debdeep Jena

Users: Kevin Lee, Shyam Bharadwaj

Affiliation: School of Electrical and Computer Engineering, Cornell University

Primary Source of Research Funding: Designing Materials to Revolutionize and Engineer our Future, E70-8276

Contact: djena@cornell.edu, KL833@cornell.edu, sb2347@cornell.edu

Website: <https://sites.google.com/a/cornell.edu/photonic-devices/home>

Primary CNF Tools Used: Veeco Icon atomic force microscope, ABM contact aligner, photolithography tools (spinners, hot plates, solvent hoods), SC4500 e-beam evaporators, AG610 RTA, PT770 ICP etcher, YES Asher, Oxford 81 RIE, profilometers, Filmetrics

Abstract:

Our main research goal is to improve and fabricate deep UV and visible photonic devices (e.g., LEDs and lasers). We grow the semiconductor thin films by molecular beam epitaxy. We use III-Nitride materials to make such devices. For deep UV devices, wide bandgap materials such as AlN, GaN and AlGa_n are the typical materials. *P*-type transport is a major challenge in UV-LEDs. As such, we are working on polarization induced and short period superlattice doping to enhance the active hole concentration in these devices. For visible LEDs, we use tunnel junctions to improve the current spreading and contact resistance.

Summary of Research:

We have grown high aluminum (Al)-content *p*-type transport layers by plasma-assisted molecular beam epitaxy (PA-MBE). These transport layers are grown on MOCVD-grown AlN on sapphire template. Using polarization induced doping, we grew magnesium (Mg)-doped graded AlGa_n layers (grading from 100% Al-content to 65%). We also grew Mg-doped AlGa_n/AlN short period superlattice structures to compare their performance. AFM images taken in CNF and XRD characterizations are shown in Figure 1.

We used standard lithography tools in CNF to fabricate transmission line measurement (TLM) structures on the *p*-type transport layers. Due to large resistivity in these *p*-type transport layers, we were not able to perform Hall measurements. Therefore, we performed temperature dependent TLM to extract the resistivity of our films and activation energy of the Mg dopant. As shown in Figure 2, the graded *p*-AlGa_n structure has improved resistivity over the standard constant *p*-AlGa_n structures. These results have been presented in the 2017 international workshop in UV materials and devices in Japan.

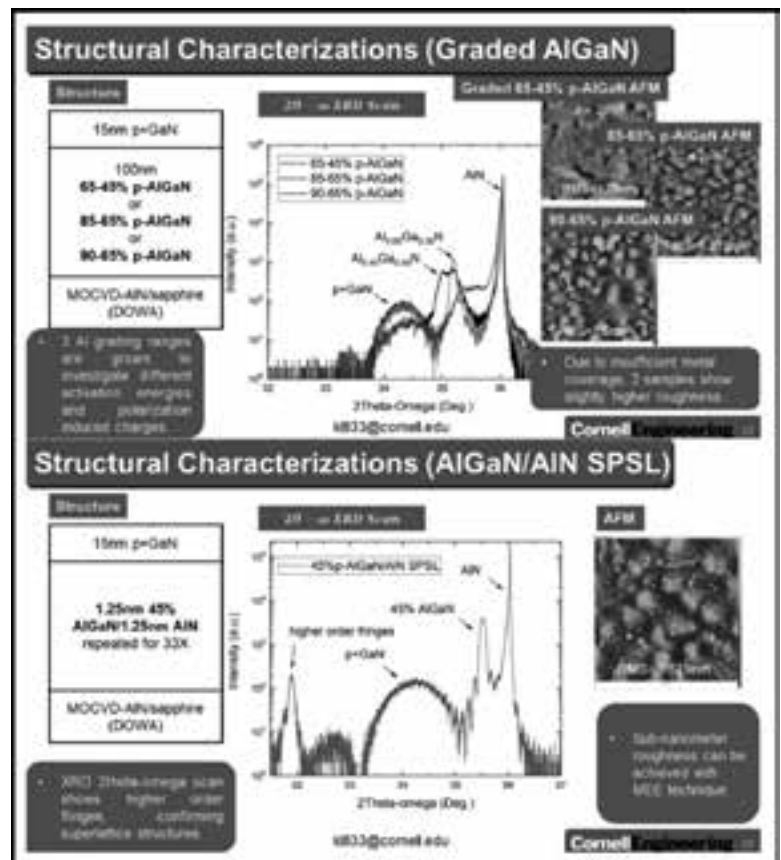


Figure 1: AFMs of grown *p*-type transport layers on AlN/sapphire substrate.

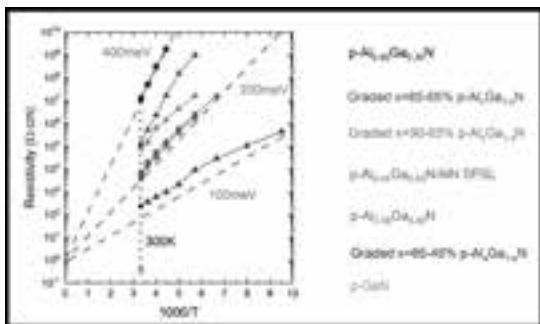
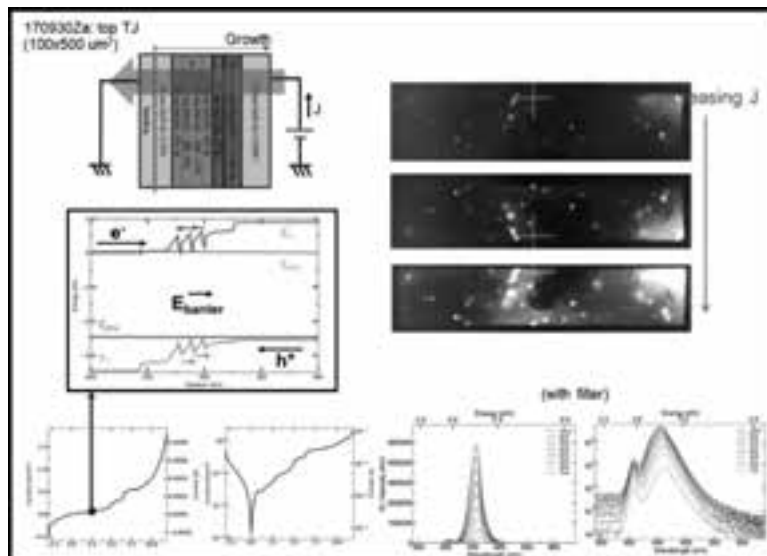


Figure 2, above: Temperature dependent TLM showed two orders less resistivity for graded AlGaIn structure over constant AlGaIn.

Figure 3, right: Summary of top tunnel junction (TJ) structure's J-V curves and electroluminescence spectrum.



Another approach to resolve the resistive p -type layer issue in nitrides is to use tunnel junction. Using tunnel junction, instead of using top p -type layer, we grew another n -type layer on top of p -layer to form a tunnel junction. This is so called top tunnel junction design. Using this strategy, it has two advantages. First, due to low resistivity in n -type layer, the current spreading is generally three orders better. Second, making contact to the n -layers is also much easier, meaning lower contact resistance.

We grew these structures on single crystal bulk gallium nitride (GaN) substrates. And we used the standard lithography tools to do MESA isolation and put down the contacts. We've successfully demonstrated both top tunnel junction blue LEDs operating at room temperature as shown in Figure 3. The next step will be measuring these devices' external quantum efficiency and output power to benchmark them with respect to other methods.

Three-Dimensional Scanner Fabrication

CNF Project Number: 2406-15

Principal Investigator: David L. Dickensheets

User: Tianbo Liu

Affiliation: Electrical and Computer Engineering Department, Montana State University

Primary Source of Research Funding: National Institutes of Health

Contact: davidd@montana.edu, tianbo.liu@msu.montana.edu

Website: <http://www.montana.edu/ddickensheets/>

Primary CNF Tools Used: Photolithography, plasma etching, electron beam evaporation wet chemical processing

Abstract:

A three-dimensional (3D) micro-electromechanical scanner that is capable of providing biaxial scanning and focus control is constructed. The scanner serves as the optical engine in a miniaturized handheld confocal microscope for the non-invasive, *in vivo* detection of skin cancer.

Introduction:

The standard method of diagnosing suspicious growths on the skin is to perform a biopsy. However not only can biopsies be painful and cause permanent scarring, they are also a sparse sampling [1,2]. It would be impractical to prescribe a biopsy for each site that looks suspicious, which leaves room for some malignant cells to go unnoticed. The good news is that a new, non-invasive method called optical biopsy is on the horizon. One of the promising types of optical biopsy is confocal laser scanning microscopy, which uses a laser to image cells under the surface of the skin [3,4]. The problem is that current confocal microscopes are too big, making it difficult to image sites that are in hard-to-reach parts of the body. A microelectromechanical system (MEMS) scanner has been constructed to address this problem by replacing the cumbersome mechanical scanning and focus elements in the conventional confocal microscope with a single 10 mm device [5,6].

Summary of Research:

The device is based on a dual axis gimbal platform that is supported by polymer hinges over a set of quadrant electrodes. At the center of the dual-axis gimbal platform is a deformable mirror that can be actuated independently using its own set of concentric electrodes. The gimbal platform along with a deformable mirror is constructed using a silicon-on-insulator (SOI) wafer, while the quadrant electrodes for scanning actuation are fabricated on a double-sided polished (DSP) silicon wafer. The fabrication process includes the making of the deformable structure, the optical surface, the electrical connections and the polymer hinges. These



Figure 1: Image of wafer after fabrication. See the full color version on the cover of this book!

are completed using microfabrication techniques such as photolithography, plasma etching, electron beam evaporation and wet chemical processing. The quadrant electrodes on the DSP wafer are fabricated using similar techniques. The two wafers are then aligned and bonded.

The release of the device uses procedures including xenon difluoride etching with the Xactix etcher to remove the device layer silicon from the SOI. Low power oxide etching employing the Oxford 81 etcher is used to remove the buried oxide layer. Figure 1 provides a picture of the completed wafer.

Conclusions:

In conclusion, we have fabricated a new polymer enhanced MEMS scan mirror that is capable of high-resolution imaging with simultaneous focus adjustment. The device is geared towards the miniaturization of confocal microscopes for a new generation of handheld optical biopsy devices. It can also be adapted to benefit a wide range of optical imaging and display applications.

References:

- [1] G. Argenziano, et al., "Accuracy in melanoma detection: a 10-year multicenter survey," *Journal of the American Academy of Dermatology*, vol. 67, no. 1, pp. 54-59. e1, 2012.
- [2] I. Kovalyshyn, S. W. Dusza, K. Siamas, A. C. Halpern, G. Argenziano, and A. A. Marghoob, "The impact of physician screening on melanoma detection," *Archives of dermatology*, vol. 147, no. 11, pp. 12691-1275, 2011.
- [3] A. Gerger, et al., "In vivo confocal laser scanning microscopy of melanocytic skin tumours: diagnostic applicability using unselected tumour images," *British Journal of Dermatology*, vol. 158, no. 2, pp. 329-333, 2008.
- [4] P. Guitera, et al., "The impact of *in vivo* reflectance confocal microscopy on the diagnostic accuracy of lentigo maligna and equivocal pigmented and nonpigmented macules of the face," *Journal of Investigative Dermatology*, vol. 130, no. 8, pp. 2080-2091, 2010.
- [5] T. Liu and D. L. Dickensheets, "Three-Dimensional beam scanner for a handheld confocal dermoscope," in *Optical MEMS and Nanophotonics (OMN), 2016 International Conference on, 2016*, pp. 1-2: IEEE.
- [6] T. Liu and D. L. Dickensheets, "MEMS 3-dimensional scanner for handheld confocal microscope," in *Optical MEMS and Nanophotonics (OMN), 2017 International Conference on, 2017*, pp. 1-2: IEEE.

Development of Single and Double Layer Anti-Reflective Coatings for Astronomical Instruments

CNF Project Number: 2458-16

Principal Investigator: Gordon Stacey¹

Users: Nicholas Cothard², Kenny Vetter³, Mahiro Abe³

Affiliation(s): 1. Department of Astronomy, 2. Department of Applied and Engineering Physics, 3. Department of Physics; Cornell University

Primary Source of Research Funding: NASA Grant NNX16AC72G

Contact: stacey@cornell.edu, nc467@cornell.edu, kju35@cornell.edu, ma797@cornell.edu

Primary CNF Tools Used: FilMetrics F50-EXR, FleXus film stress measurement, Zygo optical profilometer, ABM contact aligner, ASML 300C DUV stepper, Heidelberg DWL2000, Oxford PECVD, Anatech resist strip, Oxford 82 etcher, Unaxis 770 deep Si etcher

Abstract:

We are developing wide-bandwidth silicon substrate-based metal mesh mirrors for use in millimeter and sub-millimeter astronomical instruments. These mirrors are comprised of silicon substrates that are lithographically patterned with metal mesh reflectors on one surface and metamaterial anti-reflection coatings on their other surface. In the past year, this project has made significant progress in the development of our fabrication methods. We use standard lift-off lithography and metal evaporation tools to deposit and pattern our metal mesh filters. Our two-layer metamaterial anti-reflection coating fabrication makes extensive use of CNF's deep reactive ion etching devices and metrology tools such as profilometry and scanning electron microscopes. We are currently fabricating our meshes and anti-reflection coatings on high-resistivity silicon wafers that are low-loss, optical quality substrates. We will test the optical performance of our samples this summer using a Fourier transform spectrometer and will use the results to iterate and improve on our fabrication processes in the coming year.

Summary of Research:

The goal for this project is to fabricate silicon-substrate based metal mesh filters for use in millimeter and submillimeter astronomical instruments. This involves lithographic patterning of evaporated gold meshes on silicon wafers and etching double-layer metamaterial anti-reflection coatings (ARC) on the silicon surfaces using deep reactive ion etching (DRIE). These frequency dependent filters will be used as mirrors for Fabry-Perot interferometers (FPs) to spectroscopically observe early star and galaxy formation. The double-layer design is necessary to provide wide bandwidth transmission to span the wavelengths of interest for our instruments. The metamaterial design is necessary to match the thermal expansion coefficients of the substrate and ARC layers because warpage due to cryogenic thin film stresses would strongly affect the optical performance of our interferometry and refractive optical elements.

The bulk of our work this year has been the development of our fabrication methods for high-throughput, wide-bandwidth double-layer metamaterial ARCs. This has involved many iterations of fabrication and metrology

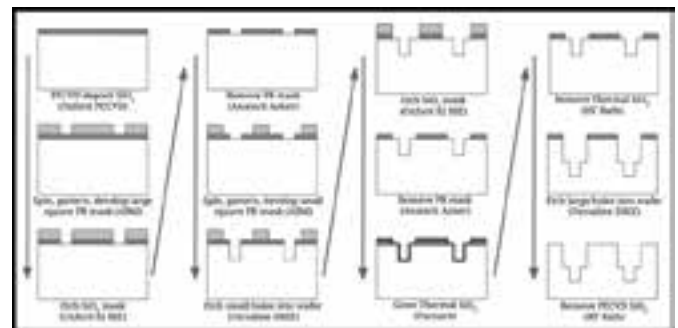


Figure 1: Process flow for fabricating a double-layer ARC on a silicon wafer. Dark grey represents thermal oxide. Light grey represents photoresist. White represents the silicon wafer.

with a plethora of tools in the CNF cleanroom. We began investigating the methods to fabricate two-layer ARCs over a year ago and presented preliminary results in an Applied Optics paper last year [1]. Since this time, we have worked to improve our control of the etched geometry. Figure 1 shows our current fabrication recipe for two-layer ARCs.

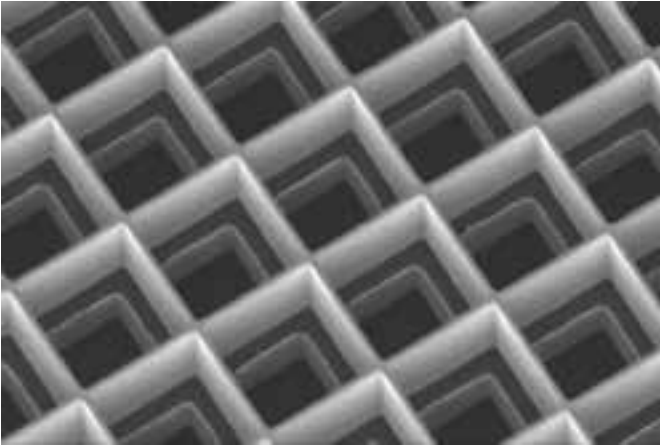


Figure 2: SEM image taken using CNF's Zeiss Ultra SEM showing successful fabrication of our two-layer metamaterial silicon ARC.

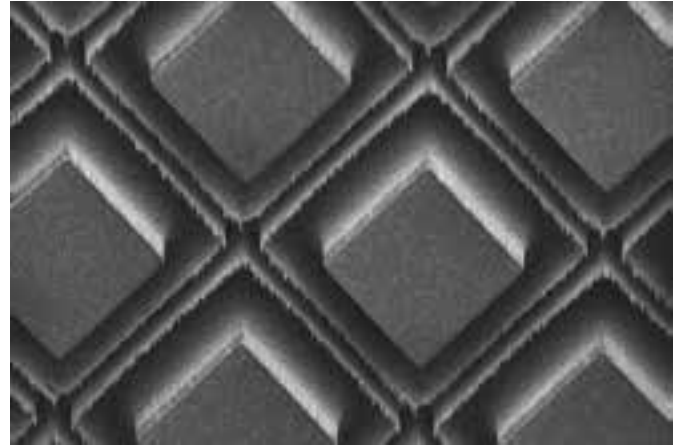


Figure 3: SEM image taken using CNF's Zeiss Ultra SEM showing a two-layer metamaterial silicon ARC with unwanted fence-like features between the upper and lower layers of the ARC.

We use stacked oxide and photoresist etch masks that are patterned on a silicon wafer before any silicon is etched. The oxide is deposited using CNF's Oxford plasma enhanced chemical vapor deposition (PECVD) and etched using the Oxford 82 etcher. Depending on the millimeter or sub-millimeter band that we are interested in, we pattern our photoresist etch masks using the ABM contact aligner or the ASML stepper with Gamma automatic coat-develop tool. With these etch masks patterned, we use either the Unaxis 770 deep silicon etcher or the Plasma-Therm deep silicon etcher. At intermediate steps inside our silicon etching, we measure the etch depth using the Zygo optical profilometer. Since last year, we have added a thermal oxide growth step and oxide removal step in between etching both silicon layers in order to clean-up the edge between both layers.

Figure 2 shows an SEM image (taken using CNF's Zeiss Ultra SEM) of a successful result of this fabrication procedure. Figure 3 shows an SEM image of the result of our old recipe, which did not include the thermal oxidation and HF bath in between the two etched layers. Notice the fence-like structure in between the upper and lower holes. Our new oxidation and removal steps can remove this unwanted structure. We are currently working to improve our control of this method and we are also looking for other methods to prevent the formation of this structure.

We are also currently fabricating these ARCs on optical quality, high-resistivity silicon wafers so that we can measure their transmittance using our lab's Fourier transform spectrometer (FTS). We have also been learning how to use negative lift-off photoresist techniques to pattern metal meshes onto silicon wafers. We have had success doing this using AZ nLOF 2020 photoresist with Microposit 1165 Remover with gold deposition using the CHA evaporator. We are beginning to fabricate these meshes on optical quality silicon so that we can measure

their frequency dependent transmittance using our lab's FTS. This summer, we will fabricate meshes of various geometries and compare to our optical models.

These mesh filters and ARCs will be used to fabricate the mirrors of astronomical FPIs, which will be used for spectroscopic measurements in two major instruments. The first will be the HIRMES (high-resolution mid-infrared spectrometer) instrument, which will fly on NASA's airborne observatory Stratospheric Observatory for Infrared Astronomy (SOFIA) [2]. The second will be the CCAT-Prime telescope which Cornell is building on Cerro Chajnantor in the Chilean Atacama Desert [3]. HIRMES will observe in the far-IR, while CCAT-Prime will observe in the millimeter and sub-millimeter. Two wafers with ARC on one side and a metalized layer on the other side will form the resonant cavity of a FPI.

In the past year we have made great steps towards achieving our goals at CNF. We have demonstrated our ability to fabricate double-layer ARCs for different millimeter, sub-millimeter and far-IR wavelengths. We have used many of the fabrication and metrology tools at CNF. Our next steps are to better characterize our etched geometries and improve our metamaterial ARCs. We will be using Fourier transform spectrometers to measure our samples' optical performance and using the results to iterate on our fabrication design.

References:

- [1] P.A. Gallardo, B.J. Koopman, N.F. Cothard, S.M.M. Bruno, G. Cortes-Medellin, G. Marchetti, K.H. Miller, B. Mockler, M.D. Niemack, G. Stacey, and E.J. Wollack, "Deep reactive ion etched anti-reflection coatings for sub-millimeter silicon optics," *Appl. Opt.* 56, 2796-2803 (2017)
- [2] <https://www.nasa.gov/feature/nasa-selects-next-generation-spectrometer-for-sofia-flying-observatory>
- [3] <http://www.ccatobservatory.org/>

Large Area Electrically Tunable Metalens

CNF Project Number: 2471-16

Principal Investigator: Professor Federico Capasso

Users: Alan She, Shuyan Zhang

Affiliation: John A. Paulson School of Engineering and Applied Sciences, Harvard University

Primary Source of Research Funding: Air Force Office of Scientific Research

Contact: capasso@seas.harvard.edu, alan.she@post.harvard.edu, shuyanzhang@seas.harvard.edu

Website: <https://www.seas.harvard.edu/capasso>

Primary CNF Tools Used: Heidelberg DWL2000, ASML DUV stepper, Gamma auto-coater, CVC sputterer, Oxford 81, 82, and 100 etchers

Abstract:

Our tunable optics technology enables dynamic tuning of metalenses with voltage-resolved precision. We have demonstrated electrically controlled focal length tuning of over 100% as well as the capability of adjusting for astigmatism and image shift at the same time. We have also developed a method for designing and fabricating metalenses of large areas: two-centimeters in diameter and beyond.

Summary of Research:

Large Area Metalenses [1]. Optical components, such as lenses, have traditionally been made in the bulk form by shaping glass or other transparent materials. Recent advances in metasurfaces provide a new basis for recasting optical components into thin, planar elements, having similar or better performance using arrays of subwavelength-spaced optical phase-shifters. The technology required to mass produce them dates back to the mid-1990s, when the feature sizes of semiconductor manufacturing became considerably denser than the wavelength of light, advancing in stride with Moore's law. This provides the possibility of unifying two industries: semiconductor manufacturing and lens-making, whereby the same technology used to make computer chips is used to make optical components, such as lenses, based on metasurfaces. Using a scalable metasurface layout compression algorithm that exponentially reduces design file sizes (by three orders of magnitude for a centimeter diameter lens) and stepper photolithography, we show the design and fabrication of metasurface lenses (metalenses) with extremely large areas, up to centimeters in diameter and beyond. Using a single two-centimeter diameter near-infrared metalens less than a micron-thick fabricated in this way, we experimentally implement the ideal thin lens equation, while demonstrating high-quality imaging and diffraction-limited focusing.

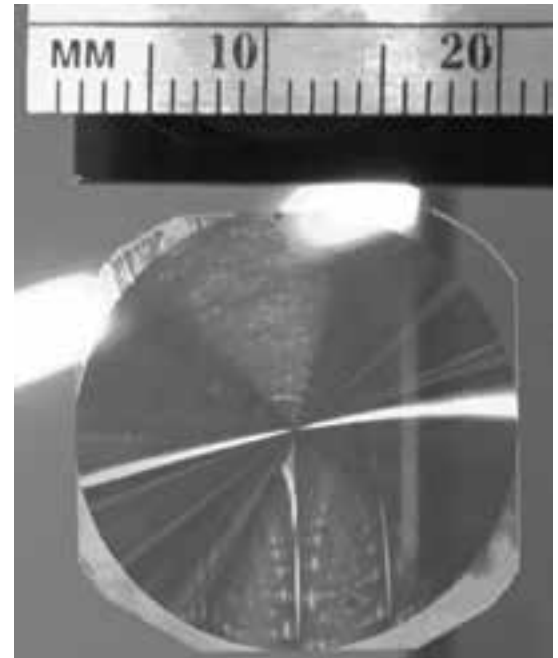


Figure 1: Our metasurface lens with diameter of 2 cm.

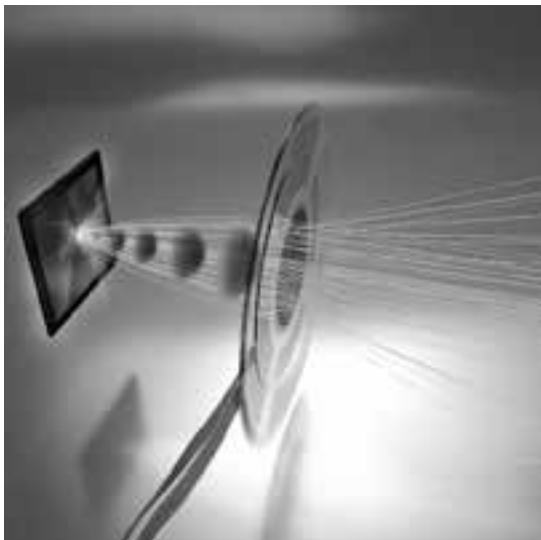


Figure 2: Schematic operation of adaptive metalens, which can perform simultaneous electrical adjustment of focal length, astigmatism, and image shift.

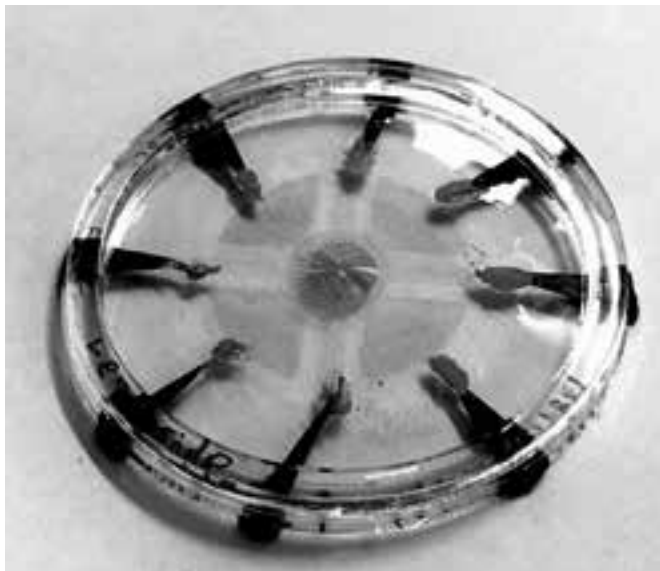


Figure 3: Photo of adaptive metalens device.

Adaptive Metalenses [2]. Focal adjustment and zooming are universal features of cameras and advanced optical systems. Such tuning is usually performed longitudinally along the optical axis by mechanical or electrical control of focal length. However, the recent advent of ultrathin planar lenses based on metasurfaces (metalenses), which opens the door to future drastic miniaturization of mobile devices such as cell phones and wearable displays, mandates fundamentally different forms of tuning based on lateral motion rather than longitudinal motion. Theory shows that the strain field of a metalens substrate can be directly mapped into the outgoing optical wavefront to achieve large diffraction-limited focal length tuning and control of aberrations. We demonstrate electrically tunable large-area metalenses controlled by artificial muscles capable of simultaneously performing focal length tuning (>100%) as well as on-the-fly astigmatism and image shift corrections, which until now were only possible in electron optics. The device thickness is only $30\ \mu\text{m}$.

Our results demonstrate the possibility of future optical microscopes that fully operate electronically, as well as compact optical systems that use the principles of adaptive optics to correct many orders of aberrations simultaneously.

References:

- [1] A. She, S. Zhang, S. Shian, D.R. Clarke, and F. Capasso, "Large area metalenses: design, characterization, and mass manufacturing," *Opt. Express* 26, 1573-1585 (2018).
- [2] A. She, S. Zhang, S. Shian, D.R. Clarke, and F. Capasso. 2018. "Adaptive metalenses with simultaneous electrical control of focal length, astigmatism, and shift." *Science Advances* 4 (2): eaap9957. doi:10.1126/sciadv.aap9957. <http://dx.doi.org/10.1126/sciadv.aap9957>.

Multi-Resonant Bianisotropic Metagratings for Ultra-Efficient Diffraction of Mid-Infrared Light

CNF Project Number: 2472-16

Principal Investigator: Gennady Shvets

User: Maxim Shcherbakov

Affiliation: School of Applied and Engineering Physics, Cornell University

Primary Source of Research Funding: ONR grant #N00014-17-1-2161

Contact: gs656@cornell.edu, mrs356@cornell.edu

Primary CNF Tools Used: JEOL 9500, even-hour evaporator, Oxford Cobra

Abstract:

We demonstrate that a bianisotropic metamaterial supporting four optical resonances of the appropriate symmetry can be used as a building block for achieving perfect diffraction of mid-infrared radiation. We design and experimentally realize such bianisotropic metamaterials. We show that near-perfect diffraction to the $+1^{\text{st}}$ diffraction order is possible, while other orders are suppressed, in the mid-infrared spectral region.

Summary of Research:

We experimentally verify the viability of the “perfectly” diffracting metagrating in the mid-IR spectral region [1]. The geometric dimensions of the designed structure and corresponding diffraction spectra have been simulated using a finite-element-method software. An undoped, double-side-polished wafer (Ultrasil, Inc.) with a device layer of $2.7 \mu\text{m}$ and a buried oxide layer of $1.0 \mu\text{m}$ was cleaned in acetone and isopropyl alcohol (IPA) and coated with two layers of positive electron beam resist: 100 nm of PMMA 950 on top of the 200 nm of PMMA 495k, baking the resist at 170°C for 15 min after each coating step. The desired pattern was exposed over the substrate at $1000 \mu\text{C}/\text{cm}^2$ (JEOL 9500FS) and developed in MIBK:IPA 1:3 solution for 75 sec, with consequent rinsing in IPA. A 60-nm-thick Cr hard mask was deposited using electron beam evaporator at a rate of 3 nm/min. After liftoff in sonicated acetone (60 sec), HBr plasma dry etching of silicon down to the $1\text{-}\mu\text{m}$ -thick buried oxide layer was carried out (Oxford Cobra), leaving the desired pattern carved in the device layer. As the last step, the residual Cr mask was removed with a Cr wet etch. The patterned area of each metagrating was $(1.5 \text{ mm})^2$. A scanning electron microscope image of the best-performance sample is given in Fig.1(a).

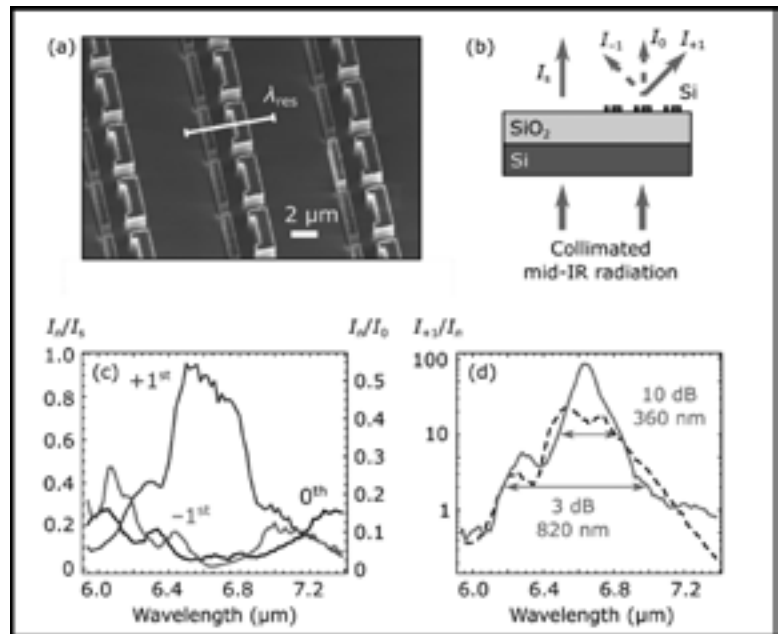


Figure 1: (a) SEM image of the best-performance metagrating. (b) Schematic of the experiment. The three measured diffraction orders in transmission, and the bare substrate transmission, are indicated by arrows. The targeted diffractive order is the $+1^{\text{st}}$. (c) Diffraction efficiency of the $+1^{\text{st}}$, 0^{th} and -1^{st} transmitted diffraction orders normalized to the bare substrate transmission measured as the function of the wavelength. The axis on the right shows absolute diffraction efficiency as normalized to the incident field intensity. (d) Diffraction contrast spectra I_{+1}/I_0 (dashed line) and I_{+1}/I_{-1} (solid line).

The normalized diffraction efficiency I_{+1}/I_s of the fabricated metagratings, defined as the ratio of the transmission I_{+1} into the targeted diffraction order to the transmission I_s through the bare Si/SiO₂ substrate, was experimentally measured. Such normalization is necessary because of the substantial (43%) amount of light experiencing reflection at the high-contrast flat Si-air and Si-SiO₂ interfaces. This artefact is due to the chosen material platform (SOI), and can be overcome by using, for example, Si-on-sapphire wafers.

A quantum cascade laser (Daylight Solutions MIRcat) was used as a source of highly collimated monochromatic tunable quasi-CW mid-IR radiation, as shown in Figure 1(b). The laser beam was softly focused with a 50-mm-focal-length lens to a 200 μm diameter spot from the back side of the wafer. The intensity of the diffracted light was measured using a pyroelectric array camera (Ophir Spiricon Pyrocam III) by integrating the intensity over the entire array. For each wavelength, the intensities of the +1st, -1st and 0th transmitted diffraction orders (I_{+1} , I_{-1} and I_0) were detected, and the +1st and -1st orders were also detected studied in reflection. The reflected diffraction orders were beyond detection limit. The bare substrate transmission I_s for the efficiency normalization of the diffracted orders was measured by passing the beam through the unstructured part of the wafer, where the device layer is etched away.

The normalized diffraction efficiencies for all transmitted diffraction orders are plotted in Figure 3(c) as a function of the incident wavelength of light. Within our experimental margin of error, the peak grating efficiency at 6.45 μm is of order 95%. Note from Figure 1(c) that the diffraction efficiency into the -1st order is even smaller than into the 0th order. Such an enormous asymmetry between the -1st and +1st orders is due to the bianisotropic nature of the metasurface.

Another important characteristic of the diffraction efficiency is the contrast between the +1st and 0th orders, defined as I_{+1}/I_0 , and the +1st and -1st orders, defined as I_{+1}/I_{-1} .

The plots of these quantities shown in Figure 1(d) indicate that the contrasts approach 20 and 80, respectively. Note that the high contrast is achieved for a fairly broad band of mid-IR wavelengths: 260 nm for 10 dB rejection, and 820 nm for the 3 dB rejection of the -1st diffraction order.

References:

- [1] Z. Fan, M.R. Shcherbakov, M. Allen, J. Allen, G. Shvets, "Perfect Diffraction with Bianisotropic Metagratings," arXiv:1802.01269 (2018).

Optical Masks for Imaging Exoplanets with Large Ground-Based Telescopes

CNF Project Number: 2499-16

Principal Investigator: Dr. Nemanja Jovanovic

Users: Christopher Alpha, Jeremy Clark, John Treichler, Nemanja Jovanovic, Olivier Guyon, Julien Lozi, Justin Knight

Affiliations: Research Corporation of the University of Hawaii; Subaru Telescope Project; University of Arizona; Cornell NanoScale Facility, Cornell University

Primary Sources of Research Funding: Subaru Telescope Project; Mt. Cuba Foundation

Contact: jovanovic.nem@gmail.com, alpha@cnf.cornell.edu, clark@cnf.cornell.edu, treichler@cnf.cornell.edu, guyon@naoj.org, lozi@naoj.org, jknight@optics.arizona.edu

Primary CNF Tools Used: ASML DUV stepper, Oxford ICE-RIE etcher

Abstract:

A stellar coronagraph is a telescope instrument that enables direct imaging of extra-solar, or exoplanets, from the ground or in space. Some components of the coronagraph system we use require microfabrication techniques to be manufactured. We report on the progress of fabricating optical masks known as complex focal plane masks for stellar coronagraphs, as well as their uses at the Subaru telescope so far.

Summary of Research:

In recent years, astronomers have used telescopes attached with instruments to estimate that approximately 50% of stars have a habitable planet (an Earth-size planet with surface temperature able to sustain liquid water). Current detection limits only allow for the radius, orbit and mass of the planet; identifying if life has developed on the planet requires direct imaging and spectroscopy. This is extremely challenging: the planet can be about a billion times fainter than the star it orbits and is located very close to it on the sky. The key to performing direct imaging and spectroscopy is a telescope instrument called a stellar coronagraph. A stellar coronagraph is designed to access light from the planet for observation by blocking, reducing, or in some way suppressing incoming starlight using a series of carefully designed optical masks.

Each mask is responsible for changing the starlight amplitude and phase to induce deep destructive interference, or cancellation, of the starlight to collect the planet signal possibly buried underneath. A simple coronagraph architecture is shown in Figure 1. It consists of optics after the telescope which focus and collimate the incoming beam at various points; doing so allows for the optical masks to suppress the starlight as discussed.

The stellar coronagraph we developed for the Subaru Coronagraphic Extreme Adaptive Optics (SCEAO) bench at the Subaru Telescope on Mauna Kea, HI, is

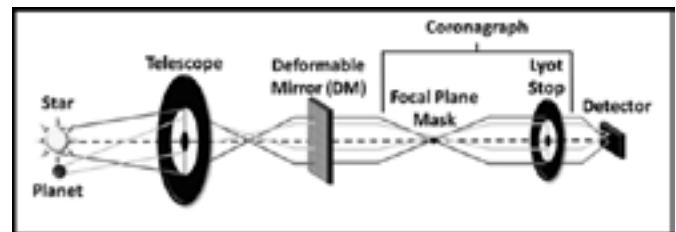


Figure 1. A stellar coronagraph. After entering the telescope, light from the planet passes through the chain of optical masks (focal plane mask, Lyot stop) unchanged, while the starlight is altered in amplitude and phase to allow the collection of planet light from the detector. The deformable mirror can be used to improve the performance of the coronagraph. Image courtesy of Kelsey Miller, University of Arizona.

known as the Phase-Induced Amplitude Apodization Complex-Mask Coronagraph (PIAACMC). It consists of several custom-fabricated optical masks including a “complex” focal plane mask. Figure 2 shows an example of a fabricated complex mask designed to modulate the amplitude and phase of starlight coming to a focus. The fabrication process for this mask used the ASML DUV stepper and an Oxford ICP-RIE etcher.

These masks consist of a tessellated pattern of hexagonal zones which vary in height; the hexagons are responsible for producing the destructive interference of the starlight

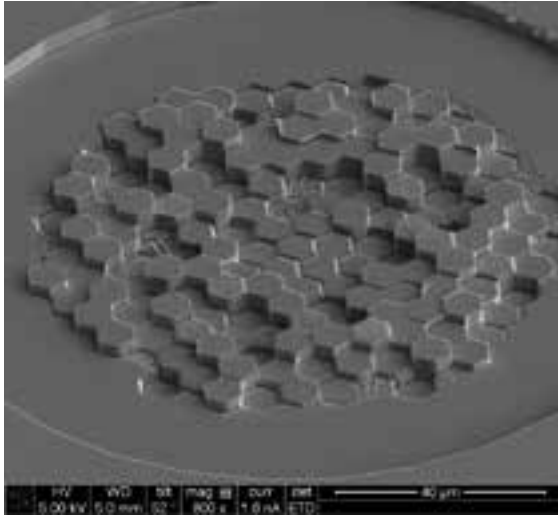
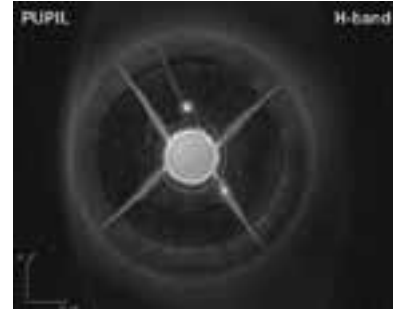


Figure 2: An early iteration of a fabricated complex mask.

on a detector. This type of focal plane mask must be fabricated using microfabrication techniques as each hexagon is typically on the order of $10\ \mu\text{m}$ wide and a few microns or less deep. Tolerances of these devices are being investigated, but the better they are made to match the original design, the better they can destructively interfere starlight at several wavelengths simultaneously.

The masks from this fabrication effort will be installed and tested at SCEXAO soon, but for now only some other masks have been put into the system. Figure 3 demonstrates the intended effect an aligned focal plane mask has in only allowing light to gather in places where it can be blocked by another optical mask. We report on some of these activities in references [1] and [2].

Figure 3:
An image of a fabricated complex-mask aligned at SCEXAO in the plane before the Lyot stop. Starlight passing through the complex-mask has been changed, but still propagates through to the features of the telescope architecture. This light will be blocked by the Lyot stop, after which the performance of the coronagraph can be measured.



References:

- [1] Julien Lozi, et al., "SCEXAO: new high-performance coronagraphs ready for science," Proc. SPIE 10706, Advances in Optical and Mechanical Technologies for Telescopes and Instrumentation III, (Publication pending).
- [2] Justin M. Knight, John Brewer, Ryan Hamilton, Karen Ward, Tom D. Milster, Olivier Guyon, "Design, fabrication, and testing of stellar coronagraphs for exoplanet imaging," Proc. SPIE 10400, Techniques and Instrumentation for Detection of Exoplanets VIII, 104000N (12 September 2017).

Description of the Exploratory Etching and Electrodeposition Project

CNF Project Number: 2527-17

Principal Investigator: Dr. David Crouse

User: Golsa Mirbagheri

Affiliation: Electrical and Computer Engineering Department, Clarkson University

Primary Source of Research Funding: CFM

Contact: dcrouse@clarkson.edu, mirbagg@clarkson.edu

Primary CNF Tools Used: Oxford 82, Oxford 100, ASML, Gamma, PECVD, Cobra

Abstract:

This project is a continuing project. We will be finishing the fabrication of the hyperbolic metamaterial structure and designing a 2nd generation of the filter that uses more of a photonics crystal resonant material within a Bragg stack. Both the hyperbolic metamaterial structure and the 2nd generation devices have compelling properties. Both show very little dispersion — meaning that their performance is not affected by the angle of incidence to the optical signal.

Project Description:

During the last year, we have further designed the hyperbolic metamaterial device and have performed much more optimization, and have taken into account practical design considerations. We are now fabricating the structure at the Cornell NanoScale Science and Technology Facility (CNF) at Cornell University. We have developed a fabrication plan and are now implementing the plan, with masks designed and fabrication processes in development.

Based on what we have learned, we are now investigating a 2nd generation device that does not use metal wires, but uses resonant cavities in the three middle layers of the Bragg stack. The resulting structure will have far less polarization dependence, will absorb less radiation, will be far easier to fabricate and manufacture, and will have a larger tuning range that allows for it to be used within pixelated wavelength filters for hyperspectral imaging applications.

We have been performing preliminary testing on the resonant cavities and have a preliminary design for operation in the midwavelength infrared range of 3-5 μm . The Bragg stack will use silicon and silicon dioxide, and potentially silicon nitride — all CMOS compatible devices — as well as having all structure features with sizes amenable to optical lithography.

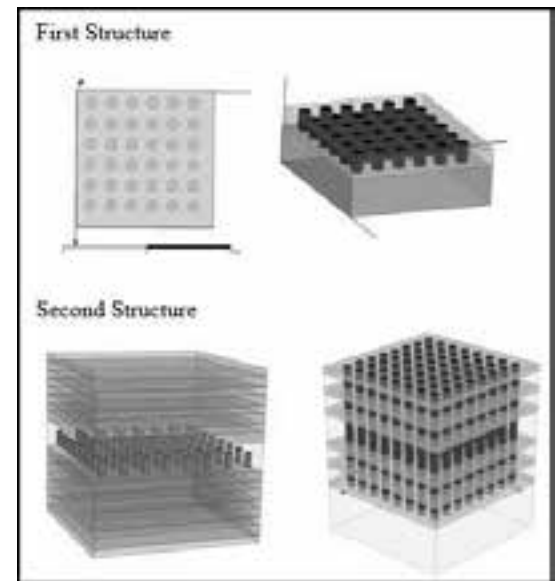


Figure 1: Schematic. Top, First Structure: The 1.5 μm SiO_2 film was deposited, patterned and etched. The holes were 0.5 μm , electroplated with Cu. Bottom, Second Structure: Alternative layers of SiO_2 and Si are deposited, patterned and etched (all through the layers), then holes electroplated with Cu.

Characterization of Magnetic Thin Films for Actuating Origami Devices

2018 CNF REU Intern: Sierra Russell

2018 CNF REU Intern Affiliation: Nanoscale Engineering and Applied Mathematics, SUNY Polytechnic Institute – Colleges of Nanoscale Science and Engineering

CNF Project: 2018 Cornell NanoScale Science and Technology Facility Research Experience for Undergraduates Program

CNF REU Principal Investigator: Professor Paul McEuen, Department of Physics, Cornell University

CNF REU Mentor: Tanner Pearson, School of Applied and Engineering Physics, Cornell University

Primary Source of CNF REU Funding: National Science Foundation via the National Nanotechnology Coordinated Infrastructure (NNCI) Grant No. ECCS-1542081

Contact: srussell@sunypoly.edu, plm23@cornell.edu, tgp34@cornell.edu

Website: http://www.cnf.cornell.edu/cnf_2018reu.html

Primary CNF Tools Used: Even-odd hour electron-beam evaporator, FlexUs film stress measurement system, P7 profilometer, ABM contact aligner, Class II resist room

Abstract:

Fabrication inspired by origami offers a novel method for the development of micron-scale machines, which have a wide range of potential applications. The use of magnetic thin films in tandem with ultra-thin atomic layer deposition (ALD) films allows for the creation of actuatable devices that can be controlled with external magnetic torques. We characterized cobalt, nickel, and iron films to compare their viability for these devices. We deposited our films via electron-beam evaporation at thicknesses of 25 nm and 50 nm and deposition rates of 0.3 Å/s and 0.6 Å/s, on top of a 10 nm thick titanium adhesion layer. We performed stress measurements of each film pre-and post-deposition, as well as thickness verification. We obtained the hysteresis curve of each film by using a vibrating sample magnetometer (VSM). We see that Fe and Co have significantly higher magnetizations than Ni, whereas Ni benefits from having the lowest stress. We also showed that the addition of a low stress polymer (SU-8) spun on top of the magnetic films may help to reduce the stress in the composite film. We discuss the implications of these results for our origami-inspired devices.

Summary of Research:

The goal of this work was to determine the viability of different magnetic materials for the fabrication of actuatable micron-scale devices. These devices, composed of a flexible ALD backbone and rigid magnetic panels, can be controlled with external magnetic

torques to create three dimensional structures from planar Si-based processing (Figure 1). We measured the stress experienced in the magnetic films, as it imparts curvature on the underlying ultrathin ALD films and alters their bending energies. We also studied the magnetic properties of the magnetic films. These include the magnetization saturation, which relates to the magnitude of the magnetic torques we can apply, and the coercive field, which is the field required to orient the magnetic moment of the film along a given axis.

We characterized three magnetic materials: cobalt, nickel, and iron. The materials were deposited via electron-beam evaporation. A 10 nm thick titanium layer was deposited prior to any magnetic films to promote adhesion to the wafer. Each material was deposited at 25 nm and 50 nm with deposition rates of 0.3 Å/s. Additionally, we deposited 50 nm of Co at a deposition rate of 0.6 Å/s to determine the effect on the stress. Once the films were deposited, the thickness was verified using a profilometer.

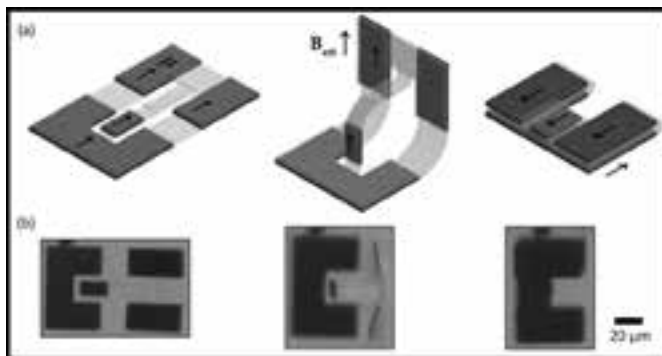


Figure 1: (a) Schematic and (b) optical image of 2D-to-3D magnetically actuated device with latching mechanism. μ represents the magnetic moment and B_{ext} the external magnetic field.

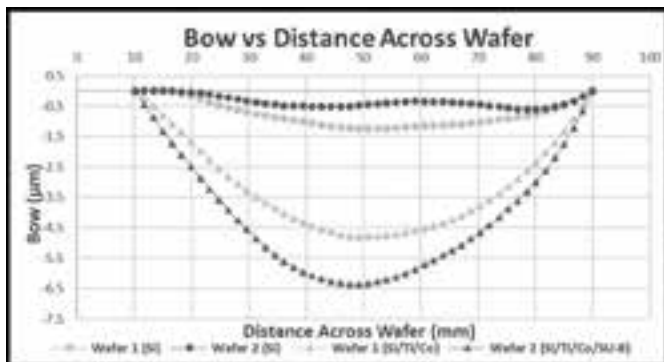


Figure 2: Bow of two wafers before and after deposition to compare the change in stress with the addition of SU-8 photoresist.

Stress measurements were taken with the FlexUs film stress measurement tool. This tool measures the bow of the wafer before and after deposition. Then it relates the change in the bow with the properties of the deposited material to determine the stress in the film. To see the influence a low stress polymer has on the overall stress in a film, 70 nm of Co was deposited on two wafers in parallel, followed by spinning 1 μm of SU-8 photoresist on one wafer (Figure 2).

Samples from each thickness of each material were put through a VSM to determine their saturated magnetizations and coercivities. The data produced by the tool provides the magnetic moment as a function of the magnetic field. We normalized the magnetic moments by the volumes of the respective films to determine their magnetizations.

Results and Conclusions:

We found that Fe films have the largest amount of stress, with both the 25 nm and 50 nm thick samples having an average stress of 820 \pm 14.9 MPa. The Co films had an average stress of 400 \pm 19.9 MPa, and the Ni films had an average stress of 170 \pm 12.0 MPa. In the case of Co, increasing the deposition rate from 0.3 $\text{\AA}/\text{s}$ to 0.6 $\text{\AA}/\text{s}$ didn't impact the stress in the film. Moreover, the addition of the SU-8 on top of the Co film did reduce the stress in the total film by approximately 90%.

The VSM data showed that Fe has the largest coercive field and magnetization saturation, while Co has the lowest coercive field and Ni has the lowest magnetization saturation (Figure 3).

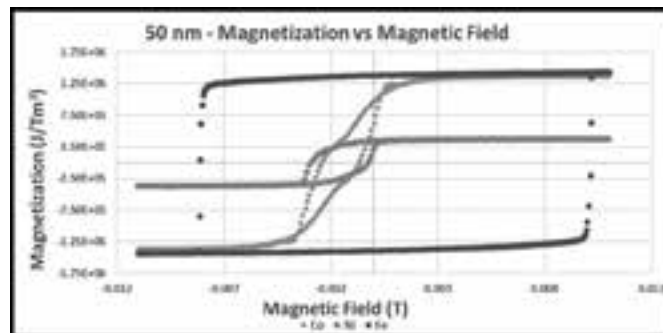


Figure 3: Magnetic hysteresis curves of 50 nm thick Co, Fe, and Ni.

The 25 nm and 50 nm samples showed similar magnetization saturations, but the coercive fields tended to increase with increasing thickness. However, we didn't expect to see Ni having a larger coercive field than Co, since Ni is considered a softer magnetic material. We think this could be due to possibly depositing oxide during our Co deposition, instead of pure Co.

We've shown that Co and Fe films have much greater stresses than Ni films, which makes them more of a risk to use as they're more likely to impact the stiffness of the ALD films in our devices. Ni films are much weaker magnets than Co and Fe films; therefore, we wouldn't be able to apply as strong of magnetic torques. To balance these factors, we can use SU-8 to reduce the stress in Co and Fe, resulting in films with both low stress and high magnetization that maximize device performance. The next steps for this project are to investigate more magnetic materials, such as magnetic alloys, and different methods of deposition.

Acknowledgements:

Thank you to Professor Paul McEuen for taking me on as an intern for this program, and Tanner Pearson for the excellent mentorship throughout the summer. This work was performed in part at the Cornell NanoScale Science & Technology Facility (CNF) and funded by the National Science Foundation via the National Nanotechnology Coordinated Infrastructure (NNCI) Grant No. ECCS-1542081.

Development of a MEMS Tool to Study the Physics of Water and Ice

2018 CNF REU Intern: Kody Whisnant

2018 CNF REU Intern Affiliation: Chemical Engineering, Wayne State University

CNF Project: 2018 Cornell NanoScale Science and Technology Facility Research Experience for Undergraduates Program

CNF REU Principal Investigator: Dr. Abraham Stroock, Smith School of Chemical and Biomolecular Engineering, Cornell

CNF REU Mentor: Hanwen Lu, Sibley School of Mechanical and Aerospace Engineering, Cornell University

Primary Source of CNF REU Funding: National Science Foundation via the National Nanotechnology Coordinated Infrastructure (NNCI) Grant No. ECCS-1542081

Contact: kody.whisnant@wayne.edu, abe.stroock@cornell.edu, hl943@cornell.edu

Website: http://www.cnf.cornell.edu/cnf_2018reu.html

Primary CNF Tools Used: ABM contact aligner, Anatech resist strip, FilMetrics film measurement system, LPCVD nitride furnace, Oxford 81/82 etchers, Oxford PECVD, SÜSS SB8e substrate bonder, SÜSS MA6-BA6 contact aligner, VersaLaser cutting/engraving tool

Abstract:

Freezing of water in confinement is commonly found in geological, biological and architectural contexts. It is believed that the phase equilibrium and crystal formation is influenced by the confinement in pore space, which often has nanoscopic dimensions. The small scale and structural complexity of porous materials hinders our ability to understand the detail kinetics and phase equilibrium of crystals in confinement. To shed light into this problem, we developed a microelectromechanical systems (MEMS) based porous system consisting of geometrically well-defined high aspect ratio nanochannels with nanoscale (30 nm to 100 nm) channel heights and micron-scale channel width. Such configurations provide a wide field of view (~microns) for direct visualization of crystallization kinetics and phase equilibrium within nanoconfinement. Channels were first fabricated via conventional photolithography techniques on silicon and glass substrates. Notably, a 200 nm silicon nitride layer was deposited via low pressure chemical vapor deposition (LPCVD) underneath the channels to enhance contrast between liquid water and ice. The final channel geometries were verified via capillary condensation within the channels. Finally, we experimentally observed the ice-water interface in nanoconfinement. The melting of confined ice is in quantitative agreement with the Gibb-Thomson relation.

Project Summary:

Introduction. Freezing of water in nanoconfinement is of great importance in geological, biological, and archeological contexts [1,2]. It is believed that the phase equilibrium of water and ice is shifted according to the Gibbs-Thomson relation [3] (Figure 1). However, owing to the small and complex geometrical nature of porous materials, the local phase equilibrium in nanoconfinement remains unresolved. Direct imaging of freezing can provide local mechanistic information on water-ice phase equilibrium and crystallization dynamics under confinement. Herein, we demonstrate the unique opportunity of observing confined phase equilibrium in a MEMS high aspect ratio nanochannel array with *in situ* phase contrast enhancement enabled by a silicon nitride (Si_3N_4) dielectric mirror [4] (Figure 2).

Fabrication and Experiment. The device fabrication process can be summarized as follows: A LPCVD Si_3N_4 layer of ~ 200 nm thickness was first deposited on a silicon wafer followed by a PECVD layer of silicon oxide with thickness corresponding to the desired channel

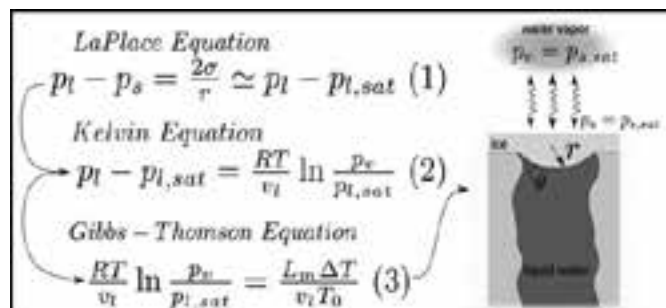


Figure 1: Liquid water in a pore can coexist, metastably, with ice and an unsaturated vapor. Capillarity between liquid and ice (Laplace) places the liquid under tension and allows for phase equilibrium (Kelvin) with the liquid under tension. This equilibrium can be expressed as the Gibbs-Thomson equation.

height. Nanochannel patterns were then transferred and patterned via photolithography. The channels were formed by etching the oxide layer with 30:1 buffered oxide etch (BOE).

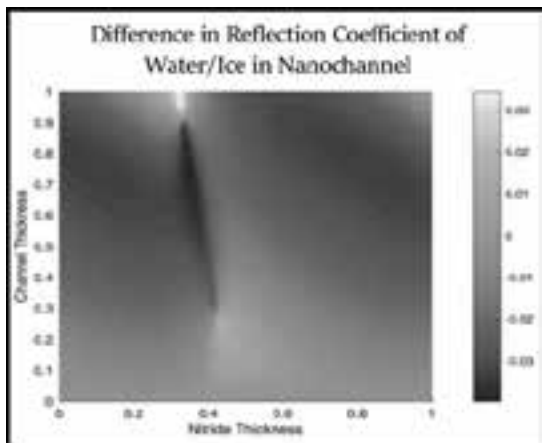


Figure 2: Calculated difference in the reflection coefficient of water and ice in the nanochannels, with axes normalized to incident wavelength. The maximum difference is found with nitride thickness in between 0.4 and 0.5, which for visible light correlates to a nitride thickness of 130 nm-260 nm. This difference is insensitive to channel thickness.

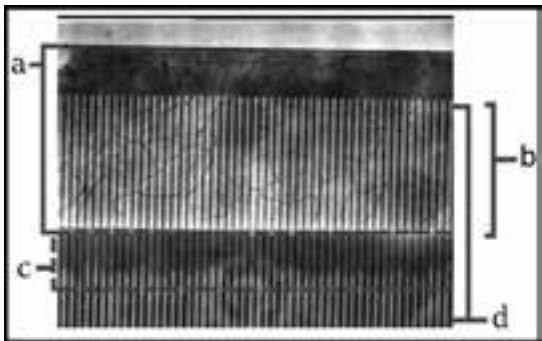


Figure 3, top: Image obtained from freezing experiment. (a) Microchannel containing bulk ice, identified by the grain boundaries present in image. (b) 500 μm channel overlap. (c) Liquid water in nanochannels (darker region) coexisting with ice (brighter region) at subfreezing temperature. (d) Nanochannel array.

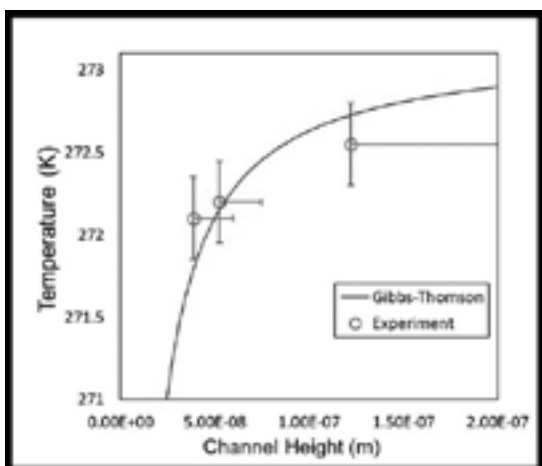


Figure 4, bottom: Melting temperatures of ice in nanochannels with different channel heights compared to the Gibbs-Thomson prediction. Values agree with those predicted by the Gibbs-Thomson relation.

For the glass wafer, a 250 nm PECVD amorphous silicon ($\alpha\text{-Si}$) layer was deposited and annealed as an etch mask. Photolithography was then used to transfer the pattern of microchannels. SF_6/O_2 reactive ion etch in the Oxford 80 etcher was used to pattern the $\alpha\text{-Si}$ etch mask and the 10 μm microchannels were etched in 49% hydrofluoric acid.

When complete, the patterned silicon and glass wafers were aligned and anodically bonded using the MA6-BA6 contact aligner and SÜSS SB8e substrate bonder. The bonded wafers were diced and microchannel inlets were cut out with the VersaLaser.

For testing, individual devices were placed in an environmental chamber with pressure and temperature regulation. Water vapor was then pumped through the chamber to fill the nanochannels with liquid water upon capillary condensation, from which the channel height was deduced. The microchannels were filled by condensation by further raising the vapor pressure to saturation. Once filled, the chamber temperature was lowered to initiate freezing in the nanochannels and confined phase equilibrium was captured with a CCD camera positioned above the chamber. The nanoconfined water-ice phase equilibrium was successfully captured as shown in Figure 3. The melting temperatures of confined ice were reported in Figure 4 and were consistent with the Gibbs-Thomson prediction.

Conclusions:

A microfluidic device consisting of high aspect ratio nanochannels was fabricated. A layer of ~ 200 nm Si_3N_4 was deposited underneath the channels, resulting in detectable contrast between the liquid water and ice in the channels. The melting temperatures of confined ice agreed with the Gibbs-Thomson relation. Continued work will focus on studying the transport dynamics of ice-water in confinement.

Acknowledgements:

Professor Abraham Stroock, Hanwen Lu, Melanie-Claire Mallison, CNF REU Program Coordinators, and CNF Staff. This work was completed in part at the Cornell NanoScale Science and Technology Facility, an NNCI member, which is supported by the NSF (Grant No. ECCS-1542081). This work was supported in part by a grant from the Air Force Office of Scientific Research (FA9550-18-1-0345).

References:

- [1] Bartels-Rausch, T., et al. "Ice structures, patterns, and processes: A view across the icefield." *Rev. Mod. Phys.* 2012, 84, 885.
- [2] Wettlaufer, J., et al. "Premelting Dynamics." *Annu. Rev. Fluid Mech.*, 2006, 38, 427-452.
- [3] Liu, Z., et al. "Measurement of freezing point depression of water in glass capillaries and the associated ice front shape." *Phys. Rev.*, 2003, 67, 6.
- [4] Li, H., et al. "Direct visualization of fluid dynamics in sub-10 nm nanochannels." *Nanoscale*, 2017, 9, 9556.

Nanosecond Spin-Orbit Torque Switching of Three Terminal Magnetic Tunnel Junctions with Low Write Error Rate

CNF Project Number: 111-80

Principal Investigator: Robert A. Buhrman

User: Shengjie Shi

Affiliation: Applied and Engineering Physics, Cornell University

Primary Source of Research Funding: Department of Defense-Intelligence Advanced Research Projects Activity

Contact: buhrman@cornell.edu, ss2882@cornell.edu

Primary CNF Tools Used: ASML, JEOL 6300 e-beam, Veeco AFM

Abstract:

Recently we reported that a significant reduction of critical switching current I_c can be achieved in tungsten-based three-terminal magnetic tunnel junctions with atomic Hf layer modification of the interfaces. This has stimulated additional work to further optimize these nanoscale structures to achieve still lower critical currents and higher speed switching for future cache memory applications. Here we report on a systematic study of the micromagnetic factors that determine both the intrinsic time scale of this nanosecond switching behavior and the degree of symmetry between the fast switching from parallel (P) to anti-parallel (AP) and the reverse. Using a modified geometry of the nanopillar magnetic tunnel junction structure we find that we are able to tune the relative speeds of reversal between two polarities. We have also designed a new spin Hall channel geometry to achieve a major reduction in channel resistance. This enables us to examine write error rates in the very high pulse current regime, $I \gg I_c$. (See Figure 1.) The results of these studies further demonstrate the feasibility of this type of three-terminal spin-orbit torque device as a high speed, energy efficient, non-volatile memory solution.

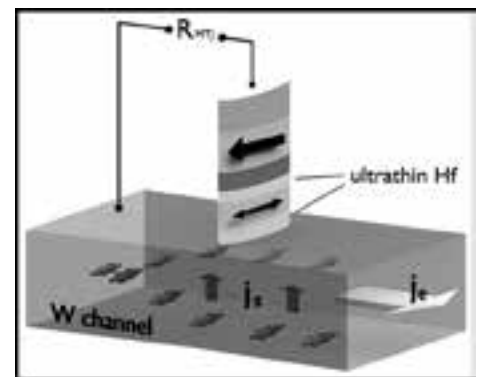


Figure 1: Schematic picture of the three terminal MTJ and measurement technique.

Summary of Research:

One of the key advances in magnetic memory technologies is the utilization of the giant spin Hall effect to switch a nanomagnet free layer in a magnetic tunnel junction (MTJ) structure. While different areas of application set different standard for what an efficient memory cell should perform, faster operation with lower energy consumption is always desired. Three-terminal MTJs are good candidates for next generation memory application due to non-volatility and zero read disturbance characteristics. However, lower write current and faster ($<1\text{ns}$) write time are required for them to replace existing techniques. We have shown that with interface modification we can achieve very low write current using a tungsten-based MTJ structure with atomic layer of Hf "spacer" and "dusting" [1]. Here we demonstrate high speed operation of these nanostructures.

We fabricate a series of MTJ pillars on top of 4 nm of PtHf alloy spin Hall channels. We show that we can achieve fast pulse switching with characteristic time scale smaller than 1 ns (Figure 2 and Figure 3), and the write error rate can be driven down below 10^{-6} , with high enough overdrive in the spin Hall channel. This extraordinary performance could potentially be due to fast domain nucleation process induced by various factors including Oersted field / field like torque / sample geometry.

Micromagnetic simulation shows that non-uniform initial state can be beneficial to switching, promoting switching speed in a preferred direction [2].

Our research shows that if we can utilize (or control) preferred non-uniform configuration and it is possible to achieve ultra-fast pulse switching in the MTJs.

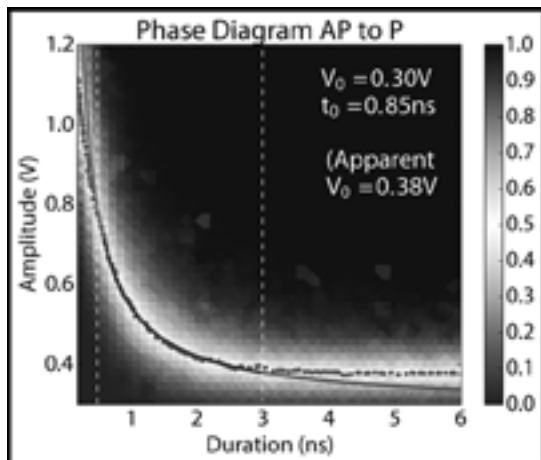


Figure 2: Switching probability of the free layer with injection of voltage pulses at various durations. Switching polarity is from AP to P.

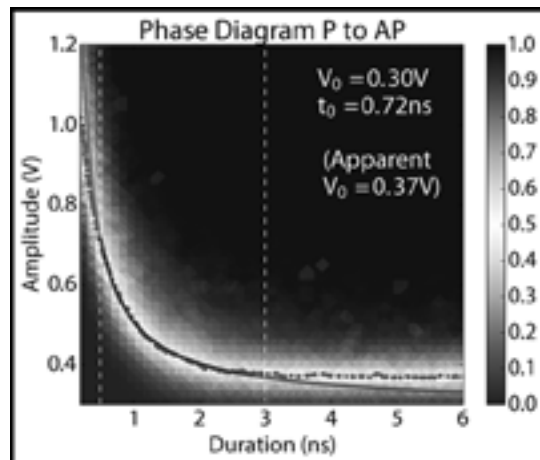


Figure 3: Switching probability of the free layer with injection of voltage pulses at various durations. Switching polarity is from P to AP.

References:

- [1] Shengjie Shi, Yongxi Ou, S. V. Aradhya, D. C. Ralph and R.A. Buhrman, Fast Low-Current Spin-Orbit-Torque Switching of Magnetic Tunnel Junctions through Atomic Modifications of the Free-Layer Interfaces. *Phys. Rev. Applied.* 9, 011002 (2018).
- [2] Aradhya, S. V., Rowlands, G. E., Oh, J., Ralph, D. C. and Buhrman, R. A. Nanosecond-Timescale Low Energy Switching of In-Plane Magnetic Tunnel Junctions through Dynamic Oersted-Field-Assisted Spin Hall Effect. *Nano Lett.* 16, 5987-5992 (2016).

Reduction of the Spin Hall Angle in Oxygen-Doped Beta Tungsten

CNF Project Number: 111-80

Principal Investigator: Robert A. Buhrman

User: Ryan Tapping

Affiliation: Applied and Engineering Physics, Cornell University

Primary Source of Research Funding: The Office of Naval Research and the National Science Foundation

Contact: buhrman@cornell.edu, rct76@cornell.edu

Primary CNF Tools Used: GCA 5x stepper; AJA sputtering tool, Veeco Icon AFM

Abstract:

Spintronic devices rely on spin currents that can be generated from charge currents flowing through certain non-magnetic metals. The spin Hall angle (SHA) is a measure of a materials' efficiency of this charge to spin current conversion. Tungsten is useful because the thin films have been shown to have a very large SHA of over 0.30, but only when the tungsten is ordered in the A15 structure (β -W) [1]. It has been previously shown that incorporation of oxygen into the tungsten during deposition can promote β -W growth and increase the SHA. Using spin-torque ferromagnetic resonance (ST-FMR) [2], we demonstrate that the SHA may actually decrease from over 0.30 to 0.10 or less as the oxygen concentration increases. We also show that the roughness of the tungsten films is approximately 0.19 ± 0.03 nm and is not significantly affected by the oxygen incorporation.

Summary of Research:

Thin film samples were deposited onto 100 mm silicon wafers using our magnetron sputtering system. The structure was $W(8)/Fe_{60}Co_{20}B_{20}(t_{FeCoB})/MgO(2)/Ta(1)$ with numbers in parenthesis representing the thickness of the layer in nanometers, and t_{FeCoB} the thickness of FeCoB, was varied between 2 and 4 nm. Oxygen was incorporated only during the sputtering of tungsten,

with the percentage corresponding to the relative amount of oxygen to argon. Stacks were then patterned into $20 \times 5 \mu m^2$ microstrips using photolithography with the 5X g-line stepper at CNF and etched using our own ion milling system. The contacts were made using the AJA sputtering system at CNF. An optical image of the microstrip is shown in Figure 1.

X-ray diffraction measurements were done on the tungsten thin films to verify that the sputtering techniques yielded β -W. Peaks were found corresponding to mostly β phase tungsten composition, and with some mixed phase α -W likely present. Resistivity measurements, using the van der Pauw method, also confirmed that the films were majority β phase, where β -W typically has a resistivity of between 100 - $300 \mu\Omega\cdot cm$ [1]. Resistivities ranged from $127 \mu\Omega\cdot cm$ for tungsten films with no oxygen incorporation to 329 , 306 , and $723 \mu\Omega\cdot cm$ for tungsten with 1.6% , 2.4% and 4.0% oxygen respectively.

The spin hall angle (SHA) was determined using spin-torque ferromagnetic resonance (ST-FMR) with analysis described by Pai, et al., for determination of the SHA [2]. This technique works by driving a microwave frequency (RF) current through the microstrip, which induces magnetic precession in the ferromagnetic layer via the spin transfer torque. A magnetic field is swept from -3000 to 3000 Oe at 45° to the microstrip and the voltage

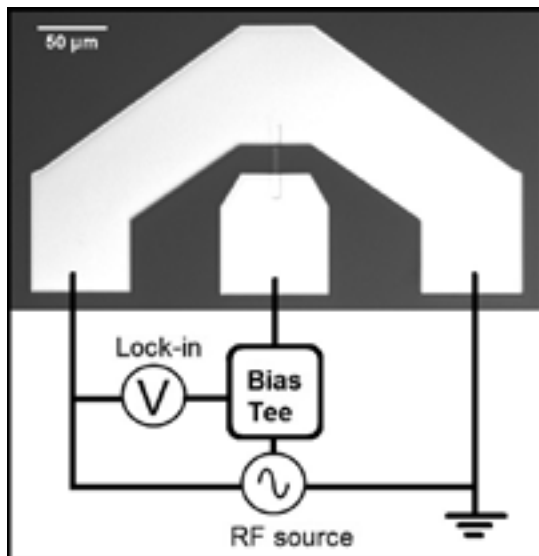


Figure 1: Microstrip after fabrication with a schematic of the ST-FMR measurement.

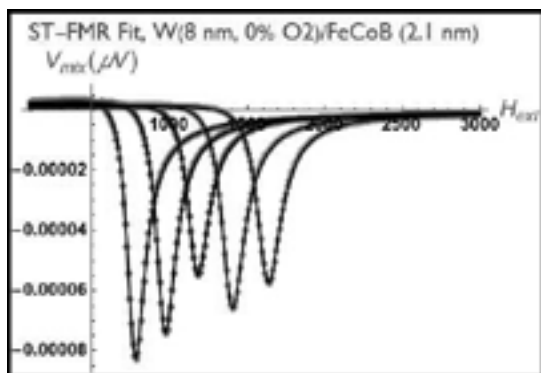


Figure 2: Voltage output from a magnetic field sweep from ST-FMR. Fits are also shown at 8, 9, 10, 11, and 12 GHz frequencies.

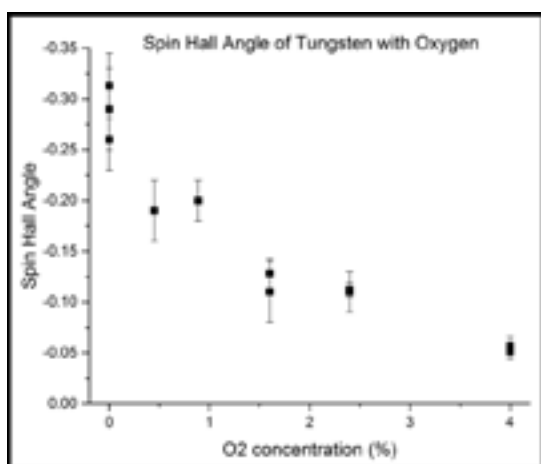


Figure 3: The spin hall angle (SHA) vs. oxygen incorporation in tungsten films.

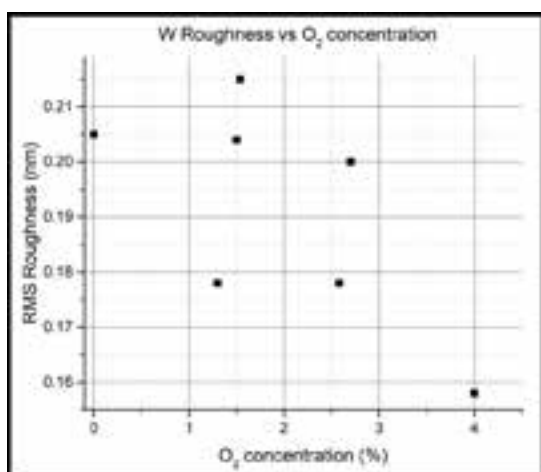


Figure 4: The roughness of tungsten films vs. oxygen incorporation shows no significant variation.

is measured by a lock-in amplifier, then the measurement is repeated for various frequencies. A lineshape analysis is done by fitting a Lorentzian function with symmetric (S) and antisymmetric (A) components as shown in Figure 2. The ratio of the prefactors S and A yield ξ_{FMR} , the spin torque efficiency. By fitting $1/\xi_{\text{FMR}}$ vs. $1/t_{\text{FeCoB}}$ the SHA is extrapolated.

For pure tungsten films with no oxygen incorporation, the SHA was found to be 0.31 ± 0.03 . However, as oxygen incorporation increased, the SHA was found to decrease, with values of 0.13 ± 0.02 and 0.06 ± 0.01 for tungsten with 1.6% and 4.0% oxygen respectively. The results of the SHA vs. oxygen incorporation for several samples are shown in Figure 3. Despite resistivity data demonstrating potentially enhanced β -W growth, the SHA reduces as oxygen is incorporated. The roughness of pure tungsten films with varying oxygen concentration were measured using the Veeco Icon AFM at CNF and all films had an rms roughness of 0.19 ± 0.03 nm, independent of oxygen concentration, as shown in Figure 4.

An explanation for the reduction in the SHA may be that the pure tungsten films were already grown in the β phase, and thus adding oxygen could not enhance the growth further. Rather, the oxygen may have only oxidized the tungsten which would also explain the increase in resistivity. This result contradicts the findings of K. Demasius, et al., which showed an enhancement of the SHA with oxygen incorporation [1].

References:

- [1] Kai-Uwe Demasius, Timothy Phung, Weifeng Zhang, Brian P. Hughes, See-Hun Yang, Andrew Kellock, Wei Han, Aakash Pushp, and Stuart S.P. Parkin, Nat. Comm. 7, 10644 (2016).
- [2] Chi-Feng Pai, Yongxi Ou, Luis Henrique Vilela-Leão, D.C. Ralph, and R.A. Buhrman, Phys. Rev. B. 92, 064426 (2015).

Study of Spin-Orbit Torques in Transition Metal Dichalcogenide / Ferromagnet Heterostructures

CNF Project Number: 598-96

Principal Investigator: Daniel C. Ralph

User: Vishakha Gupta, Gregory Stiehl, Ruofan Li

Affiliation: Physics, Cornell University

Primary Source of Research Funding: DOE Office of Science

Contact: DCR14@cornell.edu, VG264@cornell.edu, GMS263@cornell.edu, RL643@cornell.edu

Primary CNF Tools Used: AFM Veeco Icon, Zeiss Supra SEM and Nabity,

SC4500 even hour evaporator, Oxford 81 etcher, AJA sputter deposition

Abstract:

Two-dimensional (2D) transition metal dichalcogenides (TMDs) present a unique platform for spintronics because of their strong spin-orbit (S-O) couplings and atomically flat surfaces which can be readily interfaced with other materials. Our focus is the study of TMDs coupled to ferromagnets, which can lead to the generation of novel spin-orbit torques. Fabrication of these heterostructures requires special techniques to ensure that their interface remains clean and well-ordered throughout. We discuss the methods for fabricating TMD/ferromagnet devices and present electrical measurements that measure the spin-orbit torques produced.

Summary of Research:

Recent experiments have demonstrated that integrating a ferromagnetic material with a low symmetry crystalline material that possesses strong spin-orbit (S-O) coupling can generate new forms of S-O torques, which can be used to efficiently manipulate magnetic devices with perpendicular magnetic anisotropy [1,2]. Single-crystal transition metal dichalcogenides (TMDs) are a family of layered materials with strong S-O coupling that have a wide variety of crystal symmetries [3]. This makes them ideal candidate spin source materials for the generation of novel S-O torques. Here, we discuss methods to assemble heterostructures of exfoliatable TMDs (like WTe_2 , TaTe_2 , MoTe_2 , NbSe_2) and thin metallic ferromagnets for making quantitative measurements of the various torques generated.

The layers in a TMD crystal are bonded by weak van der Waal interactions and can be easily isolated by mechanical cleaving. We fabricate our samples by exfoliating the TMD from a bulk crystal using the scotch tape method, onto a high resistivity silicon wafer. The final step of the exfoliation process is carried out under high vacuum ($< 10^{-6}$ torr). This prevents degradation of the atomically flat TMD surface through absorption of water vapor and/or oxygen.

The TMD is interfaced with 6 nm of permalloy (Py = $\text{Ni}_{81}\text{Fe}_{19}$), which is deposited by grazing-angle

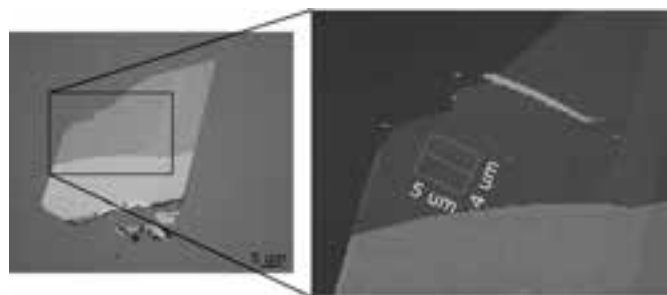


Figure 1: (left) Optical image of TMD/Py sample on a Si substrate before device patterning. The different color intensities indicate different thicknesses. (right) AFM image of the boxed region. White dashed lines indicate the active region used to make the device, with surface roughness < 300 pm and thickness 2.2 nm.

DC magnetron sputtering (with a rate < 0.2 Å/s) to minimize mechanical damage to the TMD surface. To prevent oxidation of the ferromagnet, the sample is further capped with 2 nm of aluminum. A combination of optical microscopy and atomic force microscopy (CNF AFM Veeco Icon) are used to identify thin (< 15 nm) and homogenous (surface roughness < 300 pm) regions on TMD flakes (Figure 1).

E-beam lithography (CNF Zeiss Supra SEM, Nabity) is used to pattern the selected flakes into bar geometries of $\sim 4 \times 5$ μm in size, needed to perform spin-torque



Figure 2: Optical Images of (left) Bar geometry patterned onto a TMD flake. (right) The flake around the bar is etched away using Ar ion milling. The region under the bar is protected by a hard SiO₂ mask.

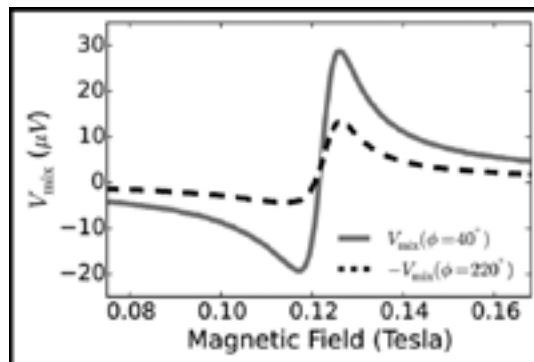


Figure 4: ST-FMR resonances for a TMD/Py sample with magnetization oriented at 40° and 220° relative to the current direction [1].

ferromagnetic resonance (ST-FMR) measurements [4,5] or second harmonic Hall measurements [6,7]. A hard mask of SiO₂ is used (CNF SC4500 even hour evaporator) to protect the active region of the device while the rest is etched out using Ar ion milling (Figure 2).

To protect the edges of the TMD/Py bilayer after ion milling, the sample is re-clamped by sputtering a thin conformal coating of SiO₂ (CNF AJA sputter deposition). A final round of e-beam lithography (CNF Zeiss Supra SEM, Nabyti) is performed to make electrical contact with the defined bars. The SiO₂ mask in the contact region is removed using reactive-ion etching (RIE) with a CHF₃/Ar mixture (CNF Oxford 81 etcher). Finally, Ti/Pt (CNF AJA sputter deposition) contacts are sputter deposited through a lift-off process.

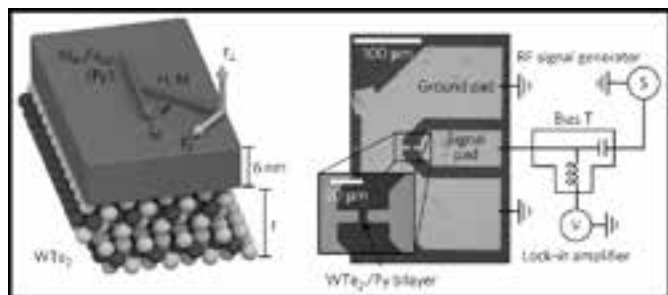


Figure 3: (left) Schematic of the heterostructure geometry [1] (right) Optical image of final device and schematic of the circuit used for ST-FMR measurements [1].

We use ST-FMR to measure the torques produced at room temperature [4,5]. As depicted in Figure 3, an RF current (8-12 GHz) is applied to the sample along with an in-plane magnetic field to tune the ferromagnet through resonance. The precessing magnetization gives rise to a changing anisotropic magnetoresistance (AMR), which mixes with the current leading to a DC signal V_{mix}

that is measured (Figure 4). By analyzing the symmetric and antisymmetric components of the V_{mix} lineshape as a function of applied field, the various torque contributions can be computed [1].

In conclusion we have provided a detailed discussion of the techniques employed in fabricating TMD/ferromagnet heterostructure devices and have presented spin-torque ferromagnetic resonance data that measures the S-O torques generated. TMDs allow for a systematic study of these torques as a function of various crystal symmetries and thicknesses [2]. These investigations provide important clues towards identifying the role of broken symmetries and bulk- vs. interface-driven mechanisms in the generation of spin-orbit torques.

References:

- [1] MacNeill, D. et al., "Control of spin-orbit torques through crystal symmetry in WTe₂/ferromagnet bilayers," *Nature Physics* 13, 300 (2017).
- [2] MacNeill, David, et al., "Thickness dependence of spin-orbit torques generated by WTe₂," *Physical Review B* 96, 054450 (2017).
- [3] Wilson, J. A., and A. D. Yoffe, "The transition metal dichalcogenides discussion and interpretation of the observed optical, electrical and structural properties," *Advances in Physics* 18, 193 (1969).
- [4] Liu, Luqiao, et al., "Spin-torque ferromagnetic resonance induced by the spin Hall effect," *Physical Review Letters* 106, 036601 (2011).
- [5] Liu, Luqiao, et al., "Spin-torque switching with the giant spin Hall effect of tantalum," *Science* 336, 555 (2012).
- [6] Hayashi, Masamitsu, et al., "Quantitative characterization of the spin-orbit torque using harmonic Hall voltage measurements," *Physical Review B* 89, 144425 (2014).
- [7] Garello, Kevin, et al., "Symmetry and magnitude of spin-orbit torques in ferromagnetic heterostructures," *Nature Nanotechnology* 8, 587 (2013).

Spin Hall Effect in CaRuO_3

CNF Project Number: 598-96

Principal Investigators: Daniel Ralph, Darrell Schlom

Users: Neal Reynolds, Hari Nair, Nathaniel Schreiber

Affiliations: Laboratory of Atomic and Solid State Physics, Materials Science and Engineering; Cornell University

Primary Source of Research Funding: National Science Foundation

Contact: dcr14@cornell.edu, schlom@cornell.edu, ndr37@cornell.edu

Primary CNF Tools Used: 5x g-line stepper, AJA sputter deposition tool, Heidelberg DWL2000

Abstract:

The spin Hall effect results in the generation of pure spin current that flows transverse to an applied electric field in non-magnetic materials. Recent experimental and theoretical work has shown that the presence and evolution of heavily-renormalized, flat, quasi-particle bands near the Fermi level can dramatically influence the magnitude of the spin Hall effect. CaRuO_3 is a so-called “Hund’s metal” in which electron correlation due Hund’s rule coupling is relevant. These strong correlations along with the large octahedral distortions in CaRuO_3 results in the emergence of flat quasi-particle bands below 120 K and a change in sign of the Hall coefficient below ~ 50 K — indications of non-trivial modifications of the Fermi surface by the quasi-particle bands as temperature is decreased. In this report we discuss the measurement of the spin Hall effect in CaRuO_3 /Permalloy ($\text{Ni}_{80}\text{Fe}_{20}$, Py) bilayers as a function of temperature.

Summary of Research:

The spin Hall effect arises from spin-dependent interaction with a material’s band structure, so-called “intrinsic” contributions, and spin-dependent scattering off of impurities in a given material, so-called “extrinsic” contributions. Intrinsic contributions to the spin Hall effect are large when in materials with strong spin orbit coupling and when the Fermi level lies within avoided crossings opened up by the strong spin orbit coupling. Materials that are expected to have large intrinsic spin Hall effects are then the late transition metals (those with 5d valence) [1], and the f-valent lanthanides [2] and actinides. Very recent work in a rare-earth Kondo lattice system has suggested that the presence of Kondo-derived heavy quasi-particle bands near the Fermi level can drive an enhancement of the spin Hall effect. The understanding of this enhancement, however, is complicated by the fact that the Kondo physics also gives rise to an enhancement of the 4f orbital bands near the Fermi level, which has been shown to independently enhance the spin Hall effect [2].

To understand the contribution of the strong correlation on the enhancement of the spin Hall effect without

4f orbitals present, we examine the spin Hall effect in calcium ruthenium trioxxygen (CaRuO_3) as a function of temperature, because it exhibits pockets of flat quasi-particle bands starting at 120 K and below. The evolution of the Fermi surface due to these bands culminates in a reversal of the Hall coefficient at ~ 50 K. Given the sensitivity of the intrinsic spin Hall effect to the material’s band structure, we expect that as temperature is decreased from room temperature we will observe a change in the spin Hall effect at these temperatures.

CaRuO_3 was grown on a neodymium gallium trioxxygen (NdGaO_3) substrate using molecular beam epitaxy (MBE) in collaboration with the Schlom group. Films were then taken to a sputter deposition system to deposit Permalloy (Py) and an aluminum capping layer. Micron-scale devices were patterned out of the films via photolithography using the 5x g-line stepper, and argon ion milling was used to define the devices. Ti/Pt liftoff leads were applied via photolithography, again with 5x g-line stepper, and the AJA sputter deposition tool. An optical image of a finished device is shown in Figure 1.

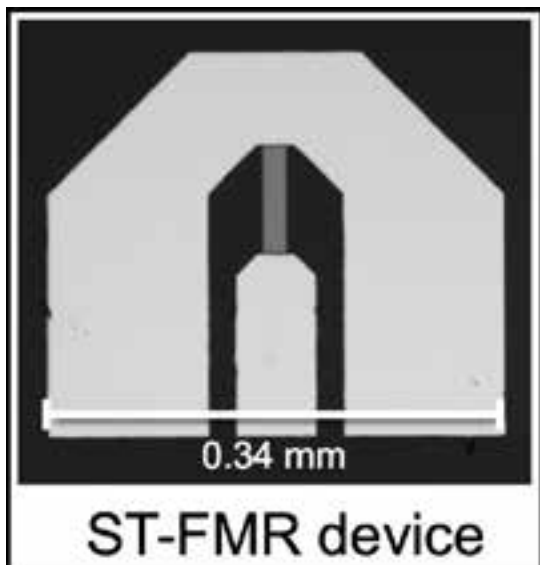


Figure 1: An optical image of a finished device used to measure the spin Hall effect via ST-FMR.

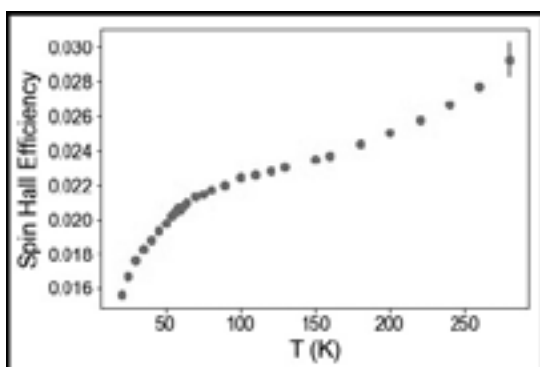


Figure 2: Spin Hall effect efficiency as a function of temperature measured by ST-FMR of a CaRuO₃/Py bilayer. The spin Hall effect decreases going from 280 K to 20 K with an inflection points at ~ 120 K and a slope change vs T at ~ 50 K consistent with the onset of the quasi-particle bands and the Hall effect coefficient sign reversal observed in CaRuO₃, respectively.

Measurements of the spin Hall effect as a function of temperature were done using spin torque-ferromagnetic resonance (ST-FMR) [3,4] in a custom He-flow cryostat. ST-FMR uses a microwave frequency signal (6-20 GHz) to excite resonant dynamics of the magnetic Py layer that then leads to a measurable voltage that is proportional to the strength of the spin Hall effect.

We report the strength of the spin Hall effect as a dimensionless efficiency calculated as the ratio of the measured spin current to applied charge current. We find a gradual decrease of the spin Hall effect with temperature, but with an inflection point ~ 120 K, consistent with the onset of the quasi-particle states, and a change in slope at ~ 50 K, commensurate with the change in Hall effect coefficient sign (Figure 2).

References:

- [1] H. L. Wang, C. H. Du, Y. Pu, R. Adur, P.C. Hammel, and F. Y. Yang, Phys. Rev. Lett. 112, 197201 (2014).
- [2] N. Reynolds, P. Jadaun, J. T. Heron, C. L. Jermain, J. Gibbons, R. Collette, R. A. Buhrman, D. G. Schlom, and D. C. Ralph, Phys. Rev. B 95, 064412 (2017).
- [3] L. Liu, T. Moriyama, D. C. Ralph, and R. A. Buhrman, Phys. Rev. Lett. 106, 036601, (2011).
- [4] L. Liu, C. F. Pai, Y. Li, H. W. Tseng, D. C. Ralph, and R. A. Burhman, Science 366, 555 (2012).

Wrapping Microdroplets with Two-Dimensional Materials

CNF Project Number: 900-00

Principal Investigators: Paul L. McEuen^{1,2}, Itai Cohen^{1,2}, Jiwoong Park^{3,4}

**Users: Kathryn L. McGill¹, Michael F. Reynolds¹, Marc Z. Miskin^{1,2},
Maritha Wang^{3,4}, Hui Gao^{3,4}, Kibum Kang^{3,4}**

Affiliations: 1. Laboratory of Atomic and Solid State Physics, Cornell University, Ithaca NY, USA; 2. Kavli Institute at Cornell for Nanoscale Science, Cornell University, Ithaca NY, USA; 3. Department of Chemistry and Chemical Biology, Cornell University, Ithaca NY, USA; 4. Department of Chemistry, Institute for Molecular Engineering, and James Franck Institute, University of Chicago, Chicago IL, USA

Primary Sources of Research Funding: Cornell Center for Materials Research with funding from the NSF MRSEC program (DMR-1719875), Air Force Office of Scientific Research (AFSOR) Multidisciplinary Research Program of the University Research Initiative Grant FA2386-13-1-4118

Contact: plm23@cornell.edu, klm274@cornell.edu, mfr74@cornell.edu

Primary CNF Tools Used: Autostep i-line stepper, Oxford 81 etcher

Abstract:

We present experiments demonstrating the wrapping of microscopic oil droplets by two-dimensional (2D) materials. We show that 2D materials such as graphene and molybdenum disulfide (MoS_2) wrap microscopic liquid drops in the same ways in which millimeter-scale drops were wrapped by thin elastic sheets [1,2].

Summary of Research:

Wrapping fluid droplets with thin elastic sheets has been used to perform capillary origami [3] and as a technique to measure bending moduli [4] of thin films. In the case where the bending energy of the sheet is much smaller than the surface tension of the droplet, the minimization of surface energy by wrapping and the inability for a planar sheet to take on Gaussian curvature determine the shape. Previous experiments include geometric wrapping patterns of droplets [2] and wrinkling of sheets on droplet surfaces [5]. Here we perform analogous experiments on the wrapping of oil droplets in water with the thinnest possible materials: one-atom-thick graphene and three-atom-thick MoS_2 .

We begin by photolithographically patterning 2D materials into a variety of simple shapes using the GCA AutoStep 200 i-line wafer stepper and the Oxford etchers at the Cornell NanoScale Science and Technology Facility. We use commercially available graphene on copper (Grolltex) and transfer it onto glass coverslips using a poly(methyl methacrylate) (PMMA) support layer. Our MoS_2 samples are grown onto glass coverslips via metal-organic chemical vapor deposition (MOCVD) by collaborators in Jiwoong Park's group at the University of Chicago, and we cover them in a protective layer of

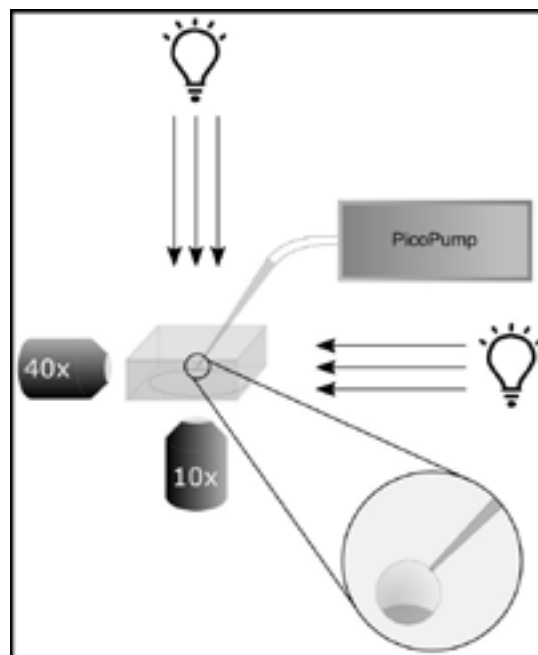


Figure 1: Schematic of setup. Inset shows Fluorinert drop with 2D material wrapping from the bottom.

PMMA during fabrication. After patterning, we etch through the PMMA/MoS₂ or graphene to define our features. We then remove the PMMA and release the graphene or MoS₂ from the glass substrate with a dilute hydrofluoric acid etch.

The experimental setup is shown schematically in Figure 1. The substrates containing the 2D material sheets are placed in a home-built cuvette filled with deionized water. Using an electronic micromanipulator (Sensapex), we position a glass micropipette filled with Fluorinert FC-70 (3M), an oil that is both denser than and index-matched to water, over the graphene/MoS₂ sheets. Droplets are formed by applying pressure spikes (Picopump, World Precision Instruments) to the micropipette, then lowered onto the 2D material sheets for pick up. We then use suction to shrink the droplet until it is completely wrapped by the 2D sheet. Simultaneously, we record the bottom and side views of the process using an inverted microscope and side-view objective, respectively.

Once we pick up the sheets, we use both the side and bottom views to simultaneously watch the wrapping process. Figure 2 shows a time series of images from both cameras as a circular MoS₂ sheet wraps a Fluorinert droplet. Frames 1 and 2 show the initial deflection of the droplet from a spherical shape due to the MoS₂ sheet. Frame 3 shows a triangular-wrapped shape, one of the typical wrapping geometries for circular sheets [2], before the shape is distorted by vacuum removal of Fluorinert in frames 5 and 6.

For circular sheets, we see triangular prisms, shown in Figure 3A, and “empanada” wrapping states. For square sheets, we see square “turnover” wrapping patterns – where the four corners are folded to the center, shown in Figure 3B. For triangular sheets, as with the circular ones, wrapping corresponds roughly to triangular prisms, shown in Figure 3C. Overall, we find that wrapping geometries are similar to those in Ref. (2) and are determined by the initial shape of the 2D material sheet.

This demonstration indicates a new route for making 3D geometries out of 2D materials by drawing on an existing literature of droplet wrapping with sheets, and it suggests the possibility of using 2D materials to perform wrapping at more complicated fluid interfaces, or to controllably form 3D microstructures. Future work includes new patterns to demonstrate capillary origami folding with 2D materials as well as wrapping droplets with devices with optical, electronic, and/or magnetic components.



Figure 2: (top) Time lapse of Fluorinert droplet wrapping by MoS₂, side view; (bottom) Time lapse of the same droplet wrapping, bottom view.

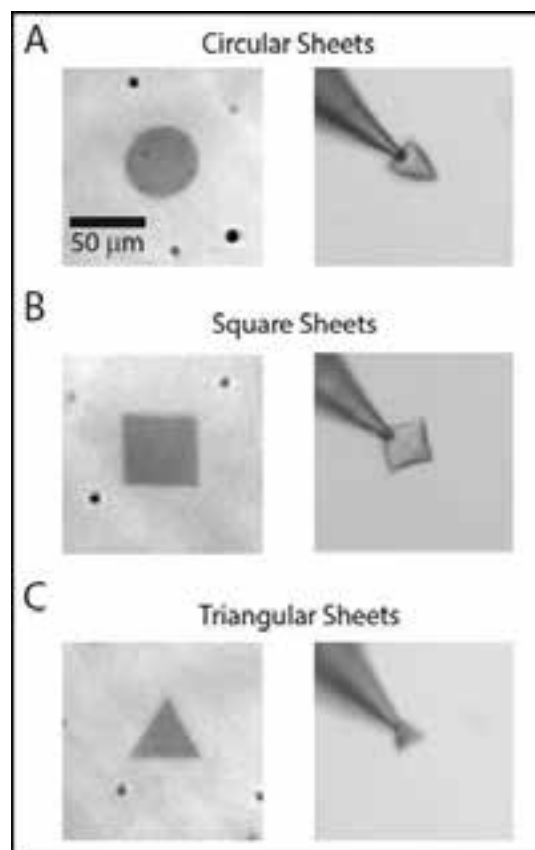


Figure 3: Final wrapped states for various sheet geometries.

References:

- [1] D. Kumar, J. D. Paulsen, T. P. Russell, N. Menon, *Science*. 359, 775 (2018).
- [2] J. D. Paulsen et al., *Nat. Mater.* 14, 1206-1209 (2015).
- [3] G. McHale, M. I. Newton, N. J. Shirtcliffe, N. R. Gherali, *Beilstein J. Nanotechnol.* 2, 145-151 (2011).
- [4] J. Bae, T. Ouchi, R. C. Hayward, *ACS Appl. Mater. Interfaces*. 7, 14734-14742 (2015).
- [5] J. Huang et al., *Science*. 317, 650-653 (2007).

Phase Transition and Equilibrium in Nanoconfinement

CNF Project Number: 1119-03

Principal Investigator: Abraham Duncan Stroock

User: Hanwen Lu

*Affiliations: Robert Fredrick Smith School of Chemical and Biomolecular Engineering,
Sibley School of Mechanical and Aerospace Engineering; Cornell University*

Primary Source of Research Funding: Air Force Office of Scientific Research (FA9550-15-1-0052)

Contact: abe.stroock@cornell.edu, HL943@cornell.edu

*Primary CNF Tools Used: Photolithography spinners, ABM contact aligner, Oxford 80s, P10 profilometer,
general chemical hood, Zeiss Ultra scanning electron microscope (SEM), SÜSS SB8e bonder*

Abstract:

Phase transitions are of natural [1,2], biological [3], and technological [4] importance. A phase transition typically takes place by nucleation catalyzed by foreign surfaces. For example, cloud formation is thought to be ice nucleation from vapor catalyzed by aerosol particles. However, due to the complex structural and chemical composition of aerosol, the exact freezing mechanism remains elusive and the lack of understanding significantly hinders our ability in predicting global radiation budget [5]. It has been proposed that nanoporous surfaces give rise to a two-step freezing process known as Pore Condensation Freezing (PCF) [6], yet the freezing transition on well-defined nanoscale roughness has not been systematically studied. Taking advantage of the nanofabrication capability at CNF, we have tackled this problem with two distinct approaches: 1) we fabricated a geometrically well-defined nanoporous membrane with Block Co-polymer (BCP) nanolithography to investigate of collective influence of nanoscopic surface topography; and 2) we fabricated high aspect ratio nanochannels via conventional lithography to directly observe phase transition in individual nanoconfinement.

Summary of Research:

Block Co-Polymer (BCP) Silicon Oxide Membrane. BCP nanolithography is a newly developed process in CNF by CNF Fellow Alex Ruyack and staff Vince Genova. BCP lithography pattern formation relies on phase separation in forming nanoscopic lamella phase aligned perpendicular to the substrate. We first spin-coated 100 nm SiO₂ PECVD film with 2% P8205-PMMA BCP. The polymer was allowed to phase separated in vacuum furnace overnight, then the PMMA is cleaved and removed leaving a coating of PS polymer with nanoscopic hollow cylinders. The porous pattern was transferred onto the substrate with plasma etching, forming a nanoporous membrane shown in Figure 1. The membrane fabricated with BCP lithography is highly mono-dispersed with typical pore radius of 13-15 nm.

The freezing efficiency of the membrane was characterized in an environmental vacuum chamber in the Stroock lab. Figure 2 reports the temperature and saturation with respect to ice (SRI) at which freezing was initiated on the membrane. The freezing behavior on the membrane first followed the liquid saturation line and then transitioned to the capillary condensation line at around 240K. This behavior is in quantitative agreement with prediction by Pore Condensation Freezing and Classical Nucleation Theory.

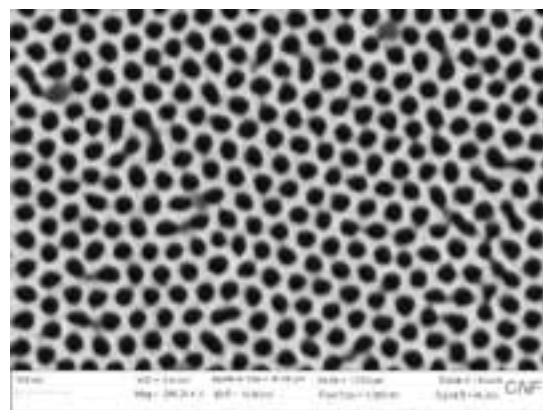


Figure 1: SEM image of BCP silicon oxide membrane. well-ordered mono-dispersed pores can be seen from a top view.

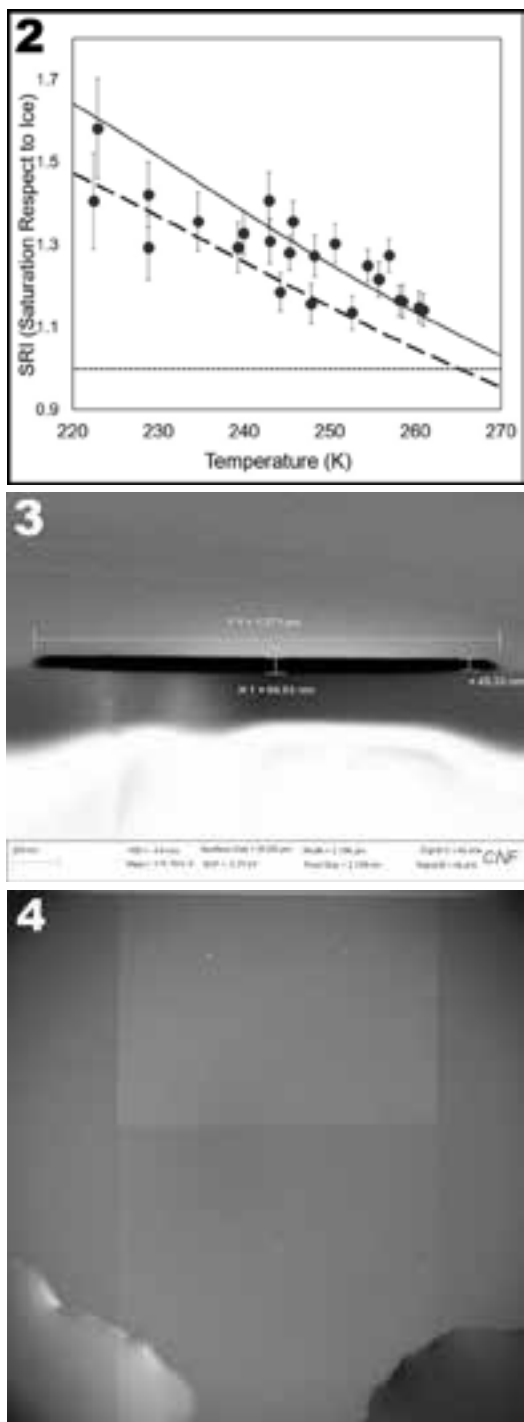


Figure 2, top: The onset of freezing transition on BCP silicon oxide membrane. the solid is the saturation line for supercooled liquid; the dotted line is the ice saturation line; the dashed line is the capillary condensation line above which supercooled liquid can capillary condense in the nanopores. The PCF predicts that freezing follows the capillary condensation line in lower temperature catalyzed by condensed liquid in the nanopore. In the figure, freezing transitioned from the liquid saturation to the capillary condensation line at around 240K. The transition temperature predicted by Classical Nucleation Theory is 243K. **Figure 3, middle:** SEM of a cleaved nanochannel cross-section. The top side of the nanochannel is the silicon side and the bottom is the Borofloat glass. **Figure 4, bottom:** The wetting front of 10 μm nanochannel array in water. The brighter portion of the channel towards the top is dry, the darker portion is filled. The lower left/right puddle is water on top of the device.

High Aspect Ratio Nanochannel. To experimentally study nucleation in single nanopore, we fabricated high aspect ratio nanochannels on silicon substrates. The micron-wide channel allows direct optical observation while the nanoscopic channel depth induces confinement effect that is distinctive from bulk phenomenon. The fabrication process is as follows; the nanochannel pattern was first created by conventional photolithography, then the substrate is etched in Oxford 80s in CF_4 plasma to create trenches ranging from 30 nm to 120 nm, the cross-sectional profile is then characterized with P10 profilometer as well as with Veeco Icon atomic force microscopy (AFM). Finally, nanochannels were anodically bonded to Borofloat glass to form a nanochannel microfluidic device. The cross-section of a bonded device with 2 μm width is shown in Figure 3.

Some variations of channel depth can be observed as well as large side wall slope short etching duration. Imbibition experiments were performed with the nanochannel devices. The wetting dynamics in nanochannels follows Washburn dynamics, i.e.: $L^2 = Dt$, where L is the wetting front position, t is time and D is a constant related to channel height. The imbibition dynamics in all experiment follows above relation with implied channel height consistent with SEM micrograph, with exception of the initial imbibition experiment. The faster dynamics is observed during the first imbibition which can be interpreted as result of flow in prewetting films and corners in perfect wetting scenario.

As experiments were repeated, the hydrophilicity of channel wall deteriorated and thus corner flow cannot be sustained. Crystallization and freezing phenomena in confinement are current being studied with these nanochannel devices.

References:

- [1] Bartels-Rausch, T. Ten things we need to know about ice and snow. *Nature* 494, 27 (2013).
- [2] Murray, B. J., O'Sullivan, D., Atkinson, J. D. and Webb, M. E. Ice nucleation by particles immersed in supercooled cloud droplets. *Chem. Soc. Rev.* 41, 6519 (2012).
- [3] Mazur, P. Cryobiology: The Freezing of Biological Systems. *Science* (80-.). 168, 939-949 (1970).
- [4] Bartels-Rausch, T. et al. Ice structures, patterns, and processes: A view across the icefields. *Rev. Mod. Phys.* 84, 885-944 (2012).
- [5] Myhre, G. et al. Anthropogenic and Natural Radiative Forcing. *Clim. Chang.* 2013 Phys. Sci. Basis. Contrib. Work. Gr. I to Fifth Assess. Rep. Intergov. Panel Clim. Chang. 659-740 (2013). doi:10.1017/ CBO9781107415324.018
- [6] Marcolli, C. Deposition nucleation viewed as homogeneous or immersion freezing in pores and cavities. *Atmos. Chem. Phys.* 14, 2071-2104 (2014).

Vortex Dynamics in Nanofabricated Superconducting Devices

CNF Project Number: 1314-05

Principal Investigator: Britton L.T. Plourde

Users: Kenneth Dodge, JJ Nelson

Affiliation: Department of Physics, Syracuse University

Primary Source of Research Funding: Army Research Office

Contact: bpourde@syr.edu, krdodgej@syr.edu, jjnelson@syr.edu

Website: <http://plourdelab.syr.edu>

Primary CNF Tools Used: ASML 300C DUV stepper, JEOL 9500, Plasma-Therm PT740

Abstract:

We fabricate superconducting microwave devices for studying the dynamics of vortices and quasiparticles at low temperatures. Vortices are quantized bundles of magnetic flux that thread many different superconductors over a particular range of applied magnetic field. Our experiments are aimed at investigating loss mechanisms that can limit the performance of superconducting circuits for quantum information processing. In addition, we are probing the microwave properties of various superconducting materials for future implementations of qubits.

Summary of Research:

Superconducting microwave circuits play an important role in quantum information processing. Circuits composed of Josephson junctions and capacitors with superconducting electrodes can serve as qubits, the fundamental element of a quantum computing architecture. Various loss mechanisms limit the ultimate performance of these devices, including trapped magnetic flux vortices. Vortices can be trapped in the superconducting electrodes when background magnetic fields are present and contribute dissipation when driven with microwave currents [1]. Thus, techniques for controlling the trapping of vortices are critical to the development of large-scale quantum information processors with superconducting circuits. In addition, investigations of microwave vortex dynamics can be a useful tool for probing new superconducting materials for use in future implementations of qubits.

We are fabricating a system of microwave resonators using a variety of superconducting thin films, including Nb, TiN, NbTiN, and disordered Al, for studying the loss contributed by trapped flux in these materials over the frequency range from 1.5-11 GHz [2]. By cooling the resonators in different magnetic fields, we are able to probe the loss from vortices as a function of field at the resonance frequencies contained in our design. We study

the microwave properties of the vortex response as a function of various parameters, including temperature, frequency, device geometry, and film disorder.

We fabricate our microwave resonators from various superconducting films, including aluminum, deposited onto silicon wafers in vacuum systems at Syracuse University or by collaborators at other institutions. We define the patterns on the ASML stepper and transfer them into the films with a combination of reactive ion etching and wet-etch processing. We measure these circuits at temperatures of 100 mK and below in our lab at Syracuse University.

References:

- [1] Song, C., Heitmann, T.W., DeFeo, M.P., Yu, K., McDermott, R., Neeley, M., Martinis, John M., Plourde, B.L.T.; "Microwave response of vortices in superconducting thin films of Re and Al"; *Physical Review B* 79, 174512 (2009).
- [2] Dodge, K., Nelson, J., Senatore, M., Xu, P., Osborn, K., Pappas, D., Plourde, B.; "Microwave Response of Vortices in Superconducting Resonators with High Kinetic Inductance"; *Bull. Am. Phys. Soc.* 2018, <http://meetings.aps.org/Meeting/MAR18/Session/Y39.11>.

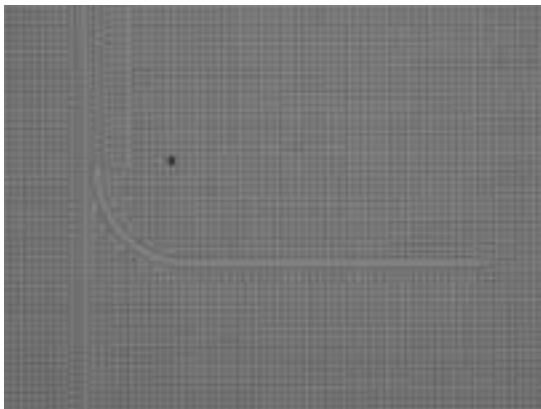


Figure 1: Coplanar waveguide resonator for probing microwave losses and magnetic field dependence in disordered superconducting aluminum thin films.

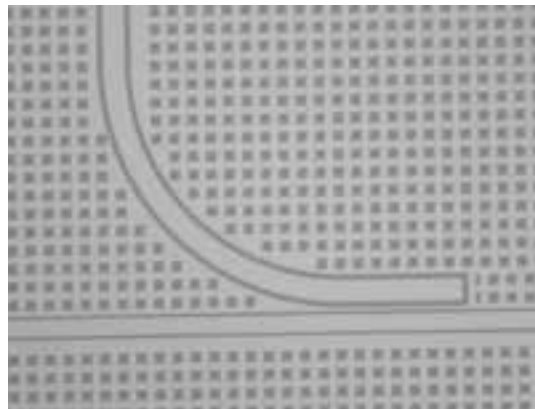


Figure 2: Capacitive coupling elbow structure for measurement of superconducting microwave resonator.

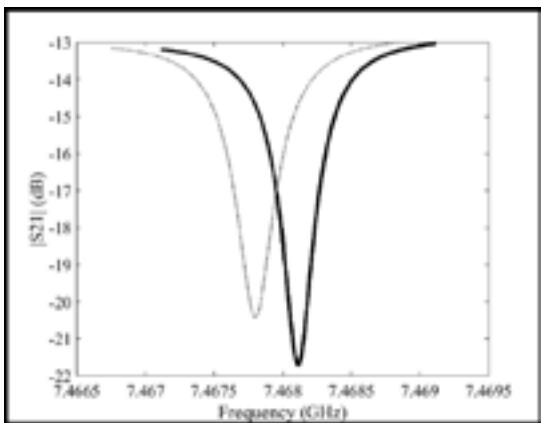


Figure 3: Measurement of microwave transmission dips corresponding to resonator patterned from disordered superconducting aluminum thin film; black (grey) curve corresponds to measurement in zero magnetic field (194 μ T).

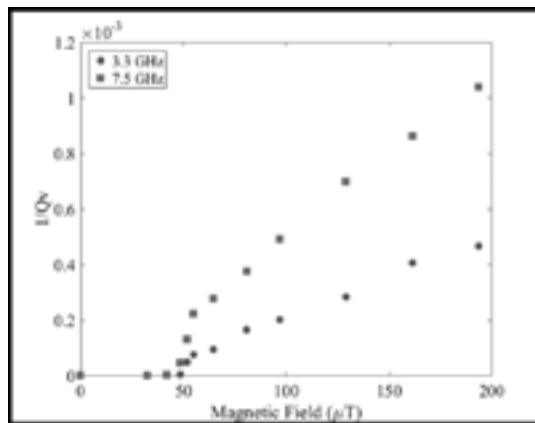


Figure 4: Microwave loss contribution from trapped vortices as a function of magnetic field in resonators patterned from disordered superconducting aluminum thin film for two different resonance frequencies.

Fabrication of Nanofluidic Cavities for Superfluid ^3He Studies

CNF Project Number: 1520-07

Principal Investigator: Jeevak M. Parpia

Users: Abhilash Thanniyil Sebastian, Nikolay Zhelev, Roberto DeAlba

Affiliation: Department of Physics, Cornell University

Primary Source of Research Funding: National Science Foundation

Contact: jmp9@cornell.edu

Website: <http://parpia.lassp.cornell.edu>

Primary CNF Tools Used: Furnaces, Oxford PECVD, contact photolithography, Oxford RIE, Plasma-Therm RIE, Unaxis DRIE, critical point dryer

Abstract:

We demonstrated nanoscale cavities that withstand 30 bar cooled to ultralow temperatures [1]. The surfaces of silicon-glass cavities are pristine having AFM characterized roughness under 1 nm [1,2]. We also examined the resonant properties of single layer graphene structures above and below room temperature. Despite extensive cleaning, there is evidence of residual polymer coatings on the surface [3].

Summary of Research:

Superfluid ^3He is a unique system for study. ^3He is a Fermion (like electrons), but its pairing into the superfluid state is more complex than its electronic counterparts producing a multiplicity of superfluid phases. In the bulk, the anisotropic A phase and the isotropically gapped B phase emerge. Confinement favors the A phase over the B phase [2,4].

The superfluid state is attained between 0 and 35 bar and between 0.9 and 2.5 mK (respectively). Below the superfluid transition, pairs condense into the coherent superfluid state. The pairing length-scale (pair diameter) varies from ~ 80 nm at 0 bar to 14 nm at high pressure. Confinement alters the phase diagram and as the ^3He

is progressively restricted to smaller sizes, the B phase should yield to the A phase and new phases should emerge.

In one series of experiments [5], we explore the thermal conductivity of confined ^3He . Two chambers are separated by a micromachined channel of dimensions $3\text{ mm} \times 100\text{ }\mu\text{m} \times 1.1\text{ }\mu\text{m}$ (Figure 1a). To fabricate this channel, 1 mm thick silicon wafers were oxidized using the oxide furnace in CNF to grow thick oxide ($> 2\text{ }\mu\text{m}$), then further oxide was deposited using the Oxford PECVD. Long channels with a width of 3 mm were patterned using contact photolithography and the oxide within them removed using both dry plasma etch (Oxford and Plasma-Therm RIE) and wet etch (6:1 BOE). Wafers were further oxidized to create a step in the Si-SiO₂ interface (modified LOCOS process) and oxide removed using HF. To define the channels further laterally to $100\text{ }\mu\text{m} \times 3\text{ mm}$, a second contact lithography step was used and the exposed Si was etched using the Unaxis DRIE to $200\text{ }\mu\text{m}$ depth. After removal of masking oxide, resist, and Bosch polymer, wafers were further oxidized with an oxide film target of 300 nm to protect surface during dicing and then diced using CNF's dicing saw. Matching glass pieces were also diced. Final step is to make the cells was to remove oxide off Si pieces, clean in SC-1 solution and bond using custom made anodic bonding jig.

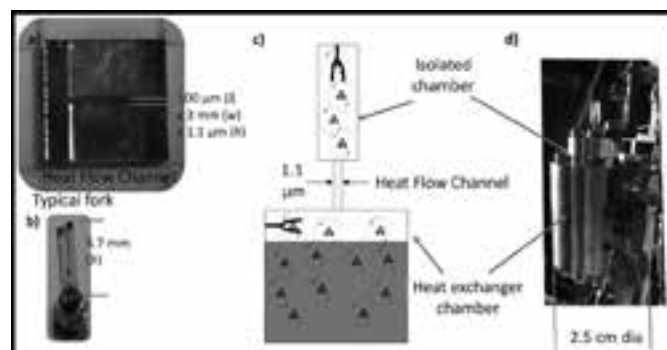


Figure 1: A. The bonded heat flow channel (5 mm square) with dimensions alongside. B. Typical quartz fork. C. Schematic of experiment. D. Photograph of experimental chamber [5]. See full color version on pages xxviii-xxix.

Chambers are monitored by Quartz “tuning fork” resonators (Figure 1b). One chamber (Fork 1) contains a heat exchanger to cool the ^3He . Fork 2 monitors the “isolated” chamber (Figure 1c,d). Pulses applied to Fork 2 heat the isolated chamber and heat flows through the micromachined channel. The relaxation following a heat pulse is measured. We have identified a thermal transport mechanism (thermomechanical heat flow) that is present only in the superfluid and then only when the mean free path is much longer than the height constraint. [5]

Measurements on supercooling of the A phase are in progress. The two phases (A and B) that are stable in the bulk are separated by a first order phase transition line. When the A phase is cooled below its stable region, it persists in a metastable state because nucleation of the B phase requires a significant energy cost. We observe

supercooling and measure the width (in temperature) of the distribution of A to B nucleation events. We intend to map the pressure dependence of the supercooling and determine if supercooling is affected by the thermal channel which favors the A phase.

We have also examined the resonant frequency and quality factor of single layer graphene resonators both above (300-500 K) and below (80-300 K) room temperature (Figure 2). The critical point dryer was an essential tool in this fabrication. We find that the resonant frequency and quality factor increase as the temperature deviates from room temperature. The results are interpreted as evidence of the persistence of traces of polymer coatings used as part of the transfer process to deposit the single layer material from growth chamber to device. [3]

Former Physics Ph.D. students Nikolay Zhelev (now Corning Research), Roberto DeAlba (now NIST), and post-doctoral scientist Abhilash Sebastian (now Aalto University) fabricated these structures before they left Cornell. Results from these structures are now emerging or have been recently published.

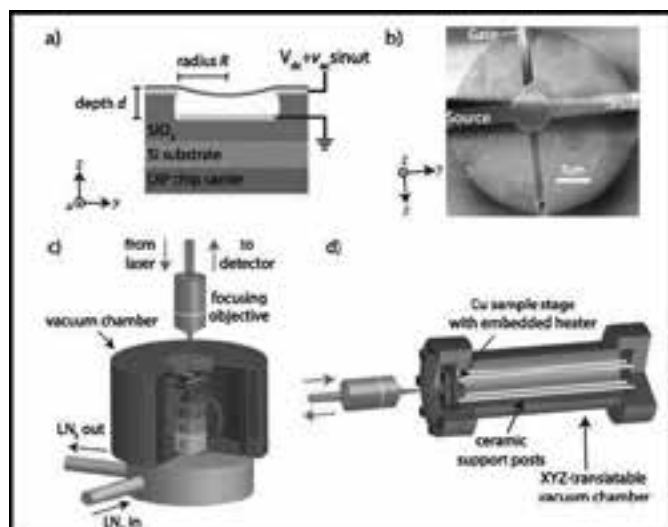


Figure 2: A. Cartoon cross-section of a graphene device. Suspended graphene (green) is pulled toward the back-gate via an applied voltage. B. False-color SEM image, showing the suspended graphene (green), metallic Source, Drain, and Gate (yellow), and surrounding SiO₂ substrate (grey). C. Liquid N₂ flow cryostat with optical access. Sample is mounted on a 24-pin Dual In-line Package (purple). D. Heated test chamber with optical window [3]. See full color version on pages xxviii-xxix.

References:

- [1] Fabrication of microfluidic cavities using Si-to-glass anodic bonding, N. Zhelev, T. S. Abhilash, R. G. Bennett, E. N. Smith, B. Ilic, L. V. Levitin, X. Rojas, A. Casey, J. Saunders, and J. M. Parpia arXiv:1805.00958.
- [2] The A-B transition in superfluid helium-3 under confinement in a thin slab geometry, N. Zhelev, T.S. Abhilash, E.N. Smith, R.G. Bennett, X. Rojas, L. Levitin, J. Saunders, and J.M. Parpia, Nature Comm. 15963 (2017).
- [3] Temperature-dependence of stress and elasticity in wet-transferred graphene membranes, Roberto De Alba, T. S. Abhilash, Aaron Hui, Isaac R. Storch, Harold G. Craighead, and Jeevak M. Parpia, Journal of Applied Physics 123, 095109 (2018).
- [4] Phase Diagram of the Topological Superfluid ^3He Confined in a Nanoscale Slab Geometry, L. V. Levitin, R. G. Bennett, A. Casey, B. Cowan, J. Saunders, D. Drung, Th. Schurig and J. M. Parpia, Science, 340 841-844, (2013).
- [5] Thermal Conductivity of ^3He confined in a 1.1 μm sized channel, Jeevak Parpia, Anna Eyal, Nikolay Zhelev, Dmytro Lotnyk, Michael Terilli, Abhilash Sebastian, Eric Smith, <http://meetings.aps.org/Meeting/MAR18/Session/A45.3>.

Fabrication of Nanoscale Josephson Junctions for Quantum Coherent Superconducting Circuits

CNF Project Number: 1735-08

Principal Investigator: Britton L.T. Plourde

Users: Caleb Howington, Indrajeet, JJ Nelson

Affiliation: Department of Physics, Syracuse University

Primary Source of Research Funding: Army Research Office

Contact: bplourde@syr.edu, cjhowing@syr.edu, indraje@syr.edu, jjnelson@syr.edu

Website: <http://plourdelab.syr.edu>

Primary CNF Tools Used: ASML 300C DUV stepper, JEOL 9500, Plasma-Therm PT740

Abstract:

We fabricate nanoscale superconductor tunnel junctions and other structures for experiments involving quantum coherent circuits. Such circuits have shown great promise in recent years for explorations of quantum mechanics at the scale of circuits on a chip and for forming qubits, the foundational elements of a quantum computer. The quantum state of these superconducting qubits can be manipulated with microwave radiation at low temperatures. In addition, we are developing alternative techniques for probing the state of these qubits and controlling their quantum state, as well as superconducting metamaterial structures with novel microwave mode spectra for coupling to superconducting qubits.

Summary of Research:

The unique properties of nanoscale Josephson junctions enable a wide range of novel superconducting circuits for investigations in many diverse areas. In recent years, circuits composed of such junctions have emerged as promising candidates for the element of a quantum computer, due to the low intrinsic dissipation from the superconducting electrodes and the possibility of scaling to many such qubits on a chip [1]. The quantum coherent properties of the circuits are measured at temperatures below 50 mK with manipulation of the qubit state through microwave excitation.

We are currently working on a variety of experiments involving these nanoscale Josephson junctions and other superconducting structures that will allow us to probe novel quantum effects in our microwave circuits. We are fabricating superconducting circuits for forming low-temperature detectors of single microwave photons and for implementing a new scheme for the efficient readout of the quantum state of superconducting qubits [2-4]. We are also working with collaborators at the University of Wisconsin, Madison to develop hybrid quantum/classical superconducting chips that allow us to perform coherent quantum control of a superconducting qubit based on digital pulses from a Single Flux Quantum (SFQ) circuit [5,6].

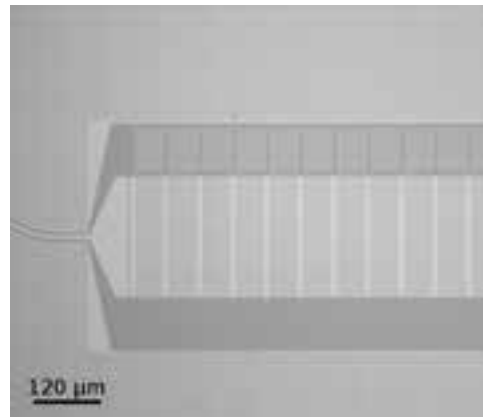


Figure 1: Optical micrograph of superconducting metamaterial transmission line resonator fabricated from Nb thin film on Si.

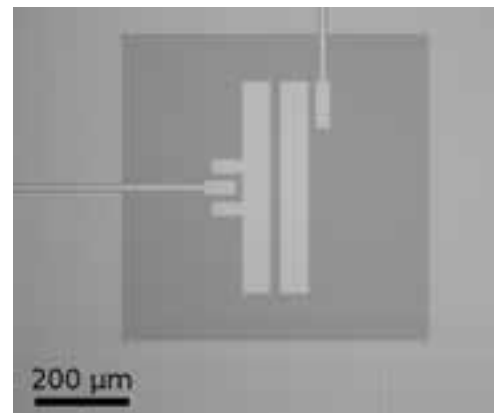


Figure 2: Optical micrograph of superconducting Nb qubit islands with coupling capacitor to metamaterial resonator.

In another effort, we are using particular combinations of superconducting lumped-circuit elements to engineer metamaterial transmission lines that exhibit novel mode structures characteristic of left-handed materials [7]. We are fabricating such metamaterial transmission lines from Al and Nb films on Si and characterizing these at low temperatures [8]. We are working on experiments to couple these left-handed lines to superconducting qubits for experiments involving the exchange of microwave photons [9].

We pattern these circuits at the CNF with nanoscale structures defined with electron-beam lithography on the JEOL 9500 integrated with photolithographically defined large-scale features. The junctions are fabricated using the standard double-angle shadow evaporation technique, in which a resist bilayer of copolymer and PMMA is used to produce a narrow PMMA airbridge suspended above the substrate. Evaporation of aluminum from two different angles with an oxidation step in between forms a small Al-AlO_x-Al tunnel junction from the deposition shadow of the airbridge. We have developed a process for defining these junctions with electron-beam lithography and we perform the aluminum evaporations in a dedicated chamber at Syracuse.

We pattern large-scale features using the ASML stepper, with electron-beam evaporation of Al, sputter-deposition of Nb, and PECVD deposition of SiO₂. Measurements of these circuits are performed in cryogenic systems at Syracuse University, including dilution refrigerators for achieving temperatures below 30 mK.

References:

- [1] Clarke, J. and Wilhelm, F.K.; "Superconducting quantum bits"; *Nature*, 453, 1031 (2008).
- [2] Govia, L.C.G., Pritchett, Emily J., Xu, Canran, Plourde, B. L. T., Vavilov, Maxim G., Wilhelm, Frank K., McDermott, R.; "High-fidelity qubit measurement with a microwave-photon counter"; *Physical Review A* 90, 062307 (2014).
- [3] Howington, Caleb, Opremcak, Alex, Pechenezhskiy, Ivan, Vavilov, Maxim, McDermott, Robert, Plourde, Britton; "Cryogenic Digital Readout of Superconducting Qubits"; *Bull. Am. Phys. Soc.* 2018, <http://meetings.aps.org/Meeting/MAR18/Session/B39.11>.
- [4] Opremcak, A, Pechenezhskiy, I., Howington, C., Christensen, B.G., Beck, M.A., Leonard Jr, E., Suttle, J., Wilen, C., Nesterov, K.N., Ribeill, G.J., Thorbeck, T., Schlenker, F., Vavilov, M.G., Plourde, B.L.T., McDermott, R.; "Measurement of a Superconducting Qubit with a Microwave Photon Counter"; arXiv:1803.01014 (2018).
- [5] McDermott, R., Vavilov, M.; "Accurate Qubit Control with Single Flux Quantum Pulses"; *Phys.Review Applied* 2, 014007 (2014).
- [6] Nelson, JJ, Leonard, E., Beck, M., Dodge, K., Howington, C., Ku, J., McDermott, R., Plourde, B. "Coherent Control of a Superconducting Transmon with Single Flux Quantum Pulses"; *Bull. Am. Phys. Soc.* 2018, <http://meetings.aps.org/Meeting/MAR18/Session/L39.5>.
- [7] Egger, D.J. and Wilhelm, F.K.; "Multimode Circuit Quantum Electrodynamics with Hybrid Metamaterial Transmission Lines"; *Physical Review Letters* 111, 163601 (2013).
- [8] Plourde, B.L.T., Wang, H., Rouxinol, F., LaHaye, M.D.; "Superconducting metamaterials and qubits"; *SPIE 9500 Proceedings, Quantum Information and Computation XIII*, 95000M (2015).
- [9] Indrajeet, Sagar, Wang, H., Hutchings, M., LaHaye, M., Plourde, B., Taketani, B., Wilhelm, F.; "Multi-mode Circuit Quantum Electrodynamics with Superconducting Metamaterial Resonators"; *Bull. Am. Phys. Soc.* 2018, <http://meetings.aps.org/Meeting/MAR18/Session/H33.9>.

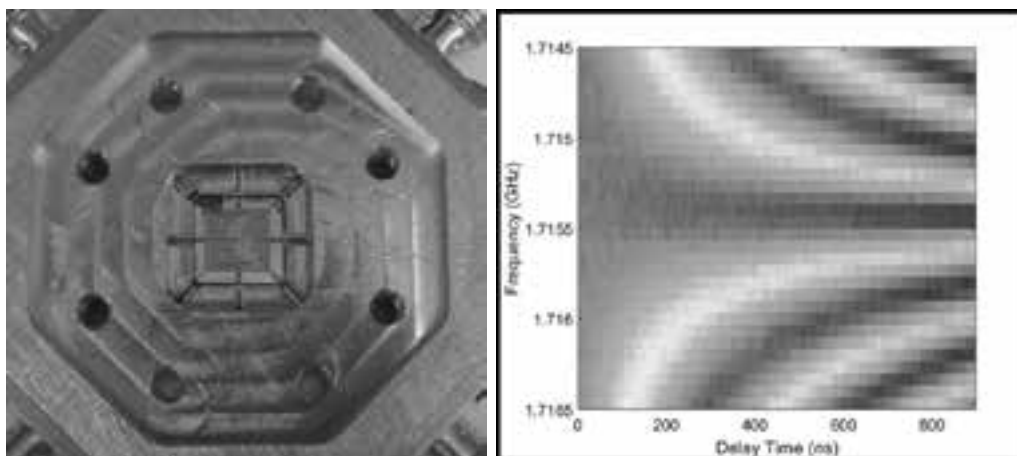


Figure 3, left: Hybrid quantum/classical chip bonded into microwave package for implementation of qubit control with superconducting digital SFQ circuit. Figure 4, right: Coherent oscillation fringes of superconducting qubit driven with on-chip superconducting SFQ digital circuit.

Fabrication of Superconducting Devices for Quantum Information Science

CNF Project Number: 1873-10

Principal Investigator: Britton L.T. Plourde

Users: Andrew Ballard, Jaseung Ku, Yebin Liu, Michael Senatore

Affiliation: Department of Physics, Syracuse University

Primary Source of Research Funding: Intelligence Advanced Research Projects Agency

Contact: bplourde@syr.edu, alballar@syr.edu, jku102@syr.edu, yliu166@syr.edu, masenato@syr.edu

Website: <http://plourdelab.syr.edu>

Primary CNF Tools Used: ASML 300C DUV stepper, JEOL 9500, Plasma-Therm PT740

Abstract:

We are fabricating nanoscale superconductor tunnel junctions and microwave resonators for investigations in quantum information science. Such circuits have shown great promise in recent years for forming qubits, the elements of a quantum computer. We are developing architectures involving multiple superconducting qubits and microwave resonators. This involves a combination of photolithographic processing and etching of large-scale features and electron-beam lithography for the tunnel junctions.

Summary of Research:

In recent years, circuits composed of nanoscale Josephson junctions have emerged as promising candidates for the foundational element of a quantum computer, due to the low intrinsic dissipation from the superconducting electrodes and the possibility of scaling to many such qubits on a chip [1]. The quantum coherent properties of the circuits are measured at temperatures below 50 mK with manipulation of the qubit state through microwave excitation.

We are working to develop architectures involving multiple superconducting qubits coupled to multiple low-loss microwave resonators [2-4]. We probe the coupling between each qubit and resonator by measuring the dispersive shift of the resonator frequency with the qubit detuned from the resonator. Some of our experiments are aimed at developing qubit designs that have reduced sensitivity to low-frequency magnetic flux noise that can lead to decoherence [2]. We are also investigating alternative qubit designs [3] that may lead to more efficient two-qubit gates for generating entanglement between circuits [4].

We pattern these circuits at the CNF with nanoscale structures defined with electron-beam lithography integrated with photolithographically defined large-scale features on Si and sapphire substrates. The junctions are fabricated using the standard double-angle shadow evaporation technique, in which a resist bilayer of copolymer and PMMA is used to produce a narrow PMMA airbridge suspended above the substrate.

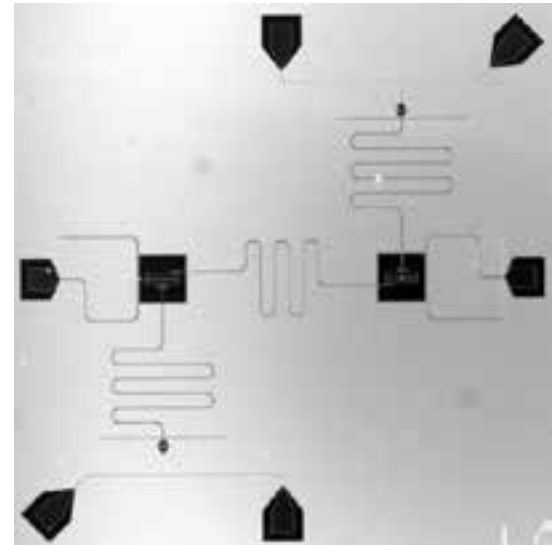


Figure 1: Optical micrograph of device with two superconducting qubits coupled by common microwave bus resonator with separate readout resonators for each qubit.

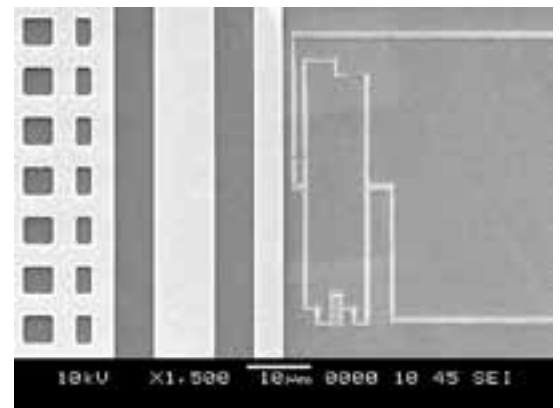


Figure 2: Scanning electron micrograph of superconducting loop with Josephson junctions for a capacitively shunted flux qubit.

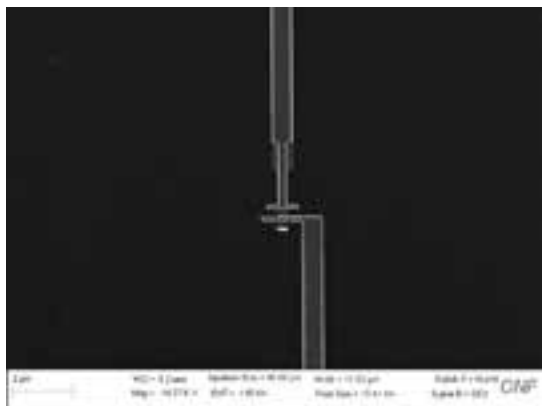


Figure 3: Scanning electron micrograph of cross-style Al-AIO_x-Al Josephson junction for superconducting qubit patterned on the JEOL 9500.



Figure 4: Optical micrograph of superconducting qubit for experiments probing the effects of magnetic flux noise on qubit decoherence.

Evaporation of aluminum from two different angles with an oxidation step in between forms a small Al-AIO_x-Al tunnel junction from the deposition shadow of the airbridge. We have developed a process for defining these junctions with electron-beam lithography on the JEOL 9500 and we perform the aluminum evaporations in a dedicated vacuum chamber at Syracuse. We pattern large-scale features using the ASML, with sputter deposition of superconducting Nb films in a dedicated vacuum system at Syracuse University. Microwave measurements of these circuits are performed in cryogenic systems at Syracuse University, including dilution refrigerators for achieving temperatures below 30 mK.

References:

- [1] Clarke, J. and Wilhelm, F.K.; "Superconducting quantum bits"; Nature, 453, 1031 (2008).
- [2] Hutchings, M. D. Hertzberg, Jared B., Liu, Y., Bronn, Nicholas T., Keefe, George A., Chow, Jerry M., Plourde, B.L.T.; "Tunable Superconducting Qubits with Flux-Independent Coherence"; Physical Review Applied 8, 044003 (2017).
- [3] Ku, Jaseung, Liu, Yebin, Plourde, Britton, Hertzberg, Jared, Brink, Markus, Magesan, Chow, Jerry; "Capacitively Shunted Flux Qubits and Asymmetric Transmons for Multi-qubit Operations"; Bull. Am. Phys. Soc. 2018, <http://meetings.aps.org/Meeting/MAR18/Session/L33.8>.
- [4] Corcoles, A. D., Gambetta, Jay M., Chow, Jerry M., Smolin, John A., Ware, Matthew, Strand, J. D., Plourde, B. L. T., Steffen, M.; "Process verification of two-qubit quantum gates by randomized benchmarking"; Physical Review A 87, 030301(R) (2013).

Anomalous Nernst Imaging of Uncompensated Moments in Antiferromagnetic FeRh Thin Films

CNF Project Number: 2091-11

Principal Investigator: Gregory D. Fuchs¹

Users: Isaiah Gray¹, Gregory M. Stiehl²

Affiliations: 1. School of Applied and Engineering Physics, 2. Department of Physics; Cornell University, Ithaca, NY

Primary Source of Research Funding: Cornell Center for Materials Research from the National Science Foundation MRSEC Program, Grant No. DMR-1719875

Contact: gdf9@cornell.edu, ig246@cornell.edu, gms263@cornell.edu

Primary CNF Tools Used: GCA 5x stepper

Abstract:

We use anomalous Nernst microscopy to image uncompensated magnetic moments in Pt/FeRh <001> bilayers as a function of temperature and magnetic field. Uncompensated moments (UMs) in antiferromagnets (AFM) have been extensively studied in ferromagnetic (FM)/antiferromagnetic (AF) bilayers, where they are responsible for exchange bias, but their structure in a single antiferromagnetic layer is less well characterized. We image the emergence of the ferromagnetic phase in the 1st-order magnetic phase transition in FeRh. Below T_N we resolve μm -scale FM domains with large, spatially inhomogeneous vertical shifts to the $M(H)$ loop. This so-called vertical exchange bias signals the presence of bulk UMs with varying degrees of exchange-coupling to the local Néel order. Our measurements provide new insight into the structure of uncompensated moments within a single antiferromagnetic thin film.

Summary of Research:

In a simplified picture of a collinear Néel antiferromagnet, each spin is compensated by an oppositely-pointing spin on an adjacent lattice site, and therefore there is no net magnetic moment. In reality, uncompensated moments (UMs) form both in the bulk and at interfaces [1]. These UMs are of great practical importance because they are directly responsible for exchange bias in antiferromagnet /ferromagnet (FM) bilayers [2]; however, they are difficult to probe directly. In this work we use anomalous Nernst microscopy to image uncompensated moments in FeRh, which undergoes a 1st-order AFM/FM phase transition near $T_N = 100^\circ\text{C}$ [3] and therefore provides an ideal platform to study the interaction of ferromagnetism and antiferromagnetism in the same material.

We study 10 nm Pt/20 nm FeRh bilayers patterned into $3\ \mu\text{m} \times 30\ \mu\text{m}$ Hall crosses. We first characterize the phase transition with anomalous Nernst imaging [4], shown in Figure 1. In agreement with previous imaging studies [5] we observe that FM domains first nucleate on defects and sample edges near 80°C , then percolate through the sample, and finally grow in size until the FM phase is uniform above 100°C .

At 25°C , we image μm -scale magnetic contrast, shown in Figure 2, which exhibits a ferromagnetic hysteresis loop averaged over the whole sample but unlike conventional FM samples does not saturate uniformly with field. Imaging at positive and negative field, we resolve signal from both unpinned domains, which switch with field, and pinned domains, which do not switch.

Plotting the average signal within adjacent μm -scale pinned domains as a function of field in Figure 3, we obtain hysteretic $M(H)$ loops characteristic of a ferromagnet, but with unusual large vertical offsets signifying spatially inhomogeneous vertical exchange bias [6]. We explain these results in terms of bulk uncompensated moments exchange-coupled to the Néel order: large ($> 1\ \mu\text{m}$) regions of UMs are strongly exchange-coupled and do not switch, while small ($< 500\ \text{nm}$) regions of UMs are weakly exchange-coupled and can be reoriented with 1 kG field.

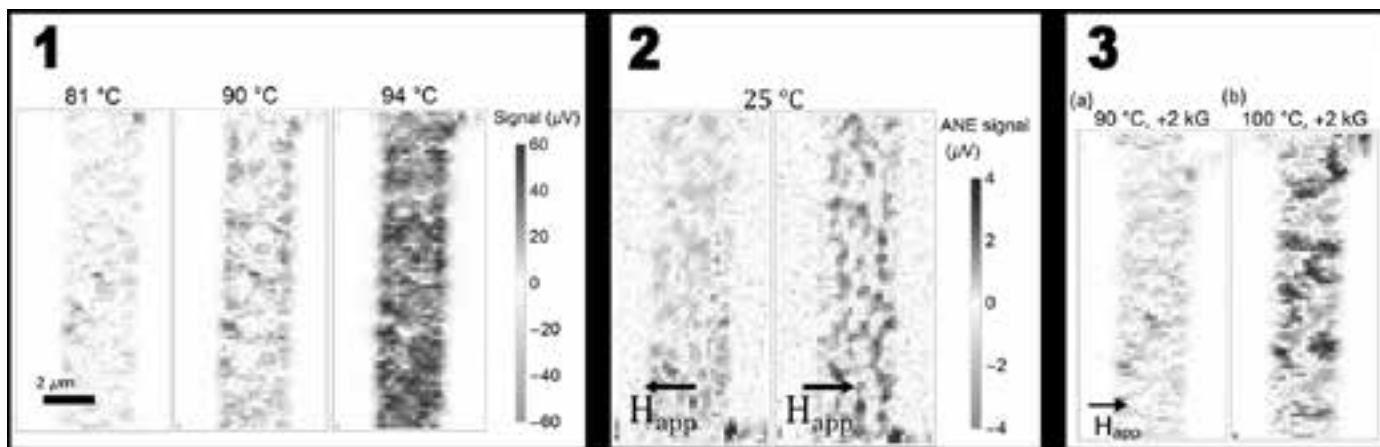


Figure 1, left: Anomalous Nernst imaging of the 1st-order magnetic phase transition in FeRh. We observe the FM phase nucleating at sample edges and defects at 81°C, percolating through the sample at 90°C, and nearly uniform at 94°C. **Figure 2, middle:** Imaging FM contrast at 25°C, nominally in the antiferromagnetic phase, at positive and negative 1.3 kG field. The signal contains both unpinned FM domains, which reverse with field, and spatially inhomogeneous pinned domains, which do not reverse up to 5 kG field. **Figure 3, right:** Average signal from adjacent pinned domains as a function of field, yielding ferromagnetic M(H) loops with giant vertical shifts (vertical exchange bias). Pinned and unpinned domains correspond to strong and weak exchange-coupling between uncompensated moments and the bulk antiferromagnetic order.

In conclusion, we image uncompensated moments in FeRh which exchange-couple to the bulk antiferromagnetic order in a complex, spatially inhomogeneous pattern. Our results establish anomalous Nernst microscopy as a powerful technique for imaging UMs in antiferromagnetic metals and provide insight into the interaction of coexisting AF and FM order in a single material.

References:

- [1] J. Nogués and I. K. Schuller, *J. Magn. Magn. Mater* 192, 203-232 (1999).
- [2] I. K. Schuller et al, *J. Magn. Magn. Mater* 416, 2-9 (2016).
- [3] J. B. McKinnon et al, *J. Phys. C: Solid State Phys.* 3, S46 (1970).
- [4] J. M. Bartell et al, *Nat Comm.* 6, 8640 (2015).
- [5] C. Baldasseroni et al, *Appl. Phys. Lett.* 100, 262401 (2012).
- [6] P.-H. Huang et al, *Appl. Phys. Lett.* 90, 062509 (2007).

Manipulating Topological Spin Textures in Spin-Valve Type Nanopillars

CNF Project Number: 2091-11

Principal Investigator: Gregory D. Fuchs

Users: Emrah Turgut, Isaiah Gray, Jason Bartell

Affiliation: Applied and Engineering Physics, Cornell University

Primary Source of Research Funding: Department of Energy

Contact: gdf9@cornell.edu, et329@cornell.edu

Primary CNF Tools Used: Heidelberg mask writer DWL 2000, GCA 5x stepper, JEOL e-beam lithography, even and odd evaporators, AJA ion mill, AJA sputtering, DISCO dicing saw

Abstract:

We study the properties of topological spin textures at nanoscale dimensions. We fabricate spin-valve nanopillars composed of a thin-film B_{20} FeGe below copper and $Ni_{80}Fe_{20}$ (permalloy) layers. Bypassing a current through these nanopillars, we explore magnetic field-dependent resistance to understand the non-trivial spin texture formed in the nanopillars, and at high current, manipulate the spin texture using spin-transfer torques. Our fabrication and characterization study of these structures is aimed at realizing future power-efficient memory devices.

Summary of Research:

Transition metal germanides (TMGs) have a non-centrosymmetric crystal structure, which creates a non-vanishing asymmetric exchange energy in addition to the common symmetric exchange in ferromagnets [1-3]. In an external magnetic field, asymmetric exchange can stabilize chiral and topological spin textures, including magnetic skyrmions and helices. These spin textures are functionally a magnetic quasi-particle in which information can be stored and manipulated with a very low energy as compared to other magnetic storage modalities.

The potential application in energy-efficient storage and logic applications makes understanding the nanoscale spin dynamics in these TMGs crucial. Studying their nanoscale spin dynamics requires the fabrication of spin valve nanopillars made of TMGs, transition metals, and ferromagnetic multilayers and with a characteristic diameter of 100 nm. The nanoscale diameter is necessary to creating large current densities and is promising for high-density magnetic storage applications. A schematic cartoon of a nanopillar is shown in Figure 1. The TMG is iron germanium (FeGe) in this case.

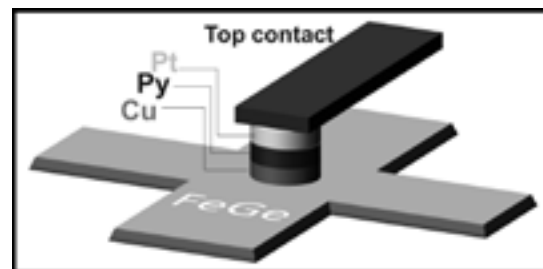


Figure 1: A cartoon picture of the nanopillar. The bottom FeGe layer is a chiral magnet that can stabilize magnetic skyrmions. The permalloy layer is a well-understood ferromagnetic layer that can generate spin current when a charge current passes through the nanopillar. The Cu layer works as spin-transport layer while decoupling the magnetic moments of permalloy and FeGe.

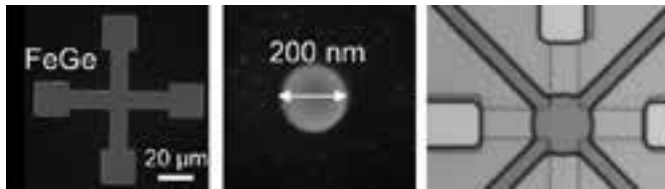


Figure 2: Micrographs of some of the steps during the nanopillar fabrication. The left and middle SEM micrographs are the bottom FeGe layer and a 200-nm-diameter pillar. The right optical micrograph is the final contact pads before deposition.

We grow FeGe on a Si <111> substrate with MBE before transferring the wafer into a sputtering system where we deposit copper, permalloy, and platinum layers under ultrahigh vacuum. Then, we fabricate magnetic nanopillars devices with multiple optical and electron-beam lithography steps, some of which are shown in Figure 2. The left and the middle images are scanning electron micrographs of the bottom FeGe layer and a 200-nm-diameter pillar, respectively. The right image is an optical micrograph of the final contact-pads before their deposition.

Our structure has complicated spin configurations due to the chiral magnetism of the FeGe layer. We study the magnetoresistance (MR) properties of the nanopillars to understand their equilibrium magnetization configurations. For example, FeGe has temperature- and field-dependent phases, including paramagnetic, spin-helix, magnetic skyrmion, and field polarized states. Moreover, the permalloy layer can stabilize magnetic vortices and multi-domain magnetic textures. By making such nanopillars, we enable interactions between these magnetic textures. We vary the sample temperature and magnetic field orientation as we measure the resistance of the nanopillar, which should reflect the magnetic configuration of the individual nanopillar.

In Figure 3, we show field-dependent MR curves at different temperatures. The left graph, Figure 3a, shows the anisotropic MR (AMR) of the bottom FeGe layer, which is isolated by measuring between bottom contacts.

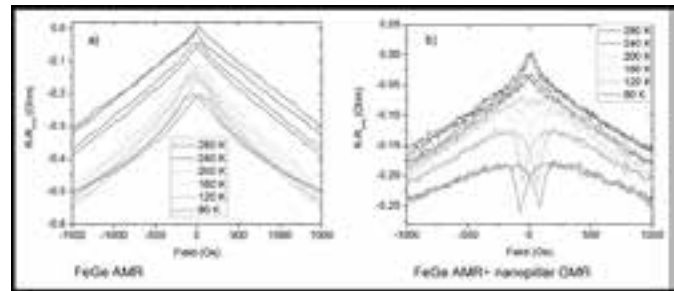


Figure 3: Magnetoresistance measurements of a nanopillar at varied temperatures. a) shows the resistance of the bottom FeGe layer only, which is a typical AMR that is less sensitive to the sample temperature. The right graph b), however, shows the combination of the FeGe AMR and the nanopillar GMR, which shows strong temperature dependence.

We observe a slight change of anisotropic MR as a function of temperature. On the other hand, Figure 3b shows both the AMR of FeGe and the giant MR (GMR) of the pillar, which is measured between the nanopillar top and bottom contacts. At high temperatures (the purple curve), FeGe is in the paramagnetic phase; therefore, we do not observe a GMR response of the FeGe/permalloy spin valve. However, at low temperatures (the red and orange curves), the GMR response is strong. As the permalloy layer switches at around 100 Oe, the total MR varies substantially.

Our experiment shows an interesting but non-trivial magnetoresistance behavior. To understanding it better, our next effort will be micromagnetic modeling.

In summary, we fabricate spin valve nanopillars and study their MR to understand topological spin textures in confined geometries. Our preliminary measurements show a strong GMR effect. Further modeling will shed light on these complicated spin configurations.

References:

- [1] Nagaosa, et al., Nature Nanotechnology 8, 899 (2013).
- [2] Turgut, et al., Physical Review B 95, 134416 (2017).
- [3] Turgut, et al., Journal of Applied Physics 122, 183902 (2017).

Diamond-Based Hybrid Quantum Mechanical Systems

CNF Project Number: 2126-12

Principal Investigator: Gregory D. Fuchs¹

Users: Huiyao Chen², Evan R. Macquarrie²

Affiliations: 1. School of Applied and Engineering Physics, 2. Department of Physics; Cornell University

Primary Source of Research Funding: Office of Naval Research (Grants No. N000141410812 and No. N000141712290)

Contact: gdf9@cornell.edu, hc846@cornell.edu

Website: <http://fuchs.research.engineering.cornell.edu>

Primary CNF Tools Used: GCA 5x stepper, Heidelberg mask writer DWL2000, AJA sputtering deposition system, YES Asher, P10 profilometer, Westbond 7400A ultrasonic wire bonder

Abstract:

Nitrogen vacancy (NV) centers are atom-like quantum emitters in diamond, with narrow orbital transition linewidth and a long-lived spin coherence that persists to room temperature. Diamond-based microelectromechanical systems (MEMS) devices integrate these quantum defects with classical mechanics, providing direct coupling between diamond NV center spin/orbital states and phonons in a mechanical resonator. We demonstrate orbital state manipulation of a single NV center with a GHz diamond high-overtone bulk acoustic resonator (HBAR). Furthermore, we are developing a new diamond MEMS device that is designed to realize the control of mechanical quantum states using diamond spins, which is potentially useful for quantum-enhanced metrology and quantum information processing.

Summary of Research:

Diamond-based hybrid quantum spin-mechanical systems marry the two fields of microelectromechanical systems (MEMS) and quantum information science with the goal of realizing coherent mechanical control of diamond nitrogen-vacancy (NV) centers [1] and quantum enhanced mechanical sensing [2]. Following the recent demonstration of coherent mechanical control of spin state of NV centers [3,4], we recently demonstrated orbital state manipulation of a single NV center using a diamond MEMS device [5].

The device adopts the design of a high-overtone bulk acoustic resonator (HBAR) device fabricated from a diamond substrate using a zinc oxide (ZnO) piezoelectric mechanical transducer. We study the resonant optical orbital transition of a single NV center under the influence of coherent phonon driving from a mechanical resonator (Figure 1). We demonstrated coherent Raman sidebands out to the ninth order and orbital-phonon interactions that mix the two excited-state orbital branches. These interactions are spectroscopically revealed through a multi-phonon Rabi splitting of the orbital branches, which scales as a function of resonator driving amplitude.

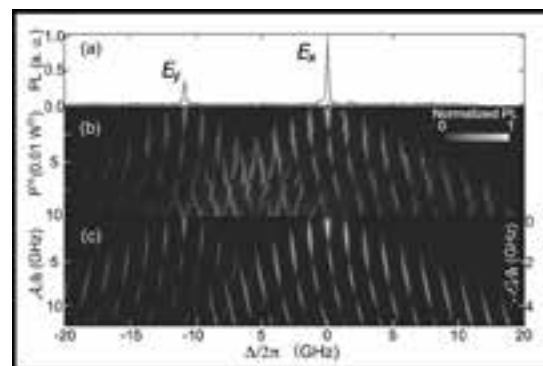


Figure 1: (a) Photoluminescence (PLE) spectrum of a NV center with orbital E-state splitting of 10.6 GHz in the absence of mechanical driving. (b) Phonon-dressed state PLE measurement with mechanical driving at 1.3844 GHz. The mechanical driving amplitude is proportional to square root of the power applied to the transducer, $P^{1/2}$. Sideband transitions and level repulsion are evident in between E states. (c) Reconstruction of experimental data through quantum master equation simulation.

We show that the application of mechanical driving to engineering NV center orbital states can potentially stabilize NV center optical transition by reducing its sensitivity to fluctuating parasitic electric fields.

For quantum-enhanced mechanical sensing, the physical interaction, NV center electron spin-phonon coupling is rather weak in the current device design, which limits their application to quantum acoustodynamics (QAD) [6]. Engineering new generation of diamond MEMS device with higher quality factors, smaller mode volumes and higher NV-center density can help increase the coupling rate, and potentially enable sensing and control of resonator mechanical state using NV centers. We are in the process of developing the next generation device (Figure 2), a parabolic diamond HBAR. The device consists a 10 μm thick diamond membrane as the substrate, fabricated through deep reactive ion etching from a 100 μm thick diamond chip. On the etched surface, we mill a parabolic solid immersion lens (SIL) using focused ion beam (Figure 3). The parabolic SIL serves two purposes: 1) create a stable plano-convex acoustic cavity to confine the active phonon mode; 2) improve light collection efficiency from NV centers in the SIL by eliminating surface refraction.

Finally, we fabricate a piezoelectric transducer (Figure 4) using photolithography and DC sputtering, whose size mode-matches with the confined acoustic beam. The device is proposed to have frequency and quality-factor product $fQ > 10^{13}$, enabling defect-assisted quantum mechanical sensing.

References:

- [1] Lee, D., et al. Topical Review: Spins and mechanics in diamond. *J. Opt.* 19 033001 (2017).
- [2] Barson, M. S.J., et al. Nanomechanical Sensing Using Spins in Diamond. *Nano Lett.* 17 (3), 1496-1503 (2017).
- [3] MacQuarrie, E. R., et al. Mechanical Spin Control of Nitrogen-Vacancy Centers in Diamond. *Phys. Rev. Lett.* 111, 227602 (2013).
- [4] Barfuss, A., et al. Strong mechanical driving of a single electron spin. *Nat. Phys.* 11, 820-824 (2015).
- [5] Chen, H. Y., et al. Orbital state manipulation of a diamond nitrogen-vacancy center using a mechanical resonator. *Phys. Rev. Lett.* 120,167401 (2018).
- [6] Chu, Y. W., et al. Quantum acoustics with superconducting qubits. *Science*, 358, 6360, 199-202 (2017).

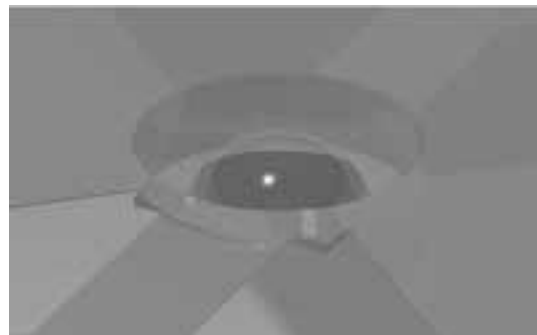


Figure 2: 3D illustration of the next generation device, with integrated plano-convex diamond acoustic cavity and mechanical transducer.

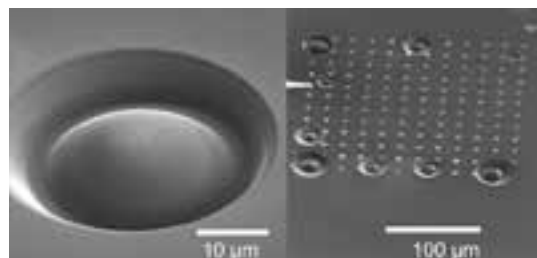


Figure 3: SEM images of solid immersion lenses on diamond milled through focused ion beam.

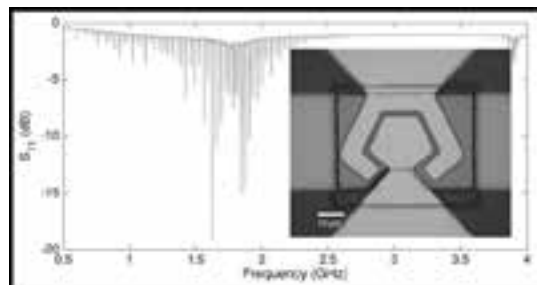


Figure 4: Electromechanical response of a HBAR sample measured by vector network analyzer. The inset shows an optical image of a device.

Properties of Isolated Defects in Hexagonal Boron Nitride

CNF Project Number: 2126-12

Principal Investigator: Gregory D. Fuchs

Users: Nicholas R. Jungwirth, Nikhil Mathur, Raphael Daveau

Affiliation: Applied and Engineering Physics, Cornell University

Primary Source of Research Funding: National Science Foundation

Contact: gdf9@cornell.edu, nrj32@cornell.edu, nm648@cornell.edu, rsd228@cornell.edu

Website: <http://fuchs.research.engineering.cornell.edu>

Primary CNF Tools Used: Scanning electron microscope, contact aligner, profilometer

Abstract:

We investigate the optical properties of defect-based single photon sources in hexagonal boron nitride (hBN) produced via solvent exfoliation (S-hBN) and mechanical exfoliation (M-hBN). Single defects found in S-hBN exhibit spectrally narrow zero-phonon emission and an absorption and emission dipole that may or may not be aligned parallel to one another. Defects found in wide area ($> 50 \times 50 \mu\text{m}$) M-hBN multilayer flakes possess a broader zero phonon line and are less bright than the defects in S-hBN flakes. To study M-hBN, we develop a reliable method for mechanically exfoliating bulk h-BN crystals and precisely transferring it to a Si/SiO₂ substrate. Optically stable defects are subsequently created in the flake via an argon plasma etch combined with a thermal annealing treatment. The investigated defects may be in regions of the flake that is in contact with the substrate or, alternatively, in regions that are suspended over pre-patterned holes. Defects in the suspended region are not influenced by the substrate and may potentially couple to the mechanical modes of the resulting hBN drumhead.

Summary of Research:

Point defects in wide bandgap semiconductors exhibit quantum emission and have been identified as candidates for applications in quantum optics, precision sensing, and quantum information technologies [1]. Defects have been optically isolated in three-dimensional materials such as diamond, SiC, ZnO, and GaN, and more recently in two-dimensional materials such as transition metal dichalcogenides (TMDs) and hexagonal boron nitride (hBN) [2-6]. The defects in hBN exhibit ultrabright and polarized single photon emission. However, these single photon sources also exhibit significant defect-to-defect variation, making the comparison of experimental results with theoretical predictions difficult. In this work we compare the optical properties of single photon sources in hBN samples produced via solvent exfoliation (S-hBN) and mechanical exfoliation (M-hBN).

Figure 1 shows a set of spectrally resolved polarization measurements made on a single defect in S-hBN. Figure 1a is a two-dimensional image plot revealing the fluorescence intensity of light emitted at a particular polarization angle. It was obtained by rotating a polarization analyzer in the collection path and collecting an emission spectrum at each orientation of the polarization analyzer. By vertically integrating the

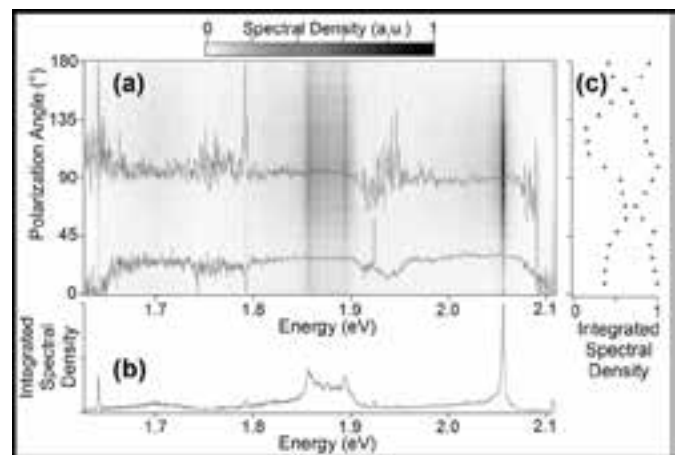


Figure 1: Spectrally resolved polarization measurements of an isolated defect in S-hBN revealing that the absorption and emission dipoles are misaligned.

columns in the plot, we recover the unpolarized emission spectrum, shown in Figure 1b. In the unpolarized emission spectrum, a narrow zero phonon line (ZPL) and phonon sideband (PSB) are evident at ~ 2.05 eV and ~ 1.88 eV, respectively. By horizontally integrating the

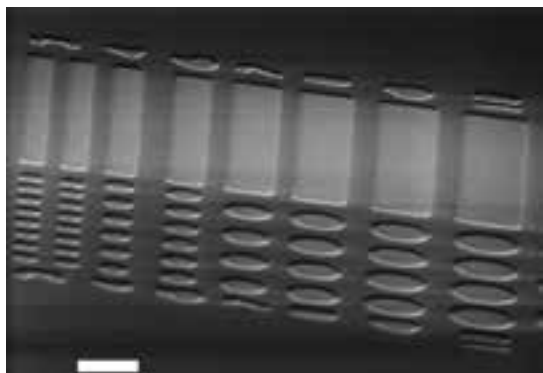


Figure 2: Scanning electron microscope image of holes and trenches fabricated onto a Si/SiO₂ substrate. The scale bar is 10 μm .

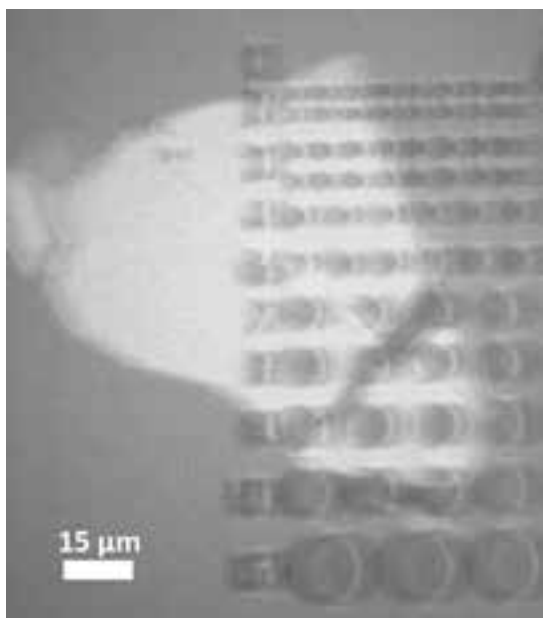


Figure 3: Optical microscope image of an hBN flake transferred to a region of the substrate containing holes and trenches.

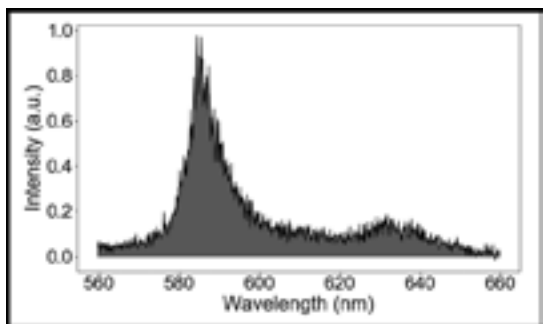


Figure 4: Emission spectrum of a single defect in M-hBN.

rows in Figure 1a we recover the spectrally averaged emission polarization profile (circles, Figure 1c). For comparison, the spectrally averaged excitation polarization profile is included as well (triangles, Figure 1c). Note that the absorption and emission dipoles are misaligned. This is confirmed by the spectrally resolved orientation of the emission and absorption dipoles, shown as the upper and lower traces, respectively, in Figure 1a.

To investigate defects in M-hBN, we developed a process of mechanically exfoliating bulk hBN crystals and precisely transferring them onto pre-patterned Si/SiO₂ substrates. Figure 2 is a scanning electron microscopy image of one such pre-patterned substrates revealing holes and trenches. Large area (> 50 \times 50 μm) M-hBN flakes may then be suspended over these holes (Figure 3). As-transferred M-hBN exhibits very low defect density, making it difficult to optically isolate individual defects. To increase the defect density, we argon etch as-transferred flakes and subsequently anneal the samples in nitrogen at 850°C for 30 minutes. After this sample treatment the defect density is enhanced and individual emitters maybe studied in suspended regions and in supported regions. Defects studied in suspended regions are not influenced by the substrate whereas defects in the supported regions may be influenced by charge traps in the underlying substrate.

Figure 4 is a room-temperature emission spectrum of a single defect in a suspended region of the M-hBN shown in Figure 3. Note that similar to S-hBN defects, this M-hBN defect also exhibits a broad ZPL and a PSB that is red-shifted from the ZPL by \sim 165 meV.

References:

- [1] J. R. Weber, W. F. Koehl, J. B. Varley, A. Janotti, B. B. Buckley, C. G. Van de Walle, and D. D. Awschalom, Proc. Natl. Acad. Sci. 107, 8513 (2010).
- [2] N. R. Jungwirth, Y. Y. Pai, H. S. Chang, E. R. MacQuarrie, K. X. Nguyen, and G. D. Fuchs, J. Appl. Phys. 116, 043509 (2014).
- [3] N. R. Jungwirth, H.-S. Chang, M. Jiang, and G. D. Fuchs, ACS Nano 10, 1210 (2016).
- [4] T. T. Tran, K. Bray, M. J. Ford, M. Toth, and I. Aharonovich, Nat. Nanotechnol. 11, 37 (2015).
- [5] N. R. Jungwirth, B. Calderon, Y. Ji, M. G. Spencer, M. E. Flatté, and G. D. Fuchs, Nano Lett. 16, 6052 (2016).
- [6] N. R. Jungwirth and G. D. Fuchs, Phys. Rev. Lett. 119, (2017).

Extreme Light-Bending and Trapping with a Simple Cubic Optical Photonic Crystal

CNF Project Number: 2173-12

Principal Investigator: Shawn-Yu Lin

Users: Brian Frey, Alex Kaiser

Affiliation: Department of Physics, Rensselaer Polytechnic Institute, Troy, NY 12180

Primary Source of Research Funding: United States Department of Energy, Office of Science, Basic Energy Sciences

Contact: sylin@rpi.edu, freyb3@rpi.edu, kaisea2@rpi.edu

Primary CNF Tools Used: PVD75 sputter deposition, AJA sputter deposition, ASML deep-ultraviolet stepper, Oxford reactive-ion-etcher, Trion inductively-coupled plasma etcher, GSI PECVD tool, Orbis chemical-mechanical polisher, Zeiss scanning electron microscope, Veeco atomic force microscope, CVC electron-beam evaporator

Abstract:

A sub-micron TiO_2 simple cubic photonic crystal with lattice constant 450 nm was fabricated and used to characterize a newly-discovered light-bending mechanism wherein the Poynting vector lies nearly parallel to the photonic crystal interface. Absorption enhancement approaching 100 times was observed compared to a reference TiO_2 film. Several enhancement peaks in the region from 600-950 nm wavelength far exceed both the ergodic and square surface-grating light-trapping limits. These results can be applied to any future light trapping applications such as phosphor-converted white light generation, water-splitting, or thin-film solar cells, where increased response in areas of weak absorption is desired.

Summary of Research:

In several areas of opto-electronics, the efficient conversion of light into useful energy is paramount. Typically, performance is limited by different factors, such as weak near-infrared absorption (crystalline silicon [1]), or charge diffusion length (amorphous silicon [2]). To circumvent these limitations while addressing cost [3], and efficiency concerns [4], it is beneficial to engineer structures that can alter the optical-path-length through these devices without using more material. This is referred to as “light trapping” [5].

In this research, we identify a precise light-trapping mechanism, which is due to photonic crystal (PC) refraction. This effect, called parallel-to-interface refraction (PIR), extends the path-length by orders of magnitude by coupling light into modes for which the Poynting vector lies nearly parallel to the PC interface [5,6]. Accordingly, we have constructed a simple cubic PC from weakly-absorbing TiO_2 to demonstrate orders-of-magnitude enhancement over a reference TiO_2 film. The conclusions that follow are general and not restricted to any material.

The structure used for this study, depicted in Figure 1.a, is a stacked, 4-layer TiO_2 simple cubic PC [7]. It was fabricated with photolithography and etch steps in a layer-by-layer process using the ASML deep-ultraviolet stepper and Oxford reactive ion etcher. A complete

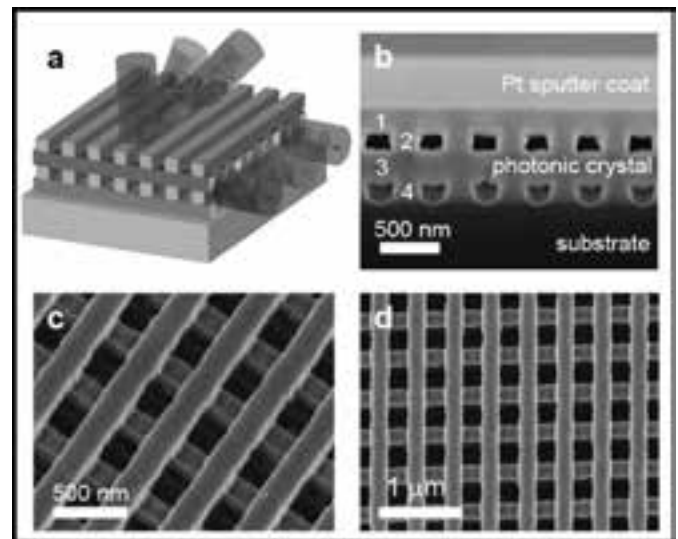


Figure 1: Schematic of a TiO_2 simple cubic photonic crystal. (a) Schematic of TiO_2 PC depicting parallel-to-interface refraction. (b) Cross-section side view, (c) perspective view, and (d) top-view pictures of fabricated TiO_2 PC.

description of the fabrication process is described elsewhere [8], but the results are summarized in Figure 1.

To investigate PIR, we measured the absorption of our PC, which is plotted in Figure 2. The absorption of a

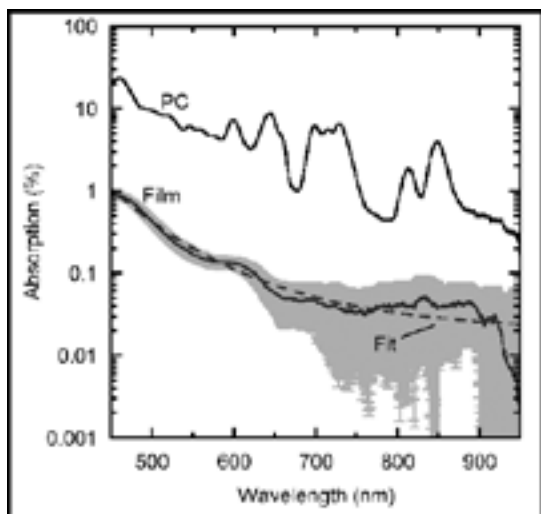


Figure 2: Absorption spectra for PC and reference film.

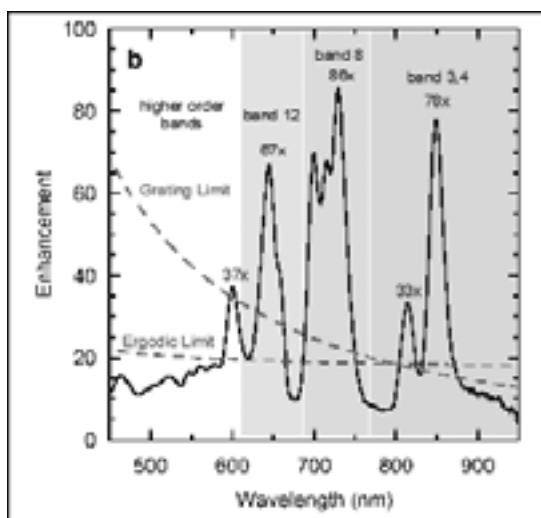


Figure 3: Absorption enhancement for PC. Also shown are the lines for the ergodic limit and 2D grating limit.

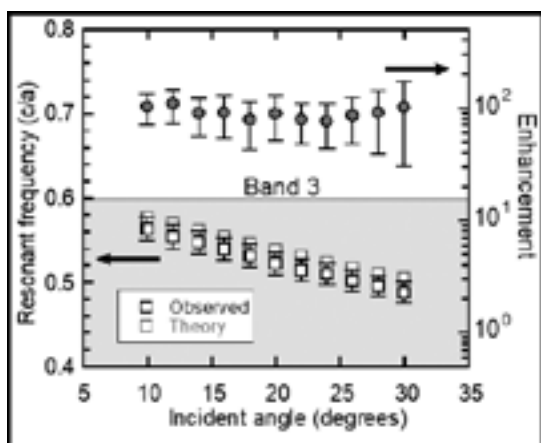


Figure 4: Absorption peak frequency and peak enhancement vs. incident angle for band 3. Filled circles are measured enhancement at the peak frequency. The bounded box shows the frequency range for band 3.

reference TiO_2 planar film of comparable thickness is also shown for comparison. Figure 2 shows that the film absorption below the bandgap is less than 1% and decays exponentially. Notably, in the range from 600-800 nm, the PC shows a series of absorption peaks that approach 10%, while the film absorption is $< 0.1\%$. Also, a pair of peaks observed for the PC between 800-900 nm with max values of $\sim 2\text{-}4\%$; here the film shows $\sim 0.03\%$ absorption.

In Figure 3, the enhancement factor η , defined as the ratio of the PC and film absorption values, is plotted as a function of wavelength. Here, the doublet of peaks observed at longer wavelengths corresponds to $\eta \sim 30$ and 80 times, respectively. The maximum enhancement for peaks in the mid-wavelength region is close to 100 times. These peaks also surpass, by multiple times, two theoretical limits also shown for comparison: one is the ergodic limit of $4n^2$ [9], and the other is based on a square surface-grating architecture [10]. To show that this is attributable to PIR, the angular dependence of the resonant frequencies for the band 3 absorption peaks is shown in Figure 4. The data not only agree well with the predicted PIR frequencies from theory, but there is a one-to-one correspondence between theory and observation and the scaling of the resonant frequency with θ_0 is virtually identical. Furthermore, the peak enhancement is approximately angle-independent at $\eta \sim 100$ times. The data experimentally validate PIR and provide direct proof of its contribution to absorption enhancement in a simple cubic PC.

PIR provides an opportunity to use simple cubic PCs as an ordered, three-dimensional network that refracts light according to the dispersion relation. This approach to absorption enhancement is amenable to infiltration by various agents, such as dyes, polymers, and nanophosphors, and is also suitable for investigating PC-induced light emission enhancement. We anticipate that the scope of these results will extend beyond thin-film solar cells to other applications, like phosphor conversion in light-emitting diodes, and water-splitting.

References:

- [1] Redfield, D. Multiple-pass thin-film silicon solar cell. *Appl. Phys. Lett.* 25, 647-648 (1974).
- [2] Carlson, D. E., and Wronski, C. R. Amorphous silicon solar cell. *Appl. Phys. Lett.* 28, 671-673 (1976).
- [3] Shah, A., Torres, P., Tscharnner, R., Wyrsh, N., and Keppner, H. Photovoltaic technology: the case for thin-film solar cells. *Science* 285, 692-698 (1999).
- [4] Vetterl, O., et al. Thickness dependence of microcrystalline silicon solar cell properties. *Sol. Energ. Mat. Sol.* 66, 345-351 (2001).
- [5] Chutinan, A., and John, S. Light trapping and absorption optimization in certain thin-film photonic crystal architectures. *Phys. Rev. A* 78, 023825 (2008).
- [6] Kuang, P., Deinega, A., Hsieh, M. L., John, S., and Lin, S. Y. Light trapping and near unity solar absorption in a three-dimensional photonic-crystal. *Opt. Lett.* 38, 4200-4203 (2013).
- [7] Frey, B. J., et al. Effectively infinite optical pathlength created using a simple cubic photonic crystal for extreme light trapping. *Sci. Rep.* 7, 4171 (2017).
- [8] Frey, B. J., Kuang, P., Lin, S. Y., Jiang, J. H., and John, S. Large area fabrication of a simple cubic metal-oxide photonic crystal for light trapping applications. *J. Vac. Sci. Technol. B* 33, 021804 (2015).
- [9] Yablonoitch, E. Statistical ray optics. *J. Opt. Soc. Am.* 72, 899-907 (1982).
- [10] Yu, Z., Raman, A., and Fan, S. Fundamental limit of light trapping in grating structures. *Opt. Express* 18, A366-A380 (2010).

Development of Scanning Graphene Hall Probes for Magnetic Microscopy

CNF Project Number: 2361-15

Principal Investigator: Katja C. Nowack

User: Brian T. Schaefer

Affiliations: Laboratory of Atomic and Solid-State Physics, Department of Physics; Cornell University

Primary Sources of Research Funding: Cornell Center for Materials Research with funding from the NSF MRSEC program (DMR-1719875), National Science Foundation Graduate Research Fellowship under Grant No. DGE-1650441

Contact: kcn34@cornell.edu, bts72@cornell.edu

Website: <http://nowack.lassp.cornell.edu/>

Primary CNF Tools Used: Veeco Icon AFM, Zeiss Supra SEM/Nabity, odd-hour evaporator, even-hour evaporator, Trion etcher, 5x stepper, Oxford 100 etcher, Plasma-Therm Versaline

Abstract:

We discuss our progress on developing scanning Hall probes using graphene as the sensitive material, with the goal to perform magnetic imaging experiments with submicron resolution. Our devices demonstrate a promising Hall sensitivity at cryogenic temperatures competitive with that of commercially available Hall probes. We plan to include a deep etch surrounding the sensitive area of the device to facilitate alignment and scanning over samples.

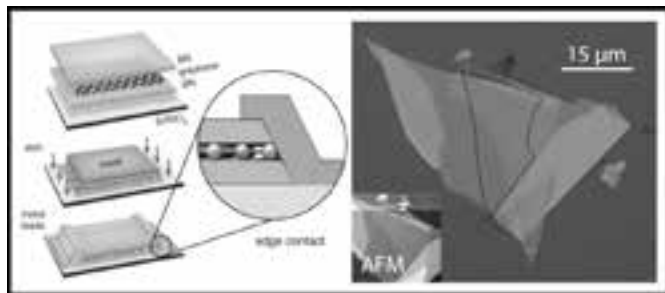


Figure 1: Left panel: overview of process from [3], used with permission. Right panel: a monolayer graphene flake (dotted outline) sandwiched between flakes of hexagonal boron nitride. Inset: AFM image, scaled down.

Summary of Research:

Scanning magnetic probe microscopy is a useful technique to study magnetism and electronic transport in materials because it provides a direct spatial map of the magnetic landscape above the sample surface. We currently use superconducting quantum interference device (SQUID) magnetometers for our imaging experiments, but these probes only operate at low temperatures and magnetic fields under ~ 1 Tesla [1]. In contrast, scanning Hall probes permit imaging in a strong magnetic field, over a much larger temperature range, and with potentially higher spatial resolution than SQUIDs [2]. To compete with the field sensitivity of a SQUID and to enable local fabrication, we choose to fabricate Hall probes from

graphene encapsulated in hexagonal boron nitride (hBN) with one-dimensional edge contacts (Figure 1). Devices made with this architecture possess a remarkably low level of disorder, permitting tunability to low carrier density ($\sim 10^{10}$ cm $^{-2}$) to maximize the Hall response while maintaining a high mobility that enables low-noise measurements [3].

Our process is derived from the steps described in Ref. [3], with the important modification to include an aligned top gate in the design (Figure 2, inset), which shields the graphene layer from electrostatic inhomogeneity on the sample. We exfoliate graphene and hBN onto silicon chips and select monolayer flakes of graphene and uniform flakes of hBN using optical and atomic-force microscopy (Veeco AFM). Using the van der Waals assembly technique [3,4], we use a polymer stamp to sequentially pick up and stack a hBN/graphene/hBN heterostructure (Figure 1). We then release the stack onto a heavily doped SiO $_2$ /Si substrate pre-patterned with alignment marks and metal contacts, dissolve the polymer in chloroform for several hours, and anneal in high vacuum at 350°C for three hours.

We again use AFM to identify regions of the stack that are flat and free of bubbles or wrinkles, and then use electron-beam lithography (Nabity) to define a metal (Cr/Au/Pt) top gate in a Hall bar or Hall cross geometry. In a second lithography step, we pattern an etch mask, leaving the edges of the top gate exposed to translate the shape of the topgate directly into the stack. We use an

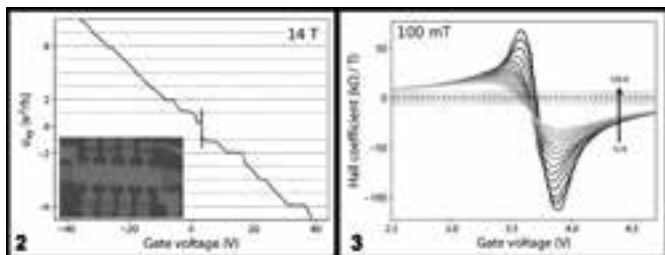


Figure 2, left: Dependence of the Hall conductance on carrier density in a large external magnetic field. The dashed lines indicate expected conductance plateaus for degenerate spin and valley Landau levels, while the dotted lines indicate the conductance plateaus for lifted spin-valley degeneracy. Inset: optical image of the device. **Figure 3, right:** Hall coefficient (sensitivity) of the device from Figure 2 measured at 100 mT and at temperatures from 15 K (dark) to 150 K (light). The light dashed line marks a typical Hall coefficient for GaAs-based Hall probes [8], and the dark dotted line marks the maximum Hall coefficient previously reported for graphene devices at room temperature [7].

inductively coupled plasma of CHF_3 , O_2 , and Ar (Trion etcher) to selectively etch hBN, creating a step-like edge profile exposing a few-nm-wide strip of graphene [5]. In a final electron-beam lithography step, we pattern, deposit, and lift off Cr/Au/Pt contacts overlapping the exposed graphene edge. To protect the devices from mechanical stresses during scanning, we evaporate an ~ 80 nm layer of SiO_2 over the completed device.

We characterize device quality by measuring Hall voltage as a function of back gate voltage in an applied magnetic field. In a large magnetic field (Figure 2), the plateaus of Hall conductance at integer multiples of the conductance quantum demonstrate that the spin-valley degeneracy of the Landau levels is fully lifted, an indication of high device quality [6]. For small magnetic fields, the Hall resistance divided by the magnetic field gives the linear Hall coefficient (Figure 3). On either side of the charge neutrality point (~ 3.7 V), the Hall coefficient reaches a maximum and then falls off inversely with the magnitude of the carrier density. Our first measurements already demonstrate a Hall coefficient competitive with that previously reported for graphene at room temperature and GaAs at cryogenic temperatures [7,8].

To adapt these devices into a geometry suitable for scanning magnetic imaging, we will soon add a deep-

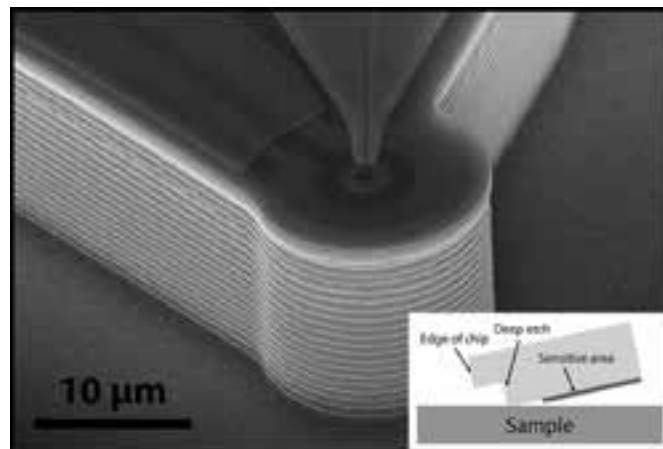


Figure 4: Deep etch surrounding the pickup loop of a SQUID magnetometer.

etched trench surrounding the sensitive area, essentially positioning the Hall cross at the corner of the chip. Figure 4 demonstrates the deep-etch feature added to a SQUID magnetometer, and the inset clarifies the alignment geometry. To achieve this structure, we pattern the chip using photolithography (5x stepper) and etch through the SiO_2 and Si layers (Oxford 100 and Plasma-Therm Versaline) to a total depth of ~ 12 μm . With the inclusion of this final step, the Hall probes will be ready to begin scanning over test samples to characterize the point spread function of the probe and to calibrate the conversion between Hall voltage and magnetic field.

References:

- [1] M. E. Huber, et al., Rev. Sci. Inst. 79, 053704 (2008).
- [2] J. R. Kirtley, et al., Rep. Prog. Phys. 73, 126501 (2010).
- [3] L. Wang, et al., Science 342, 614 (2013).
- [4] P. J. Zomer, et al., Appl. Phys. Lett. 105, 013101 (2014).
- [5] M. Ben Shalom, et al., Nat. Phys. 12, 318 (2016).
- [6] F. Amet, et al., Phys. Rev. Lett. 112, 196601 (2014).
- [7] J. Dauber, et al., Appl. Phys. Lett. 105, 013101 (2014).
- [8] K. Vervaeke, et al., Rev. Sci. Inst. 80, 074701 (2009).

Gigahertz Surface Acoustic Waves on Periodically Patterned Layered Nanostructures

CNF Project Number: 2369-15

Principal Investigator: Brian C. Daly¹

User: Weili Cui²

Affiliations: 1. Associate Professor of Physics, Vassar College; 2. Professor of Engineering, SUNY Maritime College

Primary Source of Research Funding: National Science Foundation Award Division of Materials Research-1709521

Contact: brdaly@vassar.edu, weilicui@yahoo.com

Website: <http://pages.vassar.edu/ultrafast/>

Primary CNF Tools Used: E-beam lithography, CVD, thermal evaporation

Abstract:

We used the ultrafast pump-probe technique known as picosecond ultrasonics to generate and detect surface acoustic waves on nanoscale aluminum (Al) lines on SiO₂ on silicon (Si). In all cases we identified a Rayleigh-like surface acoustic wave with wavelength equal to the pitch of the lines and frequency in the range of 5 GHz - 24 GHz. In some samples, we detected additional, higher frequency surface acoustic waves or independent modes of the Al lines with frequencies close to 50 GHz.

Summary of Research:

In recent work we measured surface acoustic waves (SAWs) in a complicated structure consisting of titanium nitride (TiN) wires of nanometer scale cross-section grown on a multilayered stack of porous and non-porous oxides on an Si wafer [1]. These unique samples yielded pitch-dependent frequencies that in some cases compared favorably with Rayleigh-like or Sezawa-like surface waves [2,3], but in other cases corresponded to modes that radiated significant acoustic energy into the substrate. In this work we studied a simpler set of samples consisting of aluminum (Al) lines on thin silicon dioxide (SiO₂) on Si and we detect multiple SAWs that can be identified by comparison with coarse-grained molecular dynamics simulations. The number of modes detected was found to depend on the pitch of the patterned Al as well as on the wavelength and polarization of the probe light. We detected Rayleigh-like SAWs and Sezawa-like SAWs with wavelength equal to the pitch of the Al lines as well as SAWs with wavelength equal to one-half or one-third of the pitch.

The ultrafast optical pump-probe experiment known as picosecond laser ultrasonics (PLU) has been described extensively in the literature [4]. We performed this experiment with a Ti:Sapphire oscillator operating at a 76 MHz repetition rate with pump wavelength of 800 nm and probe wavelengths of 800 nm or 400 nm. The ten patterned samples that we studied are illustrated schematically in Figure 1.

The samples were fabricated at the Cornell NanoScale Facility by the following process: thermal oxidation to produce the amorphous SiO₂ layer of thickness $d = 60$ or 112 nm, thermal evaporation of 25 nm of Al, and e-beam lithography and dry etching to create the nanometer scale Al pattern. The lines were etched perpendicular to the $\langle 110 \rangle$ direction in the Si substrate, they varied in pitch p ranging from 140 nm up to 1000 nm, and they were all etched near 50% (ranging from 40-60%) duty cycle. The patterned samples were placed into the optical setup, where pump and probe beams were both focused onto the same 20 μm diameter spot, so that anywhere from 20 to 140 periods of the pattern were strongly illuminated. The ultrafast pump pulses were absorbed by the Al lines, and the resulting rapid thermal expansion launched ultrasonic waves both downward into the SiO₂ film and Si substrate, and laterally as SAWs in the direction perpendicular to the line pattern. The ultrasonic waves can be detected by the time-delayed probe pulses due to transient changes in the reflectivity ΔR that they cause. The sources of these transient changes include the

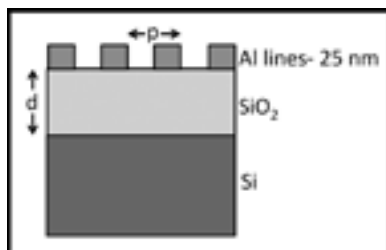


Figure 1: Schematic diagram of the samples. Film thickness d was either 60 nm or 112 nm as measured by picosecond ultrasonics. Al lines pitch p varied from 1000 nm down to 140 nm. The duty cycle was close to 50% (+/- 10%) in all cases as measured by SEM.

dependence of the optical constants of the Al on strain as well as the changes in reflectivity of the optical grating produced by the nanostructure as it responds to the acoustic oscillations.

In this work, we focus on the signals caused by laterally propagating ultrasound and not the signals caused by acoustic waves traveling normal to the sample surface.

Figure 2a shows an example of the ΔR signal with 800 nm probe as a function of probe delay time for two of the samples ($p/d = 400 \text{ nm}/112 \text{ nm}$ and $200 \text{ nm}/112 \text{ nm}$). The exponentially decaying thermal background and the initial jump at $t = 0$ have been subtracted off so that the dominant oscillations are easier to observe. Figure 2b shows the Fourier transform for these two data sets. For both samples, the data are dominated by oscillations at two frequencies. As is expected, the smaller pitch sample produces higher frequency oscillations. The frequencies of the observed oscillations are strongly dependent on the pitch of the samples, and so it is evident that they must represent SAWs, independent bar modes, or a wave propagating very near to the surface of the sample. Other data sets show as few as one or as many as seven detected surface modes, and in the following sections we identify the nature of many of these modes. After an analysis of the many detected SAW frequencies in this experiment we conclude that we detected Rayleigh-like and Sezawa-like modes with frequencies as high as 50 GHz, as well as a number of independent bar modes.

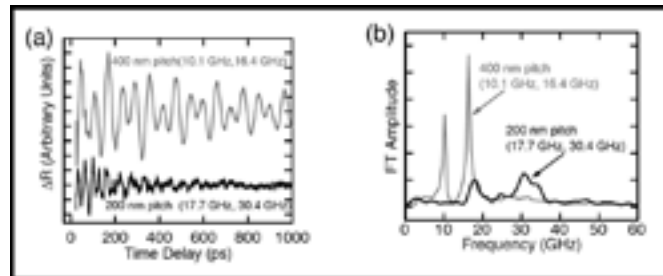


Figure 2: (a) ΔR for two samples with $d = 112 \text{ nm}$ and $p = 400 \text{ nm}$ and 200 nm . (b) Fourier transform amplitude of the signals in (a).

We compared our results to analytical calculations of an SiO_2/Si structure and to coarse-grained molecular dynamics simulations of the complete structure in order to accurately label the detected modes.

References:

- [1] M.M. Bjornsson, et. al., J. Appl. Phys. 117, 095305 (2015).
- [2] B. A. Auld, Acoustic Fields and Waves in Solids (Krieger Publishing Company, Malabar, Florida, 1990), Vol. 2, Ch. 10.
- [3] G. W. Farnell and E. L. Adler, in Physical Acoustics, edited by W. P. Mason and R. N. Thurston (Academic Press, New York, 1972), Vol. 9, p. 35.
- [4] C. Thomsen, H. T. Grahn, H. J. Maris, and J. Tauc, Phys. Rev. B 34, 4129 (1986).

Magnetic Imaging of Ionic Liquid Gated Transition Metal Dichalcogenides

CNF Project Number: 2514-16

Principal Investigator: Katja Nowack

User: Alexander Jarjour

Affiliation: Laboratory of Atomic and Solid State Physics (LASSP), Cornell University

Primary Source of Research Funding: Cornell Center for Materials Research (NSF MRSEC, DMR-1719875)

Contact: kcn34@cornell.edu, abj46@cornell.edu

Primary CNF Tools Used: Heidelberg DWL2000, SC4500 evaporators, JEOL 6300, Veeco Icon AFM, Oxford 81

Abstract:

We report progress on developing superconducting ionic liquid-gated MoS₂ devices compatible with scanned probe microscopy. We have developed a spin-on ionic gate for our MoS₂ devices, allowing us to push the material into the metallic regime. We discuss progress on improving our nanofabrication to observe superconductivity.

Summary of Research:

Atomically thin exfoliated molybdenum disulfide (MoS₂) devices have been reported to superconduct at an *n*-type charge carrier density of $\sim 10^{14}$ cm⁻² [1] with a critical temperature of approximately ~ 2 K in a monolayer [2]. To achieve the high charge carrier density ionic gating has been employed in the literature, and we wish to replicate this approach while adapting it to be compatible with mesoscale imaging. Our group is interested in imaging the magnetic response of the superconducting state, using scanning Superconducting QUantum Interference Device (SQUID) microscopy.

This technique can be used to measure the superfluid density of a superconductor as a function of temperature, which can reveal information about the order parameter [3]. Recent work on superconducting MoS₂ indicates the order parameter may not be fully gapped, suggesting a

non-Bardeen-Cooper-Schrieffer (BCS) superconducting state [4]. Superfluid density measurements would complement the existing data, further illuminating the nature of the order parameter of this system.

Our device fabrication is performed in the CNF. First, optical contact lithography is used to pattern liftoff resist for bond pads, long leads from the device area to the bond pads, and a large gate for biasing the ionic liquid. A completed device is shown in Figure 1 which includes these features. The SC4500 electron beam evaporator is then used to deposit a Ti/Pt/Au trilayer. The gold is wet etched in the gate region, exposing the platinum. Thus, the device side of the electrolytic capacitor is gold, and the gate side is platinum, with the aim of minimizing electrochemistry during gating. Using the polymer stamp transfer techniques developed for graphene

heterostructures [5], MoS₂ flakes are transferred onto these prepatterned substrates, and any polymer residue is removed by a chloroform dip. Then, contacts are patterned to the flake using the JEOL 6300 electron-beam lithography system, connecting it to the long leads and bond pads. These contacts are then metalized in the SC4500 with Ti/Au.

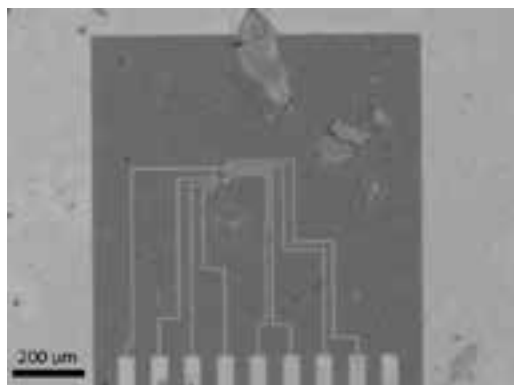


Figure 1: Spin-coated 380 nm ionic gel on MoS₂ few-layer device. Large surrounding metallic region is Pt gate, bars at bottom of image are optically patterned leads to bond pads.



Figure 2: Few layer MoS₂ device fabricated by the authors.

Next, a Hall bar geometry is defined with the JEOL 6300, and the Oxford 80 is used to etch the MoS₂. Finally, a vacuum bake is used to remove any residue from the devices. A completed MoS₂ device before liquid gating is shown in Figure 2.

In our lab, an ionic gel is prepared from diethylmethyl(2-methoxyethyl)ammonium bis(trifluoromethylsulfonyl) imide (DEME-TFSI) and polystyrene-poly(methyl methacrylate)-polystyrene (PS-PMMA-PS). In an inert atmosphere, this gel is spun onto the devices, covering the MoS₂ flake and the platinum gate. The device is then transferred into a measurement cryostat insert with < 15 minutes of total air exposure, and pumped on for > 12 hrs at room temperature to remove water. The devices are then cooled to 4 Kelvin using a helium-4

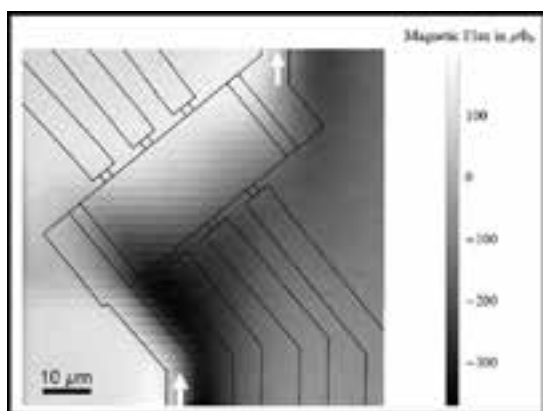


Figure 3: Scanning SQUID image of ionic liquid gated, metallic MoS₂ device. White arrows indicate current source and drain, black outline is device shape. Sample temperature approximately 10 Kelvin.

cryostat, to determine if they are superconducting. An integrated variable temperature stage allows the sample temperature to be increased to the melting point of the ionic liquid (220 K) as it is insensitive to gate voltage changes below that temperature. We have not yet observed superconductivity in our devices, but are actively working on this issue.

Magnetic imaging is performed in our 4 Kelvin cryogen-free scanning squid microscope. By spinning the gel to < 500 nm thick, we can image magnetism from currents flowing in the MoS₂ flake. Figure 3 shows such a magnetic image of one of our liquid-gated devices.

As we continue to improve our processing, we hope to soon observe superconductivity in these devices. We are working to ensure all our chemical processing is fully compatible with the MoS₂, as the superconductivity is expected to exist primarily in the first few atomic layers of the MoS₂ flake [1], which we suspect would make it sensitive to chemical processing during fabrication. We also suspect that the time in vacuum at ambient temperature may be insufficient to remove water absorbed from the air, and are working on developing a bake in the measurement cryostat to remove water from the gel.

References:

- [1] J. T. Ye, et al., Science 338, 1193 (2012).
- [2] D. Costanzo, et al., Nature Nanotechnology 11, 339 (2016).
- [3] J.A. Bert, et al., PRB Vol 86 (2012).
- [4] D. Costanzo, et al., Nature Nanotechnology 13, 483-488 (2018).
- [5] P. J. Zomer, et al., Appl. Phys. Lett. 105, 013101 (2014).

Nanoscale Periodic Features with a 5x Autostep i-line Stepper

CNF Project Number: 2217-13

Principal Investigator: Ioannis Kymissis

User: Tanya Cruz Garza

Affiliation: Department of Electrical Engineering, Columbia University, New York City, NY

Primary Source of Research Funding: National Science Foundation

Contact: johnkym@ee.columbia.edu, tanyacruzgarza@gmail.com

Website: <http://kymissis.columbia.edu>

Primary CNF Tools Used: ASML 300C DUV stepper, GCA 5x Autostep i-line stepper

Abstract:

Lithography with the ASML 300C DUV stepper has been used in previous years to produce pillar and hole features with diameters including 232 nm, 306 nm, 408 nm, and 446 nm, and with backside auto alignment on fused silica wafers. This past year, work has been furthered with the GCA 5x Autostep i-line stepper to pattern the larger of these hole features with diameters of 408 nm and 446 nm on fused silica wafers.

Summary of Research:

In previous years a process for patterning nanophotonic pillar and hole structures was developed at CNF that used the ASML 300C DUV stepper. These features were etched into the substrate material using the patterned resist as an etch mask. The ASML 300C DUV stepper process has been used to pattern 4-inch borosilicate float glass wafers ("borofloat"), 4-inch fused silica wafers, and 4-inch silicon wafers. Pillar features like those shown in Figure 1 were fabricated with diameters of 232 nm, 270 nm, 306 nm, 408 nm, 612 nm, and 816 nm. Hole features like those shown in Figure 2 were fabricated with design diameters of 306 nm, 408 nm, and 446 nm. Optimal depth of focus (DOF), exposure dose, and etch time were determined for nanophotonic patterns in fused silica by varying these parameters incrementally and examining the resultant features. Photonic crystal geometry was examined in the SEM and photonic crystal performance was assessed optically via extraction of waveguided light.

The DUV process previously developed to pattern fused silica wafers with nanophotonic pillar and hole structures was expanded to include automated backside alignment on the ASML 300C DUV stepper. Work done to enable backside alignment was achieved for up to three out of four ASML alignment marks etched into bare fused silica to a depth of 150 nm.

In previous years preliminary work was done with the GCA 5x Autostep i-line stepper to adapt the ASML 300C DUV stepper process which patterns 4-inch fused silica wafers minimum hole feature sizes of 408 nm and 446 nm. The best results of a coarse DOF and exposure dose variation study on the GCA 5x Autostep i-line stepper are shown in Figures 3 and 4. DOF and exposure

dose were determined for nanophotonic patterns in fused silica by varying these parameters incrementally and examining the resultant features. The optimal etch depth used was determined in previous work making the same features using the ASML 300C DUV stepper. Photonic crystal geometry was examined in the SEM and photonic crystal performance was. Although, there is a deformity in the holes pictured in Figures 3 and 4, the optical performance of the resultant photonic crystal pattern was comparable to those seen from the DUV lithography process.

This past year a finer DOF and exposure dose variation study on the GCA 5x Autostep i-line stepper was done focusing in on those exposure parameters which gave the best performance during the coarse study. This work was focused on the hole feature sizes of 446 nm. The resultant photonic crystal patterns are being assessed via extraction of waveguided light and the best performing of these will be further examined in the SEM to determine their geometric quality.

In summary, the process previously developed to pattern fused silica wafers with nanophotonic hole structures using the ASML 300C DUV stepper was adapted to use the GCA 5x Autostep i-line stepper for hole sizes of 408 nm and 446 nm. A coarse DOF and exposure dose variation study on the GCA 5x Autostep i-line stepper resulted in photonic crystal patterns with some geometric deformation but with comparable performance to that of those made with the DUV stepper when assessed optically via extraction of waveguided light. The results of a finer DOF and exposure dose variation study on the GCA 5x Autostep i-line stepper for hole sizes of 446 nm is currently being assessed.

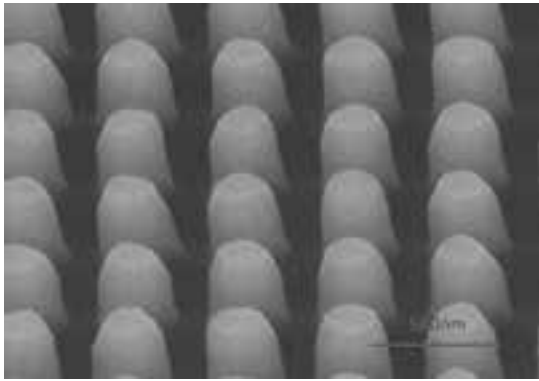


Figure 1: SEM image of photonic crystal pattern, nominally with 270 nm pillar features, fabricated fused silica with process developed with ASML 300C DUV stepper.

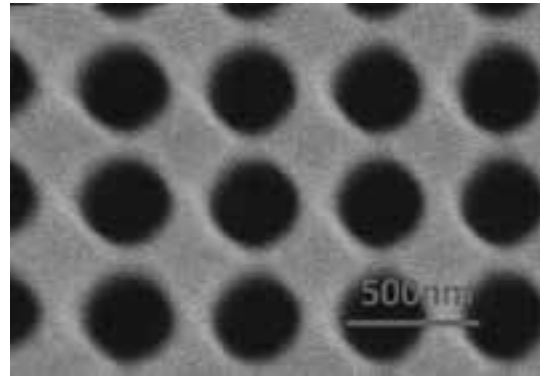


Figure 2: SEM image of photonic crystal pattern, nominally with 306 nm hole features, fabricated in fused silica with a process developed with ASML 300C DUV stepper.

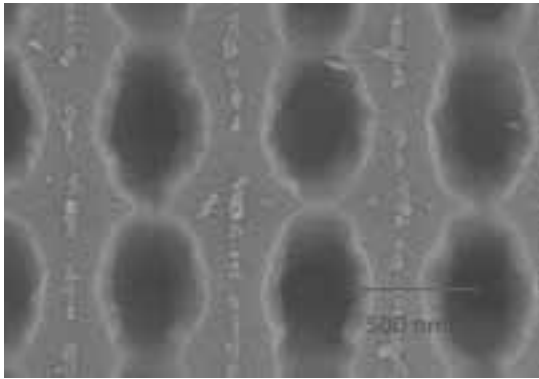


Figure 3: SEM image of photonic crystal pattern, nominally with 408 nm hole features, fabricated in fused silica with a process developed with GCA 5x stepper.

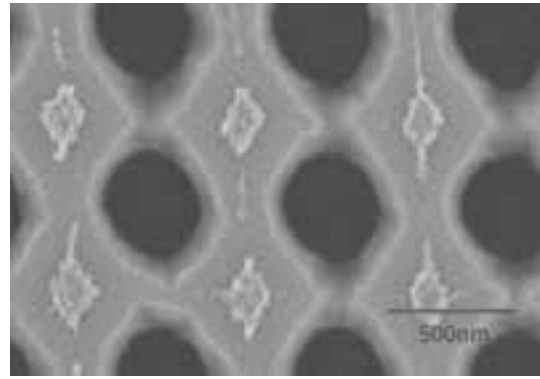


Figure 4: SEM image of photonic crystal pattern, nominally with 446 nm hole features, fabricated in fused silica with a process developed with GCA 5x stepper.

Development of GaN Vertical Trench-MOSFET with MBE Regrown Channel

CNF Project Number: 2307-14

Principal Investigators: Huili Grace Xing, Debdeep Jena

Users: Wenshen Li, Kazuki Nomoto, Zongyang Hu, Anni Wu, Jui-Yuan Hsu

Affiliations: Electrical and Computer Engineering, Material Science Engineering; Cornell University

Primary Source of Research Funding: Advanced Research Projects Agency-Energy

Contact: grace.xing@cornell.edu, WL552@cornell.edu

Primary CNF Tools Used: PT770 etcher, Autostep 200, Oxford PECVD, Oxford 81 etcher,

Heidelberg mask writer DWL2000, SC4500 odd-hour evaporator,

AJA sputter deposition, Oxford ALD FlexAL, DISCO dicing saw, Veeco Icon AFM

Abstract:

GaN vertical trench-MOSFETs incorporating molecular beam epitaxy (MBE) regrown channel are developed and investigated. The channel regrowth by MBE prevents re-passivation of the p -type GaN body while promising higher channel mobility. A respectable 600 V breakdown voltage (BV) is measured in the absence of edge termination, indicating a decent critical field strength (> 1.6 MV/cm) of the regrown channel. However, the on-resistance is limited by the highly resistive lateral channel due to Mg incorporation. With an additional n^+ buried layer, excellent on-current of 130 mA/mm and on-resistivity of 6.4 m Ω ·cm² are demonstrated, but the BV is limited by high source–drain leakage current from the channel due to drain-induced barrier lowering (DIBL) effect due to the presence of interface charge ($\sim 6 \text{ \AA} \sim 10^{12}$ cm⁻²) at the regrowth interface on etched sidewalls. This study provides valuable insights into the design of GaN vertical trench-MOSFET with a regrown channel, where simultaneous achievement of low on-resistivity and high BV is expected in devices with reduced interface charge density and improved channel design to eliminate DIBL.

Summary of Research:

GaN vertical power transistors have gained increasing interests in recent years due to the advantages over lateral transistors in high voltage/high current applications. Recently, a novel design based on trench metal oxide semiconductor field effect transistor (MOSFET) is realized by metal-organic chemical vapour deposition (MOCVD) regrowth of a thin GaN interlayer, which helps increase the channel mobility. Similar to the other MOCVD regrown devices, the buried Mg-doped p -GaN needs to be re-activated by exposing the p -GaN surface during high temperature anneal. This leads to high thermal budget and poses limitations on device geometry. Furthermore, any incomplete activation of buried p -GaN leads to reduced BV. In this report, we design a V-shaped trench MOSFET with molecular beam epitaxy (MBE) regrown unintentionally-doped (UID) GaN channel. Approximately 600 V breakdown voltage with normally-off operation is demonstrated without the need for re-activation of the buried p -GaN. To our knowledge, this is the highest BV achieved in GaN vertical transistors with MBE regrown channel.

The starting epitaxial structure is a high voltage p - n diodes structure grown by MOCVD. The schematic of the device is shown in Figure 1, which consists of a MBE regrown UID GaN channel covering the sidewall of the V-shaped trench. The conformal gate

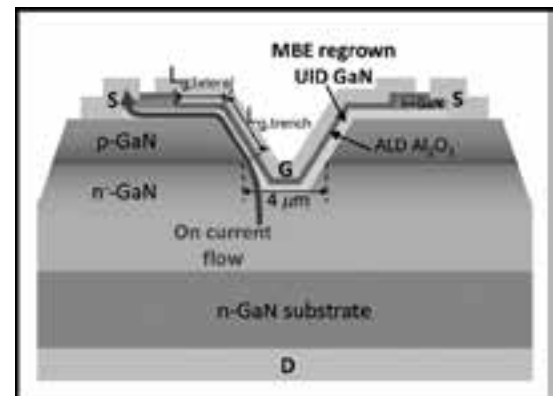


Figure 1: Schematic device structure of the GaN V-trench MOSFET.

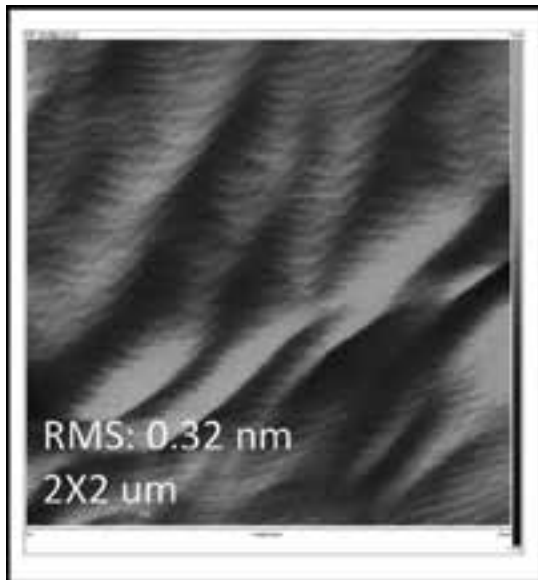


Figure 2: AFM surface morphology of the MBE regrown GaN at the trench bottom.

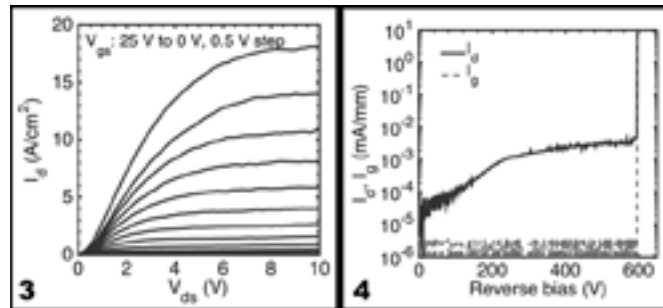


Figure 3, left: Representative I_d - V_{ds} characteristics of a Ga_2O_3 vertical power MISFET. Figure 4, right: Representative three-terminal off-state (at $V_{gs} = -15$ V) I_d/I_g - V_{ds} characteristics and breakdown voltage of Ga_2O_3 vertical power MISFETs.

ensures field-control of the regrown channel as well as the possible charge typically present at the regrowth interface. Smooth surface morphology of the regrown GaN at the trench bottom is observed by atomic force microscope (AFM) with clear atomic steps (Figure 2). The fabrication steps are as follows. A tapered trench is etched using our low damage Cl-based recipe on PT770 etcher with PECVD SiO_2 as mask. In order to reduce impurity concentration at the etched surface, a combination of UV-ozone cleaning and HF+HCl wet etch is performed before loading into the MBE chamber, where 50 nm UID GaN is regrown. A patterned n^+ -GaN regrowth is then performed for ohmic contact purpose. Since MBE chamber has no hydrogen-containing reactants, the buried p -GaN remains activated. The 30 nm Al_2O_3 gate dielectric is deposited by Oxford ALD system.

The transfer curve of a single finger device shows an on-off ratio of 10^9 and normally-off operation with a threshold voltage of ~ 16 V. The output characteristics in Figure 3 show good saturation behavior and an on-current of ~ 18 A/cm² (normalized by the trench area) at $V_{gs} = 25$ V. R_{on} is determined from the linear region to be $0.3 \Omega \cdot \text{cm}^2$. The relatively poor R_{on} and I_{on} is due to

Mg diffusion in the lateral part of the channel from the p -GaN underneath. A thin n^+ -GaN counter layer before the channel regrowth improves the channel conductivity dramatically [1]. The off-state characteristics are shown in Figure 4. Low drain leakage and a breakdown voltage of 596 V is measured with $V_{gs} = -15$ V, indicating good quality of the regrowth p - n junction interface.

In summary, record high 600 V BV is achieved among GaN vertical transistors with MBE regrown channel. No additional activation annealing of the buried p -GaN is needed, allowing for lower thermal budget and more flexible device geometry than MOCVD regrowth.

References:

- [1] W. Li, K. Nomoto, K. Lee, S. M. Islam, Z. Hu, M. Zhu, X. Gao, M. Pilla, D. Jena, and H. G. Xing, IEEE Transactions on Electron Devices 65, 2558 (2018).
- [2] W. Li, K. Nomoto, K. Lee, S. M. Islam, Z. Hu, M. Zhu, X. Gao, M. Pilla, D. Jena, and H. G. Xing, in Proc. 75th Annu. Device Res. Conf. (DRC) (2017), p. 1.

Characterization of $(\text{Al}_x\text{Ga}_{1-x})_2\text{O}_3$ Thin Films Grown on $\langle 010 \rangle \beta \text{Ga}_2\text{O}_3$ by MBE

CNF Project Number: 2443-16

Principal Investigators: Huili Grace Xing, Debdeep Jena

Users: Nicholas Tanen, Vasanth Balakrishnan

Affiliations: Materials Science and Engineering, Electrical and Computer Engineering; Cornell University

Primary Source of Research Funding: NSF -Designing Materials to Revolutionize and Engineer our Future

Contact: grace.xing@cornell.edu, djena@cornell.edu, ntj47@cornell.edu, vb322@cornell.edu

Website: <http://grace.engineering.cornell.edu>

Primary CNF Tools Used: Veeco Icon AFM

Abstract:

Electronic devices, made of wide bandgap semiconductors, show low current leakage and high breakdown fields. Oxides of aluminum, gallium, and indium (Al, Ga and In) form a class of semiconductors with promising properties. Currently HEMT transistors, fabricated of Ga_2O_3 and $(\text{Al}_x\text{Ga}_{1-x})_2\text{O}_3$ semiconductors have high breakdown voltages and low leakage currents. Hence, it is of immense interest to study and understand the growth parameters for $(\text{Al}_x\text{Ga}_{1-x})_2\text{O}_3$. Here we report our preliminary growth and surface morphology results for $(\text{Al}_x\text{Ga}_{1-x})_2\text{O}_3$ films grown on $\langle 010 \rangle - \beta$ phase Ga_2O_3 substrates by plasma-assisted molecular beam epitaxy (PAMBE). We correlate the growth parameters with quality and surface morphology of $(\text{Al}_x\text{Ga}_{1-x})_2\text{O}_3$ films.

Summary of Research:

We grew $(\text{Al}_x\text{Ga}_{1-x})_2\text{O}_3$ films with the Veeco GEN930 PAMBE system on $\langle 010 \rangle$ UID $\beta \text{Ga}_2\text{O}_3$ substrates at substrate temperature 500°C and O_2 flow 3 sccm. Based on AFM scans performed over a $2 \mu\text{m} \times 2 \mu\text{m}$ sample area, the surface structure of the film is elongated along the $\langle 100 \rangle$ direction.

At a lower Al content, Al gets incorporated in the films smoothly and for $x < 0.2$, we observe corrugated and smooth surface having very low RMS roughness. As the Al content the layers increases above a certain limit the films become amorphous and the surface roughness increases significantly. Figures 1 and 2 indicate good surface morphologies with smooth surfaces. Figure 3 on the other hand, is for a Ga rich growth regime

(high Ga BEP) which led to poor surface morphology due to Ga_2O desorption mechanism, this increased the Al incorporation in the film and made the film surface rough.

References:

- [1] Kaun, S.W., F. Wu, and J.S. Speck. " β - $(\text{Al}_x\text{Ga}_{1-x})_2\text{O}_3/\text{Ga}_2\text{O}_3 \langle 010 \rangle$ heterostructures grown on $\beta\text{-Ga}_2\text{O}_3 \langle 010 \rangle$ substrates by plasma-assisted molecular beam epitaxy." *J. of Vacuum Science and Technology A: Vacuum, Surfaces, and Films* 33.4 (2015): 041508.
- [2] Vogt, Patrick, and Oliver Bierwagen. "Reaction kinetics and growth window for plasma-assisted molecular beam epitaxy of Ga_2O_3 : Incorporation of Ga vs. Ga_2O desorption." *Applied Physics Letters* 108.7 (2016): 072101.

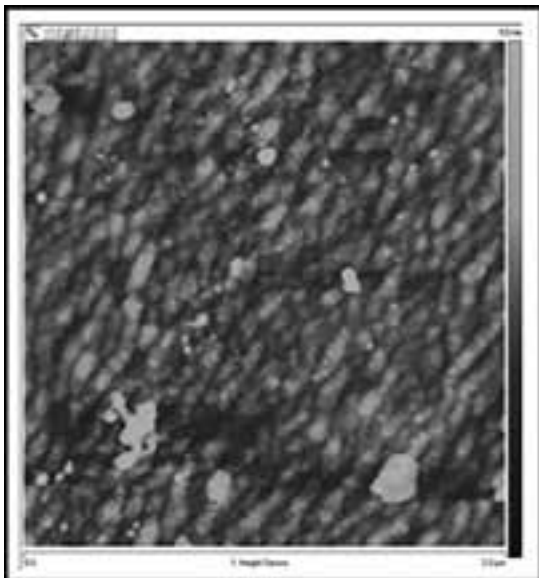


Figure 1: 2 μm × 2 μm AFM scan for Ga BEP = 3 × 10⁻⁹ (RMS = 1.08 nm).

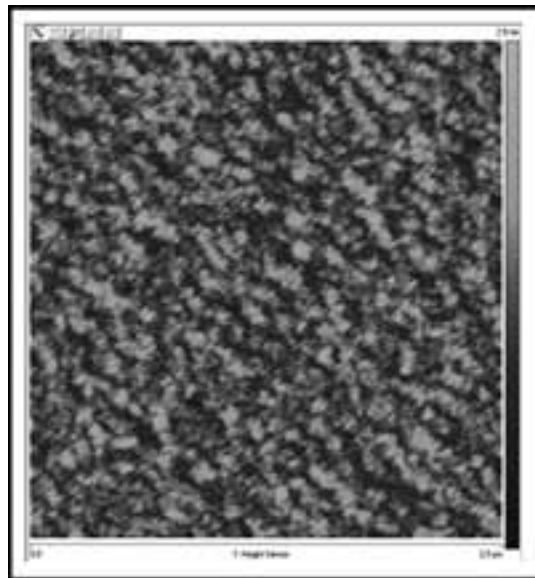


Figure 2: 2 μm × 2 μm AFM scan for Ga BEP = 5 × 10⁻⁹. (RMS = 0.272 nm).

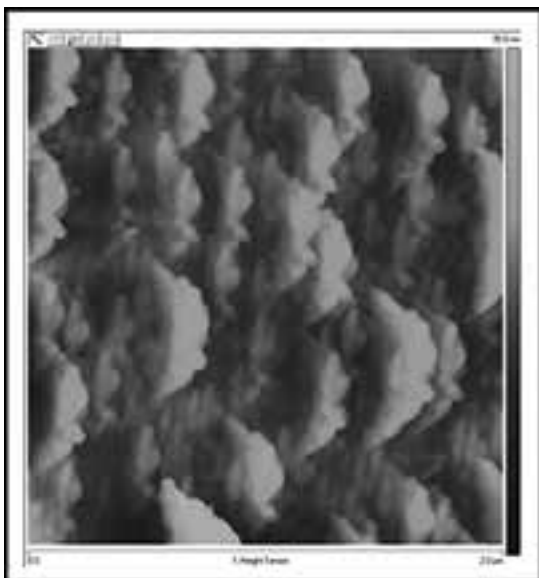


Figure 3: 2 μm × 2 μm AFM scan for Ga BEP = 30 × 10⁻⁹ (RMS = 4.45 nm).

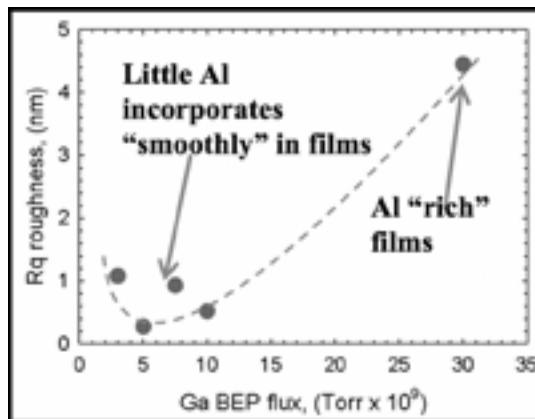


Figure 4: Graphical plot of (Al_xGa_{1-x})₂O₃ film roughness R_q vs Ga flux.

Device Processes and Electrical Characteristics of First 1 kV Ga₂O₃ Vertical Power Transistors

CNF Project Number: 2443-16

Principal Investigators: Huili Grace Xing, Debdeep Jena

Users: Zongyang Hu, Kazuki Nomoto, Wenshen Li

Affiliations: Electrical and Computer Engineering, Material Science Engineering; Cornell University

Primary Source of Research Funding: NSF, AFOSR

Contact: grace.xing@cornell.edu, zh249@cornell.edu

Primary CNF Tools Used: Oxford PECVD, e-beam lithography tools, ICP-RIE, ALD, sputtering tools

Abstract:

High-voltage vertical Ga₂O₃ MISFETs are developed employing halide vapor phase epitaxial (HVPE) layers on bulk Ga₂O₃ <001> substrates. The low charge concentration of $\sim 10^{16}$ cm⁻³ in the *n*-drift region allows three terminal breakdown voltages to reach up to 1057 V without field plates. The devices operate in the enhancement mode with a threshold voltage of ~ 1.2 - 2.2 V, a current on/off ratio of $\sim 10^8$, and an on-resistance of ~ 13 - 18 mOhm·cm², and an output current of > 300 A/cm². This is the first report of high-voltage vertical Ga₂O₃ transistors with enhancement mode operation, a significant milestone toward realizing Ga₂O₃-based power electronics.

Summary of Research:

Gallium oxide (Ga₂O₃) has emerged as a new semiconductor material for high-power applications in recent years. As the most stable form monoclinic β -Ga₂O₃ has been reported with a wide bandgap up to 4.9 eV, a high expected breakdown electric field up to 8 MV/cm and a decent intrinsic electron mobility limit of 250 cm²/Vs, which enables high-voltage and high-power operation. The experimentally reported critical electric field up to 5.2 MV/cm already exceeds that of SiC and GaN, and electron mobility of 100-150 cm²/Vs has been achieved in both bulk substrates as well as epitaxial layers. In addition, low-cost, large area single-crystal substrates allow high-quality epitaxial layers to be developed using various methods.

The past few years witnessed successful development of Ga₂O₃ lateral FETs including MOSFETs, MESFETs, nano-membrane FETs and FinFETs and vertical diodes such as SBDs and hetero-junction *p-n* diodes. However, high performance vertical power transistors on Ga₂O₃ have only been demonstrated by our group [1,2].

There are several reasons: (1) vertical power transistors require high quality epitaxial layers with minimized impurity incorporation and precisely controlled doping concentrations, (2) Vertical transistor structure design and fabrication processes are more complicated than those of lateral transistors and diodes.

In this report, we summarize the most recent development and results of Ga₂O₃ vertical transistors in our group.

We are able to combine high quality epitaxial Ga₂O₃ layers with a fully vertical Ga₂O₃ transistor process flow, and demonstrate the first 1-kV class vertical Ga₂O₃ MISFETs (or FinFETs). In addition to the high breakdown voltage, the transistor also shows

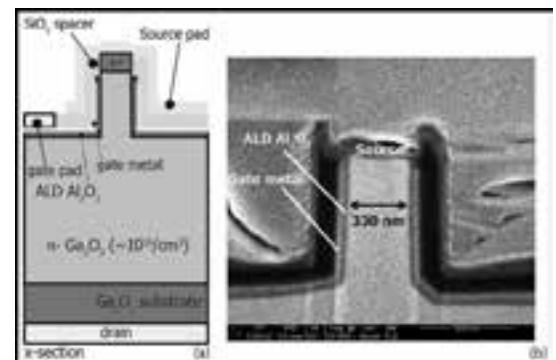


Figure 1: (a) Schematic cross-section of a Ga₂O₃ vertical power MISFET. (b) 52° SEM cross-section image of a completed Ga₂O₃ vertical Fin-MISFET showing a 330 nm wide and 795 nm long channel.

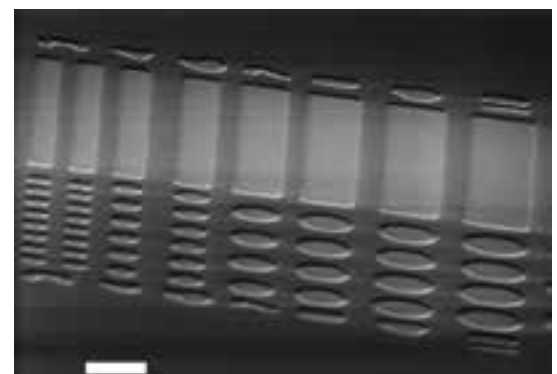


Figure 2: Representative I_d-V_{ds} characteristics of a Ga₂O₃ vertical power MISFET.

enhancement-mode operation, which is a desired feature for application as power switches.

The epitaxial layers were grown by HVPE on *n*-type bulk Ga₂O₃ <001> substrates ($n = 2 \times 10^{18} \text{ cm}^{-3}$). The 10-mm thick *n*-Ga₂O₃ epitaxial layer is doped with Si with a target doping concentration of $< 2 \times 10^{16} \text{ cm}^{-3}$.

The schematic device structure is depicted in Figure 1. A simplified process flow is described as the following:

1. Si Implantation for Top Ohmic Contacts

- SiO₂ mask deposition (Oxford PECVD)
- Si implantation with a box profile of $1\text{E}20 \text{ cm}^{-3}$
- Activation annealing at 1000°C in furnace

2. Vertical Channel Definition

- E-beam lithography and Pt metal mask deposition
- Low power ICP-RIE dry etching of Ga₂O₃
- Target channel width/height ratio of 0.3/1.0 μm

3. Gate Metallization

- Deposition of ALD Al₂O₃ ~ 30 nm
- Sputtering Cr ~ 50 nm to cover the sidewalls of the channel
- E-beam evaporation of Ti/Au as gate metal pads

4. Gate-Source Spacer Formation

- Photoresist planarization and thinning to expose top of Ga₂O₃ channels.
- Etch back ALD Al₂O₃ and Cr by dry etching
- PECVD SiO₂ spacer deposition ~ 200 nm
- Photoresist planarization and thinning
- SiO₂ spacer etch back

5. Source and Drain Metallization

- Sputter Ti/Al/Pt source metals
- Sputter Ti/Al/Pt back drain contacts

The net charge concentration ($N_D - N_A$) in the *n*-Ga₂O₃ drift layer is estimated at $1 \times 10^{15} - 1.2 \times 10^{16} \text{ cm}^{-3}$ using capacitance-voltage (C-V) measurements. The low charge concentration is essential to realize E-mode operation and high breakdown voltages.

Figure 2 shows the representative $I_d - V_{ds}$ family curves of a fabricated vertical Ga₂O₃ MOSFET with a source area of 0.33 mm × 80 mm.

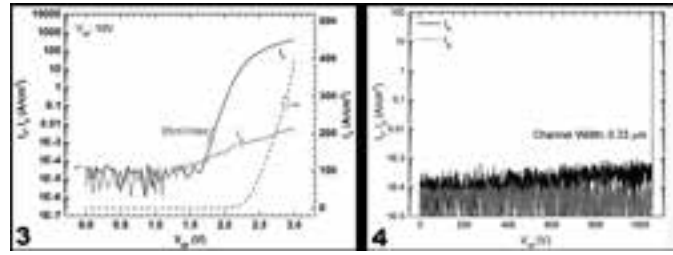


Figure 3, left: Representative $I_d/I_{dgs} - V_{gs}$ transfer characteristics in the semi-log and linear scale, along with the extracted subthreshold slope. **Figure 4, right:** Representative three-terminal off-state (at $V_{gs} = 0 \text{ V}$) $I_d/I_{dgs} - V_{ds}$ characteristics and breakdown voltage of Ga₂O₃ vertical power MISFETs.

At V_{gs} of 3 V and V_{ds} of 10 V, the drain current reaches $\sim 350 \text{ A/cm}^2$ with an associated differential on-resistance of $\sim 18 \text{ mW}\cdot\text{cm}^2$, normalized to the area of the $n^+\text{Ga}_2\text{O}_3$ source. The representative $I_d - V_{gs}$ transfer characteristics of these devices are shown in Figure 3.

The V_{th} defined by linear extrapolation of the drain current at the peak transconductance is $\sim 2.2 \text{ V}$. The subthreshold slope is measured to be $\sim 85 \text{ mV/dec}$ near a current density of 1 mA/cm^2 and the hysteresis is less than 0.2 V. The off-state leakage currents and 3-terminal breakdown voltages in these vertical power MISFETs are measured at $V_{gs} = 0 \text{ V}$.

The representative results are plotted in Figure 4: both the drain and gate leakage currents remain low, near the detection limit of the measurement instrument, before the hard breakdown near 1057 V. Two-dimensional device simulations reveal that the electric field peaks near the outer edges of the gate pads. In fact, examination of the devices after breakdown shows visible damage near the outer edges of the gate pads. Therefore, we expect that higher breakdown voltages be achieved by implementing field plates or ion implantation edge termination techniques.

References:

- [1] Z. Hu, K. Nomoto, W. Li, L. J. Zhang, J.-H. Shin, N. Tanen, T. Nakamura, D. Jena and H. G. Xing, "Vertical fin Ga₂O₃ power field effect transistors with on/off ratio $> 10^9$ ", Device Research Conf. (DRC), pp. 1-3. DOI: 10.1109/DRC.2017.7999512, June 2017.
- [2] Z. Hu, K. Nomoto, W. Li, N. Tanen, K. Sasaki, A. Kuramata, T. Nakamura, D. Jena and H. G. Xing, "Enhancement-mode Ga₂O₃ vertical Transistors with breakdown voltage $> 1 \text{ kV}$ ", IEEE Electron Device Lett., Vol. 39, No. 6, pp. 869-872. DOI: 10.1109/LED.2018.2830184, June, 2018.

Side-Coupled Microfluidics for Biosensor

CNF Project Number: 2465-16

Principal Investigators: Jiandi Wan, Stefan Preble

Users: Toby Mea, Zihao Wang

Affiliation: Microsystems Engineering Department, Rochester Institute of Technology

Primary Source of Research Funding: Moore Foundation

Contact: jdween@rit.edu, sfpeen@rit.edu, hm8168@rit.edu, zw4491@rit.edu

Primary CNF Tools Used: Heidelberg mask writer DWL2000, edge bead removal system, ABM contact aligner, SÜSS SB8e substrate bonder, DISCO dicing saw

Abstract:

A side coupled microfluidic device was designed and manufactured using standard photolithography and wafer bonding technique. Devices formed from bonding two wafers using AZ 125 nXT showed satisfactory integrity, neither breaking from the dicing step or from fluid flow that was supplied using a pulled glass capillary connected to a syringe pump.

Summary of Research:

We previously designed and fabricated an iteration of a novel biosensor combining optical and microfluidic components. While the optical components displayed satisfactory performance, the previous design's microfluidic components suffered from certain critical problems that rendered it useless, including a lack of fluid perfusability and difficulty in coupling the microchannels to an external fluid supply (i.e. syringe pump). Specifically, we had previously etched microchannels into silicon dioxide and capped the microchannels using a slab of PDMS with pre-punched through holes. However, the PDMS slab was poorly bonded to the SiO₂ and the pre-punched through-holes were not properly aligned to allow fluid perfusion.

In order to overcome these limitations in the microfluidic components, we conceptualized a different approach that utilized a photoresist adhesive bonding and side-coupled microchannels (in contrast to the top-coupled microchannels from before). Before combining the optical and microfluidic components to form a complete biosensor, we created a separate standalone microfluidic device test the effectiveness of this new approach.

The process flow for fabricating the standalone device is shown in Figure 1. Essentially, AZ 125 nXT is spun on a fused silica wafer to a thickness of approximately 20 μm and patterned using the ABM contact aligner, leaving behind the microchannel pattern. AZ 125 nXT was chosen because it could be spun to large thicknesses, but only one paper has extensively documented its use for micromachining [1]. We then spun and exposed AZ 125 nXT on a second wafer made of borosilicate glass. AZ 125 nXT is broadband sensitive, which

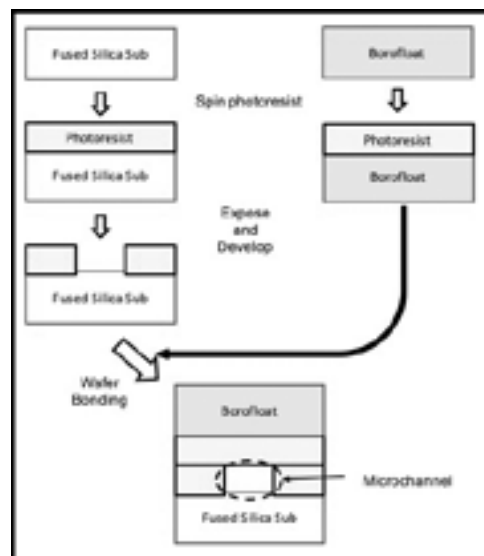


Figure 1: Process flow of fabricating side-coupled microfluidic devices.

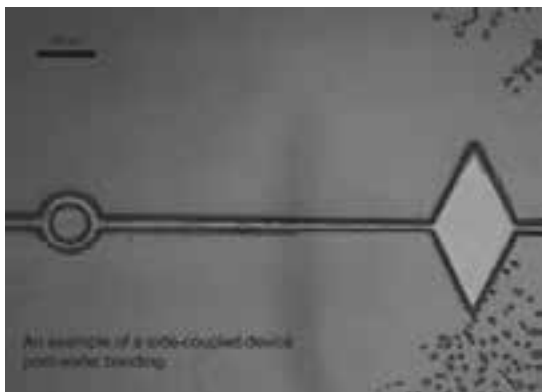


Figure 2: Micrograph showing side-coupled microfluidic device after wafer bonding.

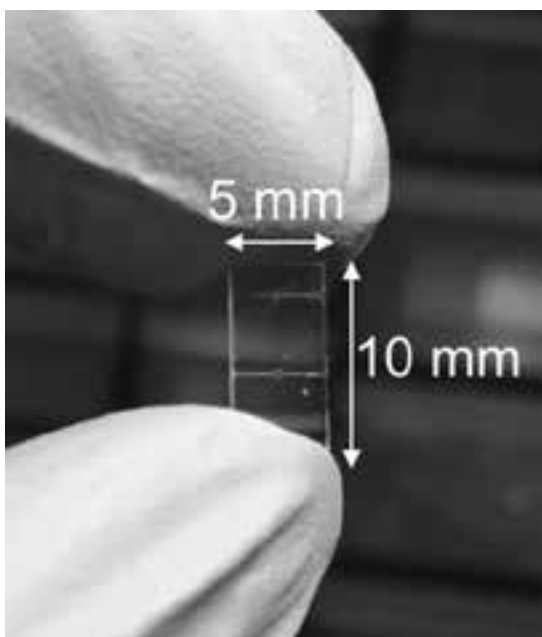


Figure 3: Snapshots of the completed side-coupled microfluidic device.

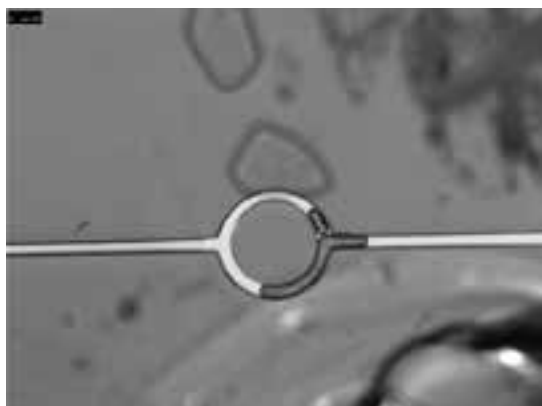


Figure 4: Snapshots of fluid perfusion through microchannels.

effectively cut the necessary exposure from the ABM contact aligner by a factor of 3. The two wafers were then bonded together using the SÜSS substrate bonder. Specifically, the two wafers were heated to 100°C and pressed against each other with a force of 1000 N to form the final device wafer. Upon bonding, the patterned photoresist showed minimal deformation, leaving the microchannels clearly defined (shown in Figure 2). Finally, using the DISCO dicing saw, the device wafer was diced into individual devices (shown in Figure 3). The wafers did not separate during the dicing step, which indicated good bonding between the wafers.

The resulting devices were then subjected to fluidic tests to investigate the perfusability of the device and the feasibility of side-coupled microfluidics. To couple the microchannels to an external syringe pump, 1 mm glass capillaries were pulled using a glass pulling machine to achieve a tip with a diameter that could fit into the microchannel inlet/outlet. In addition to being able to fit the tips into the inlet/outlet, the tip could also perfuse fluid supplied from a syringe pump (shown in Figure 4).

Pumping fluid from the syringe pump revealed that the microchannels were capable of perfusing fluid up to flows of 250 $\mu\text{L/hr}$. Therefore, we have successfully designed and fabricated a side-coupled microfluidic device that can effectively perfuse fluid.

Although side-coupled microfluidic devices have already been reported in the literature (mostly for mass spectroscopy purposes [2-3]), these experiments nonetheless demonstrated that side-coupling may be a viable strategy for realizing the microfluidic components on our proposed biosensor.

References:

- [1] T. Knoll, A. Bergmann, and D. Nussbaum, "Fabrication of microfluidic chips using lithographic patterning and adhesive bonding of the thick negative photoresist AZ 125 nXT", Proc. of SPIE, vol. 9517, 2015.
- [2] S. Koster, and E. Verpoorte, "A decade of microfluidic analysis coupled with electrospray mass spectroscopy mass spectrometer: an overview", Lab Chip, vol. 7, pp.1394-1412, 2007.
- [3] Z. L. Fang, and Q. Fang, "Development of low-cost microfluidic capillary-electrophoresis system coupled with flow-injection and sequential-injection sample introduction", Fresenius J. Anal. Chem., vol. 370, pp.978, 2001.

Size Characterization of Plasma Membrane Vesicles, Virus Particles, and Microvesicles

CNF Project Number: 2575-17

Principal Investigator: Susan Daniel

Users: Tiffany Tang, Lakshmi Nathan

Affiliation: Chemical and Biomolecular Engineering, Cornell University

Primary Source of Research Funding: National Science Foundation

Contact: sd386@cornell.edu, tt528@cornell.edu, LN258@cornell.edu

Primary CNF Tools Used: Nanosight

Abstract:

Nanosight was used to determine the concentration and size distribution of various biologically relevant particles, including viruses and plasma membrane vesicles.

Summary of Research:

Our research investigates interactions of biologically relevant particles (viruses, microvesicles, plasma membrane vesicles) on a supported lipid bilayer. Most of the particles used are generated in-house and as such, it is important to characterize them (diameter, size distribution, concentration of particles) to ensure that we are using the similar quality and concentration of particles across various experiments for consistency. The concentration is especially important as too much or too little of the plasma membrane vesicles used to form the supported lipid bilayer will influence the bilayer's diffusivity and patchiness. Typical sizes of viruses and plasma membrane vesicles that we use range from 100-200 nm and typical values of concentration are on the order of 10^8 particles/mL (for plasma membrane particles) and 10^{10} particles/mL for viruses.

After characterizing the particles, they are most often used to study the particle interaction on a supported lipid bilayer under total internal reflection fluorescence microscopy (TIRFM). TIRFM only excites fluorophores within 100 nm so we can distinguish between particles that are interacting with the bilayer versus particles that are in the bulk solution.

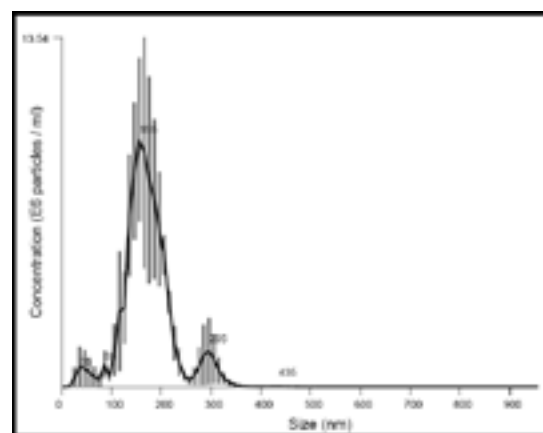


Figure 1: Concentration vs. size (nm) distribution plot for pseudotyped virus particles.

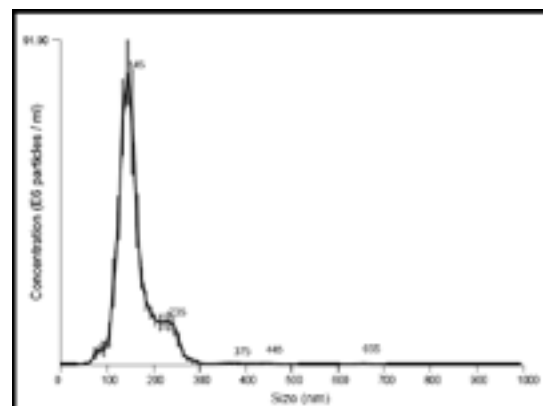


Figure 2: Concentration vs. size (nm) distribution plot for plasma membrane vesicles.

Hard Mask Fabrication from Block Copolymer Templates and Atomic Layer Deposition

CNF Fellows Project

Principal Investigators: Vince Genova³, Alan Bleier³

Users: Kyle Dorsey¹, Alex Ruyack²

Affiliation(s): 1. School of Applied and Engineering Physics, School of Electrical and Computer Engineering,
3. Cornell NanoScale Science and Technology Facility; Cornell University

Primary Source of Research Funding: National Science Foundation (Grant ECCS-1542081)

Contact: genova@cnf.cornell.edu, bleier@cnf.cornell.edu, kjd96@cornell.edu, arr68@cornell.edu

Primary CNF Tools Used: Oxford FlexAL ALD, Zeiss SEM, Oxford Cobra etcher, YES Asher

Abstract:

Block copolymer (BCP) lithography enables facile self-assembly of nanostructures at size scales inaccessible by optical lithography. We demonstrate tone-reversal and hard mask creation from BCP templates by utilizing the conformal nature of atomic layer deposition (ALD) of alumina. The alumina enables creation of hard masks that possess high etch selectivity. We demonstrate the utility of this process by fabricating high-aspect-ratio silicon nanowires with 30 nm lateral dimensions and 180 nm vertical dimensions.

Summary of Research:

Block copolymer (BCP) resists create nanoscale features through phase segregation of dissimilar polymer blocks. A variety of morphologies including pores, pillars, and lines have been demonstrated through choosing appropriate copolymer blends [1]. A challenge for the community is design of resists that possess high selectivity during etching and thermal processes. One approach is to incorporate silicon-containing compounds into the resist, such as polystyrene-polydimethylsiloxane (PS-PDMS) blends. Our approach, however, is to convert the resist pattern into a hard mask using conformal atomic layer deposition (ALD). This approach enables tone-reversal of substrate patterns and offers a broad palate of materials for the mask creation. The versatility of this approach enables device engineers to choose a hard mask with the desired etch properties.

The process flow for creating of hard masks from BCP templates is outlined in Figure 1. A BCP blend of polystyrene and poly-methylmethacrylate (PS-PMMA) is used as a template. The PS-PMMA ratio chosen produces a morphology of pores in the resist. Low-temperature ALD of alumina conformally coats the features and self-

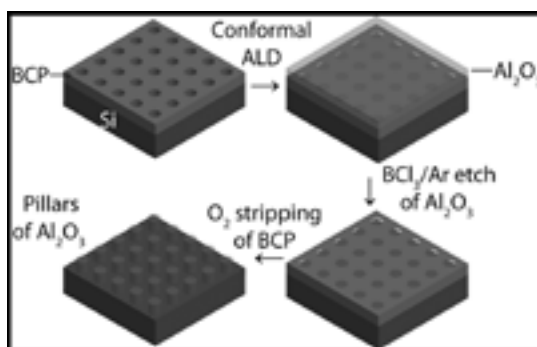


Figure 1: Process flow for hard mask creation from block copolymer templates.

planarizes by over-filling the pores. Directional etching of the over-filled alumina produces a pattern of alumina-filled pores in the BCP template. Finally, the BCP resist is stripped in a downstream oxygen plasma, leaving behind alumina pillars.

The process was characterized through visual inspection in the scanning electron microscope (SEM). Figure 2 (top) shows the formation of the pores in the BCP resist. Typical pore sizes

range between 25-30 nm. The total resist thickness is comparable to the pore size. The bottom micrograph in Figure 2 shows the wafer decorated with the remaining alumina pillars.

Optimization of the alumina etching time is essential to avoid eroding the mask. The results presented are 300 cycles of ALD alumina (nominal thickness 30 nm) and an alumina etching time of 1.5 minutes at 25 nm per minute. A slight over-etch guarantees that all of the over-filled alumina has been removed, while still remaining safely within the process window for the alumina pillar.

To demonstrate the utility and etch resistance of the alumina masks, we fabricate arrays of silicon nanowires

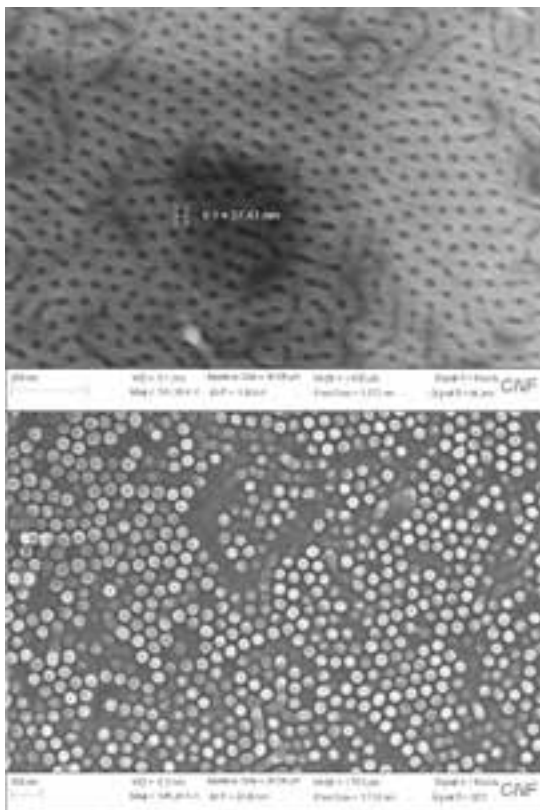


Figure 2: Scanning electron micrographs (SEMs) of the BCP tone reversal process.

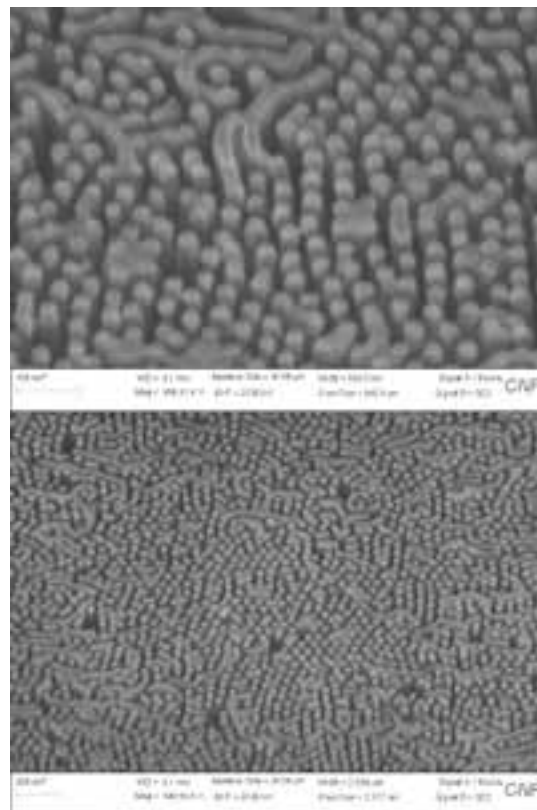


Figure 3: SEMs of high-aspect-ratio silicon nanowires fabricated from alumina masks.

by etching in an HBr/Ar plasma. Figure 3 shows successful fabrication of silicon nanowires with 30 nm diameters and heights approaching 180 nm. Pattern transfer is uniform across large areas, and is only limited by the defect density in the BCP resist. Many lithographic approaches toward vertical nanowire fabrication involve costly electron-beam lithography steps, while this approach is facile, versatile, and enables high aspect ratios. Optimization of the nanowire etch could further increase achievable aspect ratios in this system.

The ease of fabrication of silicon nanowires with high aspect ratios inspires device concepts and applications. The fabricated structures have dimensions and packing densities smaller than visible optical wavelengths. The

reflectance therefore approaches zero, as there are no smooth surfaces for reflection of light. Therefore, by doping the top layer of silicon, vertical $p-n$ junction solar cells can be fabricated that do not suffer from reflection losses.

References:

- [1] Jeong, Seong-Jun, Ju Young Kim, Bong Hoon Kim, Hyoung-Seok Moon, and Sang Ouk Kim. "Directed Self-Assembly of Block Copolymers for next Generation Nanolithography." *Materials Today* 16, no. 12 (December 1, 2013): 468-76. <https://doi.org/10.1016/j.mattod.2013.11.002>.

Photocurable Nanoimprint Lithography (P-NIL): An Enabling Technology for MEMS and Nanophotonics

CNF Fellows Project

Principal Investigator: Vincent J. Genova¹

User: Chengyu Liu^{1,2}

Affiliations: 1. Cornell NanoScale Facility, 2. School of Applied and Engineering Physics; Cornell University

Primary Source of Research Funding: National Science Foundation (Grant ECCS-1542081)

Contact: genova@cnf.cornell.edu, CL986@cornell.edu

Website: <https://confluence.cornell.edu/display/CNFUserWiki/UV+Nanoimprint+Process+using+mr-XNIL26+resist>

Primary CNF Tools Used: Nanoimprint NX-2500, MVD 100, Oxford 82 etcher,

Unaxis 770 deep Si etcher, Oxford Cobra ICP etcher, SEM

Abstract:

We evaluate a new photocurable imprint resist (mr-XNIL26) from Microresist Technology and develop a working photocurable nanoimprint process on various substrates using the Nanonex NX-2500 imprint tool.

Summary of Research:

Nanoimprint lithography (NIL) is an emerging technology that has the advantage of high throughput with sub-10 nm resolution. The resolution is largely governed by the feature dimensions of the master or template, which can be defined by advanced photolithography or electron beam lithography. NIL has been a strategic method on the ITRS roadmap for the 45 nm node and below. In addition to electronics, NIL can be a benefit to many applications including nanophotonics, biotechnology, displays, and microelectromechanical systems.

The Nanonex NX-2500 has both thermal imprint (T-NIL) and photocurable imprint (P-NIL) capabilities. The photocurable imprint module uses 200W narrow band UV lamp. A quartz template was fabricated by sputter depositing a blanket layer of chrome in which a bright and dark field line space pattern was defined with the ASML DUV (248 nm) stepper producing a minimum feature size of 250 nm. The lithographically defined pattern was then transferred into the chrome using $\text{Cl}_2/\text{O}_2/\text{Ar}$ mixed chemistry in the Trion inductively coupled plasma (ICP) tool. This etch produces smooth and perfectly anisotropic sidewall profiles, which are essential for optimum imprint replication. The chrome is used as a hard mask to etch the quartz substrate to a depth slightly less than the mr-XNIL26 resist thickness in the Oxford 80 reactive ion etching (RIE) tool using CF_4 . The chrome is then removed by immersing the substrate in liquid chrome etchant. The template is coated with FOTS in the molecular vapor deposition (MVD) system to prevent the adherence of the resist in the imprint process. The Microresist Technology P-NIL resist system evaluated

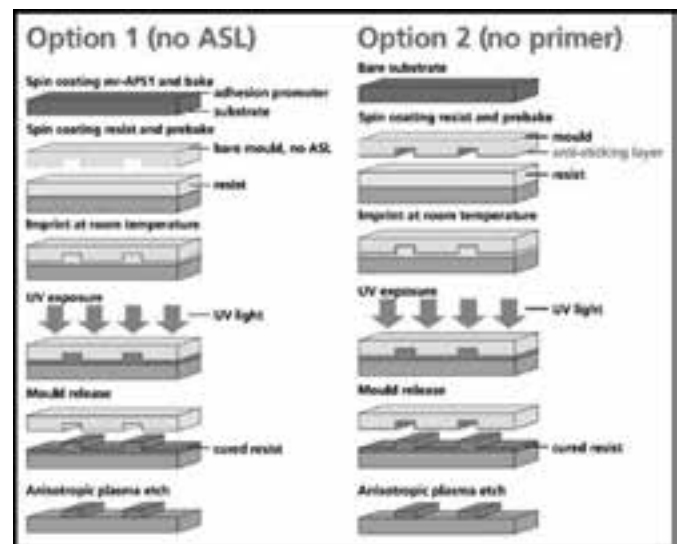


Figure 1: mr-XNIL26 P-NIL process overview from Microresist Technology.

was mr-XNIL26, which is a new fluorine-modified UV nanoimprint resist with advanced release properties. We applied the mr-XNIL26-300 nm to a silicon wafer along with Omnicoat as an adhesion promoter, although the adhesion promoter is not necessary. The imprint is performed at room temperature and at a pressure of only 10 psi which is low compared to a thermal imprint process. The UV cure time is 30 seconds. The single layer P-NIL process is illustrated in Figure 1 adopted from Microresist Technology.

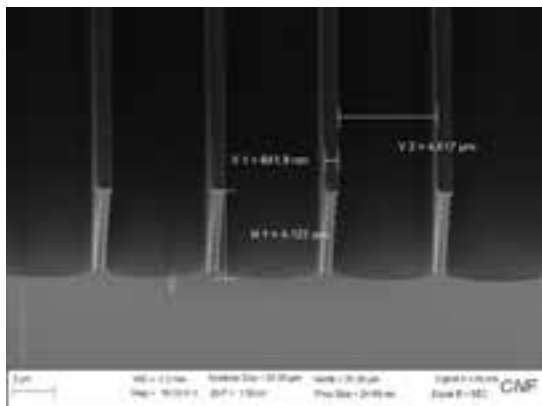


Figure 2: Bosch etch in Plasma-Therm SLR-770 of 600 nm features to an aspect ratio of 9:1.

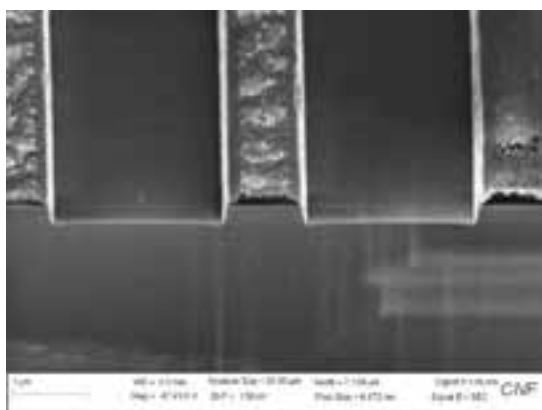


Figure 3: Oxford Cobra HBr silicon etch with a 4:1 selectivity of silicon to mr-XNIL26.



Figure 4: Silicon nitride etch using $\text{CH}_2\text{F}_2/\text{He}$ in Oxford 100 ICP.

We used option 1 where Omniccoat[®] was used as an adhesion layer in place of mr-APS1. Residual layer etching is performed in the Oxford Plasmalab 80 using oxygen at low pressure (15 mTorr) and low power (50W) to retain critical dimensions and minimize the loss of resist. The post-imprint residual thickness layer is largely dependent on pattern density and feature size. The imprinted silicon wafers were etched with the Bosch deep silicon etch and the mixed $\text{SF}_6/\text{C}_4\text{F}_8$ etch in the Plasma-Therm SLR ICP. An additional wafer was etched with HBr in the Oxford Cobra ICP. The Bosch etch is commonly used in the fabrication of MEMS devices, while the mixed etch and the HBr etch are used for nanophotonics based devices. The P-NIL process using mr-XNIL26 resist was also applied to a silicon nitride layer.

Pattern transfer into Si_3N_4 was accomplished in the Oxford Plasmalab 100 ICP using $\text{CH}_2\text{F}_2/\text{He}$ chemistry. This dielectric etch is used in the fabrication of oxide and nitride based nanophotonics devices here at CNF.

Figure 2 illustrates the results of the Bosch deep silicon etch for feature sizes of 600 nm etched to an aspect ratio of 9:1. The selectivity of silicon to the mr-XNIL26 resist is about 40:1, comparable to standard DUV and i-line photoresists. For the silicon etching with $\text{SF}_6/\text{C}_4\text{F}_8$ chemistry in the Plasma-Therm SLR-770, the selectivity of silicon to the mr-XNIL26 is 3:1, slightly less than standard DUV and i-line resists.

In Figure 3, we show the results of silicon etching in the Oxford Cobra ICP using HBr. Both the $\text{SF}_6/\text{C}_4\text{F}_8$ and the HBr etches produce highly anisotropic profiles with smooth sidewalls. Results of pattern transfer into silicon nitride using $\text{CH}_2\text{F}_2/\text{He}$ in the Oxford 100 ICP are shown in Figure 4. The $\text{CH}_2\text{F}_2/\text{He}$ chemistry is highly polymerizing and therefore highly selective with respect to imprint and conventional photoresists. The detailed process flow is posted on CNF user Wiki for reference.

In conclusion, we have evaluated a new photocurable imprint resist (mr-XNIL26) from Microresist Technology on our Nanonex NX-2500 imprint tool. This single layer resist system has been studied and the removal of residual resist has been optimized with proper plasma etch chemistry and parameters. We have then demonstrated effective pattern transfer into both silicon and silicon nitride using advanced ICP based reactive ion etching. We are currently working on combining e-beam lithography pattern and DUV pattern on one single template for imprint demonstration. We believe this process shows great potential in the fabrication of MEMS and photonics-based devices.

PS-PMMA Block Copolymer Lithography for Sub-25 nm Periodic Features

CNF Fellows Project

Principal Investigators: Vincent Genova, Alan Bleier

User: Alexander Ruyack

*Affiliations: Electrical and Computer Engineering, Cornell NanoScale Science and Technology Facility; Cornell University
Primary Source of Research Funding: National Science Foundation (Grant ECCS-1542081)*

Contact: genova@cnf.cornell.edu, bleier@cnf.cornell.edu, arr68@cornell.edu

Website: <https://confluence.cornell.edu/display/CNFUserWiki/Block+Copolymer+Resist>

Primary CNF Tools Used: ABM contact aligner, Oxford 80s, PT72, ULTRA/SUPRA scanning electron microscope (SEM), Hummer Au/Pd sputtering system, PMMA spinners, vacuum ovens, wet chemistry

Abstract:

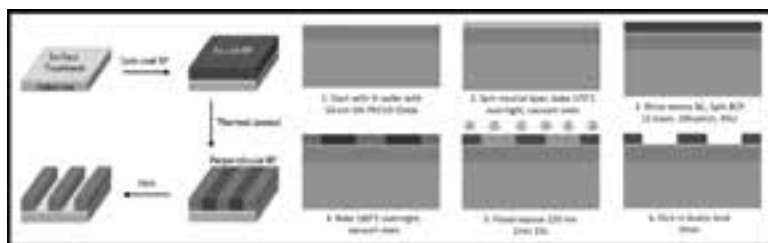
Nanolithography is a fundamental requirement for the future of electronics patterning. Current trends indicate the end of Moore's Law for traditional lithography processes. Directed self-assembly (DSA) of block copolymers (BCPs) can generate ordered, periodic arrays of various structures down to single nanometer (nm) size scale. The heterogeneous nature of these structures acts intrinsically as their own mask, enabling nm scale resolution with a flood exposure and no traditional photo mask. BCP lithography offers low-cost processing of nm scale periodic structures typically only available by e-beam lithography and can act as a complementary technology to conventional photolithography. In this work, we develop a PS-*b*-PMMA BCP lithography process on SiO₂/silicon using CNF labs and tools, achieving ~ 20 nm pattern resolution.

Summary of Research:

BCP lithography relies on the microphase separation of the two comprising polymers to achieve a nanoscale pattern. Due to the reliance on self-assembly, the resulting photolithographic features are intrinsically periodic. As such, this process is useful for applications in areas where long range repeating structures are needed, such as nano-porous substrates, nanoparticle synthesis, or high-density information storage media.

For the development of this method, we used a poly(styrene-*block*-methyl methacrylate) (PS-*b*-PMMA) block copolymer due to its popularity in literature, which stems from its excellent etch selectivity, low surface energy mismatch, and theoretical 12 nm feature size.

The typical fabrication flow for a BCP lithographic process is shown in Figure 1 (left) (adapted from [1]). First, a surface treatment is applied to create a neutral layer/brush. This prevents a surface parallel BCP domain orientation from occurring by making the substrate surface interfacial energy equal for both polymer phases. Next, the BCP is spin-coated and then thermally annealed allowing for phase separation and formation of the pattern. Finally, one phase is selectively removed, and subsequent substrate processing can occur from this point.



feature sizes and 2) evaluating inter-feature spacing. In our case, the BCP morphology is a hexagonal array of pores, so these methods were tuned to generate information on pore diameter and interpore spacing. The former was accomplished using built in ImageJ functions and the Particle Analysis tool. The latter is comprised of built in ImageJ functions along with an additional macro for K-Nearest Neighbor analysis that was expanded on from an existing implementation, as well as a custom Matlab script [3]. Again, the CNF Wiki Article has more detailed information and output examples of this image analysis.

Through this system of evaluation, we were able to achieve BCP films of 30 nm thickness with long range order. Pore sizes of ~ 23.12 nm with 1.78 nm standard deviation and interpore spacing of ~ 54.26 nm with 7.33 nm standard deviation and a circularity of ~ 0.92 were obtained. Figure 3 shows example SEM images of a typical sample. Using these films, pattern transfer through 50 to 100 nm of oxide has been achieved, as well as a subsequent Si etch (Figure 4).

In the future, we are working on various path forwards for BCP lithography implementation at the CNF. One path is further process tuning to reduce defects in the film and improve uniformity and periodicity. Beyond this, we are also looking into additional processing steps required to alter the BCP film morphology. We are working on a graphoepitaxy process that will result in parallelly aligned domains, rather than pores. Finally, we are also investigating other BCP systems for smaller features sizes (< 10 nm), such as PS-*b*-PDMS.

References:

- [1] C.M. Bates, et al., Block Copolymer Lithography, *Macromolecules*, 2014, 47 (1), pp 1-12.
- [2] Block Copolymer Resists, CNF User Wiki, Alexander Ruyack, <https://confluence.cornell.edu/display/CNFUserWiki/Block+Copolymer+Resists>.
- [3] Burri, Olivier, 2D K Nearest Neighbors Python script, GitHub repository, <https://gist.github.com/lacan/2643f2ce7e33d1bb07adafde9ff94101> (2017).

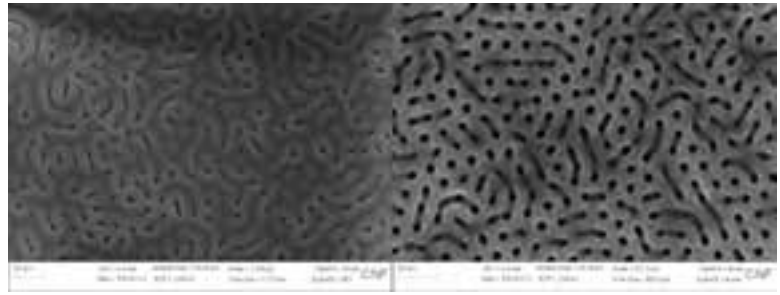


Figure 2: SEM micrographs of BCP film. Left: after annealing. Right: after etching. The increase in contrast comes from the removal of the PMMA phase in the pore regions after the etch.

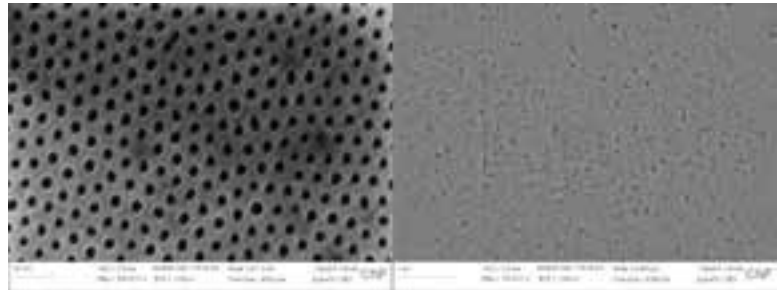


Figure 3: SEM micrographs of optimized BCP film. Left: 350kx magnification showing pore diameter and interpore spacing uniformity. Right: 50kx magnification showing long range order.

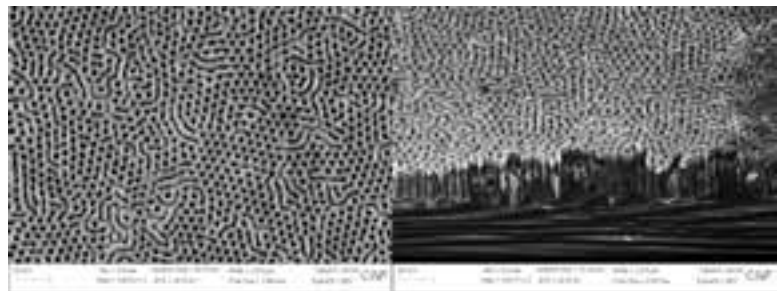


Figure 4: SEM micrograph of BCP on 50 nm of SiO₂ on Si after CH₂F₂/He and HBr/Ar etch. Left: Top down. Right: Cleaved, 45 degrees.

Index of Reports by CNF Project Number

2018 CNF REU Program Interns	1940-10	2458-16
..... 2, 64, 96, 176, 178 26 166
CNF Fellows Program	1970-10	2460-16
..... 228, 230, 232 28 44
111-80.....	1997-11	2461-16
..... 180, 182 148, 150, 152 46
150-82	2065-11	2465-16
..... 98, 100 30 224
386-90	2091-11	2470-16
..... 102, 104 200, 202 88
522-94	2123-12	2471-16
..... 106 138 168
598-96	2125-12	2472-16
..... 184, 186 74 48, 170
692-98	2126-12	2474-16
..... 4 204, 206 146
731-98	2172-12	2486-16
..... 6 154 122
762-99	2173-12	2498-16
..... 8 208 50
848-00	2214-13	2499-16
..... 10 32 172
863-00	2217-13	2502-16
..... 66 216 52
900-00	2249-13	2504-16
..... 12, 14, 108, 122, 132, 134, 188 34 54
1119-03.....	2255-13	2509-16
..... 190 156 90
1239-04	2260-13	2514-16
..... 68 36 214
1255-04	2262-13	2527-17
..... 16 38 174
1262-04	2292-14	2528-17
..... 136 158 124
1314-05	2307-14	2543-17
..... 192 218 92
1356-05	2324-15	2562-17
..... 110 80 126
1371-05	2350-15	2574-17
..... 70 82 56
1520-07	2361-15	2575-17
..... 194 210 226
1645-08	2364-15	2578-17
..... 112, 114 40, 160 94
1735-08	2369-15	2589-17
..... 196 212 58
1738-08	2385-15	2603-17
..... 18 140 128
1757-09	2387-15	2632-18
..... 20, 116 162 130
1872-10	2406-15	2636-18
..... 22, 24 164 60
1873-10	2407-15	2641-18
..... 198 118 62
1936-10	2416-16	2642-18
..... 72 142 30
	2430-16	2673-18
 42 78
	2443-16	
 84, 86, 120, 220, 222	• • •
	2446-16	
 144	
	2447-16	
 76	

Index of Reports by CNF Principal Investigators & Users

A

Abbaspourrad, Alireza ..	52
Abe, Mahiro ..	166
Abrahamsson, Sara ..	158
Agyeman-Budu, David..	154
Alden, Jonathan ..	122
Alden, Joshua S..	122
Alibakhshi, Mohammad Amin ..	32
Allen, Leslie H.	106
Alpha, Christopher.	96, 172
Anil, Vivek... ..	2
Archer, Lynden A....	76
Armbruster, Richard ..	30
Arya, Faraz Khalil... ..	146

B

Bader, Samuel..	88
Baker, Shefford ..	130
Balachandran, Vaishali..	30
Balakrishnan, Vasanth... ..	220
Ballard, Andrew..	198
Bargmann, Cori ...	158
Bartell, Jason ..	202
Beentjes, Ivan ..	118
Bender, Jay ...	118
Bharadwaj, Shyam..	162

Bircan, Baris ..	132, 134, 142
Bleier, Alan ..	228, 232
Boucher, Michael ..	74
Brock, Joel ..	154
Buhrman, Robert A.	180, 182

C

Calderon, Brian ...	124
Capasso, Federico ..	168
Chang, You-Chia .	160
Chaudhuri, Reet..	88
Chen, Huiyao... ..	204
Chen, Peng... ..	78
Chen, Wei-Liang .	20, 116
Clark, Jeremy... ..	172
Cohen, Itai ..	132, 134, 142, 188
Cordero, Roselynn..	20
Cortese, Alejandro..	12, 14, 94, 122, 134
Cosgrove, Benjamin D... ..	46
Cothard, Nicholas... ..	166
Craighead, Harold G..	6, 8
Crouse, David..	174
Cruz Garza, Tanya ..	216
Cui, Weili..	212

D

Daly, Brian C... ..212
Daniel, Susan .. 62, 226
Daveau, Raphael.206
De Micheli, Andrea J. 46
DeAlba, Roberto.194
Deng, Yue 76
Dichtel, William R..108
Dickensheets, David L... ..164
Dodge, Kenneth..192
Dorsey, Kyle.132, 134, 228
Dutta Gupta, Shourya 48

E

Encomendero, Jimy 84
Engstrom, James R..64, 68
Erickson, David... 22, 24, 60
Esposito, Edward132, 134, 142

F

Fang, Qinghua. 10
Fontes, Ernie154
Frey, Brian208
Frey, Margaret..128
Fuchs, Gregory D.... ..200, 202, 204, 206

G

Gao, Guoying 70
Gao, Hui 14, 188
Genova, Vincent J... ..228 , 230, 232
Gillilan, Richard E.. 26
Gingerich, Marcus.. 54
Gray, Isaiah200, 202
Guimarães, Marcos H.D.... .. 14
Guisado, Gabriel 28
Gupta, Manish138
Gupta, Vishakha.184
Guyon, Olivier172

H

Hanrath, Tobias... ..112, 114
Harper, Christine E. 28
He, Yang150
Hernandez, Christopher J. 28
Herzog, Walter. 16
Hickman, Austin. 88
Hoffmann, Roald 70
Hopkins, Jesse. 26
Howard-Jennings, Jordan Phillip 96
Howington, Caleb196
Hsu, Jui-Yuan... ..218
Hu, Qinan. 58
Hu, Zongyang..218, 222
Huang, Jen-Yu112
Huang, Meng... ..36, 44
Huang, Steven He... ..2
Hwang, James C.M. 90

I

Indrajeet196

J

Jadhav, Vivek... .. 32
 Jarjour, Alexander... ..214
 Jena, Debdeep
 82, 86, 88, 120, 126, 162, 218, 220, 222
 Ji, Xingchen.. ... 40, 160
 Ji, Yanxin... .. 12
 Jimenez Gordillo, Oscar A.... ..160
 Jovanovic, Nemanja172
 Jung, Seok-Heon. 96
 Jungwirth, Nicholas R.206

K

Kaiser, Alex..208
 Kang, Kibum 14, 188
 Kelp, Glen 48
 Kennedy, Brian124
 Kidd, Philip158
 Kirby, Brian..140
 Knight, Justin172
 Kosma, Vasiliki... ..102
 Ku, Jaseung..198
 Kymissis, Ioannis216

L

Lal, Amit... ..136
 Lammerding, Jan 30
 LaValley, Danielle... ..6
 Lee, Hyunjea 80
 Lee, Kevin162
 Lee, Sunwoo 94
 Leonard, Timothy 16
 Lepak, Lori42, 50
 Li, Lei 90
 Li, Mingxiao.148
 Li, Ruofan.184
 Li, Wenshen218, 222
 Li, Xiang 80
 Liang, Hanxiao148
 Lin, Qiang148, 150, 152
 Lin, Shawn-Yu.208
 Lindau, Manfred. 10, 36, 44
 Lipson, Michal 40, 160
 Liu, Chengyu... ..156, 230
 Liu, Tianbo... ..164
 Liu, Xin 44
 Liu, Yebin198
 Lozi, Julien... ..172
 Lu, Hanwen..178, 190
 Lu, Junlan. 48
 Luo, Rui150

M

Ma, Minglin.	34
Ma, Tianyu	142
Macquarrie, Evan R.	204
Manzer, Zachary..	62
Marohn, John A...	66, 74
Maroo, Shalabh C...	138
Mathur, Nikhil	206
McEuen, Paul L.	12, 14, 108, 122, 132, 134, 142, 176, 188
McGill, Kathryn L.	188
Mea, Toby.	224
Miles, Ronald N..	144
Miller, Paula	6
Miller, Steven A.	160
Mirbagheri, Golsa	174
Miskin, Marc	134, 142, 188
Mohanty, Aseema	160
Molnar, Alyosha C..	94

N

Nair, Hari..	186
Najafi, Mesbah	128
Nathan, Lakshmi	226
Nelson, JJ..	192, 196
Nomoto, Kazuki..	86, 218, 222
Norris, Samantha	12
Nowack, Katja.	210, 214

O

Ober, Christopher Kemper	20, 96, 102, 104, 114, 116
Oeschger, Taylor..	60
Ozdogan, Mehmet..	144

P

Page, Ryan	126
Pajoumshariati, Seyedramin	52
Park, Jisung..	92
Park, Jiwoong..	14, 188
Parpia, Jeevak M.	194
Paszek, Matthew.	56
Pearson, Tanner... ..	132, 176
Peles, Yoav	146
Petersen, Poul B.	72
Phare, Christopher T.	160
Plourde, Britton L.T.... ..	192, 196, 198
Plumridge, Alexander	4
Polhemus, Katherine..	140
Pollack, Lois.	4
Preble, Stefan	224

Q

Quinn, Katherine K.... ..	98
---------------------------	----

R

Ralph, Daniel 14, 184, 186
Rey, Elizabeth.. ... 22
Reynolds, Michael F.. ... 14, 134, 188
Reynolds, Neal186
Roberts, LaDeidra Monét.. ... 56
Roberts, Melanie F. 28
Roberts, Samantha P..160
Rogers, Steven.152
Rouse, Zachary130
Russell, Sierra..176
Ruyack, Alexander136, 228, 232

Song, Wei.. 34
Stacey, Gordon166
Stern, Brian160
Stiehl, Gregory184, 200
Stroock, Abraham... ..178, 190
Suh, Taewon64, 68
Suh, Young Joon.. 38
Sun, Chao108
Sun, Peter (Hanyu) 66
Sun, Xiangcheng 78
Suntivich, Jin... ..156

S

Sakai, Kazunori... .. 96, 102
Sanders, Stephanie. 72
Sawatsky, Andrew.. 16
Schaefer, Brian T.210
Schlom, Darrell... .. 92, 186
Scholtz, Juliane M.100
Schreiber, Nathaniel186
Sebastian, Abhilash Thanniyil194
Senatore, Michael... ..198
Shcherbakov, Maxim..2, 170
She, Alan168
Shi, Shengjie180
Shin, Jae Ho 82
Shin, Min Chul160
Shire, Douglas. 54
Shuler, Michael L.... ..6
Shvets, Gennady. 2, 48, 170
Singh, Ankur... .. 60

T

Tanen, Nicholas... ..220
Tang, Tiffany226
Tapping, Ryan182
Tester, Jefferson W.118
Thompson, Michael O... .. 98, 100
Tian, Harvey C.8
Towfighian, Shahrzad144
Treichler, John172
Tung, Chih-kuan. 58
Turgut, Emrah..202

V

Vemulapati, Sasank 24
Vetter, Kenny166

W

Wan, Jiandi...	..224
Wang, Maritha.188
Wang, Michelle D...	18
Wang, Ying...	..6
Wang, Zihao.224
Wanunu, Meni.	32
Whisnant, Kody178
Wiesner, Ulrich110
Windsor, Aaron ...	30
Wolfner, Mariana ...	58
Woll, Arthur.154
Wong, Patricia..	54
Wright, John.120
Wu, Anni...218
Wu, Dung-Yi114
Wu, Mingming ...	38

X

Xing, Huili Grace 80, 82, 84, 86, 88, 120, 218, 220, 222	
Xiong, Kuanchen ...	90
Xu, Helen..132
Xu, Hong...102

Y

Yalisove, Reed	64
Yang, Kou104
Ye, Fan... ..	18
Ye, Zichao106
Yin, Rose... ..	56
Yu, Fei110

Z

Zadka, Moshe..160
Zhang, Qi..110
Zhang, Shuyan168
Zhang, Yi (Johnny)100
Zhao, Ying	10
Zhelev, Nikolay...194
Zou, An.138

*The 2017-2018 CNF Research Accomplishments are also available on the web:
http://www.cnf.cornell.edu/cnf_2018cnfra.html*



0510-2844-2000